HOKKAIDO UNIVERSITY

Title	Observational Studies on Physical Properties of Molecular Gas in Nearby Galaxies
Author(s)	矢島, 義之
Degree Grantor	北海道大学
Degree Name	博士(理学)
Dissertation Number	甲第14787号
Issue Date	2022-03-24
DOI	https://doi.org/10.14943/doctoral.k14787
Doc URL	https://hdl.handle.net/2115/85889
Type	doctoral thesis
File Information	Yoshiyuki_Yajima.pdf

Hokkaido University Collection of Scholarly and Academic Papers : HUSCAP

Doctoral Dissertation

Observational Studies on Physical Properties of Molecular Gas in Nearby Galaxies

(近傍銀河における分子ガスの物理状態に関する観測的研究)

Yoshiyuki Yajima

矢島 義之

Observational Astronomy Laboratory
Department of Cosmosciences
Graduate School of Science
Hokkaido University

March, 2022

Abstract

The universe has been evolving as stars form and star formation is a main physical process in galaxies. Stars form from cold and dense molecular gas which can be traced by emission lines from rotational transitions of molecules in interstellar medium including carbon monoxide (CO). Therefore, to investigate physical properties of molecular gas and their relationships to star formation activity is crucial to understand evolution of galaxies and the universe. This dissertation addresses the four observational studies on molecular gas properties in nearby galaxies. Outlines of each study are as follows.

Variations of ^{12}CO($J=2$–1)/^{12}CO($J=1$–0) line ratio in nearby galaxies on kiloparsec scales (Yajima et al. 2021; chapter 2)

Since the raw material of stars is cold molecular gas, it is necessary to make use of lines in low-energy transitions. For this reason, molecular gas is usually observed using ^{12}CO($J=1$–0). However, recent studies often observe ^{12}CO($J=2$–1) as a molecular gas tracer because of its high observation efficiency and derived molecular gas mass from ^{12}CO($J=2$–1) integrated intensity by assuming ^{12}CO($J=2$–1)/^{12}CO($J=1$–0) line ratio $R_{2/1}$ is a constant. Hence, we study variations of $R_{2/1}$ for 24 nearby galaxies using the data by single-dish telescopes. We found that $R_{2/1}$ is largely different within and across galaxies. Accordingly, total molecular gas mass and its surface density are misled when they are derived from ^{12}CO($J=2$–1) with a fixed $R_{2/1}$. Moreover, the Kennicutt–Schmidt relation, which is a fundamental relation between star formation and molecular gas, by ^{12}CO($J=2$–1) becomes shallower than that by ^{12}CO($J=1$–0) in many galaxies. We also found that $R_{2/1}$ is correlated with star formation activity and a main physical driver to change $R_{2/1}$ is kinetic temperature $T_{\rm kin}$ of molecular gas.

Dynamical effect on molecular gas and star formation in barred spiral galaxies (Yajima et al. 2019 and its extended study; chapter 3)

Barred spiral galaxies often show lower star formation activity in their bars than that in other galactic regions, while molecular gas is rich there. In addition, strong gas dynamics in bars is inferred from both observational and theoretical studies. It is expected that molecular gas is influenced by gas dynamics and it is difficult to form stars for such molecular gas. Hence, we tried to derive number density of molecular gas $n(\rm H_2)$ in galactic regions of the barred spiral galaxy NGC 4303. $n(\rm H_2)$ is estimated from ^{12}CO($J=1$–0) and ^{13}CO($J=1$–0) data with the non-local thermodynamic equilibrium (LTE) analysis by fixing $T_{\rm kin}$. We found the positive correlation between regionally averaged star-formation efficiency (SFE) and $n(\rm H_2)$. Moreover, comparing $n(\rm H_2)$ to large-scale molecular gas velocity dispersion, we discover the increasing tendency of $n(\rm H_2)$ with velocity dispersion in the moderate dispersion range changes the decreasing tendency when velocity dispersion is too large. Furthermore, we added sample barred spiral galaxies NGC 2903 and NGC 3627 and derived $n(\rm H_2)$ without assuming $T_{\rm kin}$ by adding archival ^{12}CO($J=3$–2) data for the multi-line analysis. The positive correlation between SFE and $n(\rm H_2)$ remains, however, its scatter becomes large due to differences in the relation among the galaxies. In contrast, most regions of the galaxies tightly follow the $n(\rm H_2)$–velocity dispersion relation. It would be a universal relationship. We also discuss the thermodynamic equilibrium between molecular gas and interstellar dust and the timescale to reach the equilibrium from derived $T_{\rm kin}$ of molecular gas and dust temperature by color of infrared.

Key factor in molecular gas properties and star formation by decomposition of CO emission in Maffei 2 (Yajima and Sorai 2022; chapter 4)

Previous studies indicate that molecular gas exists in an extended, diffuse form as well as cloud-like structures known as molecular clouds. As a cause of different SFE in galaxies, this hierarchical structure of molecular gas is suggested. Molecular gas can be decomposed into the cloud component and the diffuse component using the ^{13}CO line owing to its low optical depth. Therefore, we conduct the new,

high sensitivity, and simultaneous observation of ^{12}CO($J=1$–0) and ^{13}CO($J=1$–0) toward the barred spiral galaxy Maffei 2 with the Nobeyama 45 m Telescope to investigate effects of the cloud/diffuse component fraction in molecular gas properties and star formation. ^{12}CO($J=1$–0) emission in each voxel is decomposed into the two components based on the detection of ^{13}CO($J=1$–0) at the same position and velocity. Integrated intensity ratios of ^{13}CO-detected-^{12}CO to total ^{12}CO, $R_{12(13\mathrm{det})/12}$, and ^{13}CO-detected-^{12}CO to ^{13}CO, $R_{12(13\mathrm{det})/13}$ are derived as well as the ratio of total ^{12}CO to ^{13}CO $R_{12/13}$. We found that $R_{12(13\mathrm{det})/12}$ significantly varies within the galaxy. In contrast, $R_{12(13\mathrm{det})/13}$ is almost constant in the galaxy. These results indicate that fraction of the cloud (diffuse) component of molecular gas reflected by $R_{12(13\mathrm{det})/12}$ is an effective factor to characterize properties of molecular gas and properties of the cloud component inferred from $R_{12(13\mathrm{det})/13}$ is not so different depending on galactic environments. Moreover, we found that SFE differences among galactic environments decreases when SFE is derived from ^{13}CO-detected-^{12}CO and ^{13}CO. Namely, SFE is close to a constant if the component of molecular gas which is difficult to participate in star formation is removed.

Properties of giant molecular clouds and molecular gas in the starburst galaxy NGC 1808 (chapter 5)

Since stars form in deep and dense parts in giant molecular clouds (GMCs), to reveal properties of them and their dependence on galactic environments are important. Previous studies find the similar scaling relations and properties of GMCs in the Galaxy and galaxies in the local universe including the Local Group. These results suggest that GMCs are rather uniform objects across galaxies. However, GMCs found in more extreme environments such as centers of starburst galaxies deviate from those found in normal star-forming or quiescent galaxies. Accordingly, we investigate GMC properties using the ^{12}CO($J=1$–0) data obtained with the Atacama Large Millimeter/submillimeter Array (ALMA) for the starburst barred spiral galaxy NGC 1808. We found the fraction of missing flux increases toward the center in the bar. It suggests that GMCs are shredded or converted into small clouds due to strong shear and velocity gradient along the bar. We identify GMCs with a clump finding algorithm and derive their representative properties. Virial parameter of GMCs in the bar is significantly higher than those in arms. Moreover, we can trace the evolutionary sequence of GMCs that it is difficult for them to contribute to star formation as falling along the bar and in the upstream of the central ring, whereas GMCs rapidly glow up, are compressed, and become gravitationally unbound in the downstream of the ring and the nucleus. It is perhaps a cause of starburst in the center of NGC 1808.

Contents

1 Introduction **1**

1.1 Interstellar medium . . . 1
1.2 Galaxies . . . 6
1.2.1 Morphology of galaxies . . . 6
1.2.2 Properties of galaxies . . . 8
1.3 Star formation in galaxies . . . 11
1.3.1 How to estimate activeness of star formation . . . 11
1.3.2 Kennicutt–Schmidt relation . . . 14
1.3.3 Star formation seen in barred spiral galaxies . . . 19
1.4 Physical processes of radiation from molecules and atoms in interstellar medium 24
1.4.1 Energy levels of rotational transition of molecules . . . 25
1.4.2 Emission of rotational transitions as an electric dipole radiation . . . 26
1.4.3 Emission by fine structure and hyperfine structure . . . 29
1.5 Molecular clouds . . . 29
1.5.1 Basic view of molecular clouds . . . 29
1.5.2 Fundamental relations for molecular clouds . . . 31
1.5.3 CO-to-H_2 conversion factor to derive molecular gas mass . . . 33
1.5.4 Quantities and parameters to characterize properties of molecular clouds . 37
1.6 Investigation for properties of molecular gas . . . 45
1.6.1 Probability of transitions; Einstein's coefficients and collisional rates . . . 45
1.6.2 Critical density and multiple emissions line as probes of different molecular gas properties . . . 46
1.6.3 Non-local thermodynamic equilibrium analysis and critical density considering photon trapping . . . 49
1.7 Aim of this dissertation . . . 53

2 ^{12}CO($J=2$–1)/^{12}CO($J=1$–0) line ratio in nearby galaxies on kiloparsec scales **62**

2.1 Abstract of this chapter . . . 62
2.2 Backgrounds of ^{12}CO($J=2$–1)/^{12}CO($J=1$–0) . . . 62
2.3 Data sets . . . 65
2.3.1 CO data and their analysis . . . 65
2.3.2 Intensity accuracy of CO data regarding calibration and pointing error . . . 67
2.3.3 Data in other wavelengths . . . 68
2.4 Results . . . 68

2.4.1 Maps, histograms, statistics, and radial distribution of $R_{2/1}$ . . . 68
2.4.2 Effects of $R_{2/1}$ on molecular gas mass derived from ^{12}CO($J=2$–1) . . . 75
2.4.3 Effects of $R_{2/1}$ on the Kennicutt–Schmidt relation derived from ^{12}CO($J=2$–1) . . . 78
2.5 Discussion . . . 80
2.5.1 Correlations of $R_{2/1}$ with basic properties of galaxies . . . 80
2.5.2 $R_{2/1}$ and ^{12}CO($J=1$–0)/^{13}CO($J=1$–0) ratio . . . 84
2.5.3 Non-LTE analysis using $R_{2/1}$ . . . 88
2.6 Summary of this chapter . . . 97
2.7 Appendix A: Histograms of $R_{2/1}$ in each galaxy . . . 98
2.8 Appendix B: Results of stacked spectra . . . 98

3 Dynamical effect on molecular gas and star formation in barred galaxies 104
3.1 Abstract of this chapter . . . 104
3.2 Backgrounds of molecular gas and star formation in barred galaxies . . . 104
3.3 Observations and data reduction . . . 106
3.4 Results . . . 108
3.4.1 CO emission lines . . . 108
3.4.2 Star-formation rate and efficiency . . . 108
3.4.3 Regionally averaged quantities in each galactic structure . . . 109
3.5 Discussion . . . 114
3.5.1 What $R_{12/13}$ physically means . . . 114
3.5.2 Derivation of molecular gas density via non-LTE analysis . . . 115
3.5.3 The cause of SFE and molecular gas density variations . . . 120
3.6 Discussion 2 — physical properties of molecular gas with three lines in three barred spiral galaxies . . . 123
3.6.1 Relation of SFE and $n(H_2)$, and dynamically influenced $n(H_2)$ in barred spiral galaxies . . . 128
3.6.2 Temperature of molecular gas and dust . . . 130
3.7 Summary of this chapter . . . 133

4 Key factor in molecular gas properties and star formation by decomposition of CO emission in Maffei 2 135
4.1 Abstract of this chapter . . . 135
4.2 Background of this study . . . 135
4.3 Observation and data reduction . . . 140
4.3.1 Observation settings . . . 140
4.3.2 Intensity calibration . . . 143
4.3.3 Data reduction . . . 152
4.4 Results . . . 154
4.4.1 Extraction of Galactic emission . . . 156
4.4.2 Results of Galactic removal . . . 160
4.4.3 Decomposition of ^{12}CO emission using that of ^{13}CO . . . 163
4.5 Discussion . . . 166

4.5.1 Line ratios for decomposed ^{12}CO emission and comparison with the conventional line ratio . . . 166
4.5.2 Deviations of line ratios from each mean . . . 170
4.5.3 Statistical difference of the line ratios among galactic structures . . . 172
4.5.4 Effects of the cloud-component fraction on star formation . . . 177
4.5.5 Implications . . . 179
4.6 Summary of this chapter . . . 181

5 Properties of giant molecular clouds in the starburst galaxy NGC 1808 184
5.1 Abstract of this chapter . . . 184
5.2 Background of this study . . . 184
5.3 Data and its reduction . . . 185
5.4 Results . . . 189
5.5 Discussion and summary . . . 190
5.5.1 Missing flux of the 12 m array . . . 190
5.5.2 Dependence of GMC properties on environments . . . 191

6 Conclusions of this dissertation 197

Acknowledgment 201

Bibliography 202

List of Figures

1.1 Schematic view of stellar lifecycle. . . . 2
1.2 Baryon budget in the Galaxy. . . . 3
1.3 Mass composition of the Galaxy. . . . 3
1.4 Phase diagram of interstellar medium. . . . 4
1.5 Cosmic star-formation history. . . . 5
1.6 Morphology classification based on Hubble sequence known as "Hubble's tuning fork diagram". . . . 6
1.7 Advanced morphology classification of galaxies suggested by de Vaucouleurs (1959). 7
1.8 A cut section of the body shown in figure 1.7 and representative galactic morphologies. . . . 8
1.9 Color-magnitude diagram for local galaxies. . . . 9
1.10 Basic properties of galaxies along the Hubble sequence. . . . 10
1.11 Gas fraction and molecular-atomic gas fraction along the Hubble sequence. . . . 11
1.12 Molecular gas mass fraction as a function of stellar mass in each Hubble type. . . 12
1.13 Dependence of star-formation rate to shear strength and the Hubble sequence. . 13
1.14 Core mass function and representative initial mass functions. . . . 14
1.15 The global Kennicutt–Schmidt relation for various types of local galaxies. . . . 15
1.16 The Kennicutt–Schmidt relation for local and high-z galaxies. . . . 16
1.17 Dependence of the Kennicutt–Schmidt relation on spatial resolution of data. . . . 17
1.18 The Kennicutt–Schmidt relation using dense molecular gas. . . . 18
1.19 The Kennicutt–Schmidt relation from various emission lines. . . . 18
1.20 Indices of the Kennicutt–Schmidt relation as a function of ^{12}CO rotational transitions. . . . 19
1.21 Distribution of molecular gas surface density in NGC 4303. . . . 20
1.22 Distribution of SFR surface density in NGC 4303. . . . 20
1.23 Composite image of optical, near IR, and emission lines of ions for NGC 4303 obtained with HST and MUSE on VLT. . . . 21
1.24 The spatially resolved Kennicutt–Schmidt relation in NGC 4303 and differences between galactic regions. . . . 22
1.25 Direction of gas motion in a bar. . . . 22
1.26 The schematic view of gas flows in the bar of NGC 1530. . . . 23
1.27 Schematic view of dense gas formation which leads to active star formation in the bar end of the Galaxy. . . . 24
1.28 Energy levels of rotational transitions for ^{12}CO and H_2. . . . 26
1.29 Energy levels and corresponding wavelength of C I. . . . 28

1.30 Distribution of ^{12}CO($J=1$–0) integrated intensity in the all area of the Galaxy. . 30
1.31 Distribution of ^{12}CO($J=2$–1) peak intensity in nearby galaxies at high resolution. 30
1.32 Dependence of distribution of giant molecular clouds on their mass in spiral galaxy M 51. 31
1.33 The relation between size and line width of molecular clouds in the Galaxy. . . . 32
1.34 The relation between virial mass and luminosity of molecular clouds in the Galaxy. 32
1.35 The relation between size and line width of molecular clouds found in the Galaxy and nearby galaxies. 34
1.36 The relation between virial mass and ^{12}CO luminosity for GMCs in the Galaxy and nearby galaxies. 35
1.37 Dependency of range of CO, C, C^+, and H_2 within a molecular clouds on metallicity and its size. 36
1.38 Dependency of α_{CO} on metallicity. 36
1.39 Proposed unified α_{CO} from normal Milky Way-like galaxies to ultra luminous infrared galaxies. 37
1.40 Relations between virial parameter and other properties of GMCs with and without H II found in IC 342. 38
1.41 Probability distribution functions of mean gas divergence and the relation between virial parameter and mean gas divergence with and without H II regions. 39
1.42 Relation between dimensionless star-formation efficiency and virial parameter for some example molecular clouds. 40
1.43 Star-formation efficiency per free-fall time across nearby galaxies. 40
1.44 Properties of giant molecular clouds in galactic regions of the spiral galaxy M 51. 41
1.45 The continuation of figure 1.44. 42
1.46 Properties of giant molecular clouds in representative regions of the barred spiral galaxy NGC 1300. 44
1.47 Transitions between energy levels J and $J+1$ by spontaneous emission, stimulated emission, absorption, and collisions. 46
1.48 Example of a result for non-local thermodynamic equilibrium calculations. 51
1.49 Transmission of radio at the zenith as a function of frequency at precipitable water vapor of 2 mm and 4 mm and rest frequencies of representative lines. . . . 54
1.50 ^{12}CO($J=2$–1)/^{12}CO($J=1$–0) line ratios in Orion A, B molecular clouds, M 51, and M 83. 55
1.51 Dynamical properties of molecular clouds in the bar and arms of Maffei 2. 56
1.52 A standard view of GMCs by CO lines and newly proposed hierarchical CO structures. 57
1.53 Mean spectrum averaged over the whole area of M 51 obtained from the single-dish + the interferometric data and the interferometric data only, and their spatial distributions. 58
1.54 Ratios of FWHM measured from ^{12}CO data by single-dish telescopes and H I data to that measured from the interferometer CARMA for NGC 4736 and NGC 5055 as a function of radius. 59
1.55 ^{12}CO, ^{13}CO, and C^{18}O $J=1$–0 images of the Galactic plane. 60

2.1 Consistency of integrated intensity between Sorai et al. (2019) and Kuno et al. (2007) . . . 67
2.2 $R_{2/1}$ maps and near-infrared images of all galaxies in the samples. . . . 69
2.2 (Continued.) . . . 70
2.2 (Continued.) . . . 71
2.3 Histogram of $R_{2/1}$ for all pixels of all galaxies. . . . 72
2.4 Radial distribution of $R_{2/1}$ for all galaxies. . . . 73
2.5 Rate of change in the total molecular gas mass, standard deviation of molecular gas surface density, index of the K–S relation in each galaxy . . . 75
2.6 Indices of the K–S relation derived from ^{12}CO($J=2$–1) with the constant $R_{2/1}$ of 0.7 against that from ^{12}CO($J=1$–0). . . . 76
2.7 The K–S relation of the sample galaxies derived from ^{12}CO($J=2$–1) assuming $R_{2/1}=0.7$ and from ^{12}CO($J=1$–0). . . . 77
2.8 Correlation of $R_{2/1}$ and $\Sigma_{\rm SFR}$. . . . 81
2.9 The same as figure 2.8 but for $\Sigma_{\rm mol}$. . . . 82
2.10 The same as figure 2.8 but for $\tau_{\rm dep}$. . . . 83
2.11 The same as figure 2.8 but for IR color ($I_{70\mu{\rm m}}/I_{160\mu{\rm m}}$). . . . 84
2.12 Regions for spectra stacking in NGC 628. . . . 85
2.13 The same as figure 2.12 but for NGC 2903. . . . 85
2.14 The same as figure 2.12 but for NGC 3627. . . . 86
2.15 Correlation of $R_{2/1}$ with $R_{12/13}$ measured from stacked spectra. . . . 87
2.16 Correlation of $R_{2/1}$ with $n({\rm H_2})$ and $T_{\rm kin}$ and their histograms. . . . 89
2.17 $R_{2/1}$ distribution on the $T_{\rm kin}$–$n({\rm H_2})$ plot. . . . 90
2.18 Histograms of $R_{2/1}$ in each galaxy for original resolution data. . . . 99

3.1 Images of NGC 4303 at multiple bands, CO, and velocity field. . . . 107
3.2 SFR and SFE in NGC 4303. . . . 109
3.3 Determined galactic regions of NGC 4303. . . . 110
3.4 Stacked spectra of ^{12}CO($J=1$–0), ^{13}CO($J=1$–0), and C^{18}O($J=1$–0) within each galactic structure of NGC 4303. . . . 111
3.5 $\Delta\eta_{\rm f}$ defined by equation (3.9) as a function of a given beam-filling factor. . . . 117
3.6 Example of RADEX results for the $T_{\rm kin}=15$ K case in entire arms, entire bar ends, and entire bar. . . . 118
3.7 Correlation between SFE and molecular gas density $n({\rm H_2})$ derived from RADEX for the $T_{\rm kin}=15$ K case. . . . 121
3.8 Relationship between derived $n({\rm H_2})$ and $\Delta V/\sin i$ for the $T_{\rm kin}=15$ K case. . . . 122
3.9 Galactic regions for NGC 2903, NGC 3627, and NGC 4303. . . . 124
3.10 Correlation between SFE and $n({\rm H_2})$ for NGC 2903, NGC 3627, and NGC 4303. . . . 128
3.11 The same as figure 3.10 but plotted for each galaxy. . . . 128
3.12 Relation between $n({\rm H_2})$ and velocity dispersion of molecular gas in NGC 2903, NGC 3627, and NGC 4303. . . . 129
3.13 Relation between relative velocity of molecular clouds, peak column density of molecular gas for clouds, and star formation and our expected spaces for arms, bar ends, and bars. . . . 130

3.14 Maps of dust temperature in NGC 3627 and NGC 4303. 131
3.15 Temperature of molecular gas and dust in NGC 3627 and NGC 4303. 132
3.16 Time to reach thermal equilibrium between dust and gas when $T_{\rm dust} = 15$ K and 30 K. 133

4.1 Nobeyama 45 m Radio Telescope and the receiver FOREST. 141
4.2 Observed area on the WISE 12 μm image. 142
4.3 Scan patterns of OTF for Maffei 2. 142
4.4 Example of integrated-intensity map of W3 core for the ^{12}CO($J = 1$–0) standard array. 143
4.5 Examples of the channel map at -35 km s^{-1} of the standard array for ^{12}CO($J = 1$–0) and integrated-intensity maps of the two lines. 143
4.6 Integrated-intensity maps of all 16 arrays of W3 core obtained on December 12, 2019 and identified peak positions. 144
4.7 The same as figure 4.6 but for data obtained on February 24, 2020. 145
4.8 The same as figure 4.6 but for data obtained on January 8, 2020 (windy day). . . 146
4.9 The same as figure 4.6 but for data obtained on March 12, 2020 (warm and humid day). 147
4.10 Mean spectra of each array of the data on December 12, 2019. 148
4.11 The same as figure 4.10 but for data obtained on February 28, 2020. 149
4.12 Daily variation of mean integrated-intensity in each array averaged over 7×7 pixels. 150
4.13 Correlation plots between mean integrated-intensity around the peak of the standard array for ^{12}CO($J = 1$–0). 151
4.14 The same as figure 4.13 but for the ^{13}CO($J = 1$–0) standard array. 151
4.15 Correlation plots between integrated intensities of the standard array and another array for calibration of each array. 152
4.16 Moment maps of ^{12}CO($J = 1$–0) and ^{13}CO($J = 1$–0) before the removal of Galactic emission. 154
4.17 Representative Galactic ^{12}CO($J = 1$–0) spectra at some positions. 155
4.18 Flowchart of the algorithm to separate foreground Galactic emission and background emission of Maffei 2 from observational data. 157
4.19 Channel maps at -45 km s^{-1} and 0 km $^{-1}$ after step 1 and step 3 of the Galactic removal. 159
4.20 Extracted Galactic emission at 0 km s^{-1} after step 1. 159
4.21 Example of interpolation for foreground intensity of the Galaxy along the x-axis in the step 2 of the algorithm. 160
4.22 Extracted emission of the Galaxy. 161
4.23 The same as figure 4.16 but for after the removal of Galactic emission. 162
4.24 Integrated-intensity map of C^{18}O($J = 1$–0). 164
4.25 Histogram of ^{13}CO($J = 1$–0)-nondetected and detected ^{12}CO($J = 1$–0) intensity. . 164
4.26 Representative spectra of ^{12}CO($J = 1$–0) and ^{13}CO($J = 1$–0) at some positions. . 165
4.27 Integrated intensity map of $I_{12(13\rm det)}$, $I_{12(13\rm nondet)}$, determined galactic regions, line ratio of $R_{12/13}$, $R_{12(13\rm det)/12}$, and $R_{12(13\rm det)/13}$. 167
4.28 Correlation of $R_{12/12(13\rm det)}$ and $R_{12(13\rm det)/13}$ with $R_{12/13}$. 169

4.29 Integrated-intensity ratio of ^{13}CO($J=1$–0)/C^{18}O($J=1$–0). 170
4.30 Deviations of $R_{12/13}$, $R_{12(13\mathrm{det})/12}$, $R_{12(13\mathrm{det})/13}$ from each weighted mean in the entire galaxy. 171
4.31 Violin plots of $R_{12/13}$, $R_{12(13\mathrm{det})/12}$, and $R_{12(13\mathrm{det})/13}$ in each region. 175
4.32 Matrices of p-values of the Kolmogorov–Smirnov test between each region for $R_{12/13}$, $R_{12(13\mathrm{det})/12}$, and $R_{12(13\mathrm{det})/13}$. 176
4.33 Kennicutt–Schmidt relations using I_{12}, $I_{12(13\mathrm{det})}$, and I_{13}. 178

5.1 uv coverage of the 12 m array observation and ACA observation. 186
5.2 Flux distribution of dirty images by the ALMA 12 m array and the 7 m array. . 187
5.3 Flux distribution of NGC 1808 by the ALMA TP array. 187
5.4 The same as figure 5.2 but for maps after CLEAN. 188
5.5 Integrated intensity map of the feathered data and the schematic view of structures in NGC 1808. 189
5.6 Integrated intensity map of data by the 12 m array alone and radii. 189
5.7 Mini spiral features in the 500-pc ring. 190
5.8 Fraction of missing flux for the 12 m array as a function of radius. 191
5.9 Positions of identified GMCs in the feathered data. 192
5.10 Positions of identified GMCs in the data of the 12-m array alone. 193
5.11 Dependence of representative GMC properties on the four galactic environments. 194

6.1 Classes of the hierarchical structure of ISM and types of galaxies. 199

List of Tables

1 List of abbreviations used in this dissertation. . . . xiii
2 List of variables and constants used in this dissertation. . . . xiv

1.1 Mass composition of the Galaxy. . . . 2
1.2 Rotational energy level of H_2 ($v = 0$ case) and ^{12}CO. . . . 26
1.3 Rough critical densities of representative lines considering effects of photon trapping, their rest frequencies, and electric dipole moments. . . . 52

2.1 Samples in this study. . . . 66
2.2 Statistics of $R_{2/1}$ and properties of the samples. . . . 74
2.3 Fitted parameters of the K–S relation. . . . 78
2.4 Derived physical properties of molecular gas with the non-LTE analysis. . . . 93
2.4 (Continued.) . . . 94
2.4 (Continued.) . . . 95
2.4 (Continued.) . . . 96
2.5 Results of the stacking analysis. . . . 100
2.5 (Continued.) . . . 101
2.5 (Continued.) . . . 102
2.5 (Continued.) . . . 103

3.1 Basic parameters of NGC 4303. . . . 106
3.2 Regionally averaged quantities of NGC 4303. . . . 113
3.3 Derived molecular gas densities, the optimum values of the beam filling factor, the excitation temperatures of ^{12}CO and ^{13}CO in each region. . . . 119
3.4 Basic parameters of NGC 2903. . . . 124
3.5 Basic parameters of NGC 3627. . . . 124
3.6 Integrated intensities, line ratios, SFE, and derived physical properties of molecular gas in NGC 2903. . . . 125
3.7 Integrated intensities, line ratios, SFE, and derived physical properties of molecular gas in NGC 3627. . . . 126
3.8 Integrated intensities, line ratios, SFE, and derived physical properties of molecular gas in NGC 4303. . . . 127

4.1 Parameters of Maffei 2. . . . 139
4.2 Statistics of $R_{12/13}$. . . . 172
4.3 Statistics of $R_{12(13\mathrm{det})/12}$. . . . 173

4.4 Statistics of $R_{12(13\mathrm{det})/13}$. 174

5.1 Parameters of NGC 1808. 186

Table 1: List of abbreviations used in this dissertation.

ACA	Atacama Compact Array
AGB star	asymptotic giant branch star
AGN	active galactic nucleus
ALMA	Atacama Large Millimmeter/submillimeter Array
ASTE	Atacama Submillimeter Telescope Experiment
CARMA	Combined Array for Research in Millimeter-wave Astronomy
COMING	CO Multi-line Imaging of Nearby Galaxies
FOREST	FOur-beam REceiver System on the 45 m Telescope
(F)UV	(far) ultraviolet
FWHM	full width at half maximum
GALEX	Galaxy Evolution Explorer
GMA	giant molecular cloud association
GMC	giant molecular cloud
HERACLES	HERA CO-Line Extragalactic Survey
IF	intermediate frequency
IMF	initial mass function
IPAC	Infrared Processing and Analysis Center
(N, F)IR	(near, far) infrared
IRAM	Institut de Radioastronomie Millimétrique
ISM	interstellar medium
JCMT	James Clerk Maxwell Telescope
Jy	Jansky (1 Jy = 10^{-26} W m^{-2} Hz^{-1})
K–S relation	Kennicutt–Schmidt relation
K–S test	Kolmogorov–Smirnov test
LMC	Large Magellanic Cloud
LSR	local standard of the rest
LST	local sidereal time
LTE	local thermodynamic equilibrium
M	Messier Catalogue
MW	Milky Way
NED	NASA Extragalactic Database
NGC	New General Catalogue
NRO	Nobeyama Radio Observatory
OTF	on-the-fly
P.A.	position angle
pc	parsec (1 pc $\simeq 3.08568 \times 10^{16}$ m)
PDR	photon-dominated region
RMS	root mean square
SED	spectral energy distribution
SFE	star-formation efficiency
(s)SFR	(specific) star-formation rate
SIS	superconductor-insulator-superconductor
SMC	Small Magellanic Cloud
THINGS	The H I Nearby Galaxy Survey
(U)LIRG	(ultra-)luminous infrared galaxy
VLA	Very Large Array
WISE	Wide-field Infrared Survey Explorer

Table 2: List of variables and constants used in this dissertation.

$A_{u,l}$	Einstein A coefficient from the level u to the level l
$\alpha_{\rm CO}$	CO-to-H_2 conversion factor to convert CO luminosity into molecular gas mass
$\alpha_{\rm J2000.0}$	right ascension in the Julian epoch
$\alpha_{\rm vir}$	virial parameter
b	Galactic latitude
$B_{l,u}$	Einstein B coefficient from the level l to the level u
$C_{l,u}$	probability of transition from the level l to the level u by collision
c	speed of light ($\simeq 2.9980 \times 10^8$ m s^{-1})
dv	velocity width of molecular clouds measured as FWHM
$\delta_{\rm J2000.0}$	declination in the Julian epoch
ΔV	velocity with of spectra (velocity dispersion) measured as FWHM
G	gravitational constant ($\simeq 6.6743 \times 10^{-11}$ m^3 kg^{-1} s^{-2} $\simeq 4.3009 \times 10^{-3}$ pc $M_\odot^{-1}$ (km s^{-1})^2)
h	Planck constant ($\simeq 6.6261 \times 10^{-34}$ J s)
I_X	(integrated) intensity of X
i	inclination angle of a galactic disk
J	angular momentum quantum number
$k_{\rm B}$	Boltzmann constant ($\simeq 1.3806 \times 10^{-23}$ J K^{-1})
l	Galactic longitude
$L_\odot$	solar luminosity (1 $L_\odot \simeq 3.842 \times 10^{26}$ W)
$L'_{\rm CO}$	luminosity of CO
λ	wavelength
M	mass
$M_\odot$	solar mass (1 $M_\odot \simeq 1.9884 \times 10^{30}$ kg)
$M_{\rm mol}$	mass of molecular gas
$N(X)$	column density of X
$n(X)$	number density of X
ν	frequency
$\nu_{\rm rest}$	rest frequency
$Q_1(X)$	25th percentile of X
$Q_2(X)$	median of X
$Q_3(X)$	75th percentile of X
$R_{2/1}$	integrated intensity ratio of ^{12}CO($J=2$–1)/^{12}CO($J=1$–0)
$R_{3/1}$	integrated intensity ratio of ^{12}CO($J=3$–2)/^{12}CO($J=1$–0)
$R_{12/13}$	integrated intensity ratio of ^{12}CO($J=1$–0)/^{13}CO($J=1$–0)
$R_{12({\rm 13det})/12}$	integrated intensity ratio of ^{13}CO($J=1$–0)-detected ^{12}CO($J=1$–0)/^{12}CO($J=1$–0)
$R_{12({\rm 13det})/13}$	integrated intensity ratio of ^{13}CO($J=1$–0)-detected ^{12}CO($J=1$–0)/^{13}CO($J=1$–0)
r	radius
r_{25}	B-band isophotal radius at 25 magnitude arcsec^{-2}
ρ_s	Spearman's rank correlation coefficient
$\Sigma_{\rm mol}$	surface density of molecular gas
$\Sigma_{\rm SFR}$	surface density of star-formation rate
σ	standard deviation, RMS error of data
σ_v	velocity dispersion of molecular clouds measured as the second moment
T_A^*	corrected antenna temperature
$T_{\rm ex}$	excitation temperature
$T_{\rm kin}$	kinetic temperature
$T_{\rm MB}$	main beam temperature
τ	optical depth
$\tau_{\rm dep}$	depletion time of molecular gas
$\tau_{\rm ff}$	free-fall time
$X_{\rm CO}$	CO-to-H_2 conversion factor to convert CO integrated intensity into H_2 column density
$\langle X \rangle$	mean of X

Chapter 1

Introduction

1.1 Interstellar medium

Star formation is a main physical process in the Universe and in terms of it, it is essential to study ISM. When the Universe was born at the Big Bang, matters in the Universe is only hydrogen, helium, and little lithium. As stars are born and galaxies are formed in the evolution of the Universe, heavier elements[1)] is produced via nucleosynthesis in stars. Figure 1.1 shows an artistic view of stellar lifecycle. Stars form in cold ($\sim$ 10 K), dense ($\sim 10^6$ cm^{-3}), and gravitationally contracting parts of molecular gas, which is called "molecular-cloud cores". When cores are very dense and hot enough to ignite nucleosynthesis, protostars are born. For low-mass stars (mass is less than 8 $M_\odot$[2)]) like the Sun, they live for a few $\times$ 10 Gyr and die as white dwarfs after forming planetary nebulae. High-mass stars ($M \gtrsim 8\ M_\odot$) live fast ($\sim$ 100 Myr) and explode as supernovae. The nucleus of such high-mass star formation becomes neutron stars and back holes after supernovae. In both cases, stars form from interstellar medium (ISM) and release their atmosphere and envelopes to ISM. Thus, ISM is circulating via the stellar lifecycle. Moreover, it is important to investigate properties of ISM, because stars form in it.

The material, or baryon[3)] budget in the Galaxy (the Milky Way), our living galaxy is shown in figure 1.2. Total mass of ISM in the Galaxy is $\sim 7 \times 10^9\ M_\odot$. A part of it, mass of 1.3 $M_\odot$ is consumed by star formation per year. During it, stars die and release their mass to ISM. This mass is $\sim 0.5\ M_\odot$ per year. In addition, 0.2 $M_\odot$ yr^{-1} of remnants of stars such as white dwarfs and neutron stars are formed. Since mass of consumed ISM in star formation is larger than that from died stars, the amount of ISM decreases over time. ISM will be consumed far in the future, unless ISM is supplied from the outside of the Galaxy. Such infalling, or accumulating gas is $\sim 0.5\ M_\odot$ yr^{-1} in the current Galaxy.

ISM has many compositions. Figure 1.3 and table 1.1 show mass composition in the Galaxy. The dominant component of the Galaxy is stars; it accounts for 51% of the total mass. ISM only has a small fraction of 5.8% to the total mass. Within it, most of ISM is in a form of atomic hydrogen, or "H I gas"[4)]. It is relatively warm ($\sim$ 100–1000 K) and diffuse (10^{-2}–10^1 cm^{-3}). It can be observed using the 21 cm line (named after its wavelength, the rest wavelength

[1)] Elements heavier than helium is referred as "metal" in astronomy and astrophysics.

[2)] 1 $M_\odot$ is the mass of the Sun $\simeq 1.9884 \times 10^{30}$ kg.

[3)] In astronomy and astrophysics, the term "baryon" is different from one in particle and nuclear physics. It represents the usual matter (i.e., the matter except for dark matter), not a kind of hadrons.

[4)] Roman numerals I means neutral (no ionized), i.e., atomic phase. II means singly ionized. For instance, H II is singly ionized hydrogen (H^+) and O III is doubly ionized oxygen (O^{2+}).

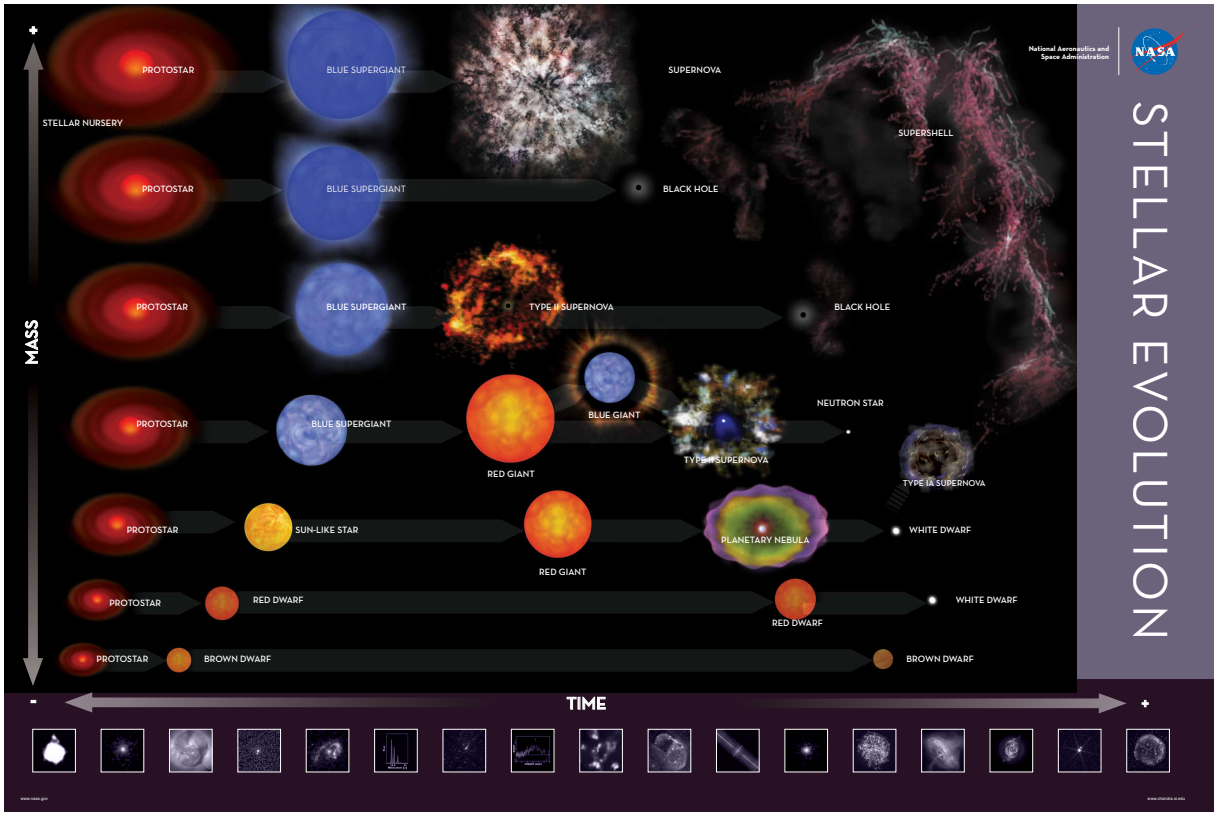

Figure 1.1: Schematic view of stellar lifecycle (retrieved from https://chandra.harvard.edu/stellarev/resources.html, credit: SAO/NASA).

Table 1.1: Mass composition of the Galaxy (Sparke and Gallagher 2007; Draine 2011, see also figure 1.3).

	Stars	Dark matter	ISM total	H II gas	H I gas	Molecular gas	Dust
Mass $[\times 10^9\ M_\odot]$	60	50	6.8	1.5	4.0	1.1	0.05

$\simeq 21.106$ cm) by the hyperfine structure of atomic hydrogen (i.e., interaction between spins of proton and electron). Although surface density of H I gas is not so high ($\Sigma_{\rm HI} \sim 10\ M_\odot\ {\rm pc}^{-2}$ at most in Galaxy and extragalaxies)[5], it extends beyond stellar distribution of galaxies (e.g., Walter et al. 2008; Nakanishi and Sofue 2016). Therefore, it becomes important in the context of galaxy evolution in the long term and slow processes seen in the edge of galaxy clusters. H I gas is stripped by ram pressure from galaxies which are falling into galaxy clusters and lost a large proportion of ISM (e.g., Kenney et al. 2004; Nakanishi et al. 2006; Chung et al. 2009) observed as "Jellyfish galaxies" (e.g., Poggianti et al. 2017; Jáchym et al. 2019). As a result, star formation is stopped, or "quenched" in these galaxies (e.g., Gunn and Gott 1972; Peng et al. 2015; Morokuma-Matsui et al. 2021).

The second large component is ionized hydrogen denoted as "H II gas". It is a hot ($\sim 10^4$ K) and relatively diffuse ($\sim 10^{-1}$–10^2 cm^{-3}) component and observed in star-forming regions (ionized by radiation from newly born stars) and outer edges of galaxies (ionized by high energy

[5] 1 pc $\simeq 3.0857 \times 10^{13}$ km $\simeq 2.0627 \times 10^5$ au.

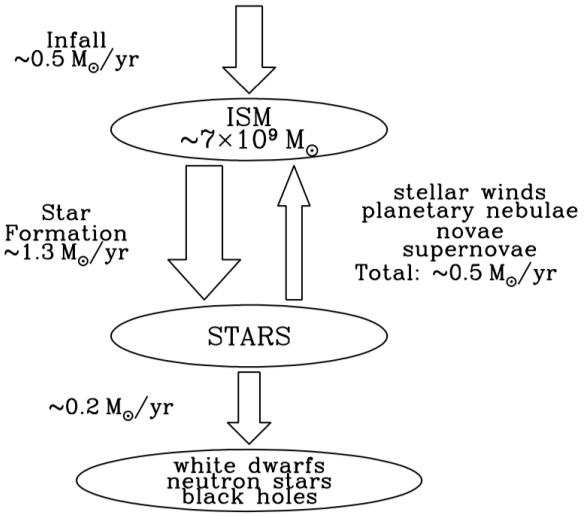

Figure 1.2: Baryon budget in the Galaxy (Draine 2011).

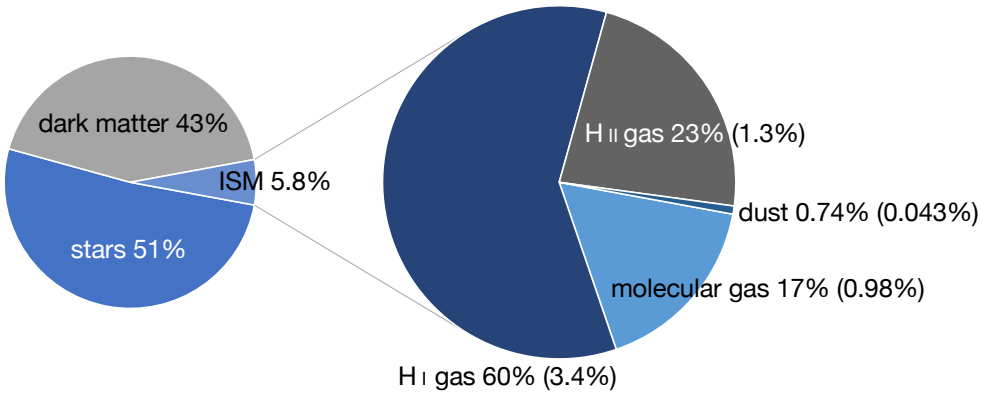

Figure 1.3: Mass composition of the Galaxy (Sparke and Gallagher 2007; Draine 2011). Values in parentheses is percentage of total mass (stars + dark matter + ISM). See also table 1.1.

intergalactic-radiation). It can be observed by Hα line[6)], radio continuum of free-free radiation around the 100 GHz band, and radio recombination line of hydrogen. Since these lines are relevant to star formation activity, star-forming regions are called "H II region". Moreover, they are used to estimate how stars are born in a unit time. This is described more detail in section 1.3.

The third large component is molecular gas, the main topic of this dissertation. It account for only 17% of total ISM in the Galaxy, it is important phase, because molecular gas is the direct raw-material of stars. Stars form in gravitationally shrinking, dense gas. Therefore, gas which can form stars should be cold. If gas is warm or hot, it cannot shrink due to internal energy. Molecular gas is a cold ($\sim$ 10–30 K) and dense ($\gtrsim 10^2$ cm^{-3}) phase and consists of molecular hydrogen (H_2). Then molecular gas is named "molecular". Other than molecular hydrogen, many molecules such as carbon monoxide (^{12}CO), its isotopologues (e.g., ^{13}CO, C^{18}O)[7)], ammonia

[6)] Emission line from the atomic hydrogen which is de-excited from $n = 3$ to $n = 2$.

[7)] In this dissertation, atomic mass number of the most abundant isotope (for example,^{16}O for oxygen) in molecular formulae is omitted except for ^{12}CO. This is because to clearly denote it as the distinct molecule from ^{13}CO. The term

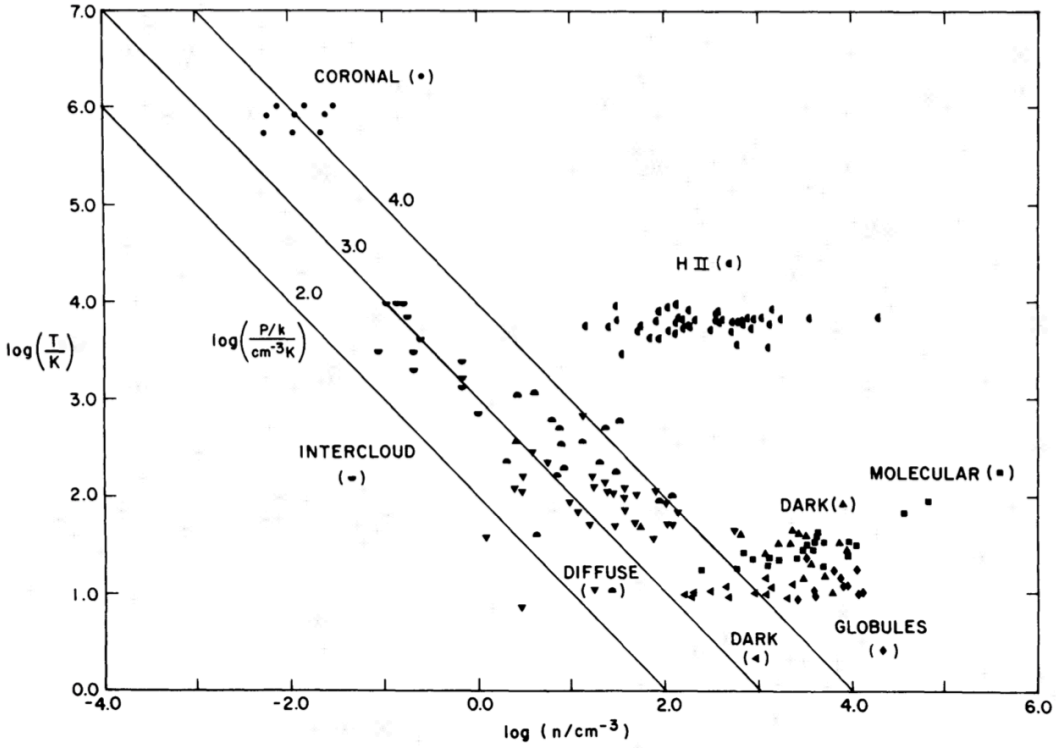

Figure 1.4: Phase diagram of interstellar medium (Myers 1978). "Coronal" is a kind of ionized (H II) gas, "intercloud" and "diffuse" are H I gas, and "dark", "grobules" are molecular phase. Pressure of ISM ($nT/k_{\rm B}$, where n is number density, T is temperature, and $k_{\rm B}$ is the Boltzmann constant) is constant of $nT/k_{\rm B} = 10^2, 10^3, 10^4$ cm^{-3} K on solid lines from top left to bottom right.

(NH_3), hydrogen cyanide (HCN), carbon monosulfide (CS), silicon monoxide (SiO), and ethanol (CH_3COOH) are found. About the investigation of molecular gas, more detail description is produced in section 1.4 and later.

Figure 1.4 summarizes phases of ISM on the phase diagram (temperature–density plot). These phases in ISM is roughly under the pressure equilibrium except for ionized gas in H II regions and dense molecular gas. This diagram is like a part of the stellar evolution shown in figure 1.1. That is, stars form in cold, dense molecular gas and die releasing ionized, hot gas to interstellar space. Such hot gas is cooled and form cold H I gas ("diffuse" gas in the figure) so called "cold neutral medium" (CNM) via warm H I gas ("intercloud" gas in the figure) so called "warm neutral medium" (WNM). Then, cool H I gas is cooled further, cold molecular gas is formed, which is a raw material of stars. The diagram of figure 1.4 traces the lifecycle of ISM as well as stellar evolution of figure 1.1.

Back to figure 1.3, the most smallest fraction is interstellar dust. It mainly consists of carbon or silicate. Its existence can be confirmed by dark lanes, or dust lanes in optical images of the Galaxy and extragalaxies. The amount of dust is very small, it exerts significant influences on energy distribution of radiation as a function of wavelength and chemical processes. Dust grains scatter and absorb radiation whose wavelength is shorter than $\lesssim 10^0$ μm (i.e., electromagnetic waves shorter than near infrared). When they absorb radiant energy, they re-emit the energy

"CO" in the dissertation indicates the total carbon monoxide including ^{12}CO and its isotopologues.

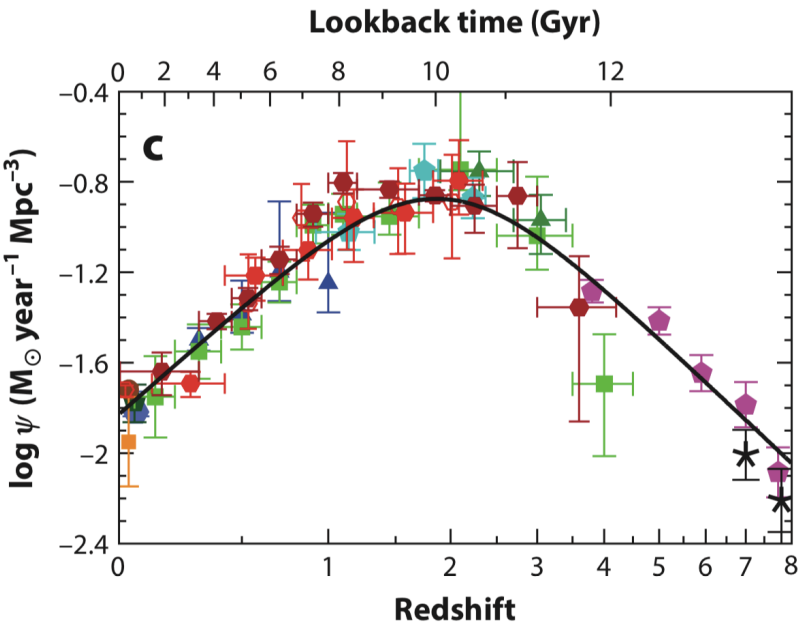

Figure 1.5: Cosmic star-formation history (Madau and Dickinson 2014). ψ in the vertical axis is star-formation-rate volume density (mass of stars born in a unit time per unit volume).

in mid- to far-infrared regime (10^1 μm $\lesssim \lambda \lesssim 10^3$ μm). As a result, spectral energy distribution (SED) and extinction curve changes (e.g, Weingartner and Draine 2001). Moreover, dust grains behave like a catalyst in chemical reactions. Because density of ISM is very low compared with laboratory conditions on the ground, gas-phase reactions seldom occur. Instead, atoms and molecules sticking the surface of dust can evoke chemical reactions on the surface. In addition, dust can absorb heat of reaction, thus reactions are stable. For instance, formation of molecular hydrogen from atomic hydrogens occur on the dust.

To investigate molecular gas in the Universe is essential to understand how stars form. Moreover, it is important in terms of evolution of the Universe. Figure 1.5 shows cosmic star-formation history. Here, redshift z the horizontal axis is determined as the following equation;

$$z \equiv \frac{\lambda_{\rm obs}}{\lambda_{\rm rest}} - 1, \tag{1.1}$$

where $\lambda_{\rm obs}$ is observed wavelength and $\lambda_{\rm rest}$ is rest wavelength. According to the Hubble's law, the more distant object has the more higher receding velocity. Thus, wavelength from the more distant objects gets longer due to the Doppler effect. Since distant objects observed at present is the past image, redshift can be convert into look-back time. In the early Universe, star-formation activity gradually increases as time passed. It is at the peak around $z = 2$. This duration is called "cosmic noon". After that, star formation gradually declines by about 1 dex to the present time. So sometimes the current state is called "cosmic dusk" and "cosmic morning" for the early Universe. Star formation has been changed as the Universe evolves. Hence, to reveal factors and causes for molecular gas to characterize star formation is also important to understand the evolution of the Universe and galaxies, because stars are born from molecular gas in galaxies.

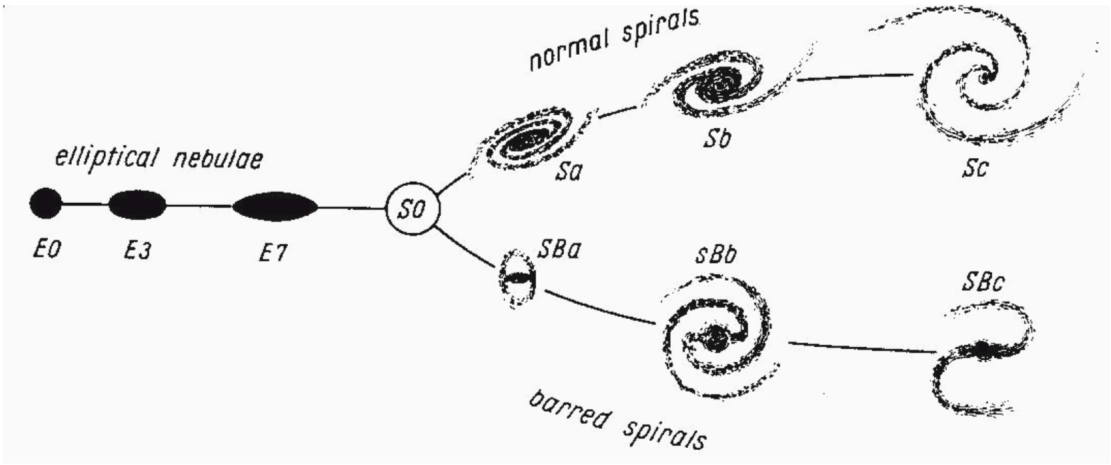

Figure 1.6: Morphology classification based on the Hubble sequence known as "Hubble's tuning fork diagram" (Hubble 1936).

1.2 Galaxies

In this section, we introduce galaxies, mainly their morphologies and properties.

1.2.1 Morphology of galaxies

The first classification of galactic morphologies were done by Edwin P. Hubble (Hubble 1936). His classification is shown in figure 1.6. He roughly classified galaxies into three types; elliptical-like ("elliptical nebulae" in figure 1.6), spiral-like ("normal spirals"), and intermediates (lenticular-like). Furthermore, he added additional types for spiral-like galaxies whether they have the bar structure near the center ("barred spirals"). He denoted "En" as a symbol for *elliptical nebulae*. Here, n is an integer part of 10ϵ, where ϵ is ellipticity derived from fitting of elliptical-like galaxy. Lenticular-like one is denoted as "S0". Normal spirals are denoted as "Sa", "Sb", and "Sc" ... depending on the tightness of wounded spiral-shaped arms (spiral arms or simply arm). That is, a galaxy which has tightly wounded spiral arms is "Sa" and one that which has loosely wounded spiral arm is "Sc". Barred spirals are denoted as "SB" So, galaxies with tightly wounded spiral arms and the bar structure is "SBa" and loosely wounded barred spiral is "SBc". The alignment from ellipticals to S0, Sa (SBa), ..., Sc (SBc) is called "the Hubble sequence" and the diagram of figure 1.6 is called "Hubble's tuning fork diagram". At present, *elliptical nebulae*[8)] are called "elliptical galaxies", intermediate galaxies are "lenticular galaxies", *normal spirals* are "spiral galaxies", and *barred spirals* are barred spiral galaxies.

He called that galaxies become "early type" as the Hubble sequence goes to left, and "late type" as goes to right. This does not mean that early-type galaxies are in an early evolutionally stage and late-type galaxies are in late evolutionally stage. In other words, galaxies do not evolve changing their morphology along the Hubble sequence from ellipticals to lenticulars, tightly wounded spirals, and loosely wounded spirals. Nevertheless, the term of "early type" and "late type" have been used nowadays.

[8)] At that time, whether galaxies are beyond the Galaxy or nebulae in the Galaxy was not clearly recognized. Therefore, extragalaxies were sometimes called "nebulae" then.

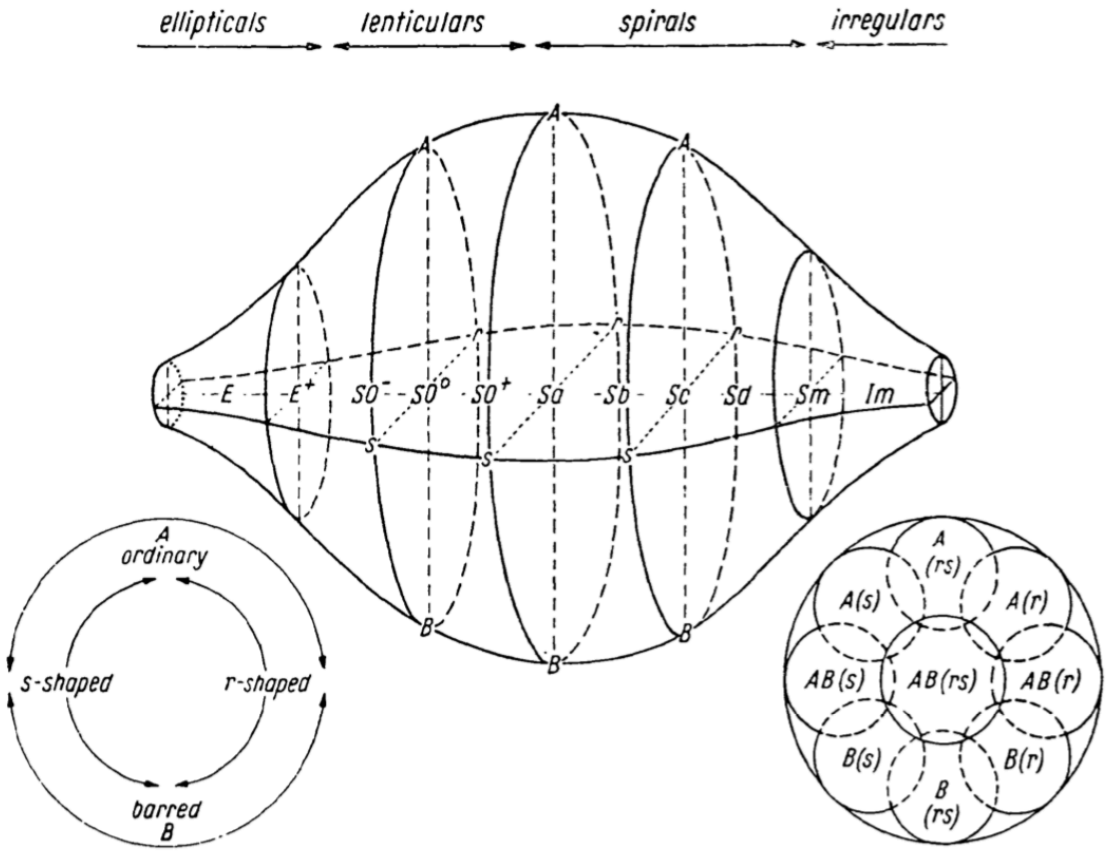

Figure 1.7: Advanced morphology classification of galaxies from Hubble (1936) suggested by de Vaucouleurs (1959). Hubble sequence is aligned in the order of elliptical galaxies, lenticular galaxies, spiral galaxies, and irregular galaxies along the spine of the body. Morphology becomes ordinary spiral without bar (A) upward, and barred (B) downward. Spiral features are clear (s) toward the near side of the body. Spirals are ambiguous and ring-like structure is significant (r) toward the far side. An intermediate one is represented like "AB(rs)". See also figure 1.8.

As observational technologies improved from the age of Hubble (1936), many types of galaxies was found. de Vaucouleurs (1959) ameliorated the Hubble's classification. It is shown in figure 1.7. He added "Sd", "Sm" galaxies and irregular galaxies as more late-type galaxies along the Hubble sequence. Here, "m" indicates Magellanic, implied Magellanic Clouds, which are satellite dwarf galaxies of the Galaxy. In addition, intermediate barred galaxies are newly classified. As a vertical axis to the Hubble sequence, ordinal spiral without bar, intermediate bar, clear bar is distributed. They denote as "A", "AB", and "B", respectively.

He also expand the Hubble sequence into a three-dimensional body. The spine of the body is along the Hubble sequence; ellipticals, lenticulars, spirals, and irregulars. A vertical axis indicates the strength of the bar. The other vertical axis represents whether galaxies are spiral-like or ring-like. For figure 1.7, spiral features are clearer toward the near side, and spiral features are ambiguous and the ring-like structure is dominant toward the far side along the axis. The former and the latter is denoted as "(s)" and "(r)", respectively, and the intermediate one is "(rs)". For spiral galaxies, strongly barred spiral galaxies with clear spiral features are expressed as "SB(s)" and galaxies with intermediate bar and intermediate spirals are "SAB(rs)". Example

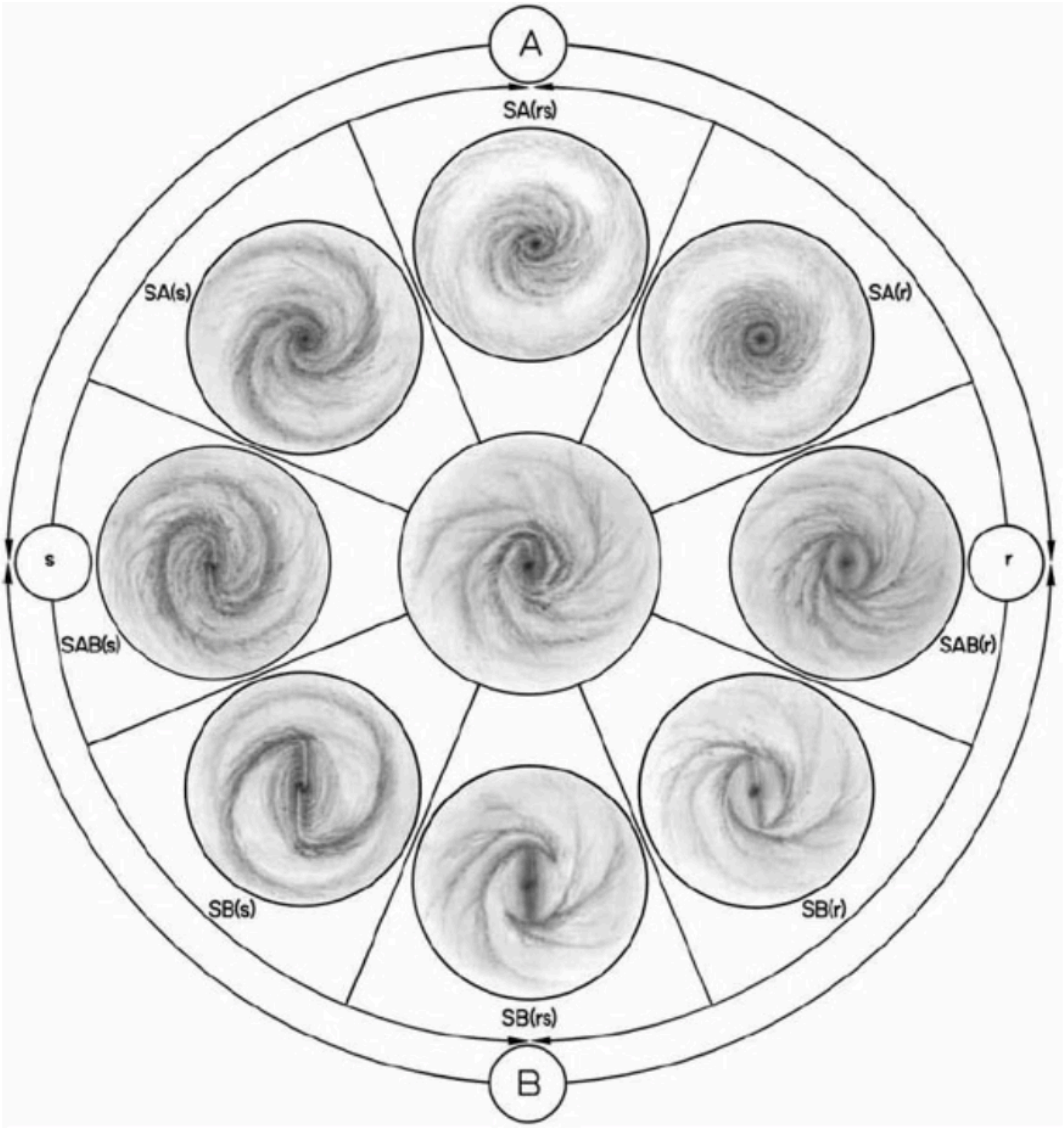

Figure 1.8: A cut section of the body shown in figure 1.7. Representative galactic morphologies are shown in each part. As figure 1.7, morphologies show ordinary spiral galaxies without bar (A) upward. The bar structures is significant (B) downward. Spiral structures are clear (s) toward left and they diminish and show ring structures (r) toward right.

galactic morphologies for a cut section of the body at spiral galaxies is shown in figure 1.8. The Galaxy is classified as "SB(r)bc" (Kennicutt 2001), Andromeda Galaxy (M 31) is "SA(s)b", and Triangulum Galaxy (M 33) is "SA(s)cd" (de Vaucouleurs et al. 1991). Here, "bc" and "cd" indicate intermediate between "b" and "c", and "c" and "d" along the Hubble sequence, respectively.

1.2.2 Properties of galaxies

In the last subsection, we introduce classifications for morphologies of galaxies. It has been reported that properties of galaxies differs from morphologies. For example, the bimodality of galaxies are found (Baldry et al. 2004). Figure 1.9 shows the result. When local galaxies

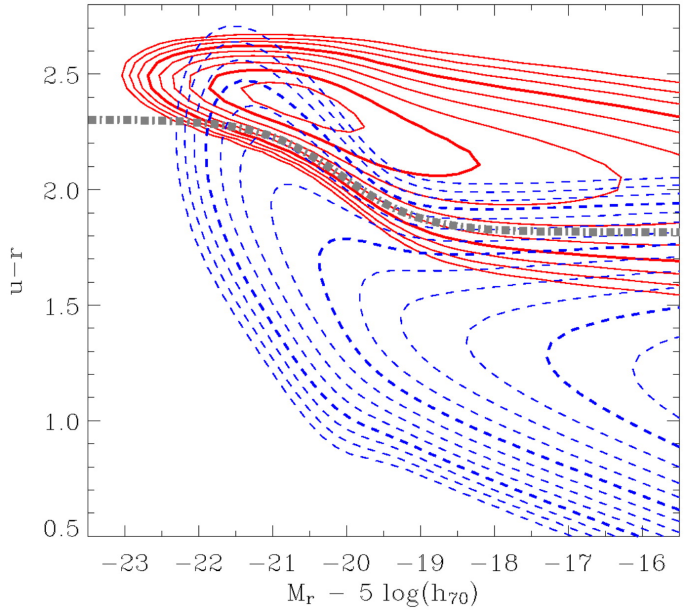

Figure 1.9: Color-magnitude diagram for local galaxies (Baldry et al. 2004). This shows bimodality of galaxies. The vertical axis is difference of magnitude in the u band and the r band, and the horizontal axis is absolute magnitude at the r band. Red solid contours represent density of *red component* (massive, passive star-forming activity) and blue dashed are *blue component* (relatively less massive, active star-formation).

are plotted on the color–magnitude plane[9)], the two components are appeared. One is the red[10)] component, which is massive and passively star-forming objects. The other is the blue component, which is relatively less massive and shows active star-formation. The former consists of early-type galaxies such as elliptical galaxies and S0 galaxies. The latter is the ensemble late-type galaxies such as spiral galaxies and irregular galaxies. Hence, early-type galaxies typically does not show star formation, or they are quenched, and late-type galaxies are sites of star formation. This result is seen in another study (Colombo et al. 2018) that shows dependency of star-formation rate surface density $\Sigma_{\rm SFR}$ on the Hubble sequence; see panel a) of figure 1.10. $\Sigma_{\rm SFR}$ in elliptical and S0 galaxies is lower by ~ 2 dex than late-type galaxies.

Not only star-formation activity, gas properties are also different between galaxies' types. Figure 1.11 shows total gas mass fraction to stellar mass $[M({\rm H_2}) + M({\rm HI})]/M_{\rm star}$, molecular gas mass fraction to stellar mass $M({\rm H_2})/M_{\rm star}$, and molecular gas mass fraction to atomic gas mass $M({\rm H_2})/M({\rm HI})$ along the Hubble sequence by Boselli et al. (2014). As galaxies become late type, total gas fraction and molecular gas fraction tend to increases. On the other hand, molecule-atomic gas fraction decreases from early type to late type. It is ambiguous when we see medians for solid markers (blue large markers), however, $M({\rm H_2})/M({\rm HI})$ ratio certainly decreases considering open markers. These tendencies are confirmed by other previous studies (e.g., Young and Scoville 1991; Nishiyama and Nakai 2001).

When molecular gas mass fraction is considered as a function of stellar mass, results are

[9)] "Color" is referred as difference of magnitude or ratio of flux of different bands. They are equivalent, because magnitude is logarithmic scale of flux.

[10)] In astronomy and astrophysics, the concept of "red" and "blue" are generalized. That is, "red" is referred when magnitude at longer wavelength is brighter than that at shorter wavelength.

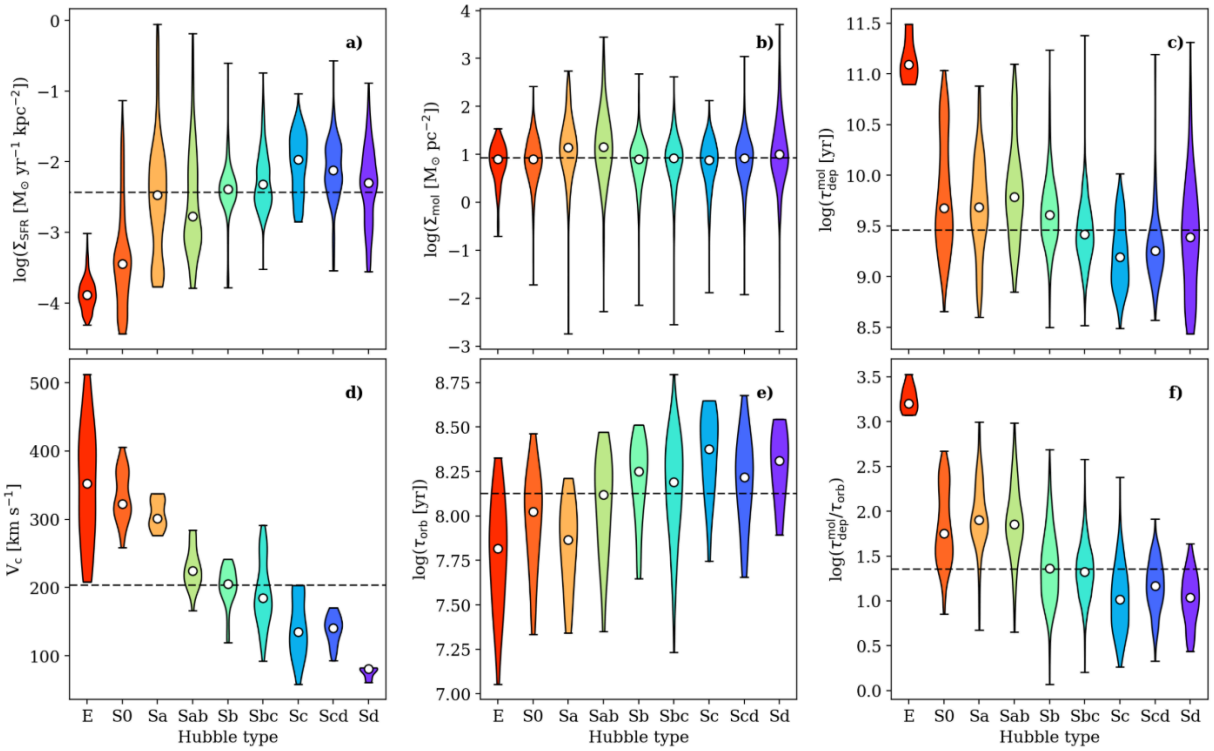

Figure 1.10: Basic properties of galaxies along the Hubble sequence (Colombo et al. 2018). a) surface density of star-formation rate. b) surface density of molecular gas. c) depletion time of molecular gas. d) rotation speed of the galactic disk. e) orbital timescale of the galactic disk. f) ratio of molecular gas depletion-time to orbital timescale.

shown in figure 1.12 (Sorai et al. 2019). For early-type galaxies, molecular gas mass fraction decreases as stellar mass increases. In contrast, it increases as stellar mass increases for late-type galaxies. According to these results avobe, early-type galaxies are typically gas poor and late-type galaxies are (molecular) gas rich and have a large amount of cold-gas reservoir as H I. Hence, to investigate star formation from molecular gas in galaxies, it is essential to observe and study late-type galaxies not early-type galaxies.

Note that the amount of molecular gas itself is less in early-type galaxies than that in late-type galaxies. Based on panel b) of figure 1.10, molecular gas mass is not so different between the Hubble types. Being different between early- and late-type is molecular gas fraction against stelar mass.

Depletion time of molecular gas defined as a ratio of molecular gas mass to star-formation rate (described more detail in section 1.3) also depends on the Hubble type. Panel c) of figure 1.10 shows differences of molecular gas depletion-time. Depletion time is much longer in elliptical galaxies than in other types. Other early-type galaxies such as S0 galaxies is slightly longer by ~ 0.7 dex than very late-type galaxies such as Sc and Sd galaxies. This tendency was not seen in past, early studies (Young and Scoville 1991). The lower star-formation rate as well as long depletion time of molecular gas in early-type galaxies are attributed to strong shear motion within these galaxies (figure 1.13) due to rapid rotating velocity.

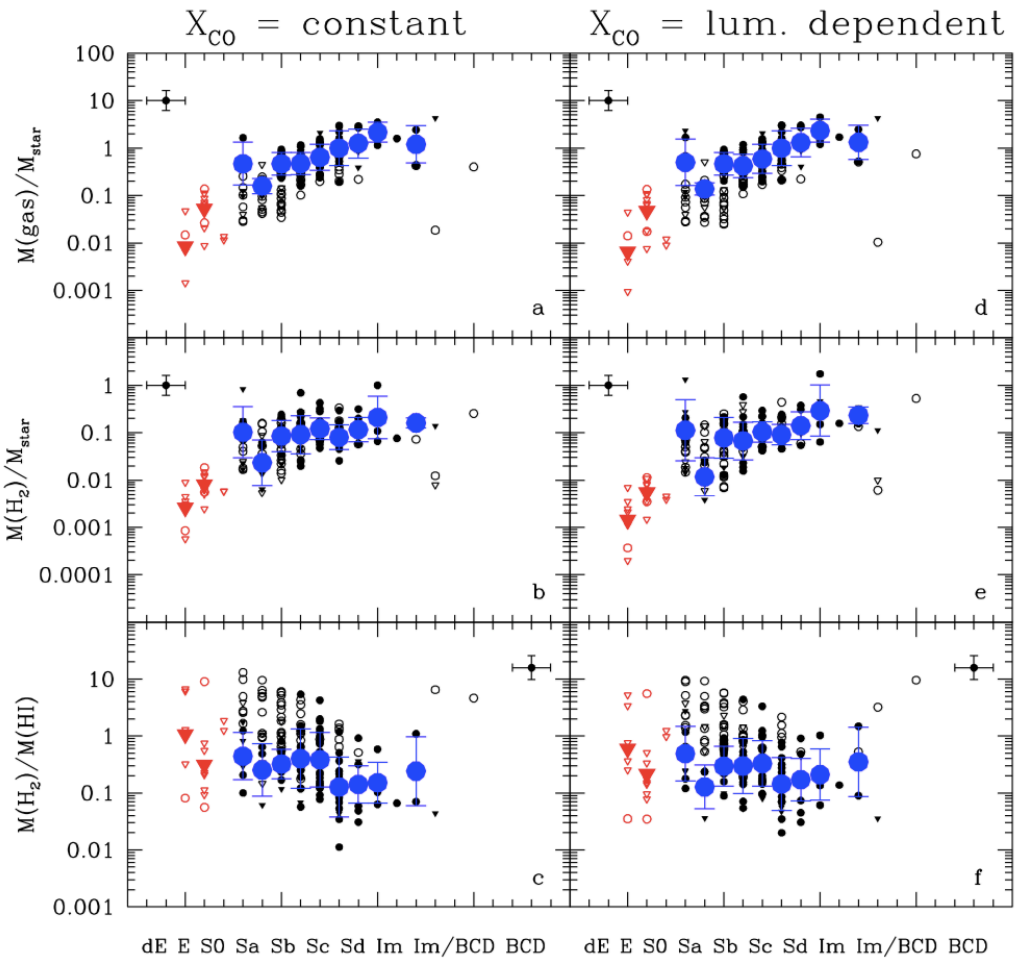

Figure 1.11: Gas fraction and molecular-atomic gas fraction along the Hubble sequence (Boselli et al. 2014). $X_{\rm CO}$ is the conversion factor from emission of ^{12}CO line to molecular gas mass. This is described more detail in section 1.5.3. Red markers are early-type galaxies and blacks are late-type galaxies. Filled markers indicate H I gas is not deficient and open ones show H I deficient. Triangles are $3\,\sigma$ upper limits. Large markers with error bars indicate median and standard deviation for filled markers.

1.3 Star formation in galaxies

In this section, quantify of star formation, the fundamental relation of star formation in galaxies, and phenomena seen in barred spiral galaxies.

1.3.1 How to estimate activeness of star formation

To quantify activeness of star-formation activity, an indicator of it is needed. This is "star-formation rate" (SFR) which is already appeared in the dissertation. It is defined as mass of newly born stars per unit time; thus its unit is $M_\odot$ yr^{-1}. It is difficult to directly measure total mass of new born stars from observational data due to limited resolution and sensitivity. Therefore, SFR is derived from total high-mass stars indirectly. Since high-mass stars are short lived, total mass of new born stars can be estimated, assuming distribution of new born mass.

As mentioned in section 1.1, H II gas is related to star forming activity. To ionize atomic

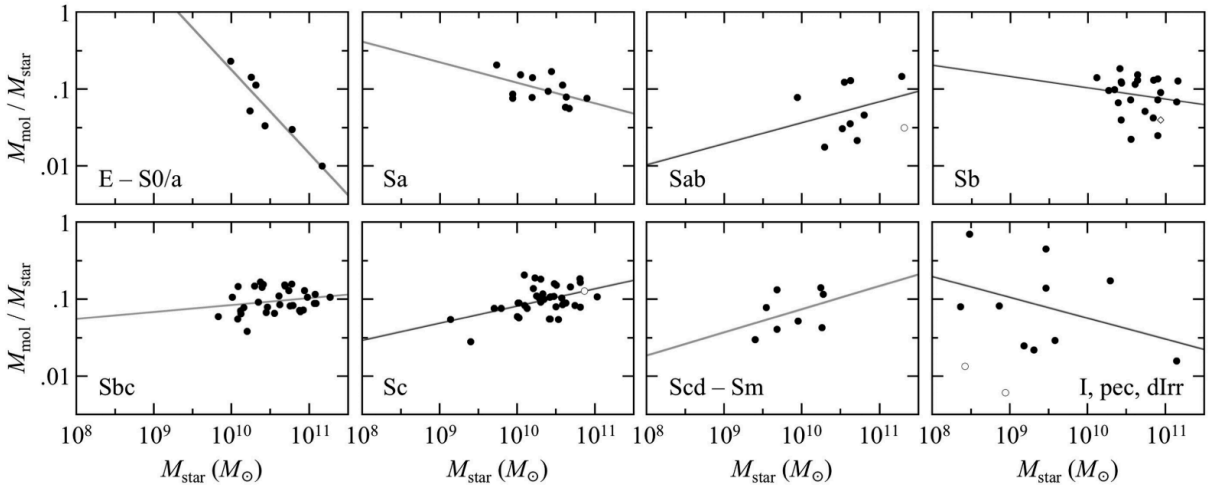

Figure 1.12: Molecular gas mass fraction as a function of stellar mass in each Hubble type. (Sorai et al. 2019).

hydrogen, the energy of 13.6 eV is needed;

$$\mathrm{H} + 13.6\,\mathrm{eV} \rightarrow \mathrm{H}^+ + e^-. \tag{1.2}$$

This energy corresponds to the wavelength of 91.1 nm[11], which is in the short wavelength of far-ultraviolet (FUV) regime. Only massive and young stars can emit at the wavelength. Hence, emission such as Hα line (the rest wavelength is 656.3 nm in a red optical light regime), free-free radiation, radio recombination line which can be observed in H II gas traces such young, massive stars. Hα line traces star formation whose mass is higher than 15 $M_\odot$ and timescale is younger than 3–10 Myr (Hao et al. 2011; Murphy et al. 2011; Kennicutt and Evans 2012).

Not only Hα and other tracers of ionized gas, FUV emission also traces young massive stars. Since temperature of surface of high-mass stars such as O and B stars is $\gtrsim 10^4$ K, FUV emission is directly observed from high-mass stars. FUV is absorbed in the atmosphere, so that it cannot be observed from the ground and can obtained from satellites in the orbit around the Earth. The most famous satellite for ultraviolet astronomy is Galaxy Evolution Explorer (GALEX) by NASA, which can observe FUV at wavelengths of 134.4–178.6 nm (Morrissey et al. 2007). FUV traces 10–100 Myr-aged young, massive stars (Hao et al. 2011; Murphy et al. 2011; Kennicutt and Evans 2012).

Although Hα line and FUV can directly observe massive young stars, they are easily scattered or absorbed by interstellar dust due to their short wavelength. This lead to underestimated SFR as it is and correction of extinction is needed. Dust re-emits absorbed energy as far infrared (FIR) emission. In particular, 24 μm (or 22 μm) of FIR intensity from hot dust has widely been made use of correction of extinction (e.g., Calzetti et al. 2005; 2007; Kennicutt et al. 2007; Rieke et al. 2009; Casasola et al. 2017). According to the Wien's displacement law;

$$\left(\frac{\lambda_{\max}}{\mu\mathrm{m}}\right) \simeq 2897.77 \Big/ \left(\frac{T}{\mathrm{K}}\right), \tag{1.3}$$

[11] In this connection, the dissociation energy of H_2 into H I is 4.47 eV. It corresponds to 277 nm and it is in the near-ultraviolet (NUV) band of GALEX (177.1–283.1 nm).

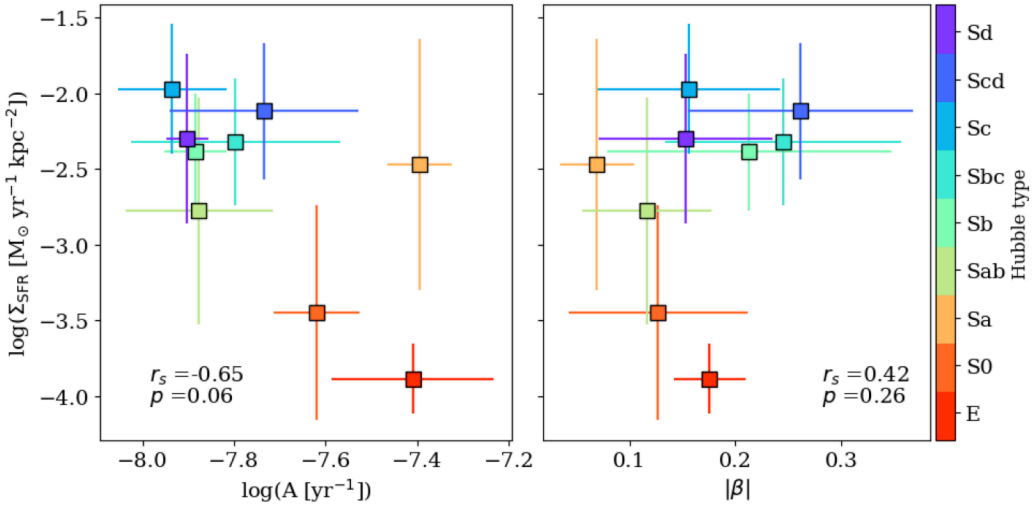

Figure 1.13: Dependence of star-formation rate on shear strength (left panel) and shape of rotation curve (right panel) with the Hubble sequence (Colombo et al. 2018).

dust temperature whose radiant power has the peak around 24 μm is $\sim$ 120 K. As well as FUV, FIR is absorbed and cannot be observed from the ground, space IR satellites and telescopes such as Spitzer Space Telescope and Wide-field Infrared Survey Explorer (WISE) are used for observations of the band (Engelbracht et al. 2007; Wright et al. 2010). Alternatively, total luminosity in infrared regime by the SED fitting can be used to derive SFR (e.g., Kennicutt 1998a; 2009; Hao et al. 2011). Obscured SFR traced by FIR is dominant compared with unobscured SFR by Hα and FUV. The former is often higher by 1 dex and more than the latter in massive, molecular-gas rich, star-forming galaxies (i.e., normal spiral galaxies rather than dwarf and irregular galaxies; e.g., Leroy et al. 2008).

With the combination of an obscured tracer and an unobscured tracer, SFR can be derived. In this regard, since these tracers reflect only young massive stars, the distribution of masses for newly born stars need to be assumed in order to take less massive stars into account. This mass distribution is called "initial mass function" (IMF). IMF is usually described as

$$\frac{dN}{d\log M} \propto M^{-\gamma}, \tag{1.4}$$

or

$$\frac{dN}{dM} \propto M^{-(\gamma+1)}, \tag{1.5}$$

where N is number of stars at the mass M and $-\gamma$ is the slope of the distribution in the logarithmic plot for equation (1.4)[12]. Salpeter (1955) firstly determined $\gamma = 1.35$ from observational results (the Salpeter ISM). In studies of galaxies, the Kroupa IMF (Kroupa 2001) (adopted various γ depending on stellar mass), the Chabrier IMF (Chabrier 2003) (adopted simple log-normal), and the `STARBURST99` model (Leitherer et al. 1999) are often applied in addition to the Salpeter IMF.

In many cases, IMF is fixed over galaxies. However, it should change depending on environments around and within galaxies. To reveal dependence of IMF is essential for all studies

[12] In this dissertation, "log" means $\log_{10}$. The natural logarithm $\log_e$ is denoted as "ln" if it appears.

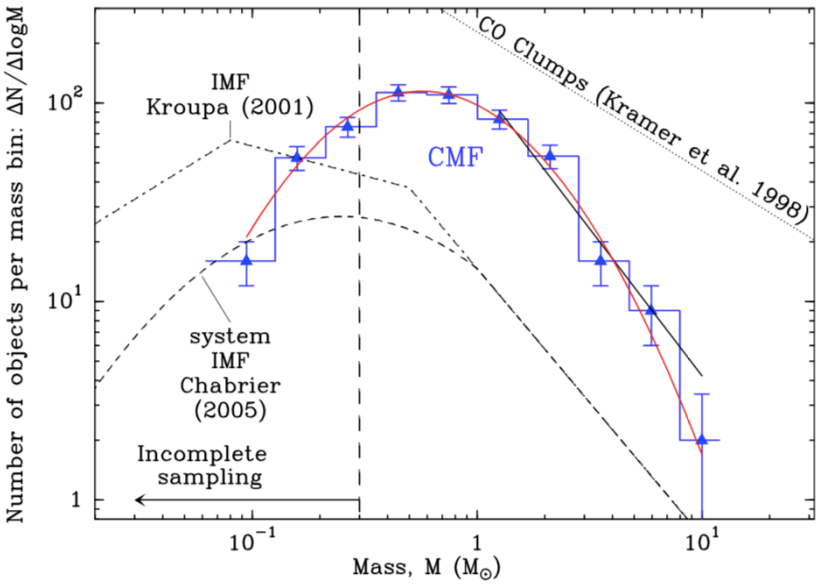

Figure 1.14: Core mass function (CMF) and representative initial mass functions (IMFs) (André et al. 2010).

relevant to star formation. As the first clue, it is reported that IMF is analogous to mass function of molecular cloud core; core mass function (CMF; e.g., Motte et al. 1998; André et al. 2010). The result of André et al. (2010) is shown in figure 1.14. Most of surveys for molecular cloud core are in contexts of inner Galaxy studies. Even in the current status, core surveys for extragalaxies is yet difficult, because molecular cloud mores are too small and emission lines which selectively trace dense molecular gas (this is described more detail in section 1.6.2) is very weak. IMF likewise CMF variations and their dependence on galactic environments are an open question.

1.3.2 Kennicutt–Schmidt relation

A most fundamental relation connecting star formation and gas is the Kennicutt–Schmidt (K–S) relation (Schmidt 1959; Kennicutt 1989). It is described as

$$\Sigma_{\rm SFR} \propto \Sigma_{\rm gas}^{N}, \tag{1.6}$$

where $\Sigma_{\rm SFR}$ is surface density of SFR and $\Sigma_{\rm gas}$ is that of gas (either molecular gas + atomic gas, atomic gas only, atomic gas only). N is the slope in a double logarithmic plot. Originally, N is reported in a range of $1 < N \lesssim 1.5$, so the relation is super linear in most of cases. Kennicutt (1998b) found that $N = 1.4$ (see figure 1.15). It extends over 5–7 orders of magnitude for $\Sigma_{\rm SFR}$ and $\Sigma_{\rm gas}$. This result is averaged over each galaxy; that is, $\Sigma_{\rm SFR}$ and $\Sigma_{\rm gas}$ are derived averaging the all area of galaxies. Thus, each data point represents one galaxy. Spatially resolved K–S relations (plotting $\Sigma_{\rm SFR}$ and $\Sigma_{\rm gas}$ at each pixel) is one of the advanced topic from the global K–S relation (e.g., Rahman et al. 2011; 2012; Shetty et al. 2014b; Utomo et al. 2017; Takeuchi, T. T. 2021 in prep.). The super linearity of the relation is also seen in some of spatially resolved studies (e.g., Kennicutt et al. 2007; Momose et al. 2010; Liu et al. 2011; Momose et al. 2013;

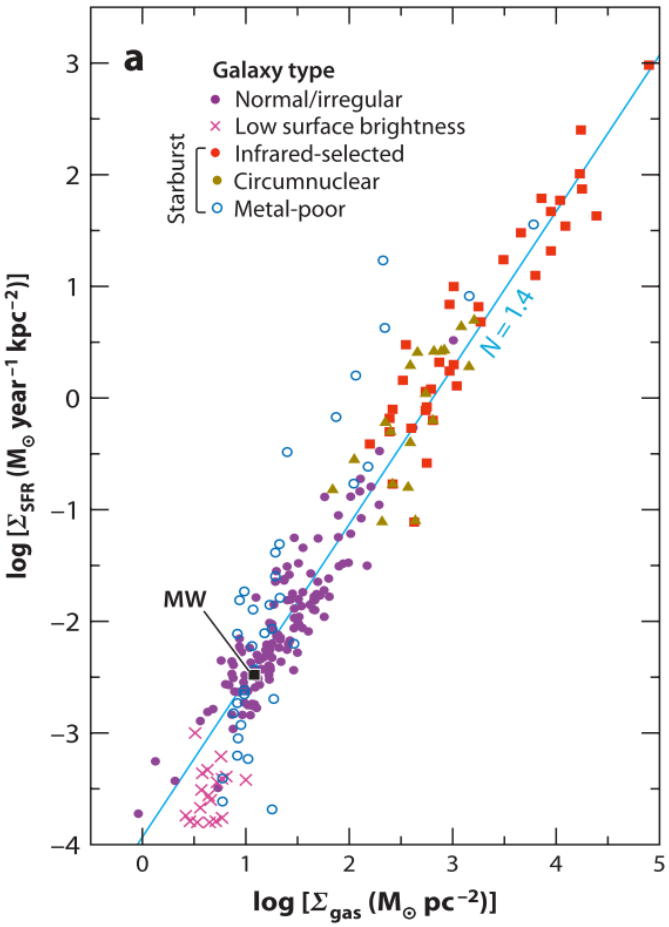

Figure 1.15: The global Kennicutt–Schmidt relation for various types of local galaxies (Kennicutt and Evans 2012).

Hatakeyama et al. 2017). Nowadays, the K–S relation is extended to the three-dimensional space adding stellar surface density Σ_* (mainly by the ALMA–MaNGA QUEnching and STar Formation (ALMaQUEST) survey: Lin et al. 2019; Ellison et al. 2020; Lin et al. 2020; Ellison et al. 2021).

The index N of the K–S relation is thought to have physical means of star formation (e.g., Elmegreen 2002; 2015; Krumholz and McKee 2005; Komugi et al. 2006; Krumholz et al. 2009b; Tan 2010). For instance, $N = 1$ indicates that star formation is linearly increased to gas surface density, or column density of gas. Therefore, gravitational instability is a dominant effect of onset of star formation. The linearity of the K–S relation also means timescale, or efficiency of star formation is constant over galaxies. $N = 1.5$ prefers star formation occurs at free-fall time (see section 1.5.4 more detail), i.e., the dynamical star-formation scenario (rapid star-formation; e.g., Goldreich and Kwan 1974; Krumholz and McKee 2005; Hayward and Hopkins 2017; Krumholz et al. 2017), which is opposite to the turbulence-regulated star-formation scenario (slow star-formation; e.g., Zuckerman and Evans 1974; Hennebelle and Chabrier 2011; Padoan and Nordlund 2011; Federrath and Klessen 2012). $N = 2$ is supposed to be produced by star formation caused by cloud-cloud collision (reflects timescale of collisions among molecular

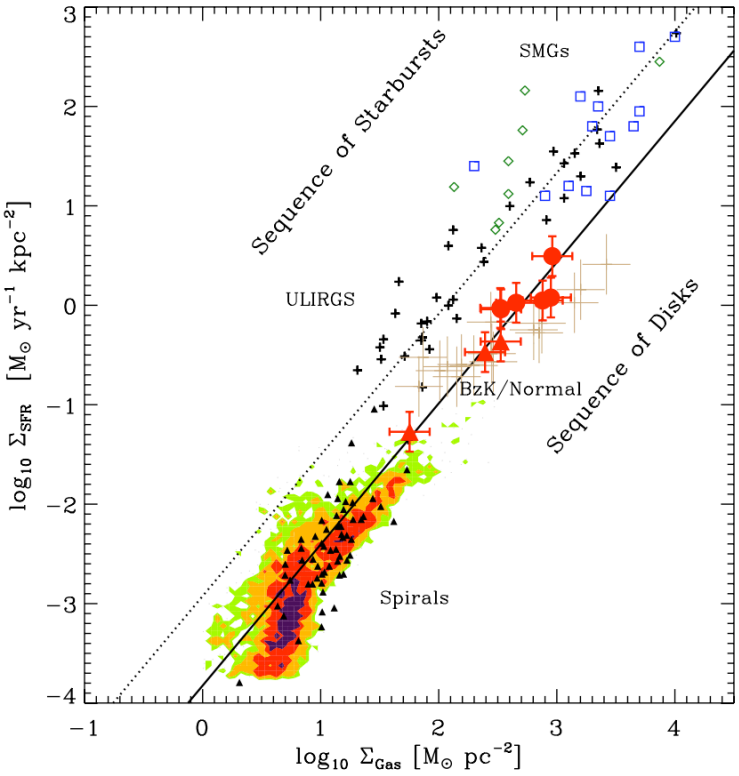

Figure 1.16: The Kennicutt–Schmidt relation for local and high-z galaxies (Daddi et al. 2010). The lower solid line is the result for local spiral galaxies, normal galaxies in $0.5 \lesssim z \lesssim 1.5$, and BzK galaxies. Its slope is 1.42. The upper dotted line is that for ultra-luminous infrared galaxies (ULIRGs) and submillimeter galaxies (SMGs).

clouds) (Habe and Ohta 1992).

This relation is appeared not only local galaxies but also higher-z (early Universe) galaxies. Daddi et al. (2010) showed that BzK galaxies and normal galaxies in the age of $0.5 \lesssim z \lesssim 1.5$ are on the extension of local, nearby spiral galaxies (figure 1.16). BzK galaxies are star-forming galaxies in $1.4 \lesssim z \lesssim 2.5$ which locate characteristic positions in the color-color diagram of B, z[13], and K bands (Cimatti et al. 2002; Daddi et al. 2004). Contrary, ultra-luminous infrared galaxies (ULIRGs) and submillimmeter galaxies (SMGs) which harbor more active star-formation shift upward by 0.9 dex on the K–S relation. They called these two phases "sequence of disks" and "sequence of starbursts".

The broken part of the color-shaded region at $\Sigma_{\rm gas} \sim 10\ M_\odot\ {\rm pc}^{-2}$ of figure 1.16 (the original result is by Bigiel et al. 2008) is supposed to be due to saturation of H I gas. Most of gas where its surface density is less than $10\ M_\odot\ {\rm pc}^{-2}$ is atomic phase. When $\Sigma_{\rm HI}$ exceeds the value, formation of H_2 is enhanced and stars form at solar metallicity (Krumholz et al. 2009a). Since SFR is independent of mass or surface density of H I gas, such brake of the K–S relation at $10\ M_\odot\ {\rm pc}^{-2}$ can be seen. Of course, value of $\Sigma_{\rm HI}$ to reach the saturation depends on not only metallicity but also strength of interstellar radiation field and gas number density (e.g., Elmegreen 1993).

The K–S relation is *broken down*, when the spatial resolution of used data is too high. Onodera et al. (2010) showed the scatter (tightness) of the relation depends on the spatial

[13] Note that z here is the name of a photometric band in near IR around $\lambda = 900$ nm, not redshift.

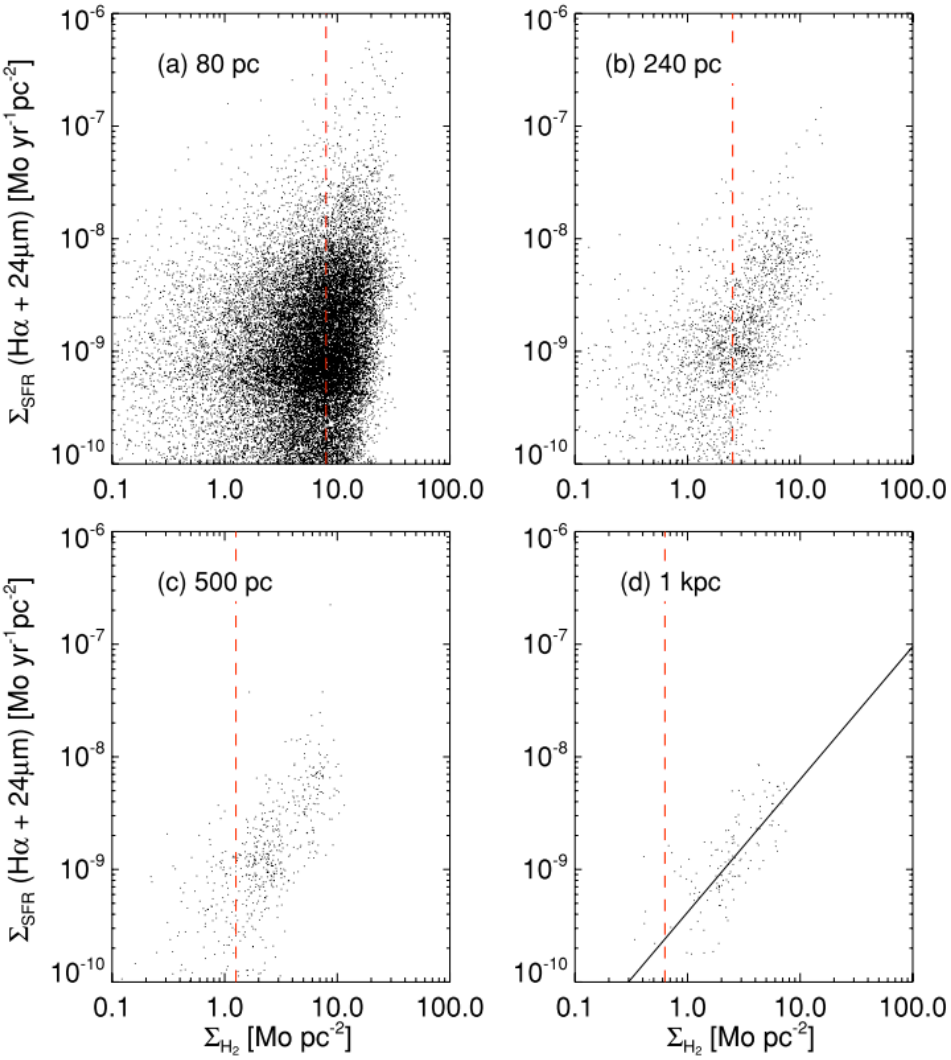

Figure 1.17: Dependence of the Kennicutt–Schmidt relation on spatial resolution of data (Onodera et al. 2010). Vertical red dashed lines represent $2\,\sigma$ sensitivity of molecular gas surface density.

resolution. Their results are shown in figure 1.17. When the resolution is $\gtrsim$ 500 pc, the K–S relation is tight and shows the clear tendency. However, it becomes ambiguous and scatter is larger and larger as the resolution gets better. At 80 pc resolution, the relation is completely disappeared. This is because sites of star formation and position of its natal gas is no longer the same and higher resolution can resolve this difference. According to their result, considering resolution is important to study the K–S relation, because it changes depending on the resolution.

Whereas the K–S relation using total gas, it is reported that when using only dense molecular gas, the relation shows linearity (Gao and Solomon 2004a, Gao and Solomon 2004b; Bigiel et al. 2016). Figure 1.18 shows the K–S relation for dense molecular gas. The horizontal axis is luminosity of emission line from rotational transition of HCN. Emission from this molecule can selectively observe dense molecular gas (see section 1.6.2 more detail). Similar results are seen based on dust extinction for molecular clouds in the Galaxy (e.g., Lada et al. 2010). These results suggest that tracers of molecular gas changes the result of the K–S relation.

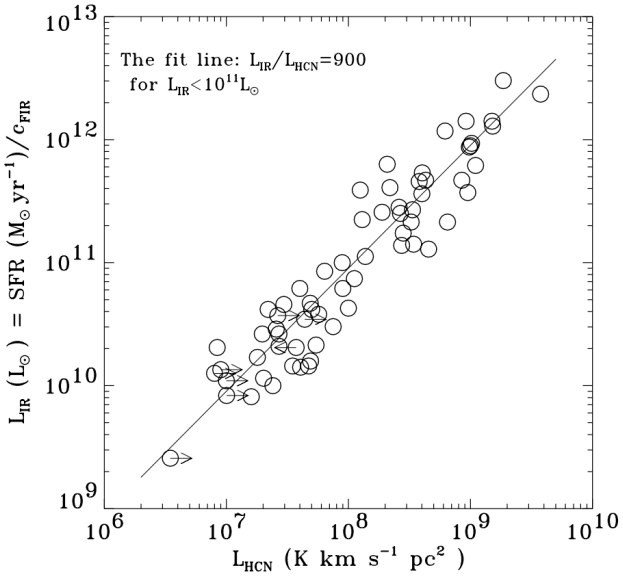

Figure 1.18: The Kennicutt–Schmidt relation using dense molecular gas (Gao and Solomon 2004b).

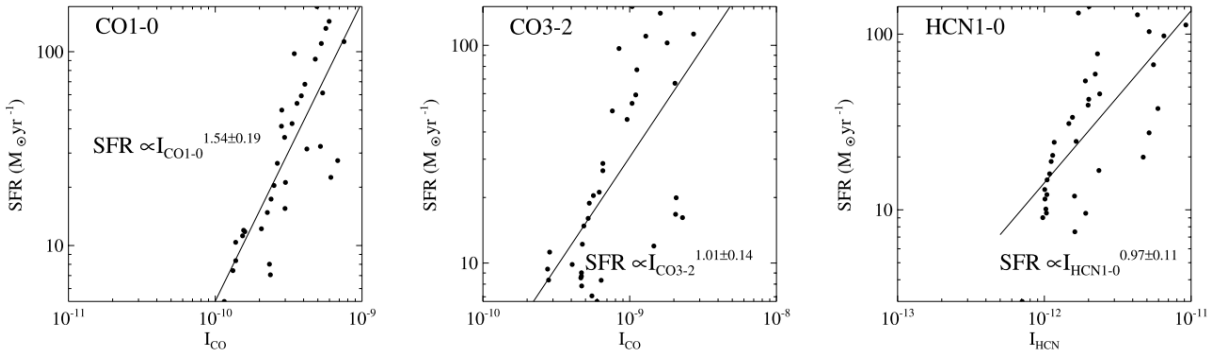

Figure 1.19: The Kennicutt–Schmidt relation from ^{12}CO($J=1$–0), ^{12}CO($J=3$–2), and HCN($J=1$–0) (Narayanan et al. 2008).

Not only HCN line as a dense molecular gas tracer, emission line from rotational transition of ^{12}CO at a higher excitation state also tends to produce a lower index of the K–S relation. Energy levels of ^{12}CO rotational transitions are described in section 1.4.1 more detail. Narayanan et al. (2008) showed that while the K–S relation is super linear when using ^{12}CO($J=1$–0), that from ^{12}CO($J=3$–2) is linear likewise HCN($J=1$–0) as reported by Gao and Solomon (2004b) (figure 1.19). In conjunction with their results, Bayet et al. (2009) reported that indices of the K–S relation gradually decrease as energy of rotational transitions increases as shown in figure 1.20. In fact, studies for the spatially resolved K–S relation using ^{12}CO($J=2$–1), which is the higher energy transition than ^{12}CO($J=1$–0) by one level argue that the linear relation rather than super linear (e.g., Bigiel et al. 2008; Leroy et al. 2008; Schruba et al. 2011; Leroy et al. 2013). These linear K–S relations may be due to usage of ^{12}CO($J=2$–1) as suggested by Momose et al. (2013). We should pay attention to properties of molecular gas traced by used emission line to study the K–S relation.

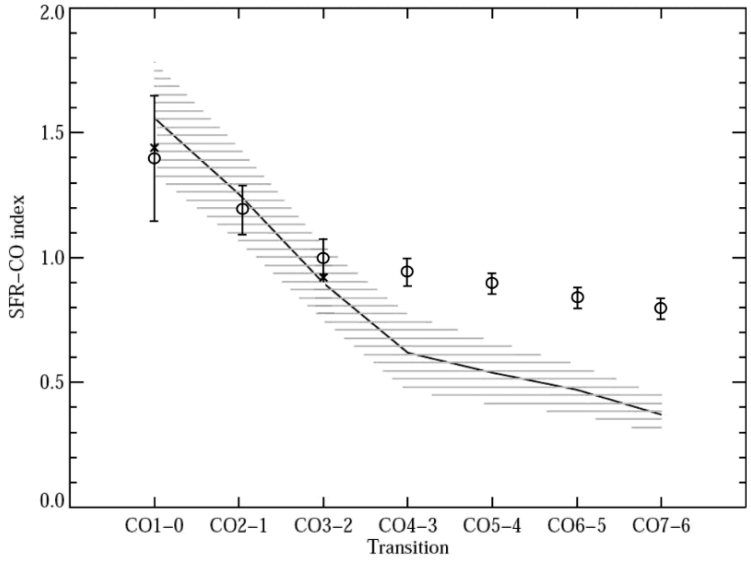

Figure 1.20: Indices of the Kennicutt–Schmidt relation as a function of ^{12}CO rotational transitions (Bayet et al. 2009). The gray shaded area and the black dashed line is the prediction by Narayanan et al. (2008).

1.3.3 Star formation seen in barred spiral galaxies

Barred spiral galaxies introduced in section 1.2.1 often show characteristic star formation. For example, Handa et al. (1991) reported that flux ratio of FUV to ^{12}CO($J = 1$–0) is much smaller in the bar than that in the center and spiral arms of the nearby barred spiral galaxy M 83. It indicates that star formation is passive, although molecular gas is rich. As another example, distribution of molecular gas and SFR in the barred spiral galaxy NGC 4303 are shown in figure 1.21 (Sun et al. 2018) and 1.22 (Yajima et al. 2019) in addition to the stellar images in figure 1.23. There are few newly born stars along the bar, while the amount of molecular gas is large (about the position of the bar, see the left panel of figure 1.23). Low SFR can be appeared in the composite image including emission lines from ions which trace star-forming regions as shown in the right panel of figure 1.23. Other barred spiral galaxies shows few star-forming regions in spite of rich molecular gas along the bar (e.g., Sheth et al. 2000; Sheth et al. 2002). This low activeness of star formation in the bar is often seen in relatively early-type ("b"–"c" of the Hubble sequence) barred spiral galaxies and more late-type barred spiral galaxies show active star formation along the bar (Phillips 1996).

Because of low SFR despite plenty of molecular gas in the bar, results for the bar is located at distinct positions compared to other regions of the disk such as spiral arms on the plot of the spatially resolved K–S relation. Figure 1.24 shows the spatially resolved K–S relation in NGC 4303 with color code of representative galactic regions (Momose et al. 2010). Markers for the bar shift toward the bottom right to those for arms in the plot, because $\Sigma_{\rm SFR}$ is lower and $\Sigma_{\rm H_2}$ is a little bit higher in the bar than in arms for this galaxy. Here, star-formation efficiency (SFE) is defined to express activeness of star-formation activity considering gas mass;

$$\left(\frac{\rm SFE}{\rm yr^{-1}}\right) \equiv \left(\frac{\Sigma_{\rm SFR}}{M_\odot\ {\rm yr^{-1}\ pc^{-2}}}\right) \Big/ \left(\frac{\Sigma_{\rm gas}}{M_\odot\ {\rm pc^{-2}}}\right). \tag{1.7}$$

The denominator of gas is usually referred as molecular gas + atomic gas or molecular gas only.

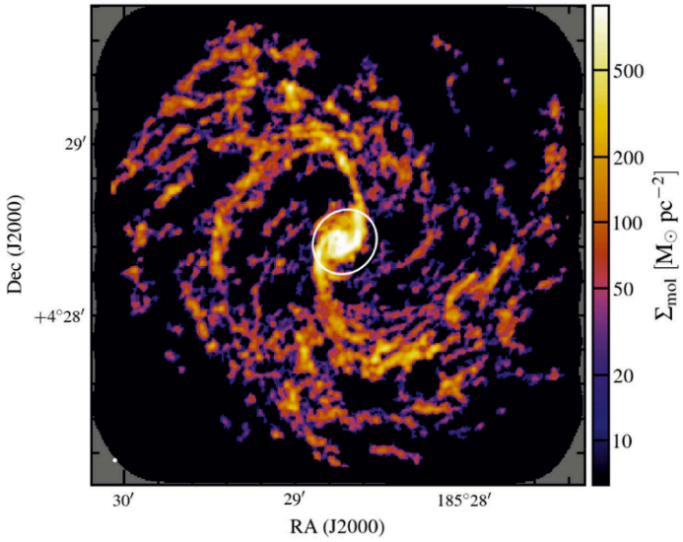

Figure 1.21: Distribution of molecular gas in NGC 4303 (Sun et al. 2018).

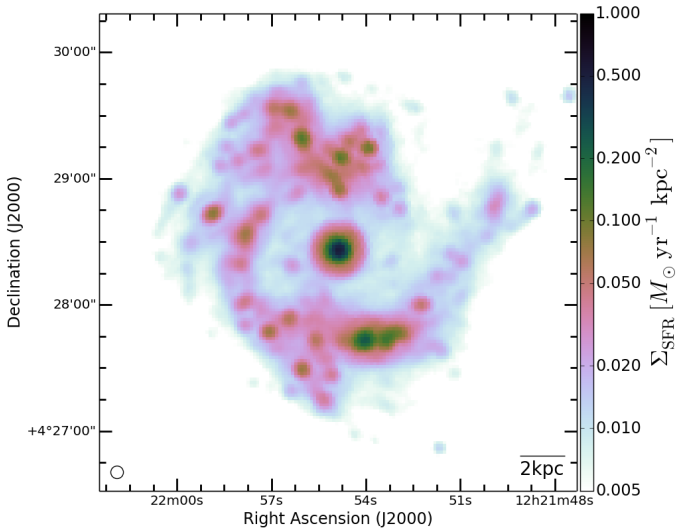

Figure 1.22: Distribution of SFR surface density in NGC 4303 (Yajima et al. 2019).

High SFE means stars form more efficiently per unit gas mass. The inverse number of SFE is also called "gas depletion time" which is usually denoted as $\tau_{\rm dep}$. Based on results of Momose et al. (2010), SFE in the bar is lower by 26% than the mean over the while disk and by 43% than the mean in arms. Lower SFE in the bar than in the center and arms is confirmed by many case-studies including for each barred galaxies including Momose et al. (2010) (e.g., M 83: Hirota et al. 2014, M 100: Pan and Kuno 2017; NGC 1300: Maeda et al. 2020b, NGC 2903: Muraoka et al. 2016, NGC 3627: Watanabe et al. 2011; Law et al. 2018, NGC 4303: Yajima et al. 2019, NGC 6946: Pan et al. 2015a, and Maffei 2: Yajima & Sorai 2021 in prep.).

Note that the definition of star-formation efficiency in the context of studies about star formation in the Galaxy is different from equation (1.7). Star-formation efficiency $\epsilon_{\rm SF}$ in the

Figure 1.23: (Left) Color composite image (B band around 450 nm is in blue and I band around 814 nm is in yellow) of NGC 4303 obtained with Hubble Space Telescope (HST). This image was retrieved from https://esahubble.org/images/potw1324a/ (credit: ESA/Hubble & NASA). (Right) The same as the left panel but including emission lines of ions (G band around 475 nm and [O III] emission line at 499 nm are in blue, R band around 625 nm is in green, [S II] line at 673 nm is in yellow, and I band around 775 nm and Hα line at 656 nm are in red) obtained with the Multi-Unit Spectroscopic Explorer (MUSE) mounted on Very Large Telescope (VLT). This image was retrieved from https://www.eso.org/public/images/eso2110b/ (credit: ESO/PHANGS). See also Emsellem et al. (2021) about the Physics at High Angular Resolution in Nearby GalaxieS (PHANGS)–MUSE survey.

context of studies within the Galaxy is

$$\varepsilon_{\rm SF} \equiv \frac{M_*}{M_{\rm gas} + M_*}, \tag{1.8}$$

where M_* is mass of newly born stars (young stellar objects; YSOs). Thus, *star-formation efficiency* in the context of extragalactic studies has the dimension of $(\text{time})^{-1}$ and that in the context of studies within the Galaxy is dimensionless.

These depressions of star formation in bars are supposed to be gas dynamics within it. Figure 1.25 (Regan et al. 1999) and 1.26 (Downes et al. 1996) show gas dynamics in a bar (figure 1.26 is gas dynamics of the specific bar of NGC 1530). Due to the non-axisymmetric gravitational-potential of a bar, gas loses its angular momenta (the potential of the bar transfers angular momenta of gas to the bar itself). As a result, gas accumulates in narrow lanes and falls into the galactic center through these lanes. Velocity of this inward motion is ~ 100 km s^{-1} (e.g., Reynaud and Downes 1998; Sorai et al. 2000) These lanes are called "offset ridges" of the bar. Since offset ridges are seen on the leading side to the rotation direction of a galaxy, they are also referred as "offset ridges at the leading side". They are visible in optical images of barred spiral galaxies as dust lanes (see figure 1.23). Along offset ridges, there is velocity gradient accelerating toward the center. This inflow gas can increase central concentration of molecular gas (e.g., Sakamoto et al. 1999; Kuno et al. 2007) and can also induce active star formation in centers (e.g., Sakamoto et al. 1999; Jogee et al. 2005; Schinnerer et al. 2006; Haan et al. 2009;

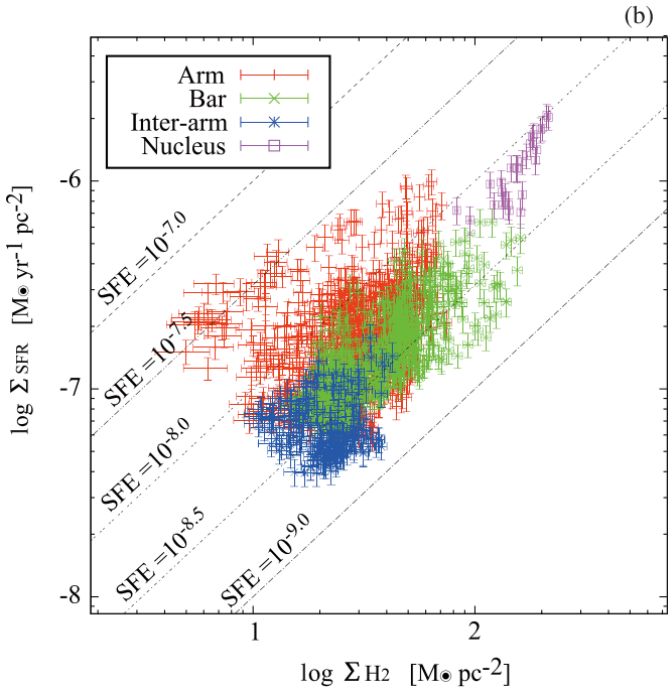

Figure 1.24: The spatially resolved Kennicutt–Schmidt relation in NGC 4303 and differences between galactic regions (Momose et al. 2010). Dashed-dotted lines from bottom left to top right indicate SFE is a constant.

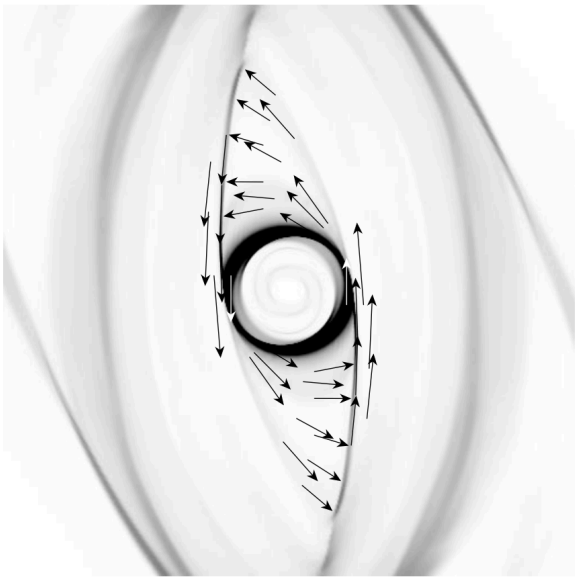

Figure 1.25: Direction of gas motion in a bar (Regan et al. 1999). The background gray scale is gas surface density.n

Muraoka et al. 2019).

Moreover, spraying gas from conjunctions of offset ridges and the inner ring pours on the other side of offset ridge (orbits through offset ridges and trace the outline of the bar is called "x_1 orbits" and those around the inner ring at the center of the bar is called "x_2 orbits";

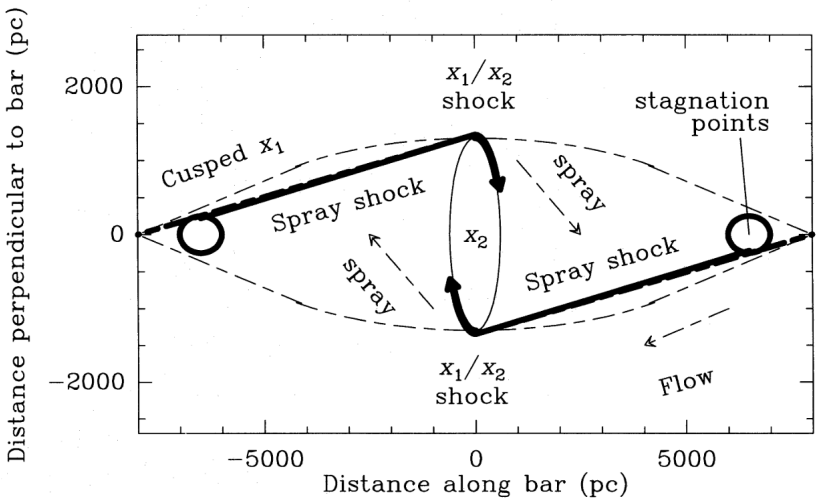

Figure 1.26: The schematic view of gas flows in the bar of NGC 1530 (Downes et al. 1996).

e.g., Athanassoula 1992a; 1992b). It forms shock fronts because spraying gas injects at a high velocity and direction of gas motion suddenly changes; gas in upstream of offset ridges has outward velocity-components but gas streams inward. This velocity jump is > 100 km s^{-1} (e.g., Reynaud and Downes 1998). It has been suggested that these strong non-circular motion such as shear by velocity gradient along bars, shock on offset ridges, and large velocity dispersion (sudden changes of velocity vector) prevent molecular gas from becoming dense and from forming stars (references above).

In addition to the violent gas dynamics which disturb star formation, galactic bars can promote star formation at the tip, or ends of the bar. Orbits of gas near bar ends is crossing to the self-orbit. Therefore, gas accumulates and stagnates at the position as shown in figure 1.26 (see also Blitz et al. 1993; Renaud et al. 2015). This stagnation increases probability of interactions among gas and can compress gas which triggers star formation. Also, radial gas motion affects star formation at bar ends. Figure 1.27 (Kohno et al. 2021b) shows the schematic view of gas motion and formation of dense gas and massive stars at the end of the bar in the Galaxy. As shown figure 1.25 and 1.26, velocity vectors of gas motion has the outward component in upstream of offset ridges. Because of it, gas from the bar and that on a circular orbit in the disk outside the bar collides. As a result, gas is effectively compressed and become dense and it can start massive-star formation. Not only the bar end of our Galaxy, but also other extragalaxies shows active star formation in their bar ends regions and bar-arm transition regions (e.g., M 83, NGC 1530, NGC 3627, NGC 4303).

According to these differences of star formation in barred spiral galaxies such as depression of SFR and SFE in the bar and intense star formation at bar ends, it is suggested that structures in galaxies alter properties of molecular gas. Furthermore, as its consequence, star formation activity varies from positions to position within galaxies, i.e., among regions of galaxies. Hence, barred spiral galaxies are a good laboratory to investigate factors for molecular gas which exert influences on star formation owing to intensive environments by bars. This is a motivation of studies for molecular gas in barred spiral galaxies.

Note that barred spiral galaxies *do not always* show low star formation activity. Some recent

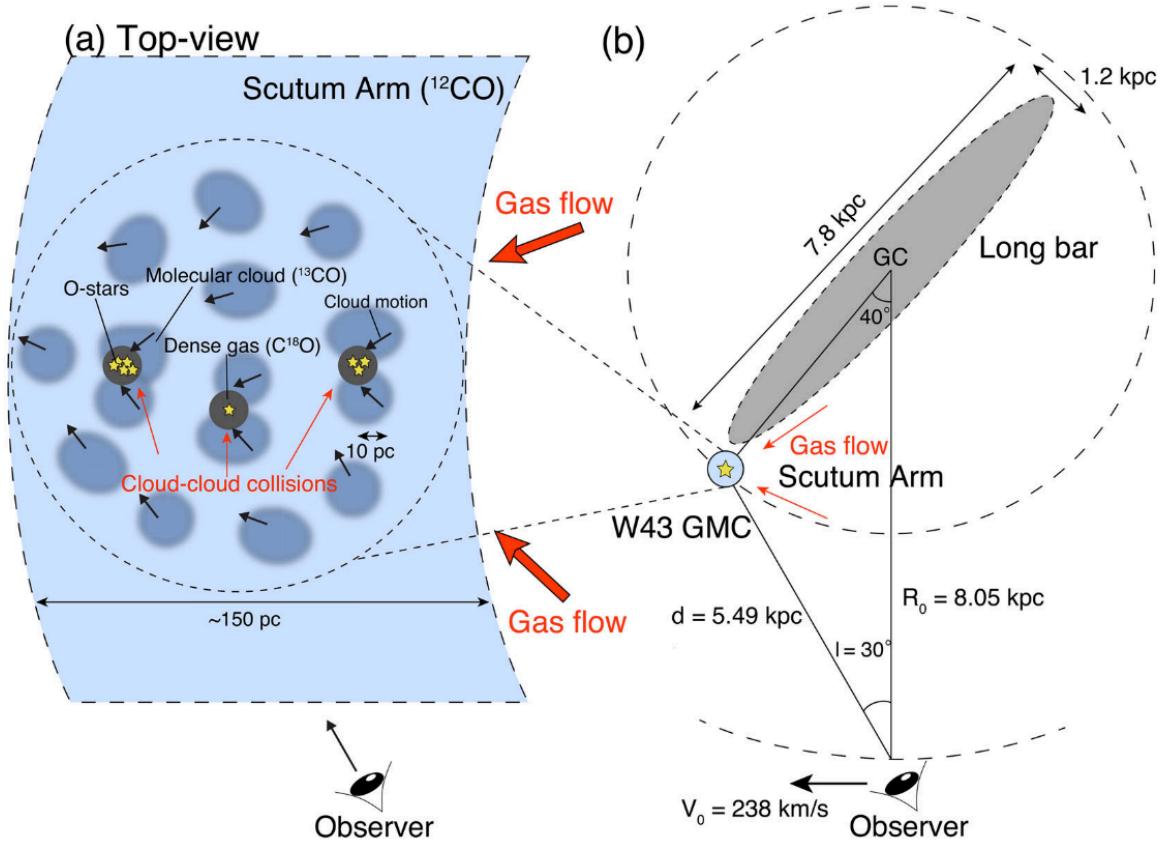

Figure 1.27: Schematic view of dense gas formation which leads to active star formation in the bar end of the Galaxy. (Kohno et al. 2021b). "GC" is Galactic Center, "Scutum Arm" is a spiral arm of the Galaxy, and W43 is a massive-star-formation region found at the end of the Galactic bar. The Galactic bar is denoted as the gray ellipse. Directions of gas motion are denoted as red arrows.

surveys with statistical analysis for a number of barred galaxies suggest that effects of bars are limited to star formation. For example, Díaz-García et al. (2021) observed molecular gas along bars in 12 strongly barred spiral galaxies with Institut de Radioastronomie Millimétrique (IRAM) 30 m telescope. They argued not all strong bars prefer inhibit of star formation, although SFE tends to be low in bars for massive barred galaxies. In addition, Querejeta et al. (2021b) reported that there is no statistically significant differences of SFR and molecular gas depletion time between arms and bars using PHANGS–ALMA samples (Leroy et al. 2021c).

1.4 Physical processes of radiation from molecules and atoms in interstellar medium

Prior to describing molecular gas, I introduce physics of radiation processes from molecules and atoms in ISM. Emission from them is direct observable quantities and probes for ISM including molecular gas.

1.4.1 Energy levels of rotational transition of molecules

Molecular gas can be observed from emission lines from rotational transitions of molecules. This is because energy gaps for rotational transition is the lowest than those for vibration of molecules and transitions of electrons, and molecular gas is cold. That is, molecules cannot emit radiation by vibrational transition and electronic transitions because of low energy in cold molecular gas.

In classical mechanics, rotating energy $E_{\rm rot}$ can be expressed by

$$E_{\rm rot} = \frac{L^2}{2I}, \tag{1.9}$$

where L is angular momentum and I is moment of inertia. Go on to quantum mechanics, the Hamiltonian of the rotator $\hat{\mathcal{H}}_{\rm rot}$ for a rotating molecule can be written as

$$\hat{\mathcal{H}}_{\rm rot} = \frac{\hat{\boldsymbol{L}}^2}{2I}, \tag{1.10}$$

where $\hat{\boldsymbol{L}}$ is the operator of angular momentum;

$$\hat{\boldsymbol{L}}^2 = -\hbar^2 \left[\frac{1}{\sin\theta} \frac{\partial}{\partial\theta} \left(\sin\theta \frac{\partial}{\partial\theta} \right) + \frac{1}{\sin^2\theta} \frac{\partial^2}{\partial\varphi^2} \right], \tag{1.11}$$

and $\hbar$ is the reduced Planck constant. The energy eigenvalue E_J of the system is

$$\begin{aligned} \hat{\mathcal{H}}_{\rm rot} \left| J, M \right\rangle &= E_J \left| J, M \right\rangle & (1.12)\\ &= \frac{\hbar^2 J(J+1)}{2I} \left| J, M \right\rangle & (1.13)\\ &= hBJ(J+1) \left| J, M \right\rangle, & (1.14) \end{aligned}$$

where $|J, M\rangle$ is the eigenstate which have the angular momentum quantum number J and the magnetic quantum number M, h is the Planck constant. B is called "the molecular rotation constant" which is defined as

$$B \equiv \frac{h}{8\pi^2 I}. \tag{1.15}$$

The energy difference $\Delta E_{J+1,J}$ is

$$\begin{aligned} \Delta E_{J+1,J} &\equiv E_{J+1} - E_J & (1.16)\\ &= \frac{\hbar^2}{I}(J+1). & (1.17) \end{aligned}$$

According to equation (1.17), the energy difference and rest frequency of emission line $\nu_{\rm rest} = \Delta E_{J+1,J}/h$ becomes larger and larger by a factor of $J+1$ as the excitation level increases as shown in figure 1.28 and table 1.2.

^{12}CO is the third abundant molecule followed by molecular hydrogen and helium, although its abundance ratio to H_2, $[^{12}{\rm CO}]/[{\rm H_2}]$, is $\sim 10^{-4}$ (e.g., Frerking et al. 1982; Langer et al. 1989; Pineda et al. 2008). The first excited state $J=1$ of ^{12}CO corresponds to only ~ 5.5 K, which is cooler or comparable to temperature of cold molecular gas. Therefore, ^{12}CO is easily excited to this level even in cold molecular gas and emit radiation as emission line. Here, emission line by transition of $J=1$–0 is denoted as "$^{12}{\rm CO}(J=1\text{–}0)$" (already appeared in section 1.3.2) whose $\nu_{\rm rest}$ is 115.271202 GHz. Although corresponding temperatures of energy levels for $J \geq 2$ are relatively higher than the typical temperature of molecular gas, these gaps are not too

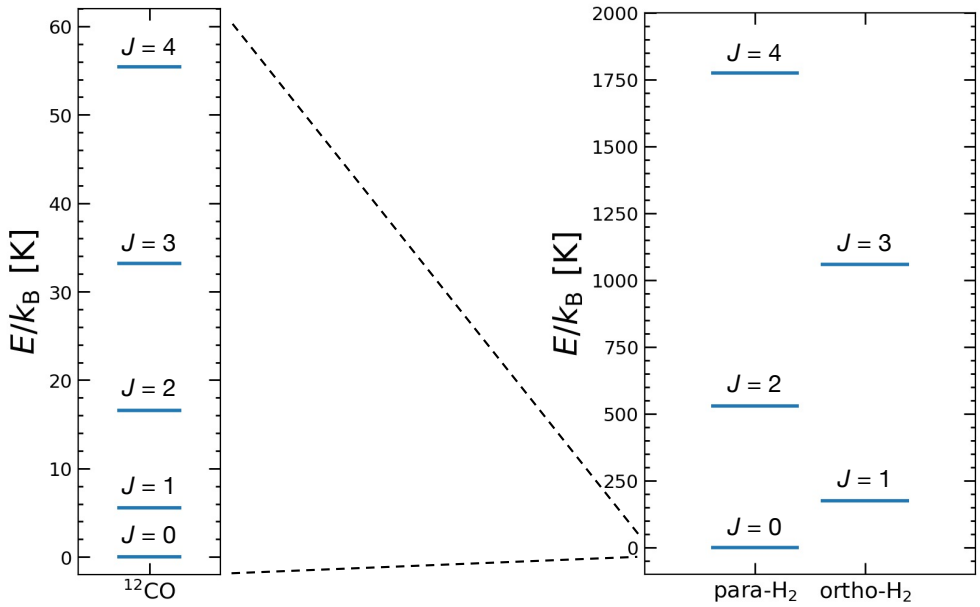

Figure 1.28: Energy levels of rotational transitions for ^{12}CO and H_2. Note that the typical temperature of molecular gas is $\sim$ 10–30 K.

Table 1.2: Rotational energy level of H_2 ($v = 0$ case) and ^{12}CO.

	^{12}CO				H_2			
Level	$J=1$	$J=2$	$J=3$	$J=4$	$J=1$	$J=2$	$J=3$	$J=4$
Energy E/k_B [K]	5.54	16.6	33.2	55.4	177	530	1060	1770

high to excite ^{12}CO. Thus, ^{12}CO($J=2$–1) ($\nu_{\rm rest}$ is 230.538000 GHz) and ^{12}CO($J=3$–2) ($\nu_{\rm rest}$ is 345.795990 GHz) are also observed in cold molecular gas, while these lines is usually weaker than ^{12}CO($J=1$–0) except for extreme environments such as massive-star forming regions, galactic centers, and starburst galaxies.

The energy difference between the ground state of the vibration and the first excited state is much larger than that of the rotational transition (for CO molecule, the energy difference of $v=1$–0 is larger by approximately 500 times than that of $J=1$–0 in $v=0$). Therefore, emission of the vibrational transition cannot be observed in the ISM which is a raw material of stars. It can be observed only in high temperature environment such as circumstellar medium and circumnuclear disk of active galactic nuclei (AGNs).

1.4.2 Emission of rotational transitions as an electric dipole radiation

Strictly speaking, emission lines from rotational transition of molecules are produced by perturbation of different eigenstates and electromagnetic field with the electric dipole moment in a molecule. In other words, radiation from rotational transitions are a kind of that from an electric dipole moment. Therefore, I describe emission of rotational transitions considering an electric dipole moment

Considering the electric dipole moment $\boldsymbol{p}$ which consists of two particles charged q at the displacement vector $\boldsymbol{d}$ ($\boldsymbol{p} = q\boldsymbol{d}$) rotating at the angular velocity ω, mean radiant power $\langle P \rangle$

averaged over one period is

$$\langle P \rangle = \frac{\omega^4 |\boldsymbol{p}|^2}{12\pi\varepsilon_0 c^3} \tag{1.18}$$

from electromagnetism, where ε_0 is the dielectric constant of vacuum[14)], c is the speed of light. Using mean electric dipole moment $\boldsymbol{\mu} = \boldsymbol{p}/2$ of the system, equation (1.18) becomes

$$\langle P \rangle = \frac{\omega^4}{3\pi\varepsilon_0 c^3} |\boldsymbol{\mu}|^2. \tag{1.19}$$

Thus, the mean energy of the rotational transition $J+1 \to J$, $P_{J+1,J}$ can be similarly written as

$$\langle P_{J+1,J} \rangle = \frac{\omega^4}{3\pi\varepsilon_0 c^3} |\boldsymbol{\mu}_{J+1,J}|^2, \tag{1.20}$$

where $\boldsymbol{\mu}_{J+1,J}$ is the electric dipole moment of the transition $J+1 \to J$, which can be calculated as

$$\boldsymbol{\mu}_{J+1,J} = \langle \psi_J | \, \hat{\boldsymbol{\mu}} \, | \psi_{J+1} \rangle \tag{1.21}$$

where $\hat{\boldsymbol{\mu}}$ is the electric dipole moment operator, $|\psi_J\rangle$ and $|\psi_{J+1}\rangle$ is the eigenstate of level J and $J+1$, respectively. Since $\omega = 2\pi\nu$ and $\boldsymbol{\mu}_{J+1,J} = \sqrt{(J+1)/(2J+3)}\boldsymbol{\mu}$, equation (1.20) becomes

$$\langle P_{J+1,J} \rangle = \frac{16\pi^3\nu^4}{3\varepsilon_0 c^3} \frac{J+1}{2J+3} \mu^2. \tag{1.22}$$

This is the mean radiant power from a molecule with the electric dipole moment μ of the transition $J+1 \to J$ per unit time.

Here, we introduce the Einstein's A coefficient $A_{J+1,J}$. It is defined as the probability of transition from the level $J+1$ to J for one molecule per unit time. Since the time-averaged radiant energy $\langle P_{J+1,J} \rangle$ can be represented as equation (1.22) and a photon has the discrete energy $h\nu$, the number of photons emitted from a molecule via the transition in unit time (i.e., the probability of the transition) is

$$A_{J+1,J} = \frac{\langle P_{J+1,J} \rangle}{h\nu} \tag{1.23}$$

$$= \frac{16\pi^3\nu^3}{3\varepsilon_0 h c^3} \frac{J+1}{2J+3} \mu^2. \tag{1.24}$$

Since $A_{J+1,J} \propto \nu^3 (J+1)\mu^2/(2J+3)$, it depends on only species and transitions of the molecule. It represents the probability of simultaneous emission per unit time.

According to equation (1.22) and (1.24), it is deduced that molecules whose μ is zero such as homonuclear diatomic molecules cannot radiate energy as an electric dipole. Accordingly, H_2 molecule, which is the most abundant species in molecular gas cannot be observed as the electric dipole radiation. Instead, it can emit energy as the electric quadrupole moment radiation. However, emission from an electric quadrupole radiation is much weaker than that from a dipole. It stands for higher energy level (difficult to excite) in quantum mechanics. The lowest energy level of para-H_2 (spins of the two protons are antiparallel) is $\sim$ 530 K and that of ortho-H_2 (spins of the two protons are parallel) is $\sim$ 883 K (note that $J = 0,\ 2,\ 4\ \ldots$ for para-H_2 and $J = 1,\ 3,\ 5,\ \ldots$ for ortho-H_2, because the selection rule for the quadrupole is $\Delta J = \pm 2$, whereas that for the dipole is $\Delta J = \pm 1$; see figure 1.28). Temperatures of excited energy levels for H_2 is

[14)] The form of this equation is in the MKS unit case. In the CGS system, $\varepsilon_0 = 1/4\pi$

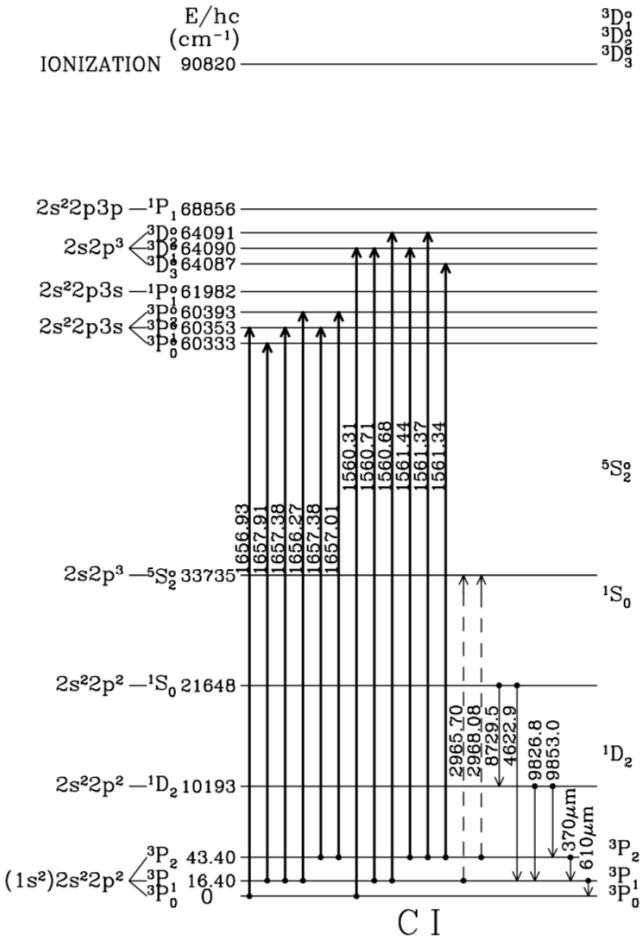

Figure 1.29: Energy levels and corresponding wavelength of of C I (Draine 2011).

much higher than the typical temperature of molecular gas. Emission from H_2 is observable only from warm gas surrounding massive-star forming regions, for example. On the other hand, CO molecules have electric dipole moment ($^-C \equiv O^+$)[15]. Hence, emission line from ^{12}CO, especially $^{12}CO(J=1\text{–}0)$ is used as a tracer of molecular gas instead of H_2 with reasons of easily excited, easily observed for ^{12}CO emission lines.

H_2 transition in the lowest energy level is 0–0 S(0) (corresponding $\sim$ 530 K). Here "0–0" indicates transition of vibration and "S(0)" indicates transition of $J=2\text{–}0$, i.e., $(v=0, J=2) \rightarrow (v=0, J=0)$. In general, a transition of $(v=v_u, J=J_u) \rightarrow (v=v_l, J=J_l)$ is denoted as "v_u–v_l S(J_l)" when $J_l = J_u - 2$, "v_u–v_l Q(J_l)" when $J_l = J_u$, and "v_u–v_l O(J_l)" when $J_l = J_u + 2$. Therefore, H_2 transition of $(v=1, J=3) \rightarrow (v=0, J=1)$ which is often observed at 2.1 μm is denoted as "1–0 S(1)".

[15] CO is in the resonance of $^-C \equiv O^+$, C = O, and $^+C - O^-$, and the first one is dominant because of stability. Therefore, mean electric dipole moment of CO is C→O, whereas electronegativity of oxygen is higher than that of carbon.

1.4.3 Emission by fine structure and hyperfine structure

In ISM, emission line by fine structure of atomic carbon is also observed. The lowest energy transition is [C I] ($^3P_1 \to {}^3P_0$)[16] ($\nu_{\rm rest}$ is 492.1607 GHz). Here, "3" in top left is multiplicity of total spin angular momentum of electrons in the outermost subshell, $2S+1$ (S is the total spin of outer most electrons). In this case, spin angular momenta for two electrons in the $2p$ subshell is the same (carbon's electron configuration is $1s^2 2s^2 2p^2$). "P" means total orbital angular momentum number L is 1 (S for $L=0$, P for $L=1$, D for $L=2$ like name of subshells). The number of subscript is the total angular momentum $J = |\boldsymbol{L}+\boldsymbol{S}|$. That is, the transition of atomic carbon above is $(J,L,S) = (1,1,1) \to (0,1,1)$[17]. This notation is called "term symbol" and assumes the LS coupling (Russell–Saunders coupling). Figure 1.29 shows energy levels of C I.

As mentioned in section 1.1, H I gas is observed with the 21 cm line ($\lambda_{\rm rest}$ is 21.106114 cm; $\nu_{\rm rest}$ is 1420.405752 MHz). It is produced by the hyperfine structure for the atomic hydrogen. The energy split ΔE by the interaction with spin of electron and that of atomic nucleus can be expressed as

$$\Delta E = g(I)\frac{m_e}{m_p}\frac{chR\alpha^2}{n^3}\left[\frac{F(F+1)-I(I+1)-J(J+1)}{J(J+1)(2L+1)}\right], \tag{1.25}$$

where $\boldsymbol{J} = \boldsymbol{L}+\boldsymbol{S}$ is total spin of electrons, $\boldsymbol{I}$ is total spin of atomic nucleus, $\boldsymbol{F} = \boldsymbol{J}+\boldsymbol{I}$ is total spin of atom, $g(I)$ is g-factor for atomic nucleus (in this case, proton), m_e is mass of electron, m_p is that of proton, R is the Rydberg constant, α is the fine-structure constant, and n is principal quantum number. For atomic hydrogen at the ground state, ΔE between $F=1$ (spins of proton and electron are parallel) and $F=0$ (spins of proton and electron are antiparallel) is

$$\Delta E = \frac{8}{3}g(I)\frac{m_e}{m_p}\frac{chR\alpha^2}{n^3}, \tag{1.26}$$

since $L=0$, $S=1/2$, $J=1/2$, $I=1/2$, and $n=1$. It corresponds to the wavelength of ~ 21 cm.

1.5 Molecular clouds

1.5.1 Basic view of molecular clouds

Molecular gas is distributed as cloud-like structures. They are called "molecular clouds". Figure 1.30 and 1.31 show distributions of molecular gas in the Galaxy and nearby galaxies at high resolution. They show that molecular gas is not widely and extendedly but unevenly distributed as the cloud-like form. Their typical size of molecular clouds ranges $\sim$ 1–100 pc. Mass ranges from 10^3–10^6 up to $\sim 10^7\ M_\odot$. Large and massive clouds ($\gtrsim$ a few $\times$ 10 pc, $\gtrsim 10^4\ M_\odot$) are usually called "giant molecular clouds" (GMCs). More massive and larger structures than GMCs are referred to as "giant molecular cloud associations" (GMAs). In contrast, small and less massive clouds than GMCs are called "dark clouds". These properties are summarized in Goldsmith (1987).

As shown in figure 1.30, molecular clouds are mainly distributed on the midplane of galactic disks (usually within the width of $|z| \lesssim 50$ pc). In addition, they trace galactic structures such

[16] Sometimes simply denoted as "[C I]($J=1$–0)."
[17] Note that $J = L+S, L+S-1, \ldots, |L-S|$.

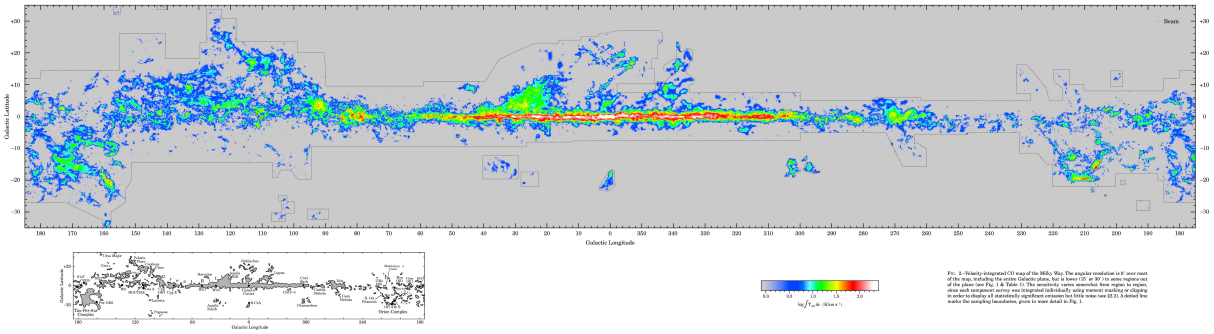

Figure 1.30: Distribution of ^{12}CO($J=1$–0) integrated intensity in the all area of in the Galaxy (Dame et al. 2001).

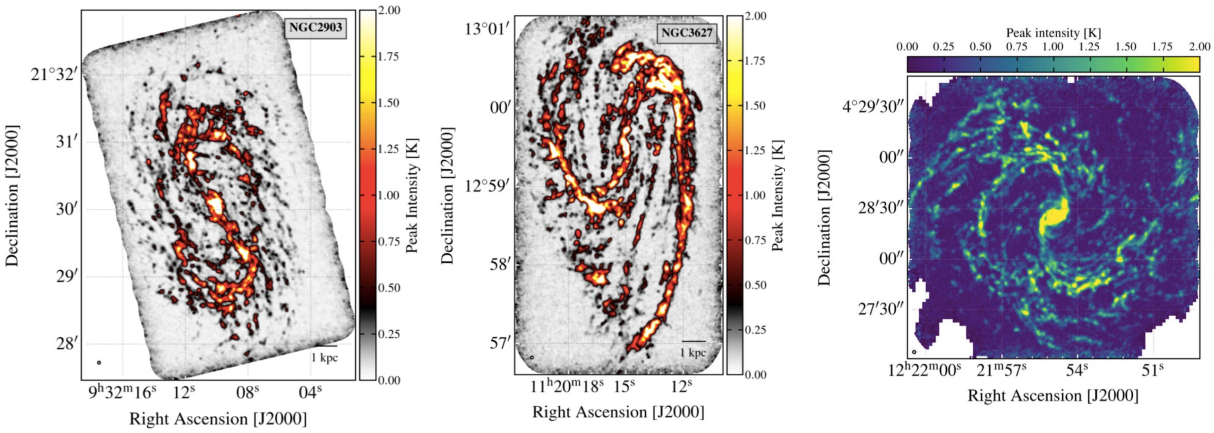

Figure 1.31: Distribution of ^{12}CO($J=2$–1) peak intensity in nearby galaxies at high resoution (left: NGC 2903, center: NGC 3627, right: NGC 4303). Left and center panels are from Leroy et al. (2021c) and the right panel is from Leroy et al. (2021a). See also figure 1.21.

as spiral arms, bars on the top-down view of galactic disks like figure 1.31. Massive GMCs prefer such galactic structures. Figure 1.32 shows dependence of distributions on mass of GMCs in the spiral galaxy M 51 (Miyamoto et al. 2014). Massive GMCs whose mass is $\gtrsim 10^6\ M_\odot$ usually located on spiral arms. On the other hand, less massive GMCs than those are uniformly distributed in the disk including inter-arm (see also Koda et al. 2009). According to these results, it is supposed that molecular clouds are collected by structures and grow up by agglomeration within them (e.g., Koda et al. 2016). In the outside of structures such as inter-arm, shear is strong, so that massive and large molecular clouds are destroyed, while small and less massive ones can be survived (e.g., Miyamoto et al. 2014; Pettitt et al. 2018). Also, in such low column density environments, the self-shielding of hydrogen is not effective. Therefore, H_2 molecule is easily dissociated by interstellar and circumgalactic emission.

Incidentally, the unit of peak intensity is "K" in figure 1.31. This is because the unit of radio intensity is described as temperature. According to the Planck function

$$B_\nu(\nu, T) = \frac{2h\nu^3}{c^2} \frac{1}{\exp\left(h\nu/k_\mathrm{B}T\right) - 1}, \tag{1.27}$$

temperature T is uniquely determined at any intensity with a given frequency, because

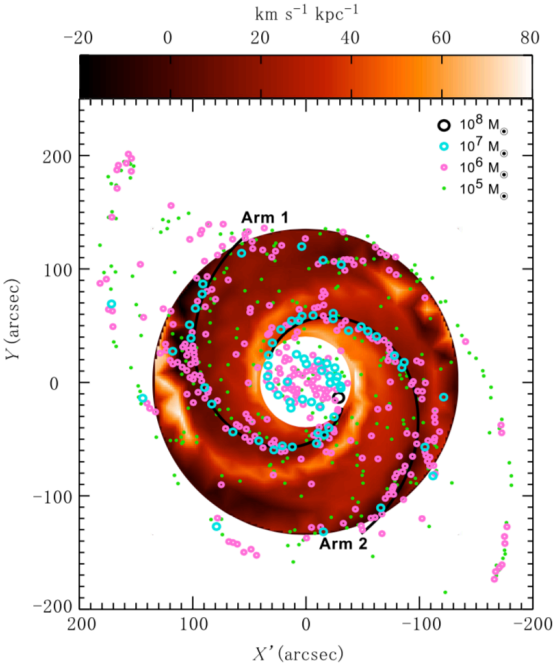

Figure 1.32: Dependence of distribution of giant molecular clouds on their mass in spiral galaxy M 51 (Miyamoto et al. 2014). Two spiral arms are shown as solid black curves. The background color scale shows strength of shear.

$\partial B_\nu / \partial T > 0$. Especially, temperature corresponds to intensity one by one in the Rayleigh–Jeans limit ($h\nu / k_\mathrm{B} T \ll 1$) as described by

$$B_\nu \simeq \frac{2\nu^2 k_\mathrm{B} T}{c^2}. \tag{1.28}$$

Since the Rayleigh–Jeans approximation is conventionally valid in radio astronomy, expressing radio intensity in temperature has been widely used. This temperature scale representing radio intensity is referred to as "brightness temperature".

1.5.2 Fundamental relations for molecular clouds

Early stage observations toward molecular clouds in the Galaxy (e.g., Scoville et al. 1987; Solomon et al. 1987) revealed fundamental relations of molecular clouds. One is the relation between size and line width of molecular clouds. Figure 1.33 shows the relation. It is described as

$$\sigma_v \propto \sqrt{S}, \tag{1.29}$$

where σ_v is velocity dispersion of molecular clouds along the line of sight (i.e., one dimensionon) and S is the size of molecular clouds. Thus, more larger molecular clouds have more larger velocity dispersion. This relation was originally discovered by Larson (1981), so these are also called "the Larson's scaling relation".

As shown in figure 1.33 velocity dispersion of molecular clouds of a few km s^{-1} is much larger than that expected from the Maxwell distribution at its temperature ($\sim$ 10 K) for molecular hydrogen ($\sim$ 0.3 km s^{-1}). It is understood that observed velocity dispersion of molecular clouds

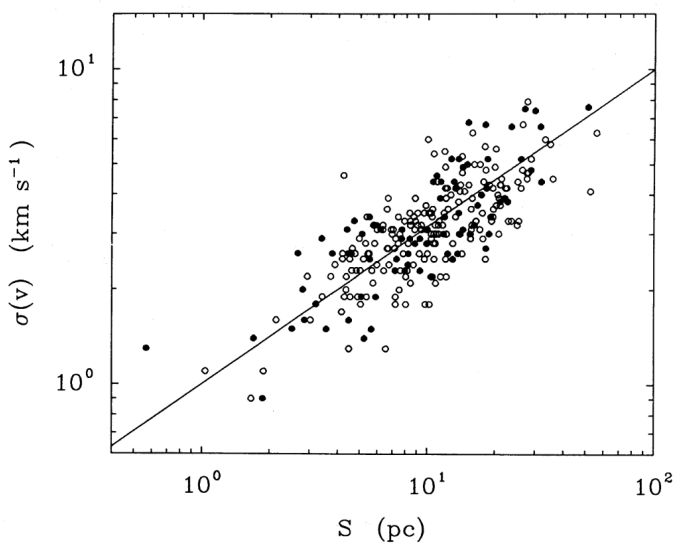

Figure 1.33: The relation between size and line width of molecular clouds in the Galaxy (Solomon et al. 1987). Solid markers are molecular clouds whose distance is determined with reliability and open markers are not. The solid line indicates $\sigma(v) \propto \sqrt{S}$.

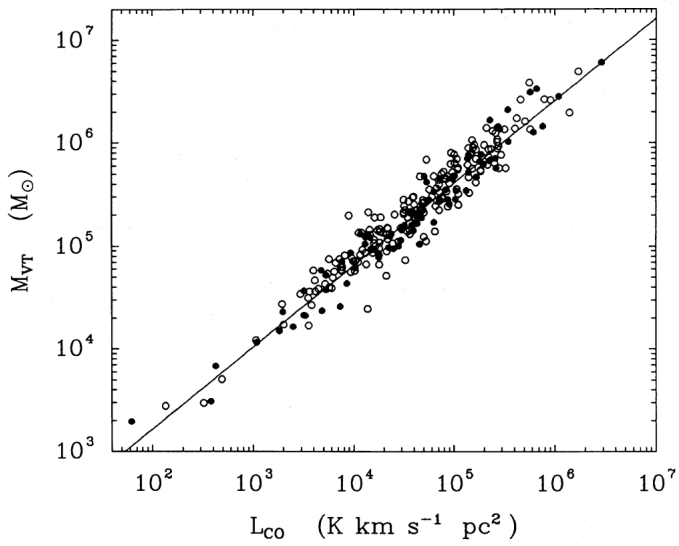

Figure 1.34: The relation between virial mass and luminosity of molecular clouds in the Galaxy (Solomon et al. 1987). Markers are the same as figure 1.33. The solid line indicates $M_{\rm VT} \propto L_{\rm CO}^{0.81}$.

are due to turbulence of gas. As a main mechanism to generate turbulence, explosions of supernovae has been suggested (e.g., Koyama and Ostriker 2009; Hennebelle and Falgarone 2012).

The second fundamental relation is one between virial mass and luminosity[18)] of ^{12}CO line. Figure 1.34 shows it. Here, virial mass is the mass estimated from the virial equilibrium. Virial equilibrium is achieved in self-gravitating systems, i.e., inward force by its gravity and

[18)] Luminosity in astronomy and astrophysics is defined as the total radiant energy from an object enclosing the all solid angle 4π sr per unit time. Thus, its unit has the same dimension of "W". In contrast, luminosity of emission line is defined as the product of velocity-integrated intensity and its emitting area. Therefore, its unit is "K km s^{-1} pc^2".

outward force by internal energy and pressure are balanced. In this case, kinetic energy T and gravitational potential energy W of the system satisfy the following condition;

$$2T + W = 0. \tag{1.30}$$

From line width of emission line, T can be estimated and as a result, mass can be derived from W. Its mass, or virial mass $M_{\rm vir}$ ($M_{\rm VT}$ in figure 1.34) is expressed as

$$M_{\rm vir} = \frac{3(5-2k)}{G(3-k)}{\sigma_v}^2 R, \tag{1.31}$$

where G is the gravitational constant, R is radius of a cloud, and k is power-law index of volume density along the radius of a cloud; $\rho \propto r^{-k}$ (Solomon et al. 1987; MacLaren et al. 1988; Bertoldi and McKee 1992; Bolatto et al. 2013b). Solomon et al. (1987) (the result of figure 1.34) adopted $k = 1$.

Figure 1.34 suggests that there is a relatively linear relation between virial mass and luminosity of ^{12}CO. Since molecular clouds are considered to be self-gravitating objects, this relation indicates a conversion factor from luminosity of ^{12}CO line into mass of molecular clouds; the CO-to-H_2 conversion factor (Bolatto et al. 2013b). Solomon et al. (1987) also considered that emission from a cloud is not absorbed by the foreground cloud along the line of sight because of their different receding velocity (i.e., the Doppler effect) and observed luminosity of ^{12}CO is proportional to number of clouds, or molecular gas mass. This is sometimes referred to as "mist model" of molecular clouds (see also Dickman et al. 1986).

These two fundamental relations have been updated by later observations. Bolatto et al. (2008) reported the similar size–line width relation for molecular clouds in nearby and the Local Group galaxies found in the Galaxy ($\sigma_v \propto r^{0.6\pm0.1}$). Leroy et al. (2015) compiled their result and other studies of the relation. Figure 1.35 shows it. They argued that velocity dispersion of molecular clouds largely varies depending on galaxies and environments (disk or galactic center), however, it roughly follow the size–line width relation of $\sigma_v \propto r^{0.5}$.

For the virial mass–^{12}CO luminosity relation, Bolatto et al. (2008) found the almost linear relation ($M_{\rm vir} \propto L_{\rm CO}^{1.00\pm0.04}$) for nearby and the Local Group galaxies. Donovan Meyer et al. (2013) conducted the survey toward nearby galaxies as the CArma and NObeyama Nearby galaxies (CANON) survey (Koda et al. 2011) and also found the relation between virial mass and ^{12}CO luminosity which is the close to linear ($M_{\rm vir} \propto L_{\rm CO}^{1.11\pm0.29}$). These results are shown in figure 1.36. They support the existence that there is a factor which converts ^{12}CO luminosity or integrated intensity into molecular gas mass and its column density along a line of sight. Similar relations found in the Galaxy and extragalaxies (see also Hirota et al. 2011; Rebolledo et al. 2012; Colombo et al. 2014; Faesi et al. 2018; Hirota et al. 2018) suggest that molecular clouds may be rather universal objects (see also Young and Scoville 1991; Fukui and Kawamura 2010) as mentioned by Bolatto et al. (2008).

1.5.3 CO-to-H_2 conversion factor to derive molecular gas mass

As previously seen, an important physical quantity of molecular clouds is mass (of course mass is the fundamental quantity in any fields of science). According to the almost linear relation between virial mass and luminosity of ^{12}CO line, mass of molecular clouds (gas) and column

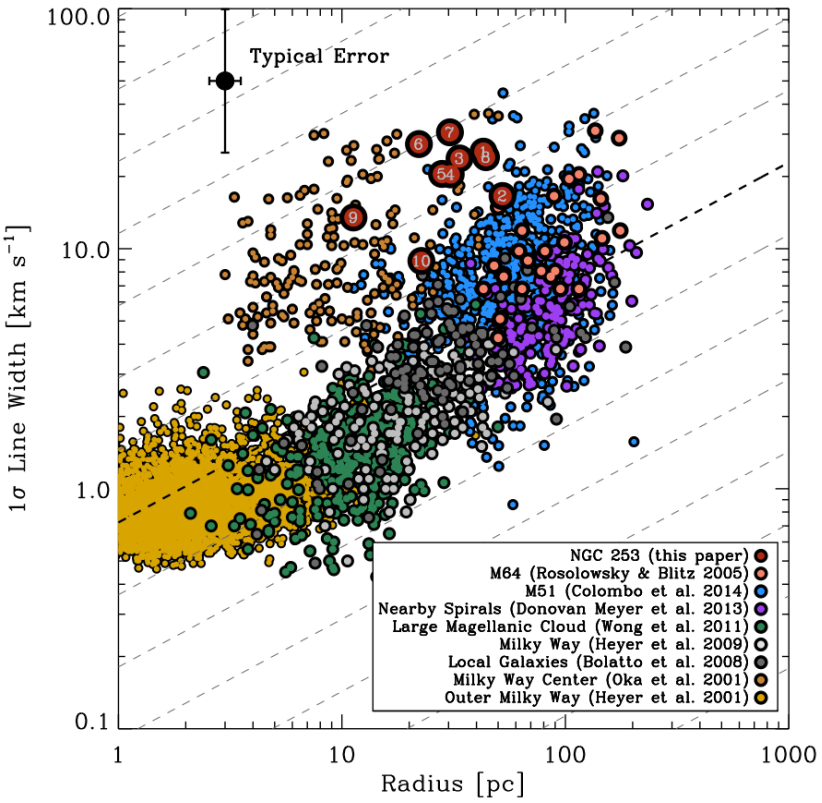

Figure 1.35: The relation between size and line width of molecular clouds found in the Galaxy and nearby galaxies (Leroy et al. 2015). Results of other studies (Rosolowsky and Blitz 2005; Colombo et al. 2014; Donovan Meyer et al. 2013; Wong et al. 2011; Heyer et al. 2009; Bolatto et al. 2008; Oka et al. 2001; Heyer et al. 2001) are also compiled. Dashed lines indicate $\sigma \propto \sqrt{r}$.

density of molecular gas can be derived from luminosity of ^{12}CO line, assuming they are under the virial equilibrium. Its conversion factor is called the "CO-to-H_2 conversion factor", which is usually denoted as $X_{\rm CO}$ and $\alpha_{\rm CO}$. $X_{\rm CO}$ converts integrated intensity of ^{12}CO($J=1$–0), $I_{^{12}{\rm CO}(J=1-0)}$, into column density of H_2, $N_{\rm H_2}$, along the line of sight;

$$\left(\frac{N_{\rm H_2}}{\rm cm^{-2}}\right) = \left[\frac{I_{^{12}{\rm CO}(J=1-0)}}{\rm K\,km\,s^{-1}}\right]\left[\frac{X_{\rm CO}}{\rm cm^{-2}\,(K\,km\,s^{-1})^{-1}}\right]. \tag{1.32}$$

The other factor $\alpha_{\rm CO}$ converts luminosity of ^{12}CO($J=1$–0), $L'_{^{12}{\rm CO}(J=1-0)}$, into molecular gas mass, $M_{\rm mol}$, including the mass contribution of helium;

$$\left(\frac{M_{\rm mol}}{M_\odot}\right) = \left[\frac{L'_{^{12}{\rm CO}(J=1-0)}}{\rm K\,km\,s^{-1}\,pc^2}\right]\left[\frac{\alpha_{\rm CO}}{M_\odot\,({\rm K\,km\,s^{-1}\,pc^2})^{-1}}\right]. \tag{1.33}$$

Equation (1.33) is equivalent to derivation of molecular gas surface density, $\Sigma_{\rm mol}$;

$$\left(\frac{\Sigma_{\rm mol}}{M_\odot\,{\rm pc^{-2}}}\right) = \cos i\left[\frac{I_{^{12}{\rm CO}(J=1-0)}}{\rm K\,km\,s^{-1}}\right]\left[\frac{\alpha_{\rm CO}}{M_\odot\,{\rm pc^{-2}}\,({\rm K\,km\,s^{-1}})^{-1}}\right], \tag{1.34}$$

where i is inclination angle of the galactic disk. From the result of Solomon et al. (1987) (figure 1.34), $X_{\rm CO} = 2.1\times10^{20}$ cm^{-2} (K km s^{-1})$^{-1}$ [corresponding $\alpha_{\rm CO}$ is 4.5 $M_\odot$ (K km s^{-1} pc^2)$^{-1}$] is suggested (Bolatto et al. 2013b) [although Solomon et al. (1987) themselves derived $X_{\rm CO} = 3.0\times10^{20}$ cm^{-2} (K km s^{-1})$^{-1}$].

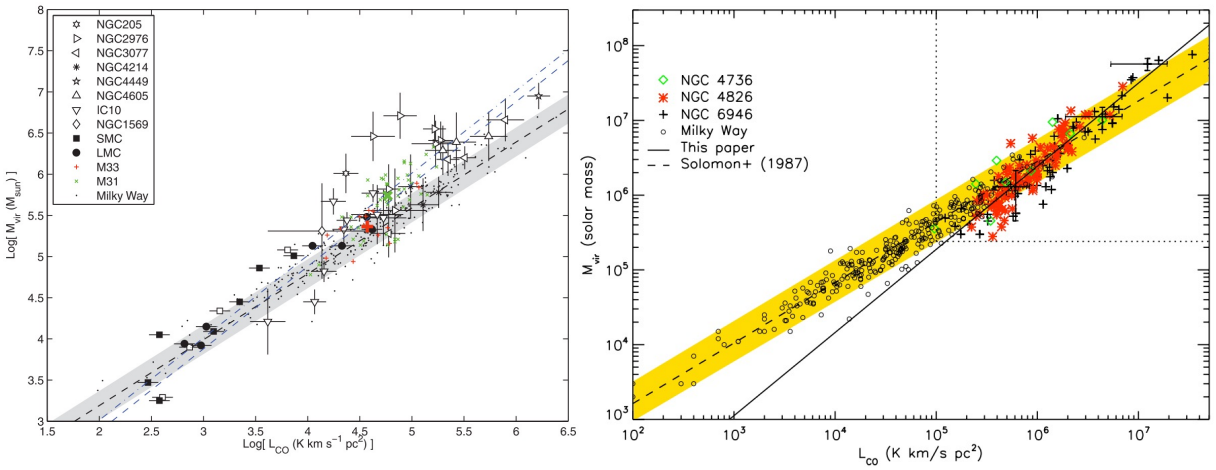

Figure 1.36: The relation between virial mass and ^{12}CO luminosity for GMCs in the Galaxy and nearby galaxies. The left panel is from Bolatto et al. (2008) and right panel is from Donovan Meyer et al. (2013). In left panel, the black dashed line is the relation by Solomon et al. (1987) and the shaded region indicates its $1\,\sigma$ range. Blue dashed and dash-dotted lines are the regression line for all clouds and that for only dwarf galaxies, respectively. Solid markers are observational results baed on ^{12}CO($J=1$–0) and open ones are based on ^{12}CO($J=2$–1) observations. In the right panel, dotted lines indicates sensitivity of their data. The yellow shaded region is a factor of two range of the CO-to-H_2 conversion factor $X_{\rm CO}$ based on Solomon et al. (1987). The best-fit result is $M_{\rm vir} \propto L_{\rm CO}^{1.00\pm0.04}$ for the left panel and $M_{\rm vir} \propto L_{\rm CO}^{1.11\pm0.29}$ for the right panel.

$X_{\rm CO}$ has been vigorously studied based on the virial equilibrium (e.g., Scoville et al. 1987; Solomon et al. 1987; Bolatto et al. 2008; Donovan Meyer et al. 2013), emission line from isotopologues of ^{12}CO molecule (e.g., Goldsmith et al. 2008; Pineda et al. 2008; Cormier et al. 2018), extinction and FIR emission from dust (e.g., Pineda et al. 2008; Pineda et al. 2010; Leroy et al. 2011; Planck Collaboration et al. 2011; Paradis et al. 2012; Sandstrom et al. 2013; Yasuda et al. 2021) assuming mass ratio of dust and gas is constant, and γ-ray by the pion π^0 destruction process $\pi^0 \rightarrow 2\gamma$ (e.g., Strong and Mattox 1996). The pion is formed by collisions between cosmic ray and atomic nuclei. Summarized many studies about CO-to-H_2 conversion factor, the value of $X_{\rm CO} = 2.0 \times 10^{20}$ cm^{-2} (K km s^{-1})$^{-1}$ [$\alpha_{\rm CO} = 4.3\ M_\odot$ (K km s^{-1} pc^2)$^{-1}$, alternatively 4.35 $M_\odot$ (K km s^{-1} pc^2)$^{-1}$ is also often used] is recommended for the Galaxy and normal, star-forming extragalaxies (Bolatto et al. 2013b).

In low-metallicity galaxies such as dwarf galaxies (e.g., LMC and SMC), CO molecules are easily dissociated, because self-shielding of CO molecules are not effective due to low abundance of CO; high-energy interstellar radiation and cosmic ray can incident in deep of molecular gas as shown in figure 1.37. As a result, most carbon is in a form of C and C^+ and CO emission is very weak, which leads to high $X_{\rm CO}$ (e.g., Mizuno et al. 2001; Fukui et al. 2008; Wolfire et al. 2010; Leroy et al. 2011; see figure 1.38). In these low-metallicity galaxies, emission lines by the fine structure of carbon, [C I] and [C II] introduced in section 1.4.3 are good tracers of molecular gas instead of CO line.

In starburst and (ultra-)luminous infrared galaxies which are actively forming stars, $X_{\rm CO}$ is lower than the normal star forming galaxies (e.g., Downes and Solomon 1998; Bryant and Scoville 1999; Narayanan et al. 2011; 2012; Papadopoulos et al. 2012a). This because higher excitation condition of ^{12}CO, which increases emissivity of ^{12}CO lines. Moreover, optical depth

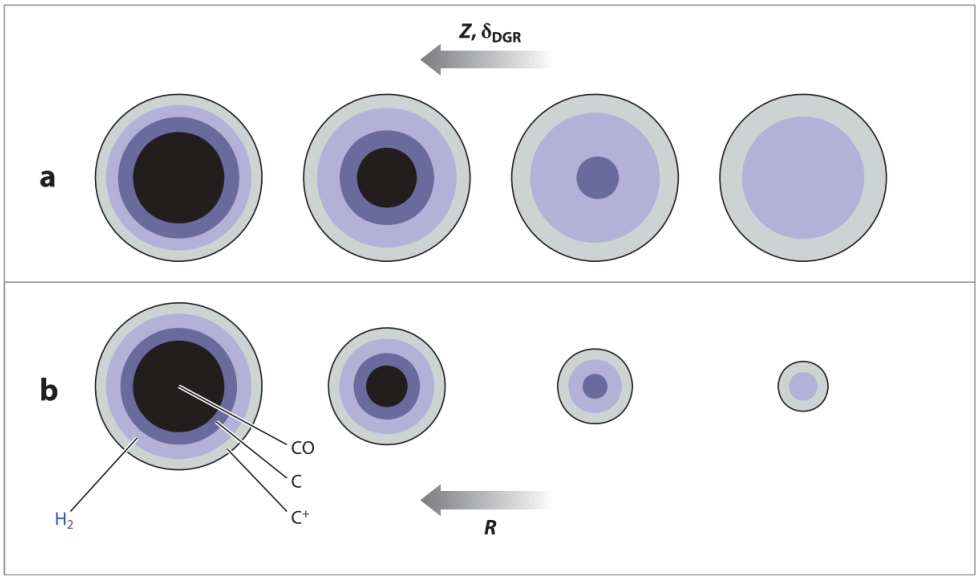

Figure 1.37: Dependency of range of CO, C, C^+, and H_2 within a molecular clouds on metallicity and its size (Bolatto et al. 2013b). Z and $\delta_{\rm DGR}$ means metallicity and dust-to-gas ratio. Effects by size of molecular clouds is the same as that of metallicity (bottom panel; R is radius).

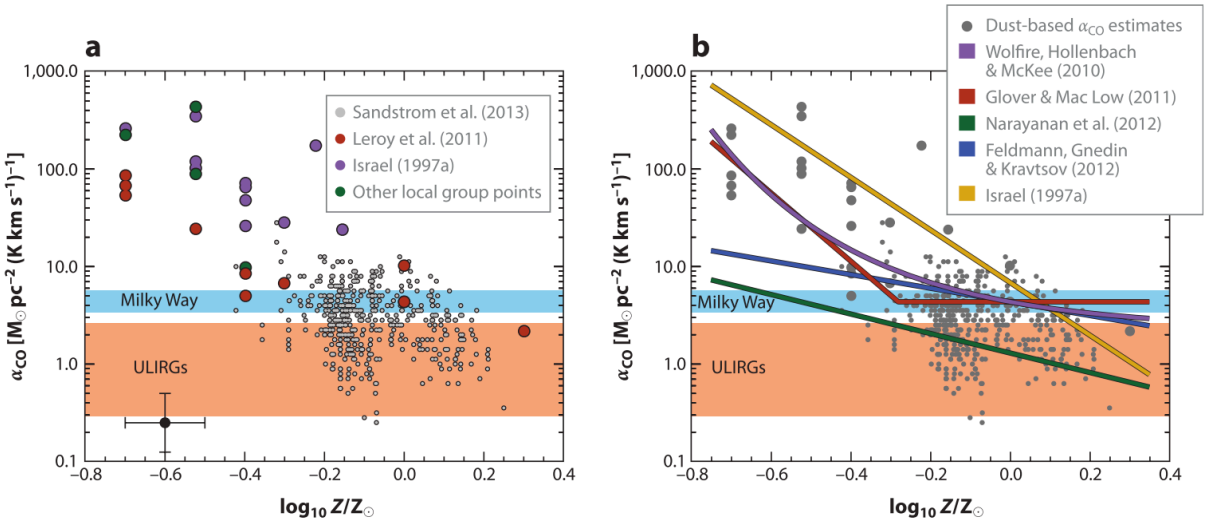

Figure 1.38: Dependency of $\alpha_{\rm CO}$ on metallicity compiled other studies (Sandstrom et al. 2013; Leroy et al. 2011; Israel 1997; Wolfire et al. 2010; Glover and Mac Low 2011; Narayanan et al. 2011; Feldmann et al. 2012) by Bolatto et al. (2013b). $Z_\odot$ is the solar metallicity ($1\ Z_\odot \simeq 8.9$ measured as $12+\log[{\rm O/H}]$). Blue- and red-shaded areas are their recommended range of $\alpha_{\rm CO}$ for the Milky Way-like galaxies and ULIRGs.

can decrease in such hot environments. It also reduces $X_{\rm CO}$. For the unified description from dwarf, low metallicity galaxies to ULIRGs, Bolatto et al. (2013b) proposed the equation for $\alpha_{\rm CO}$,

$$\alpha_{\rm CO} \simeq 2.9 \exp\left(\frac{0.4}{Z'\Sigma_{\rm GMC}^{100}}\right)\left(\frac{\Sigma_{\rm tot}}{100\ M_\odot\ {\rm pc}^{-2}}\right)^{-\gamma} M_\odot\ ({\rm K\ km\ s^{-1}\ pc^2})^{-1} \tag{1.35}$$

where Z' is metallicity normalized by the solar metallicity (i.e., $Z' \equiv Z/Z_\odot$), $\Sigma_{\rm GMC}^{100}$ is the

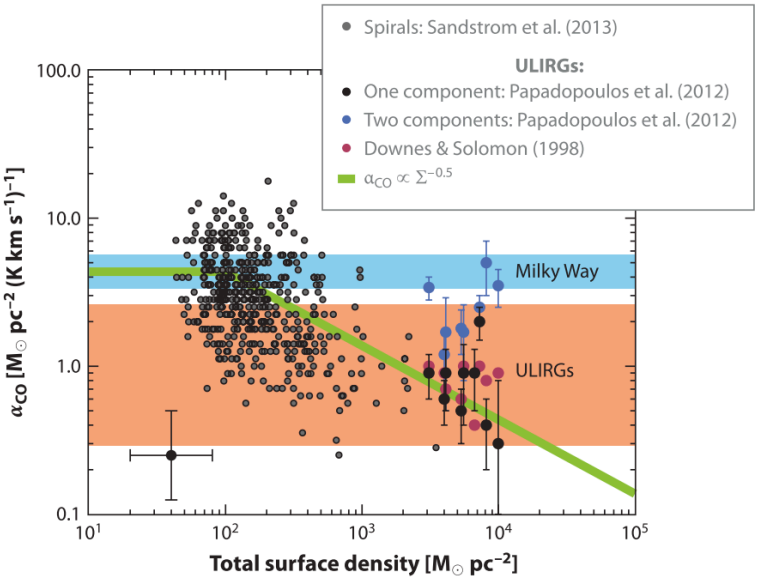

Figure 1.39: Proposed unified $\alpha_{\rm CO}$ from normal Milky Way-like galaxies to ultra luminous infrared galaxies compiled other studies (Sandstrom et al. 2013; Papadopoulos et al. 2012a; Downes and Solomon 1998) by Bolatto et al. (2013b). Total surface density is including gas and stellar components. The green thick line indicates $\alpha_{\rm CO} \propto \Sigma_{\rm tot}^{-0.5}$ when $\Sigma_{\rm tot} > 100\,M_\odot\,{\rm pc}^{-2}$.

characteristic molecular gas surface density ($\Sigma_{\rm GMC}^{100} \equiv \Sigma_{\rm GMC}/100\,M_\odot\,{\rm pc}^{-2}$), $\Sigma_{\rm tot}$ is total baryonic mass surface density including the stellar content, and γ is

$$\gamma = \begin{cases} 0.5 & (\text{if } \Sigma_{\rm GMC} > 100\,M_\odot\,{\rm pc}^{-2}), \\ 0 & (\text{otherwise}). \end{cases} \tag{1.36}$$

Aside from whether we adopt equation (1.35), we should take into account that $X_{\rm CO}$ and $\alpha_{\rm CO}$ in dwarf galaxies, starburst galaxies, (U)LIRGs, and extremely high-surface-density environments are different from that in the Galaxy and normal spiral galaxies.

1.5.4 Quantities and parameters to characterize properties of molecular clouds

In this subsection, I introduce other fundamental quantities to characterize properties of molecular gas. As seen in section 1.5.2, direct observable quantities of molecular clouds are their size (radius, R), velocity dispersion, σ_v, luminosity (integrated intensity). From these quantities, virial mass is derived from equation (1.31). In addition, mass inferred from ^{12}CO luminosity, $M_{\rm mol}$, is derived with the appropriate assumption of $\alpha_{\rm CO}$ explained in section 1.5.3.

Here, to express how the virial equilibrium is satisfied or how the gravitational force and the internal energy is balanced within a cloud, "virial parameter", $\alpha_{\rm vir}$, is introduced by Bertoldi

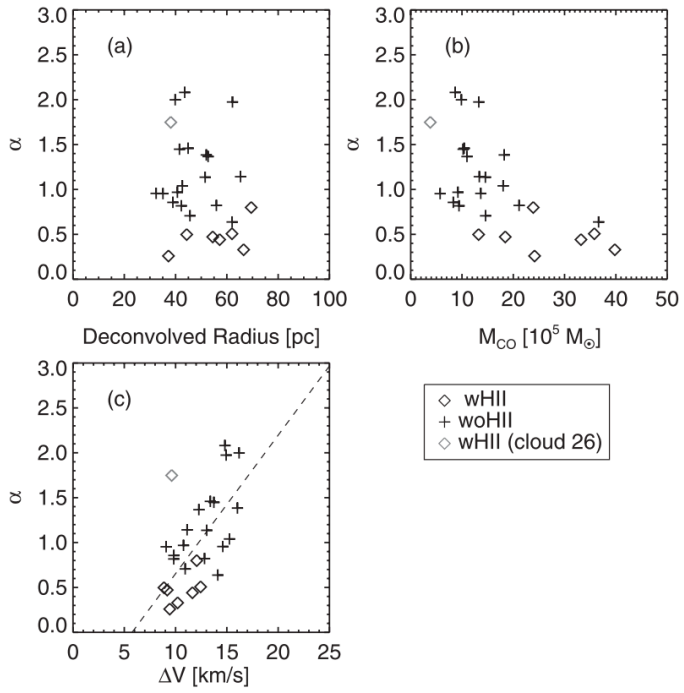

Figure 1.40: Relations between virial parameter and radius (a), mass from ^{12}CO luminosity (b), and velocity dispersion (c) for GMCs with and without H II regions found in the nearby barred spiral galaxy IC 342. Properties of GMCs with and without star formation with virial parameter (Hirota et al. 2011). The light diamond marker (cloud 26) is a peculiar cloud in their paper. In panel (c), the dashed line is the best-fitting line.

and McKee (1992). It is defined as

$$\alpha_{\rm vir} \equiv \frac{5{\sigma_v}^2 R}{GM_{\rm mol}} \tag{1.37}$$

$$\simeq \frac{M_{\rm vir}}{M_{\rm mol}} \tag{1.38}$$

$$\simeq \frac{2T}{|W|} \tag{1.39}$$

Strictly speaking, $M_{\rm vir}$ is expressed as equation (1.31) and equation (1.37) is the case of $k = 0$. Although equation (1.37) neglects density profile in molecular clouds, the factor of $3(5-2k)/(3-k)$ in equation (1.31) weakly depends on k. Therefore, the definition of $\alpha_{\rm vir}$ expressed as equation (1.37) is widely accepted, whereas $\alpha_{\rm vir}$ might be derived as the ratio of $M_{\rm vir}/M_{\rm mol}$ like equation (1.38). When the virial equilibrium is attained, $\alpha_{\rm vir} \simeq 1$. When $\alpha_{\rm vir} < 1$, the molecular cloud are collapsing (contracting) and form stars. Usually, molecular clouds are considered to be unbound and will be dissipated or confined by pressure of outer medium when $\alpha_{\rm vir} > 2$, i.e., $T > |W|$ from equation (1.39).

Since $\alpha_{\rm vir}$ reflects strength of gravitational boundness in a cloud, it is expected that stars easily form in molecular clouds with with lower $\alpha_{\rm vir}$ than unity and it is difficult to form stars for clouds with higher $\alpha_{\rm vir}$ than unity. In fact, high resolution observations show the expectation. Figure 1.40 shows correlations between virial parameter and radius, mass, and line width, respectively for GMCs with and without H II regions for GMCs in the nearby barred spiral galaxy

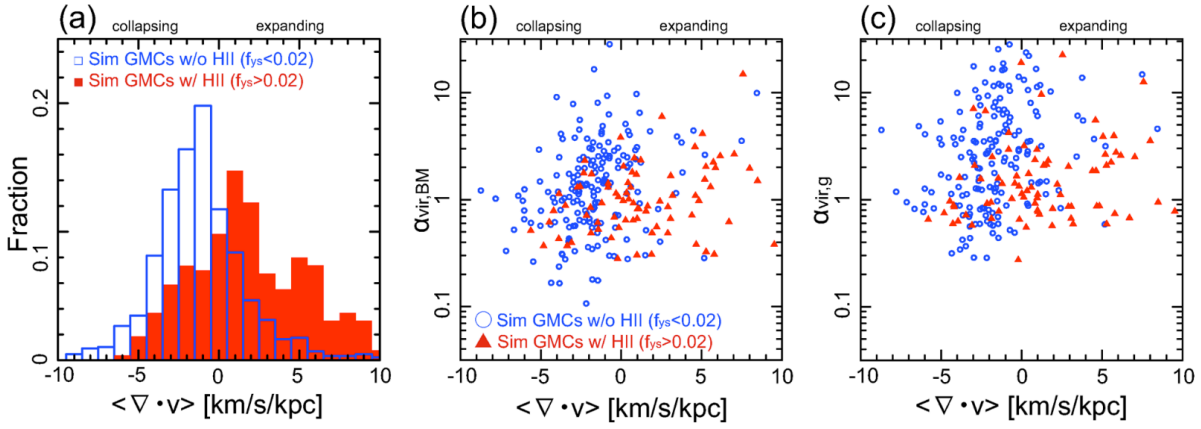

Figure 1.41: (a) Probability distribution functions of mean gas divergence in molecular clouds with and without H II regions. (b) The relation between virial parameter based on the definition of equation (1.37) and gas divergence in clouds with and without H II regions. (c) The same as (b) but the definition of $\alpha_{\rm vir}$ is $\alpha_{\rm vir,g} \equiv 2T/|W|$. Note that a cloud is collapsing (contracting) when $\langle \nabla \cdot \boldsymbol{v} \rangle < 0$ and expanding when $\langle \nabla \cdot \boldsymbol{v} \rangle > 0$. These results are produced by Baba et al. (2017).

IC 342. GMCs associated with star formation clearly have lower $\alpha_{\rm vir}$.

However, some theoretical simulations suggest a caveat of virial parameter in terms of star formation. Baba et al. (2017) shows the relation between virial parameter and mean divergence for gas particles $\langle \nabla \cdot \boldsymbol{v} \rangle$ using the smoothed particle hydrodynamic (SPH) simulation. Figure 1.41 shows their results. They revealed that virial parameter no longer indicates whether clouds are really contracting or expanding without relying on the definition of virial parameter. Moreover, virial parameter is not correlated with star formation; there is no tendency that collapsing clouds ($\langle \nabla \cdot \boldsymbol{v} \rangle < 0$) are more star-forming one. They also argued that virial parameter is high even for a completely gravitationally collapsing cloud (i.e., velocity dispersion is produced by gravitational collapse not internal turbulence).

Nevertheless, it may be danger that these results are believed as general consequences. They also examined probability distribution functions of $\langle \nabla \cdot \boldsymbol{v} \rangle$ and showed that molecular clouds with H II regions tend to be expanding. They attributed these expanding clouds to feedback from young stars. Therefore, gas particles associated with H II regions seen in this simulation is heavily affected by stellar feedback. In contrast, it is not yet clear that how observed molecular gas is influenced by it.

Furthermore, Pettitt et al. (2018) showed that there is no clear relation between dimensionless star-formarion efficiency $\varepsilon_{\rm SF}$ as defined by equation (1.8) and virial parameter. Their results shows figure 1.42. They found that there is no correlation between star-formation efficiency and virial parameter of molecular clouds. They also mentioned that virial parameter is significantly different among clouds even when they are located at a similar environment (i.e., within the same arm) and close positions. The linear relation of $\epsilon_{\rm SF}$ to $\alpha_{\rm vir}$ might be seen if highly unbound clouds (Cloud3, 8, 9 in figure 1.42) are excluded according to the main text of the paper. Finally, they proposed that $\alpha_{\rm vir}$ is possibly a poor indicator to reflect capacity for star formation of a molecular cloud, and it prefer an indicator of formations for star-forming cores within a cloud.

Note that molecular clouds does not always form stars when $\alpha_{\rm vir} > 2$ (i.e., unbound state).

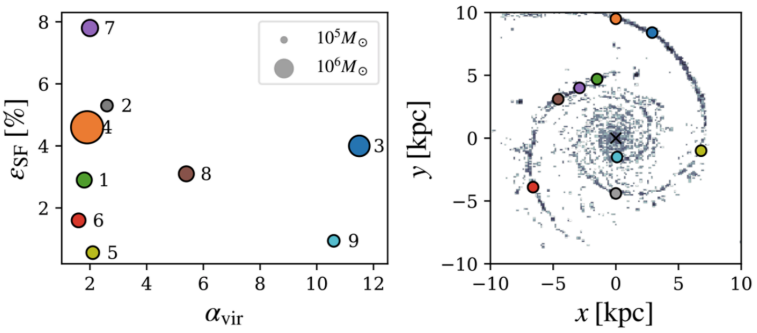

Figure 1.42: Relation between dimensionless star-formation efficiency and virial parameter (left) and positions of their clouds (right) (Pettitt et al. 2018).

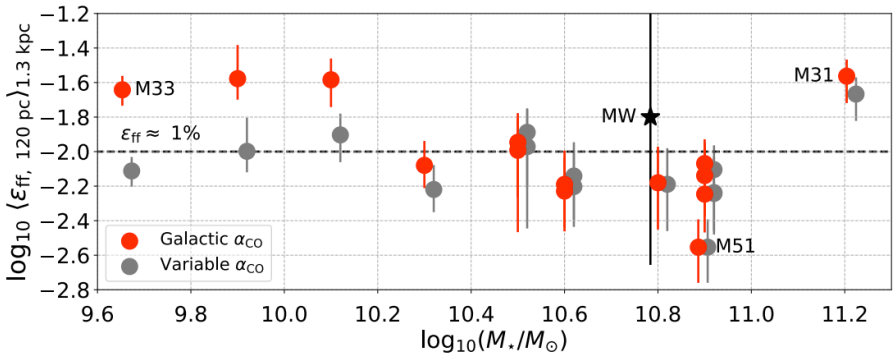

Figure 1.43: Star-formation efficiency per free-fall time $\varepsilon_{\rm ff}$ across nearby galaxies as a function of total stellar mass within each galaxy (Utomo et al. 2018). Each marker is the median of $\varepsilon_{\rm ff}$ in each galaxy and each errorbar indicates 16th–84th percentile (equivalent to $1\,\sigma$) range. Markers of $\varepsilon_{\rm ff}$ derived from variable $\alpha_{\rm CO}$ considering metallicity are shifted by +0.02 dex for clarify. The result for the Galaxy ("MW" in the plot) is based on Evans et al. (2014) and Lee et al. (2016).

Even if a molecular cloud is gravitationally unbound, dense molecular gas deep inside of the cloud is bound and can form stars including OB stars according to theoretical simulations (e.g., Clark et al. 2005; Dobbs et al. 2011a; Ward et al. 2014).

In addition to virial parameter, the other fundamental quantity to characterize properties of molecular clouds is "free-fall time", $\tau_{\rm ff}$. It is derived from a calculation of hydrodynamics and expressed as

$$\tau_{\rm ff} = \sqrt{\frac{3\pi}{32G\rho}}, \tag{1.40}$$

where ρ is volume density of a molecular cloud. It is usually derived from mass of GMCs and its radius. Radius along the line of sight is assumed to be not so changed. In most of case, geometric mean of radii along the major and minor axis is used as the representative radius of a cloud and to derive volume of GMCs (e.g., Colombo et al. 2014; Hirota et al. 2018; Schruba et al. 2019). Free-fall time is the timescale of collapsing a molecular cloud by only its self-gravity. That is, after the time of $\tau_{\rm ff}$ is passed, a cloud is collapsed to one point. Free-fall time usually ranges 1–10 Myr (e.g., Freeman et al. 2017; Hirota et al. 2018; Rosolowsky et al. 2021).

Since free-fall time provides a simple timescale of star formation, we can defined SFE per

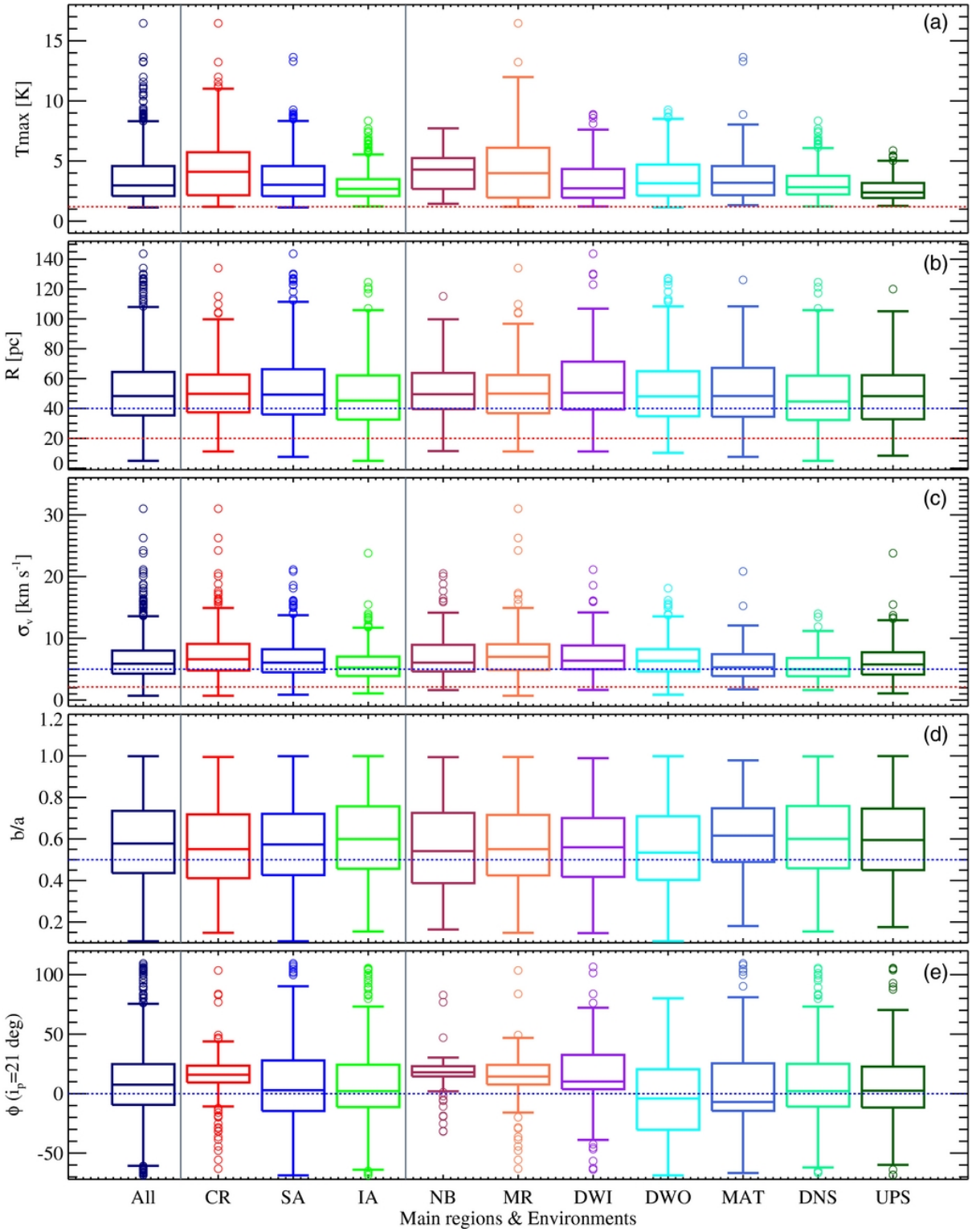

Figure 1.44: Properties of giant molecular clouds in galactic regions of the spiral galaxy M 51 (Colombo et al. 2014). The 2nd–4th box-whisker plots are results for representative galactic environments ("CR": center, "SA": spiral arms, "IA": inter-arm). More detailed regions (5th–11th box-whisker plots) are nuclear bar ("NB"), molecular ring ("MR"), inner density-wave spiral arms ("DWI"), outer density-wave spiral arms ("DWO"), material arms ("MAT"), downstream of spiral arms ("DNS"), and upstream ("UPS"). For the definition, see figure 2 of Colombo et al. (2014). Compared quantities of GMCs are (a) peak intensity, (b) radius, (c) velocity dispersion, (d) axis ratio of the major and minor, (e) position angle of the major axis of GMCs.

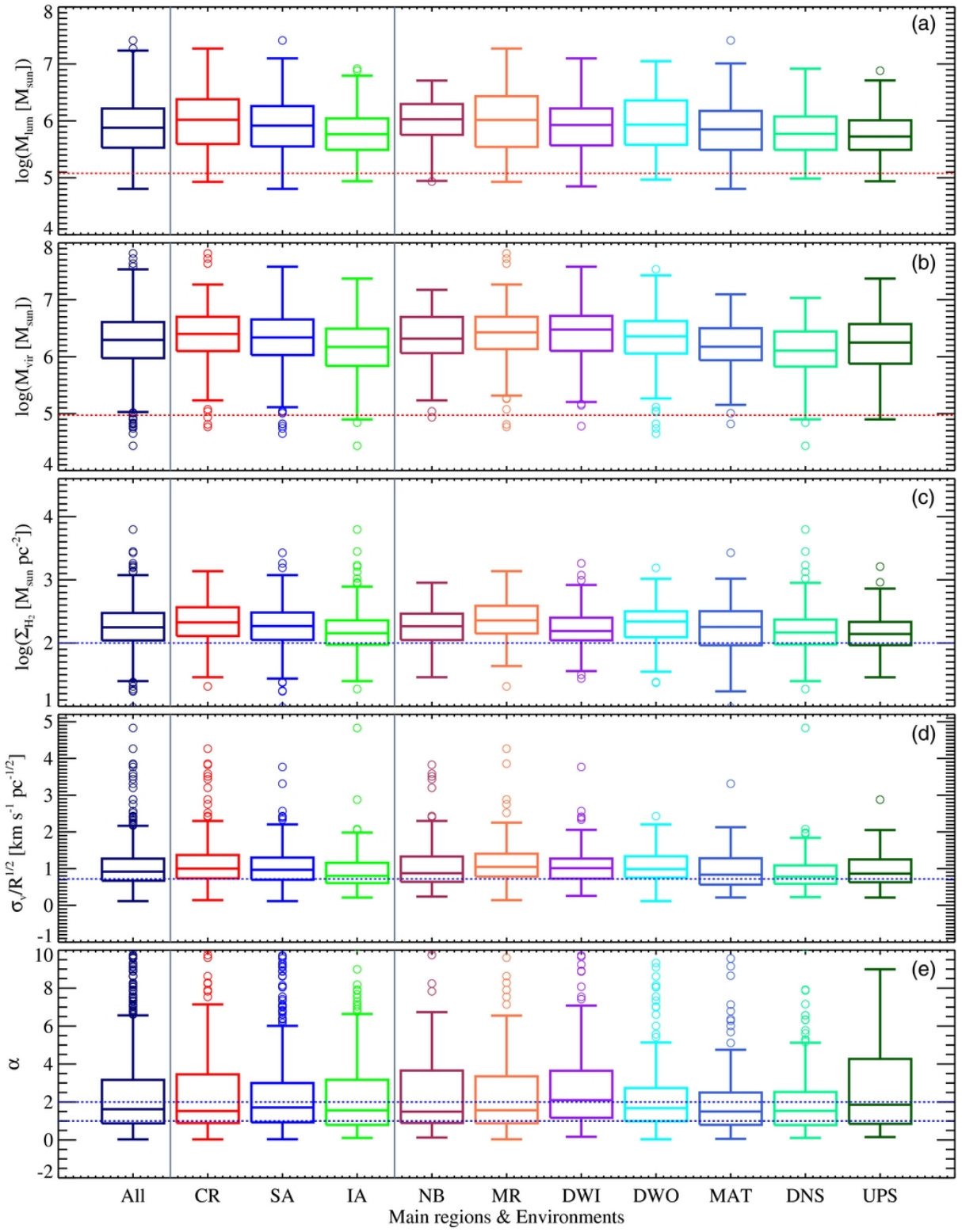

Figure 1.45: The continuation of figure 1.44. Compared quantities of GMCs are (a) molecular gas from ^{12}CO($J=1$–0) luminosity, (b) virial mass, (c) surface density, (d) the ratio of velocity dispersion to square root of radius, (e) virial parameter.

free-fall time $\varepsilon_{\rm SF}$;

$$\varepsilon_{\rm ff} \equiv \frac{\tau_{\rm ff}}{\tau_{\rm dep}} = \tau_{\rm ff} \frac{\Sigma_{\rm SFR}}{\Sigma_{\rm mol}}, \tag{1.41}$$

where $\tau_{\rm dep}$ is depletion time of molecular gas, which is the reciprocal of SFE defined as equation (1.7). According to equation (1.41), $\tau_{\rm ff}$ is simply $\propto 1/\sqrt{\rho}$, i.e., $\propto 1/\sqrt{n({\rm H_2})}$, where $n({\rm H_2})$ is number density of H_2 in a molecular cloud. Usually, $\tau_{\rm dep}$ is in the order of 0.1–1 Gyr, so that $\varepsilon_{\rm SF}$ is only a few or a few $\times$ 0.1 %. Utomo et al. (2018) derived mean $\varepsilon_{\rm SF}$ averaged over the 1.3 kpc scale using 120 pc resolution data for some nearby galaxies and showed $\varepsilon_{\rm SF} \lesssim 1\%$ in many galaxies (see also Leroy et al. 2017a). Therefore, star formation is very inefficient compared to the simple free-fall by pure self-gravity. This is because internal turbulence prevents molecular clouds from collapsing at free-fall time (based on the view from the turbulence-regulated star-formation scenario) or clouds are actually collapsing at free-fall time, however, they are dissipated by stellar and supernovae feedback from already formed stars (based on the view from the dynamical star-formation scenario), which are briefly introduced in section 1.3.2.

Using properties of molecular clouds such as mass, size, line width, and virial parameter and free-fall time, dependences of GMC properties on environments and regions where they locate have been studied. Colombo et al. (2014) examined differences of GMC properties in the spiral galaxy M 51 between environments within the galaxy using high resolution data obtained from the PdBI Arcsecond Whirlpool Survey (PAWS; Schinnerer et al. 2013) carried out with Institut de Radioastronomie Millimétrique (IRAM) 30 m telescope and Plateau de Bure Interferometer (PdBI). Figure 1.44 and 1.45 show their results. Although GMCs in inter-arm prefer low peak intensity, low velocity dispersion, low mass (both luminosity based and virial), and low surface density, other properties are not so different between the galactic center, spiral arms, and inter-arm. They also reported that mass spectrum (mass function) for each galactic environment is significantly different. Moreover, Donovan Meyer et al. (2013) showed that virial parameter are not significantly different between arms, inter-arm, and galactic centers of NGC 4736, NGC 4826, and NGC 6946 obtained by the CANON survey.

In more extreme environments such as bars of barred spiral galaxies, the same tendency is seen. Freeman et al. (2017) shows no evidence of not varying GMC properties (internal pressure, surface density, free-fall time) outside the nucleus of the nearby barred spiral galaxy M 83 obtained with only the 12 m array of Atacama Large Millimeter/submillimeter Array (ALMA).

Hirota et al. (2018) showed GMC properties in M 83 using the combined data of the ALMA 12 m array with the Atacama Compact Array [ACA; the 7 m array + the total power (TP) array]. GMCs in the galactic center tend to have higher peak intensity, higher velocity dispersion, larger mass, higher surface density, shorter free-fall time than other regions (note that compared to similar properties of GMCs between the center and the disk of M 51, M 83 has the starburst nucleus whereas star formation at the center of M 51 is more quiescent than M 83, so that GMCs in the center of M 83 is outstanding different properties compared to those in disk). In the bar of M 83, peak intensity, velocity dispersion, mass, surface density, and virial parameter are relatively higher and larger than those in arms. However, larger velocity dispersion and higher velocity dispersion are attributed to larger size of GMCs. The ratio of velocity dispersion to peak intensity, which is equivalent to virial parameter eliminating the effect of different radius is not so different between arms and the bar.

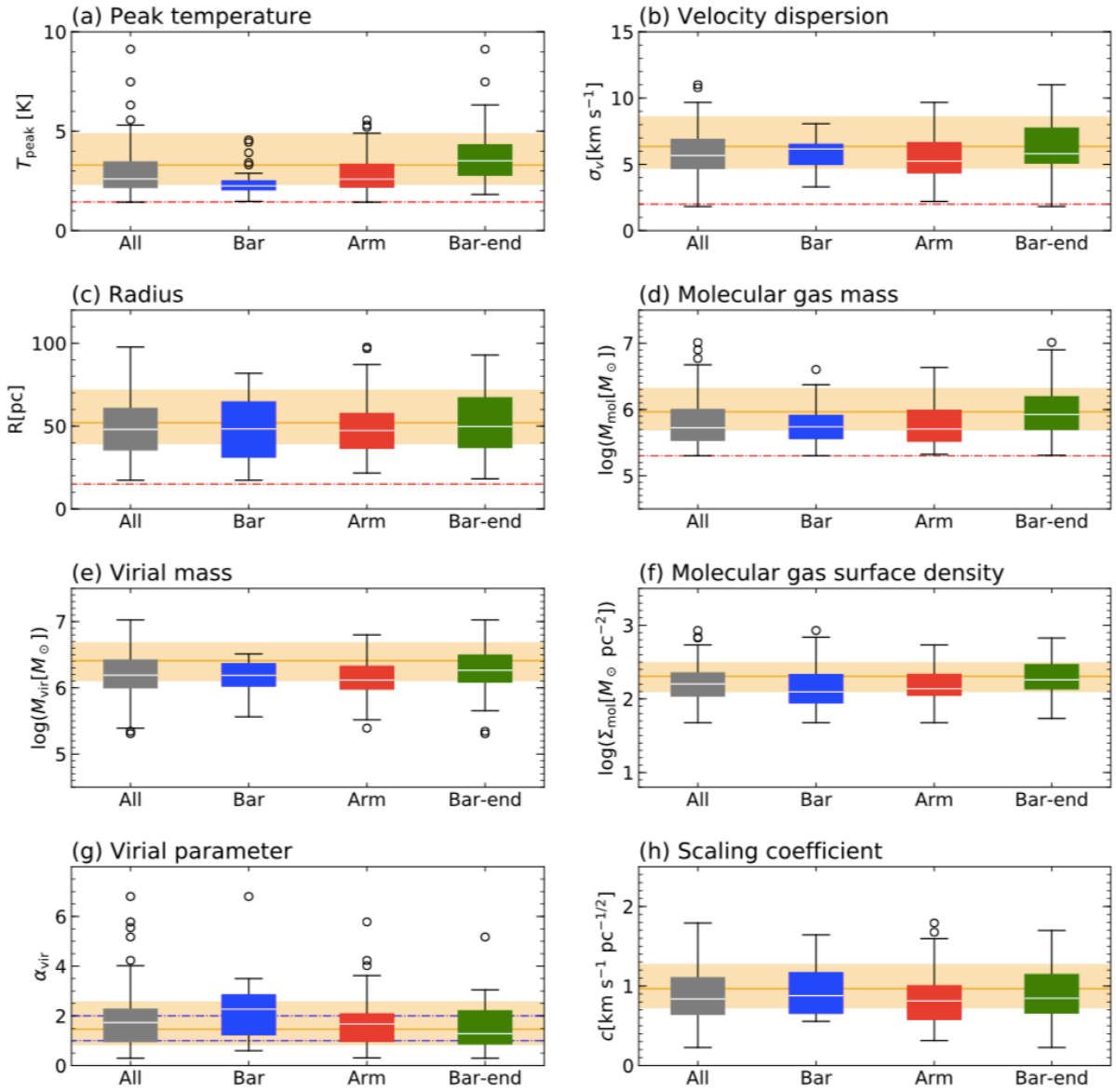

Figure 1.46: Properties of giant molecular clouds in representative regions of the barred spiral galaxy NGC 1300 (Maeda et al. 2020a).

The tendency that interferometric data alone shows more uniform properties of GMCs within a galaxy is also seen in another barred spiral galaxies M 100 reported by Pan and Kuno (2017). They showed that GMA properties (mass, surface density of molecular gas and SFR, velocity dispersion, virial parameter, and SFE) are largely different between the center, the bar, and arms using combined ALMA 12 m array and ACA data. In contrast, these variations among the galactic regions are weakened when data from ALMA 12 m array alone is used.

As an extreme example of a strongly barred spiral galaxy, Maeda et al. (2020a) reported properties of GMCs in NGC 1300, which is the prototypical SB galaxy. Their results are shown in figure 1.46. They argued that although the median of virial parameter in the bar is higher than those in arms and bar ends, the statistical test denies its significance. They concluded that the cause of low SFE observed in the bar is not the property of GMCs that are hard to

gravitationally contract and there is another possibility to induce difference of SFE. According to these results above, molecular clouds, at least found as GMCs in extragalaxies are possibly somewhat robust and universal objects against surrounding environments and galactic structures as seen in their fundamental relations described in section 1.5.2.

Note that we should take the method of analysis for derivation of GMC properties into account. Sun et al. (2018), Sun et al. (2020), and Rosolowsky et al. (2021) reported wide variations of GMC properties using the PHANGS–ALMA data (Leroy et al. 2021c). However, they derived GMC properties without identification of them. They assume that the size of GMCs are the same as the beam size (spatial resolution) and derived properties at each pixel which are sampling by half size of the beam (i.e., Nyquist sampling). This analysis can analyze all ^{12}CO data at all positions, however, it leads to large variations of properties for GMCs, because ^{12}CO emission which is not identified as a GMC is considered as a GMC. Therefore, we should pay attention to analysises of GMC studies.

1.6 Investigation for properties of molecular gas

In this section, I introduce how we estimate and infer properties of molecular gas, especially using multiple emission lines and multiple molecules.

1.6.1 Probability of transitions; Einstein's coefficients and collisional rates

In section 1.4.2, I introduce the Einstein's A coefficient as equation (1.24). It represents the probability of spontaneous emission, or spontaneous transition from the upper level to the lower level. There are other processes for transitions; absorption, stimulated emission, and transitions by collisions between molecules and atoms.

The probability of absorption and transition from the level J to $J+1$ per unit time is $B_{J,J+1}\bar{J}_\nu$, where $B_{J,J+1}$ is the Einstein's B coefficient and $\bar{J}_\nu$ is mean radiation field, which is derived by

$$\bar{J}_\nu = \frac{1}{4\pi}\int I_\nu d\Omega = \frac{1}{4\pi}\int_0^\pi d\theta \int_0^{2\pi} d\varphi \; I_\nu \sin\theta. \tag{1.42}$$

Here I_ν is intensity of incident emission. The probability of stimulated emission of $J+1 \to J$ per unit time is expressed as $B_{J+1,J}\bar{J}_\nu$ using the Einstein's B coefficient. These Einstein's coefficients $A_{J+1,J}$, $B_{J,J+1}$, and $B_{J+1,J}$ are related to each other with the Einstein's relation;

$$A_{J+1,J} = \frac{2h\nu^3}{c^2} B_{J+1,J}, \tag{1.43}$$

$$B_{J,J+1} = \frac{g_{J+1}}{g_J} B_{J+1,J}, \tag{1.44}$$

where g_{J+1} and g_J are statistical weights (degeneracy) at the level $J+1$ and J, respectively. In this case, $g_{J+1} = 2J+3$ and $g_J = 2J+1$.

The probability of transitions by collision is $C_{J,J+1}$ and $C_{J+1,J}$ for $J \to J+1$ and $J+1 \to J$, respectively. They are also called collisional rates. $C_{J+1,J}$ is

$$C_{J+1,J} = n_{\rm col}\gamma_{J+1,J}, \tag{1.45}$$

where $n_{\rm col}$ is number density of the collisional partner (in molecular gas, it is H_2), and $\gamma_{J+1,J}$ is the downward collisional rate coefficient. The collisional rate coefficient is mean of the product

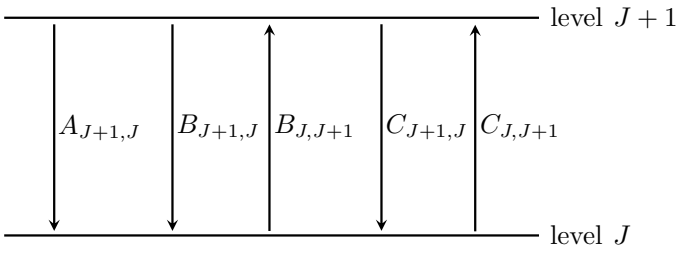

Figure 1.47: Transitions between energy levels J and $J+1$ by spontaneous emission ($A_{J+1,J}$), stimulated emission ($B_{J+1,J}$), absorption ($B_{J,J+1}$), and collisions ($C_{J+1,J}$, $C_{J,J+1}$).

of the collisional cross section σ and velocity v by the Maxwell distribution f_v (van der Tak et al. 2007; Draine 2011);

$$\gamma_{J+1,J} \equiv \int_0^\infty \sigma v f_v dv \tag{1.46}$$

$$= \int_0^\infty \sigma v \times 4\pi \left(\frac{\mu}{2\pi k_{\rm B} T_{\rm kin}}\right)^{3/2} \exp\left(-\frac{\mu v^2}{2k_{\rm B}T_{\rm kin}}\right) v^2 dv, \tag{1.47}$$

where μ is the reduced mass of the collision partners and $T_{\rm kin}$ is kinetic energy (temperature characterized by the Maxwell distribution). It also expressed as

$$\gamma_{J+1,J} = \left(\frac{8k_{\rm B}T_{\rm kin}}{\pi\mu}\right)^{1/2} \left(\frac{1}{k_{\rm B}T_{\rm kin}}\right)^2 \int_0^\infty \sigma E \exp\left(-\frac{E}{k_{\rm B}T_{\rm kin}}\right) dE, \tag{1.48}$$

using the collisional energy E because $E = \mu v^2/2$. Often $\gamma_{J+1,J}$ is approximately considered to be $\approx \sigma\langle v\rangle$, so that

$$C_{J+1,J} \approx n({\rm H_2})\sigma\langle v\rangle, \tag{1.49}$$

and $\gamma_{J+1,J} \propto \sqrt{T_{\rm kin}}$ (e.g., Goldreich and Kwan 1974; Spitzer 1978). Figure 1.47 summarizes physical processes of transitions with important coefficients. Using these coefficients above, time variation of the number density at the energy level i is in general

$$\frac{dn_i}{dt} = n_j \left[\sum_{j>i}(A_{j,i} + B_{j,i}\bar{J}_\nu + C_{j,i}) + \sum_{j<i}(B_{j,i}\bar{J}_\nu + C_{j,i})\right] - n_i \left[\sum_{j>i}(B_{i,j}\bar{J}_\nu + C_{i,j}) + \sum_{j<i}(A_{i,j} + B_{i,j}\bar{J}_\nu + C_{i,j})\right], \tag{1.50}$$

where n_i is the number density at the energy level i. Note that the selection rule for rotational transitions is $\Delta J = \pm 1$.

1.6.2 Critical density and multiple emissions line as probes of different molecular gas properties

If transitions are dominantly occurred by collisions (i.e., $A_{J+1,J} \ll C_{J+1,J}$), energy interaction is enough to attain the thermodynamic equilibrium. In this case, the distribution of molecules at each energy level becomes the Boltzmann distribution at the surrounding temperature $T_{\rm kin}$;

$$\frac{n_{J+1}}{n_J} = \frac{g_{J+1}}{g_J} \exp\left(-\frac{\Delta E_{J+1,J}}{k_{\rm B}T_{\rm kin}}\right). \tag{1.51}$$

However, energy interaction of molecules in ISM is usually too weak to attain the thermodynamic equilibrium, because their density and temperature are too low. In such case, the distribution of molecules at each energy level is

$$\frac{n_{J+1}}{n_J} = \frac{g_{J+1}}{g_J} \exp\left(-\frac{\Delta E_{J+1,J}}{k_{\rm B} T_{\rm ex}}\right), \tag{1.52}$$

where $T_{\rm ex}$ is called "excitation temperature" and usually $T_{\rm ex} \leq T_{\rm kin}$. In addition, $C_{J+1,J}$ and $C_{J,J+1}$ are related to each other;

$$C_{J,J+1} = \frac{g_{J+1}}{g_J} C_{J+1,J} \exp\left(-\frac{\Delta E_{J+1,J}}{k_{\rm B} T_{\rm ex}}\right). \tag{1.53}$$

From the Einstein's relations equation (1.43) and (1.44), and equation (1.53), we can obtain

$$\frac{n_{J+1}}{n_J} = \frac{\dfrac{g_{J+1}}{g_J}\left[\dfrac{c^2}{2h\nu^3}\bar{J}_\nu A_{J+1,J} + C_{J+1,J}\exp\left(-\dfrac{h\nu}{k_{\rm B}T_{\rm ex}}\right)\right]}{A_{J+1,J}\left(1 + \dfrac{c^2}{2h\nu^3}\bar{J}_\nu\right) + C_{J+1,J}}. \tag{1.54}$$

When $\bar{J}_\nu = 0$ (i.e., no incident radiation), equation (1.54) is

$$\frac{n_{J+1}}{n_J} = \frac{g_{J+1}}{g_J} \exp\left(-\frac{h\nu}{k_{\rm B}T_{\rm ex}}\right)\left(\frac{A_{J+1,J}}{C_{J+1,J}} + 1\right)^{-1}. \tag{1.55}$$

If $A_{J+1,J} \ll C_{J+1,J}$, n_{J+1}/n_J becomes much smaller than the expected one by the Boltzmann distribution in the thermal equilibrium. That is, molecules are not excited to higher energy levels. In contrast, when $A_{J+1,J} \gg C_{J+1,J}$, n_{J+1}/n_J is close to that of the Boltzmann distribution at the temperature $T_{\rm kin} > T_{\rm ex}$, i.e., molecules are well excited to higher levels for the temperature. Therefore, whether $C_{J+1,J}$ is higher than $A_{J+1,J}$ is important for excitation of molecules.

Here, we can define "critical density" $n_{\rm crit}$ as

$$n_{\rm crit} \equiv \frac{A_{J+1,J}}{\gamma_{J+1,J}} \approx \frac{A_{J+1,J}}{\sigma_{\rm col}\langle v\rangle}, \tag{1.56}$$

from $A_{J+1,J}/C_{J+1,J}$ and equations (1.45) and (1.49). It represents the threshold of umber density of medium (such as H_2 and H I) to approach the thermodynamic equilibrium. Namely, if $n(H_2)$ is higher than $n_{\rm crit}$ of a kind of molecules, the molecules are well excited to higher energy levels and close to the thermal equilibrium. Contrary, when $n(H_2) < n_{\rm crit}$, the molecules are not sufficiently excited. In other words, when $n(H_2)$ is higher than $n_{\rm crit}$ for the transition $J+1 \to J$ of a kind of molecules, it is expected that adequate strong line by the transition of the molecules are observed, whereas if not, the emission line is very weak and possibly cannot be detected. Hence, each emission line from different transitions and different molecules traces different part of molecular gas where its density is different.

According to the formula of the Einsteins A coefficient, equation (1.24), and frequency of the emission line by the $J+1 \to J$ transition is $\propto (J+1)$ (cf. equation 1.17), $A_{J+1,J}$ is roughly proportional to $J^3\mu^2$. Therefore, $n_{\rm crit}$ becomes higher and higher as energy level of transition is higher and electric dipole moment is larger. For example, the electric dipole moment of ^{12}CO, CS, HCN, HCO^+ are 0.11 D, 1.96 D, 2.99 D, 3.93 D (Debye)[19], respectively (see also table 1.3

[19] 1 D $= 10^{-18}$ esu cm $\simeq 3.3356 \times 10^{-30}$ C m.

in the next subsection). This is a reason emission lines from CS, HCN, and HCO^+ are used as a dense gas tracer as seen in section 1.3.2, although their energy gap $\Delta E_{J+1,J}$ is smaller than that of ^{12}CO[20)] (e.g., Gao and Solomon 2004a; 2004b; Bigiel et al. 2016; Bešlić et al. 2021). This is also a reason that ^{12}CO is easy to observe even in diffuse molecular gas because of its low electric dipole moment. For the same molecule, it is expected that lines by higher energy transitions such as $^{12}CO(J=2\text{–}1)$, $^{12}CO(J=3\text{–}2)$, $^{12}CO(J=4\text{–}3)$ trace denser gas than what $^{12}CO(J=1\text{–}0)$ traces. Specific values of $n_{\rm crit}$ are listed in the next subsection.

Note that the concept of critical density neglects variations of temperature. When temperature of molecular gas is high, $\langle v \rangle$ in equation (1.56) increases. As a result, critical density decreases and the emission line can be observed even though density of molecular gas is not changed. In this sense, temperature and density are degenerated to observed emission lines. To resolve this degeneracy, the non-local thermodynamic equilibrium analysis is needed if gas is not in the thermodynamic equilibrium.

Also, emission lines whose $n_{\rm crit}$ is higher can increase when column density of gas increases. That is, column density as an extensive variable and volume density as an intensive variable are degenerated to observed intensity of emission lines. For this reason, usually ratio of two different emission lines are used to infer properties of molecular gas, i.e., (integrated) intensity ratios of different emission lines are probes of molecular gas properties.

$HCN/^{12}CO$ and $HCO^+/^{12}CO$ line ratios are usually referred to as dense gas fraction (e.g., Gao and Solomon 2004b; Usero et al. 2015; Bigiel et al. 2016; Gallagher et al. 2018a; 2018b; Jiménez-Donaire et al. 2019; Querejeta et al. 2019; Bešlić et al. 2021). Some of these studies showed that there is no positive correlation between SFE and dense gas fracton and SFE by dense gas ($\equiv$ SFR/dense gas mass) drops at high Σ_* and high pressure environments such as galactic centers (Usero et al. 2015; Bigiel et al. 2016; Jiménez-Donaire et al. 2019; Querejeta et al. 2019). Jiménez-Donaire et al. (2019) also reported that SFE by dense gas is negatively correlated with dense gas fraction, while usual SFE is positively correlated with dense gas fraction. To interpret these discrepancies, it is suggested that relative overdensity of gas to the background and surrounding environments is important for star formation, rather than the simple threshold of gas density (e.g., Federrath and Klessen 2012). Perhaps more careful treatments and detail discussions with star formation are necessary for these dense gas tracers.

For higher excitation transitions of ^{12}CO, Muraoka et al. (2007) measured the radial distribution of $^{12}CO(J=3\text{–}2)/^{12}CO(J=1\text{–}0)$ integrated intensities, $I_{^{12}CO(J=3-2)}/I_{^{12}CO(J=1-0)} \equiv R_{3/1}$, in the nearby barred spiral galaxy M 83. They found that there is a positive correlation between azimuthally averaged $R_{3/1}$ and SFE. They suggested that $R_{3/1}$ represents dense gas fraction of molecular gas and active star formation is enhanced by larger such dense gas because $^{12}CO(J=3\text{–}2)$ traces denser gas than that $^{12}CO(J=1\text{–}0)$ traces.

In distant infrared-bright galaxies, it is reported that $R_{3/1}$ is much larger than that in local and normal disk galaxies. In such systems, $R_{3/1}$ ranges from 0.6 to 1.0 (e.g., Iono et al. 2009; Mao et al. 2010; Papadopoulos et al. 2012b), while it is ~ 0.3 in the Galaxy and normal spiral galaxies (e.g., Fixsen et al. 1999; Muraoka et al. 2007; Morokuma-Matsui and Muraoka 2017; Li et al. 2020). These high values of $R_{3/1}$ is often attributed to promoted excitation of CO due to high temperature of molecular gas induced by more active star formation compared with

[20)] $\nu_{\rm rest}$ of $CS(J=1\text{–}0)$, $HCN(J=1\text{–}0)$, and $HCO^+(J=1\text{–}0)$ is 48.99 GHz, 88.63 GHz, and 89.19 GHz, respectively. All of them are lower than that of $^{12}CO(J=1\text{–}0)$, 115.27 GHz (see also table 1.3 in the next subsection).

local galaxies rather than number density variations. Note that if only $R_{3/1}$ is available, it is difficult to distinguish whether molecular gas is warm or dense when $R_{3/1}$ is high. There is a degeneracy between warm, diffuse condition and cold, dense condition under the same ^{12}CO($J=3$–2)/^{12}CO($J=1$–0) ratio (e.g., Muraoka et al. 2012); we need another line to constrain the condition of molecular gas.

1.6.3 Non-local thermodynamic equilibrium analysis and critical density considering photon trapping

When molecular gas is in the thermodynamic equilibrium, observed intensity of a line is equivalent to $T_{\rm kin}$ in the brightness temperature scale (see section 1.5.1) when the source is completely filled with the beam of the telescope. In this case, the distribution of molecules at each energy levels follows the Boltzmann distribution at $T = T_{\rm kin}$ like equation (1.51) and we can estimate the number of molecules at each level from column density, and finally number density can be derived. Namely, physical properties can be solved with only one line under the thermodynamic equilibrium. Even if the system is not totally in the equilibrium, the assumption is sometimes applicable when we consider the limited small extent. This situation is called "local thermodynamic equilibrium" (LTE) approximation. It is often valid in studies for ISM and star formation in the Galaxy, because their spatial scale is small and they observe relatively dense environments.

However, LTE is often no longer valid in extragalactic studies, because the spatial scale is larger and observed gas includes diffuse environments. In such case, the distribution of molecules in each energy level is the Boltzmann distribution at an unknown temperature $T_{\rm ex}$ as expressed by equation (1.52). Moreover, $T_{\rm ex}$ is different from different combination of levels, i.e., $T_{\rm ex}$ between the level $J+1$ and J is not the same as that between J and $J-1$. In such situation, physical properties of molecular gas cannot be derived from a single emission line.

Non-LTE analysis is a tool to estimate physical properties such as $n({\rm H_2})$ and $T_{\rm kin}$ when the LTE approximation is invalid (e.g., Goldreich and Kwan 1974; Scoville and Solomon 1974; Leung and Liszt 1976; van der Tak et al. 2007). It iteratively solves the radiative transfer equation and the statistical population of energy levels and find the solution until calculations converges. Here, I introduce the radiative transfer equation.

The one dimensional radiative transfer equation along the ray is described by

$$\frac{dI_\nu}{d\tau_\nu} = -I_\nu + \mathcal{S}_\nu, \tag{1.57}$$

where I_ν is intensity, τ_ν is "optical depth", $\mathcal{S}_\nu$ is the "source function" defined as $\varepsilon_\nu/\kappa_\nu$ where ε_ν is emissivity per unit volume and κ_ν is the volume absorption coefficient. Subscripts ν indicate they are functions of frequency. τ_ν is defined as

$$d\tau_\nu = \kappa_\nu dx. \tag{1.58}$$

Therefore, it is calculated by integration along the line of the ray,

$$\tau_\nu = \int d\tau_\nu = \int \kappa_\nu dx. \tag{1.59}$$

When the system is in the thermodynamic equilibrium, $\mathcal{S}_\nu = B_\nu(T_{\rm kin})$ (the Planck function) expressed by equation (1.27) according to the Kirchhoff's law. If the medium is uniform, equation

(1.57) becomes

$$I_\nu = I_\nu(0)e^{-\tau_\nu} + \mathcal{S}_\nu(1 - e^{-\tau_\nu}), \tag{1.60}$$

where $I_\nu(0)$ is the background intensity. Usually the cosmic microwave background (CMB), i.e., $B_\nu(T_{\rm bg} = 2.73\,{\rm K})$ is assumed as $I_\nu(0)$.

It is difficult to solve the radiative transfer equation, equation (1.60), and the statistical equilibrium for energy level populations, equation (1.50), because they are coupled in the term of $\bar{J}$. In other words, the solution of the radiative transfer equation for the local radiation field depends on the solution of the energy level populations and vise versa. It leads to extensive calculations and finer resolutions for numerical calculations (more grids are needed). To solve this complexity, escape probability of photon at a position in gas β_ν is introduced (Sobolev 1960). For instance, $\beta_\nu = 1$ means photon completely escapes and photon is completely trapped at a position in gas when $\beta_\nu = 0$. It is called "photon trapping" or "radiative trapping".

When the velocity along the line of sight is proportional to position or distance (such as radius), β_ν is

$$\beta_\nu = \frac{1 - e^{-\tau_\nu}}{\tau_\nu} \tag{1.61}$$

by Castor (1970). The concept of the escape probability of photon is invented in studies of stellar atmosphere, Goldreich and Kwan (1974) applied it to molecular clouds by considering molecular clouds are shrinking or expanding with the velocity $v \propto r$ and successfully derived physical properties of molecular gas. This is referred to as the "large velocity gradient" (LVG) approximation or the "Sobolev approximation". Besides equation (1.61), there are some variations to express β_ν. For example, for a homogeneous slab, $\beta_\nu = (1 - e^{-3\tau_\nu})/3\tau_\nu$, for a uniform sphere, $\beta_\nu = 1.5[1 - 2/\tau_\nu^2 + (2/\tau_\nu + 2/\tau_\nu^2)e^{-\tau_\nu}]/\tau_\nu$ (de Jong et al. 1975; Osterbrock and Ferland 2006; van der Tak et al. 2007).

Since optical depth can be expressed for a line by the transition from level $u \to l$ as

$$\tau_\nu = \frac{c^3}{8\pi\nu_{u,l}} \frac{A_{u,l}N}{1.064dv} \left(x_l \frac{g_u}{g_l} - x_u \right), \tag{1.62}$$

where $\nu_{u,l}$ is the correspond frequency, N is column density of molecule considered, dv is velocity dispersion of a molecular cloud, and x_i is the fractional population at the level i when the medium is uniform (van der Tak et al. 2007). Therefore, N/dv is an important factor for non-LTE calculations. In LVG calculations assuming velocity gradient, it corresponds to $N/(dV/dr)$, i.e., column density of molecule per unit velocity gradient. At a given $n({\rm H_2})$, $T_{\rm kin}$, and N/dv, intensity of the emission line can be derived by non-LTE calculations. However, we cannot estimate both $n({\rm H_2})$ and $T_{\rm kin}$ simultaneously, because there are infinite combinations of them to reproduce observed intensity. In additions, sources of emission lines are usually smaller than the beam size, so that observed intensity is weaker by the factor of $\Omega_{\rm source}/\Omega_{\rm beam}$, where $\Omega_{\rm source}$ is the solid angle of the source and $\Omega_{\rm beam}$ is that of the beam of the telescope. It is known as the "beam dilution effect". To settle these problems, two line ratios by three different lines are used. That is, intensities of three lines are unknown quantities and $n({\rm H_2})$, $T_{\rm kin}$, and N/dv are like conditions to solve them in non-LTE calculations.

Figure 1.48 shows an example result of the non-LTE analysis using the code RADEX (van der Tak et al. 2007). Observed line ratios are reproduced The blue and black lines correspond to combinations of $n({\rm H_2})$ and $T_{\rm kin}$ which reproduce observed line ratios at a fixed N/dv. $n({\rm H_2})$

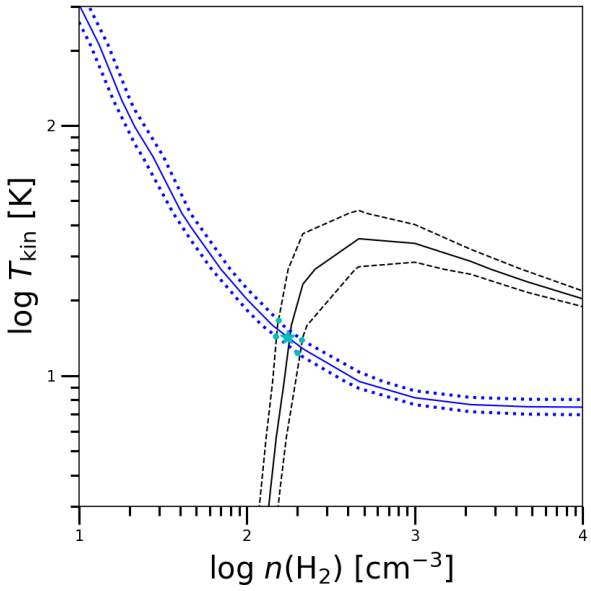

Figure 1.48: Example of a result for non-LTE calculations by RADEX (van der Tak et al. 2007). Blue lines indicate integrated intensity ratio of ^{12}CO($J=2$–1)/^{12}CO($J=1$–0) and black are that of ^{12}CO($J=1$–0)/^{13}CO($J=1$–0) (dotted and dashed lines are their errors). Number density and temperature at the intersection of the two lines corresponds to physical properties inferred from the two line ratios. Their errors correspond to the spatial extent of the area where dotted and dashed lines are overlapped.

and $T_{\rm kin}$ at the intersection of these two lines are derived properties from two line ratios. In this way, we can estimate $n(\mathrm{H_2})$ and $T_{\rm kin}$ from observed line ratios backward with the non-LTE analysis. We note that usually non-LTE calculations assume the medium is uniform. Moreover, taking ratios of intensities from two lines to eliminate the beam dilution effect is based on the assumption that solid angle of the two sources are the same. Such a model is the "one-zone model" and if we adopt it nevertheless it is not valid, there is no solution (i.e., no intersection in the plot like figure 1.48). In this case, obtained properties of molecular gas is averaged within the beam (and averaged along the line of sight when we use observed integrated intensity ratios, i.e., averaged along the velocity axis). To consider two- or more zones, a more sophisticated calculation code is needed.

Using the escape probability of photon, mean radiation field $\bar{J}_\nu$ can be expressed as

$$\bar{J}_\nu = (1-\beta_\nu)B_\nu(T_{\rm ex}) + \beta_\nu B_\nu(T_{\rm bg}). \tag{1.63}$$

The statistical equilibrium of energy level populations is also described as

$$\frac{dn_u}{dt} = -\beta_\nu n_u A_{u,l} + \beta_\nu n_l \frac{g_u}{g_l} A_{u,l} \cdot \frac{c^2}{2h\nu^3} B_\nu(T_{\rm bg}) \left(1 - \frac{n_u g_l}{n_l g_u}\right) + n_l C_{l,u} - n_u C_{u,l}, \tag{1.64}$$

when the simple two energy levels (u and l) is considered using the Einstein's relation (cf. equation 1.43 and 1.44, see Draine 2011). Equation (1.64) indicates that the Einstein A coefficient is reduced by the factor of β_ν, because only net transitions from which photon is not trapped in gas can contribute to time variation of number density at each level. Recalling the critical

Table 1.3: Rough critical densities of representative lines considering effects of photon trapping, their rest frequencies, and electric dipole moments (cf. Leroy et al. 2017b).

Line	$n_{\rm crit}$ [cm^{-3}]	$\nu_{\rm rest}$ [GHz]	μ [D]
^{12}CO($J=1$–0)	10^2	115.271	0.110
^{12}CO($J=2$–1)	10^3	230.538	0.110
^{12}CO($J=3$–2)	10^4	345.796	0.110
^{13}CO($J=1$–0)	10^3–10^4	110.201	0.110
C^{18}O($J=1$–0)	10^4–10^5	109.780	0.110
CS($J=2$–1)	10^5	97.981	1.958
HCN($J=1$–0)	10^5	88.632	2.985
HCO$^+$($J=1$–0)	10^4–10^5	89.189	3.900

density once defined by equation (1.56), it can be re-defined considering the photon trapping;

$$n_{\rm crit} \equiv \frac{\beta_\nu A_{J+1,J}}{\gamma_{J+1,J}}. \tag{1.65}$$

Hence, critical density is also effectively reduced by the factor of β_ν. Critical densities of optically thick ($\tau_\nu \gg 1$) lines is lower than that expected only their $A_{J+1,J}$ and $\gamma_{J+1,J}$.

Table 1.3 summarizes $n_{\rm crit}$ for representative emission lines considering photon trapping. ^{12}CO molecules have small electric dipole moment and their lines are usually optically thick. Thus, ^{12}CO($J=1$–0) line, the lowest energy transition of the molecule can trace low density and cold (i.e., low energy) molecular gas, which is a direct raw material of stars. This is also a reason that this line is usually used as a tracer of molecular gas in addition to the low excitation energy as seen in section 1.4.1. Higher transitions of ^{12}CO such as ^{12}CO($J=2$–1) and ^{12}CO($J=3$–2) have higher critical densities than that of ^{12}CO($J=1$–0). We note that these ^{12}CO lines can be observed with adequate strong intensity even if molecular gas density is lower than their $n_{\rm crit}$ (i.e., even of they are sub-tharmal), because they are optically thick. Molecules with high electric dipole moments have high $n_{\rm crit}$ as explained in section 1.6.2.

Low-J emission lines from isotopologues of ^{12}CO, ^{13}CO and C^{18}O, also have higher $n_{\rm crit}$ by one–two orders of magnitude than that of ^{12}CO($J=1$–0), while their electric dipole moment and energy levels are almost the same as ^{12}CO. This is because photon trapping for these lines is not effective; critical densities are not reduced by small β_ν. ^{13}CO($J=1$–0) and C^{18}O($J=1$–0) are usually optically thin, at least not optically thick ($\tau_\nu \lesssim 1$), because abundance ratio of ^{13}CO and C^{18}O is small. In this way, we can also trace different molecular gas with different physical properties using optically thin lines from low abundant isotopologues (e.g., Polk et al. 1988; Wilson and Walker 1994; Sakamoto et al. 1997a; Hüttemeister et al. 2000; Paglione et al. 2001; Meier and Turner 2004; Hirota et al. 2010; Watanabe et al. 2011; Morokuma-Matsui et al. 2015; Muraoka et al. 2016; Roman-Duval et al. 2016; Cao et al. 2017; Cormier et al. 2018; Torii et al. 2019; Morokuma-Matsui et al. 2020).

[^{12}C]/[^{13}C] abundance ratio is ~ 30 at the Galactic center, ~ 50 at 5 kpc of Galactocentric radius, and ~ 70 for local ISM clouds (nearby the Solar System, Langer and Penzias 1990; Milam et al. 2005). [^{13}CO]/[C^{18}O] abundance ratio in the Galaxy is reported as 5–10 (e.g., Langer and Penzias 1990; Wouterloot et al. 2008). ^{13}C is produced by the carbon-nitrogen-oxygen (CNO)

cycle in asymptotic giant branch (AGB) stars (Pagel 1997);

$$^{12}\mathrm{C} + \mathrm{p} \rightarrow {}^{13}\mathrm{N} + \gamma \tag{1.66}$$
$$^{13}\mathrm{N} \rightarrow {}^{13}\mathrm{C} + e^{+} + \nu_e \tag{1.67}$$
$$^{13}\mathrm{C} + \mathrm{p} \rightarrow {}^{14}\mathrm{N} + \gamma \tag{1.68}$$
$$^{14}\mathrm{N} + \mathrm{p} \rightarrow {}^{15}\mathrm{O} + \gamma \tag{1.69}$$
$$^{15}\mathrm{O} \rightarrow {}^{15}\mathrm{N} + e^{+} + \nu_e \tag{1.70}$$
$$^{15}\mathrm{N} + \mathrm{p} \rightarrow {}^{12}\mathrm{C} + {}^{4}\mathrm{He}, \tag{1.71}$$

where γ is γ-ray and ν_e is electron neutrino. Since AGB stars are the final evolutionary state for low- and intermediate-mass stars ($0.8\ M_\odot < M < 8\ M_\odot$), ^{13}C is reproduced and released into ISM from these stars.

On the other hand, ^{12}C is produced by the triple-alpha process (e.g., Timmes et al. 1995);

$$^{4}\mathrm{He} + {}^{4}\mathrm{He} \rightarrow {}^{8}\mathrm{Be} + \gamma \tag{1.72}$$
$$^{8}\mathrm{Be} + {}^{4}\mathrm{He} \rightarrow {}^{12}\mathrm{C} + \gamma \tag{1.73}$$

in high-mass stars. Lifetime of high-mass stars is short, whereas low- and intermediate-mass stars are longer than them. Therefore, rate of a release for ^{12}C is more rapid than ^{13}C; the abundance of ^{13}C more gradually increases in ISM. It is also indicated by the fact that there is a discrepancy between $[^{12}\mathrm{C}]/[^{13}\mathrm{C}]$ in the Earth (~ 90; Clayton and Nittler 2004) and nearby molecular clouds and star forming regions around the Solar System (~ 70). $[^{12}\mathrm{C}]/[^{13}\mathrm{C}]$ isotropic ratio in the Earth is fixed when the Earth formed 4.6 Gyr ago. Isotropic ratios also reflect such chemical nucleosynthesis evolution. Note that studies of isotropic ratios are limited in the Galaxy in most of cases, because emission lines to derive it are very weak. Observed emission lines should be optically thin so that intensity is proportional to column density of the molecule. Thus, extragalactic studies of isotropic ratios are usually limited to nearby starburst galaxies and (U)LIRGs where adequate intensity of lines is expected to be observed (e.g., Henkel et al. 1993; 1998; Mao et al. 2000; Martín et al. 2010).

1.7 Aim of this dissertation

I introduce basic view and concepts which are relevant to this dissertation. In the end of this chapter, I describe fundamental motivations of our studies and the dissertation.

As mentioned in section 1.4.1, 1.4.2, 1.6.2, and 1.6.3, ^{12}CO($J = 1$–0) is a fundamental line to study cold molecular gas, which is a raw material of stars and relatively lower dense. However, its rest frequency ($\nu_{\mathrm{rest}} = 115.271202$ GHz) is close to the O_2 absorption band at 118 GHz. Therefore, this line is absorbed to a small extent by the atmosphere. It is an issue of observations for nearby galaxies and ISM in the Galaxy which are not significantly red-shifted. The typical system noise temperature (the temperature corresponding to total noise in the telescope and attenuation by the atmosphere) of ^{12}CO($J = 1$–0) is ~ 300 K at zenith. On the other hand, that of ^{13}CO($J = 1$–0) ($\nu_{\mathrm{rest}} = 110.201353$ GHz) is ~ 150 K; it reduces by 50% when frequency is just different from about 5 GHz.

Figure 1.49 shows transmission of radio as a function of frequency. According to it, transparent of ^{12}CO($J = 1$–0) is $\sim 70\%$. It causes observations of this line to take a longer time (decrease

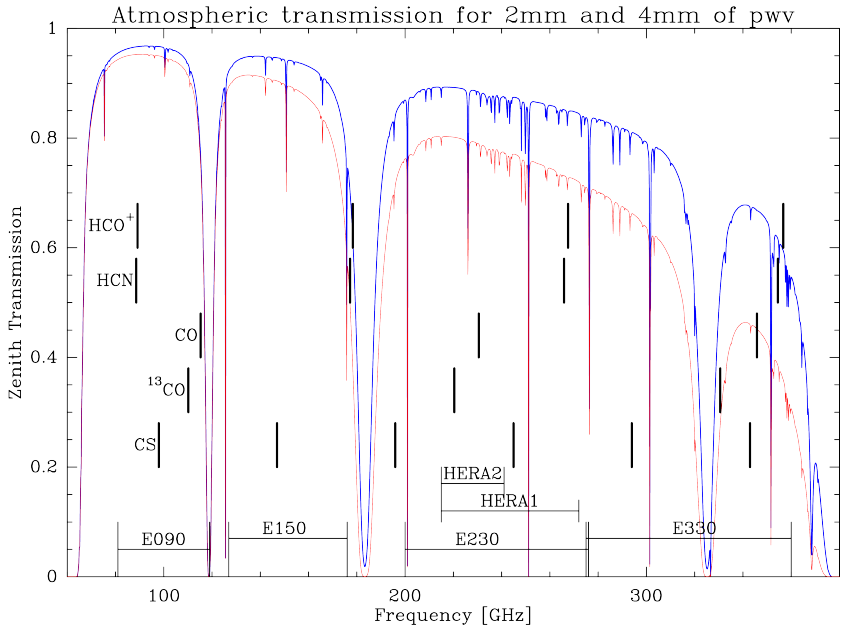

Figure 1.49: Transmission of radio at the zenith as a function of frequency at precipitable water vapor (PWV) of 2 mm (blue) and 4 mm (red). Rest frequencies of representative lines are also plotted. Lines by the same species of molecules are plotted at the same height. Lowest frequencies for each molecule correspond to the $J = 1$–0 transition except for CS (it is $J = 2$–1). This image is retrieved from https://publicwiki.iram.es/EmirforAstronomers (credit: IRAM).

observation efficiency). To avoid this issue, recent observations of molecular gas in the local universe often utilize ^{12}CO($J = 2$–1) line ($\nu_{\rm rest}$ = 230.538000 GHz, e.g., Leroy et al. 2009; Leroy et al. 2013; Druard et al. 2014; Sun et al. 2018; Muraoka et al. 2020; Brown et al. 2021; Leroy et al. 2021c). Since there is no absorption band by molecules in the atmosphere at 230 GHz (see figure 1.49), observation efficiency of ^{12}CO($J = 2$–1) is better than that of ^{12}CO($J = 1$–0). Although ^{12}CO($J = 2$–1) is more sensitive to water vapor than ^{12}CO($J = 1$–0) because of higher frequency, cites of observatory and telescopes of short millimeter-wave is usually located in dry climate, thus it is not an issue in most of cases.

Moreover, it is reported that ^{12}CO $J = 2$–1/$J = 1$–0 line ratio, $I_{^{12}{\rm CO}(J=2-1)}/I_{^{12}{\rm CO}(J=1-0)} \equiv R_{2/1}$ and peak intensity ratio of these lines are constant in galactic disks (Leroy et al. 2009) and their contrasts in galaxies are relatively small (Leroy et al. 2013). Based on these results, molecular gas mass is derived from ^{12}CO($J = 2$–1) line by assuming $R_{2/1}$ is a constant over and across galaxies and discuss the K–S relations and GMC properties (e.g., Bigiel et al. 2008; 2011; Leroy et al. 2013; Sun et al. 2018; 2020; Rosolowsky et al. 2021). However, there are also studies $R_{2/1}$ depends on environments. Representative results of $R_{2/1}$ distributions are shown in figure 1.50. In individual molecular clouds, it is higher around H II regions and lower in the outer edge (e.g., Sakamoto et al. 1994; Nishimura et al. 2015; Kohno et al. 2021a). In galaxies, it is usually high in centers and arms, especially in their downstream, and low in inter-arm (e.g., Sakamoto et al. 1997b; Koda et al. 2012; 2020; den Brok et al. 2021). $R_{2/1}$ is also correlated with physical properties and star formation activity (e.g., Koda et al. 2012; 2020; den Brok et al. 2021; Leroy et al. 2021b). Therefore, effects of the assumption to consider that $R_{2/1}$ is a constant is examined. This is a motivation for us to study $R_{2/1}$ in nearby galaxies. Its results

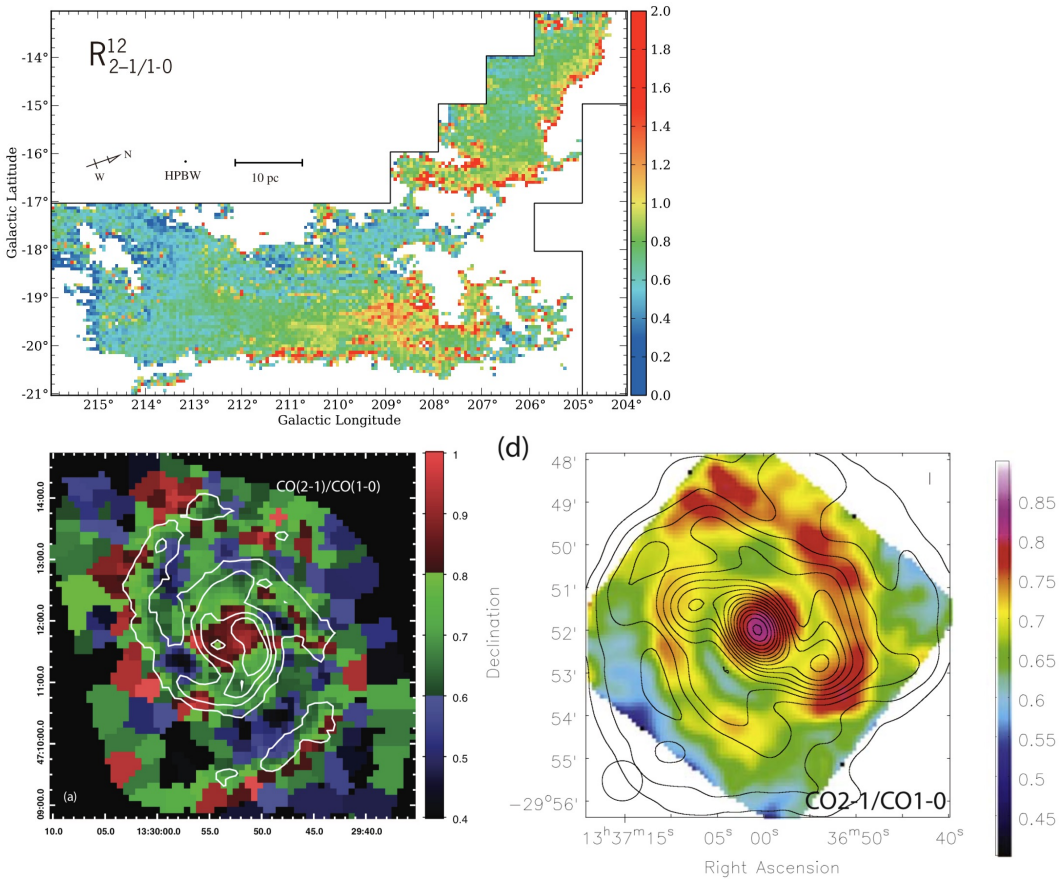

Figure 1.50: ^{12}CO($J=2$–1)/^{12}CO($J=1$–0) line ratios in Orion A, B molecular clouds (top; Nishimura et al. 2015), M 51 (bottom left; Koda et al. 2012), and M 83 (bottom right; Koda et al. 2020).

are described in chapter 2.

The second motivation of our studies are peculiarity of star formation seen in barred spiral galaxies. As already introduced in section 1.3.3, SFR and SFE are suppressed in bars and enhanced in bar ends. In addition, gas dynamics is more violent and extreme there than that in arms (see figure 1.25–1.27). Based on these facts, molecular gas and clouds in bars and bar ends are significantly influenced by surrounding gas dynamical environments and as a result, star-formation activity there is different from other galactic regions. In other words, barred spiral galaxies are the best laboratories to investigate effects of gas dynamics on molecular gas properties and star formation.

In fact, it is suggested that molecular clouds are gravitationally unbound in the bar for the nearby barred spiral galaxy Maffei 2 by Sorai et al. (2012). They modeled dynamical properties of molecular clouds from observed integrated intensity, peak intensity, and FWHM of spectra of ^{12}CO($J=1$–0). Figure 1.51 shows their result. They indicated that most molecular clouds in the bar are gravitationally unbound due to enhanced velocity dispersion within clouds but not in arms It can lead to lower SFR and SFE in bars of barred spiral galaxies.

The result remind us that number density of molecular gas and clouds are lower in bars than arms in barred galaxies which show depression of star formation in their bars. However, quantitative derivations of molecular gas number density is technically difficult, because it needs

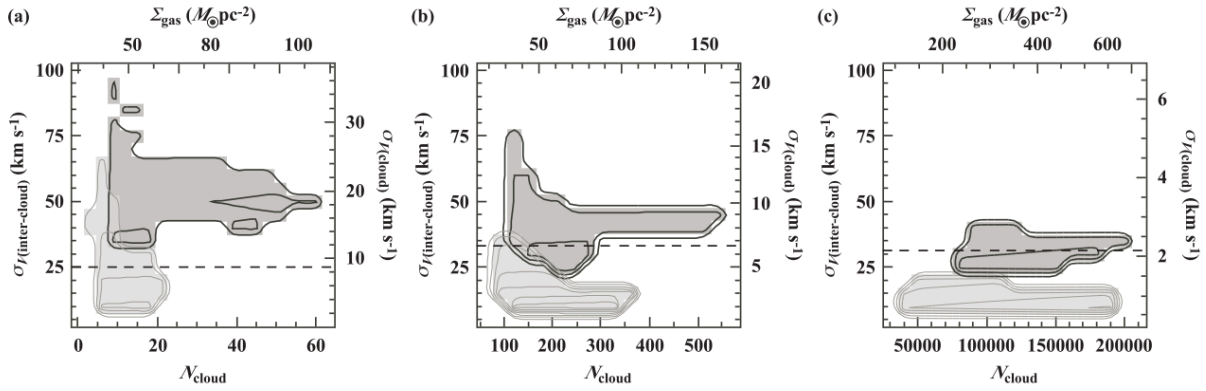

Figure 1.51: Dynamical properties of molecular clouds in the bar and arms of Maffei 2 (Sorai et al. 2012). They assumed clouds' dynamical properties from observed integrated intensity, peak intensity, and velocity width of ^{12}CO($J=1$–0) spectra by fixing $n(\mathrm{H_2})$, $T_{\rm kin}$, diameter of clouds with LVG calculations. Panels (a), (b), (c) correspond to results for diffuse, moderate, and dense clouds. Velocity dispersion between clouds, $\sigma_{V\rm (inter-clouds)}$, and number of clouds in the beam, $N_{\rm cloud}$ are free parameters. Velocity dispersion in each cloud, $\sigma_{V\rm (cloud)}$, is derived assuming the Larson's scaling relation is satisfied between the beam size and $\sigma_{V\rm (inter-clouds)}$, i.e., the scale factor between $\sigma_{V\rm (inter-clouds)}$ and the square root of the beam size is applied to the relation between $\sigma_{V\rm (cloud)}$ and the square root of the cloud's radius. Horizontal dashed lines are the threshold that whether clouds are gravitationally unbound or not (clouds above the dashed line are unbound). Light gray and dark gray areas are results of clouds in arms and the bar, respectively.

data of more than three emission lines. Usually molecular emission lines except for low-J ^{12}CO lines are weak and observational time-cost is high in normal galaxies. Then, the survey for an extensive number of nearby galaxies with simultaneous observations of multiple emission lines, CO Multi-line Imaging of Nearby Galaxies (COMING; Sorai et al. 2019) was recently carried out. Its data makes it possible to perform multi-line analyses of molecular gas in barred spiral galaxies. Therefore, we study properties of molecular gas in barred spiral galaxies using data obtained by COMING. It is described in chapter 3.

The third motivation of our study stems from the concept of the hierarchical structures of molecular gas traced by CO lines. Figure 1.52 shows the schematic view of the concept. CO-trasing molecular gas is considered to be conventionally cloud-like structures like GMCs as seen in figure 1.30 and 1.31. As an alternative and advanced view of it, Shetty et al. (2014a) proposed the hierarchical structures seen in CO lines to interpret non-linearity of the K–S relation (it is equivalent to differences in SFE) seen in many galaxies. They suggested that GMCs considered so far are relatively dense gas and there is also diffuse and extended gas surrounding it which is also traced by CO. Such diffuse gas seems to be difficult to participate in star formation. Namely, not all molecular gas is contributed to star formation, which leads to different SFE in galaxies. The negative correlation between SFE and fraction of diffuse molecular gas is actually shown (Maeda et al. 2020b).

Diffuse molecular gas traced by CO, especially ^{12}CO($J=1$–0) is in fact indicated by comparison of data from interferometric observations and single-dish observations. Here, I briefly explain why the existence of diffuse gas is confirmed from the comparison of them. According to the van Citter–Zernike theorem, the intensity distribution on the sky $T(x, y, \nu)$ is related to

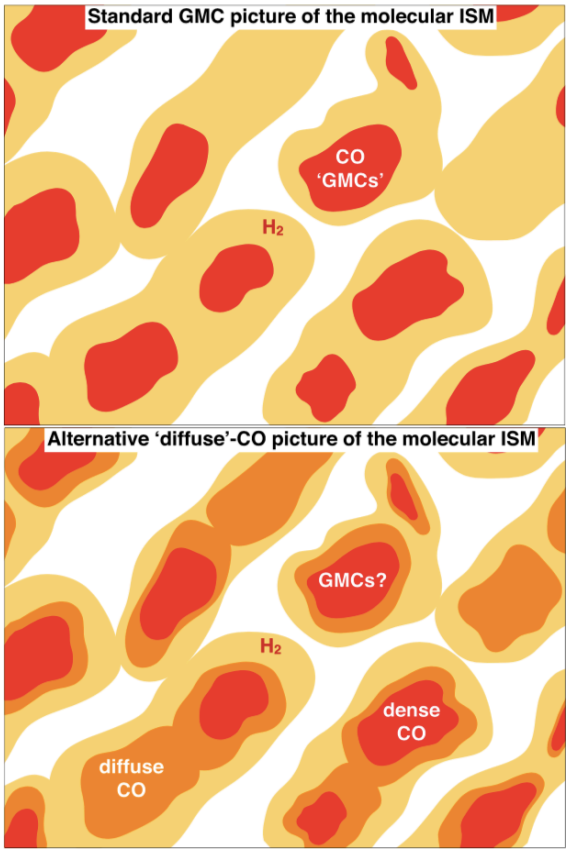

Figure 1.52: A standard (conventional) view of GMCs by CO lines (top) and newly proposed hierarchical CO structures (bottom) by Shetty et al. (2014a).

the "visibility" $\mathcal{V}(u, v, \nu)$ via the Fourier transformation;

$$T(x, y, \nu) = \mathcal{F}[\mathcal{V}(u, v, \nu)], \tag{1.74}$$

where $\mathcal{F}$ means the Fourier transformation and (u, v) is the spatial coordinate defined by

$$(u, v) \equiv \frac{1}{\lambda_{\rm obs}}(\boldsymbol{D} \cdot \boldsymbol{e}_x, \boldsymbol{D} \cdot \boldsymbol{e}_y), \tag{1.75}$$

where $\boldsymbol{D}$ is the baseline vector between two antennas which compose an interferometer and $\boldsymbol{e}_i$ is the unit vector along i (namely, this coordinate is on the ground seen from the object). The visibility is proportional to the cross spectrum, here denoted as $\hat{C}_{1,2}(u, v, \nu)$ calculated between the antenna 1 and 2. $\hat{C}_{1,2}(u, v, \nu)$ is the Fourier transformed the cross-correlation function $C_{1,2}(u, v, \tau)$;

$$\hat{C}_{1,2}(u, v, \nu) = \mathcal{F}[C_{1,2}(u, v, \tau)]. \tag{1.76}$$

$C_{1,2}(u, v, \tau)$ is derived from the cross-correlation function between electric field received by the antenna 1 at the aperture, $\varepsilon_1(u, v, t)$, and that by the antenna 2, $\varepsilon_2(u, v, t)$;

$$C_{1,2}(u, v, \tau) = \langle \varepsilon_1(u, v, t) * \varepsilon_2(u, v, t') \rangle. \tag{1.77}$$

Therefore, $T(x, y, \nu)$ (what we would like to obtain as observational data) can be derived by cross-correlation functions obtained from many combinations of antennas.

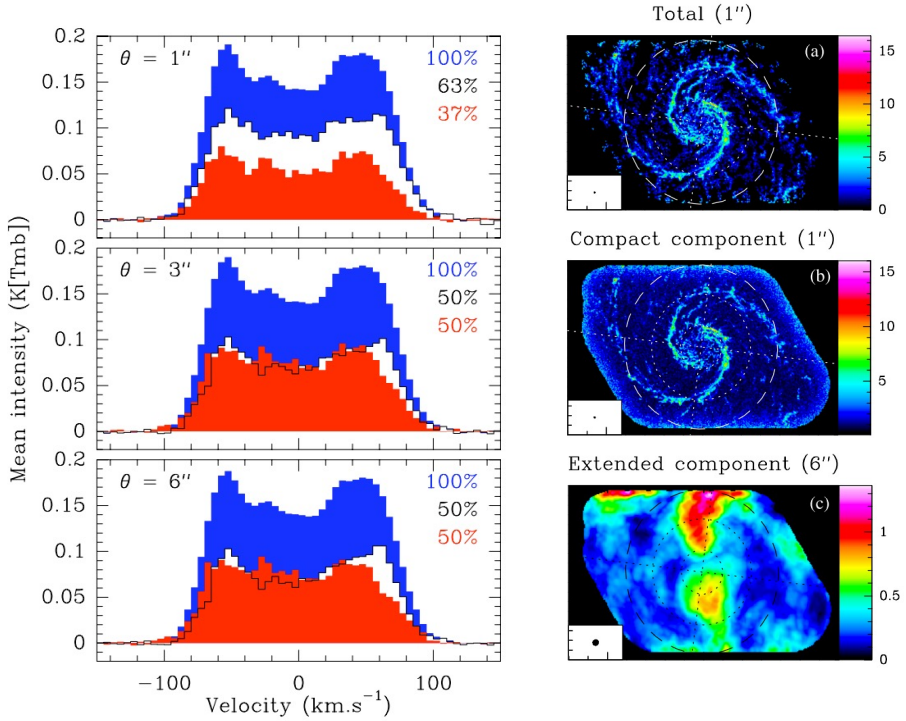

Figure 1.53: (Left column) Mean spectrum averaged over the whole area of M 51 obtained from the single-dish (IRAM 30 m telescope) + the interferometric (PdBI) data (blue), the interferometric data only (red), and their difference (white) at the resolution of 1″, 3″, and 6″ (Pety et al. 2013). Their proportions are denoted at top right corners in each panel. (Right column) Peak intensity map of the total component (top), compact component traced by only the interferometer (middle), and extended component. The unit is "K".

Since (u, v) corresponds to the wave-number space of $T(x, y)$, visibilities at small $\sqrt{u^2 + v^2}$ distance are comparable with spatially extended distribution on the sky. On the other hand, visibilities far from the origin (large $\sqrt{u^2 + v^2}$) correspond to spatially compact structures. Realistically, the number of antennas constituting the interferometer is limited, thus sampled visibilities are sparse on (u, v). Therefore, there is a limit to response the maximum spatial scale which is determined by the minimum $|\boldsymbol{D}|$ (the shortest baseline of antennas). The spatial scale is referred to as the "maximum recoverable scale" (MRS). Also, *sensitivity* depends on density of antennas on the (u, v) plane. *Sensitivity* in obtained observational data by the interferometer alone decreases as the spatial scale of the object is larger and larger, and at last, information of the structure larger than the MRS is completely lacked. It is known as the "missing flux" problem for interferometers.

To solve the issue, combining data obtained with the single dish observations is usually performed. This is because single dish telescopes can sample continuous visibilities within the distance of $\sqrt{u^2 + v^2}$ equivalent with their diameter. Single dish telescopes fill up visibilities at small $\sqrt{u^2 + v^2}$ distances on the (u, v) plane. Hence, contribution of diffuse gas can be estimated by comparing combined data with the interferometer and the single dish, and the interferometric data alone.

Figure 1.53 (Pety et al. 2013) shows mean spectrum averaged over the entire area of M 51 obtained from the PAWS survey (Schinnerer et al. 2013). They found $\sim 50\%$ of ^{12}CO($J = 1$–0)

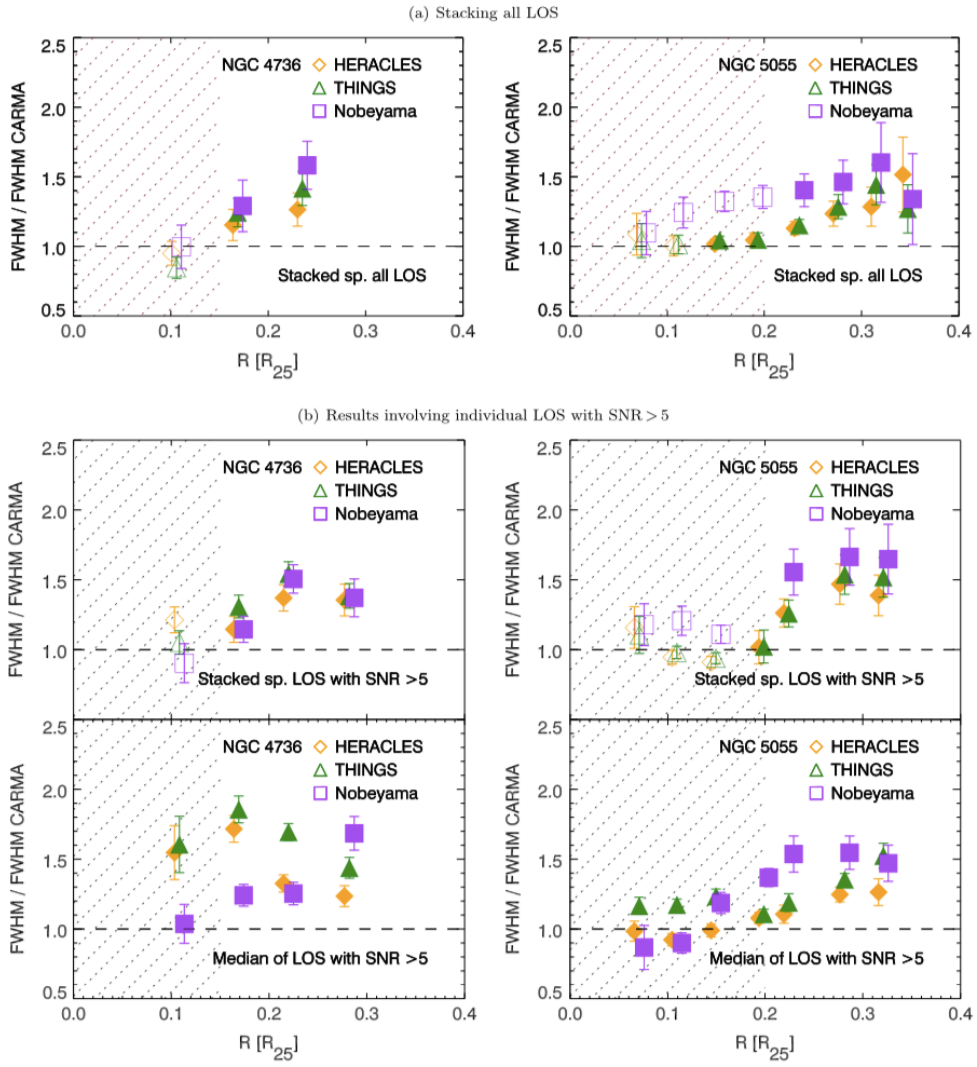

Figure 1.54: Ratios of FWHM measured from ^{12}CO data by single-dish telescopes and H I data to FWHM by the interferometer Combined Array for Research in Millimeter-wave Astronomy (CARMA) as a function of radius normalized by the B-band isophotal radius at 25 magnitude arcsec^{-2}, R_{25}, for NGC 4736 (left column) and NGC 5055 (right column) by Caldú-Primo et al. (2015). FWHM is derived by stacked spectra at all line of sights (top row), stacked at spectra with high signal-to-noise ratio ($S/N > 5$) (middle row) in annuli. For the bottom row, median of FWHM of spectra with $S/N > 5$ in annuli are plotted. Orange diamonds are the ^{12}CO($J = 2$–1) observations HERA CO-Line Extragalactic Survey (HERACLES; Leroy et al. 2009) carried out with the IRAM 30 m Telescope. Green triangles are The H I Nearby Galaxy Survey (THINGS; Walter et al. 2008) carried out with the Very Large Array (VLA). Purple squares are the ^{12}CO($J = 1$–0) survey Nobeyama CO Atlas of Nearby Galaxies (Kuno et al. 2007) carried out with the Nobeyama 45 m Telescope. The beam smearing effect is dominant in shaded areas.

flux is recovered by the interferometer alone. About a half of ^{12}CO($J = 1$–0) emission is from the extended component which cannot be observed by the interferometer. They argued that the diffuse component is the extralpanar molecular gas (gas above and below the midplane of the galactic disk) assuming observed velocity dispersion is along the vertical axis to the disk.

The existence of diffuse molecular gas is also confirmed from FWHM of spectra by the combined (interferometer + single dish) data and interferometric data. Figure 1.54 (Caldú-

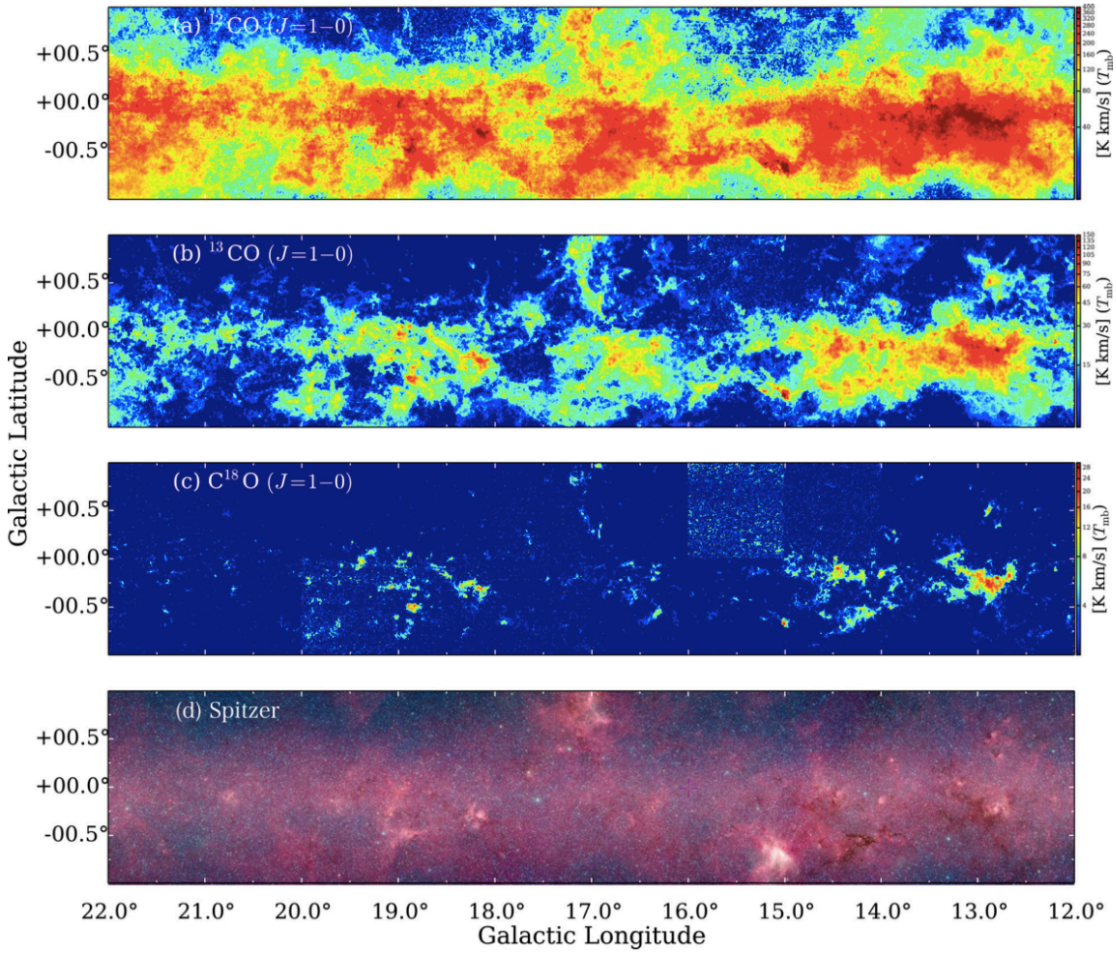

Figure 1.55: ^{12}CO, ^{13}CO, and C^{18}O $J=1$–0 images of the Galactic plane (Umemoto et al. 2017).

Primo et al. 2015) shows ratios of FWHM of spectra by ^{12}CO observations with single dish telescopes (Kuno et al. 2007; Leroy et al. 2009) and the H I observation (Walter et al. 2008) to FWHM of spectra by the interferometric observation with the Combined Array for Research in Millimeter-wave Astronomy (CARMA) for NGC 4736 and NGC 5055. They found that FWHM of single dish observations and the H I observation is usually larger by $\sim$ 20–60% than that from the interferometric observation. It indicates that there is the extended molecular gas component whose spatial extent may be comparable with that of H I gas.

Such diffuse molecular gas is seen in the survey for the Galactic plane. Figure 1.55 shows ^{12}CO, ^{13}CO, and C^{18}O $J=1$–0 integrated intensity maps obtained from the FOREST Unbiased Galactic Plane Imaging Survey with the Nobeyama 45 m Telescope (FUGIN; Umemoto et al. 2017). The image of ^{12}CO($J=1$–0) indicates the extended and diffuse molecular gas over the Galactic disk. In contrast, ^{13}CO($J=1$–0) traces more structured, cloud-like molecular gas because it is optically thin as mentioned in section 1.6.3. ^{13}CO($J=1$–0) is not scarcely detected in inter-clouds' complexes. That is, molecular gas can be decomposed into the two components, the GMC-like component and the diffuse component as suggested by Liszt et al. (2010) and Shetty et al. (2014a). In addition, properties of the cloud component can be inferred with the combination of ^{12}CO($J=1$–0) and ^{13}CO($J=1$–0), because ^{13}CO($J=1$–0) traces inner molecular gas

within clouds. Hence, we can examine which is the effective factor to characterize properties of molecular gas and star formation activity, the fraction of the cloud/diffuse component molecular gas or differences in properties of the cloud component. To investigate it, we conducted new ^{13}CO($J = 1$–0) observations toward the nearby barred spiral galaxy Maffei 2. Its results are described in chapter 4.

Chapter 2

Variations of ^{12}CO($J = 2$–1)/^{12}CO($J = 1$–0) line ratio in nearby galaxies on kiloparsec scales: validity of the assumption that the ratio is a constant

2.1 Abstract of this chapter

While molecular gas mass is usually derived from ^{12}CO($J = 1$–0) — the most fundamental line to explore molecular gas — it is often derived from ^{12}CO($J = 2$–1) assuming a constant ^{12}CO($J = 2$–1)/^{12}CO($J = 1$–0) line ratio ($R_{2/1}$). We present variations of $R_{2/1}$ and effects of the assumption that $R_{2/1}$ is a constant in 24 nearby galaxies using ^{12}CO data obtained with the Nobeyama 45-m radio telescope and IRAM 30-m telescope. The median of $R_{2/1}$ for all galaxies is 0.61, and the weighted mean of $R_{2/1}$ by ^{12}CO($J = 1$–0) integrated-intensity is 0.66 with a standard deviation of 0.19. The radial variation of $R_{2/1}$ shows that it is high ($\sim$0.8) in the inner $\sim$1 kpc while its median in disks is nearly constant at 0.60 when all galaxies are compiled. In the case that the constant $R_{2/1}$ of 0.7 is adopted, we found that the total molecular gas mass derived from ^{12}CO($J = 2$–1) is underestimated/overestimated by $\sim$20%, and at most by 35%. The scatter of a molecular gas surface density within each galaxy becomes larger by $\sim$30%, and at most by 120%. Indices of the spatially resolved Kennicutt–Schmidt relation by ^{12}CO($J = 2$–1) are underestimated by 10–20%, at most 39% in 17 out of 24 galaxies. $R_{2/1}$ has good positive correlations with star-formation rate and infrared color, and a negative correlation with molecular gas depletion time. There is a clear tendency of increasing $R_{2/1}$ with increasing kinetic temperature ($T_{\rm kin}$). Further, we found that not only $T_{\rm kin}$ but also pressure of molecular gas is important to understand variations of $R_{2/1}$. Special considerations should be made when discussing molecular gas mass and molecular gas properties inferred from ^{12}CO($J = 2$–1) instead of ^{12}CO($J = 1$–0).

2.2 Backgrounds of ^{12}CO($J = 2$–1)/^{12}CO($J = 1$–0)

Molecular gas is a crucial component in the interstellar medium (ISM) because star formation is the main physical process in the universe, and stars form from cold molecular gas. Therefore,

it is essential to understand the properties of molecular gas to investigate galaxies and their evolution. ^{12}CO($J=1$–0) line has been used as a tracer for cold molecular gas (e.g., Solomon et al. 1987; Young and Scoville 1991) because H_2 molecule cannot be directly observed in cold environments due to no electric dipole moment. Since the $J=1$ energy level of a ^{12}CO molecule is low ($\Delta E/k_{\rm B} \sim 5.5$ K, where ΔE is energy gap and $k_{\rm B}$ is the Boltzmann constant), ^{12}CO is easily excited to the $J=1$ level and emit ^{12}CO($J=1$–0) line even in cold conditions. In addition, the critical density of ^{12}CO($J=1$–0) is a few hundred cubic centimeters in an optical thick region. This value is quite lower than that of other molecular gas tracers. Furthermore, ^{12}CO is an abundant molecule in the ISM except hydrogen and helium, has large dissociation energy, and its abundance ratio is nearly uniform in molecular clouds. Thus, ^{12}CO($J=1$–0) is the most useful line to study the bulk of cold molecular gas. Molecular gas surface density ($\Sigma_{\rm mol}$) in galactic disks is usually derived from the following equation with the integrated intensity of ^{12}CO($J=1$–0), $I_{^{12}{\rm CO}(1-0)}$,

$$\left(\frac{\Sigma_{\rm mol}}{M_\odot\ {\rm pc}^{-2}}\right) = 1.36 \times 3.20\ \cos i \left[\frac{I_{^{12}{\rm CO}(1-0)}}{\rm K\ km\ s^{-1}}\right] \left[\frac{X_{\rm CO}}{2.0 \times 10^{20}\ {\rm cm^{-2}\ (K\ km\ s^{-1})^{-1}}}\right], \tag{2.1}$$

where i is the inclination angle of the galactic disk, $X_{\rm CO}$ is the CO-to-H_2 conversion factor that converts $I_{^{12}{\rm CO}(1-0)}$ into column density of H_2. Helium in molecular gas contributes the factor of 1.36 and the other factor 3.20 represents the unit conversion of K km s^{-1} into $M_\odot$ pc^{-2}. The product of $1.36 \times 3.20 = 4.35$ in units of $M_\odot$ pc^{-2} (K km s^{-1})$^{-1}$ corresponding to $X_{\rm CO} = 2.0 \times 10^{20}$ cm^{-2} (K km s^{-1})$^{-1}$ is also widely used as the CO-to-H_2 conversion factor that converts $I_{^{12}{\rm CO}(1-0)}$ into $\Sigma_{\rm mol}$ [or luminosity of ^{12}CO($J=1$–0) into molecular gas mass] usually denoted as "$\alpha_{\rm CO}$" (e.g., Bolatto et al. 2013b; Leroy et al. 2013; Schruba et al. 2019).

When the atmosphere is extremely dry, which is common at sites of short-millimeter and submillimeter telescopes, the observation efficiency of ^{12}CO($J=1$–0) for the local universe is usually lower than that with ^{12}CO($J=2$–1). This is because the rest frequency of ^{12}CO($J=1$–0), 115 GHz, is close to the O_2 absorption band at 118 GHz, and the ^{12}CO($J=2$–1) attenuation caused by water vapor is small at its rest frequency of 230 GHz in such sites. Thus, ^{12}CO($J=2$–1) is often used to observe molecular gas instead of ^{12}CO($J=1$–0) (e.g., Leroy et al. 2009, hereafter L09; Druard et al. 2014; Sun et al. 2018). In this case, $\Sigma_{\rm mol}$ is derived from the following equation instead of equation 1 by assuming the integrated-intensity ratio of ^{12}CO($J=2$–1)/^{12}CO($J=1$–0) (hereafter, $R_{2/1}$),

$$\left(\frac{\Sigma_{\rm mol}}{M_\odot\ {\rm pc}^{-2}}\right) = 1.36 \times 3.20\ \cos i\ R_{2/1}^{-1} \left[\frac{I_{^{12}{\rm CO}(2-1)}}{\rm K\ km\ s^{-1}}\right] \left[\frac{X_{\rm CO}}{2.0 \times 10^{20}\ {\rm cm^{-2}\ (K\ km\ s^{-1})^{-1}}}\right],$$

where $I_{^{12}{\rm CO}(2-1)}$ is the integrated intensity of ^{12}CO($J=2$–1). The value of 0.7–0.8 is usually assumed to be a constant $R_{2/1}$ (e.g., L09; Leroy et al. 2013).

Although ^{12}CO($J=2$–1) is used as a proxy of ^{12}CO($J=1$–0), the energy of ^{12}CO $J=2$ level ($\Delta E/k_{\rm B} \sim 16.5$ K) is higher than that in the typical cold molecular clouds (~ 10 K). Therefore, it is possible that ^{12}CO molecules are not well excited to reach the $J=2$ level based on molecular gas properties (e.g., Peñaloza et al. 2017). Molecular gas traced by ^{12}CO($J=2$–1) is warmer and/or denser than that traced using ^{12}CO($J=1$–0). $R_{2/1}$ is influenced by the physical conditions of molecular gas.

The systematic variations of $R_{2/1}$ have been reported in previous observations of molecular gas in the Milky Way. For nearby giant molecular clouds (GMCs), while $R_{2/1}$ is medium ($\sim$ 0.7–

0.8) in the ridges of GMCs, it exceeds unity in interfaces of H II regions and OB associations, and it is relatively low in the peripheries of GMCs ($\sim$ 0.5) (Sakamoto et al. 1994; Nishimura et al. 2015). GMCs with active star formation tend to show high $R_{2/1}$ while those with quiescent star formation show low ratios. In large scales of the Milky Way, $R_{2/1}$ decreases from 0.75 at 4 kpc to 0.5 at 8 kpc as a function of the Galactocentric radius (Sakamoto et al. 1995; Sakamoto et al. 1997b). Further, a $R_{2/1}$ gradient appears across spiral arms; it gradually increases toward the downstream of arms. In addition, $R_{2/1}$ shows higher values that are close to unity in the Galactic center compared with the Galactic disk (Oka et al. 1998; Sawada et al. 2001).

For external galaxies, a pioneering study by Braine and Combes (1992) reported that there is a moderate positive correlation between $R_{2/1}$ and infrared (IR) color, and they attempted to infer molecular gas properties from $R_{2/1}$ around the center of nearby galaxies. High $R_{2/1}$ (0.9 with the scatter of $\sim$ 0.3) was reported in the Large Magellanic Cloud (LMC), and positions where $R_{2/1}$ is high do not always coincide with massive star-formation regions (Sorai et al. 2001). It was argued that it reflects dense molecular gas, which is ready to form stars and is not due to warmed gas by radiations from massive stars, whereas the low metallicity environment in LMC may also influence $R_{2/1}$. In several nearby galaxies, the median of $R_{2/1}$ in disks is approximately constant ($\sim$ 0.8) and $R_{2/1}$ increases ($>$ 1) in the center similar to that in the Milky Way (L09), while some galaxies show a nearly constant $R_{2/1}$ in the entire galaxy including the center (e.g., M 33; Druard et al. 2014). Leroy et al. (2013) reported the median of 0.66 with standard deviations of $\sim$ 0.3 for approximately 30 nearby galaxies. Based on this result, some studies using ^{12}CO($J=2$–1) data assumed the constant $R_{2/1}=0.7$ and converted the intensity of the line into that of ^{12}CO($J=1$–0) to derive molecular gas mass and its surface density.

A detailed study to understand $R_{2/1}$ as a probe of molecular gas properties in the extragalactic field reported that while typical $R_{2/1}$ is $\sim$ 0.7, it is relatively high (0.8–0.9) in the leading side (the downstream) of the spiral arms and low (0.4–0.6) in the inter-arms for M 51 as well as the Milky Way (Koda et al. 2012). In addition, they found that $R_{2/1}$ increases as surface density of star-formation rate ($\Sigma_{\rm SFR}$) and star-formation efficiency (SFE) in this galaxy. They also suggested that high $R_{2/1}$ is relevant to warm molecular gas by active star formation and compressed molecular gas before star formation. With regard to $R_{2/1}$ and star formation activity, it was found that the correlation of $R_{2/1}$ with IR color is better than that of $R_{2/1}$ with far-ultraviolet (FUV), and far IR intensities in M 83 (Koda et al. 2020). It was argued that these are attributed to warm molecular gas heated by dust, UV photons, and cosmic ray from supernovae, considering high $R_{2/1}$ in the downstream of arms where many massive stars are seen.

As described above, $R_{2/1}$ has systematic variations within and among galaxies, and it reflects molecular gas conditions such as temperature. Hence, it would be possible that molecular gas mass, its related quantities and relations derived from ^{12}CO($J=2$–1) with assumed constant $R_{2/1}$ are misled (e.g., Momose et al. 2013) although there remains the uncertainty of the CO-to-H_2 conversion factor. It is better to test the validity of the assumption that $R_{2/1}$ is constant, and its effect on derived quantities and relations which are relevant to molecular gas, especially for many types of galaxies. Furthermore, the causes of $R_{2/1}$ variations should be investigated with physical properties of molecular gas.

The largest CO-mapping survey for nearby galaxies in the world, CO Multi-line Imaging

of Nearby Galaxies (COMING; Sorai et al. 2019[1)], hereafter S19) was carried out using the receiver FOur-beam REceiver System on the 45-m Telescope (FOREST; Minamidani et al. 2016) installed on the Nobeyama 45-m telescope. COMING mapped 147 nearby galaxies in ^{12}CO, ^{13}CO, and C^{18}O $J=1$–0 lines. The addition of other CO-mapping surveys such as Kuno et al. (2007) (hereafter, K07) and L09 enable us to investigate spatial $R_{2/1}$ variations in many types of nearby galaxies and the effects of the assumption for a constant $R_{2/1}$ in a large area of galaxies. With those CO data, we verify the assumption of fixed $R_{2/1}$. The key questions in this paper are as follows: (i) How does the assumption of a constant $R_{2/1}$ affect molecular gas mass itself and its relevant relations? Is the assumption that $R_{2/1}$ is a constant reasonable?; (ii) What changes $R_{2/1}$? How does $R_{2/1}$ vary depending on molecular gas properties?

The remainder of this chapter is organized as follows. In section 2.3, the samples of this study, analysis of CO cubes, intensity accuracy of CO considering calibration and pointing, and ancillary data sets are explained. The spatial distribution, statistics, and radial distribution of $R_{2/1}$ are described in the first half of section 2.4. In the latter half of the section, we report effects of the constant $R_{2/1}$ on molecular gas mass, its scatter within a galaxy, and the $\Sigma_{\rm SFR}$–$\Sigma_{\rm mol}$ relation (i.e., the molecular gas Kennicutt–Schmidt relation). To investigate the relation of $R_{2/1}$ and molecular gas properties, the correlations of representative quantities and $R_{2/1}$ are examined in the first half of section 2.5. We attempted to derive the intrinsic properties of molecular gas, number density, and kinetic temperature from ^{12}CO($J=1$–0), ^{12}CO($J=2$–1), and ^{13}CO($J=1$–0) for COMING galaxies and compared them with $R_{2/1}$. These discussions and implications are described in the latter half of section 2.5. Finally, the conclusions of this paper are provided in section 2.6.

2.3 Data sets

2.3.1 CO data and their analysis

^{12}CO($J=1$–0) data used in this paper were taken from COMING firstly. Refer to sections 3 and 4 in S19 for details about the settings of observations, calibration, and data reduction for COMING. In addition, Nobeyama CO Atlas of Nearby Spiral Galaxies (K07) is used as the second reference of ^{12}CO($J=1$–0) data. Since the samples of K07 includes galaxies with large appearances, it makes it possible to discuss variations of $R_{2/1}$ in large area of galaxies. For the ^{12}CO($J=2$–1) reference, we use HERA CO-Line Extragalactic Survey (HERACLES; L09) carried out with the IRAM 30-m telescope.

The ^{12}CO($J=1$–0) data obtained by K07 and ^{12}CO($J=2$–1) data obtained by L09 were convolved to match the angular resolution of 17″, which is the original resolution of COMING. Before measurements of $R_{2/1}$, the coordinates for all CO cubes were matched and regridded so that the grid size becomes 8″. Then, velocity channels were binned so that the velocity resolution is 20 km s^{-1}. These processes were performed to improve signal-to-noise ratio (S/N). After that, the baseline was subtracted.

The method of baseline subtraction is the same as COMING Auto-Reduction Tool (COMING ART; see section 4.2 in S19 for detail), however, signal channels are defined by ^{12}CO($J=2$–1), not by ^{12}CO($J=1$–0) because ^{12}CO($J=2$–1) data achieves a much better sensitivity than that

[1)] See also ⟨https://astro3.sci.hokudai.ac.jp/~radio/coming/⟩

Table 2.1: Samples in this study.

galaxy	D [Mpc] (1)	i [deg] (2)	P.A. [deg] (3)	Res. [kpc] (4)	^{12}CO(1–0) ref. (5)
NGC 337	18.9	44.5	119.6	1.6	S19
NGC 628	9.02	7	20	0.74	S19
NGC 2146	27.7	62	−43.5	2.3	S19
NGC 2798	29.6	60.7	158.7	2.4	S19
NGC 2841	14.60	73.7	152.6	1.2	S19
NGC 2903	9.46	67	−155	0.78	S19
NGC 2976	3.63	64.5	−25.5	0.30	S19
NGC 3034	3.53	81	68	0.34	S19
NGC 3077	3.81	38.9	63.8	0.31	S19
NGC 3184	8.7	21	−174	0.72	K07
NGC 3198	13.40	71.5	−145.0	1.1	S19
NGC 3351	10.7	41	−168	0.88	K07
NGC 3521	14.20	63	−19	1.2	S19
NGC 3627	9.04	52	176	0.75	S19
NGC 3938	17.9	20.9	−154.0	1.5	S19
NGC 4214	2.93	30	65	0.24	S19
NGC 4254	16.5	42	66	1.4	K07
NGC 4321	16.5	27	138	1.4	K07
NGC 4536	16.5	64.2	−54.5	1.4	S19
NGC 4559	7.31	63.1	−36.8	0.60	S19
NGC 4569	16.5	64	22	1.4	K07
NGC 4579	16.5	41.7	92.1	1.4	S19
NGC 4736	4.3	40	−61	0.4	K07
NGC 5055	9.04	61	98	0.75	S19
NGC 5194	7.7	20	176	0.63	K07
NGC 5457	7.2	18	42	0.59	K07
NGC 5713	19.5	33	−157	1.6	S19
NGC 6946	5.5	40	−118	0.5	K07
NGC 7331	13.90	75.8	167.7	1.1	S19

(1) Adopted distance.
(2) Inclination angle of the disk.
(3) Position angle of the major axis of the disk for the redshifted side (against the north direction, the positive values correspond to the counterclockwise direction).
(4) The linear scale corresponded to the angular resolution of 17″ along the major axis of the disk.
(5) References of ^{12}CO($J=1$–0) data.
References of D, i, P.A. are the same as in S19 or K07.

of ^{12}CO($J=1$–0). That is, the result that whether the channel is a 'signal' or 'noise' for each channel of ^{12}CO($J=2$–1) in a position was applied to that of ^{12}CO($J=1$–0) at the channel of the same velocity in the position. This methodology does not induce any biases for ^{12}CO($J=1$–0) and ^{12}CO($J=2$–1) integrated-intensities because the sensitivities of the ^{12}CO($J=2$–1) data are much better than those of ^{12}CO($J=1$–0). The threshold to evaluate each channel as a 'signal' or a 'noise' is set as $3\,\sigma$, where σ is the root mean square (R.M.S.) measured in the defined emission-free velocity range beforehand.

The samples in this study consist of 29 galaxies that are overlapped between S19 + K07, and

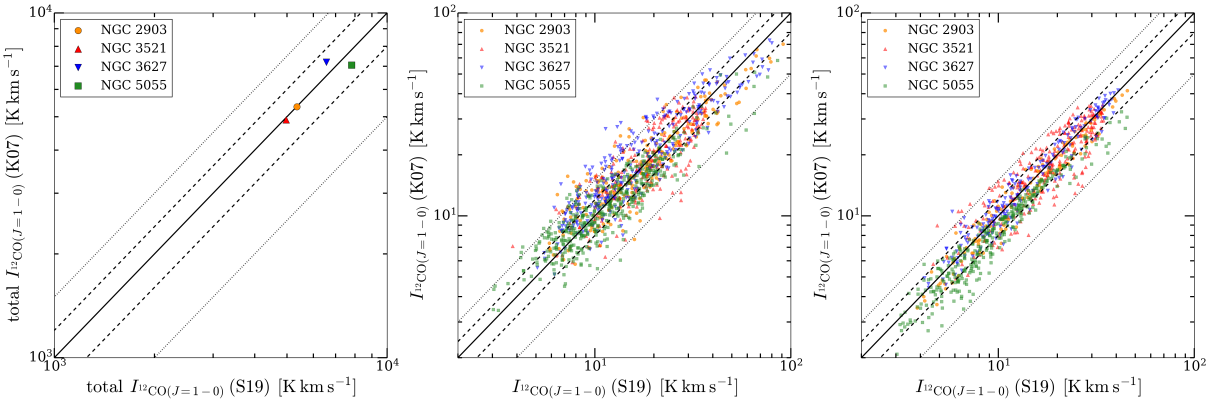

Figure 2.1: Consistency of integrated intensity for NGC 2903, NGC 3521, NGC 3627, and NGC 5055 between S19 and K07 summing up within the whole disk, which corresponds to total flux (left), at the original resolution and grid size (center) and convolved data so that the resolution and grid size are fixed to 1.5 kpc and 650 pc (right), respectively. Pixels below 5 σ are masked in the center and right panel. The solid, dashed, and dotted lines in each panel indicate inconsistency of 0%, ±20%, and ±50%, respectively.

L09. They are listed in table 2.1. For the overlapped galaxies between S19 and K07 (NGC 2903, NGC 3351, NGC 3521, NGC 3627, NGC 5055), we used S19 data except for NGC 3351 because the baseline of the S19 data for this galaxy is heavily undulated.

2.3.2 Intensity accuracy of CO data regarding calibration and pointing error

Intensity accuracy of CO data is important to study $R_{2/1}$ because its contrast is relatively small (usually $R_{2/1} = 0.4$–1.0) as argued in Koda et al. (Koda et al. 2012; Koda et al. 2020). Therefore, calibration and pointing error is an issue in this paper. We demonstrated how intensity of ^{12}CO($J = 1$–0) data is accurate with overlapped 4 galaxies (NGC 2903, NGC 3521, NGC 3627, NGC 5055) between S19 and K07. Although NGC 3351 is an overlapped galaxy, the baseline of this galaxy is heavily undulated and thus, we excluded this galaxy to test intensity consistency. Both S19 and K07 data was regridded and the baseline was subtracted in the same way described in section 2.3.1.

We firstly tested consistency of total integrated-intensity within the whole disk (i.e., total flux) for S19 and K07 data and integrated intensity at position-to-position in the original resolution (17″) and grid size (8″). The left and center panel of figure 2.1 shows correlations of total integrated-intensities and integrated intensities at each pixel, respectively. The threshold was set to be 5 σ in the central panel. The difference of total integrated-intensity is at most $\sim 10\%$. The scatter of intensity at position-to-position is $\sim 25\%$ in the R.M.S. level within each galaxy. Hence, calibration error of ^{12}CO($J = 1$–0) used in this paper is up to 10% and intensity accuracy including pointing error and calibration error is 25% at the original resolution.

In section 2.4.3 and 2.5.1, we use convolved CO data so that the spatial resolution and grid size are fixed to 1.5 kpc and 650 pc, respectively. In addition, we stacked spectra within concentric annuli in disks and galactic structures in analyses of section 2.5.2 and 2.5.3. Thus, we next tested consistency of convolved S19 and K07 data to match the resolution of 1.5 kpc and grid size of 650 pc. The right panel of figure 2.1 shows consistency of integrated intensity between S19 and K07 for convolved data. The scatter at position-to-position in this case is

$\sim$ 15% in each galaxy. Therefore, intensity error combining calibration and pointing error in section 2.4.3 and 2.5.1 is 15%. Since in stacking analysis, spectra are stacked in a large area (galactic components and concentric annuli whose width is $r_{25}/8$ where r_{25} is B-band isophotal radius at 25 mag arcsec^{-2}), intensity error due to pointing error will be negligible.

We would like to note that intensity accuracy of ^{13}CO($J=1$–0) against ^{12}CO($J=1$–0) is relatively good because ^{13}CO($J=1$–0) data was taken simultaneously with ^{12}CO($J=1$–0) in COMING observations. In addition, since COMING applied the On-The-Fly (OTF) mode in their observation, while observation in K07 applied the Position-Switch, calibration and pointing accuracy of S19 would be better than that of K07.

We could not test how calibration/pointing error of ^{12}CO($J=2$–1) data is in the same way of S19 and K07 because there is no available archival data of the line. However, L09 mentioned that daily variations of ^{12}CO($J=2$–1) intensity at high S/N regions is 20%. Therefore, intensity error of ^{12}CO($J=2$–1) combining calibration and pointing error is 20%, which is quite better than that of ^{12}CO($J=1$–0). Assuming the fraction of contribution by pointing error is the same as the ^{12}CO($J=1$–0) case, calibration error of ^{12}CO($J=2$–1) will be $\sim$ 8%. Hence, there will be also calibration error of $\sim$ 10% in ^{12}CO($J=2$–1) data, which is common in short millimeter-wave observations. Similarly, intensity error due to calibration/pointing error in convolved ^{12}CO($J=2$–1) data will be $\sim$ 12%. To summarize above descriptions, $R_{2/1}$ error due to calibration error is 13%, due to calibration+pointing error at original angular resolution is 32%, and at fixed spatial resolution and grid size is 19%, respectively.

2.3.3 Data in other wavelengths

Star-formation rate (SFR) was derived from FUV and 22-μm band intensity based on the following equation by Casasola et al. (2017) and Leroy et al. (2008) that adopted the Kroupa initial mass function (IMF; Kroupa 2001) as with the method in other COMING papers (e.g., Muraoka et al. 2019; Takeuchi et al. 2020 in prep.):

$$\left(\frac{\Sigma_{\rm SFR}}{M_\odot\ {\rm yr}^{-1}\ {\rm kpc}^{-2}}\right) = 1.59\cos i\left[3.2\times10^{-3}\left(\frac{I_{22\mu{\rm m}}}{{\rm MJy\ sr}^{-1}}\right) + 8.1\times10^{-2}\left(\frac{I_{\rm FUV}}{{\rm MJy\ sr}^{-1}}\right)\right],$$

where $I_{22\mu{\rm m}}$ and $I_{\rm FUV}$ are intensities of the 22-μm and FUV band. The FUV maps were obtained with the GALEX Ultraviolet Atlas of Nearby Galaxies (Gil de Paz et al. 2007) and were retrieved from the NASA/IPAC Extragalactic Database (NED). The 22-μm maps obtained with the WISE band 4 were retrieved from the NASA/IPAC Infrared Science Archive.

In addition, the IR color that represents dust temperature is used as an indicator of ISM conditions. To measure the IR color in many galaxies as much as possible, we used the intensity ratio of the 70-μm to 160-μm band obtained with Herschel/PACS. This filter selection reduces the sample number of galaxies because of a lack of samples in the far-infrared range.

2.4 Results

2.4.1 Maps, histograms, statistics, and radial distribution of $R_{2/1}$

Figure 2.2 shows the $R_{2/1}$ maps for our sample galaxies in the original resolution of COMING (17″). Here, error of $R_{2/1}$ is derived from that of $I_{^{12}{\rm CO}(1-0)}$ and $I_{^{12}{\rm CO}(2-1)}$ based on propagation of

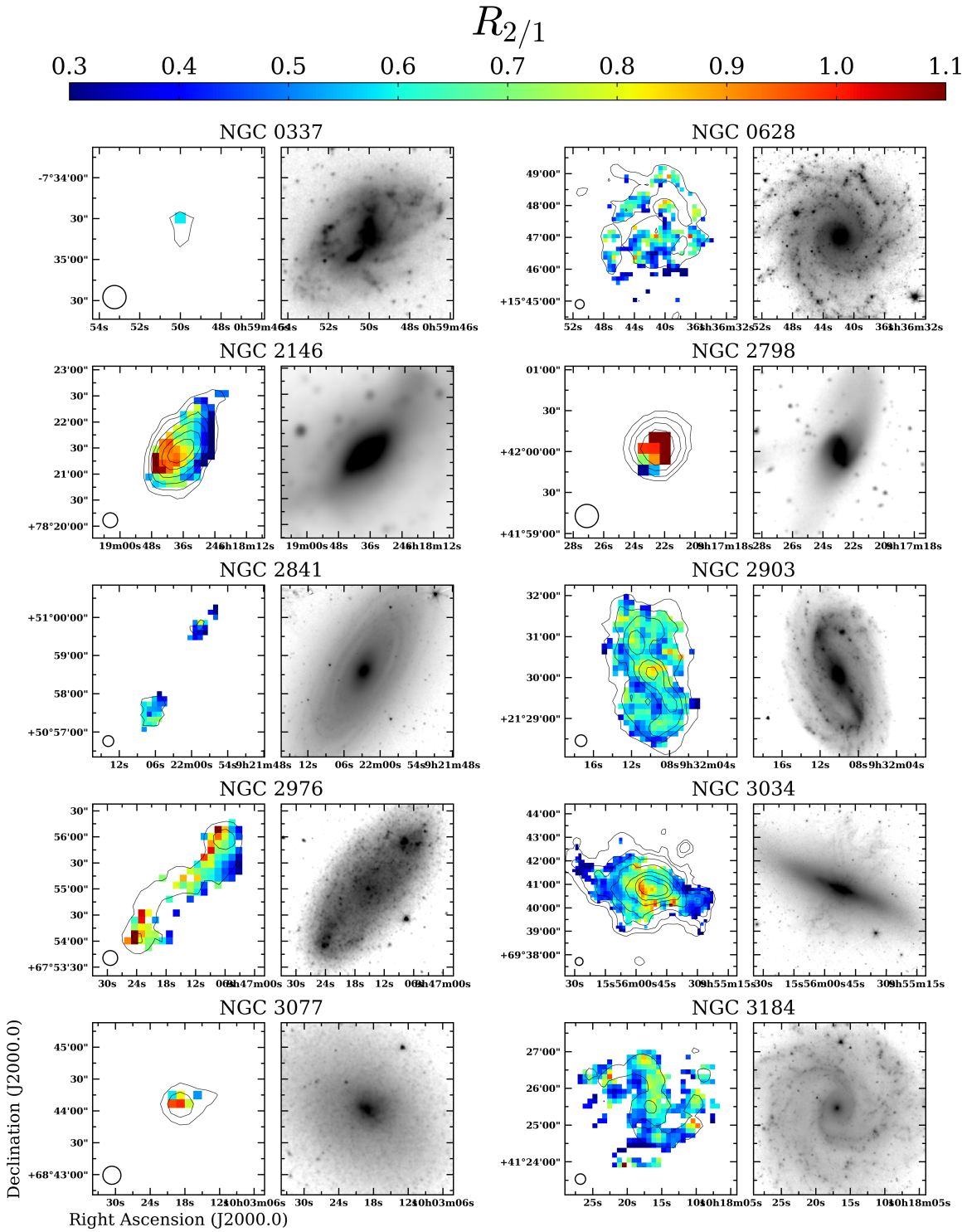

Figure 2.2: $R_{2/1}$ maps (left) and near-infrared images in gray scale (right) of all galaxies in the samples. In $R_{2/1}$ maps, pixels are masked when either integrated intensities of ^{12}CO($J=1$–0) or ^{12}CO($J=2$–1) at the pixel do not reach $4.5\,\sigma$. The middle of the color bar corresponds to $R_{2/1} = 0.7$, which is the usually assumed value for a constant $R_{2/1}$. Open circles in the bottom left corner in each panel indicate the angular resolution of 17″. Black contours indicate the integrated intensity of ^{12}CO($J=2$–1) at levels 2, 5, 10, 20, 50, 100, and 200 K km s^{-1}. The reference of near-infrared data is Spitzer/IRAC 3.6-μmimages obtained by the S^{4}G survey (Sheth et al. 2010) except for NGC 2146. For NGC 2146, the WISE 3.4-μmimage is used alternatively.

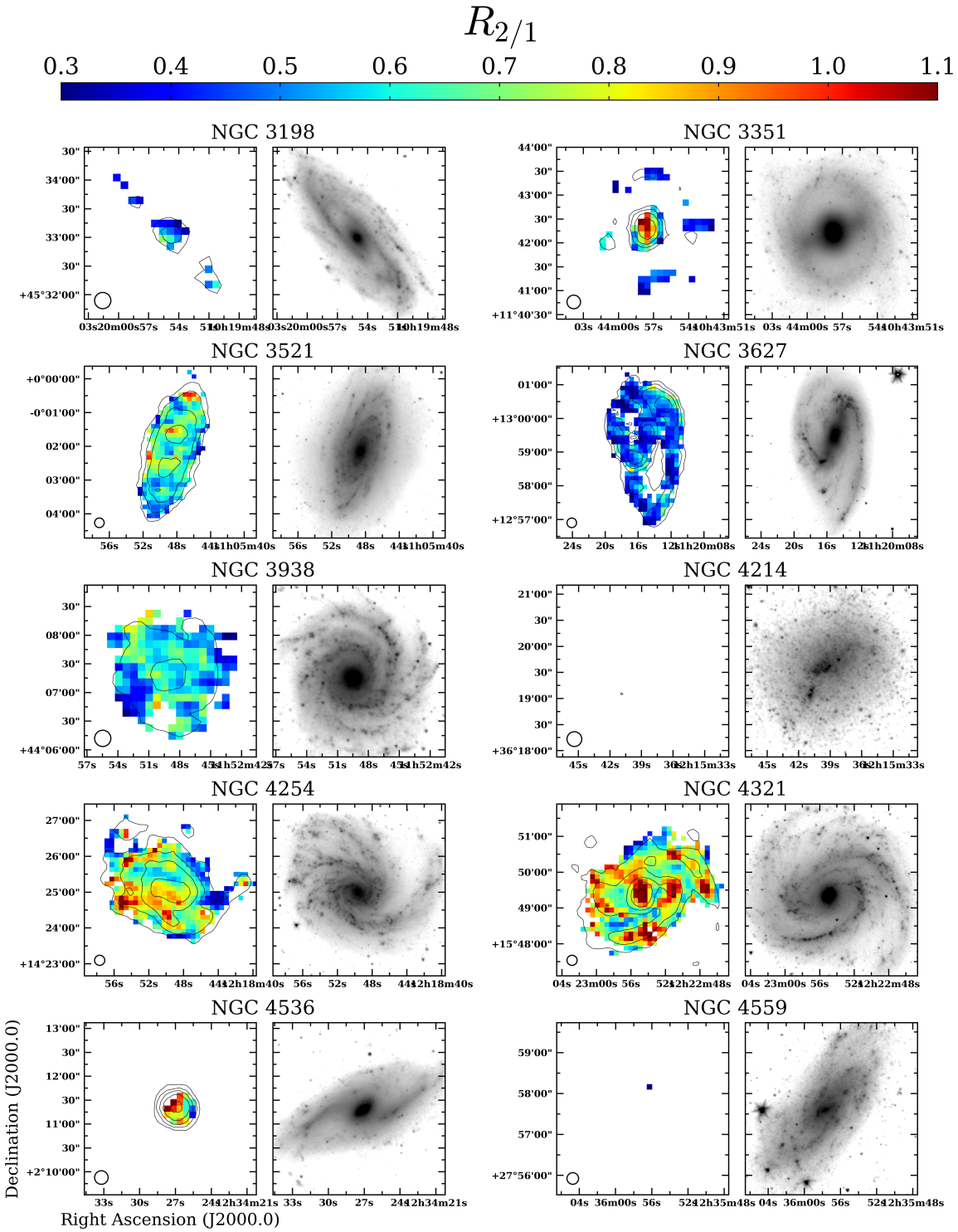

Figure 2.2: (Continued.)

their error. Each galaxy shows various $R_{2/1}$. For example, NGC 2798 and NGC 4736 show higher (> 0.9) $R_{2/1}$ in large area. $R_{2/1}$ is low (< 0.6) in most positions of NGC 2841 and NGC 3627. Some galaxies have significant variations within each galaxy. NGC 2146 and NGC 5713 show an $R_{2/1}$ gradient from ~ 1.2 to 0.4. In NGC 4321, $R_{2/1}$ is clearly high ($\gtrsim 1.0$) in the center

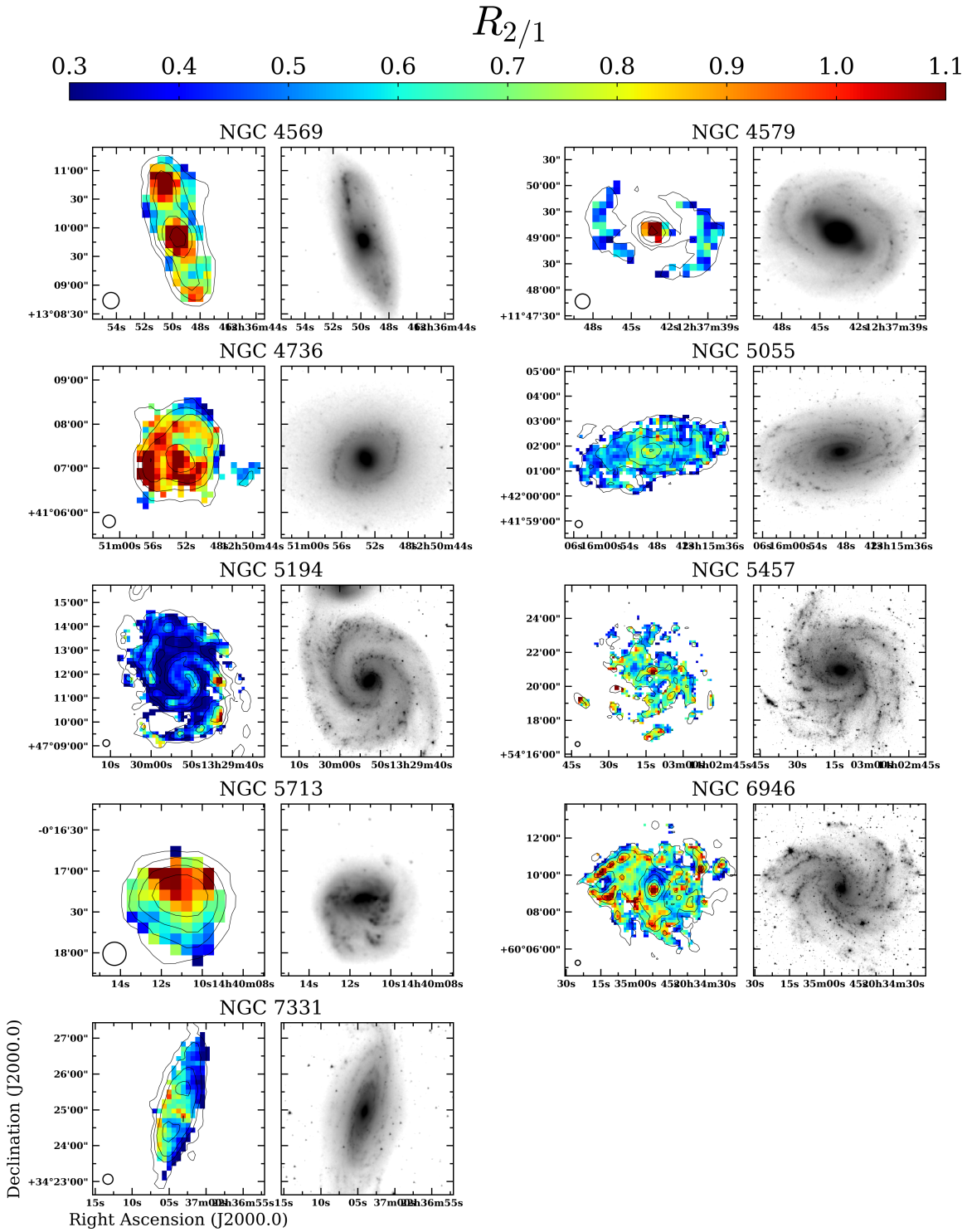

Figure 2.2: (Continued.)

and bar ends, low ($\lesssim 0.6$) in inter-arms, and intermediate (0.7–0.8) in arms. In NGC 3351 and NGC 4579, $R_{2/1}$ is low in the ring-like structure, whereas $R_{2/1}$ is high in the center.

Some galaxies show gradation of $R_{2/1}$ from a side to the other (e.g., NGC 2146, NGC 2798, NGC 5713, NGC 7331). We tested these gradations are due to the systematic pointing offset

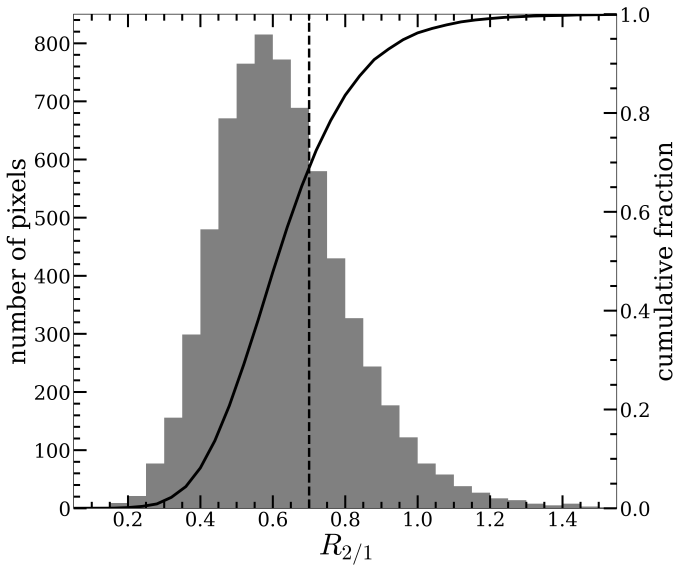

Figure 2.3: Histogram of $R_{2/1}$ for all pixels of all galaxies. The solid line shows the cumulative distribution function and the dashed line indicates $R_{2/1} = 0.7$.

between ^{12}CO($J=1$–0) and ^{12}CO($J=2$–1) observations with spectra at some doubtful positions and residual maps of the first moment maps derived from the lines. According to the test, there is no indication of systematic pointing offset. Gradations of $R_{2/1}$ may be caused by interactions (e.g., NGC 2146, NGC 2798, NGC 5713) or appearance of disk due to three-dimensional warp (NGC 7331).

Note that the result for NGC 5194 is not consistent with Koda et al. (2012). They reported that intensities of ^{12}CO($J=1$–0) data obtained in K07 (the original map is from Nakai et al. 1994) for this galaxy is ~ 2 times higher than that of Koda et al. (2011). They argued that a calibration error in the data of Nakai et al. (1994) was caused by difficulties in the calibration method at that time.

Figure 2.3 shows the histogram of $R_{2/1}$ and the cumulative distribution function for all pixels in all galaxies in the samples. As shown in the figure, the constant value of 0.7 assumed in many cases so far is rather large. The peak of the histogram is in the range of 0.55–0.60; the most frequently appearing value of $R_{2/1}$ is lower than 0.7. Cumulative fraction also indicates $R_{2/1} = 0.7$ is quite higher in our samples (cumulative fraction at $R_{2/1} = 0.7$ is $\sim 70\%$). This is significant even considering $R_{2/1}$ error of 13% due to calibration error of CO data. The median, mean weighted by ^{12}CO($J=1$–0) integrated-intensity, and standard deviation of $R_{2/1}$ combined for all galaxies are 0.61, 0.66, and 0.19, respectively.

The median we obtained ($R_{2/1} = 0.61$) is slightly lower than the value ($R_{2/1} = 0.67$) reported in Leroy et al. (2013), while this difference would not be significant considering $R_{2/1}$ error due to calibration error is 13% (section 2.3.2). If this difference is significant, this discrepancy may have originated from differences in observed areas. Most ^{12}CO($J=1$–0) data Leroy et al. (2013) used are from Usero et al. (2015), which observed specific positions in a galaxy where ^{12}CO($J=2$–1) is strong. Their observed areas in each galaxy usually include the center of the galaxy where $R_{2/1}$ tends to be high as mentioned in the next paragraph. These results and statistics of $R_{2/1}$

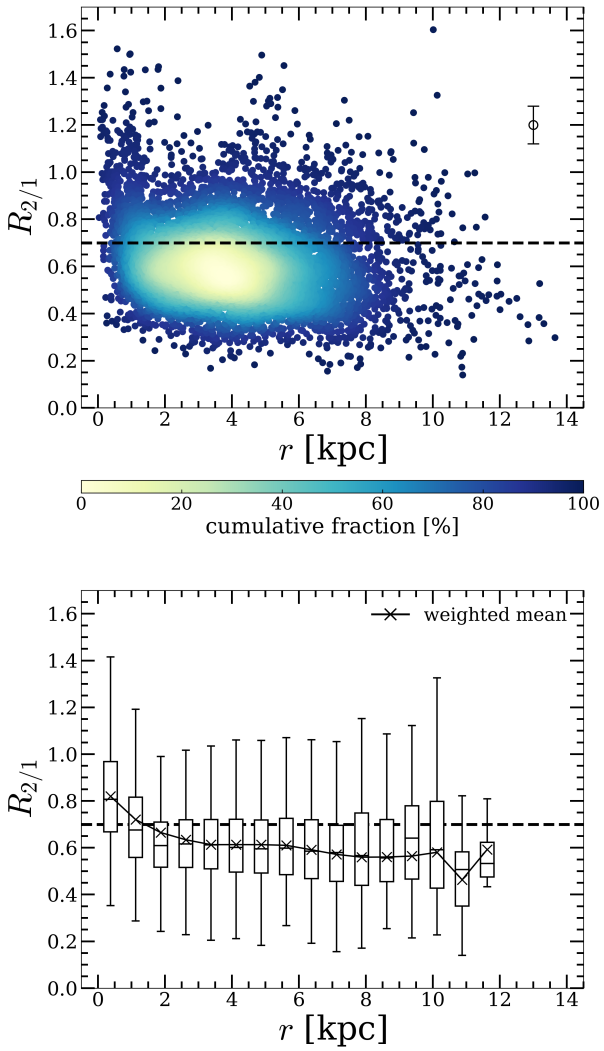

Figure 2.4: Radial distribution of $R_{2/1}$ for all galaxies. The dashed line in the both panels indicates $R_{2/1} = 0.7$. (Top) Scatter plot of $R_{2/1}$ against the galactocentric radius. The colors indicate the cumulative fraction of data. The typical error of $R_{2/1}$ is shown on the top right with the open circle marker. (Bottom) Box plot for the top panel. Each bin is 0.75 kpc in width. Cross markers show mean $R_{2/1}$ in a bin weighted by ^{12}CO($J = 1$–0) integrated-intensity. The upper whisker extends up to the maximum value and the lower whisker extends down to the minimum value in each bin unless the maximum value is less than $Q_3 + 1.5$IQR and the minimum value is larger than $Q_1 - 1.5$IQR, where Q_1 is the 25th percentile, Q_3 is 75th percentile, and IQR is the interquartile range defined as $Q_3 - Q_1$. Otherwise, the upper whisker extends up to $Q_3 + 1.5$IQR and the lower whisker extends down to $Q_1 - 1.5$IQR without outliers for simplicity.

such as median, $Q_2(R_{2/1})$, and weighted mean, $\overline{R_{2/1}}$, for each galaxy are summarized in table 2.2 with some properties of galaxies related to star formation. The relations between $R_{2/1}$ and these properties of galaxies are discussed in section 2.5.1. The histograms of $R_{2/1}$ for each galaxy are shown in section 2.7.

Figure 2.4 shows $R_{2/1}$ as a function of the galactocentric radius for all galaxies. Both the median and weighted mean of $R_{2/1}$ in the disk region ($r > 2$ kpc) are nearly constant at 0.60. Although $R_{2/1}$ in the disk is lower than 0.7, it tends to exceed 0.7 in central regions. Both

Table 2.2: Statistics of $R_{2/1}$ and properties of the samples.

galaxy	$Q_2(R_{2/1})$	$\overline{R_{2/1}}$	$\sigma(R_{2/1})$	$\overline{\Sigma_{\rm mol}}$ $[M_\odot\,{\rm pc}^{-2}]$	$\overline{\Sigma_{\rm SFR}}$ $[10^{-2}\,M_\odot\,{\rm yr}^{-1}\,{\rm kpc}^{-2}]$	$\overline{\tau_{\rm dep}}$ [Gyr]	$\overline{I_{70\mu{\rm m}}}/\overline{I_{160\mu{\rm m}}}$
	(1)	(2)	(3)	(4)	(5)	(6)	(7)
All	0.61	0.66	0.19	—	—	—	—
NGC 337	—*	—*	—*	—*	—*	—*	—*
NGC 628	0.54	0.54	0.14	17.5	0.962	1.82	0.363
NGC 2146	0.66	0.73	0.23	113	27.9	0.406	1.22
NGC 2798	0.99	1.0	0.33	44.0	17.8	0.248	1.45
NGC 2841	0.51	0.50	0.12	4.34	0.287	1.51	0.210
NGC 2903	0.59	0.62	0.11	21.8	1.93	1.13	—†
NGC 2976	0.67	0.67	0.20	3.13	0.527	0.594	0.483
NGC 3034	0.56	0.67	0.15	23.2	3.75	0.617	1.43
NGC 3077	—*	—*	—*	—*	—*	—*	—*
NGC 3184	0.55	0.56	0.14	14.5	0.756	1.91	0.307
NGC 3198	0.46	0.47	0.10	6.37	0.915	0.697	0.493
NGC 3351	0.48	0.73	0.21	19.4	3.20	0.608	0.765
NGC 3521	0.61	0.63	0.12	31.2	2.17	1.43	0.423
NGC 3627	0.46	0.46	0.10	39.0	2.96	1.32	0.543
NGC 3938	0.56	0.56	0.11	20.5	1.43	1.44	0.409
NGC 4214	—*	—*	—*	—*	—*	—*	—*
NGC 4254	0.70	0.72	0.17	39.8	3.27	1.21	0.483
NGC 4321	0.76	0.83	0.18	26.7	2.00	1.33	0.421
NGC 4536	0.79	0.84	0.24	54.7	11.5	0.474	1.18
NGC 4559	—*	—*	—*	—*	—*	—*	—*
NGC 4569	0.76	0.89	0.25	27.5	1.63	1.69	0.420
NGC 4579	0.50	0.63	0.20	20.1	0.890	2.25	0.396
NGC 4736	0.84	0.88	0.24	20.8	2.90	0.718	0.870
NGC 5055	0.54	0.56	0.11	18.2	0.87	2.11	0.330
NGC 5194	0.40‡	0.41‡	0.16‡	—§	2.98	—§	0.436
NGC 5457	0.62	0.64	0.18	15.3	0.89	1.72	0.336
NGC 5713	0.72	0.80	0.24	61.3	9.35	0.656	0.804
NGC 6946	0.67	0.71	0.17	29.6	1.85	1.60	0.491
NGC 7331	0.53	0.55	0.17	18.3	1.11	1.65	0.426

(1) Median of $R_{2/1}$.
(2) Mean of $R_{2/1}$ weighted by integrated intensity of ^{12}CO($J=1$–0) averaged over the pixels where $R_{2/1}$ is significantly measured (cf. figure 2.2).
(3) Standard deviation of $R_{2/1}$.
(4)–(5) Mean surface density of molecular gas and SFR. The area used to derive these means are the same as column (2).
(6) Mean depletion time derived as total molecular gas mass over total SFR within the area used in column (2).
(7) Mean IR color derived as total luminosity of 70 μmover that of 160 μmwithin the area used in column (2).
* There are few or no pixels to measure $R_{2/1}$.
† Archival data is not available.
‡ There may be calibration error of CO data.
§ Not derived due to the possibility of calibration error.

the median and weighted mean is 0.83 in the inner 0.75 kpc (the innermost bin of the bottom panel of figure 2.4). The usually assumed constant value of 0.7 for $R_{2/1}$ is common only for the transition region of the galactic center and the disk (1 kpc $\lesssim r \lesssim$ 2 kpc).

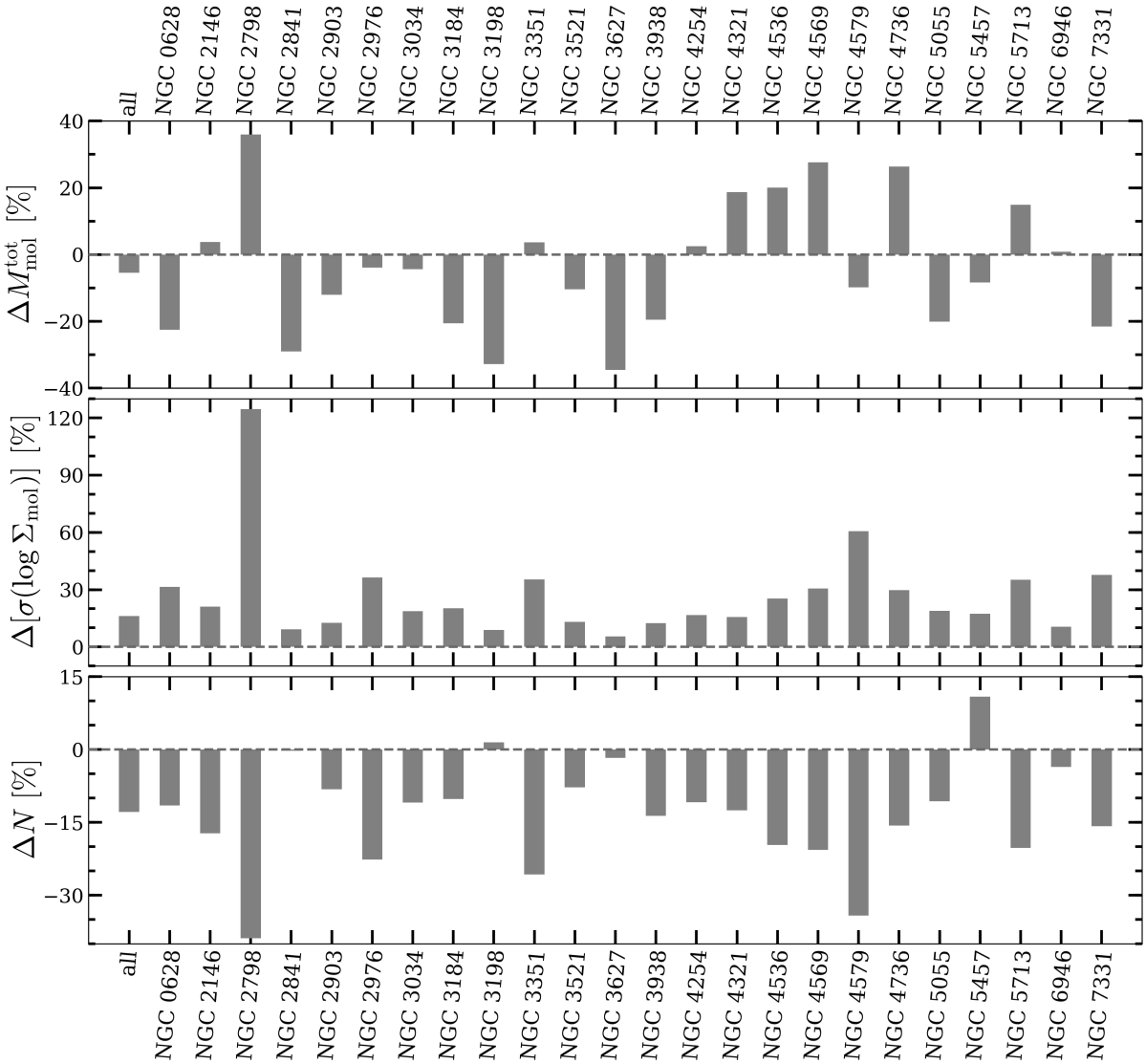

Figure 2.5: Rate of change in the total molecular gas mass $\Delta M_{\rm mol}^{\rm tot}$ (top), standard deviation of molecular gas surface density $\Delta[\sigma(\log \Sigma_{\rm mol})]$ (middle), and index of the K–S relation ΔN (bottom) in each galaxy.

2.4.2 Effects of $R_{2/1}$ on molecular gas mass derived from ^{12}CO($J = 2$–1)

As effects originated from the assumption that $R_{2/1}$ is a constant, we report that how molecular gas mass is underestimated or overestimated and how the scatter of molecular gas surface density within a galaxy changes. We adopted the standard CO-to-H_2 conversion factor $X_{\rm CO}$ of 2.0×10^{20} cm^{-2} (K km s^{-1})$^{-1}$ (Bolatto et al. 2013b) for the entire area of all galaxies based on the widely used method.

The top panel of figure 2.5 shows how the total molecular gas mass within a galaxy changes (rate of change in total molecular gas mass; $\Delta M_{\rm mol}^{\rm tot}$) when the molecular gas mass is derived from ^{12}CO($J = 2$–1) with the $R_{2/1}$ of 0.7 compared with the case wherein $M_{\rm mol}^{\rm tot}$ is derived from CO($J = 1$–0). For instance, $\Delta M_{\rm mol}^{\rm tot} = -20\%$ indicates that the total molecular gas mass derived from ^{12}CO($J = 2$–1) is underestimated by 20%. NGC 337, NGC 3077, NGC 4214, and NGC 4559

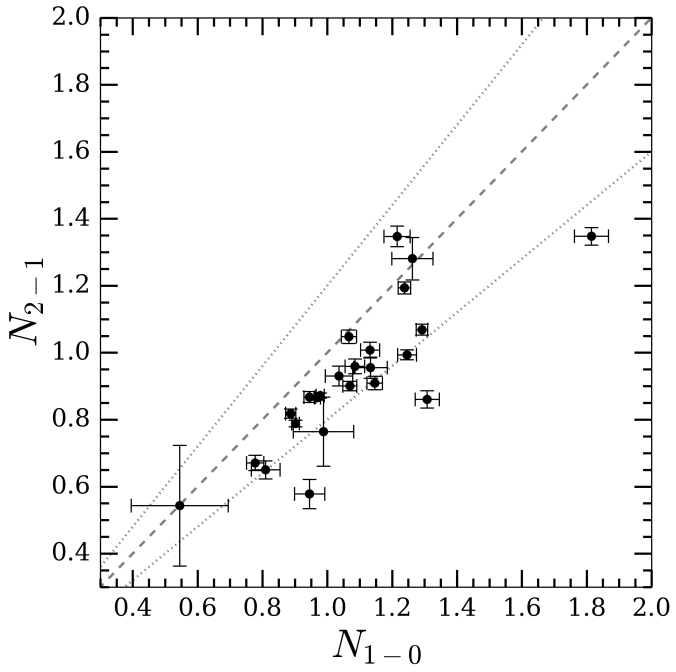

Figure 2.6: Indices of the K–S relation derived from ^{12}CO($J=2$–1) with the constant $R_{2/1}$ of 0.7 (N_{2-1}) against that from ^{12}CO($J=1$–0) (N_{1-0}). The diagonal dashed line indicates $N_{2-1} = N_{1-0}$. Dotted lines indicate that N_{2-1} is higher and lower by 20% than N_{1-0}.

are omitted because $R_{2/1}$ cannot be significantly measured in most positions in these galaxies (figure 2.2) and NGC 5194 is omitted due to the possibility of the calibration problem as mentioned in section 2.4.1.

As $\overline{R_{2/1}}$ deviates from 0.7 (table 2.2), the total molecular gas mass within a galaxy is underestimated or overestimated when the molecular gas mass is derived from ^{12}CO($J=2$–1) assuming the constant $R_{2/1}$ of 0.7. For instance, the total molecular gas mass is underestimated by $\sim 30\%$ for galaxies that show low $\overline{R_{2/1}}$ ($\lesssim 0.50$; e.g., NGC 2841, NGC 3198). Further, it is overestimated by $\sim 30\%$ when $\overline{R_{2/1}}$ is high ($\gtrsim 0.9$; e.g., NGC 2798, NGC 4569, NGC 4736). For the most deviated galaxy, the molecular gas mass is underestimated by $\sim 35\%$ in NGC 3627.

The middle panel of figure 2.5 shows the change rate of standard deviation for $\log \Sigma_{\rm mol}$, $\Delta[\sigma(\log \Sigma_{\rm mol})]$, in each galaxy when $R_{2/1}$ is assumed to be the constant. $\Delta[\sigma(\log \Sigma_{\rm mol})]$ is positive for all galaxies and exceeds 30% in some galaxies (NGC 628, NGC 2798, NGC 2976, NGC 3351, NGC 5713, and NGC 7331), and the highest one reaches 120% (NGC 2798). When the scatter of $R_{2/1}$, $\sigma(R_{2/1})$, is relatively large ($\gtrsim 0.2$) or when $\overline{R_{2/1}}$ deviates from 0.7, $\Delta[\sigma(\log \Sigma_{\rm mol})]$ tends to be large. In contrast, when $\sigma(R_{2/1})$ is small, $\Delta[\sigma(\log \Sigma_{\rm mol})]$ is also small (e.g., NGC 3627). These results indicate that not only the total molecular gas mass but also molecular gas surface density and its relevant quantities in positions-to-position are misled by the assumption of the constant $R_{2/1}$. This becomes an issue when spatially resolved data are used, which has been the standard recently.

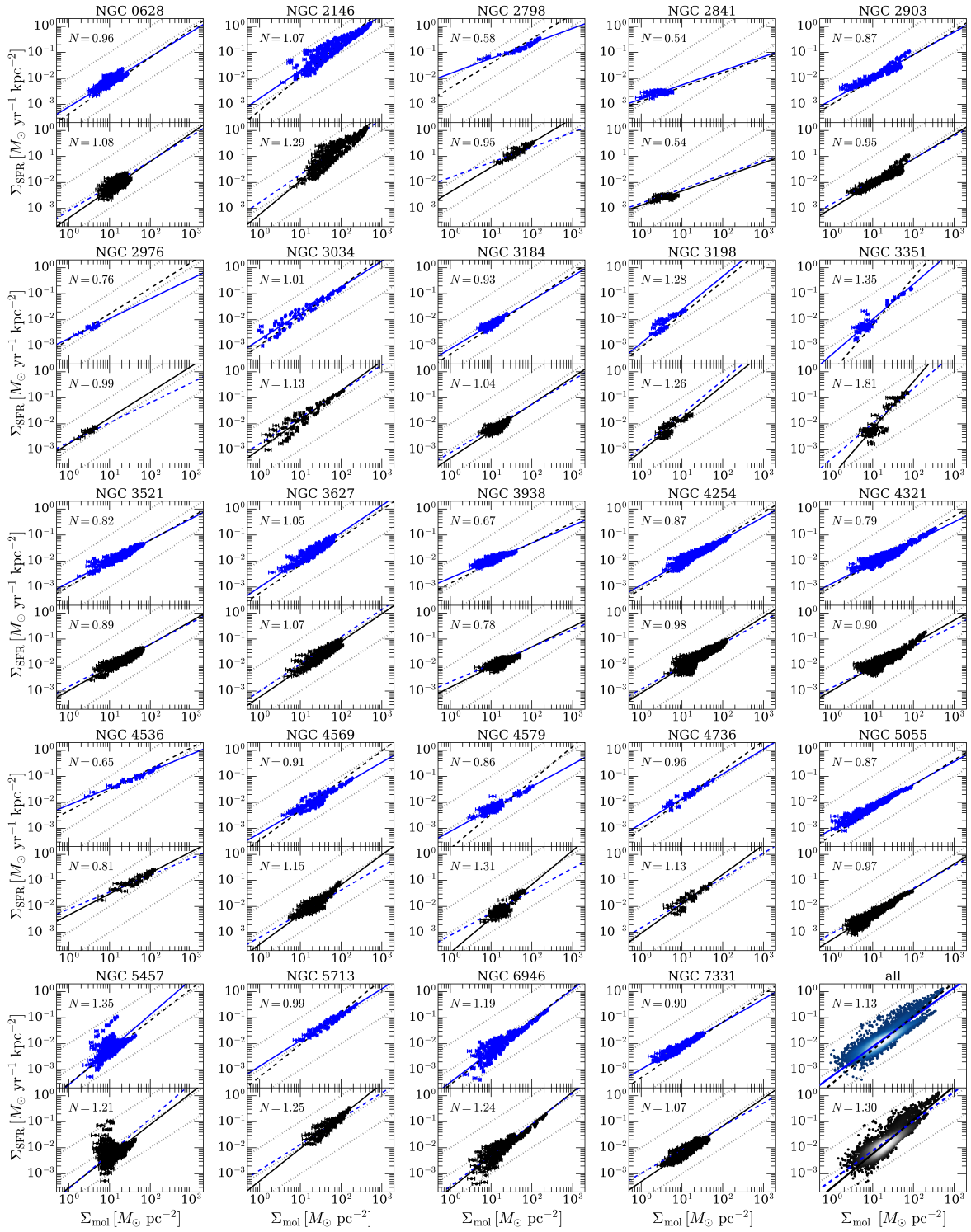

Figure 2.7: The K–S relation of the sample galaxies derived from ^{12}CO($J = 2$–1) assuming $R_{2/1} = 0.7$ (top panels, blue plots) and from ^{12}CO($J = 1$–0) (bottom panels, black plots). The index of each panel is provided on the top left. Solid lines and dashed lines indicate regression lines of the panel and the other panel, respectively. Dotted lines indicate that the depletion time of molecular gas is 10^{-1} Gyr, 10^{0} Gyr, and 10^{1} Gyr from bottom to top. The K–S plot of all galaxies (excluding NGC 337, NGC 3077, NGC 4214, NGC 4559, and NGC 5194) is shown in the panel at the bottom right corner.

Table 2.3: Fitted parameters of the K–S relation.

galaxy	N_{1-0}	N_{2-1}	ΔN [%]	A_{1-0}	A_{2-1}	ΔA [%]
	(1)	(2)	(3)	(4)	(5)	(6)
All	1.299 ± 0.005	1.132 ± 0.004	-12.8	-3.537 ± 0.008	-3.253 ± 0.007	-8.02
NGC 337	—	—	—	—	—	—
NGC 628	1.08 ± 0.03	0.96 ± 0.02	-11.5	-3.37 ± 0.05	-3.10 ± 0.04	-8.05
NGC 2146*	1.29 ± 0.02	1.07 ± 0.02	-17.2	-3.24 ± 0.03	-2.77 ± 0.03	-14.3
NGC 2798	0.95 ± 0.05	0.58 ± 0.04	-38.8	-2.37 ± 0.06	-1.81 ± 0.04	-23.5
NGC 2841	0.5 ± 0.1	0.5 ± 0.2	-0.24	-2.9 ± 0.4	-2.8 ± 0.4	-2.87
NGC 2903	0.95 ± 0.02	0.87 ± 0.02	-8.18	-2.99 ± 0.03	-2.82 ± 0.03	-5.64
NGC 2976	0.99 ± 0.09	0.8 ± 0.1	-22.7	-2.8 ± 0.2	-2.7 ± 0.2	-1.54
NGC 3034	1.13 ± 0.03	1.01 ± 0.02	-10.9	-2.99 ± 0.04	-2.77 ± 0.04	-7.27
NGC 3077	—	—	—	—	—	—
NGC 3184	1.04 ± 0.04	0.93 ± 0.03	-10.2	-3.33 ± 0.07	-3.12 ± 0.05	-6.21
NGC 3198	1.26 ± 0.06	1.28 ± 0.06	1.48	-3.06 ± 0.08	-2.90 ± 0.08	-5.22
NGC 3351	1.81 ± 0.05	1.35 ± 0.03	-25.7	-4.02 ± 0.07	-3.34 ± 0.04	-16.9
NGC 3521	0.89 ± 0.02	0.82 ± 0.01	-7.77	-2.98 ± 0.03	-2.83 ± 0.02	-4.98
NGC 3627	1.07 ± 0.02	1.05 ± 0.02	-1.73	-3.23 ± 0.04	-3.01 ± 0.03	-6.89
NGC 3938	0.78 ± 0.03	0.67 ± 0.02	-13.6	-2.86 ± 0.05	-2.65 ± 0.04	-7.19
NGC 4214	—	—	—	—	—	—
NGC 4254	0.98 ± 0.01	0.872 ± 0.008	-10.8	-3.08 ± 0.02	-2.93 ± 0.01	-4.94
NGC 4321	0.90 ± 0.01	0.79 ± 0.01	-12.5	-2.98 ± 0.02	-2.87 ± 0.02	-3.92
NGC 4536	0.81 ± 0.04	0.65 ± 0.03	-19.7	-2.33 ± 0.06	-2.10 ± 0.03	-9.81
NGC 4559	—	—	—	—	—	—
NGC 4569	1.15 ± 0.02	0.91 ± 0.02	-20.6	-3.46 ± 0.04	-3.19 ± 0.04	-7.89
NGC 4579	1.31 ± 0.04	0.86 ± 0.03	-34.2	-3.78 ± 0.06	-3.12 ± 0.05	-17.5
NGC 4736	1.13 ± 0.05	0.96 ± 0.03	-15.7	-3.04 ± 0.07	-2.82 ± 0.05	-7.16
NGC 5055	0.969 ± 0.009	0.866 ± 0.007	-10.6	-3.28 ± 0.02	-3.04 ± 0.01	-7.36
NGC 5457	1.21 ± 0.04	1.35 ± 0.03	10.9	-3.55 ± 0.06	-3.58 ± 0.04	1.07
NGC 5713*	1.25 ± 0.03	0.99 ± 0.01	-20.2	-3.28 ± 0.05	-2.87 ± 0.02	-12.5
NGC 6946	1.24 ± 0.02	1.19 ± 0.02	-3.56	-3.58 ± 0.03	-3.49 ± 0.03	-2.52
NGC 7331	1.07 ± 0.02	0.90 ± 0.01	-15.8	-3.31 ± 0.03	-2.99 ± 0.02	-9.7

(1) Index of the K–S relation derived from ^{12}CO($J=1$–0).
(2) Index of the K–S relation derived from ^{12}CO($J=2$–1) and the constant $R_{2/1}$ of 0.7.
(3) Change rate of index.
(4) Intercept of the K–S relation derived from ^{12}CO($J=1$–0).
(5) Intercept of the K–S relation derived from ^{12}CO($J=2$–1) and the constant $R_{2/1}$ of 0.7.
(6) Change rate of intercept.
* The spatial resolution is different from 1.5 kpc (cf. table 2.1).

2.4.3 Effects of $R_{2/1}$ on the Kennicutt–Schmidt relation derived from ^{12}CO($J=2$–1)

Next, we investigate how the Kennicutt–Schmidt (K–S) relation (Schmidt 1959; Kennicutt 1989) changes when the molecular gas surface density is derived from ^{12}CO($J=2$–1) and the fixed $R_{2/1}$ compared with that derived from ^{12}CO($J=1$–0). The molecular K–S relation is described as

$$\log\left(\frac{\Sigma_{\rm SFR}}{M_\odot\ {\rm yr}^{-1}\ {\rm kpc}^{-2}}\right) = N \log\left(\frac{\Sigma_{\rm mol}}{M_\odot\ {\rm pc}^{-2}}\right) + A, \tag{2.2}$$

where N is the index and A is the intercept on the double-logarithmic plot. Several studies suggested that this relation, in particular N, reflects the processes of star formation in galaxies (e.g., Elmegreen 2002; Krumholz and McKee 2005; Komugi et al. 2006; Tan 2010; Takeuchi, T., T. et al. 2020 in preparation). Therefore, we focused on how N changes in this study.

When the spatial resolution is changed, the result of the K–S relation also changes (Onodera et al. 2010). Thus, we smoothed ^{12}CO cubes and $\Sigma_{\rm SFR}$ maps so that the spatial resolution is the same value of 1.5 kpc for all galaxies except for NGC 337, NGC 2146, and NGC 5713. Since the original spatial resolution of these three galaxies is larger than 1.5 kpc (table 2.1), we did not smooth them. We also regridded ^{12}CO cubes and $\Sigma_{\rm SFR}$ maps to fix spatial sampling (i.e., pixel size) for all galaxies. The pixel size is set to 650 pc which is slightly smaller than the Nyquist sampling. For convolved and regridded data, pixels whose S/N of integrated-intensities does not reach $4.5\,\sigma$ were masked. We made K–S plots from ^{12}CO($J=1$–0) by adopting the standard $X_{\rm CO}$ of 2.0×10^{20} cm^{-2} (K km s^{-1})$^{-1}$ for the entire area of all galaxies according to the widely used method. The K–S plots from ^{12}CO($J=2$–1) are obtained by converting ^{12}CO($J=2$–1) intensity into that of ^{12}CO($J=1$–0) with the constant $R_{2/1}$ of 0.7, which is the same method employed in previous studies about the K–S relation with ^{12}CO($J=2$–1) (e.g., Bigiel et al. 2008).

We fitted the K–S relation with the ordinary least-squares (OLS) bisector method Isobe et al. (1990) and derived N and A of the relation made with ^{12}CO($J=1$–0) and ^{12}CO($J=2$–1), respectively. Indices derived from ^{12}CO($J=1$–0) and ^{12}CO($J=2$–1) (hereafter, N_{1-0} and N_{2-1}, respectively), intercepts from the two ^{12}CO lines (similarly, A_{1-0} and A_{2-1}, respectively), and their rates of change (ΔN and ΔA) are listed in table 2.3. The bottom panel of figure 2.5 indicates the change rate of indices; figure 2.6 shows the correlation plot of N_{2-1} against N_{1-0}. The K–S plots of each galaxy are shown in figure 2.7. We could not fit the K–S relation for NGC 337, NGC 3077, NGC 4214, and NGC 4559 because the number of pixels at which $R_{2/1}$ is significantly measured is not enough. Therefore, these four galaxies were excluded from the K–S relation of all compiled galaxies in the samples (the last panel in figure 2.7).

We find that indices decrease typically by 10–20%, up to 39%, when the relation is derived from ^{12}CO($J=2$–1) with the constant $R_{2/1}=0.7$ in 17 galaxies. The K–S relation using molecular gas surface density derived by this method produces a lower index than that derived by ^{12}CO($J=1$–0) for most galaxies. This tendency is the same as Momose et al. (2013) that discussed the discrepancy between their super-linear slope of the K–S relation derived by ^{12}CO($J=1$–0) and the linear slope derived by ^{12}CO($J=2$–1) reported in Bigiel et al. (2008). The significant change ($\Delta N < -20\%$) of the index is shown in NGC 2798, NGC 2976, and NGC 3351. In these galaxies, $\sigma(R_{2/1})$ within a galaxy tends to be relatively larger than others (table 2.2). When the variation of $R_{2/1}$ in a galaxy is small (e.g., NGC 3198, NGC 3627), ΔN is small ($|\Delta N| \lesssim 2\%$). The differences of the K–S relation for all sample galaxies also shows a lower index ($\Delta N = -13\%$).

We interpret these underestimated indices of the K–S relation derived from ^{12}CO($J=2$–1) as follows. $R_{2/1}$ is often higher than 0.7 when $\Sigma_{\rm SFR}$ and $\Sigma_{\rm mol}$ are high (the top right on the K–S plot), while $R_{2/1}$ is prone to be lower than 0.7 when $\Sigma_{\rm SFR}$ and $\Sigma_{\rm mol}$ are low (the bottom left on the K–S plot). Here, we mean that "$\Sigma_{\rm mol}$" is derived from ^{12}CO($J=1$–0). As a result, molecular gas surface density derived from ^{12}CO($J=2$–1) with the fixed $R_{2/1}$ of 0.7 is overestimated (data points move to right in the plot) where $\Sigma_{\rm SFR}$ and $\Sigma_{\rm mol}$ are high, and it is underestimated (data

points move to left in the plot) where $\Sigma_{\rm SFR}$ and $\Sigma_{\rm mol}$ are low (we examine correlations of $R_{2/1}$, $\Sigma_{\rm SFR}$, and $\Sigma_{\rm mol}$ in section 2.5.1; figures 2.8 and 2.9). This becomes prominent in galaxies whose $\sigma(R_{2/1})$ is large, as seen in the plot of NGC 2798, NGC 3351, and NGC 4579 of figure 2.7. We note that indices are underestimated even if $R_{2/1}$ is assumed as the mean or median of $R_{2/1}$ in a galaxy.

When the K–S relation is derived from higher-J ^{12}CO lines such as ^{12}CO($J=3$–2), the same tendency of lower indices is seen (Morokuma-Matsui and Muraoka 2017). Dense gas tracers also produce nearly linear K–S relations, whereas ^{12}CO($J=1$–0) produces super-linear relations (e.g., Gao et al. 2007; Kennicutt 1989). According to these results, it seems that indices of the K–S relation become low when the relation is derived from the molecular gas, that is more related to star-formation activity. We conclude that the K–S relation, the basic relation of molecular gas with star formation, will be misinterpreted, in addition to total molecular gas within a galaxy and surface density of molecular gas when ^{12}CO($J=2$–1) is used as a molecular gas tracer with a fixed $R_{2/1}$. Previous studies of the K–S relation using molecular gas surface density derived from this method would underestimate their indices.

2.5 Discussion

2.5.1 Correlations of $R_{2/1}$ with basic properties of galaxies

To investigate how $R_{2/1}$ changes depending on basic properties of galaxies such as $\Sigma_{\rm SFR}$, correlations of $R_{2/1}$ with representative quantities are examined in this subsection. The spatial resolution and grid spacing are fixed to be 1.5 kpc and 650 pc except for NGC 337, NGC 2146, and NGC 5713, similar to the K–S relation case (these three galaxies were analyzed with their original resolution as shown in table 2.1).

First, we describe the correlation of $R_{2/1}$ with $\Sigma_{\rm SFR}$. The top panel of figure 2.8 shows the correlation plot of $R_{2/1}$ against $\Sigma_{\rm SFR}$ for spatially resolved data and integrated data over the pixels where $R_{2/1}$ is significantly measured (table 2.2, figure 2.2). The bottom panel of the figure shows the box plot for the top panel binned with 0.2 dex and the mean $R_{2/1}$ weighted by ^{12}CO($J=1$–0) integrated-intensity in each bin. The Spearman's rank correlation coefficient (ρ_s) for the spatially resolved case and the integrated one are 0.47 and 0.51, respectively. Although the scatter is rather large, $Q_2(R_{2/1})$ and $\overline{R_{2/1}}$ in each bin clearly increase from ~ 0.4 to ~ 0.9 as $\Sigma_{\rm SFR}$ increases. This result is consistent with Koda et al. (2012) and Koda et al. (2020), whereas the spatial resolution of the former is approximately twice higher than ours. From this result, possibilities are as follows: one main physical factor to change $R_{2/1}$ can be star-formation feedback (i.e., high $R_{2/1}$ is a result and high $\Sigma_{\rm SFR}$ is a cause) or $R_{2/1}$ becomes high because the molecular gas is dense and as a result, the star-formation rate is high (i.e., high-density condition is a cause and high $R_{2/1}$ and high $\Sigma_{\rm SFR}$ are results). Otherwise, this correlation might be just mere coincidence.

Second, we investigate the dependence of $R_{2/1}$ on $\Sigma_{\rm mol}$ as shown in figure 2.9. Mean $\Sigma_{\rm mol}$ is derived by the same method of that for mean $\Sigma_{\rm SFR}$ case. $R_{2/1}$ loosely increases from ~ 0.55 to ~ 0.8 as $\Sigma_{\rm mol}$ increases according to the bottom panel, while there seems to be no clear tendency according to the scatter plot in the top panel. The ρ_s for the spatially resolved and global result is 0.28 and 0.51, respectively. Since the tendency of $R_{2/1}$ against $\Sigma_{\rm SFR}$ is clearer

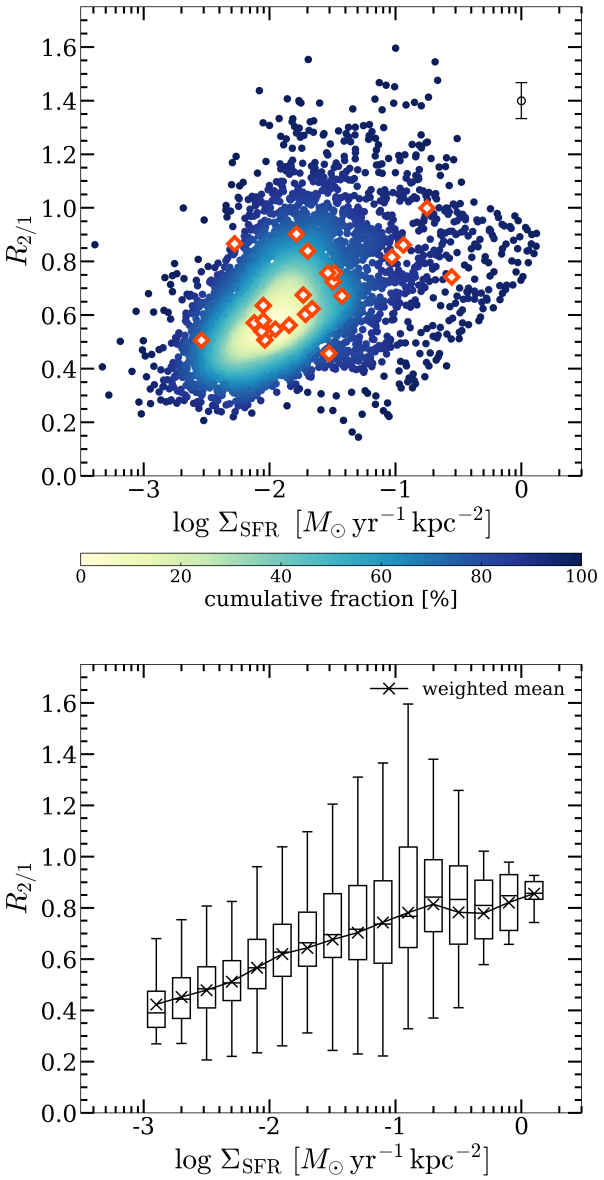

Figure 2.8: (Top) Correlation of spatially resolved data (circles) and integrated data over the whole galaxy (open orange diamonds) of $R_{2/1}$ and $\Sigma_{\rm SFR}$. The colors indicate the cumulative fraction of data points. The typical error of $R_{2/1}$ is shown on the top right in the panel. Errors of $\Sigma_{\rm SFR}$ is negligible. (Bottom) Box plot and $\overline{R_{2/1}}$ in each bin (cross markers) for the top panel. The bin width is 0.2 dex. Settings of the box plot are the same as figure 2.4.

than that against $\Sigma_{\rm mol}$, the lower indices of the K–S relation using molecular gas mass derived from ^{12}CO($J=2$–1) (discussed in section 2.4.3) are mainly due to fluctuated $R_{2/1}$ by $\Sigma_{\rm SFR}$ rather than $\Sigma_{\rm mol}$.

Third, the correlation between $R_{2/1}$ and the depletion time of molecular gas ($\tau_{\rm dep}$) is examined. The $\tau_{\rm dep}$ is derived as the following equation:

$$\left(\frac{\tau_{\rm dep}}{\rm yr}\right) = \left(\frac{\Sigma_{\rm mol}}{M_\odot\ {\rm pc}^{-2}}\right) \Big/ \left(\frac{\Sigma_{\rm SFR}}{M_\odot\ {\rm yr}^{-1}\ {\rm pc}^{-2}}\right). \tag{2.3}$$

Figure 2.10 shows the relation between $R_{2/1}$ and $\tau_{\rm dep}$ in the same way as figure 2.8. Mean $\tau_{\rm dep}$

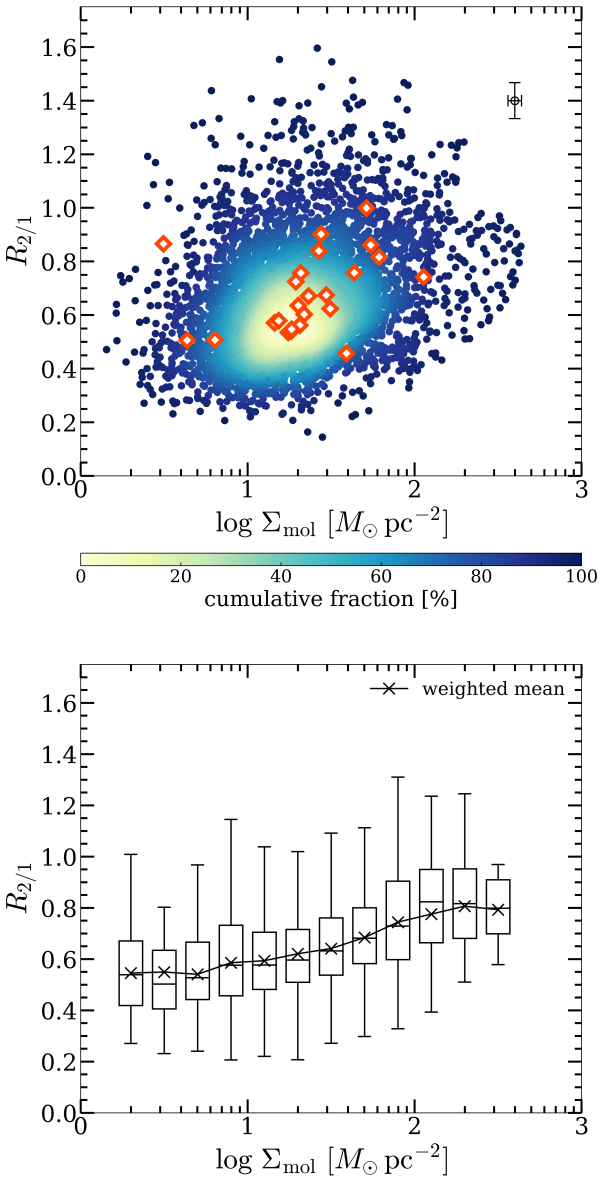

Figure 2.9: The same as figure 2.8 but for $\Sigma_{\rm mol}$.

is derived by dividing total molecular gas mass by total SFR within the pixels where $R_{2/1}$ is significantly measured. Both the top and bottom panels show significantly decreased $R_{2/1}$ as $\tau_{\rm dep}$ increases. This relation is also consistent with Koda et al. (2012) (note that their horizontal axis is proportional to SFE that is equivalent to the reciprocal number of $\tau_{\rm dep}$). The ρ_s for the spatially resolved and integrated case is -0.47 and -0.50, respectively. $Q_2(R_{2/1})$ and $\overline{R_{2/1}}$ decrease from ~ 1.2 to ~ 0.45 when $\tau_{\rm dep}$ increases from ~ 0.1 Gyr to ~ 5 Gyr. Therefore, $R_{2/1}$ may be related to an efficient conversion from molecular gas into stars because of the dense condition (e.g., Muraoka et al. 2016; Yajima et al. 2019). As another possibility, molecular gas is easily warmed by active star formation (heat source) with poor molecular gas (low heat capacity) when $\tau_{\rm dep}$ is short. These possibilities are relevant to the dense or warm conditions of molecular gas likely mentioned in the $\Sigma_{\rm SFR}$ case.

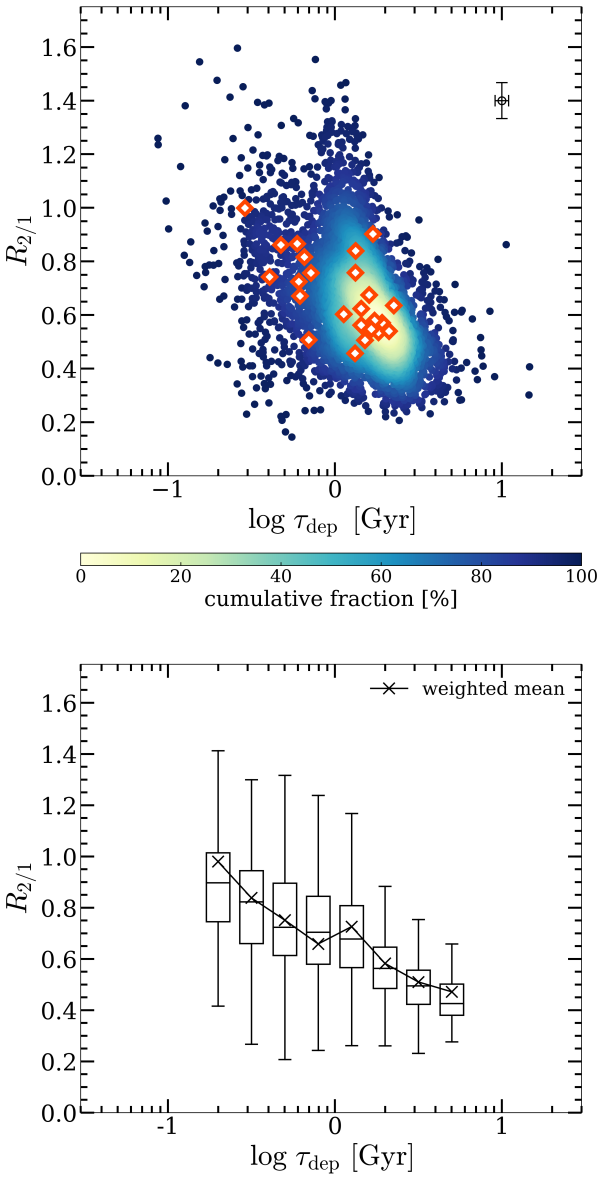

Figure 2.10: The same as figure 2.8 but for $\tau_{\rm dep}$.

Finally, the correlation of $R_{2/1}$ with IR color is examined. The IR color is derived from Herschel/PACS 70-μmand 160-μmintensity ratios. Usually, the peak of spectral energy distribution (SED) for cool dust, which is dominant in ISM, is around the 160-μmband. Therefore, this band selection well reflects dust temperature, especially in the present case of lacking data of the long-wavelength side for most of the sample galaxies. Cool dust temperature may also be a good probe of ISM conditions. Since there is no archival data of PACS for NGC 2903, we do not derive IR color for this galaxy. Figure 2.11 shows the correlation between $R_{2/1}$ and IR color and the box plot in the same manner as figure 2.8. The mean IR color is derived from the ratio of total intensity of $I_{70\mu\rm m}$ to that of $I_{160\mu\rm m}$ within the pixels where $R_{2/1}$ is significantly measured. The ρ_s of the spatially resolved and integrated case is 0.39 and 0.49. Both $Q_2(R_{2/1})$ and $\overline{R_{2/1}}$ increase from ~ 0.4 to ~ 0.85 as IR color increases (corresponding dust temperature

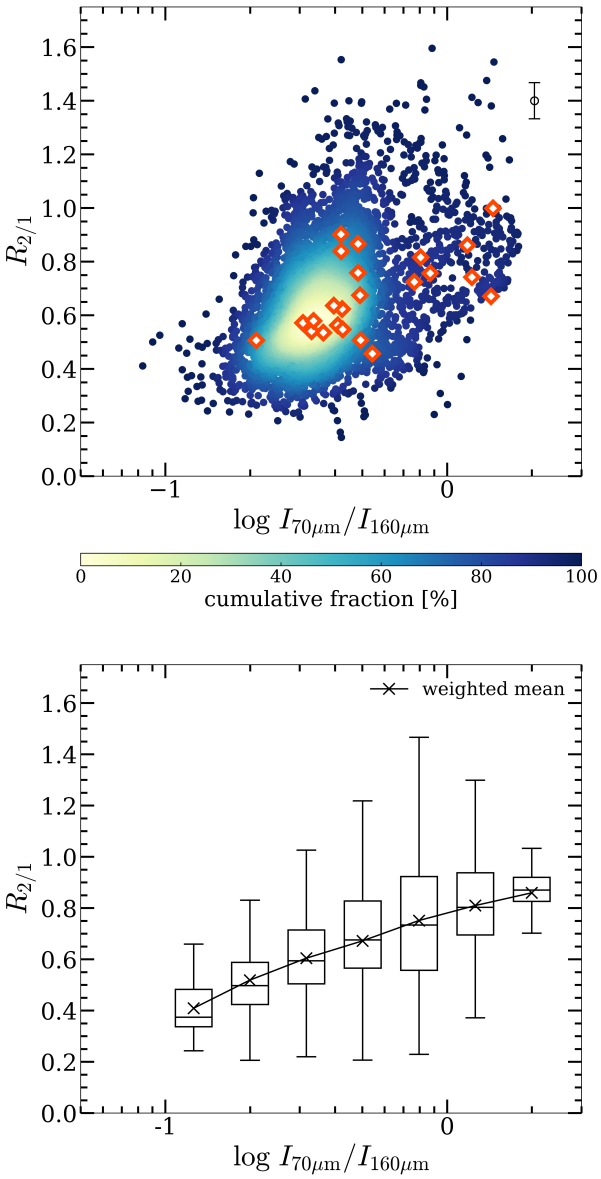

Figure 2.11: The same as figure 2.8 but for IR color ($I_{70\mu m}/I_{160\mu m}$). Errors of IR color is negligible.

is from $\sim$ 15 K to $\sim$ 35 K) similarly to the Σ_{SFR} case. The tendency is consistent with Koda et al. (2020). However, the correlation coefficient between $R_{2/1}$ and IR color is higher than that for $R_{2/1}$ and Σ_{SFR} in their paper, whereas it is not higher (0.47 and 0.39) in our results. This difference may be originated from far IR band selection and sample selection because their resolution is comparable to ours (their resolution is 1.2 kpc and ours is 1.5 kpc).

2.5.2 $R_{2/1}$ and ^{12}CO($J=1$–0)/^{13}CO($J=1$–0) ratio

From this subsection, we investigate how properties of molecular gas themselves (such as density and temperature) change $R_{2/1}$. We obtained ^{13}CO($J=1$–0) maps of the COMING galaxies in our samples. Therefore, the number density of molecular gas, $n(H_2)$, and the kinetic temperature of molecular gas, T_{kin}, can be derived with a non-local thermodynamic equilibrium (non-LTE)

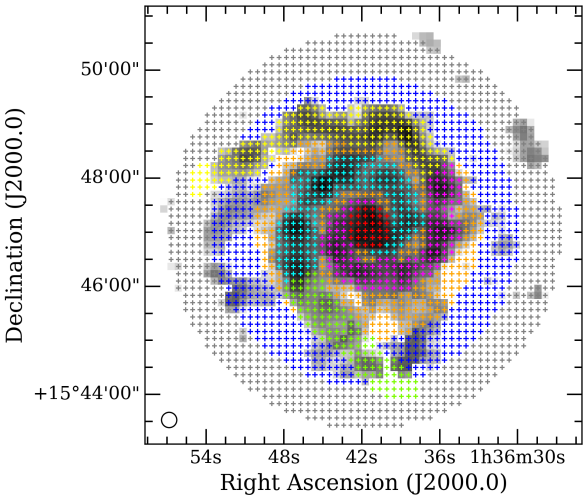

Figure 2.12: Regions for spectra stacking in NGC 628: center (red), inner arm 1 (magenta), inner arm 2 (cyan), outer arm 1 (yellow), outer arm 2 (yellow green), inter-arm 1 (orange), inter-arm 2 (blue), and outer disk (gray). Gray scale is the integrated-intensity map of ^{12}CO($J = 2$–1) obtained by L09.

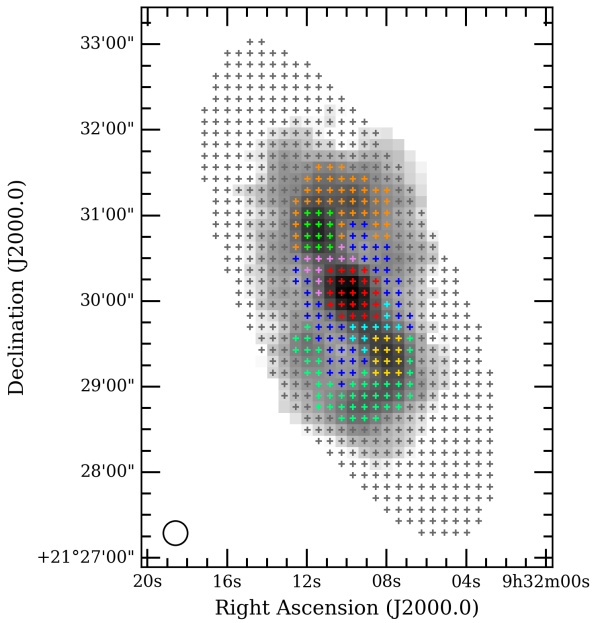

Figure 2.13: The same as figure 2.12 but for NGC 2903: center (red), northern bar (purple), southern bar (cyan), northern bar end (yellow green), southern bar end (yellow), northern arm (orange), southern arm (mint), inter-arm (blue), and outer disk (gray). The reference of ^{12}CO($J = 2$–1) data is the same as figure 2.12.

analysis with integrated-intensity ratios of the three lines (Scoville and Solomon 1974; Goldreich and Kwan 1974).

Since ^{13}CO($J = 1$–0) emission is weak compared with ^{12}CO lines, we measured the integrated intensity with the velocity-alignment stacking analysis (Schruba et al. 2011; Morokuma-Matsui et al. 2015) within concentric annuli or galactic structures such as arms and the bar. We

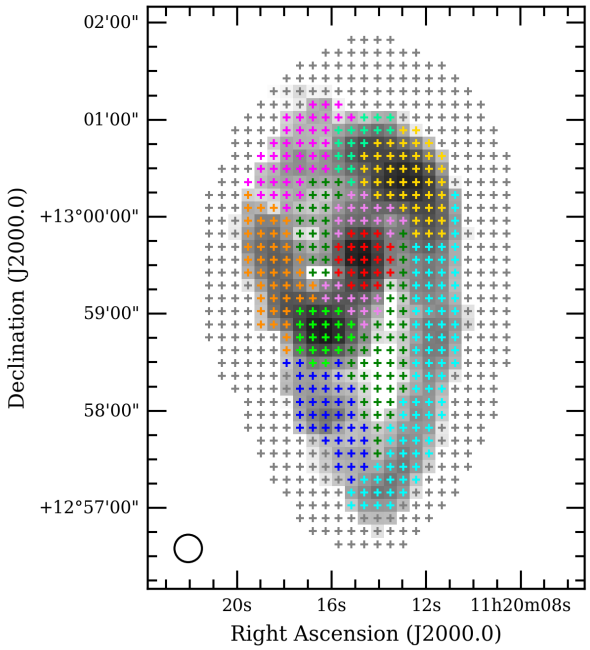

Figure 2.14: The same as figure 2.12 but for NGC 3627: center (red), bar (purple), northern bar end (yellow), southern bar end (yellow green), western arm (cyan), eastern arm (orange), southern stream (blue), northern offset stream (mint), arm-bar end interacting region (magenta), inter-arm (green), and outer disk (gray). The reference of ^{12}CO($J=2$–1) data is the same as figure 2.12.

determined galactic structures for NGC 628, NGC 2903, and NGC 3627 because the structures of these three galaxies can be clearly seen in the integrated-intensity maps of the ^{12}CO lines. The determined structures are shown in figures 2.12–2.14. For other galaxies, the regions for spectra stacking are determined as concentric annuli whose width is $r_{25}/8$. To align spectra along the velocity axis, we used the first-moment maps of H I obtained by The H I Nearby Galaxy Survey (THINGS; Walter et al. 2008) if a galaxy was observed in the survey. The H I first-moment maps enable us to stack spectra even in outer disks. When H I data is not available, the first-moment maps of ^{12}CO($J=2$–1) are used.

Integrated intensities, integrated-intensity ratios, and full width at half maximum (FWHM) of stacked spectra are summarized in section 2.8. The $3\,\sigma$ lower limit of ^{12}CO($J=1$–0)/^{13}CO($J=1$–0) integrated-intensity ratio (hereafter, denoted as $R_{12/13}$) is adopted when S/N of ^{13}CO($J=1$–0) integrated-intensity is lower than $3\,\sigma$. Prior to the non-LTE analysis, we discuss the relation of $R_{2/1}$ and $R_{12/13}$ as a bare observed quantity. Figure 2.15 shows the correlation plot of $R_{2/1}$ against $R_{12/13}$.

Regions where S/N of ^{13}CO($J=1$–0) is poor (derived as only the upper limit of integrated intensity) even with stacking are mainly inter-arms and outer disks. Since the area where ^{13}CO($J=1$–0) is emitted is much smaller than that of ^{12}CO lines in such regions, a different beam-filling factor may be effective, i.e., the line ratio is no longer a probe of molecular gas properties.

In figure 2.15, it appears that there are two components (or groups): one is that both $R_{2/1}$ and $R_{12/13}$ are high and the other is not so high $R_{2/1}$ ($\lesssim 0.7$) with various $R_{12/13}$ ($\sim$ 7–20). The

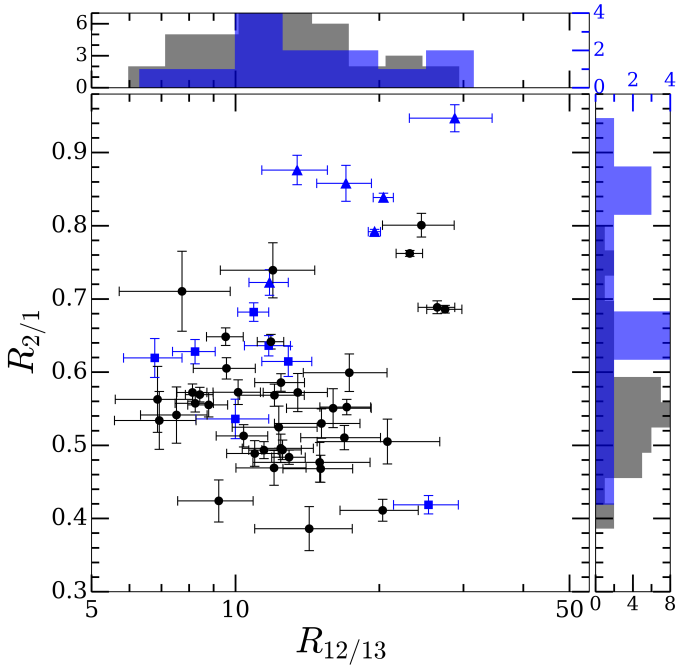

Figure 2.15: Correlation of $R_{2/1}$ with $R_{12/13}$ measured from stacked spectra. Black circle markers represent results in disks, blue triangles indicate galactic centers with active star formation (mean $\Sigma_{\rm SFR}$ in inner $r_{25}/8$ or the region defined as "center" is $> 0.1\ M_\odot\ {\rm yr}^{-1}\ {\rm kpc}^{-2}$; NGC 2146, NGC 2903, NGC 3034, NGC 3351, NGC 4536, and NGC 5713), and blue squares indicate galactic centers with quiescent star formation (mean $\Sigma_{\rm SFR}$ in the region is lower than the value). Black histograms are results of disk regions (black plots) and blue histograms are results of galactic centers (blue plots). Colors of tick labels correspond to those of histograms.

former largely includes central regions of galaxies with active star formation (mean $\Sigma_{\rm SFR}$ within inner $r_{25}/8$ or within the region defined as "center" is higher than $0.1\ M_\odot\ {\rm yr}^{-1}\ {\rm kpc}^{-2}$; NGC 2146, NGC 2903, NGC 3034, NGC 3351, NGC 4536, and NGC 5713). The latter corresponds to galactic disks and centers with quiescent star formation (mean $\Sigma_{\rm SFR}$ in the region is lower than the value above). The same tendency of decreasing $R_{2/1}$ with increasing $R_{12/13}$ can be seen in results of another survey (Cormier et al. 2018). It is likely that systematic differences of molecular gas properties between the central region and the disk influencing $R_{2/1}$ and $R_{12/13}$ are seen in the figure. Among galactic structures in disks (arms, inter-arms, and bars etc.), $R_{2/1}$ tends to be relatively low in bars and inter-arms, and high in arms and bar ends, although the contrast of $R_{2/1}$ is low (see results of stacked spectra for NGC 628, NGC 2903, and NGC 3627 in section 2.8). In addition, the tendency of $R_{2/1}$ and $R_{12/13}$ among these structures roughly follow the disk-phase feature (i.e., $R_{2/1}$ decreases as $R_{12/13}$ increases). Previous studies about $R_{12/13}$ suggested that high $R_{12/13}$ indicates low $n({\rm H_2})$ (e.g., Meier and Turner 2004), high $T_{\rm kin}$ (e.g., Paglione et al. 2001), or low abundance of ^{13}CO due to selective photodissociation (e.g., Davis 2014). Since $R_{2/1}$ is also high in galactic centers with active star formation, both high $n({\rm H_2})$ and high $T_{\rm kin}$ conditions are possible.

2.5.3 Non-LTE analysis using $R_{2/1}$

To compare $R_{2/1}$ with intrinsic molecular gas properties, $n(\mathrm{H_2})$ and T_{kin} are derived with the non-LTE analysis. In this study, we made use of the 1D non-LTE radiative transfer code RADEX (van der Tak et al. 2007). Settings for RADEX are based on those in Yajima et al. (2019).

Input parameters for calculations are $R_{2/1}$, $R_{12/13}$, column density of ^{12}CO of all energy levels ($\mathcal{N}_{^{12}\mathrm{CO}}$), that of ^{13}CO ($\mathcal{N}_{^{13}\mathrm{CO}}$), and FWHM of a GMC's spectrum (dv). To derive $\mathcal{N}_{^{12}\mathrm{CO}}$ and $\mathcal{N}_{^{13}\mathrm{CO}}$ from column density of $\mathrm{H_2}$ with observed $I_{^{12}\mathrm{CO}(1-0)}$, abundance ratios of $[^{12}\mathrm{CO}]/[\mathrm{H_2}]$, $[^{12}\mathrm{CO}]/[^{13}\mathrm{CO}]$, and X_{CO} were basically adopted as 8.5×10^{-5} (Pineda et al. 2008), 70 (the solar neighborhood value; Milam et al. 2005), and 2.0×10^{20} cm^{-2} (K km s^{-1})$^{-1}$ (Bolatto et al. 2013b), respectively. For the central region of galaxies, $[^{12}\mathrm{CO}]/[^{13}\mathrm{CO}]$ and X_{CO} were also adopted as 40 and 1.0×10^{20} cm^{-2} (K km s^{-1})$^{-1}$, respectively, to reflect the environment of galactic centers (e.g., Meier and Turner 2001; Oka et al. 2001). The escape probability of photon was calculated based on the Sobolev approximation (Sobolev 1960).

The FWHM of GMCs dv was estimated by assuming that dv in a region is proportional to the FWHM of the stacked spectrum in the region as described below. This is because molecular gas is a continuous medium and GMCs do not have a rigid boundary. Thus, internal kinematics of GMCs is likely to be influenced by dynamics of surrounding gas (i.e., large-scale dynamics), especially in bar ends and bars where large velocity dispersion can be seen. In addition, since our velocity resolution is 20 km s^{-1} and our spatial resolution is a kpc order, which are much wider than the typical velocity width of GMCs and much larger than the typical size of them, FWHM of a stacked spectrum, ΔV, reflects velocity dispersion among molecular clouds within the beam. This is a good indicator of large-scale dynamics of molecular gas.

At first, ΔV of a stacked spectrum within the entire disk in each galaxy was measured (hereafter, this ΔV is denoted as ΔV_{disk}) and the dv of 5.0 km s^{-1} was adopted corresponding to ΔV_{disk}. This velocity of 5.0 km s^{-1} as the standard of dv in the entire disk was determined based on the typical FWHM of GMCs in the disk of the Milky Way (e.g., Heyer et al. 2009). Next, the dv of 20 km s^{-1} was adopted corresponding to ΔV of the galaxy center (hereafter, denoted as $\Delta V_{\mathrm{center}}$). This 20 km s^{-1} is based on FWHM of GMCs found in the central region of galaxies and the Milky Way (e.g., Oka et al. 2001; Leroy et al. 2015). Then, the dv for each region (i.e., each annulus or galactic structure) was calculated by linearly interpolating or extrapolating with its ΔV, ΔV_{disk}, and $\Delta V_{\mathrm{center}}$. That is, the dv for region i (dv_i) is determined by the following equation:

$$\left(\frac{dv_i}{\mathrm{km\,s^{-1}}}\right) = a\left(\frac{\Delta V_i}{\mathrm{km\,s^{-1}}}\right) + b, \tag{2.4}$$

where

$$a \equiv (20\,\mathrm{km\,s^{-1}} - 5\,\mathrm{km\,s^{-1}}) \Big/ \left[\left(\frac{\Delta V_{\mathrm{center}}}{\mathrm{km\,s^{-1}}}\right) - \left(\frac{\Delta V_{\mathrm{disk}}}{\mathrm{km\,s^{-1}}}\right)\right], \tag{2.5}$$

$$b \equiv 20\,\mathrm{km\,s^{-1}} - a\left(\frac{\Delta V_{\mathrm{center}}}{\mathrm{km\,s^{-1}}}\right), \tag{2.6}$$

and ΔV_i is the FWHM of the stacked spectrum in the region. The reason why the dv for the innermost region is fixed to be 20 km s^{-1} is $\Delta V_{\mathrm{center}}$ mainly reflects not velocity dispersion in a large scale but the velocity gradient due to the rigid rotation of the galactic disk. High-resolution observations support increasing dv as close to the galactic center in inner disks (e.g., Sun et al.

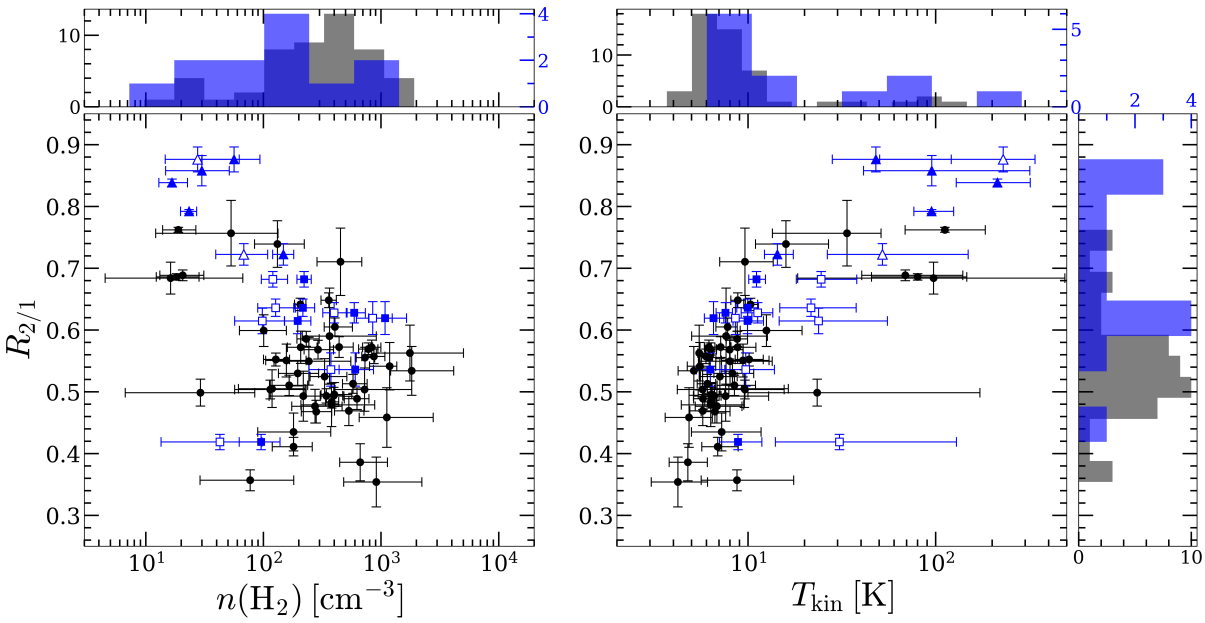

Figure 2.16: Correlation of $R_{2/1}$ with $n(\mathrm{H_2})$ (left) and T_{kin} (right) and their histograms. Black circle markers represent results in disks and those of blue filled triangle and square are galactic centers with active and quiescent star formation as with figure 2.15. Blue open markers correspond to central regions in which different [^{12}CO]/[^{13}CO] and X_{CO} are adopted. As with the plots, black histograms are results of disk regions and blue histograms are results of galactic centers. Colors of tick labels correspond to those of histograms. Blue histograms exclude the results for which different [^{12}CO]/[^{13}CO] and X_{CO} are adopted (open blue markers).

2020). Note that dv is not monotonically increases towards the center in outer disks. Since ΔV in outer disks is almost constant, dv is also constant (see the result of NGC 5055 in section 2.8).

Derived $n(\mathrm{H_2})$, T_{kin}, and ancillary results of excitation temperature for ^{12}CO($J=1$–0), ^{12}CO($J=2$–1), and ^{13}CO($J=1$–0) [$T_{\mathrm{ex}}^{12(1-0)}$, $T_{\mathrm{ex}}^{12(2-1)}$, $T_{\mathrm{ex}}^{13(1-0)}$], and optical depth of these lines [$\tau_{12(1-0)}$, $\tau_{12(2-1)}$, $\tau_{13(1-0)}$] are listed in table 2.4. Errors of $n(\mathrm{H_2})$ and T_{kin} are derived from errors of $R_{2/1}$ and $R_{12/13}$. Namely, four pairs of [$n(\mathrm{H_2})$, T_{kin}] are obtained from $R_{2/1} \pm dR_{2/1}$ and $R_{12/13} \pm dR_{12/13}$ (where $dR_{2/1}$ and $dR_{12/13}$ are errors of $R_{2/1}$ and $R_{12/13}$, respectively). Errors of $n(\mathrm{H_2})$, T_{kin} toward the positive direction are adopted as $\max[X_i, i = 1, 2, 3, 4] - X_0$, where X_0 is $n(\mathrm{H_2})$ and T_{kin} derived from $R_{2/1}$ and $R_{12/13}$, and X_i is $n(\mathrm{H_2})$ and T_{kin} derived from $R_{2/1} \pm dR_{2/1}$ and $R_{12/13} \pm dR_{12/13}$. Errors of $n(\mathrm{H_2})$, T_{kin} toward the negative direction are adopted as $X_0 - \min[X_i, i = 1, 2, 3, 4]$. Errors of other ancillary quantities such as intrinsic intensities and excitation temperature are nearly the same factor of errors for $n(\mathrm{H_2})$ and T_{kin}. There are no solutions of RADEX calculations in several regions. These are caused by the low S/N of ^{13}CO($J=1$–0) even with stacking. It is also possible that the one-zone model adopted for RADEX is not valid because the area seen in ^{13}CO($J=1$–0) is much smaller than those seen in ^{12}CO($J=1$–0) and ^{12}CO($J=2$–1). Based on these RADEX results, we examined the $R_{2/1}$ dependence on $n(\mathrm{H_2})$ and T_{kin} as shown in figure 2.16.

There is a clear tendency that $R_{2/1}$ increases with T_{kin}, while $R_{2/1}$ seems to decrease with increasing $n(\mathrm{H_2})$. The Spearman's rank correlation for $R_{2/1}$ and T_{kin} is 0.67 with a p-value of $\mathcal{O}(10^{-9})$ and that for $R_{2/1}$ and $n(\mathrm{H_2})$ is -0.36; however, it is not statistically significant with the

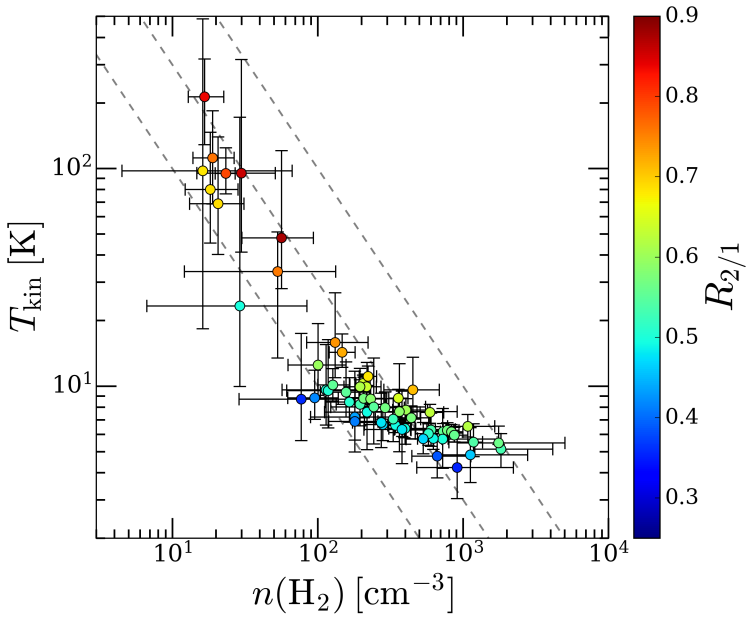

Figure 2.17: $R_{2/1}$ distribution on the $T_{\rm kin}$–$n(\rm H_2)$ plot. Dashed lines indicate that pressure divided by $k_{\rm B}$ is 10^3 K cm^{-3}, 3×10^3 K cm^{-3}, and 10^4 K cm^{-3} from bottom to top.

significance level of 5% (p-value is 0.06). In addition, the tendency of increased $R_{2/1}$ with $T_{\rm kin}$ is not changed even when different [^{12}CO]/[^{13}CO] and $X_{\rm CO}$ for galactic centers {[^{12}CO]/[^{13}CO] = 40 and $X_{\rm CO} = 1.0 \times 10^{20}$ cm^{-2} (K km s^{-1})$^{-1}$} are adopted. The result indicates that the variations of $R_{2/1}$ in galaxies seen in kpc-scale resolutions reflect the temperature of molecular gas. As discussed in section 2.5.1, the positive correlation between $R_{2/1}$ and $\Sigma_{\rm SFR}$ indicates that $R_{2/1}$ varies depending on $T_{\rm kin}$ or $n(\rm H_2)$ [high $\Sigma_{\rm SFR}$ enhances $T_{\rm kin}$ and $R_{2/1}$ or high $n(\rm H_2)$ induces high $\Sigma_{\rm SFR}$ and $R_{2/1}$]. Based on the results of the non-LTE analysis, the correlation implies the former case. Radiation feedback from stars warms dust and molecular gas directly and/or dust warms molecular gas; therefore, $R_{2/1}$ becomes high, as suggested by Koda et al. (2020).

Moreover, it seems that there are two phases of molecular gas. One is relatively dense (10^2–10^3 cm^{-3}) and cold (5–10 K) with $R_{2/1} \lesssim 0.7$. Its correlation of $R_{2/1}$ with $T_{\rm kin}$ is tight and steep but no clear correlation with $n(\rm H_2)$. The other is the diffuse (20–300 cm^{-3}), warm (30–200 K) with high $R_{2/1}$, and it is loosely correlated with $T_{\rm kin}$ and $n(\rm H_2)$. The former corresponds to results for disk regions and galactic centers with quiescent star formation (low $R_{2/1}$ and low $R_{12/13}$ indicated by black markers and blue squares in figure 2.15). The latter is the central regions of galaxies with active star formation (high $R_{2/1}$ and high $R_{12/13}$) indicated by blue triangles in the figure. Differences of molecular gas properties in disks and galactic centers are tested with the Kolmogorov–Smirnov test (i.e., for black and blue histograms in figure 2.16). It is confirmed that the hypothesis that $T_{\rm kin}$ and $R_{2/1}$ are the same between the disks and galactic centers is rejected at the significance level of 5%; however, that for $n(\rm H_2)$ cannot be rejected at the same level (p-value is 0.15). In short, differences of molecular gas phases in disks and centers are clearly seen in $R_{2/1}$ and physical properties planes, especially for $T_{\rm kin}$, at the kpc-scale resolutions.

The relation between $R_{2/1}$ and $n(\rm H_2)$ seems inconsistent with other studies for GMCs

(Sakamoto et al. 1994; Nishimura et al. 2015; Peñaloza et al. 2018), although the negative correlation of $R_{2/1}$ with $n(H_2)$ is not statistically significant. For instance, $R_{2/1}$ is high in not only warm environments but also dense regions such as ridges and filaments in molecular clouds in these studies. The discrepancy is because spatial scale is quite different between ours (kpc scale) and theirs (order of pc scale), and dynamic range of characteristic $n(H_2)$ is much wider for cloud-scale studies than galactic-scales. If observations with such high spatial resolution for galaxies is conducted, high $R_{2/1}$ with high $n(H_2)$ would appear. Furthermore, observations for molecular clouds in the Milky Way do not contain high $R_{2/1}$ and high $R_{12/13}$ environments (common in galactic centers with active star formation) that show warm and diffuse conditions via non-LTE calculations. Thus, the discrepancy possibly originated from observed environments (represented on the $R_{2/1}$–$R_{12/13}$ plane). Related to it, this negative correlation would be produced by data distribution of the bimodality of molecular gas properties seen in figure 2.15.

Moreover, studies of molecular gas in other galactic centers support our results of high $R_{2/1}$ with warm diffuse molecular gas seen in central regions with active star formation. For example, Meier et al. (2000) suggested that there are two phases of molecular gas: warm diffuse layers and cold dense clumps in the starburst nucleus of IC 342. In addition, low-J ^{12}CO lines, in particular ^{12}CO($J=2$–1), are dominantly emitted in such warm diffuse molecular gas. Israel and Baas (2003) modeled properties of molecular gas in the center of IC 342 and Maffei 2 (this galaxy also has the modest starburst nucleus) with transitions of ^{12}CO from $J=1$ to $J=4$; those of ^{13}CO from $J=1$ to $J=3$ and [C I]. Further, they argued the existence of the warm diffuse molecular gas of $T_{\rm kin} \sim 100$–150 K and $n(H_2) \sim 10^2$ cm^{-3} associated with the photon-dominated region (PDR), and the cold dense clumps of $T_{\rm kin} \sim 10$–20 K and $n(H_2) \sim 10^3$ cm^{-3}. It was also suggested that this warm diffuse molecular gas accounts for approximately 2/3 of the total molecular gas. Our results of physical properties with high $R_{2/1}$ reflect such hot diffuse molecular gas related to PDR.

Figure 2.17 shows $R_{2/1}$ distribution on the $T_{\rm kin}$–$n(H_2)$ plot. Most of molecular gas is nearly under the pressure equilibrium of a few 10^3 K cm^{-3}. This figure indicates that both $T_{\rm kin}$ and pressure of molecular gas are important for variations of $R_{2/1}$ in galaxies. That is, even when pressure is so high ($\gtrsim 3 \times 10^3$ K cm^{-3}), $R_{2/1}$ is not always high (~ 0.5–0.6) as long as $T_{\rm kin}$ is low ($\lesssim 10$ K). Similarly, $R_{2/1}$ is not always very high (< 0.8) even when $T_{\rm kin}$ is high ($\gtrsim 30$ K) as long as pressure is not relatively high ($\sim 10^3$ K cm^{-3}).

Our results of $R_{2/1}$ and molecular gas properties suggest an issue of molecular gas mass derived from ^{12}CO($J=2$–1) according to fluctuated $R_{2/1}$ and $X_{\rm CO}$ as follows. Some studies reported that $X_{\rm CO}$ is lower in galactic centers, (ultra-) luminous infrared galaxies, and mergers than that in disks (i.e., hosting active star formation; e.g., Oka et al. 2001; Narayanan et al. 2011; Papadopoulos et al. 2012a; Sandstrom et al. 2013[2)]; Yasuda et al. 2020 in prep). In these systems, $R_{2/1}$ should be higher than in normal disks considering our results (e.g., figure 2.4, 2.8, 2.11, 2.16, and 2.17). In addition, the recent synthetic observation of ^{12}CO($J=1$–0) and ^{12}CO($J=2$–1) in a 3D magneto-hydrodynamics simulation (Gong et al. 2020) shows that $X_{\rm CO}$ is low in the environments where $R_{2/1}$ is high. Hence, the molecular gas mass derived from ^{12}CO($J=2$–1) is more overestimated in active star-formation environments when the constant $R_{2/1}$ and $X_{\rm CO}$ are adopted because $M_{\rm mol} \propto I_{^{12}{\rm CO}(2-1)} \times X_{\rm CO}/R_{2/1}$. When $R_{2/1}$ increases and

[2)] Sandstrom et al. (2013) assumed the constant $R_{2/1}$ to derive molecular gas mass from ^{12}CO($J=2$–1), however, the tendency of lower CO-to-H$_2$ conversion factors in galactic centers can also be seen in ^{12}CO($J=1$–0)-based studies.

$X_{\rm CO}$ decreases, the fluctuation of $X_{\rm CO}/R_{2/1}$ is amplified. Based on the reported variations of $X_{\rm CO}/R_{2/1}$ so far, active star-formation environments lead to more overestimated molecular gas if ^{12}CO($J=2$–1), constant $X_{\rm CO}$, and fixed $R_{2/1}$ are used compared with the ^{12}CO($J=1$–0) case.

Table 2.4: Derived physical properties of molecular gas with the non-LTE analysis.

galaxy	region*	$n(H_2)$ [cm^{-3}] (1)	T_{kin} [K] (2)	$T_{ex}^{12(1-0)}$ [K] (3)	$T_{ex}^{12(2-1)}$ [K] (4)	$T_{ex}^{13(1-0)}$ [K] (5)	$\tau_{12(1-0)}$ (6)	$\tau_{12(2-1)}$ (7)	$\tau_{13(1-0)}$ (8)
NGC 628	center	$(1.1^{+0.6}_{-0.3}) \times 10^3$	$6.5^{+0.9}_{-0.7}$	6.3	6.1	4.4	18	22	0.41
	inner arm1	$(1.9^{+1.0}_{-0.6}) \times 10^2$	$8.2^{+2.5}_{-1.7}$	6.9	6.1	3.4	19	26	0.64
	inner arm2	$(2.1^{+0.8}_{-0.5}) \times 10^2$	$8.8^{+2.2}_{-1.6}$	7.4	6.6	3.5	20	29	0.7
	outer arm2	$(6.6^{+4.7}_{-2.2}) \times 10^2$	$4.8^{+1.3}_{-1.0}$	4.5	4.0	3.3	13	10	0.26
	inter-arm1	$(1.8^{+1.9}_{-0.9}) \times 10^2$	$7.2^{+4.5}_{-2.2}$	5.9	5.0	3.2	17	20	0.49
	center†	$(8.5^{+3.9}_{-2.3}) \times 10^2$	$8.5^{+1.9}_{-1.5}$	7.8	7.2	4.9	9.8	15	0.45
NGC 2146	center	$(1.7^{+0.6}_{-0.4}) \times 10^1$	210^{+110}_{-80}	14	14	3.5	18	40	1.6
	ring1	$(2.1^{+1.1}_{-0.7}) \times 10^1$	69^{+71}_{-29}	10	9.4	3.2	20	38	1.2
	ring2	$(2.9^{+5.5}_{-2.2}) \times 10^1$	23^{+149}_{-13}	7.0	6.0	3.0	19	27	0.74
	center†	—	—	—	—	—	—	—	—
NGC 2841	ring2	$(1.2^{+0.2}_{-0.4}) \times 10^3$	$5.5^{+1.2}_{-0.8}$	5.4	5.1	4.0	17	17	0.36
	ring3	$(1.8^{+2.3}_{-0.6}) \times 10^3$	$5.1^{+0.9}_{-0.9}$	5.0	4.8	4.0	15	14	0.3
	ring4	$(1.1^{+1.7}_{-0.5}) \times 10^3$	$4.8^{+1.6}_{-1.2}$	4.7	4.3	3.6	14	12	0.27
NGC 2903	center	$(1.5^{+0.3}_{-0.3}) \times 10^2$	$14^{+3.0}_{-2.0}$	11	9.9	3.9	20	38	1.1
	northern bar	$(1.0^{+0.6}_{-0.4}) \times 10^2$	$13^{+7.0}_{-3.0}$	8.5	7.5	3.4	20	33	0.9
	southern bar	$(1.1^{+1.2}_{-0.6}) \times 10^2$	$9.6^{+5.9}_{-3.0}$	7.0	6.0	3.2	19	27	0.68
	northern bar end	$(3.6^{+0.6}_{-0.5}) \times 10^2$	$8.8^{+0.9}_{-0.7}$	7.9	7.4	4.0	19	30	0.67
	southern bar end	$(2.3^{+0.7}_{-0.4}) \times 10^2$	$8.7^{+1.2}_{-1.1}$	7.5	6.7	3.6	20	29	0.69
	northern arm	$(4.0^{+1.7}_{-0.8}) \times 10^2$	$7.8^{+1.0}_{-1.0}$	7.1	6.6	3.8	19	26	0.59
	southern arm	$(7.3^{+1.5}_{-1.1}) \times 10^2$	$6.2^{+0.5}_{-0.6}$	5.9	5.5	3.9	18	20	0.42
	inter-arm	—	—	—	—	—	—	—	—
	outer disk	$(1.2^{+1.1}_{-0.6}) \times 10^2$	$9.5^{+6.8}_{-3.1}$	7.0	6.0	3.2	19	26	0.63
	center†	$(6.8^{+4.1}_{-2.9}) \times 10^1$	52^{+97}_{-26}	12	11	4.1	10	22	1.1
NGC 2976	center	—	—	—	—	—	—	—	—
	ring1	$(5.3^{+8.0}_{-4.1}) \times 10^1$	34^{+17}_{-20}	12	11	3.6	18	38	1.2
	ring2	$(1.3^{+0.9}_{-0.5}) \times 10^2$	$16^{+11}_{-5.0}$	11	10	3.9	19	39	1.1
	ring3	$(4.5^{+2.3}_{-1.7}) \times 10^2$	$9.6^{+4.0}_{-2.6}$	8.8	8.4	4.5	19	32	0.68

Table 2.4: (Continued.)

galaxy	region*	$n(H_2)$ [cm^{-3}] (1)	T_{kin} [K] (2)	$T_{ex}^{12(1-0)}$ [K] (3)	$T_{ex}^{12(2-1)}$ [K] (4)	$T_{ex}^{13(1-0)}$ [K] (5)	$\tau_{12(1-0)}$ (6)	$\tau_{12(2-1)}$ (7)	$\tau_{13(1-0)}$ (8)
NGC 3034	center	$(2.3^{+0.4}_{-0.4}) \times 10^1$	95^{+30}_{-19}	13	12	3.5	18	40	1.6
	ring1	$(1.9^{+0.8}_{-0.5}) \times 10^1$	110^{+70}_{-40}	12	11	3.4	19	40	1.4
	ring2	$(1.8^{+1.0}_{-0.6}) \times 10^1$	80^{+66}_{-35}	10	9.3	3.2	20	38	1.2
	center†	—	—	—	—	—	—	—	—
NGC 3198	center	$(6.0^{+2.6}_{-1.6}) \times 10^2$	$6.3^{+1.2}_{-1.0}$	5.9	5.5	3.7	17	19	0.42
	ring1	$(2.2^{+2.6}_{-1.1}) \times 10^2$	$7.6^{+5.3}_{-2.5}$	6.4	5.6	3.3	18	22	0.53
	center†	$(3.7^{+2.0}_{-1.3}) \times 10^2$	$9.7^{+4.1}_{-2.5}$	7.7	6.7	4.1	9.3	14	0.51
NGC 3351	center	$(5.6^{+3.7}_{-2.6}) \times 10^1$	48^{+73}_{-20}	16	16	4.1	18	43	1.8
	ring1	$(3.6^{+5.5}_{-1.5}) \times 10^2$	$7.6^{+5.1}_{-2.6}$	7.0	6.4	3.7	20	27	0.62
	ring2	$(7.2^{+11.0}_{-3.2}) \times 10^2$	$5.7^{+2.2}_{-1.5}$	5.5	5.0	3.7	16	17	0.36
	center†	$(2.8^{+3.5}_{-1.3}) \times 10^1$	230^{+110}_{-180}	16	16	4.2	12	30	1.6
NGC 3521	center	$(2.2^{+0.6}_{-0.4}) \times 10^2$	$9.9^{+1.4}_{-1.2}$	8.3	7.6	3.7	20	32	0.79
	ring1	$(2.1^{+0.2}_{-0.2}) \times 10^2$	$10^{+1.0}_{-1.0}$	8.5	7.8	3.7	20	33	0.81
	ring2	$(1.3^{+0.4}_{-0.3}) \times 10^2$	$10^{+2.0}_{-2.0}$	7.6	6.6	3.3	20	30	0.76
	ring3	$(1.6^{+0.7}_{-0.5}) \times 10^2$	$9.4^{+3.5}_{-2.2}$	7.4	6.5	3.4	19	28	0.71
	center†	$(1.3^{+0.6}_{-0.4}) \times 10^2$	$22^{+16}_{-7.0}$	10	8.9	4.0	9.8	19	0.83
NGC 3627	center	$(9.5^{+4.3}_{-3.3}) \times 10^1$	$8.8^{+3.0}_{-1.8}$	6.0	5.0	3.1	18	21	0.54
	bar	$(1.8^{+0.8}_{-0.6}) \times 10^2$	$6.9^{+2.0}_{-1.2}$	5.6	4.8	3.2	17	18	0.46
	northern bar end	$(3.4^{+0.4}_{-0.4}) \times 10^2$	$6.6^{+0.6}_{-0.5}$	6.0	5.3	3.5	18	20	0.55
	southern bar end	$(3.9^{+0.8}_{-0.6}) \times 10^2$	$6.4^{+0.6}_{-0.6}$	5.8	5.2	3.5	17	19	0.45
	western arm	$(2.8^{+1.0}_{-0.7}) \times 10^2$	$6.7^{+1.4}_{-1.0}$	5.9	5.1	3.3	18	20	0.48
	eastern arm	$(6.2^{+1.6}_{-1.4}) \times 10^2$	$5.7^{+0.8}_{-0.6}$	5.4	5.0	3.6	16	17	0.37
	offset stream	$(1.7^{+0.7}_{-0.5}) \times 10^2$	$8.4^{+2.5}_{-1.6}$	6.8	5.9	3.3	19	26	0.64
	southern arm	$(2.7^{+1.9}_{-1.0}) \times 10^2$	$6.8^{+2.5}_{-1.6}$	6.0	5.2	3.4	18	20	0.49
	arm-bar end inter. region	$(7.7^{+10.3}_{-4.8}) \times 10^1$	$8.7^{+8.8}_{-3.1}$	5.4	4.5	3.0	17	17	0.45
	center†	$(4.3^{+5.4}_{-2.9}) \times 10^1$	31^{+98}_{-17}	6.1	5.1	3.2	9.1	11	0.42

Table 2.4: (Continued.)

galaxy	region*	$n(H_2)$ [cm^{-3}] (1)	T_{kin} [K] (2)	$T_{ex}^{12(1-0)}$ [K] (3)	$T_{ex}^{12(2-1)}$ [K] (4)	$T_{ex}^{13(1-0)}$ [K] (5)	$\tau_{12(1-0)}$ (6)	$\tau_{12(2-1)}$ (7)	$\tau_{13(1-0)}$ (8)
NGC 3938	center	$(5.9^{+1.4}_{-0.9}) \times 10^2$	$7.6^{+0.7}_{-0.8}$	7.1	6.7	4.1	18	25	0.51
	ring1	$(4.4^{+1.4}_{-0.7}) \times 10^2$	$7.1^{+1.0}_{-0.8}$	6.6	6.1	3.8	19	24	0.52
	ring2	$(2.9^{+1.0}_{-0.7}) \times 10^2$	$8.0^{+1.4}_{-1.2}$	7.0	6.4	3.6	19	26	0.6
	ring3	$(1.8^{+3.2}_{-0.8}) \times 10^3$	$5.5^{+1.1}_{-0.1}$	5.4	5.2	4.2	16	16	0.3
	center†	$(4.0^{+1.1}_{-0.8}) \times 10^2$	$11^{+2.0}_{-2.0}$	9.0	8.1	4.5	9.8	17	0.6
NGC 4536	center	$(3.0^{+2.1}_{-1.5}) \times 10^1$	95^{+222}_{-54}	16	15	3.8	18	42	1.8
	center†	—	—	—	—	—	—	—	—
NGC 4579	center	—	—	—	—	—	—	—	—
	ring1	$(2.4^{+3.1}_{-1.2}) \times 10^2$	$8.0^{+5.4}_{-2.6}$	6.9	6.2	3.5	19	26	0.62
	ring2	$(3.3^{+1.8}_{-0.8}) \times 10^2$	$7.1^{+1.7}_{-1.5}$	6.3	5.7	3.5	18	22	0.52
	center†	—	—	—	—	—	—	—	—
NGC 5055	center	$(2.2^{+0.3}_{-0.3}) \times 10^2$	$11^{+1.0}_{-1.0}$	9.2	8.6	3.9	20	35	0.87
	ring1	$(7.8^{+1.6}_{-1.4}) \times 10^2$	$6.3^{+0.5}_{-0.4}$	6.0	5.6	4.0	18	20	0.42
	ring2	$(3.8^{+0.5}_{-0.4}) \times 10^2$	$6.3^{+0.5}_{-0.4}$	5.8	5.1	3.4	17	19	0.45
	ring3	$(5.8^{+1.8}_{-1.1}) \times 10^2$	$6.1^{+0.7}_{-0.7}$	5.7	5.2	3.6	17	18	0.41
	ring4	$(4.0^{+1.6}_{-0.9}) \times 10^2$	$6.4^{+1.1}_{-1.0}$	5.9	5.2	3.5	17	19	0.45
	ring5	$(3.8^{+5.0}_{-1.7}) \times 10^2$	$6.3^{+3.2}_{-1.9}$	5.7	5.1	3.4	17	19	0.43
	ring6	$(9.1^{+13.0}_{-4.3}) \times 10^2$	$4.2^{+1.8}_{-1.2}$	4.0	3.7	3.2	11	7.1	0.19
	center†	$(1.2^{+0.4}_{-0.2}) \times 10^2$	$24^{+13}_{-6.0}$	11	9.8	4.1	10	21	0.95
NGC 5713	center	—	—	—	—	—	—	—	—
	ring1	—	—	—	—	—	—	—	—
	ring2	$(1.6^{+5.1}_{-1.2}) \times 10^1$	97^{+390}_{-79}	9.9	9.2	3.2	19	37	1.1
	center†	—	—	—	—	—	—	—	—

Table 2.4: (Continued.)

galaxy	region*	$n(\mathrm{H_2})$ [cm^{-3}]	$T_{\rm kin}$ [K]	$T_{\rm ex}^{12(1-0)}$ [K]	$T_{\rm ex}^{12(2-1)}$ [K]	$T_{\rm ex}^{13(1-0)}$ [K]	$\tau_{12(1-0)}$	$\tau_{12(2-1)}$	$\tau_{13(1-0)}$
		(1)	(2)	(3)	(4)	(5)	(6)	(7)	(8)
NGC 7331	center	$\left(2.0^{+0.6}_{-0.4}\right)\times10^2$	$9.9^{+2.1}_{-1.6}$	8.2	7.4	3.6	19	31	0.77
	ring1	$\left(8.3^{+1.6}_{-1.4}\right)\times10^2$	$6.2^{+0.5}_{-0.3}$	6.0	5.6	4.0	18	21	0.42
	ring2	$\left(8.7^{+2.1}_{-1.8}\right)\times10^2$	$6.0^{+0.5}_{-0.4}$	5.8	5.4	3.9	18	20	0.41
	ring3	$\left(5.3^{+1.8}_{-1.3}\right)\times10^2$	$5.7^{+1.1}_{-0.8}$	5.4	4.8	3.5	16	16	0.38
	center†	$\left(9.8^{+5.3}_{-4.1}\right)\times10^1$	$24^{+32}_{-9.0}$	9.5	8.4	3.8	10	19	0.86

(1) Number density of molecular gas.
(2) Kinetic temperature of molecular gas.
(3) Excitation temperature of ^{12}CO($J=1$–0).
(4) The same as (3) but for ^{12}CO($J=2$–1).
(5) The same as (3) but for ^{13}CO($J=1$–0).
(6) Optical depth of ^{12}CO($J=1$–0).
(7) The same as (6) but for ^{12}CO($J=2$–1).
(8) The same as (6) but for ^{13}CO($J=1$–0).
Results of (1)–(8) are obtained from the one-zone model of RADEX.
* In annuli cases, regions of each annulus are named 'ring1', 'ring2'... in order from the galactic center.
† Adopted $X_{\rm CO}$ and [^{12}CO]/[^{13}CO] are different to reflect environments in galactic centers.

2.6 Summary of this chapter

We present the variations of ^{12}CO($J=2$–1)/^{12}CO($J=1$–0) line ratio ($R_{2/1}$) within and among galaxies, the effects of the assumption that $R_{2/1}$ is a constant on the derivation of molecular gas mass, and the properties of molecular gas reflecting variations of $R_{2/1}$ in 24 nearby galaxies on kpc scales. The main conclusions of this paper are as follows:

1. The median and mean $R_{2/1}$ weighted by ^{12}CO($J=1$–0) integrated-intensity for spatially resolved data of galaxies in our samples are 0.61 and 0.66, respectively, with the standard deviation of 0.19. $R_{2/1}$ varies from 0.4 to 0.9 among and within galaxies. While $R_{2/1}$ in the galactic centers (inner $\sim$ 1 kpc) is typically higher ($\sim$ 0.8), the median of $R_{2/1}$ in disks (exterior to $\sim$ 2 kpc) is nearly constant at 0.60. (Section 2.4.1, figure 2.2, 2.3, 2.4, and table 2.2.)

2. The total molecular gas mass within a galaxy derived from ^{12}CO($J=2$–1) is underestimated or overestimated by $\sim$ 20% for most galaxies, and at most by 35%, when $R_{2/1}$ is assumed to be the constant of 0.7. In addition, the scatter of molecular gas surface density ($\Sigma_{\rm mol}$) by ^{12}CO($J=2$–1) within a galaxy increases in all galaxies. Its change rate exceeds $\sim$ 30% in some galaxies, and it is 120% in the highest case when the constant $R_{2/1}$ is adopted. This increased scatter of $\Sigma_{\rm mol}$ is serious for mapping (spatially resolved) observations. (Section 2.4.2, and figure 2.5.)

3. The indices of the Kennicutt–Schmidt relation using molecular gas surface density derived from ^{12}CO($J=2$–1) and $R_{2/1}=0.7$ become lower by 10–20%, up to 39% compared with that using ^{12}CO($J=1$–0) for 17 galaxies out of 24. This is because $R_{2/1}$ tends to be higher than 0.7 when $\Sigma_{\rm SFR}$ and $\Sigma_{\rm mol}$ are high while $R_{2/1}$ is often lower than 0.7 when $\Sigma_{\rm SFR}$ and $\Sigma_{\rm mol}$ are low. Underestimated indices are prominent when the scatter of $R_{2/1}$ within a galaxy is large. (Section 2.4.3, figure 2.5, 2.6, 2.7, and table 2.3.)

4. $R_{2/1}$ has positive correlations with $\Sigma_{\rm SFR}$ and IR color and the negative correlation with depletion time of molecular gas. These suggest that $R_{2/1}$ becomes high by warmed molecular gas from stars (stars influence on molecular gas properties and $R_{2/1}$). Otherwise, $R_{2/1}$ is high because molecular gas is dense; as a result, star formation is active (molecular gas properties influence on star formation activity and $R_{2/1}$). There is no clear tendency between $R_{2/1}$ and $\Sigma_{\rm mol}$. (Section 2.5.1, figure 2.8, 2.9, 2.10, and 2.11.)

5. Comparing $R_{2/1}$ with ^{12}CO($J=1$–0)/^{13}CO($J=1$–0) line ratio ($R_{12/13}$) measured within each galactic structure or concentric annulus, there seems to be two components; one is both $R_{2/1}$ and $R_{12/13}$ are high, and the other is relatively low $R_{2/1}$ with various $R_{12/13}$. The former corresponds to molecular gas in galactic centers with active star formation (mean $\Sigma_{\rm SFR}$ within inner $r_{25}/8$ or the region defined as "center" is higher than 0.1 $M_\odot$ yr^{-1} kpc^{-2}) and the latter corresponds to that in disk regions and centers of galaxies with quiescent star formation (mean $\Sigma_{\rm SFR}$ in the region is lower than the above value). (Section 2.5.2, and figure 2.15.)

6. According to the non-LTE analysis, there is a clear tendency that $R_{2/1}$ increases with $T_{\rm kin}$; however, $R_{2/1}$ and $n(\rm H_2)$ show a rather negative correlation but it is not statistically

significant. This suggests that variations of $R_{2/1}$ on kpc scales imply the temperature of molecular gas. The dependence of $R_{2/1}$ on $n(H_2)$ would appear when the spatial resolution is higher. Stellar radiation feedback influences molecular gas properties and $R_{2/1}$. The bimodality caused by differences of properties between galactic centers and disks seen on the $R_{2/1}$–$R_{12/13}$ plane can also be seen on the $R_{2/1}$–T_{kin} and $R_{2/1}$–$n(H_2)$ plots. Molecular gas in the centers is warm and diffuse, and its $R_{2/1}$ has relatively loose correlations between T_{kin} and $n(H_2)$. The disk phase molecular gas is cold, relatively dense, and its $R_{2/1}$ is tightly correlated with T_{kin}; however, it has no relation with $n(H_2)$. (Section 2.5.3, and figure 2.16.)

7. Not only T_{kin} but also pressure of molecular gas is important to understand $R_{2/1}$ variations in galaxies. Namely, even when pressure is so high ($\gtrsim 3 \times 10^3$ K cm^{-3}), $R_{2/1}$ is not always high ($\sim$ 0.5–0.6) as long as T_{kin} is low ($\lesssim$ 10 K). Likewise, even when T_{kin} is high ($\gtrsim$ 30 K), $R_{2/1}$ is not always very high (< 0.8) as long as pressure is not relatively high ($\sim 10^3$ K cm^{-3}). (Section 2.5.3, and figure 2.17.)

8. Considering variations of the CO-to-H_2 conversion factor X_{CO}, molecular gas mass in active star-formation environments such as galactic centers and (U)LIRGs is more overestimated when it is derived from ^{12}CO($J=2$–1) and the constant $R_{2/1}$ of 0.7. This is because molecular gas mass is $\propto I_{^{12}CO(2-1)} \times X_{CO}/R_{2/1}$, X_{CO} decreases, and $R_{2/1}$ increases [where $I_{^{12}CO(2-1)}$ is integrated intensity of ^{12}CO($J=2$–1)]. As a result, fluctuations of $X_{CO}/R_{2/1}$ are amplified. (Section 2.5.3.)

2.7 Appendix A: Histograms of $R_{2/1}$ in each galaxy

Figure 2.18 shows histograms of $R_{2/1}$ in each galaxy for data of the original resolution of 17″.

2.8 Appendix B: Results of stacked spectra

Table 2.5 summarizes parameters of stacked spectra in each region of galaxies.

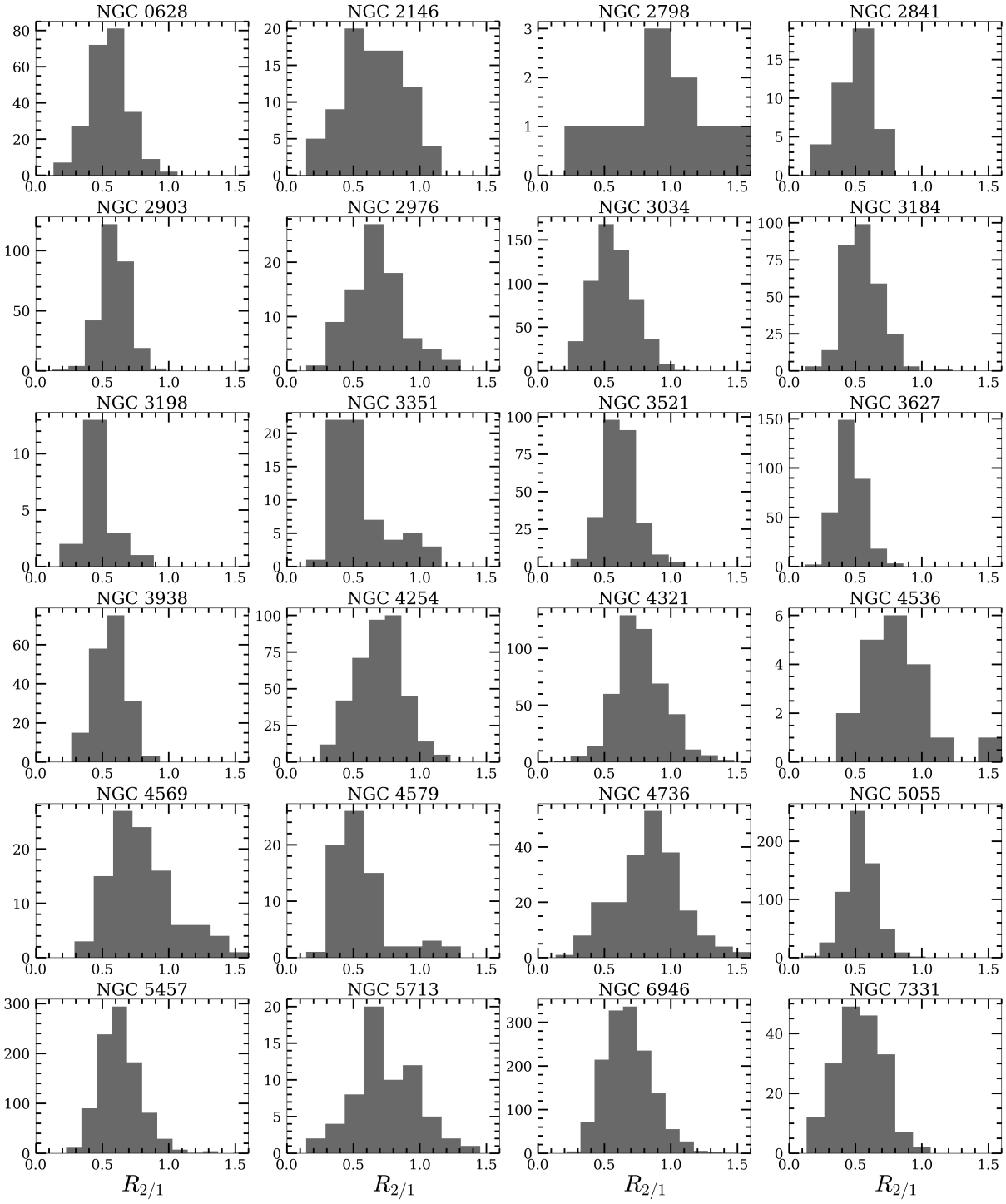

Figure 2.18: Histograms of $R_{2/1}$ in each galaxy for original resolution data.

Table 2.5: Results of the stacking analysis.

galaxy	region	$I_{^{12}\mathrm{CO}(1-0)}$ [K km s^{-1}] (1)	$I_{^{12}\mathrm{CO}(2-1)}$ [K km s^{-1}] (2)	$I_{^{13}\mathrm{CO}(1-0)}$ [K km s^{-1}] (3)	$R_{2/1}$ (4)	$R_{12/13}$ (5)	ΔV [km s^{-1}] (6)
NGC 628	center	6.8 ± 0.3	4.23 ± 0.09	1.0 ± 0.1	0.62 ± 0.03	6.8 ± 0.9	30 ± 2
	inner arm1	5.3 ± 0.2	2.80 ± 0.05	0.35 ± 0.07	0.53 ± 0.02	15.1 ± 3.1	28 ± 2
	inner arm2	5.1 ± 0.2	2.93 ± 0.05	0.38 ± 0.06	0.57 ± 0.03	13.5 ± 2.1	37 ± 2
	outer arm1	3.0 ± 0.2	1.92 ± 0.06	< 0.07	0.65 ± 0.06	> 41.1	28 ± 4
	outer arm2	3.8 ± 0.3	1.47 ± 0.06	0.27 ± 0.06	0.39 ± 0.03	14.3 ± 3.3	27 ± 3
	inter-arm1	3.1 ± 0.2	1.37 ± 0.03	< 0.07	0.43 ± 0.03	> 42.9	32 ± 4
	inter-arm2	1.6 ± 0.1	0.69 ± 0.04	< 0.04	0.44 ± 0.04	> 37.3	30 ± 5
NGC 2146	center	148 ± 1	123.9 ± 0.3	7.2 ± 0.4	0.839 ± 0.006	20.4 ± 1.0	202 ± 3
	ring1	52.3 ± 0.6	36.0 ± 0.2	2.0 ± 0.2	0.689 ± 0.009	26.4 ± 2.3	150 ± 4
	ring2	16.4 ± 0.6	8.2 ± 0.1	< 0.18	0.50 ± 0.02	> 92.8	160 ± 21
	ring3	6.5 ± 0.5	3.7 ± 0.2	< 0.2	0.57 ± 0.05	> 31.8	71 ± 12
NGC 2841	ring1	5.1 ± 0.2	2.2 ± 0.1	0.55 ± 0.1	0.42 ± 0.03	9.2 ± 1.7	88 ± 8
	ring2	3.7 ± 0.2	2.01 ± 0.09	0.49 ± 0.07	0.54 ± 0.04	7.5 ± 1.2	58 ± 6
	ring3	2.4 ± 0.1	1.29 ± 0.06	0.35 ± 0.06	0.53 ± 0.04	6.9 ± 1.3	59 ± 5
	ring4	1.6 ± 0.1	0.74 ± 0.06	< 0.05	0.46 ± 0.05	> 30.8	67 ± 10
NGC 2903	center	46 ± 1	33.5 ± 0.2	3.9 ± 0.4	0.72 ± 0.02	11.8 ± 1.1	157 ± 13
	northern bar	21.7 ± 0.8	13.0 ± 0.3	1.3 ± 0.2	0.60 ± 0.03	17.3 ± 3.4	94 ± 7
	southern bar	28.0 ± 0.7	14.1 ± 0.2	< 0.35	0.50 ± 0.02	> 79.2	151 ± 4
	northern bar end	41.7 ± 0.7	27.0 ± 0.2	4.4 ± 0.4	0.65 ± 0.01	9.5 ± 0.8	101 ± 3
	southern bar end	36.5 ± 0.7	21.4 ± 0.2	2.9 ± 0.3	0.59 ± 0.01	12.5 ± 1.5	119 ± 4
	northern arm	19.7 ± 0.4	11.9 ± 0.1	2.1 ± 0.3	0.61 ± 0.01	9.6 ± 1.4	65 ± 2
	southern arm	18.8 ± 0.5	10.4 ± 0.1	2.1 ± 0.2	0.56 ± 0.02	8.8 ± 0.8	65 ± 4
	inter-arm	13.8 ± 0.4	7.0 ± 0.1	< 0.16	0.51 ± 0.02	> 85.5	82 ± 5
	outer disk	3.9 ± 0.2	1.98 ± 0.06	0.19 ± 0.05	0.51 ± 0.03	20.8 ± 6.0	53 ± 5
NGC 2976	center	3.1 ± 0.3	2.61 ± 0.09	< 0.12	0.84 ± 0.08	> 24.9	33 ± 5
	ring1	2.6 ± 0.2	1.98 ± 0.08	< 0.05	0.76 ± 0.05	> 49.0	31 ± 4
	ring2	3.3 ± 0.1	2.41 ± 0.05	0.27 ± 0.06	0.74 ± 0.04	12.0 ± 2.7	30 ± 2
	ring3	2.0 ± 0.1	1.44 ± 0.07	0.26 ± 0.07	0.71 ± 0.05	7.7 ± 2.0	31 ± 4
	ring4	0.6 ± 0.1	0.41 ± 0.04	< 0.05	0.7 ± 0.2	> 11.0	28 ± 9

Table 2.5: (Continued.)

galaxy	region	$I_{^{12}\mathrm{CO}(1-0)}$ [K km s^{-1}] (1)	$I_{^{12}\mathrm{CO}(2-1)}$ [K km s^{-1}] (2)	$I_{^{13}\mathrm{CO}(1-0)}$ [K km s^{-1}] (3)	$R_{2/1}$ (4)	$R_{12/13}$ (5)	ΔV [km s^{-1}] (6)
NGC 3034	center	462 ± 2	365.5 ± 0.4	23.6 ± 0.7	0.792 ± 0.003	19.5 ± 0.6	147 ± 1
	ring1	204 ± 1	155.4 ± 0.2	8.8 ± 0.6	0.762 ± 0.004	23.2 ± 1.5	137 ± 2
	ring2	115.0 ± 0.8	78.9 ± 0.2	4.2 ± 0.4	0.686 ± 0.005	27.4 ± 2.3	126 ± 2
	ring3	60.8 ± 0.8	38.5 ± 0.1	1.5 ± 0.2	0.633 ± 0.008	41.7 ± 7.0	112 ± 3
	ring4	33 ± 1	24.56 ± 0.1	1.1 ± 0.2	0.74 ± 0.03	29.5 ± 6.3	106 ± 13
	ring5	33.9 ± 0.9	19.33 ± 0.07	< 0.26	0.57 ± 0.01	> 128	105 ± 6
	ring6	27.9 ± 0.8	15.6 ± 0.1	< 0.26	0.56 ± 0.02	> 108	102 ± 7
	ring7	23.1 ± 0.9	12.83 ± 0.07	< 0.21	0.56 ± 0.02	> 107	91 ± 9
	ring8	17.0 ± 0.7	9.9 ± 0.1	< 0.19	0.58 ± 0.03	> 88.5	82 ± 8
	ring9	13.5 ± 0.7	8.23 ± 0.08	< 0.22	0.61 ± 0.03	> 60.9	82 ± 12
	ring10	11.6 ± 0.5	7.15 ± 0.09	< 0.21	0.62 ± 0.03	> 56.0	87 ± 15
	ring11	11.2 ± 0.6	7.25 ± 0.09	< 0.25	0.65 ± 0.04	> 44.1	91 ± 18
NGC 3198	center	8.0 ± 0.3	4.3 ± 0.1	0.8 ± 0.1	0.54 ± 0.03	10.0 ± 1.7	92 ± 7
	ring1	4.0 ± 0.3	1.98 ± 0.06	< 0.1	0.49 ± 0.04	> 41.9	63 ± 8
	ring2	1.9 ± 0.2	1.26 ± 0.04	< 0.05	0.68 ± 0.07	> 34.5	42 ± 9
NGC 3351	center	17.5 ± 0.4	15.4 ± 0.1	1.3 ± 0.2	0.88 ± 0.02	13.5 ± 2.1	194 ± 8
	ring1	3.1 ± 0.4	1.8 ± 0.1	< 0.13	0.59 ± 0.08	> 23.2	96 ± 29
	ring2	3.6 ± 0.2	1.79 ± 0.06	< 0.13	0.50 ± 0.03	> 28.1	41 ± 5
	ring3	2.7 ± 0.3	1.08 ± 0.05	< 0.09	0.41 ± 0.05	> 29.8	40 ± 9
	ring4	1.5 ± 0.2	0.64 ± 0.04	< 0.07	0.42 ± 0.07	> 21.5	33 ± 13
NGC 3521	center	32.3 ± 0.6	20.5 ± 0.2	2.8 ± 0.3	0.64 ± 0.01	11.7 ± 1.3	165 ± 13
	ring1	27.7 ± 0.4	17.8 ± 0.1	2.3 ± 0.1	0.64 ± 0.01	11.9 ± 0.8	118 ± 3
	ring2	16.8 ± 0.3	9.28 ± 0.08	1.0 ± 0.1	0.55 ± 0.01	17.1 ± 2.1	92 ± 3
	ring3	5.7 ± 0.3	3.15 ± 0.06	0.36 ± 0.07	0.55 ± 0.03	16.0 ± 3.2	88 ± 9
	ring4	2.1 ± 0.2	0.96 ± 0.05	< 0.09	0.46 ± 0.05	> 24.1	49 ± 9
	ring5	1.2 ± 0.1	0.59 ± 0.04	< 0.06	0.51 ± 0.07	> 19.3	56 ± 13

Table 2.5: (Continued.)

galaxy	region	$I_{^{12}\mathrm{CO}(1-0)}$ [K km s^{-1}] (1)	$I_{^{12}\mathrm{CO}(2-1)}$ [K km s^{-1}] (2)	$I_{^{13}\mathrm{CO}(1-0)}$ [K km s^{-1}] (3)	$R_{2/1}$ (4)	$R_{12/13}$ (5)	ΔV [km s^{-1}] (6)
NGC 3627	center	50.4 ± 0.7	21.1 ± 0.6	2.0 ± 0.3	0.42 ± 0.01	25.3 ± 3.9	164 ± 9
	bar	24.7 ± 0.8	10.2 ± 0.2	1.2 ± 0.2	0.41 ± 0.01	20.3 ± 3.8	108 ± 11
	northern bar end	31.9 ± 0.6	15.7 ± 0.2	2.8 ± 0.2	0.49 ± 0.01	11.5 ± 0.8	68 ± 3
	southern bar end	41 ± 1	20.3 ± 0.2	3.3 ± 0.3	0.49 ± 0.01	12.5 ± 1.2	96 ± 11
	western arm	13.7 ± 0.4	6.4 ± 0.1	0.9 ± 0.1	0.47 ± 0.02	15.1 ± 2.5	48 ± 2
	eastern arm	18.4 ± 0.4	9.0 ± 0.2	1.7 ± 0.2	0.49 ± 0.02	11.0 ± 1.4	68 ± 3
	offset stream	19.1 ± 0.5	9.7 ± 0.2	1.1 ± 0.2	0.51 ± 0.02	16.9 ± 3.2	60 ± 3
	southern arm	11.1 ± 0.6	5.3 ± 0.1	0.7 ± 0.2	0.48 ± 0.03	15.0 ± 4.1	45 ± 3
	arm-bar end inter. region	12.3 ± 0.4	4.4 ± 0.1	< 0.19	0.36 ± 0.02	> 65.4	51 ± 3
	inter-arm	10.0 ± 0.5	4.7 ± 0.1	< 0.14	0.47 ± 0.03	> 70.5	86 ± 9
	outer disk	2.6 ± 0.2	1.03 ± 0.07	< 0.09	0.39 ± 0.05	> 30.4	58 ± 12
NGC 3938	center	9.5 ± 0.2	5.98 ± 0.09	1.2 ± 0.1	0.63 ± 0.02	8.2 ± 0.8	43 ± 2
	ring1	6.4 ± 0.2	3.68 ± 0.05	0.63 ± 0.07	0.57 ± 0.02	10.1 ± 1.2	29 ± 1
	ring2	4.3 ± 0.1	2.46 ± 0.04	0.36 ± 0.05	0.57 ± 0.02	12.1 ± 1.9	28 ± 1
	ring3	2.4 ± 0.2	1.36 ± 0.04	0.35 ± 0.06	0.56 ± 0.05	6.9 ± 1.3	27 ± 3
	ring4	1.02 ± 0.09	0.55 ± 0.03	< 0.03	0.54 ± 0.06	> 29.7	24 ± 3
NGC 4536	center	34 ± 1	29.7 ± 0.2	2.0 ± 0.3	0.86 ± 0.02	17.0 ± 2.2	161 ± 17
	ring1	6.5 ± 0.4	4.9 ± 0.1	< 0.14	0.74 ± 0.05	> 45.1	136 ± 23
	ring2	2.2 ± 0.2	1.34 ± 0.07	< 0.1	0.61 ± 0.07	> 22.8	80 ± 16
NGC 4579	center	13.0 ± 0.7	10.1 ± 0.2	< 0.35	0.78 ± 0.05	> 37.0	154 ± 36
	ring1	5.5 ± 0.4	3.05 ± 0.09	< 0.2	0.55 ± 0.04	> 28.0	50 ± 6
	ring2	5.1 ± 0.2	2.68 ± 0.07	0.41 ± 0.08	0.52 ± 0.03	12.3 ± 2.5	50 ± 4
	ring3	2.8 ± 0.3	1.30 ± 0.08	< 0.13	0.47 ± 0.06	> 21.0	46 ± 11

Table 2.5: (Continued.)

galaxy	region	$I_{^{12}\mathrm{CO}(1-0)}$ [K km s^{-1}] (1)	$I_{^{12}\mathrm{CO}(2-1)}$ [K km s^{-1}] (2)	$I_{^{13}\mathrm{CO}(1-0)}$ [K km s^{-1}] (3)	$R_{2/1}$ (4)	$R_{12/13}$ (5)	ΔV [km s^{-1}] (6)
NGC 5055	center	40.0 ± 0.6	27.3 ± 0.3	3.7 ± 0.3	0.68 ± 0.01	10.9 ± 0.8	120 ± 4
	ring1	20.1 ± 0.3	11.4 ± 0.1	2.4 ± 0.2	0.569 ± 0.01	8.4 ± 0.6	71 ± 2
	ring2	14.0 ± 0.2	6.79 ± 0.08	1.08 ± 0.09	0.484 ± 0.01	12.9 ± 1.0	53 ± 1
	ring3	8.5 ± 0.2	4.38 ± 0.07	0.82 ± 0.1	0.51 ± 0.02	10.4 ± 1.3	47 ± 2
	ring4	5.5 ± 0.2	2.74 ± 0.07	0.44 ± 0.07	0.5 ± 0.02	12.4 ± 2.1	44 ± 2
	ring5	2.7 ± 0.2	1.28 ± 0.05	< 0.06	0.48 ± 0.04	> 42.4	43 ± 4
	ring6	1.8 ± 0.2	0.65 ± 0.04	< 0.06	0.35 ± 0.04	> 30.5	49 ± 8
	ring7	1.1 ± 0.2	0.54 ± 0.06	< 0.06	0.51 ± 0.09	> 18.1	49 ± 12
NGC 5713	center	36.3 ± 0.7	34.4 ± 0.2	1.3 ± 0.2	0.95 ± 0.02	28.8 ± 5.7	112 ± 5
	ring1	20.7 ± 0.4	16.6 ± 0.1	0.8 ± 0.1	0.80 ± 0.02	24.5 ± 4.2	80 ± 4
	ring2	10.4 ± 0.4	7.1 ± 0.1	< 0.12	0.68 ± 0.03	> 86.2	61 ± 6
	ring3	5.7 ± 0.3	3.4 ± 0.1	< 0.11	0.59 ± 0.03	> 50.2	54 ± 5
NGC 7331	center	28.6 ± 0.9	17.6 ± 0.2	2.2 ± 0.3	0.61 ± 0.02	12.9 ± 1.6	143 ± 21
	ring1	35.2 ± 0.7	20.1 ± 0.1	4.3 ± 0.3	0.57 ± 0.01	8.1 ± 0.6	119 ± 9
	ring2	23.0 ± 0.4	12.8 ± 0.1	2.8 ± 0.3	0.56 ± 0.01	8.2 ± 0.8	114 ± 4
	ring3	11.6 ± 0.6	5.46 ± 0.1	1.0 ± 0.2	0.47 ± 0.02	12.0 ± 2.0	86 ± 10
	ring4	5.8 ± 0.4	2.60 ± 0.07	< 0.14	0.45 ± 0.04	> 40.6	93 ± 23
	ring5	3.1 ± 0.3	1.18 ± 0.07	< 0.11	0.38 ± 0.04	> 29.1	74 ± 20
	ring6	1.9 ± 0.2	0.66 ± 0.05	< 0.08	0.34 ± 0.05	> 23.5	67 ± 14

(1) Integrated intensity of stacked ^{12}CO($J = 1$–0) spectra.
(2) The same as (1) but for ^{12}CO($J = 2$–1).
(3) The same as (1) but for ^{13}CO($J = 1$–0).
(4) Integrated-intensity ratio of stacked ^{12}CO($J = 2$–1) to that for ^{12}CO($J = 1$–0).
(5) The same as (4) but for stacked ^{12}CO($J = 1$–0)/^{13}CO($J = 1$–0).
(6) FWHM of stacked ^{12}CO($J = 1$–0) spectra.

Chapter 3

Dynamical effect on density of molecular gas and star formation in barred spiral galaxies

3.1 Abstract of this chapter

We present the results of ^{12}CO($J = 1$–0) and ^{13}CO($J = 1$–0) simultaneous mappings toward the nearby barred spiral galaxy NGC 4303 as a part of the CO Multi-line Imaging of Nearby Galaxies (COMING) project. Barred spiral galaxies often show lower star-formation efficiency (SFE) in their bar region compared to the spiral arms. In this paper, we examine the relation between the SFEs and the volume densities of molecular gas $n(\mathrm{H_2})$ in the eight different regions within the galactic disk with CO data combined with archival far-ultraviolet and 24 μm data. We confirmed that SFE in the bar region is lower by 39% than that in the spiral arms. Moreover, velocity-alignment stacking analysis was performed for the spectra in the individual regions. The integrated intensity ratios of ^{12}CO to ^{13}CO ($R_{12/13}$) range from 10 to 17 as the results of stacking. Fixing a kinetic temperature of molecular gas, $n(\mathrm{H_2})$ was derived from $R_{12/13}$ via non-local thermodynamic equilibrium (non-LTE) analysis.s The density $n(\mathrm{H_2})$ in the bar is lower by 31–37% than that in the arms and there is a rather tight positive correlation between SFEs and $n(\mathrm{H_2})$, with a correlation coefficient of ~ 0.8. Furthermore, we found a dependence of $n(\mathrm{H_2})$ on the velocity dispersion of inter-molecular clouds ($\Delta V/\sin i$). Specifically, $n(\mathrm{H_2})$ increases as $\Delta V/\sin i$ increases when $\Delta V/\sin i < 100$ km s^{-1}. On the other hand, $n(\mathrm{H_2})$ decreases as $\Delta V/\sin i$ increases when $\Delta V/\sin i > 100$ km s^{-1}. These relation are seen even other barred spiral galaxies NGC 2903 and NGC 3627 are compiled. The relations indicate that the variations of SFE could be caused by the volume densities of molecular gas, and the volume densities could be governed by the dynamical influence such as cloud-cloud collisions, shear and enhanced inner-cloud turbulence.

3.2 Backgrounds of molecular gas and star formation in barred spiral galaxies

In the local universe, most of baryons in galaxies exist as stars and they are made from cold molecular gas. That is, studying molecular gas, which is a raw material of the main component

of galaxies is very important to understand galaxy evolution and formation. Star-formation activity in barred spiral galaxies is often significantly different between in spiral arms and in their bar. For example, previous studies have revealed that there are little new stars in the bar, while young stars are mainly distributed in spiral arms (e.g., Sheth et al. 2000; Sheth et al. 2002; Koda and Sofue 2006). In other words, star-formation rate (SFR) is lower in the bar than that in arms. Star-formation efficiency (SFE) is defined as the ratio of SFR to gas mass. In barred spiral galaxies, SFE is also lower in the bar (Handa et al. 1991; Momose et al. 2010; Watanabe et al. 2011; Hirota et al. 2014).

Sorai et al. (2012) suggested that most of molecular clouds in the offset ridges at leading sides of the bar are not gravitationally bound. They concluded that vigorous gas motion in the bar ridges makes molecular gas unbound and SFE in the bar decreases since it is hard for molecular clouds to shrink and form stars; molecular clouds in the bar ridges may exist as diffuse gas.

Several studies have tried to reveal the relation between physical properties of molecular gas and star formation. The HCN molecule can trace high dense molecular gas because of its large electric dipole moment. Therefore, integrated intensity ratio of HCN and ^{12}CO emission lines can be regarded as a dense gas fraction of molecular gas. There are several studies which have revealed that dense gas fraction has a positive correlation with both SFR and SFE (e.g., Solomon et al. 1992; Gao and Solomon 2004a; Gao and Solomon 2004b; Muraoka et al. 2009; Usero et al. 2015; Bigiel et al. 2016). According to these results, it seems that dense gas fraction determines the activity of star formation. Hence, it is important to understand how dense or diffuse molecular gas is distributed within a galaxy, i.e., volume density distribution.

However, deriving volume density of molecular gas (hereafter, we phrase "density" as "volume density") is not easy. It cannot be estimated from only one emission line because one intensive variable such as an intensity of a line cannot constrain extensive variables such as density and temperature of molecular gas. Thus, it is necessary to observe multiple lines Unfortunately, since molecular emission lines excluding low-excitation line of ^{12}CO are usually weak, this confines observation targets to luminous (e.g., starburst galaxies; Iono et al. 2007; Pan et al. 2015b) or very near galaxies (e.g., galaxies in the Local Group; Minamidani et al. 2011, Muraoka et al. 2012). Therefore, molecular gas density in the bar of barred spiral galaxies is not yet clear.

A newly developed instrument enables us to observe weak lines with bright CO line simultaneously. CO Multi-line Imaging of Nearby Galaxies (COMING) project[1)] (Sorai et al. 2019), one of the legacy projects of Nobeyama Radio Observatory (NRO) produced ^{12}CO($J=1$–0), ^{13}CO($J=1$–0) and C^{18}O($J=1$–0) simultaneous mappings toward a hundred and several tens of galaxies with the Nobeyama 45-m telescope and the multi-beam receiver FOur-beam REceiver System on 45-m Telescope (FOREST; Minamidani et al. 2016).

Muraoka et al. (2016) investigated physical properties of molecular gas in the barred spiral galaxy NGC 2903. They found a positive correlation between SFE and $n(\mathrm{H_2})$ among the regions. As one of the papers from the COMING project, this paper presents the decreased SFEs in the bar caused by a lower density condition of molecular gas as shown in Muraoka et al. (2016). In addition, we also discuss the causes of SFE and $n(\mathrm{H_2})$ variations within a barred spiral galaxy as an extended study.

To investigate the density of molecular gas in the bar, we study the barred spiral galaxy

[1)] Official homepage is ⟨https://astro3.sci.hokudai.ac.jp/~radio/coming/index.html⟩

NGC 4303 (M 61) which is one of the targets in the COMING project. Figure 3.1 (a) shows the Spitzer/IRAC 3.6 μm image obtained by Sheth et al. (2010). This galaxy has three spiral arms (northern, eastern, and western), the bar and the bright nucleus. The northern arm exists roughly from $(\alpha, \delta)_{\rm J2000.0} = (12^{\rm h}21^{\rm m}54^{\rm s}, 4^\circ29')$ to $(12^{\rm h}21^{\rm m}57^{\rm s}, 4^\circ29'30'')$ and the eastern one is from $(12^{\rm h}21^{\rm m}56^{\rm s}, 4^\circ29')$ to $(12^{\rm h}21^{\rm m}56^{\rm s}, 4^\circ27'24'')$ via $(12^{\rm h}21^{\rm m}58^{\rm s}, 4^\circ28'20'')$ (see also figure 3.3). NGC 4303 is considered as a member of the Virgo cluster. Because this galaxy is located in the outer region of the cluster, H I depletion is not seen in this galaxy (Cayatte et al. 1990). NGC 4303 can be observed in the face-on view (the inclination angle is 27°) and previous surveys showed that there is plenty of molecular gas in its bar (e.g., Kuno et al. 2007). Hence, we can clearly recognize the bar and it is not difficult to analyze molecular gas in the bar. Moreover, it is already confirmed in NGC 4303 that SFE in the bar is lower than that in arms by Momose et al. (2010). Therefore, this galaxy is one of the best objects to observe for discussing differences of molecular gas properties among the galactic structures. Basic parameters of NGC 4303 are listed in table 3.1.

3.3 Observations and data reduction

We made simultaneous mappings of ^{12}CO($J = 1$–0), ^{13}CO($J = 1$–0) and C^{18}O($J = 1$–0) lines toward NGC 4303 on 2016 February 12 and 13 with the Nobeyama 45-m radio telescope as a part of the COMING project. The multi-beam receiver FOREST was used as the receiver front-end; it is a four-beam dual polarization receiver with sideband separation mixers. The beam size is 15″.0 and 14″.0 at 110 GHz and 115 GHz, respectively, and the beam separation is 50″.

We adopted the On-The-Fly (OTF) mapping mode and used two scan patterns parallel to the major axis (X scan) and the minor axis (Y scan) of this galaxy, where the position angle of the X scan was set as −48° against the north. The scan separation was 4″.975, and the scan speeds were 15″.1 s^{-1} for the X scan and 14″.8 s^{-1} for the Y scan. The mapping area was 5′.3 × 5′.1, which corresponds to 27 × 25 kpc in this galaxy at the adopted distance and the inclination angle of this galaxy. The receiver backend we used was SAM45 (Kuno et al. 2011;

Table 3.1: Basic parameters of NGC 4303.

Parameter	Value
Morphological type*	SAB(rs)bc
Map center†	
Right ascension (J2000.0)	$12^{\rm h}21^{\rm m}54^{\rm s}.895$
Declination (J2000.0)	+04°28′25″.13
Distance‡	16.5 Mpc
$V^*_{\rm LSR}$	1563 km s^{-1}
Inclination angle§	27°
Position angle§	−36°.4
Linear scale	80.0 pc arcsec^{-1}
Nucleus type‖	H II, Seyfert 2

* de Vaucouleurs et al. (1991).
† Argyle and Eldridge (1990).
‡ Mei et al. (2007).
§ Salo et al. (2015).
‖ Filippenko and Sargent (1985), Ho et al. (1997).

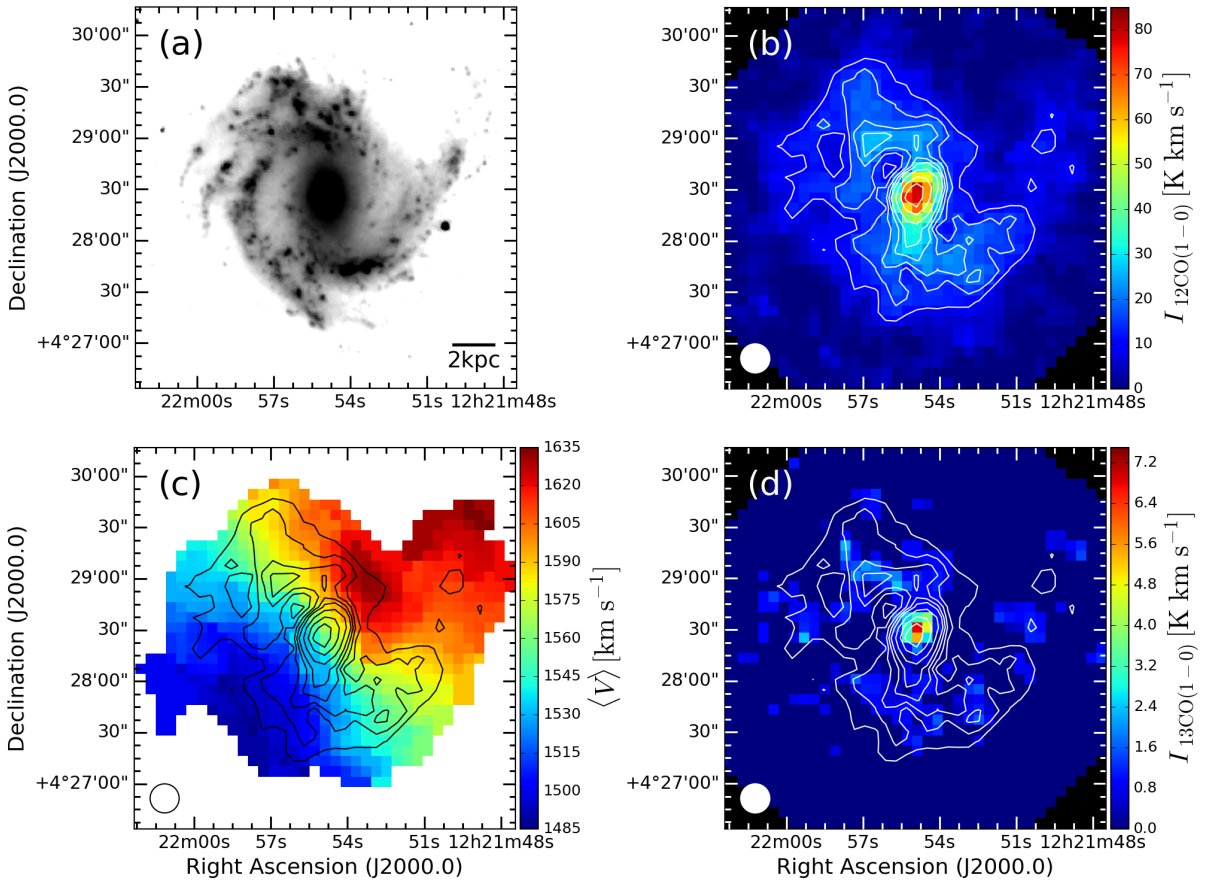

Figure 3.1: (a) Spitzer/IRAC 3.6 μm image of NGC 4303 from S^{4}G survey (Sheth et al. 2010). (b) The velocity-integrated intensity map of ^{12}CO($J=1$–0) line. Contour levels are 10, 15, 20, 25, 30, 40, 55, 70 K km s^{-1}. The map-averaged 1 σ error of integrated intensities is 1.3 K km s^{-1}. The white circle in the lower left corner represents the beam size of the Nobeyama 45-m telescope. (c) The intensity-weighted mean velocity field (color) measured by ^{12}CO($J=1$–0) line overlaid on ^{12}CO($J=1$–0) integrated intensities (contours). Contours are the same as (b). To get accurate velocity field map, we masked channels whose intensity is lower than 4 σ. (d) The velocity-integrated intensity map of ^{13}CO($J=1$–0) line overlaid on ^{12}CO($J=1$–0) integrated intensities (contour). Contours are the same as (b).

Kamazaki et al. 2012). The total bandwidth and frequency resolution were 2 GHz and 488 kHz, respectively, which corresponds to 5330 km s^{-1} and 1.3 km s^{-1} at 115 GHz.

The line intensity was calibrated by the chopper wheel method, yielding an antenna temperature, T_{A}^{*}, corrected both atmospheric and antenna ohmic losses. The main beam brightness temperature, T_{MB}, was converted from T_{A}^{*}, by observing a standard source, the carbon star IRC +10216. The telescope pointing was checked and corrected every 30–50 minutes by observing the quasar 3C 273, and the resultant pointing error was approximately 3″. The system noise temperature in T_{A}^{*} was 280–380 K at 115 GHz and 140–190 K at 110 GHz during the observations.

We used the auto-reduction system COMING ART (Sorai et al. 2019) for data reduction including removal of bad data, binning up of channels, basket-weaving (Emerson and Gräve 1988), regridding and subtracting the baseline with the first- and third-degree polynomials. This system was developed by members of the COMING project and based on the OTF data analysis

package NOSTAR (Sawada et al. 2008) distributed by NRO. The final velocity resolution and pixel scale were set to be 10 km s^{-1} and 6″.0, respectively. An effective angular resolution after map-smoothing is 17″ for all three lines, corresponding to 1.4 kpc in this galaxy. The root mean square (RMS) noise levels of the maps were $\Delta T_{\rm MB} = 73$ mK, 37 mK and 36 mK for ^{12}CO, ^{13}CO and C^{18}O, respectively.

3.4 Results

3.4.1 CO emission lines

Figure 3.1 (b) shows the velocity-integrated intensity $I_{^{12}\rm CO} \equiv \int T_{\rm MB,^{12}CO} dv$ (zeroth moment) map of ^{12}CO($J = 1$–0). Comparing the IRAC 3.6 μm image [figure 3.1 (a)], the western arm is clearly seen in the ^{12}CO line, whereas the eastern and the northern arms are ambiguous. Assuming the standard CO-to-H$_2$ conversion factor $X_{\rm CO} = 2.0 \times 10^{20}$ cm^{-2} (K km s^{-1})$^{-1}$ (Bolatto et al. 2013b), the surface density of molecular gas mass $\Sigma_{\rm mol}$ is measured by the following equation:

$$\left(\frac{\Sigma_{\rm mol}}{M_\odot\ {\rm pc}^{-2}}\right) = 1.36 \times 3.20 \cos i \left(\frac{I_{^{12}\rm CO}}{\rm K\ km\ s^{-1}}\right) \left\{\frac{X_{\rm CO}}{2.0 \times 10^{20}\,{\rm cm^{-2}}\ ({\rm K\ km\ s^{-1}})^{-1}}\right\} \tag{3.1}$$

where i is the inclination angle of this galaxy and a factor 1.36 is contribution of helium mass in molecular gas. The other factor 3.20 represents the coefficient for conversion of units from cm^{-2} to $M_\odot$ pc^{-2}. The total molecular gas mass in the map is $(9.40 \pm 0.06) \times 10^9$ $M_\odot$. This is almost consistent with previous results, such as Kuno et al. (2007) (9.7×10^9 $M_\odot$) and Momose et al. (2010) (9.1×10^9 $M_\odot$) corrected with the same distance, $X_{\rm CO}$ and the inclination angle. Figure 3.1 (c) shows the intensity-weighted mean velocity field $\langle V \rangle$ measured with ^{12}CO by the following equation: $\langle V \rangle \equiv \int v T_{\rm MB,^{12}CO} dv / \int T_{\rm MB,^{12}CO} dv$ (1st moment). To measure $\langle V \rangle$ accurately, velocity channels whose intensity is lower than 4 σ are masked.

Figure 3.1 (d) shows the ^{13}CO integrated intensity map. Because of low abundance of ^{13}C, the ^{13}CO emission is optically thin and very weak. Thus, the signal-to-noise ratio (S/N) is poor, although the RMS noise level of ^{13}CO is about half of that of ^{12}CO. Emission of ^{13}CO can be mainly seen from the galactic center. We could not detect any emission of C^{18}O($J = 1$–0).

3.4.2 Star-formation rate and efficiency

From the combination of far ultraviolet (FUV) or Hα line, and far infrared intensities, SFR can be derived (e.g., Calzetti et al. 2007, Kennicutt et al. 2007, Leroy et al. 2008). In this paper, we adopted the following equation reported by Leroy et al. (2008):

$$\left(\frac{\Sigma_{\rm SFR}}{M_\odot\ {\rm yr^{-1}\ kpc^{-2}}}\right) = \cos i \left[8.1 \times 10^{-2} \left(\frac{I_{\rm FUV}}{\rm MJy\ sr^{-1}}\right) + 3.2^{+1.2}_{-0.7} \times 10^{-3} \left(\frac{I_{24\mu\rm m}}{\rm MJy\ sr^{-1}}\right)\right], \tag{3.2}$$

where $I_{\rm FUV}$ and $I_{24\mu\rm m}$ are intensities of FUV and 24 μm continuum, respectively. This equation adopts Kroupa initial mass function (IMF, Kroupa 2001) with mass range of 0.1–120 $M_\odot$. Note that SFR assuming this IMF is less by 1/1.59 than that derived by the Salpeter IMF (Salpeter 1955) of 0.1–100 $M_\odot$ (Leroy et al. 2008).

We made use of GALEX FUV (Gil de Paz et al. 2007) and Spitzer/MIPS 24 μm (Bendo et al. 2012) archival data downloaded from the NASA/IPAC Extragalactic Database[2)] (NED). Since

[2)] ⟨https://ned.ipac.caltech.edu⟩

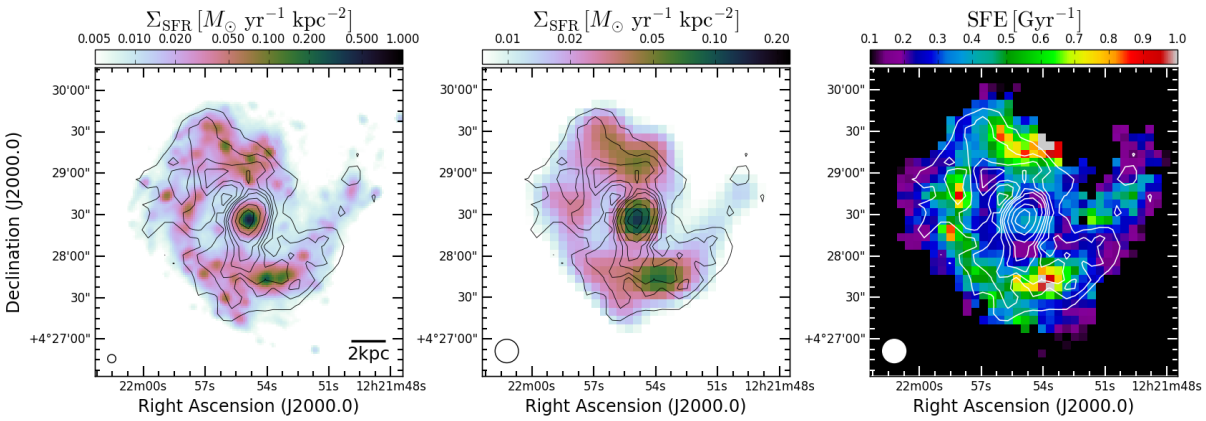

Figure 3.2: (Left) Surface density of SFR in NGC 4303 (color) overlaid on ^{12}CO($J=1$–0) integrated intensities (contours). The angular resolution of this panel is 6″.0 (the open circle in the bottom left corner) and the pixel scale is 1″.5 which are the same as the Spitzer/MIPS 24 μm data. (Center) Convolved and regridded SFR surface density in NGC 4303. The angular resolution and the grid spacing are the same as our CO data (17″ and 6″, respectively). The open circle in the bottom left corner indicates the angular resolution of this panel. (Right) The SFE map (color) of NGC 4303 overlaid on the ^{12}CO($J=1$–0) integrated intensity map (contours). Pixels whose integrated intensity of ^{12}CO($J=1$–0) line is below 3 σ were masked. The angular resolution (the open circle in the bottom left corner) and the grid spacing are the same as the middle panel (17″ and 6″, respectively).

the original angular resolution of GALEX FUV and Spitzer/MIPS 24 μm data are 4″.0 and 6″.0, respectively, the FUV and 24 μm data were convolved to match Gaussian beams of 17″, which is the same as our CO data. They were also regridded into 6″.0 to match our CO data because their pixel scale are 1″.5. To exhibit lower Σ_{SFR} in the bar, we also made a Σ_{SFR} map whose resolution is 6″.0 and pixel scale is 1″.5 from convolved FUV and original 24 μm image. The left panel of figure 3.2 shows it as a high resolution Σ_{SFR} map. SFE can be calculated by the following equation:

$$\left(\frac{\mathrm{SFE}}{\mathrm{yr}^{-1}}\right) = \left(\frac{\Sigma_{\mathrm{SFR}}}{M_\odot\ \mathrm{yr}^{-1}\ \mathrm{pc}^{-2}}\right) \Big/ \left(\frac{\Sigma_{\mathrm{mol}}}{M_\odot\ \mathrm{pc}^{-2}}\right). \tag{3.3}$$

SFEs in each pixel were measured with our ^{12}CO data and the convolved and regridded SFR map (the middle panel of figure 2). The right panel of figure 3.2 shows the result.

In the higher resolution Σ_{SFR} map (the left panel of figure 3.2) there are little newborn stars in the bar, while many clumpy structures (HII regions) are found in bar ends and spiral arms. The central region of NGC 4303 also shows higher SFR. In the right panel of figure 3.2, SFE was measured for pixels whose $I_{^{12}\mathrm{CO}}$ is larger than 3 σ error. SFE is higher in spiral arms, especially the northern arm and the southern bar end. On the other hand, SFE is depressed in the bar, outer disk and inter-arms region.

3.4.3 Regionally averaged quantities in each galactic structure

To compare physical quantities such as Σ_{mol}, Σ_{SFR} and SFE among galactic structures, we separated NGC 4303 into eight components: the center, northern bar, southern bar, northern bar end, southern bar end, northern arm, eastern arm and western arm according to figure 3.3. To determine each region, we referred ^{12}CO($J=1$–0) contours and the near infrared image in

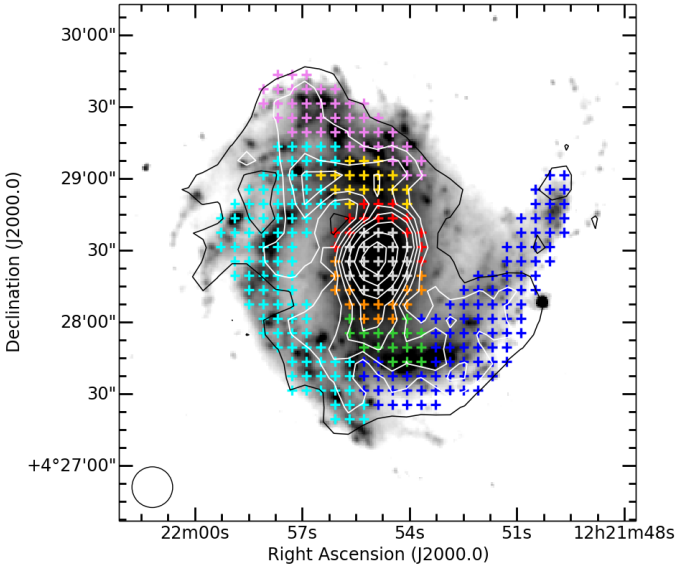

Figure 3.3: The separated regions based on the galactic structures: the center (gray), the northern bar (red), the southern bar (orange), the northern bar end (yellow), the southern bar end (green), the northern arm (purple), the eastern arm (cyan) and the western arm (blue) overlaid on the Spitzer/IRAC 3.6 μm image (gray scale) and ^{12}CO($J=1$–0) integrated intensities (contours). Contours are the same as figure 3.1 (b). The open circle in the bottom left corner represents the beam size of the Nobeyama 45-m telescope 17″. Each cross marker corresponds to pixels of the COMING original data (6″ × 6″).

figure 3.1 (a). We measured $\Sigma_{\rm mol}$, $\Sigma_{\rm SFR}$ and SFE in each region. Regionally averaged $\Sigma_{\rm SFR}$ was measured from the convolved and regridded map to match our CO data (the middle panel of figure 3.2) and SFE was measured from regionally averaged $\Sigma_{\rm SFR}$ over $\Sigma_{\rm mol}$, not averaged SFE in each pixel. Averaged $\Sigma_{\rm mol}$, $\Sigma_{\rm SFR}$ and SFE are listed in table 3.2.

Even though the left panel of figure 3.2 shows prominently lower $\Sigma_{\rm SFR}$ in the bar, regionally averaged values listed in table 3.2 are not so different compared with that in the arms. This is because the convolution process smooths distribution of $\Sigma_{\rm SFR}$ and it closes the spatial gap within this galaxy (cf. the left and middle panel of figure 2). The SFE in the bar is lower by approximately 39% than that in the arms. By contrast, SFE in bar ends is slightly higher (by $\sim$ 10%) than that in arms. Momose et al. (2010) also reported that the SFE in the bar of NGC 4303 is lower by 43% than that in the arms region. Our result is almost consistent with Momose et al. (2010) and the difference would be originated from the definition of each region and the angular resolution (17″ and 6″).

To derive density of molecular gas, we need integrated intensity ratios; the ratio of $I_{^{12}\rm CO}$ to $I_{^{13}\rm CO} \equiv R_{12/13}$ needs to be measured. However, as shown in figure 3.1 (d), ^{13}CO($J=1$–0) line is not strong enough to measure integrated intensities. Therefore, we performed the stacking analysis (Schruba et al. 2011; Morokuma-Matsui et al. 2015) in order to measure ^{13}CO($J=1$–0) integrated intensity $I_{^{13}\rm CO}$ accurately. The process of the stacking analysis is as follows: Firstly, spectra are shifted along the velocity axis according to intensity-weighted mean velocity field measured in ^{12}CO($J=1$–0) [figure 3.1 (c)]. Secondly, these velocity-shifted spectra are averaged. In this way, the noise level decreases and we can get a S/N-improved spectrum although spatial information is lost. Since the grid size of the data we used for the stacking analysis is 6″ (the

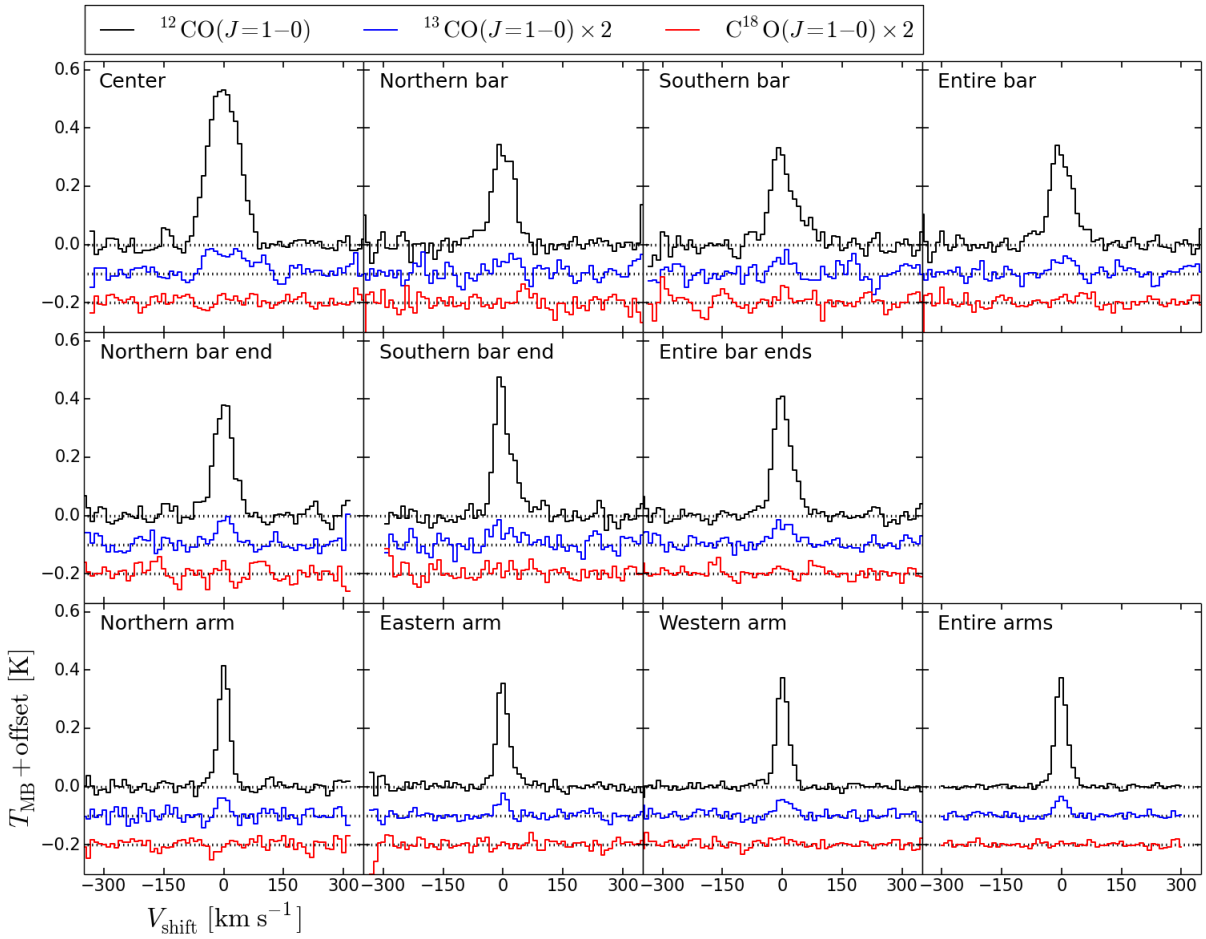

Figure 3.4: Stacked ^{12}CO(J = 1–0) (black), ^{13}CO(J = 1–0) (blue) and C^{18}O(J = 1–0) (red) spectra in each region. Offsets are 0, −0.1, −0.2 K for ^{12}CO(J = 1–0), ^{13}CO(J = 1–0) and C^{18}O(J = 1–0), respectively. Intensities of ^{13}CO(J = 1–0) and C^{18}O(J = 1–0) spectra are multiplied by two.

same as COMING original data, see figure 3.3), the spectra are oversampled.

Figure 3.4 shows stacked ^{12}CO(J = 1–0), ^{13}CO(J = 1–0) and C^{18}O(J = 1–0) spectra in each region. Parameters of stacked spectra are also summarized in Table 3.2. We measured integrated intensities for ^{12}CO(J = 1–0) and ^{13}CO(J = 1–0) stacked spectra, which is significantly detected. Note that integrated intensities in some regions such as the entire bar are not necessarily average of values in its finer regions such as the northern and southern bars. This is because integrated intensities can be changed if S/N of stacked spectra is different and it depends on how spectra are stacked. Thanks to the stacking analysis, ^{13}CO(J = 1–0) emission could be detected in all regions. On the other hand, C^{18}O(J = 1–0) emission line could not be detected.

The number of stacked spectra is approximately 15 for each part of the bar, the bar ends and the center, 40 for the northern arm and 90 for the eastern and the western arm (figure 3.3). Correspondingly, the noise level after stacking in the above-mentioned regions is typically 20, 15, 10 mK for ^{12}CO, and 11, 9, 5 mK for ^{13}CO, respectively. The resultant noise levels of stacked spectra are approximately larger by a factor of $\sim$ 1.2 than expected (the inverse number of square root of the number of the stacked spectra). This would be due to oversampling of the spectra, i.e., the noises for adjacent spectra are not random because of oversampling.

While several studies have reported that $R_{12/13}$ is high in starburst galaxies, luminous and ultra luminous infrared galaxies (LIRG, ULIRG; e.g., Aalto et al. 1991; Aalto et al. 1995), it ranges 5–18 for normal spiral galaxies (Paglione et al. 2001; Cao et al. 2017; Cormier et al. 2018; Morokuma-Matsui et al. 2020). Measured $R_{12/13}$ from stacked spectra in each region of NGC 4303 are consistent with such normal galaxies. Furthermore, $R_{12/13}$ is lower in the bar and rather higher in the bar end and the center where star formation is suppressed and enhanced, respectively. This tendency is seen in another nearby barred spiral galaxy NGC 3627 (Watanabe et al. 2011; Morokuma-Matsui et al. 2015). We discuss physical reasons for $R_{12/13}$ variations of details in the next section.

The 3σ lower limits of the ^{13}CO/C^{18}O integrated intensity ratios are also measured for the representative regions (the entire arms, the entire bar ends, the bar and the center). They typically range from 2.2 (for the entire bar) to 4.4 (for the center). This result falls within the range of the values for other local spiral galaxies (e.g., Jiménez-Donaire et al. 2017).

In addition, the full width at half maximum (FWHM) of ^{12}CO($J=1$–0) line profiles ΔV was measured without Gaussian fitting. We interpolated channels so that velocity whose intensity becomes the half of the peak was determined. Among stacked spectra, we found that ^{12}CO($J=1$–0) spectra in spiral arms look sharp in profile, while they are rather broader in the bar. In fact, the ΔV is smaller in the spiral arm regions than the bar regions.

Table 3.2: Regionally averaged quantities of NGC 4303.

	$\Sigma_{\rm mol}$	$\Sigma_{\rm SFR}$	SFE	$I_{^{12}\rm CO}$	$I_{^{13}\rm CO}$	$R_{12/13}$	ΔV
	$[M_\odot\ {\rm pc}^{-2}]$	$[10^{-2}\ M_\odot\ {\rm yr}^{-1}\ {\rm kpc}^{-2}]$	$[10^{-10}\ {\rm yr}^{-1}]$	[K km s^{-1}]	[K km s^{-1}]		[km s^{-1}]
	(1)	(2)	(3)	(4)	(5)	(6)	(7)
Center	201 ± 2.5	$6.49^{+0.57}_{-0.33}$	$3.23^{+0.29}_{-0.17}$	51.2 ± 1.0	4.5 ± 0.3	11.4 ± 0.8	95 ± 5
Northern bar	83.5 ± 2.1	$2.38^{+0.23}_{-0.14}$	$2.85^{+0.29}_{-0.18}$	22.6 ± 0.9	1.4 ± 0.3	16.6 ± 3.4	65 ± 4
Southern bar	88.8 ± 2.4	$2.09^{+0.20}_{-0.12}$	$2.36^{+0.24}_{-0.15}$	22.9 ± 0.9	1.4 ± 0.2	16.4 ± 2.8	59 ± 12
Entire bar	86.1 ± 1.6	$2.23^{+0.16}_{-0.09}$	$2.60^{+0.19}_{-0.12}$	23.5 ± 0.7	1.4 ± 0.2	17.0 ± 2.3	64 ± 4
Northern bar end	82.3 ± 1.8	$3.51^{+0.33}_{-0.19}$	$4.27^{+0.41}_{-0.25}$	23.0 ± 0.8	2.1 ± 0.2	10.8 ± 1.3	53 ± 4
Southern bar end	89.4 ± 2.1	$4.46^{+0.45}_{-0.26}$	$5.00^{+0.52}_{-0.32}$	23.1 ± 0.6	2.3 ± 0.4	10.2 ± 1.9	41 ± 4
Entire bar ends	85.7 ± 1.4	$3.97^{+0.28}_{-0.16}$	$4.63^{+0.33}_{-0.20}$	22.6 ± 0.5	2.1 ± 0.2	10.7 ± 1.1	51 ± 3
Northern arm	55.6 ± 1.0	$2.97^{+0.18}_{-0.10}$	$5.34^{+0.34}_{-0.21}$	14.7 ± 0.4	1.1 ± 0.2	13.7 ± 2.6	32 ± 2
Eastern arm	53.4 ± 0.6	$2.20^{+0.08}_{-0.05}$	$4.13^{+0.17}_{-0.11}$	14.0 ± 0.3	1.1 ± 0.1	12.5 ± 1.1	35 ± 2
Western arm	52.3 ± 0.6	$2.03^{+0.09}_{-0.05}$	$3.87^{+0.19}_{-0.11}$	14.4 ± 0.3	1.1 ± 0.1	13.2 ± 1.6	34 ± 1
Entire arms	53.3 ± 0.4	$2.27^{+0.06}_{-0.04}$	$4.26^{+0.12}_{-0.07}$	14.1 ± 0.2	1.1 ± 0.1	12.5 ± 1.1	34 ± 1

(1) Mean surface density of molecular gas.
(2) Mean surface density of SFR.
(3) Mean SFE.
(4) Integrated intensity of ^{12}CO derived from stacked spectra.
(5) Integrated intensity of ^{13}CO derived from stacked spectra.
(6) Integrated intensity ratio of ^{12}CO to ^{13}CO derived from (4) and (5).
(7) FWHM of stacked ^{12}CO spectra.

3.5 Discussion

3.5.1 What $R_{12/13}$ physically means

If ^{12}CO($J=1$–0) emission is optically thick, ^{13}CO($J=1$–0) is optically thin and the LTE assumption is applicable, $R_{12/13}$ is proportional to ${\tau_{13}}^{-1}$, where τ_{13} is optical depth of ^{13}CO. In addition, when excitation temperature of ^{13}CO, $T_{\rm ex,13}$ satisfies $T_{\rm ex,13} \gg 5.3$ K [$\sim h\nu_{^{13}\rm CO}/k_{\rm B}$, where h is the Planck constant, $\nu_{^{13}\rm CO}$ is the rest frequency of ^{13}CO($J=1$–0) and $k_{\rm B}$ is the Boltzmann constant], τ_{13} is approximately proportional to $\mathcal{N}_{^{13}\rm CO}/({T_{\rm kin}}^2 dv)$, where $\mathcal{N}_{^{13}\rm CO}$ is column density of ^{13}CO and dv is velocity dispersion within a molecular cloud. Therefore, some studies suggest that $R_{12/13}$ strongly depends on $T_{\rm kin}$ (e.g., Paglione et al. 2001; Hirota et al. 2010). However, it could be doubtful that ^{13}CO satisfies LTE condition because of its low abundance ratio and low column density. In this subsection, we discuss what changes $R_{12/13}$ focusing particularly on the chemical abundance ratio, velocity dispersion and physical properties of molecular gas such as $n(\rm H_2)$ and $T_{\rm kin}$.

When $T_{\rm kin} \lesssim 35$ K, chemical fractionation (e.g., $^{12}\rm CO + {}^{13}C^+ \rightleftharpoons {}^{13}CO + {}^{12}C^+$) is promoted (e.g., Langer et al. 1984; Liszt 2007). In addition, ^{13}CO can be selectively dissociated by radiation from massive stars (e.g., Davis 2014). On the other hand, Szűcs et al. (2014) showed there are no strong effects on the ^{13}CO abundance ratio by selective photodissociation. Milam et al. (2005) indicated both processes of chemical fractionation and selective photodissociation are inconsistent with the abundance ratios of [^{12}C]/[^{13}C] in the Milky Way. Cao et al. (2017) presumed the effects on $R_{12/13}$ by changes in the chemical abundance ratio are small enough to be easily washed out by other factors based on the discrepancy between the $R_{12/13}$ and the abundance ratios of [^{12}C]/[^{13}C] in the Galactic center and inner disk of the Milky Way. Hence, we consider $R_{12/13}$ is mainly changed by other factors except for the abundance ratio.

Next, how can velocity dispersion influence $R_{12/13}$? If velocity dispersion is large, τ_{13} becomes thin. Watanabe et al. (2011) reported the spatially resolved $R_{12/13}$ in the barred spiral galaxy NGC 3627 and $R_{12/13}$ in the bar is less than in other regions such as the spiral arms. They argue the depletion of $R_{12/13}$ would be caused by the optically thinner ^{13}CO due to high velocity dispersion in the bar. By contrast, Meier and Turner (2004) showed there is no correlation between $R_{12/13}$ and the velocity dispersions of ^{13}CO spectra in the nucleus of NGC 6946. Cao et al. (2017) also showed no correlations between $R_{12/13}$ and the intensity-weighted velocity dispersions of ^{12}CO spectra for 11 galaxies. Note that their spatial resolution is different. Watanabe et al. (2011) performed a single-dish observation and the resolution is ~ 1 kpc. While the others were interferometric, thus the spatial resolution corresponds to sub-kpc or a few 100 pc. As seen above, the effect of velocity dispersion on $R_{12/13}$ is under debate. Therefore, we need to calculate τ_{13} practically in a certain way.

At last, we examine the effects of physical properties such as density or temperature. As mentioned in the first part of this subsection, if the four conditions (the optical depth of ^{12}CO, $\tau_{12} \gg 1$, $\tau_{13} \ll 1$, the LTE approximation and $T_{\rm ex,13} \gg 5.3$ K) are applicable, $R_{12/13}$ is proportional to ${T_{\rm kin}}^{-2}$. However, if the LTE approximation is not applicable, the temperature dependence of $R_{12/13}$ becomes weak as suggested in Paglione et al. (2001). Alternatively, Meier and Turner (2004) and Meier et al. (2008) suggested that sub-thermally excited ^{13}CO is significant to variations of $R_{12/13}$. The critical density of ^{13}CO($J=1$–0) is $\sim 2 \times 10^3$ cm^{-3}, whereas

that of ^{12}CO($J=1$–0) is $\sim$ 300 cm^{-3}. Therefore, when $n(H_2)$ becomes less than $\sim 2 \times 10^3$ cm^{-3}, ^{13}CO becomes strongly sub-thermalized and the intensity of ^{13}CO($J=1$–0) is rapidly decreased. That is, $R_{12/13}$ is sensitive to the change in $n(H_2)$. Although one may presume that kinetic temperatures are higher in vicinities of star-forming regions, several studies reported the kinetic temperatures around it are not higher than other regions (e.g., Meier and Turner 2004; Schinnerer et al. 2010). Feedback from massive stars would have a small impact on kinetic temperature of molecular gas. Hence, we suggest that $R_{12/13}$ can be an indicator of $n(H_2)$, as long as ^{13}CO is strongly sub-thermalized.

3.5.2 Derivation of molecular gas density via non-LTE analysis

With the non-local thermodynamic equilibrium (non-LTE) analysis, we can derive density and kinetic temperature of molecular gas from measured integrated intensity ratios by modeling observed emission lines. It presumes internal motion of a molecular cloud with microscopic turbulences or a systematic acceleration field to calculate escape probability of photons, and computes intensities of emission lines. The latter case is called the large velocity gradient (LVG) method (e.g., Scoville and Solomon 1974; Goldreich and Kwan 1974). In this study, we use an open source code for the non-LTE analysis RADEX (van der Tak et al. 2007)[3)] based on the former case.

Settings of non-LTE analysis

RADEX solves the statistical equilibrium equations and the radiative transfer equation iteratively for an input molecule at a given kinetic temperature T_{kin} and a number density of molecular hydrogen $n(H_2)$, and outputs a brightness temperature T_b and an integrated intensity I of a single molecular cloud for each emission line of the molecule. However, this computed I cannot be compared with observed integrated intensities directly because observation results are affected by beam dilution. This problem can be solved by taking a ratio of two integrated intensities in order to cancel the beam dilution effect with assumptions that the medium is uniform and the solid angle subtended by emissions of each line is the same. In summary, RADEX computes integrated intensity ratios assuming $n(H_2)$ and T_{kin} of molecular gas.

RADEX can select three types of a cloud geometry (expanding or shrinking sphere, uniform sphere, plane slab) to calculate photon escape probability. We adopted the expanding and shrinking model, and in that case it is calculated with the Sobolev approximation (Sobolev 1960). Collision partners to ^{12}CO and ^{13}CO were set only to H_2. The brightness temperature of the background radiation was set to 2.73 K. To derive both of $n(H_2)$ and T_{kin} simultaneously, three emission lines, or two independent integrated intensity ratios are needed at least. There are two available lines. However, we have only one integrated intensity ratio $R_{12/13}$. In this paper, RADEX is calculated with a fixed T_{kin} (T_{kin} = 10, 15, 20 K). According to the previous subsection, this assumption is not invalid because T_{kin} would not exert a strong influence on $R_{12/13}$.

In RADEX calculations, a ^{12}CO column density ($\mathcal{N}_{^{12}CO}$), ^{13}CO column density ($\mathcal{N}_{^{13}CO}$) and FWHM of a cloud (dv) are needed as input parameters. $\mathcal{N}_{^{12}CO}$ and $\mathcal{N}_{^{13}CO}$ are measured with the

[3)] See also ⟨http://home.strw.leidenuniv.nl/~moldata/radex_manual.pdf⟩

following equations by additionally assuming the abundance ratio of ^{12}CO to H_2 ($[^{12}\mathrm{CO}]/[\mathrm{H_2}]$) and ^{13}CO to ^{12}CO ($[^{13}\mathrm{CO}]/[^{12}\mathrm{CO}]$):

$$\left(\frac{\mathcal{N}_{^{12}\mathrm{CO}}}{\mathrm{cm^{-2}}}\right) = \frac{[^{12}\mathrm{CO}]}{[\mathrm{H_2}]}\left(\frac{I_{^{12}\mathrm{CO}}}{\mathrm{K\ km\ s^{-1}}}\right)\left\{\frac{X_{\mathrm{CO}}}{\mathrm{cm^{-2}\ (K\ km\ s^{-1})^{-1}}}\right\}\frac{1}{\eta_{\mathrm{f}}}, \tag{3.4}$$

$$\left(\frac{\mathcal{N}_{^{13}\mathrm{CO}}}{\mathrm{cm^{-2}}}\right) = \frac{[^{13}\mathrm{CO}]}{[^{12}\mathrm{CO}]}\left(\frac{\mathcal{N}_{^{12}\mathrm{CO}}}{\mathrm{cm^{-2}}}\right), \tag{3.5}$$

where η_{f} is a beam-filling factor. Because the beam size of our CO data corresponds to 1.4 kpc at NGC 4303, this is quite a lot larger than the typical scale of molecular clouds. As a consequence, observed integrated intensities are much less than the intrinsic intensity of a cloud. Therefore, η_{f} is necessary for measuring a column density of a molecular cloud.

We first applied $X_{\mathrm{CO}} = 2.0 \times 10^{20}$ cm^{-2} (K km s^{-1})$^{-1}$ and assumed $[^{12}\mathrm{CO}]/[\mathrm{H_2}] = 8.5 \times 10^{-5}$ which is considered as the standard value for the Solar neighborhood (e.g., Frerking et al. 1982; Langer et al. 1989; Pineda et al. 2008). Milam et al. (2005) measured radial distribution of $[^{12}\mathrm{C}]/[^{13}\mathrm{C}]$ in the Galaxy and found that the relation $[^{12}\mathrm{C}]/[^{13}\mathrm{C}] = 6.21\,D\,[\mathrm{kpc}] + 18.71$ where D is the distance from the Galactic center. ^{13}C is produced in the carbon-nitrogen-oxygen (CNO) cycle and this process occurs mainly in asymptotic giant branch (AGB) stars (Pagel 1997). What causes the abundance gradient of ^{13}C, however, is still unclear. In this study, we adopted the local interstellar medium value of $[^{12}\mathrm{CO}]/[^{13}\mathrm{CO}] = 68$ measured by Milam et al. (2005).

Since molecular clouds are not like discrete balls but a continuous medium, the line widths due to internal cloud motion (dv) as an input parameter of RADEX was set depending on ΔV. In other words, they do not have the rigid boundary and internal cloud motion is likely to be affected by dynamics of surrounding gas. If ΔV increases, dv should also increase. As mentioned above, the beam size of our observation is much larger than that of molecular clouds. Therefore, one can assume that there are thousands of molecular clouds in the field of view of the telescope. In addition, measured ΔV is a few tens km s^{-1} (table 3.2), although the typical line width of a cloud is a few km s^{-1}. Thus, ΔV represents the velocity dispersion among the molecular clouds in the beam. We first defined dv as 5.0 km s^{-1} for the entire arms region. This is the typical FWHM of emission lines from molecular clouds in the Galaxy (e.g., Heyer et al. 2009). For other regions, we determined dv by the following equation.

$$\left(\frac{dv}{\mathrm{km\ s^{-1}}}\right)_i = 5.0 \times \left(\frac{\Delta V}{\mathrm{km\ s^{-1}}}\right)_i \Bigg/ \left(\frac{\Delta V}{\mathrm{km\ s^{-1}}}\right)_{\mathrm{entire\ arms}} \tag{3.6}$$

where the subscript i represents each region name and $\Delta V_{\mathrm{entire\ arms}} = 34$ km s^{-1} (table 3.2).

How to estimate a beam-filling factor

To set a beam-filling factor η_{f} in equation (3.4), we developed a method to estimate the best value of η_{f}. If the observed line is optically thick, molecular clouds do not overlap and sensitivity within the beam is uniform, η_{f} can be approximately assumed as

$$\eta_{\mathrm{f}} \simeq \frac{T_{\mathrm{peak,obs}}}{T_{\mathrm{model}}}, \tag{3.7}$$

where $T_{\mathrm{peak,obs}}$ is the observed peak intensity and T_{model} is the brightness temperature of a molecular cloud calculated by a model.

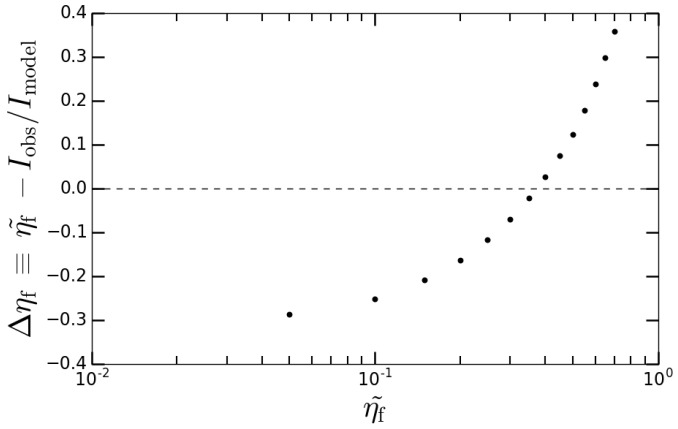

Figure 3.5: $\Delta\eta_{\rm f}$ defined by equation (3.9) as a function of a given beam-filling factor $\tilde{\eta}_{\rm f}$. This is the result for the entire arms and $T_{\rm kin} = 15$ K case. In this case, the optimum value of the beam-filling factor can be estimated to be 0.35–0.4.

However, peak intensity is no longer available to estimate $\eta_{\rm f}$ for our observation. Because the velocity resolution is 10 km s^{-1} in our observation, it is not enough to measure the true peak intensity. Moreover, profiles of observed spectra would be almost Dirac's delta function-like shape if molecular clouds in the beam do not have inter-clouds velocity dispersion. Nevertheless, molecular clouds in the beam actually have inter-clouds velocity dispersion as mentioned above. Hence, $T_{\rm peak,obs}$ becomes less than $\eta_{\rm f} T_{\rm model}$. The observed peak intensity does not reflect the amount of molecular clouds in the beam.

Even if the amount of molecular gas in the beam is constant, it is possible that the observed peak intensity changes due to inter-clouds velocity dispersion. On the other hand, the observed integrated intensity would not depend on its velocity dispersion if the overlaps of molecular clouds in the beam can be ignored. Therefore, we decided the best $\eta_{\rm f}$ using the observed integrated intensities in the following way. As an analogous to equation (3.7) of the static-clouds motion case, $\eta_{\rm f}$ can be

$$\eta_{\rm f} \simeq \frac{I_{\rm obs}}{I_{\rm model}}, \tag{3.8}$$

where $I_{\rm obs}$ is the observed integrated intensity and $I_{\rm model}$ is the integrated intensity calculated by RADEX. Hence, when a given beam-filling factor $\tilde{\eta}_{\rm f}$ is the optimum value, it satisfies the following equation:

$$\Delta\eta_{\rm f} \equiv \tilde{\eta}_{\rm f} - \frac{I_{\rm obs}}{I_{\rm model}} = 0. \tag{3.9}$$

Note that the fraction $I_{\rm obs}/I_{\rm model}$ in equations (3.8) and (3.9) is not constant; $I_{\rm model}$ is computed by RADEX and it needs a given beam-filling factor $\tilde{\eta}_{\rm f}$ as an input parameter according to equation (3.4). Namely, $I_{\rm model}$ varies depending on a given parameter $\tilde{\eta}_{\rm f}$.

For the estimation of the optimum value of a beam-filling factor, ^{12}CO($J = 1$–0) was used as the reference line, i.e., $I_{\rm obs}$ and $I_{\rm model}$ were applied to measured $I_{^{12}{\rm CO}(1-0)}$ with stacked spectra and results of calculations by RADEX, respectively. Firstly, we input $\tilde{\eta}_{\rm f} = 0.05$–0.7 with an interval of 0.05 and computed $\Delta\eta_{\rm f}$ with RADEX for each $\tilde{\eta}_{\rm f}$. Figure 3.5 shows how $\Delta\eta_{\rm f}$ is changed depending on each given $\tilde{\eta}_{\rm f}$ for the $T_{\rm kin} = 15$ K, entire arms case. From this result, we can assume that the optimum value of the beam-filling factor ranges from 0.35 to 0.40, since

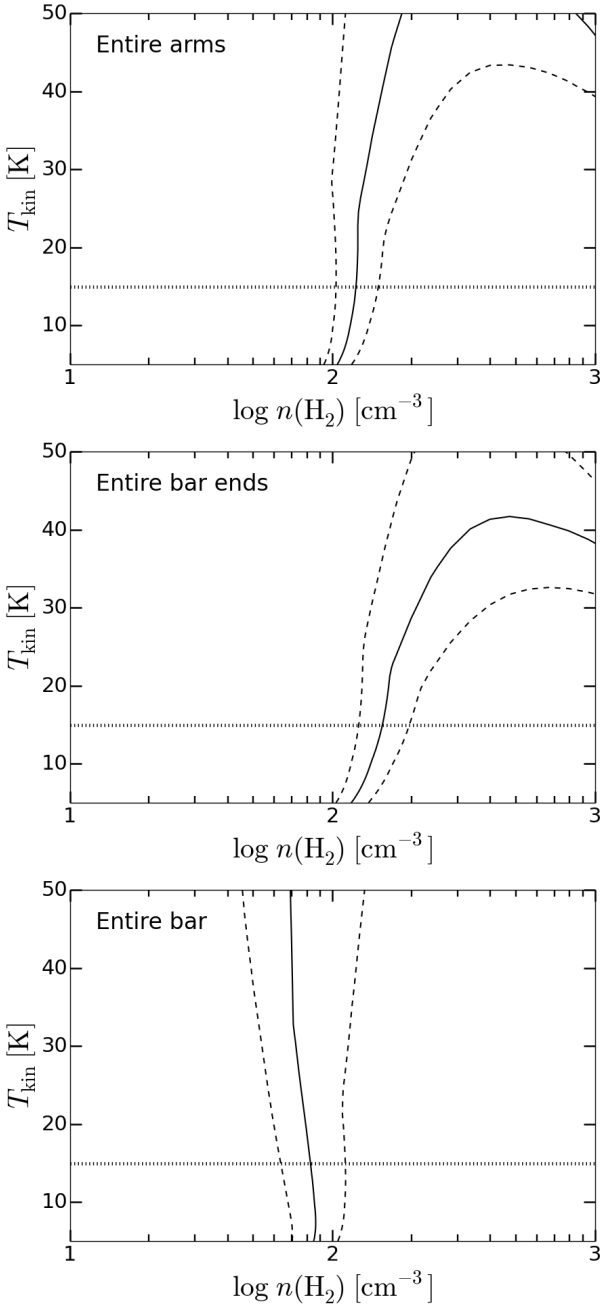

Figure 3.6: Results of RADEX calculation for $T_{\rm kin} = 15$ K in entire arms (top), entire bar ends (middle) and entire bar (bottom). Solid lines indicate the densities and the kinetic temperatures of molecular gas which reproduce observed $R_{12/13}$. Dashed lines represent $1\,\sigma$ error of $R_{12/13}$. The intersections of the solid line and the dotted line correspond to the derived densities.

the sign of $\Delta\eta_{\rm f}$ changes between these values. Secondly, we input $\tilde{\eta_{\rm f}}$ from the value whose sign changes in the next step, to the next value of it with an interval of 0.01. In figure 3.5 case, for example, $\tilde{\eta_{\rm f}}$ is input in range of 0.35–0.40 with a step of 0.01. Then we chose $\tilde{\eta_{\rm f}}$ whose $\Delta\eta_{\rm f}$ is the nearest to zero and considered it as the best $\eta_{\rm f}$. In this way, the optimum value of the beam-filling factor is defined.

Table 3.3: Derived molecular gas densities, the optimum values of the beam filling factor, the excitation temperatures of ^{12}CO and ^{13}CO in each region.

	$T_{\rm kin} = 10$ K				$T_{\rm kin} = 15$ K				$T_{\rm kin} = 20$ K			
	$n(H_2)$ [10^2 cm^{-3}]	$\eta_{\rm f}$	$T_{\rm ex,12}$ [K]	$T_{\rm ex,13}$ [K]	$n(H_2)$ [10^2 cm^{-3}]	$\eta_{\rm f}$	$T_{\rm ex,12}$ [K]	$T_{\rm ex,13}$ [K]	$n(H_2)$ [10^2 cm^{-3}]	$\eta_{\rm f}$	$T_{\rm ex,12}$ [K]	$T_{\rm ex,13}$ [K]
	(1)	(2)	(3)	(4)	(1)	(2)	(3)	(4)	(1)	(2)	(3)	(4)
Northern bar	$1.3^{+0.7}_{-0.4}$	0.53	7.5	3.3	$0.86^{+0.54}_{-0.27}$	0.38	9.3	3.4	$0.68^{+0.45}_{-0.22}$	0.32	10	3.5
Southern bar	$1.3^{+0.6}_{-0.3}$	0.59	7.5	3.4	$0.87^{+0.42}_{-0.24}$	0.42	9.3	3.5	$0.68^{+0.35}_{-0.20}$	0.35	10	3.5
Entire bar	$1.2^{+0.4}_{-0.3}$	0.56	7.5	3.3	$0.82^{+0.29}_{-0.19}$	0.40	9.2	3.4	$0.66^{+0.25}_{-0.16}$	0.34	10	3.5
Northern bar end	$2.3^{+0.7}_{-0.5}$	0.54	8.5	3.8	$1.5^{+0.5}_{-0.3}$	0.36	11	4.0	$1.2^{+0.4}_{-0.3}$	0.29	13	4.2
Southern bar end	$2.5^{+1.4}_{-0.7}$	0.69	8.5	3.9	$1.7^{+1.0}_{-0.5}$	0.46	11	4.1	$1.4^{+0.9}_{-0.4}$	0.37	13	4.3
Entire bar ends	$2.3^{+0.6}_{-0.4}$	0.55	8.5	3.8	$1.6^{+0.4}_{-0.3}$	0.37	11	4.0	$1.3^{+0.4}_{-0.2}$	0.30	13	4.2
Northern arm	$1.6^{+0.8}_{-0.5}$	0.61	8.0	3.5	$1.1^{+0.6}_{-0.3}$	0.43	10	3.7	$0.86^{+0.53}_{-0.27}$	0.35	12	3.7
Eastern arm	$1.9^{+0.4}_{-0.3}$	0.53	8.2	3.6	$1.2^{+0.3}_{-0.2}$	0.36	10	3.8	$1.0^{+0.3}_{-0.2}$	0.30	12	3.9
Western arm	$1.7^{+0.5}_{-0.3}$	0.57	8.1	3.6	$1.1^{+0.4}_{-0.2}$	0.39	10	3.7	$0.91^{+0.30}_{-0.20}$	0.32	12	3.8
Entire arms	$1.9^{+0.4}_{-0.3}$	0.56	8.2	3.6	$1.2^{+0.3}_{-0.2}$	0.37	10	3.8	$1.0^{+0.2}_{-0.2}$	0.31	12	3.9

(1) Number density of H_2.
(2) Estimated beam-filling factor.
(3) Excitation temperature between the level $J = 0$ and 1 for ^{12}CO.
(4) The same as (3) but for ^{13}CO.

As described in table 3.1, NGC 4303 has a nucleus classified as type H II (Filippenko and Sargent 1985) and type 2 Seyfert (Ho et al. 1997). Thus, it is considered that AGN feedback may have some impacts on molecular gas in the galactic center. Moreover, chemical compositions and the $X_{\rm CO}$ in the central region may be different from the disk (e.g., Bolatto et al. 2013b). Therefore, we excluded the central region for non-LTE analysis.

Results of non-LTE analysis

Figure 3.6 shows the calculation results of RADEX for the entire arms, entire bar ends and entire bar at the $T_{\rm kin}$ = 15 K case. Solid lines indicate $n(\rm H_2)$ and $T_{\rm kin}$ which produce the measured $R_{12/13}$ in each region and dotted lines are its 1 σ error. The derived $n(\rm H_2)$ corresponds to the intersection of solid and dotted lines.

All the derived densities of molecular gas and the optimum values of a beam-filling factor for each region and fixed kinetic temperature are listed in table 3.3. The molecular gas densities in the arms range from approximately 100–200 cm^{-3}, which is almost consistent with the results of giant molecular clouds in the spiral arms of M 51 (Schinnerer et al. 2010). In addition, our results fall into the range of strongly sub-thermal ^{13}CO as described in section 3.5.1. Therefore, the assumption of fixed $T_{\rm kin}$ is not a serious problem.

According to table 3.3, $n(\rm H_2)$ in the bar is lower by approximately 37% ($T_{\rm kin}$ = 10 K), 31% ($T_{\rm kin}$ = 15 K), 34% ($T_{\rm kin}$ = 20 K) than that in spiral arms. Hence, we confirmed that the density of molecular gas in the bar where the SFE also decreases is lower than that in the spiral arms. Moreover, we found that the $n(\rm H_2)$ in bar ends is larger by approximately 21% ($T_{\rm kin}$ = 10 K), 33% ($T_{\rm kin}$ = 15 K), 33% ($T_{\rm kin}$ = 20 K) than that in the arms. Calculated $\eta_{\rm f}$ are not so different for each region, whereas they are likely to depend on $T_{\rm kin}$ ($\eta_{\rm f}$ is $\sim$ 0.5 for $T_{\rm kin}$ = 10 K, $\sim$ 0.4 for $T_{\rm kin}$ = 15 K and $\sim$ 0.3 for $T_{\rm kin}$ = 20 K). These differences are caused by the fact that integrated intensities calculated by RADEX ($I_{\rm model}$) are sensitive to $T_{\rm kin}$ rather than $n(\rm H_2)$. The higher $T_{\rm kin}$ is, the larger $I_{\rm model}$ is in equations (3.8) and (3.9) and as a result, the ratio $I_{\rm obs}/I_{\rm model}$ becomes smaller and the optimum value of beam-filling factors is smaller.

The excitation temperatures of ^{12}CO(J = 1–0), $T_{\rm ex,12}$ and $T_{\rm ex,13}$ calculated by RADEX are also listed in table 3.3. Since $\mathcal{N}_{^{13}\rm CO}$ is lower, ^{13}CO is strongly sub-thermalized. Optical depths of ^{12}CO and ^{13}CO, τ_{12} and τ_{13} is almost constant among the regions: τ_{12} = 20, 19–20, 18–20, and τ_{13} = 0.77–0.82, 1.0–1.1, 1.2–1.3 for the $T_{\rm kin}$ = 10, 15, 20 K cases, respectively. One may assume that the optical depths could be lower in the bar than that of others, because the line widths are larger. We note that the large column densities in the bar cancel this effect [see also equation (21) in van der Tak et al. (2007)]. In addition, the derived τ_{13} are much larger than those in Cormier et al. (2018), although the results of $R_{12/13}$ for NGC 4303 are consistent with theirs. This may be because a $T_{\rm ex,13}$ they assumed is much higher (20–30 K) than our derived ones, which lead to lower value of τ_{13} [see also equation (3) in Cormier et al. (2018)]. Several studies have reported $\tau_{13} \sim 1$, for example, Roman-Duval et al. (2010), Hacar et al. (2016) and Torii et al. (2021). Thus, our results of $\tau_{13} \sim 1$ are not unique.

3.5.3 The cause of SFE and molecular gas density variations

We show the double logarithmic correlation plot between SFEs and $n(\rm H_2)$ for the $T_{\rm kin}$ = 15 K case in figure 3.7. The gray dashed line in the figure indicates the least squares law fitting. In

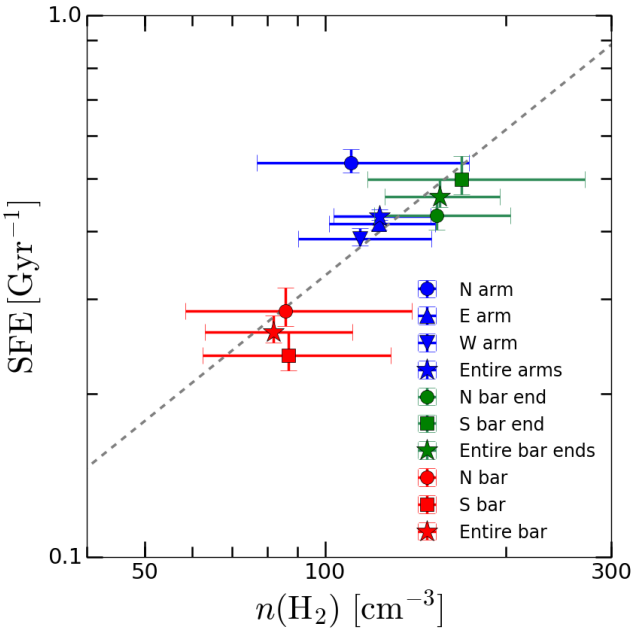

Figure 3.7: Correlation between SFE and molecular gas density $n(H_2)$ derived from RADEX for the $T_{kin} = 15$ K case. The gray dashed line indicates the least square fitting.

the double logarithmic plot case, the correlation coefficient is 0.83, 0.82, 0.83 for $T_{kin} = 10$, 15, 20 K, respectively. This positive correlation is the second case subsequently to Muraoka et al. (2016) for NGC 2903. According to Muraoka et al. (2016), the correlation coefficient for the double logarithmic SFE–$n(H_2)$ plot is 0.71, which is the similar result to that for this study (note that they reported not the correlation coefficient but the coefficient of determination R^2). To investigate whether the relation between SFE and $n(H_2)$ is almost the same for other galaxies, more samples and further studies are needed.

The northern arm seems to have a deviation from the correlation as shown in figure 3.7. The reason may be that molecular gas has been halfway to depletion although it was plenty before the current active star formation in the northern arm. As a result, the SFE becomes relatively larger than that of others. It is also possible that an interaction with other galaxies may produce compact dense molecular clouds in the northern arm, which could not be detected in our observation, even though the kpc-scale averaged density of molecular gas is lower. The deviation from the usual spider pattern for the mean velocity field is seen at near the root of the northern arm according to figure 3.1 (c). In fact, Cayatte et al. (1990) argued that many supernovae and H II regions in NGC 4303 indicate recent star-burst activity, and this may be due to a tidal interaction with its companions NGC 4292 and NGC 4301 (NGC 4303A).

Even though there are some deviations, we can conclude that the variation of SFEs within NGC 4303 is caused by the different densities of molecular gas. Then, the next question appears: why do the densities of molecular gas vary among the galactic structures? We discuss the reason for the various molecular gas densities in the following.

Many previous studies based on both observations and simulations have reported that non-circular motion is large in the bar (e.g., Athanassoula 1992a; Reynaud and Downes 1998; Watanabe et al. 2011; Fujimoto et al. 2014; Maeda et al. 2018; Sun et al. 2018). Therefore, we in-

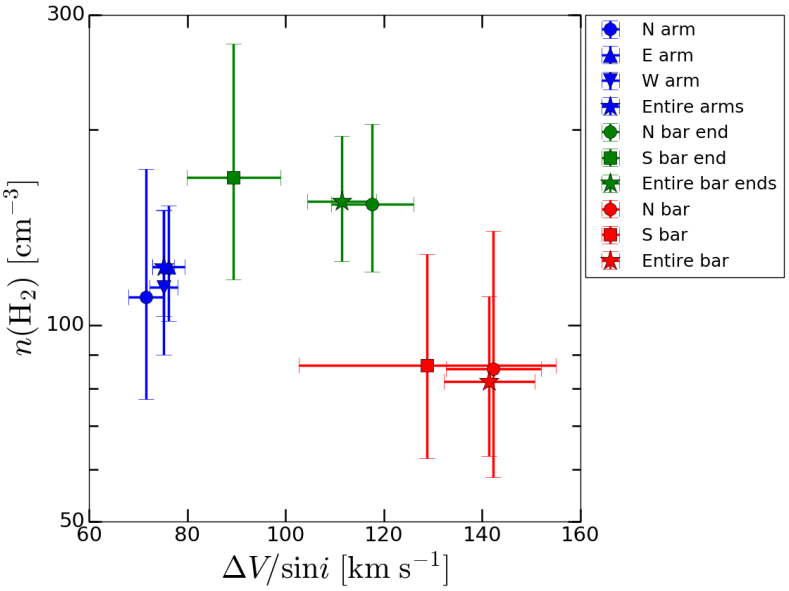

Figure 3.8: Relationship between derived $n(H_2)$ and $\Delta V/\sin i$ for the $T_{\rm kin} = 15$ K case.

vestigate the reason of the lower density condition of molecular gas in the bar by focusing on dynamics of molecular gas in each region. As discussed in subsection 3.5.2, the FWHM of observed and stacked spectra ΔV represents the velocity dispersion of inter-molecular clouds in the beam. Since the galactic disk is tilted against the observer, the observed velocity becomes larger by a factor of $\sin i$ than that for the face-on case. Hence, the quantity $\Delta V/\sin i$ could indicate the velocity dispersion of inter-molecular clouds projected on the galactic disk. We examine the relation between $n(H_2)$ and $\Delta V/\sin i$.

Figure 3.8 shows $n(H_2)$ in the $T_{\rm kin} = 15$ K case against $\Delta V/\sin i$ for each region. It is clear that when $\Delta V/\sin i \lesssim 100$ km s^{-1} (from the arms to the bar end region), $n(H_2)$ increases as $\Delta V/\sin i$ increases. On the other hand, when $\Delta V/\sin i \gtrsim 100$ km s^{-1} (from the bar end to the bar region), $n(H_2)$ decreases as $\Delta V/\sin i$ increases. That is, we found that if inter-clouds velocity dispersion is moderate, density of molecular gas get denser and if velocity dispersion is too large, it becomes lower inversely: the $n(H_2)$–$\Delta V/\sin i$ relationship with the asymmetric-"Λ" like shape. This can be also seen in $T_{\rm kin} = 10$ K and 20 K cases. In summary, we can conclude that density of molecular gas could vary depending on the dynamical effect such as inter-clouds velocity dispersion. From the next paragraph, we further discuss what processes influence on $n(H_2)$ for the lower and higher inter-clouds velocity dispersion regimes, respectively.

For the $\Delta V/\sin i \lesssim 100$ km s^{-1} (the positive correlation regime between $n(H_2)$ and $\Delta V/\sin i$) case, moderate velocity dispersion seems to enhance density of molecular gas. The tendency is explained if cloud-cloud collisions (Habe and Ohta 1992) occur more frequently due to reasonable inter-clouds' motion, which would increase the probability of collisions or interactions with molecular clouds.

In figure 3.8, molecular gas density is increased in bar ends where the inter-clouds velocity dispersions are moderate. It is possible that orbits of molecular gas have self-intersections around the bar end (e.g., Blitz et al. 1993; Downes et al. 1996). This fact may be the reason for moderate velocity dispersion and the increased probability of collisions. In consequence of such processes,

the molecular gas densities would become higher in the bar ends. In fact, for the star-forming region W 43, which is considered to be located in the bar end of the Galaxy (e.g., Nguyen Luong et al. 2011), it would be a cloud-cloud collisions site (e.g., Motte et al. 2014).

On the other hand, for the $\Delta V/\sin i \gtrsim 100$ km s^{-1} (the negative correlation) regime, collision speed could become higher than that of the moderate case. Therefore, because of such high collision speed, molecular clouds could be destroyed (e.g., Tubbs 1982). In another aspect of destructive colliding, Takahira et al. (2014) showed that if molecular clouds collide at high speed, many molecular cloud cores are formed. However, they do not have enough time to accrete molecular gas. As a result, molecular cloud cores cannot grow and mean density does not become higher. In addition to the cloud-cloud collision scenario, large velocity dispersion of inter-clouds should enhance inner-cloud velocity dispersion, or turbulence. This causes molecular clouds to gravitationally contract hardly (e.g., Sorai et al. 2012; Nimori et al. 2013). Finally, strong shear motion could become dominant in such a vigorous environment. Therefore, molecular clouds would be stripped, shredded and finally destroyed (e.g., Athanassoula 1992a). Understanding which is the most dominant process in the bar is a remaining issue.

3.6 Discussion 2 — physical properties of molecular gas with three lines in three barred spiral galaxies

Up to section 3.5, the analysis is based on the two lines. Due to this, we have to assume $T_{\rm kin}$ to derive $n(\rm H_2)$. In order to derive $n(\rm H_2)$ with more confidence, we further analyzed properties of molecular gas by adding data of another line. Moreover, we tried to add sample barred spiral galaxies.

As long as we searched for archival data of another ^{12}CO line for barred spiral galaxies in the COMING sample, we found that ^{12}CO($J=3$–2) data ($\nu_{\rm rest}$ = 345.796 GHz) obtained with the 4×4 multi-beam receiver Heterodyne Array Receiver Program (HARP; Buckle et al. 2009) mounted on the James Clark Maxwell Telescope (JCMT) was best. Data was downloaded via the Canadian Astronomy Data Centre[4)]. ^{12}CO($J=3$–2) archival data was available for only NGC 2903, NGC 3627, and NGC 4303. NGC 2903 was observed in only northern part. There are also other barred spiral galaxies whose ^{12}CO($J=3$–2) archival data is available in the COMING sample galaxies, however, the apparent size of the bar is too small to analyze or CO emission is very weak and the stacking analysis could not be performed. The original observational data has the frequency axis not velocity, the frequency resolution is ~ 0.488 MHz, which is too fine, and the original resolution is 14″. Therefore, we converted the frequency axis into the velocity axis, binned up velocity channels so that the velocity resolution of ~ 10 km s^{-1}, and convolved the data to much the COMING data. Basic parameters of NGC 2903 and NGC 3627 are listed in table 3.4 and 3.5.

Galactic structures for NGC 2903 and NGC 3627 are defined as shown in figure 3.9. They are based on ^{12}CO($J=1$–0) contours and 3.6 μm images. Apart from the northern bar end of NGC 3627, Watanabe et al. (2011) defined the "offset stream" extending from the bar end to the east. Our definition followed it. In addition, the northern and southern bar in NGC 4303 defined in figure 3.3 are combined to increase S/N. Spectra of ^{12}CO($J=1$–0), ^{12}CO($J=3$–2),

[4)] http://www.cadc-ccda.hia-iha.nrc-cnrc.gc.ca/en/search/

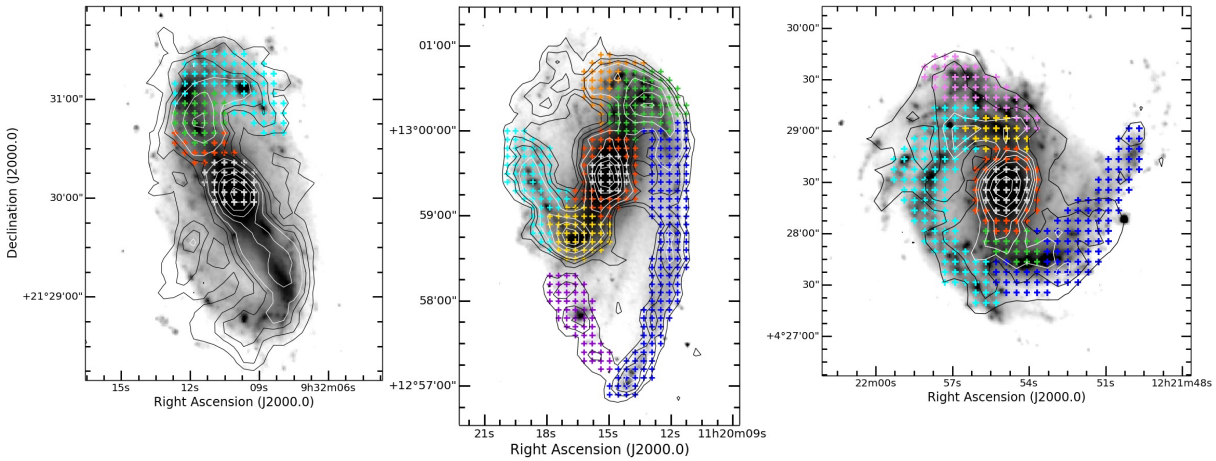

Figure 3.9: Galactic regions for NGC 2903 (left), NGC 3627 (center), and NGC 4303 (right). In NGC 2903, the center (white), the northern bar (red), the northern bar end (green), and the northern arm (cyan) are determined. In NGC 3627, the center (white), the bar (red), the northern bar end (green), the southern bar end (yellow), the western arm (blue), the eastern arm (cyan), the southern arm (purple), and the offset stream (orange) are determined. In NGC 4303, most regions are the same as figure 3.3, but the northern and southern bar are combined to increase S/N. The background gray scale is Spitzer/IRAC 3.6 μm images obtained by Sheth et al. (2010) and contours are ^{12}CO($J=1$–0) integrated intensity. The reason regions are determined in only the northern part for NGC 2903 is JCMT ^{12}CO($J=3$–2) data is covered with this area.

and ^{13}CO($J=1$–0) were stacked within each region using ^{12}CO($J=1$–0) velocity field maps. Then, integrated intensity ratios of ^{12}CO($J=3$–2)/^{12}CO($J=1$–0), $R_{3/1}$, were derived. From it and $R_{12/13}$, mean $n(\mathrm{H_2})$ in each region was also derived without assuming $T_{\rm kin}$ with the same settings of RADEX described in section 3.5.2. $R_{3/1}$, $R_{12/13}$, and derived physical properties of molecular gas from RADEX such as $n(H_2)$ and $T_{\rm kin}$ are listed in table 3.6–3.8.

Table 3.4: Basic parameters of NGC 2903.

Parameter	Value
Morphological type*	SAB(rs)bc
Right ascension (J2000.0)†	$09^{\rm h}32^{\rm m}10^{\rm s}.11$
Declination (J2000.0)†	$+21°30'03''.0$
Distance‡	9.46 Mpc
$V_{\rm LSR}^{\S}$	549 km s^{-1}
Inclination angle‖	67°
Position angle‖	$-155°.4$
Linear scale	45.9 pc arcsec^{-1}
Nucleus type#	H II

* de Vaucouleurs et al. (1991).
† Jarrett et al. (2003).
‡ Tully et al. (2013).
§ Kuno et al. (2007).
‖ Chung et al. (2009).
NED.

Table 3.5: Basic parameters of NGC 3627.

Parameter	Value
Morphological type*	SAB(s)b
Right ascension (J2000.0)†	$11^{\rm h}20^{\rm m}14^{\rm s}.964$
Declination (J2000.0)†	$+12°59'29''.54$
Distance‡	9.04 Mpc
$V_{\rm LSR}^{\S}$	724 km s^{-1}
Inclination angle§	52°
Position angle§	176°.4
Linear scale	43.8 pc arcsec^{-1}
Nucleus type‖	LINER, Seyfert 2

* de Vaucouleurs et al. (1991).
† Evans et al. (2010).
‡ Tully et al. (2013).
§ Kuno et al. (2007).
‖ NED.

Table 3.6: Integrated intensities, line ratios, SFE, and derived physical properties of molecular gas in NGC 2903.

	$I_{^{12}\mathrm{CO}(1-0)}$ [K km s^{-1}]	$I_{^{12}\mathrm{CO}(3-2)}$ [K km s^{-1}]	$I_{^{13}\mathrm{CO}(1-0)}$ [K km s^{-1}]	$R_{3/1}$	$R_{12/13}$	ΔV [km s^{-1}]	SFE [10^{-10} yr^{-1}]	$n(\mathrm{H_2})$ [10^2 cm^{-3}]	T_{kin} [K]	T_{dust} [K]
	(1)	(2)	(3)	(4)	(5)	(6)	(7)	(8)	(9)	(10)
Nothern bar	22.8 ± 0.9	6.41 ± 0.13	2.29 ± 0.22	0.281 ± 0.012	9.9 ± 1.0	86.0 ± 7.3	$4.07^{+0.43}_{-0.27}$	$2.18^{+0.51}_{-0.39}$	$14.1^{+2.1}_{-1.7}$	—
Northern bar end	39.2 ± 0.7	11.6 ± 0.17	3.38 ± 0.25	0.296 ± 0.006	11.6 ± 0.9	96.1 ± 4.0	$2.36^{+0.18}_{-0.11}$	$1.38^{+0.26}_{-0.21}$	$17.8^{+2.4}_{-2.0}$	—
Northern arm	18.5 ± 0.4	5.08 ± 0.07	1.91 ± 0.14	0.275 ± 0.006	9.7 ± 0.7	53.5 ± 2.7	$4.81^{+0.26}_{-0.16}$	$2.23^{+0.33}_{-0.29}$	$13.6^{+1.3}_{-1.1}$	—

(1) Integrated intensity of ^{12}CO($J = 1$–0) derived from stacked spectra.
(2) The same as (1) but for ^{12}CO($J = 3$–2).
(3) The same as (1) but for ^{13}CO($J = 1$–0).
(4) Integrated-intensity ratio of ^{12}CO($J = 3$–2)/^{12}CO($J = 1$–0).
(5) Integrated-intensity ratio of ^{12}CO($J = 1$–0)/^{13}CO($J = 1$–0).
(6) Full-width at half maximum of stacked spectra.
(7) Regionally averaged SFE.
(8) Number density of H_2 derived from RADEX.
(9) Kinetic temperature of H_2 derived from RADEX.
(10) Dust temperature derived from Herschel/PACS 70 and 160 μm.

Table 3.7: Integrated intensities, line ratios, SFE, and derived physical properties of molecular gas in NGC 3627.

	$I_{^{12}\mathrm{CO}(1-0)}$ [K km s^{-1}]	$I_{^{12}\mathrm{CO}(3-2)}$ [K km s^{-1}]	$I_{^{13}\mathrm{CO}(1-0)}$ [K km s^{-1}]	$R_{3/1}$	$R_{12/13}$	ΔV [km s^{-1}]	SFE [10^{-10} yr^{-1}]	$n(\mathrm{H_2})$ [10^2 cm^{-3}]	T_{kin} [K]	T_{dust} [K]
	(1)	(2)	(3)	(4)	(5)	(6)	(7)	(8)	(9)	(10)
Entire bar	29.8 ± 0.6	8.24 ± 0.23	0.85 ± 0.18	0.276 ± 0.009	35.0 ± 7.4	125.5 ± 13.6	$2.52^{+0.15}_{-0.09}$	$0.49^{+0.41}_{-0.23}$	$34.0^{+28.4}_{-13.2}$	31.1
Northern bar end	35.3 ± 0.6	12.34 ± 0.21	3.14 ± 0.16	0.349 ± 0.008	11.3 ± 0.6	60.9 ± 3.3	$5.31^{+0.30}_{-0.18}$	$1.29^{+0.17}_{-0.14}$	$20.9^{+2.3}_{-2.0}$	31.6
Southern bar end	39.7 ± 0.9	18.19 ± 0.25	3.52 ± 0.27	0.458 ± 0.012	11.3 ± 0.9	101.9 ± 9.9	$7.63^{+0.55}_{-0.33}$	$0.98^{+0.23}_{-0.20}$	$32.3^{+8.2}_{-5.8}$	33.2
Entire bar ends	37.2 ± 0.6	14.92 ± 0.20	3.04 ± 0.18	0.402 ± 0.008	12.2 ± 0.7	77.4 ± 4.1	$6.47^{+0.31}_{-0.18}$	$0.94^{+0.15}_{-0.14}$	$29.2^{+4.8}_{-3.9}$	31.9
Eastern arm	20.6 ± 0.4	7.96 ± 0.27	1.93 ± 0.20	0.385 ± 0.015	10.7 ± 1.1	66.5 ± 3.0	$3.66^{+0.19}_{-0.12}$	$1.37^{+0.38}_{-0.28}$	$22.0^{+5.4}_{-3.8}$	29.8
Western arm	17.7 ± 0.4	4.18 ± 0.15	1.04 ± 0.09	0.236 ± 0.010	17.1 ± 1.5	40.5 ± 1.8	$2.52^{+0.09}_{-0.06}$	$0.63^{+0.17}_{-0.14}$	$24.7^{+6.7}_{-4.7}$	28.3
Southern arm	13.4 ± 0.6	4.31 ± 0.23	1.13 ± 0.15	0.321 ± 0.022	11.9 ± 1.7	29.7 ± 2.4	$5.44^{+0.39}_{-0.25}$	$1.18^{+0.47}_{-0.32}$	$20.2^{+7.4}_{-4.6}$	29.8
Offset stream	20.9 ± 0.5	6.00 ± 0.14	1.44 ± 0.12	0.287 ± 0.010	14.5 ± 1.3	50.7 ± 3.9	$5.00^{+0.41}_{-0.25}$	$0.79^{+0.20}_{-0.16}$	$23.8^{+5.8}_{-4.2}$	30.7
Entire arms	17.9 ± 0.3	5.62 ± 0.12	1.26 ± 0.08	0.314 ± 0.008	14.2 ± 0.9	40.0 ± 1.7	$3.50^{+0.10}_{-0.06}$	$0.80^{+0.14}_{-0.12}$	$26.2^{+4.6}_{-3.7}$	29.0

(1)–(10) The same as table 3.6 but for NGC 3627.

Table 3.8: Integrated intensities, line ratios, SFE, and derived physical properties of molecular gas in NGC 4303.

	$I_{^{12}\mathrm{CO}(1-0)}$ [K km s^{-1}]	$I_{^{12}\mathrm{CO}(3-2)}$ [K km s^{-1}]	$I_{^{13}\mathrm{CO}(1-0)}$ [K km s^{-1}]	$R_{3/1}$	$R_{12/13}$	ΔV [km s^{-1}]	SFE [10^{-10} yr^{-1}]	$n(\mathrm{H_2})$ [10^2 cm^{-3}]	T_{kin} [K]	T_{dust} [K]
	(1)	(2)	(3)	(4)	(5)	(6)	(7)	(8)	(9)	(10)
Entire bar	23.5 ± 0.7	4.37 ± 0.15	1.38 ± 0.18	0.186 ± 0.009	17.0 ± 2.3	64.2 ± 4.2	$2.60^{+0.19}_{-0.11}$	$0.77^{+0.30}_{-0.22}$	$18.6^{+5.7}_{-3.9}$	26.4
Northern bar end	23.0 ± 0.8	8.12 ± 0.23	2.12 ± 0.24	0.353 ± 0.016	10.8 ± 1.3	53.4 ± 3.8	$4.27^{+0.41}_{-0.25}$	$1.42^{+0.45}_{-0.32}$	$19.9^{+5.1}_{-3.7}$	27.7
Southern bar end	23.1 ± 0.6	7.25 ± 0.24	2.28 ± 0.42	0.313 ± 0.013	10.2 ± 1.9	40.6 ± 4.3	$4.99^{+0.52}_{-0.31}$	$1.79^{+0.87}_{-0.55}$	$16.2^{+4.9}_{-3.3}$	28.0
Entire bar ends	22.6 ± 0.5	7.72 ± 0.20	2.12 ± 0.21	0.341 ± 0.012	10.7 ± 1.1	50.6 ± 3.2	$4.63^{+0.33}_{-0.20}$	$1.51^{+0.39}_{-0.29}$	$18.8^{+3.7}_{-2.8}$	27.8
Nothern arm	14.7 ± 0.4	4.36 ± 0.16	1.07 ± 0.20	0.297 ± 0.014	13.7 ± 2.6	32.5 ± 1.6	$5.35^{+0.33}_{-0.21}$	$0.90^{+0.53}_{-0.34}$	$22.6^{+11.6}_{-6.5}$	27.7
Eastern arm	14.0 ± 0.3	3.74 ± 0.06	1.12 ± 0.10	0.266 ± 0.007	12.5 ± 1.2	34.6 ± 1.5	$4.13^{+0.17}_{-0.10}$	$1.25^{+0.30}_{-0.23}$	$17.4^{+3.0}_{-2.3}$	27.0
Western arm	14.4 ± 0.3	3.40 ± 0.12	1.09 ± 0.13	0.256 ± 0.009	13.2 ± 1.6	34.1 ± 1.3	$3.87^{+0.18}_{-0.11}$	$1.18^{+0.36}_{-0.27}$	$16.6^{+3.6}_{-2.7}$	26.0
Entire arms	14.1 ± 0.2	3.76 ± 0.06	1.13 ± 0.10	0.266 ± 0.006	12.5 ± 1.1	34.1 ± 1.0	$4.26^{+0.12}_{-0.07}$	$1.21^{+0.26}_{-0.21}$	$17.5^{+2.7}_{-2.1}$	26.7

(1)–(10) The same as table 3.6 but for NGC 4303.

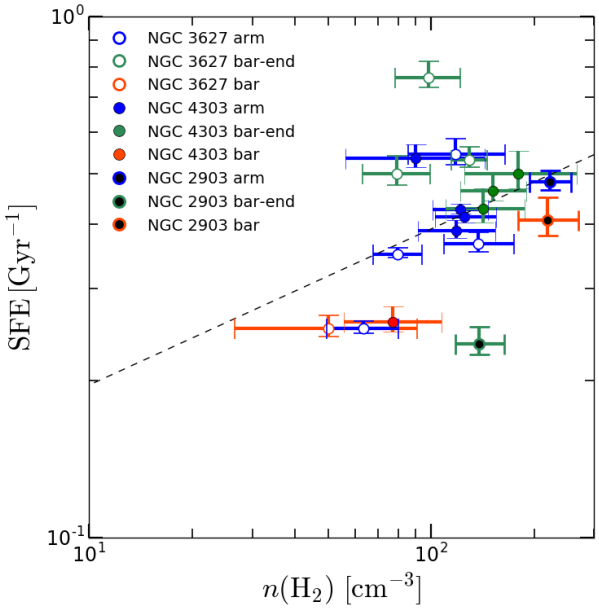

Figure 3.10: Correlation between SFE and $n(H_2)$ for NGC 2903 (black-filled markers), NGC 3627 (open markers), and NGC 4303 (filled markers). Blue, green, and red correspond to arms, bar ends, and bar respectively. The gray dashed line is the filled line.

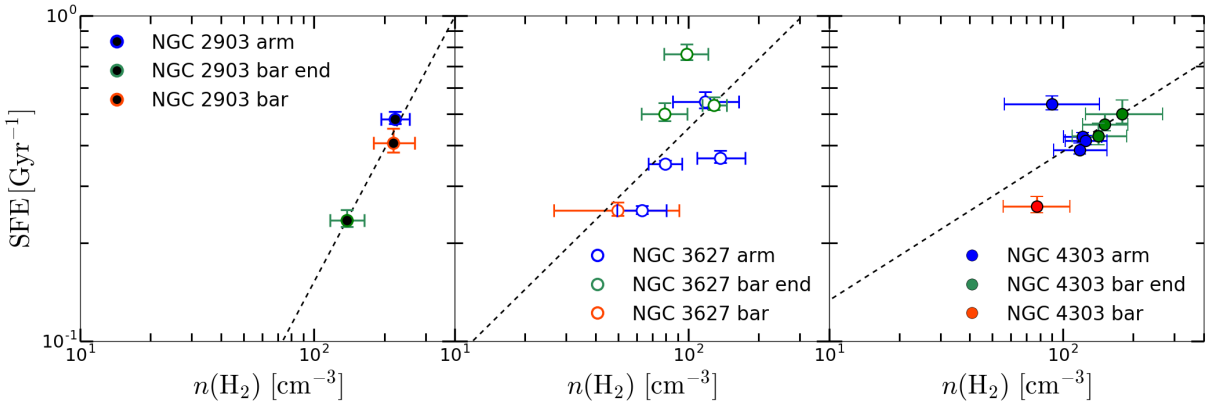

Figure 3.11: The same as figure 3.10 but plotted for each galaxy.

3.6.1 Relation of SFE and $n(H_2)$, and dynamically influenced $n(H_2)$ in barred spiral galaxies

Figure 3.10 shows the correlation between SFE and $n(H_2)$ for NGC 2903, NGC 3627, and NGC 4303. Its Pearson's correlation coefficient is 0.38. Although the moderate positive correlation is seen between them, scatter is large and it is not clearer than seen in figure 3.7. It may be due to differences among galaxies, thus we also examine the correlation for each galaxy.

Figure 3.11 shows correlations of SFE and $n(H_2)$ in each galaxy. The Pearson's correlation coefficient is 0.98, 0.64, 0.57 for NGC 2903, NGC 3627, and NGC 4303, respectively. Although the result for NGC 2903 is not confident because of few data points, it is found that large scatter seen in figure 3.10 is caused by various slopes of the SFE–$n(H_2)$ relation among galaxies. We

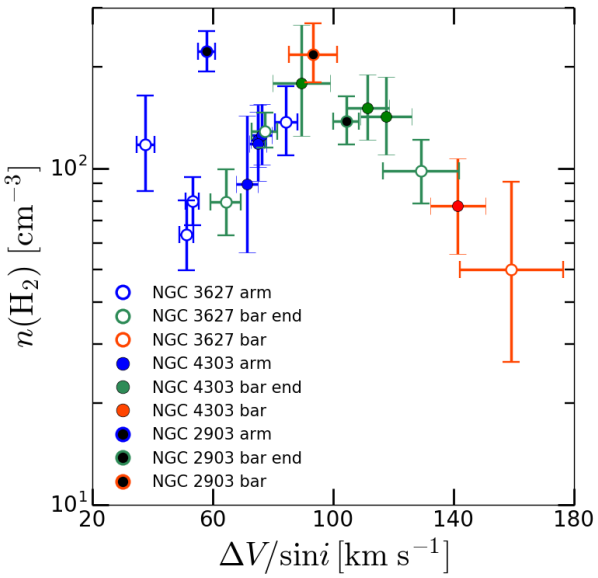

Figure 3.12: Relation between $n(H_2)$ and velocity dispersion of molecular gas in NGC 2903, NGC 3627, and NGC 4303. The effect of inclination of galactic disks is corrected. Markers and their color-codes are the same as figure 3.10.

also mention that the correlation for NGC 2903 is very steeper than other galaxies and derived $n(H_2)$ is systematically higher than other galaxies. Therefore, when markers for NGC 2903 are excluded in figure 3.10, the Pearson's correlation coefficient is 0.55. It significantly increases.

The positive correlation between SFE and $n(H_2)$ is probably the case for galaxies, taking account of the results by Muraoka et al. (2016). Moreover, figure 3.11 presents a new question; what determine the slope of the regression line for SFE and $n(H_2)$ like that of the K–S relation. Perhaps properties of barred spiral galaxies such as strength of bars, bar ellipticity, strength of non-circular motion of gas in bars, and arm class can affect this relation.

Using $n(H_2)$ derived from the three lines, we examine the $n(H_2)$–$\Delta V/\sin i$ relation seen in figure 3.8 again. Figure 3.12 shows the relation for the three galaxies. As seen in figure 3.8, $n(H_2)$ increases when $\Delta V/\sin i < 100$ km s^{-1} and decreases when $\Delta V/\sin i > 100$ km s^{-1}. This relation still appears even when $n(H_2)$ is derived from the three lines and other galaxies are added. Moreover, the bar of NGC 2903, which shows relatively higher $n(H_2)$ follows the relation. Molecular gas density in bars is not always lower than arms and bar ends, however, its variations are determined by large scale gas dynamics. This $n(H_2)$–$\Delta V/\sin i$ relation may be the universal relation for galaxies.

Recently Enokiya et al. (2021) reported the relation between relative velocity of molecular clouds, peak column density of molecular gas for clouds, and resultant star formation. Their result is shown in figure 3.13. They argued that star formation is enhanced as relative velocity (collision speed) between clouds and column density are high along the solid line in figure 3.13. However, they found the cloud without OB stars even with high relative velocity (the marker labelled "Foot print MC" in the figure). They argued that even when relative speed is high, low column density conditions prevent star formation. From the result, it is expected that there may be another sequence above the solid line in figure 3.13 and star formation in molecular clouds

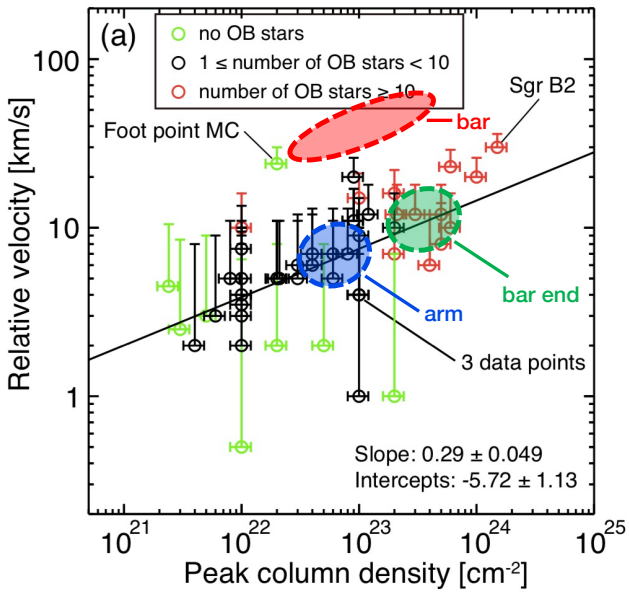

Figure 3.13: Relation between relative velocity of molecular clouds, peak column density of molecular gas for clouds, and star formation by Enokiya et al. (2021). Green, black, and red markers are molecular clouds which contain no OB stars, 1–9 OB stars, and $\geq$ 10 OB stars, respectively. The expected typical values for "arm", "bar end", and "bar" are plotted on the plot in blue, green, and red, respectively.

on the sequence is suppressed, i.e., green, black, and red markers are shifted toward top right on the sequence.

If we consider so, molecular clouds in arms and bar ends are on the solid line of figure 3.13 and higher SFE in bar ends than that in arms is interpreted by moderately higher relative speed and higher column density as well as the increased probability of cloud-cloud collisions. Bars showing lower SFE may be on the sequence above the solid line. One possible cause of quiescent star formation in bars is too high relative velocity considering its column density. In fact, Maeda et al. (2021) reported that there are small, less massive molecular clouds in the bar of NGC 1300 and estimated collision speed is high in the bar. Note that NGC 1300 is relatively gas poor in its bar, however, NGC 2903, NGC 3627, and NGC 4303 analyzed above are gas rich there. Furthermore, the horizontal axis of figure 3.13 is column density of molecular clouds. On the other hand, estimated column density from COMING's data is mean column density averaged within the beam (kpc scales). We need higher resolution data like PHANGS's (their images for the same galaxies are shown in figure 1.31) to investigate the relation of figure 3.13 in barred spiral galaxies more detail.

3.6.2 Temperature of molecular gas and dust

Since we utilize three lines, $T_{\rm kin}$ of molecular gas is also derived. As a discussion of molecular gas temperature, we compare $T_{\rm kin}$ and dust temperature. Dust temperature is derived from 70 μm and 160 μm images by the Photometric Array Camera and Spectrometer (PACS) mounted on the Herschel Space Observatory (Pilbratt et al. 2010; Poglitsch et al. 2010). These archival data was available for only NGC 3627 and NGC 4303, thus we cloud not derive dust temperature for NGC 2903.

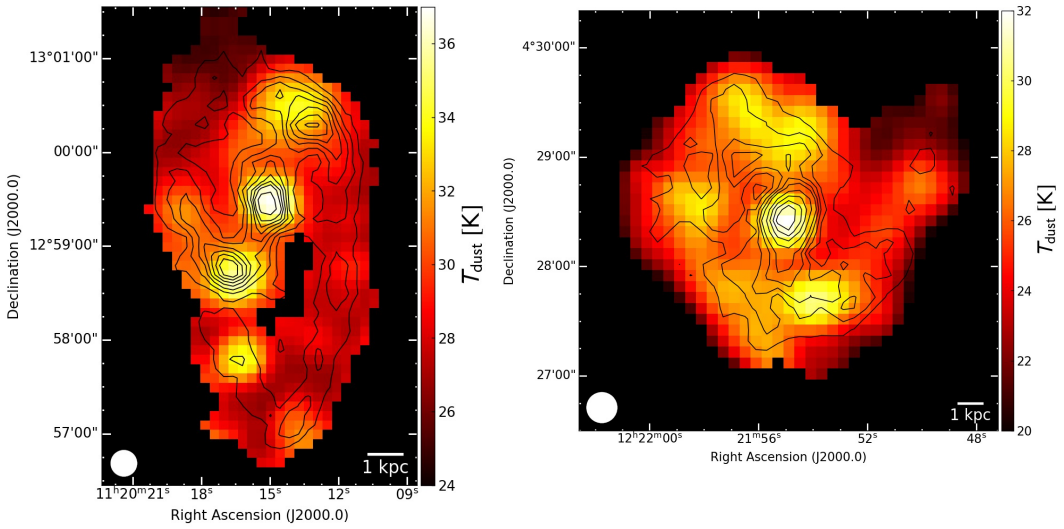

Figure 3.14: Maps of dust temperature in NGC 3627 (left) and NGC 4303 (right).

For interstellar dust, it is known that optical depth is related to frequency;

$$\tau_\nu \propto \nu^\beta, \tag{3.10}$$

where β is called the "emissivity index" or "power-law index of the absorption efficiency" (Tabatabaei et al. 2007; Xilouris et al. 2012). When the size of dust grains is much smaller than the wavelength, $\beta = 2$, and when the dust size is comparable to the wavelength and dust grains are amorphous, $\beta = 1$ (e.g., Draine 2011). When dust is in the thermal equilibrium at the dust temperature $T_{\rm dust}$ and the background radiation is negligible, the radiative transfer equation becomes

$$I_\nu = B_\nu(T_{\rm dust})(1 - e^{-\tau_\nu}). \tag{3.11}$$

Usually dust emission is optically thin, thus,

$$I_\nu \propto \nu^\beta B_\nu(T_{\rm dust}). \tag{3.12}$$

Namely, $T_{\rm dust}$ can be derived using the color at the frequency of ν_1 and ν_2 by assuming β;

$$\frac{I_{\nu_1}}{I_{\nu_2}} = \left(\frac{\nu_1}{\nu_2}\right)^\beta \frac{B_\nu(\nu_1, T_{\rm dust})}{B_\nu(\nu_2, T_{\rm dust})}. \tag{3.13}$$

Equation (3.13) cannot be solved analytically, we derived $T_{\rm dust}$ using the bisection method. β is fixed to be 1.5, which corresponds to the situation that small and large, amorphous dust grains are mixed. Figure 3.14 shows $T_{\rm dust}$ maps for NGC 3627 and NGC 4303. Regionally averaged $T_{\rm dust}$ in each region is listed in table 3.6–3.8.

Figure 3.15 shows the relation between $T_{\rm kin}$ and $T_{\rm dust}$ in NGC 3627 and NGC 4303. $T_{\rm kin}$ is lower by ~ 10 K than $T_{\rm dust}$ in most regions of these galaxies. Hence, dust and gas are not in the thermodynamic equilibrium in the galactic scale. It suggest that dust may be easily heated by stellar radiation taking into account that $T_{\rm dust}$ maps are similar to those of SFR. In contrast, thermal interaction between dust and gas is supposed to be difficult. Accordingly, we try to estimate timescale to reach the thermodynamic equilibrium.

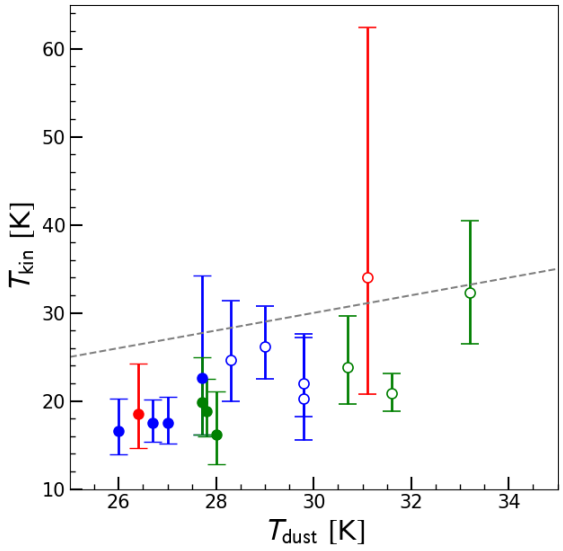

Figure 3.15: Molecular gas $T_{\rm kin}$ and $T_{\rm dust}$ in NGC 3627 and NGC 4303. The gray dashed line is $T_{\rm kin} = T_{\rm dust}$. Open markers are results for NGC 3627 and filled markers are for NGC 4303. Blue, green, and red markers correspond to arms, bar ends, and bars, respectively. Error of $T_{\rm dust}$ is negligible.

Energy interaction by collision between dust grains and gas particle i (e.g., H, H_2, H^+, e^-) can be represent by the following equation when dust has no charge (Draine 2011);

$$\frac{dE_{\rm dust}}{dt} = \sum_i n_i \sqrt{\frac{8k_{\rm B}T_{\rm gas}}{\pi m_i}} \pi a^2 \times \alpha_i \times 2k_{\rm B}(T_{\rm gas} - T_{\rm dust}), \tag{3.14}$$

where n_i is number density of gas particle i, $T_{\rm gas}$ is (kinetic) temperature of gas, m_i is mass of gas particle i, a is radius of dust, α_i is the accommodation coefficient between dust and gas particle i, and $T_{\rm dust}$ is dust temperature. The accommodation coefficient represents inelasticity for collision of dust and gas and ranges $0 \leq \alpha_i \leq 1$. When dust and gas completely collide elastically, $\alpha_i = 0$ and in an inelastic collision case, $\alpha_i = 1$. Usually α_i is simply assumed as ~ 0.5. From this equation, time to reach thermal equilibrium is estimated. Assuming that dust interacts with only gas collisions, i.e., not affected by radiation from stars etc. and the collisional parter of dust is H_2, equation (3.14) becomes

$$t_{\rm TE} = \pm \frac{2}{A\sqrt{T_{\rm dust}}} \left[\tanh^{-1} \sqrt{\frac{T_{\rm gas}}{T_{\rm dust}}} - \tanh^{-1} 1 \right], \tag{3.15}$$

by solving the differential equation, where $t_{\rm TE}$ is time to reach thermodynamic equilibrium between dust and gas and

$$A \equiv -\frac{2}{3Nk_{\rm B}} \pi a^2 \times \alpha_{\rm H_2} \times 2k_{\rm B} n({\rm H_2}) \sqrt{\frac{8k_{\rm B}}{\pi m_{\rm H_2}}}, \tag{3.16}$$

because $dE_{\rm dust}/dt = -dE_{\rm gas}/dt$ and $E_{\rm gas} = 3Nk_{\rm B}T_{\rm gas}/2$[5)] (here N is number of H_2 colliding with dust during dt, N is assumed to be $n_{\rm H_2}$). The sign is + when $T_{\rm gas} < T_{\rm dust}$ and vise versa.

[5)] Although we consider diatomic molecule (H_2), degrees of freedom for rotation are frozen out in low temperature environments such as molecular gas.

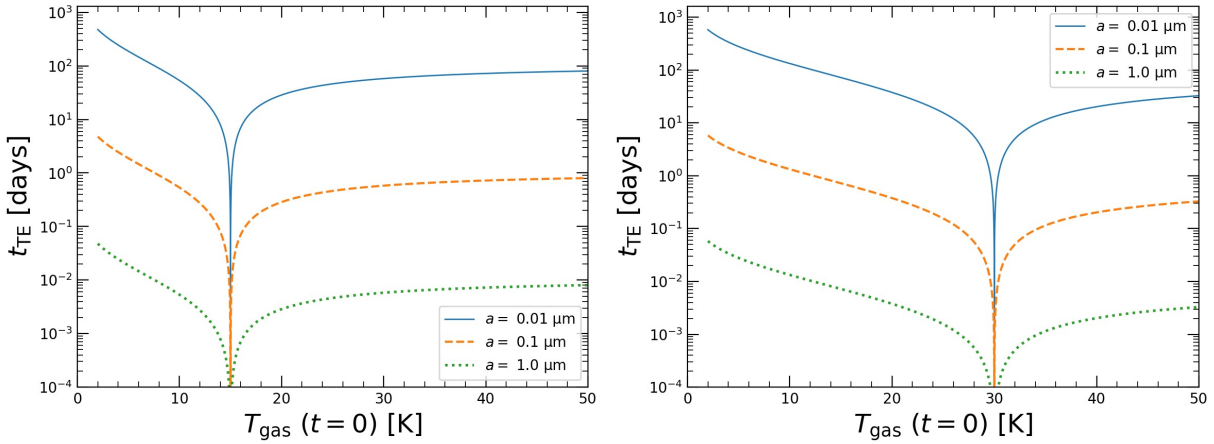

Figure 3.16: Time to reach thermal equilibrium between dust and gas t_{TE} when $T_{dust} = 15$ K (left) and $T_{dust} = 30$ K (right). a is dust size.

Adopting $n(H_2) = 100$ cm^{-3}, $N = 100$, $\alpha_{H_2} = 0.5$, t_{TE} is calculated as a function of T_{gas} at a fixed dust size and T_{dust}.

Figure 3.16 shows t_{TE} as a function of T_{gas} at $t = 0$ and the dust size a. Time for thermodynamic equilibrium is of the order of a few hours to a few years depending on the dust grain size. Dust and gas instantly reach equilibrium if their energy interaction is only collision. However, dust is warmer than molecular gas in most of cases as seen in figure 3.15. Dust is easily affected by other heat sources such as stars and it is difficult to satisfy thermodynamic equilibrium with molecular gas. Their thermal equilibrium could be reached only in the depth of molecular clouds without star formation (i.e., without heat source by radiation).

3.7 Summary of this chapter

We present the results of simultaneous ^{12}CO($J = 1$–0) and ^{13}CO($J = 1$–0) mappings toward the nearby barred spiral galaxy NGC 4303 with the Nobeyama 45-m telescope and the receiver FOREST as the NRO legacy project COMING. Main conclusions in this paper are as follows:

1. Galactic structures can be seen in ^{12}CO($J = 1$–0). ^{13}CO($J = 1$–0) is detected mainly at the galactic center and C^{18}O($J = 1$–0) is not detected from our map.

2. We separated NGC 4303 into eight regions (the center, northern bar, southern bar, northern bar end, southern bar end, northern arm, eastern arm, western arm) based on its structures. Regionally averaged molecular gas surface densities (Σ_{mol}), surface densities of star-formation rates (Σ_{SFR}) and star-formation efficiencies (SFE) are measured in each region.

3. The SFE in the bar is lower by approximately 39% than that in the spiral arms. This tendency is consistent with previous studies about barred spiral galaxies. In addition, the SFE in the bar ends is slightly larger ($\sim 10\%$) than that in the spiral arms.

4. From stacking analysis for each galactic region, we can successfully detect ^{12}CO($J = 1$–0) and ^{13}CO($J = 1$–0) lines and measure their integrated intensities for all regions.

$C^{18}O(J=1–0)$ line cannot be detected significantly even with stacking.

5. Based on measured integrated intensity ratios of $^{12}CO(J=1–0)$ and $^{13}CO(J=1–0)$ line from stacked spectra, we derive volume densities of molecular gas $n(H_2)$ at a fixed kinetic temperature T_{kin} for each region via non-LTE analysis. To perform non-LTE analysis, we developed a way to obtain the correct beam dilution effect. As a result, beam-filling factors are not so different among the regions.

6. Results of non-LTE analysis show the $n(H_2)$ in the bar is lower by 31–37% than that in the arms. We confirm that in the bar where the SFE is low, volume density of molecular gas is also low. Moreover, the $n(H_2)$ in the bar ends is higher by 21–33% than that in the arms.

7. There is a positive correlation between SFE and derived $n(H_2)$ among the regions. The correlation coefficient is 0.82–0.83. Hence, the variations of SFE within NGC 4303 would be caused by the different volume densities of molecular gas.

8. We found that when inter-clouds velocity dispersion is moderate ($\Delta V/\sin i \lesssim 100$ km s^{-1}), $n(H_2)$ tends to be larger as velocity dispersion increases. On the other hand, when velocity dispersion is too large ($\Delta V/\sin i \gtrsim 100$ km s^{-1}), $n(H_2)$ decreases as velocity dispersion increases. This suggests that volume density of molecular gas would be influenced by dynamical effects indicated by inter-clouds velocity dispersion.

9. The relation between $n(H_2)$ and $\Delta V/\sin i$ could be interpreted as follows: In the moderate $\Delta V/\sin i$ situation, cloud-cloud collisions could occur frequently. By contrast, when $\Delta V/\sin i$ exceeds 100 km s^{-1}, molecular clouds would be shredded and destroyed. It is also possible that molecular clouds are hard to shrink by self-gravity due to enhanced inner turbulences and cores in molecular clouds being unable to grow enough because of high collision speed.

10. We derived $n(H_2)$ without fixing T_{kin} by adding archival $^{12}CO(J=3–2)$ by JCMT. Moreover, NGC 2903 and NGC 3627 are added as sample galaxies. Even when sample galaxies are added, the positive correlation between SFE and $n(H_2)$ appears. However, the scatter is large. It is due to differences in correlations among galaxies.

11. The relation between $\Delta V/\sin i$ and $n(H_2)$ is clearly seen even when the three galaxies are compiled. The velocity where the tendency of increase and decrease of $n(H_2)$ change remains at $\Delta V/\sin i \sim 100$ km s^{-1}. This relation may be the universal for galaxies.

12. T_{dust} is derived from Herschel/PACS 70 and 160 μm data for NGC 3627 and NGC 4303 to compare molecular gas T_{kin} by the triple-line analysis. T_{kin} is lower than T_{dust} in most regions. We estimate the timescale to reach the thermodynamic equilibrium between dust and molecular gas if the energy interaction is by only collisions. We found that dust and molecular gas instantly reach the thermodynamic equilibrium within a few days–a few years. Therefore, radiative heating of dust grains are not negligible and the thermodynamic state can be achieved within only deep inside molecular clouds without radiation source.

Chapter 4

Key factor in molecular gas properties and star formation by decomposition of CO emission in Maffei 2

4.1 Abstract of this chapter

Molecular gas exists in the diffuse component in addition to cloud-like structures. The cloud-phase molecular gas is traced by ^{13}CO line because of its low opacity, while ^{12}CO line traces all molecular gas. To reveal how significantly the cloud/diffuse-component molecular gas fraction changes properties of molecular gas compared to properties of the cloud component themselves, we conducted ^{12}CO($J=1$–0) and ^{13}CO($J=1$–0) observations toward the barred spiral galaxy Maffei 2 with the Nobeyama 45 m telescope. Since Galactic emission is seen at specific velocities, we developed a new algorithm to separate emission of Maffei 2 and the Galaxy, and the latter is successfully extracted. ^{12}CO is three-dimensionally decomposed into the two components based on ^{13}CO detection at the same voxel. The luminosity of ^{12}CO without ^{13}CO accounts for 38% of the total luminosity. The integrated-intensity ratio of ^{13}CO-detected ^{12}CO to total ^{12}CO, $R_{12(13\mathrm{det})/12}$, which reflects fraction of the cloud component shows significant variation (from 0 to 1) as well as the conventional ^{12}CO/^{13}CO line ratio, $R_{12/13}$ (from 8 to 23) in the galaxy. In contrast, ^{13}CO-detected-^{12}CO/^{13}CO line ratio, $R_{12(13\mathrm{det})/13}$, which implies properties of the cloud component (especially density of molecular gas) is rather constant of $\sim$9. The Kolmogorov–Smirnov test for line ratios between galactic structures shows that p-values systematically decrease from $R_{12/13}$ to $R_{12(13\mathrm{det})/12}$, and increase in only disk regions from $R_{12/13}$ to $R_{12(13\mathrm{det})/13}$. Moreover, we found that differences in star-formation efficiency between galactic structures are lowered by $\sim$40%, when molecular gas mass is estimated from ^{13}CO-detected ^{12}CO and ^{13}CO instead of ^{12}CO alone. Our results suggest that proportion of the cloud/diffuse-component molecular gas is a key factor to characterize properties of molecular gas and star formation, and effects of galactic structures are not strong enough to change clouds' properties, whereas they promote transition of the cloud/diffuse component.

4.2 Background of this study

To investigate properties of molecular gas in which stars form is crucial, because star formation is a main process in galaxies. Star-formation activity quantified as star-formation rate (SFR)

and star-formation efficiency (SFE) varies within and among galaxies (e.g., Leroy et al. 2008; Rahman et al. 2012; Leroy et al. 2013; Utomo et al. 2017; Kreckel et al. 2018; Muraoka et al. 2019; Villanueva et al. 2021). In particular, barred spiral galaxies often show distinct difference in SFR and SFE along their bars. They are lower in bars than the center, bar ends, and spiral arms, even though molecular gas is rich there (e.g., Sheth et al. 2002; Momose et al. 2010; Watanabe et al. 2011; Hirota et al. 2014; Yajima et al. 2019; Maeda et al. 2020b; Iles et al. 2022). As its reason, it is suggested that mean density of molecular gas is lower in the bar than that in other galactic regions (Muraoka et al. 2016; Yajima et al. 2019).

Recent studies also showed that the three-dimensional Kennicutt–Schmidt (K–S) relation (Schmidt 1959; Kennicutt 1989) using volume density of gas and SFR is tighter than the usual two-dimensional one (Bacchini et al. 2019). SFR is well described by density structures of ISM in a simulation (Wada and Norman 2007). Typically 45% of ^{12}CO emission is not overlapped with H II regions (Schinnerer et al. 2019; Pan et al. 2022). About a half of molecular gas is in a quiescent state before star formation. On the contrary, a large fraction of molecular gas may not be used in star formation. These results above indicate that solely considering the amount of (molecular) gas at a line of sight, or surface density is not enough for star formation. In other words, all molecular gas perhaps does not always participate in star formation even though molecular gas is rich. Physical conditions determine how easy molecular gas contributes to star formation.

Since molecular gas is considered to be distributed in galaxies as giant molecular clouds (GMCs), one candidate to represent quality of molecular gas is properties of GMCs such as density and virial paramter. Properties of GMCs have been investigated in many observational studies (e.g., Rosolowsky et al. 2007; Leroy et al. 2017a; Hirota et al. 2018; Sun et al. 2018; Muraoka et al. 2020; Sun et al. 2020; Tokuda et al. 2020; Rosolowsky et al. 2021) as well as theoretical studies (e.g., Dobbs et al. 2011a; Fujimoto et al. 2014; Nguyen et al. 2018; Pettitt et al. 2018; Fujimoto et al. 2020; Treß et al. 2021). Some of these argue that although mass spectra vary among galactic regions, properties of GMCs which seem to be relevant to star formation (e.g., number density, virial parameter, free-fall time) is not outstandingly different between environments within galaxies (Rebolledo et al. 2012; Donovan Meyer et al. 2013; Colombo et al. 2014; Freeman et al. 2017; Nguyen et al. 2018; Fujimoto et al. 2020; Jeffreson et al. 2020; Maeda et al. 2020a; Pettitt et al. 2020). Further, GMCs found in galaxies are similar to those in the Galaxy (e.g., Bolatto et al. 2008; Fukui and Kawamura 2010). In simulations, properties of clouds in the Milky Way-like galaxies and Large Magellanic Cloud (LMC)-like galaxies are also similar across the cosmic time (Guszejnov et al. 2020). These results suggest that molecular clouds' properties may be rather unchanging, whereas clouds are easily aggregated (e.g., Koda et al. 2009; Miyamoto et al. 2014; Koda et al. 2016) and dissipated (e.g., Baba et al. 2017; Kruijssen et al. 2019).

Molecular gas exists in a form of not only cloud-like structures seen as GMCs, but also in the extended, diffuse, and not structured component. It has been revealed that the amount of this diffuse molecular gas is non-negligible in galaxies. Garcia-Burillo et al. (1992) found that extended ^{12}CO emission up to $\sim$ 1 kpc above and below the midplane of NGC 891. Pety et al. (2013) reported that 50% of ^{12}CO emission in M 51 is from diffuse and extra-planar molecular gas with the scale height of $\sim$ 200 pc by deriving from missing flux of an interferometer. Moreover,

line width of ^{12}CO is comparable to that of H I gas, indicating ^{12}CO emission has a similar spatial extent of H I (Caldú-Primo et al. 2013). Theoretical modeling also found that there are two-component molecular disks (the thick disk in addition to the ordinal thin disk) in many nearby galaxies (Patra 2020). The fraction of molecular gas in the thick disk accounts for 70% of the total molecular gas mass (Patra 2021). The thick molecular disk is also found in the Galaxy (Busch et al. 2021; Su et al. 2021).

In terms of missing flux, line width of ^{12}CO derived from interferometric observations is narrower than that from single-dish observations (Caldú-Primo et al. 2015; Caldú-Primo and Schruba 2016). The fraction of missing flux by interferometers is usually 40–90% of total flux in galaxies (e.g., Engargiola et al. 2003; Heyer et al. 2004; Rosolowsky et al. 2007; Hirota et al. 2014; Caldú-Primo et al. 2015; Hirota et al. 2018; Querejeta et al. 2021a). Rosolowsky et al. (2007) showed that 90% of diffuse molecular gas which is not identified as GMCs surrounds them. Liszt et al. (2010) estimated that approximately 2/3 of ^{12}CO luminosity is from diffuse molecular gas at the Solar circle.

Fraction of missing flux (diffuse-component gas fraction) varies within galaxies. Pan and Kuno (2017) reported that difference in properties of GMC associations (GMAs) disappear when missing flux is not considered. They argued that the diffuse component is non-negligible when environmental dependence of molecular gas is discussed. Maeda et al. (2020b) also showed that fraction of missing flux differs among galactic structures (arms, bar ends, and bar) from 30% to 90%.

Such diffuse molecular gas is probably difficult to contribute to star formation (timescale of star formation is long). Shetty et al. (2014b) argued that the non-linearity of the K–S relation seen in many galaxies (i.e., difference in SFE) is due to hierarchical structures of molecular gas. Namely, ^{12}CO line traces diffuse and extended molecular gas as well as GMCs. In fact, Maeda et al. (2020b) showed the negative correlation of SFE and missing flux fraction. Moreover, Sawada et al. (2012a, 2012b) found that highly structured (i.e., more clumpy) molecular gas traces spiral arms of the Galaxy and H II regions are aligned along such gas. The degree of how molecular gas is structured is important for star formation.

These indications above motivate us to reveal that proportion of the diffuse/cloud-like component to total molecular gas is the main factor to determine molecular gas properties and star formation in comparison with properties of GMCs themselves. For the derivation of the diffuse component, a Fourier transformation-based method is proposed (Hygate et al. 2019). However, it is difficult to infer properties of inner molecular gas of GMCs with ^{12}CO line alone due to its high opacity even in high-resolution observations, although conventional properties such as virial parameter can be derived. Furthermore, reliable decomposition of molecular gas is hard with ^{12}CO line alone, because it cannot be distinguished whether observed cloud-like structures are really "clouds" or they just look like so due to high column density with diffuse molecular gas. Alternatively, usage of ^{13}CO line helps to decompose molecular gas into the two components as proposed by Liszt et al. (2010) and Shetty et al. (2014b), because it is optically thin.

Actually, ^{13}CO line traces more structured, inner, cloud-like molecular gas according to observational results for the Galaxy (e.g., Goldsmith et al. 2008; Sawada et al. 2012b; Umemoto et al. 2017) and galaxies with high resolution data (e.g., Schinnerer et al. 2010; Rebolledo et al. 2012; Pan et al. 2015b; Bešlić et al. 2021). Moreover, virial parameter of Galactic GMCs derived

from ^{13}CO line is relatively lower than that from ^{12}CO line (e.g., Benedettini et al. 2021; Evans et al. 2021). GMCs showing high SFR and SFE also tend to be bright in ^{13}CO line (e.g., Hirota et al. 2011; Rebolledo et al. 2012). These results imply that ^{13}CO line traces molecular gas which is more contributable to star formation than what ^{12}CO traces.

^{12}CO($J=1$–0)/^{13}CO($J=1$–0) integrated-intensity ratio, $R_{12/13}$, varies depending on environments of galaxies and spatial scales of observational data. $R_{12/13}$ at galactic scales is $\sim$ 10–30 in nearby galaxies (e.g., Sakamoto et al. 1997b; Meier and Turner 2004; Hirota et al. 2010; Watanabe et al. 2011; Morokuma-Matsui et al. 2015; Cao et al. 2017; Cormier et al. 2018; Muraoka et al. 2016; Yajima et al. 2019; Israel 2020; Yajima et al. 2021), and high ($\gtrsim$ 30) in the center of galaxies with active star formation (e.g., Aalto et al. 1995; Hüttemeister et al. 2000; Paglione et al. 2001; Aalto et al. 2010; Pan et al. 2015b; Saito et al. 2015; Morokuma-Matsui et al. 2020; Yajima et al. 2021). On smaller spatial scales of GMCs and in Galactic studies, $R_{12/13}$ is small ($\sim$ 3–7, e.g., Solomon et al. 1979; Polk et al. 1988; Wilson and Walker 1994; Tosaki et al. 2007; Hirota et al. 2011; Roman-Duval et al. 2016; Torii et al. 2019). Some studies attribute these variations of $R_{12/13}$ to the diffuse component which do not be traced by ^{13}CO (Polk et al. 1988; Wilson and Walker 1994; Sakamoto et al. 1997b; Hüttemeister et al. 2000; Hirota et al. 2010; Morokuma-Matsui et al. 2015). Polk et al. (1988) showed that $R_{12/13}$ increases as averaged regions to derive $R_{12/13}$ become wider. Wilson and Walker (1994) also indicated that $R_{12/13}$ derived from a single-dish observation is higher due to missing flux of ^{12}CO line than that from interferometric data.

Decomposition of molecular gas traced by ^{12}CO line into the cloud and diffuse components using ^{13}CO line has been already successfully done in several studies. For example, Polk et al. (1988) and Wilson and Walker (1994) derived that the fraction of the diffuse phase to total molecular gas is 30–60% from $R_{12/13}$. Goldsmith et al. (2008) decomposed pixels where integrated intensity of ^{12}CO($J=1$–0) is significantly measured into the two components based on whether ^{13}CO($J=1$–0) integrated-intensity is measured or not for the Taurus molecular cloud. They found 37% of the total ^{12}CO($J=1$–0) luminosity is from the ^{13}CO($J=1$–0)-non-detected pixels. Roman-Duval et al. (2016) three-dimensionally separated ^{12}CO($J=1$–0) emission into the two components based on detection of ^{13}CO($J=1$–0) at each voxel for inner and outer Galaxy. Diffuse molecular gas which is traced by only ^{12}CO($J=1$–0) accounts for 25% of total molecular gas. Morokuma-Matsui et al. (2015) decomposed velocity-aligned stacked ^{12}CO($J=1$–0) spectra in NGC 3627 into the sharp and broad Gaussians using the peak-intensity ratios of stacked ^{12}CO($J=1$–0) and ^{13}CO($J=1$–0) spectra. They considered that the he narrow line-width component is optically thick and the broad line-width component is non-optically thick and diffuse molecular gas. They argued that about more than half of ^{12}CO emission is from the diffuse component.

However, the decomposition of molecular gas using ^{12}CO and ^{13}CO lines at present is limited to the samples above, because ^{13}CO-line mappings take a high cost and are challenging for galaxies due to weakness of the line. Moreover, using ^{13}CO line to decompose ^{12}CO emission needs high sensitivity, in particular three-dimensional decomposition. In addition, these studies lack more extreme dynamical environments such as bars and bar ends where properties of molecular gas are expected to be strongly influenced by gas dynamics than arms (e.g., Yajima et al. 2019). It is necessary to carry out a new and high-sensitivity mapping of ^{13}CO line covered with a large

area toward other galaxies to compare properties of molecular gas among various environments for molecular gas. Hence, we conducted the ^{13}CO($J=1$–0) and ^{12}CO($J=1$–0) simultaneous mapping of the entire disk of the nearby barred spiral galaxy Maffei 2.

We consider ^{13}CO($J=1$–0) as a tracer of clumpy, more structured molecular gas existing as GMCs, ^{12}CO($J=1$–0) as a tracer of total molecular gas including the diffuse component. $R_{12/13}$ within GMCs is considered to indicate how molecular gas is *condensed*. It is sometimes considered to reflect optical depth of ^{13}CO($J=1$–0) under the assumption of the local thermodynamic equilibrium (LTE), considering that ^{12}CO($J=1$–0) is optically thick and ^{13}CO($J=1$–0) is optically thin (e.g., Paglione et al. 2001; Hirota et al. 2010; Cao et al. 2017; Morokuma-Matsui et al. 2020). However, ^{13}CO($J=1$–0) is thermalized when molecular gas density is $\gtrsim$ a few $\times$ 10^3–10^4 cm^{-3} (e.g., Leroy et al. 2017b) and it is usually sub-thermal (e.g., Yajima et al. 2021). In this case, $R_{12/13}$ is sensitive to density of molecular gas (e.g., Meier and Turner 2004; Yajima et al. 2019). We refer to molecular gas detected in both ^{12}CO($J=1$–0) and ^{13}CO($J=1$–0) as the "cloud component/phase" and that detected in ^{12}CO($J=1$–0) but not in ^{13}CO($J=1$–0) as the "diffuse component/phase". With high-sensitivity ^{13}CO($J=1$–0) data from our observation, we decompose ^{12}CO emission three-dimensionally and to investigate how significantly the cloud/diffuse-phase molecular gas fraction changes properties of molecular gas and star formation in comparison with effects of clouds' properties.

There are advantages to observe Maffei 2. Since this galaxy is one of the nearest barred galaxies (the distance is 3.49 Mpc; Tully et al. 2013), the spatial resolution reaches a few $\times$ 100 pc even with single-dish telescopes. Archival ^{12}CO data of Maffei 2 shows that it is molecular gas rich, which implies that ^{13}CO line is not too weak to be observed. Therefore, the ^{13}CO mapping of the whole disk with a reasonable time is attained using current multi-beam and sensitive receivers mounted on singe-dish telescopes. In addition, Maffei 2 has the strong bar, which is expected to significantly affect properties of molecular gas as suggested by Sorai et al. (2012). For these reasons, we observed this galaxy with the Nobeyama 45 m telescope and the

Table 4.1: Parameters of Maffei 2.

Parameter	Value
Right Ascension (J2000.0)*	$02^{\rm h}41^{\rm m}55^{\rm s}.017$
Declination (J2000.0)*	$+59°36'15''.41$
Morphological type†,‡	SAB(rs)bc?, SBb(s) pec
Distance§	3.49 Mpc
Inclination angle‖	63°
Position angle‖	−145°
Linear scale	16.9 parsec arcsec^{-1}
System velocity (LSR)#	−31.6 km s^{-1}
total $L'_{^{12}{\rm CO}(1-0)}$#	4.84×10^8 K km s^{-1} pc^2
total $L'_{^{13}{\rm CO}(1-0)}$#	3.21×10^7 K km s^{-1} pc^2

* Evans et al. (2010).
† de Vaucouleurs et al. (1991).
‡ Hurt et al. (1993a).
§ Tully et al. (2013).
‖ Jarrett et al. (2003), corrected so that the angle is between the north and the red-shifted major axis, positive corresponds to counterclockwise.
this study.

FOur-beam REceiver System on the 45 m Telescope (FOREST; Minamidani et al. 2016).

Since Maffei 2 is behind the Galaxy ($l \sim 136°.5$, $b \sim -0°.325$), electromagnetic waves whose wavelength is shorter than near infrared (NIR) are seriously attenuated by dust in the Galaxy. Due to it, Maffei 2 was discovered by Maffei (1968) later than other nearby galaxies catalogued in the Messier and New General Catalogue in spite of its proximity. CO emission from this galaxy was firstly detected in an early stage of CO observations for galaxies (Rickard et al. 1977). Maffei 2 has the starburst nucleus (e.g., Seaquist et al. 1976; Turner and Ho 1994), thus many observations have been carried out toward its center (e.g., Ishiguro et al. 1989; Hurt and Turner 1991; Hurt et al. 1993b; Sorai et al. 2002; Israel and Baas 2003; Kuno et al. 2008; Meier et al. 2008; Meier and Turner 2012). Asymmetric structure of Maffei 2 seen in NIR, ^{12}CO, and H I (Hurt et al. 1993a; Hurt et al. 1996; Jarrett et al. 2003; Kuno et al. 2007) indicates a recent interaction with a companion. Parameters of Maffei 2 are listed in table 4.1.

4.3 Observation and data reduction

4.3.1 Observation settings

Observations toward Maffei 2 were carried out from December 2019 to March 2020 (in the semester 2019) with the Nobeyama 45 m Telescope (upper panel of figure 4.1) of Nobeyama Radio Observatory (NRO). Proposal ID is CG191002 (PI: Y. Yajima) and the observation was allocated in local sidereal time (LST) 2–10h. The frontend was the 2×2 multi-beam focal-plane dual-polarization 2SB SIS mixer receiver, FOur-beam REceiver System on the 45 m Telescope (FOREST); Minamidani et al. (2016) (bottom panel of figure 4.1). Its original beam size is 15″ at 110 GHz. The local frequency was set to be 105.131484 GHz so that ^{12}CO($J = 1$–0) (rest frequency 115.271202 GHz) and ^{13}CO($J = 1$–0) (rest frequency 110.201353 GHz) lines are in upper sideband (USB) and these lines are observed simultaneously. The receiver backend was the FX-type correlator, Spectral Analysis Machine for the 45 m Telescope (SAM45) (Kuno et al. 2011; Kamazaki et al. 2012). The total bandwidth and frequency resolution were set to be 2 GHz and 488 kHz, respectively. Received radio signals are separated into 16 arrays (A01–A16, 4 beams × 2 polarizations × 2 IF bands). A01–A08 correspond to ^{12}CO($J = 1$–0) and A09–A16 correspond to ^{13}CO($J = 1$–0). The Y-factor of the attenuator which is used when the hot load is inserted in front of the receiver was optimized in every observation day based on system noise temperature $T_{\rm sys}$ and outside temperature $T_{\rm atm}$ using the following equation:

$$T_{\rm sys} = \frac{T_{\rm atm}}{10^{Y/10} - 1}. \tag{4.1}$$

The typical system noise temperature is 150–200 K at 110 GHz and 300–500 K at 115 GHz in $T_{\rm A}^*$ scale during observations.

The observation mode was on-the-fly (OTF) using two scan patterns parallel to the major axis of the galaxy (X scan) and the minor axis (Y scan). The observed area was 8′10″ × 3′30″ that covers the entire CO-disk (figure 4.2). This area corresponds to 8.3 kpc × 7.8 kpc at the adopted distance. Scan patterns are shown in figure 4.3. The position angle of the X scan was 27° against north. This angle is determined based on the already existing data by Kuno et al. (2007) so that it is roughly the same as that of CO-disk of Maffei 2. The separation of each scan was 5″, time for one scan was 20 seconds, and dump time is 0.1 seconds. X and Y scan were

Figure 4.1: (Top) Nobeyama 45 m Radio Telescope. This picture was taken in January 4, 2018 during observations of Sorai et al. (2019). (Bottom) The receiver FOREST in the machine room of the Nobeyama 45 m Telescope. Radio enters from right to the left side of the receiver. This picture was taken in September 5, 2019.

separated into 2 parts and 4 parts, respectively in the practical observation to reduce intervals of pointing observations. For instance, Y scan has 109 lows and it takes approximately 1.7 hours to complete 1 map of Y scan. Pointing of the telescope becomes incorrect if observation of the target continues for such long time. The total ONs source time was approximately 25 hours. The radio absorber was inserted in front of the receiver every $\sim$ 12 minutes for intensity calibration based on the chopper-wheel method (Ulich and Haas 1976) after a scan row.

The OFF point was observed after every scan row. The position of OFF point was (α,

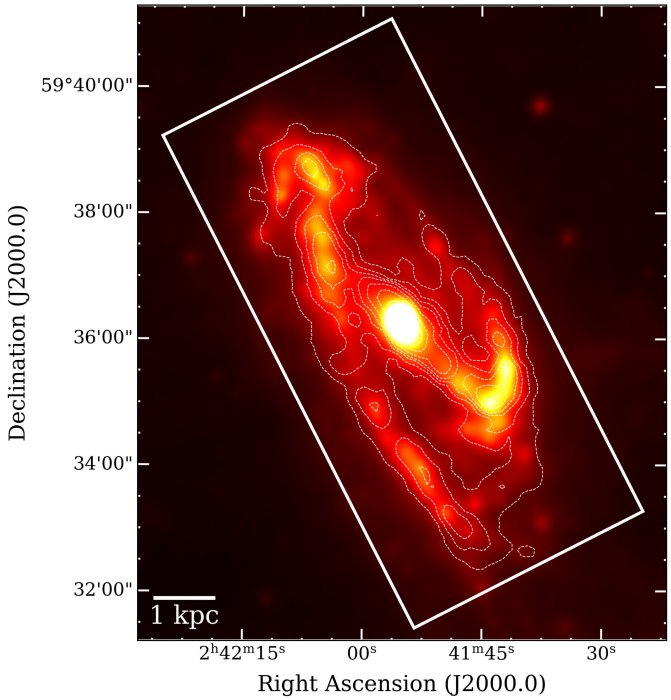

Figure 4.2: Observed area (rectangle) on the WISE 12 μm image. Narrow white contours are the distribution of ^{12}CO($J=1$–0) integrated-intensity shown in figure 4.23.

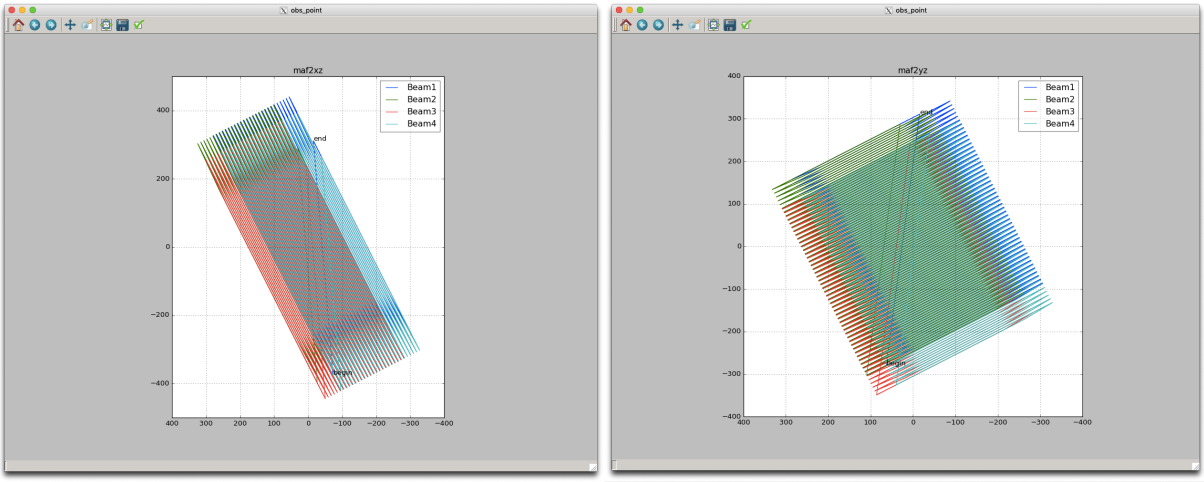

Figure 4.3: Scan patterns of X scan (left) and Y scan (right). The coordinate of maps is ($\alpha_{\mathrm{J2000.0}}$, $\delta_{\mathrm{J2000.0}}$) in arcsec. The origin of the coordinate corresponds to the center of the map. Tracks of each beam are represented with blue, green, red, and cyan lines. The final observational area is overlapped region of beam 1–4.

$\delta)_{\mathrm{J2000.0}} = (02^{\mathrm{h}}42^{\mathrm{m}}03^{\mathrm{s}}.017, 59°23'45''.410)$. This is little far from Maffei 2 compared with other extragalactic observations because this galaxy is close to the Galactic midplane (Galactic latitude $\sim 0.3°$) and the OFF point must avoid Galactic emission. We set this OFF position according to AKARI 90 and 140 μm band images (Murakami et al. 2007). To corroborate that Galactic emission is not detected at this OFF point, we observed this position with FOREST position

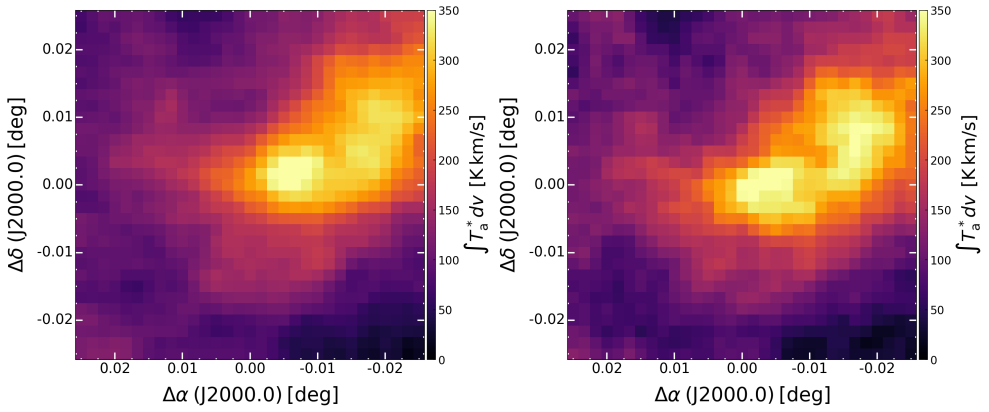

Figure 4.4: Example of integrated-intensity map of W3 core for ^{12}CO($J=1$–0) of the standard array. The left image was obtained on December 12, 2019 and the right one was obtained on February 24, 2020. The grid size is the same as Maffei 2's data (6″).

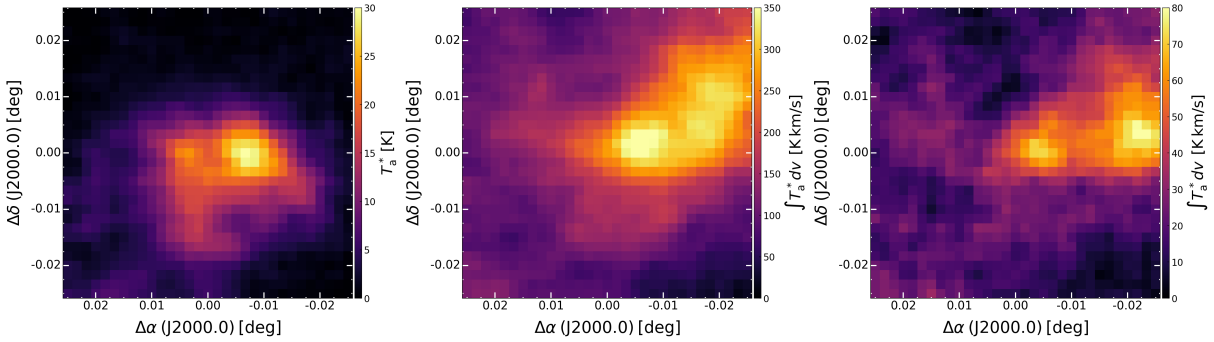

Figure 4.5: (Left) Channel map at -35 km s^{-1} of the standard array for ^{12}CO($J=1$–0) (A01). (Center) The integrated-intensity map of A01. (Right) The integrated-intensity map of the standard array for ^{13}CO($J=1$–0) (A09). These data was obtained on December 12, 2019.

switch mode on the first observation date. To check the pointing accuracy, the SiO maser source IRC+60092 was observed every 0.5–1 hour. We discarded data whose offset is larger than 5″ from the previous pointing observation. The typical pointing accuracy is 2″–3″.

4.3.2 Intensity calibration

As the standard source for intensity calibration, W3 core (W3 Main; Westerhout 1958), the star-forming region in the Galaxy, located at $(\alpha, \delta)_{\mathrm{J2000.0}} = (02^{\mathrm{h}}25^{\mathrm{m}}40^{\mathrm{s}}.660, 62^{\circ}05'52''.112)$ was observed around the fixed LST every observation to roughly keep the elevation angle of the telescope constant. In main observations, it was observed around LST 6:00 and in compensated observations, it was observed around LST 8:30 (compensated observations were allocated in LST 6–10h). The observed area covers the $3' \times 3'$ area of W3 core and the scanning pattern is applied only along the right ascension (east–west direction). This is the default setting by NRO. The radio absorber was inserted in front of the receiver every $\sim$ 12 minutes after a scan row likewise in the main observation of Maffei 2.

To use intensity of the standard source for calibration, mean integrated-intensity around the peak in its map of the standard array of each line has to be measured. Thus, the position

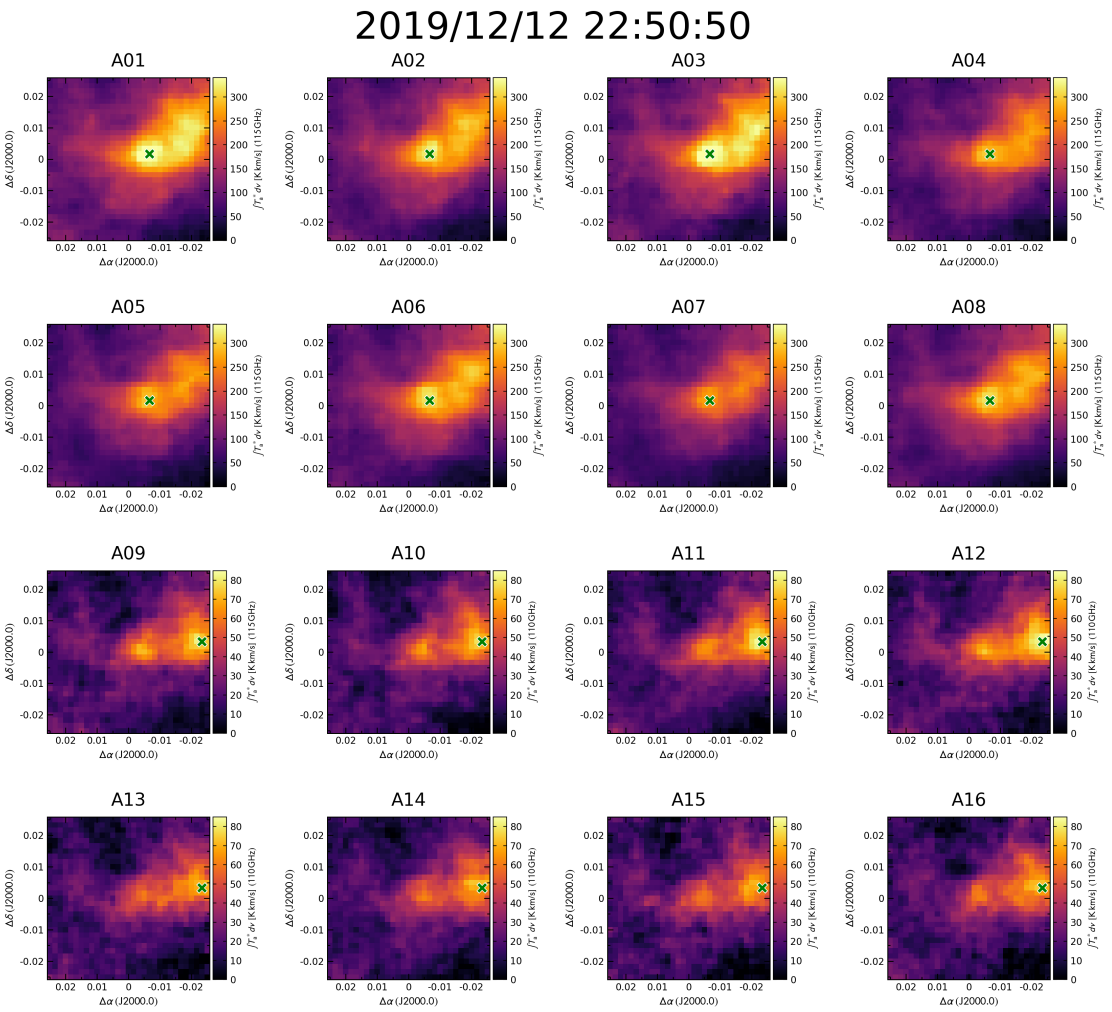

Figure 4.6: Integrated-intensity maps of all 16 arrays of W3 core obtained on December 12, 2019. A01–A08 correspond to ^{12}CO($J=1$–0) and A09–16 correspond to ^{13}CO($J=1$–0). Identified peak positions are denoted by cross markers.

of the peak of the integrated-intensity map is need to be identified. The standard array of ^{12}CO($J=1$–0) and ^{13}CO($J=1$–0) is set to be A01 and A09, respectively because of stability of another array of the beam 1, which is along the optical axis of the telescope (A02 and A10). Note that pointing observations for the standard source was not performed, because the mapping area is so large that the peak position includes its area. Therefore, the peak position is different every observation day as shown in figure 4.4. Furthermore, the secondary peak seen in northwest of the primary peak seen around the center of the map is sometimes brighter than the primary one. For these reasons, the peak position cannot be determined simply by seeking the pixel where the integrated intensity is maximum. This is also the case for ^{13}CO($J=1$–0). We identified the peak position based on a channel map at a certain velocity.

When the channel map at -35 km s^{-1} of ^{12}CO($J=1$–0), the peak position in the map is offset but close to the peak position in the integrated-intensity map (figure 4.5). According to this, the peak position is searched at first. Next, the shifted position by 1 pixel toward the north from the peak position of the channel map is identified as the peak of the integrated-intensity map.

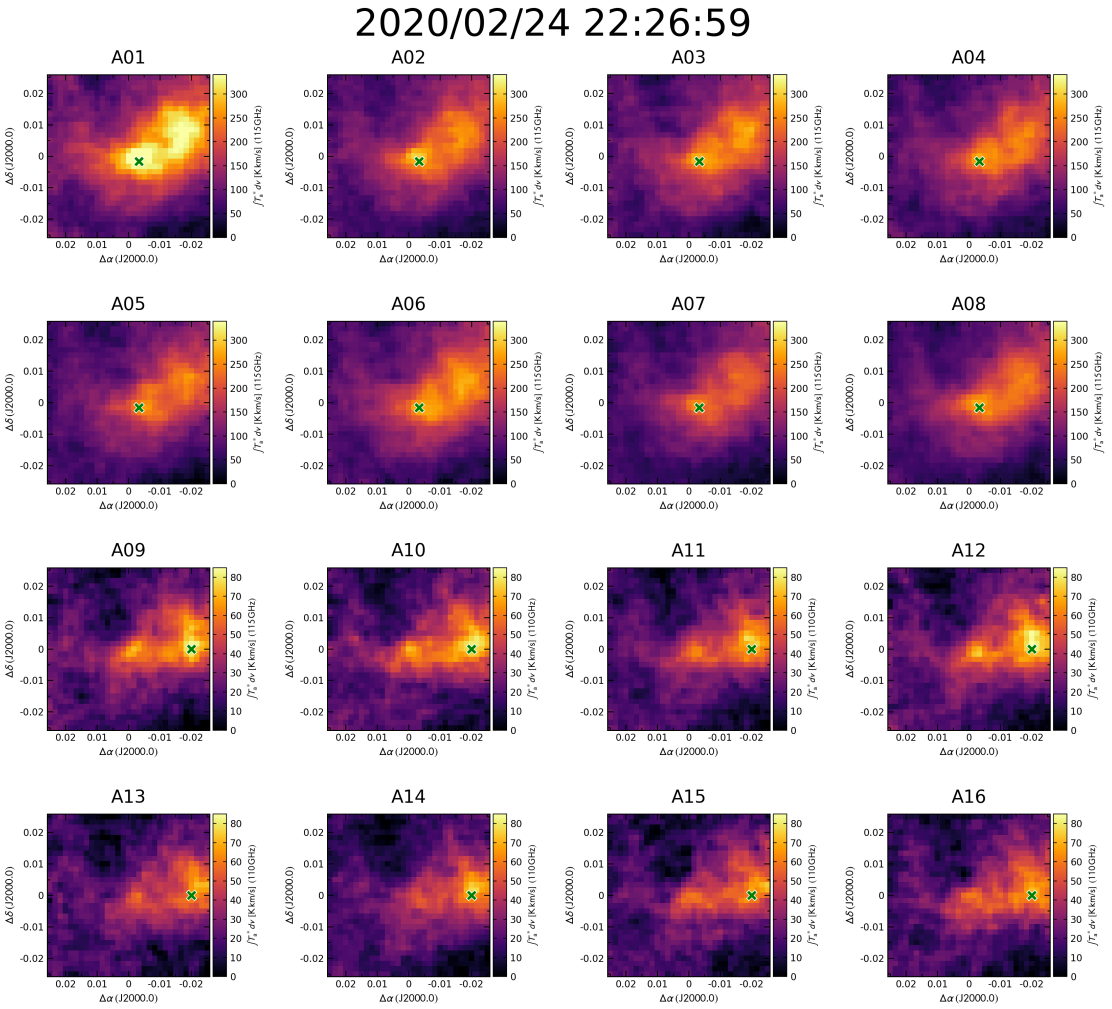

Figure 4.7: The same as figure 4.6 but for data obtained on February 24, 2020.

For the identification of the peak position of ^{13}CO($J=1$–0) integrated-intensity map, the peak of the integrated-intensity map of the line is usually seen in west of the peak of ^{12}CO($J=1$–0) (figure 4.5). Hence, the shifted position by 1 pixel toward the north and by 10 pixels toward the west from the peak of the channel map is identified as the peak of ^{13}CO($J=1$–0) integrated-intensity map. These offsets from the peak of the channel map were determined through trial and error and by checking by eye. These identified peak positions are applied to other arrays of each line. Note that channel maps of ^{13}CO($J=1$–0) cannot be used for identification of the peak if the line, because the peak position is invalid due to poor S/N when it was rainy, very humid, and probably bad seeing[1)]. Examples of identified peak positions are shown in figure 4.6 and 4.7. Owing to the method above, we can track the position of the peak integrated-intensity and integrated intensities around the peak can be derived more accurately. In this way, intensity calibration for ^{12}CO($J=1$–0) and ^{13}CO($J=1$–0) was done separately.

After the identification of the peak position, it was determined that whether W3 core's data on each observational day can be used to intensity calibration considering data quality and

[1)] The equipment for the measurement of seeing in the observatory has been broken since the semester 2019 due to lack of parts to be fixed. Thus, seeing could not be measured during our observations.

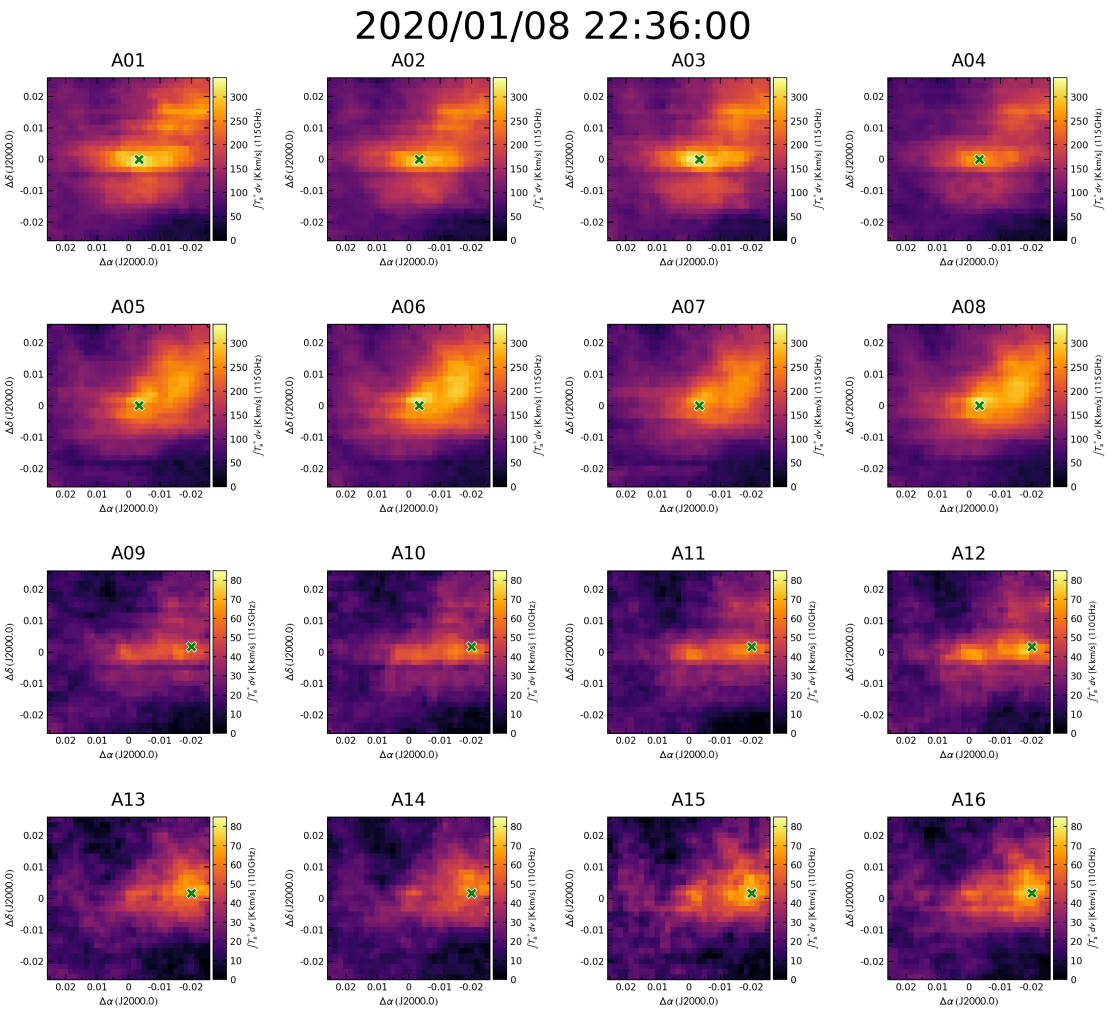

Figure 4.8: The same as figure 4.6 but for data obtained on January 8, 2020 (windy day).

reliability. To do this, we checked integrated-intensity maps and mean spectra averaging around the peak. When it was windy, obtained data of W3 core shows scanning-like patterns as shown in figure 4.8 due to shaken pointing by strong wind. Also, when it was rainy or very humid (as a result of warm condition which increase the amount of saturated water vapor), observed intensity of W3 core becomes very weak and the structure of it cannot be seen (figure 4.9). In addition, mean spectra around the peak usually shows double peaks for ^{12}CO($J = 1$–0) (figure 4.10) if the data is reliable (obtained on a fine day). However, their double peaks sometimes disappear in some arrays when the atmospheric condition is not good (figure 4.11). These data is not reliable as the standard source and cannot be used to intensity calibration. Hence, these data are excluded from used data for intensity calibration.

Figure 4.12 shows daily variations of mean integrated-intensity averaged over 7×7 pixels around the peak for each array. If the averaging range is too small, bright pixels are not used for calibration when the identified peak position is slightly shifted. To the contrary, if the averaging range is too large, pixels with poor S/N are used to calibration, which decreases calibration accuracy. Averaging over 7×7 is just right area (thus, mean spectra shown in figure 4.10 and

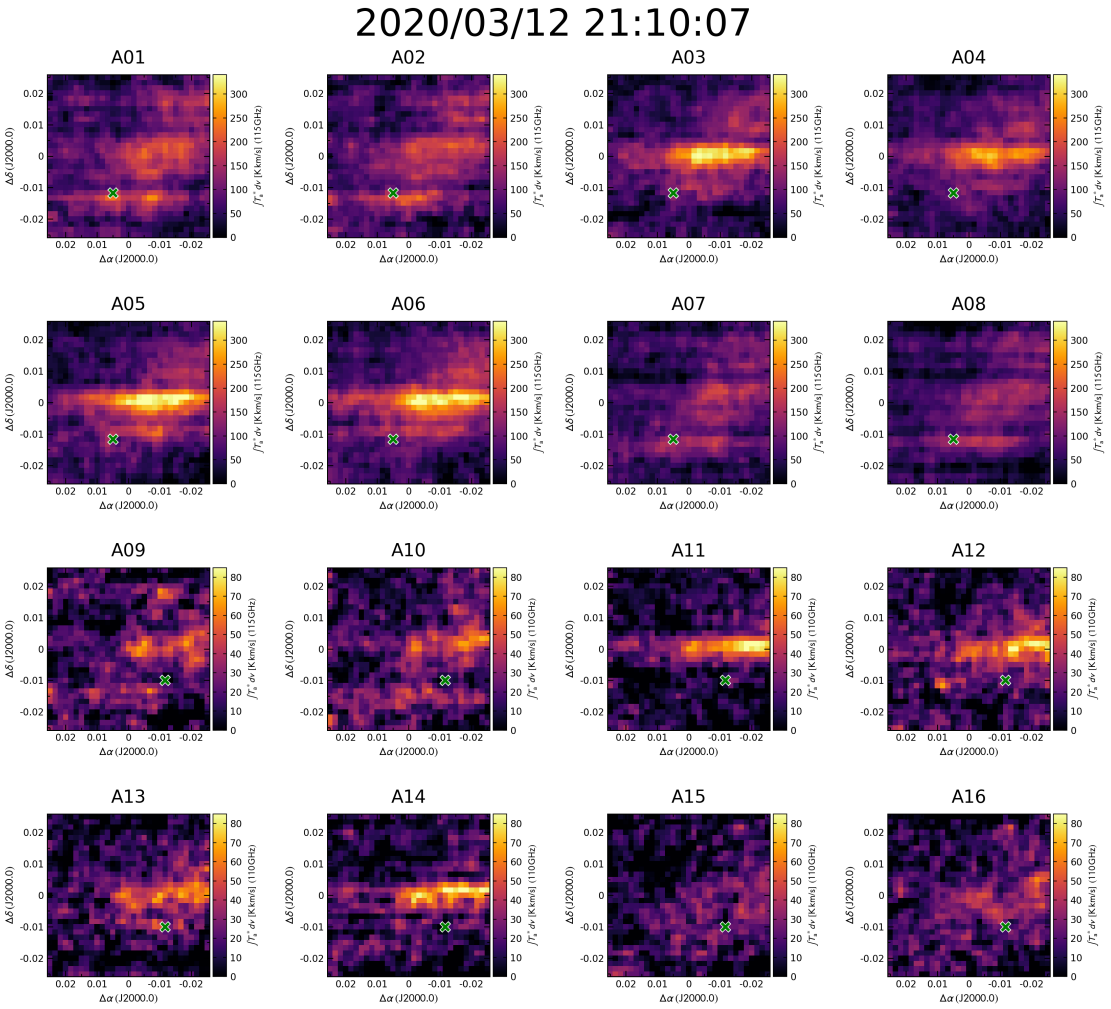

Figure 4.9: The same as figure 4.6 but for data obtained on March 12, 2020 (warm and humid day).

4.11 is also averaged over 7×7 pixels around the peak). Fluctuations of used data for calibration are almost within the uncertainty of the chopper-wheel method of 10% (Ulich and Haas 1976). Although intensity variations are within the expectation, we attempt to investigate what affects variations of intensity.

Figure 4.13 and 4.14 shows correlations between mean integrated-intensities for data which is determined to be used and factors which can influence on observed intensity. ^{12}CO($J = 1$–0) intensity is rather strongly correlated with elevation angle of the telescope, system noise temperature (corrected the elevation angle effect), water vapor, pointing offset, and outside temperature. In these factors, tendencies with elevation angle, system noise temperature, and outside temperature are consistent with the expectation. In contrast to ^{12}CO($J = 1$–0), ^{13}CO($J = 1$–0) shows no clear tendency with those factors. This would be because ^{12}CO($J = 1$–0) tends to be affected by atmosphere conditions than ^{13}CO($J = 1$–0), since ^{12}CO($J = 1$–0) is more absorbed by the atmosphere. Therefore, intensity variations of the standard source would be due to changes of atmospheric conditions not telescope's structural deformation by gravity and wind. Since it is difficult to correct weather effects and it is possible to introduce additional error when we

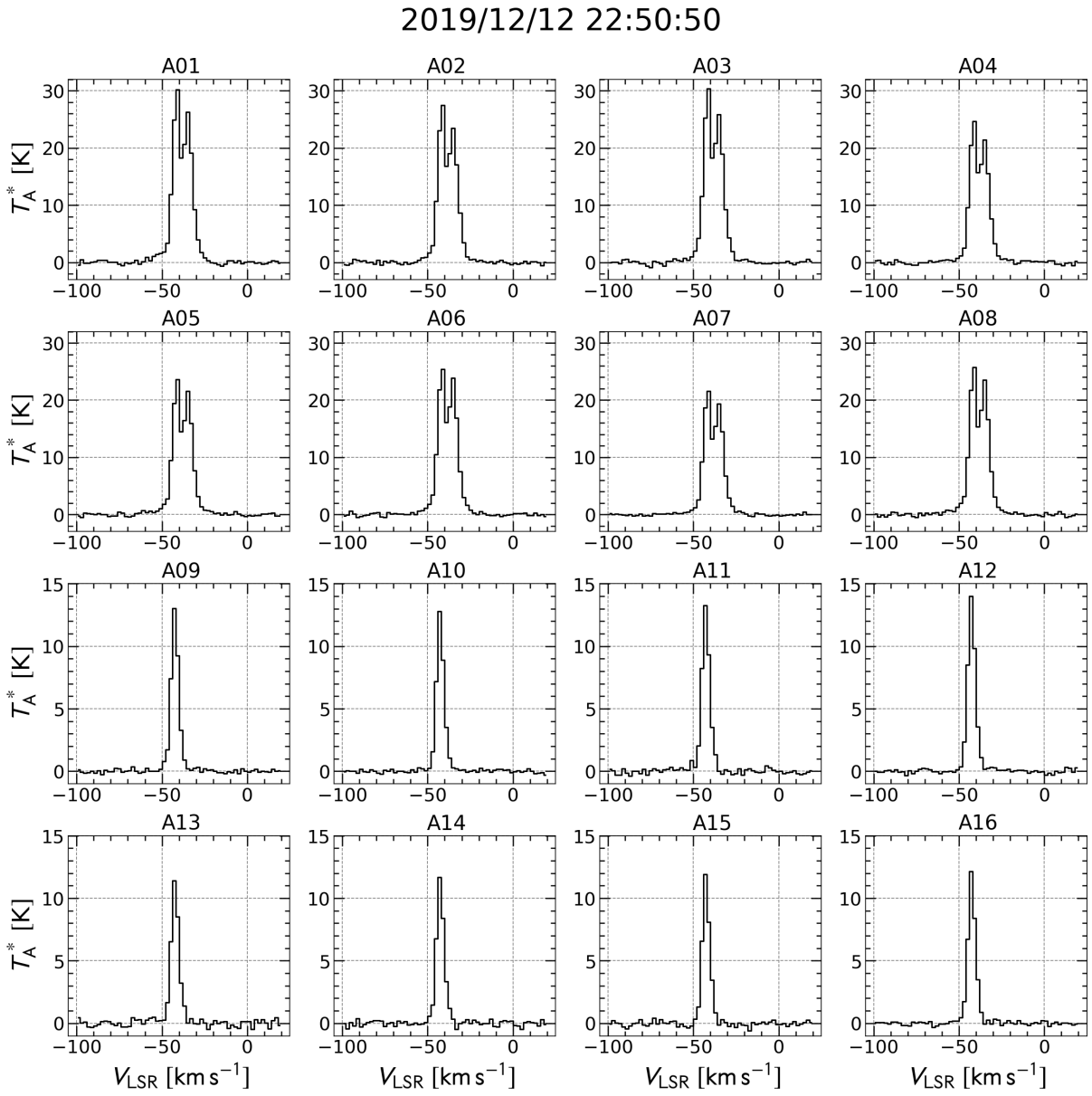

Figure 4.10: Mean spectra of each array of the data on December 12, 2019. Mean spectra are derived by averaging 7×7 pixels around the peak.

correct intensity day by day, intensity was calibrated by averaging mean integrated intensity of W3 core within a certain period, not calibrated each day. Averaged intervals were set during the main observation and compensated observation.

Intensity in the corrected antenna temperature T_A^* scale was converted into the main beam temperature $T_{MB} = T_A^*/\eta_{MB}$ scale with the published value of the main beam efficiency η_{MB} ($\equiv \Omega_{MB}/\Omega_A$, where Ω_{MB} is solid angle of the main beam and Ω_A is total solid angle of the antenna including side-lobes) by NRO. Unfortunately, η_{MB} at 110 GHz in the semester 2019 could not measured by the observatory due to COVID-19. Therefore, intensity calibration was done using beam efficiencies at 115 and 110 GHz measured in the semester 2017 and observational data of W3 core obtained by Sorai et al. (2019) during the semester. Used values of η_{MB} at

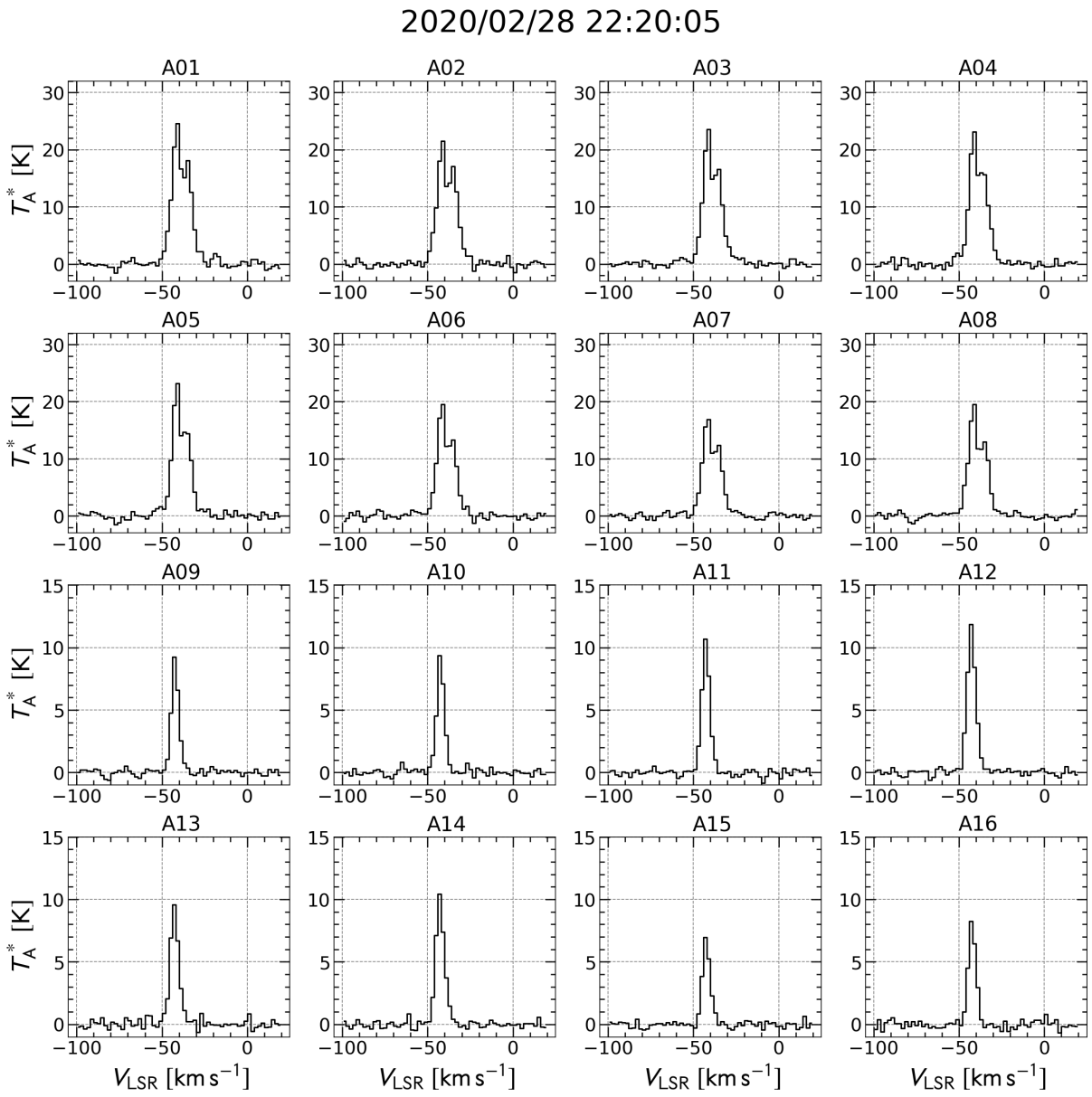

Figure 4.11: The same as figure 4.10 but for data obtained on February 28, 2020.

110 and 115 GHz measured in the semester 2017 is 0.44 and 0.43, respectively. The $\eta_{\rm MB}$ of the semester 2019 $\eta_{\rm MB,2019}$ is estimated by the following equation:

$$\eta_{\rm MB,2019} = \eta_{\rm MB,2017} \frac{\langle I_{\rm std,2019} \rangle}{\langle I_{\rm std,2017} \rangle}, \tag{4.2}$$

where $\eta_{\rm MB,2017}$ is the main beam efficiency of the semester 2017, $I_{\rm std,2019}$ is mean integrated-intensity of the standard array averaged over a term in the semester 2019, and $I_{\rm std,2017}$ is that for the semester 2017. Observed intensity of ^{12}CO($J = 1$–0) is surprisingly weak for results of arrays of beam 3 and 4 (A05–A08) on the first and second date of the semester 2017 (see figure 4.12). This is not an issue because only A01 is used to calibration for data of this semester.

Intensity calibration for other arrays except for the standard array was done by making

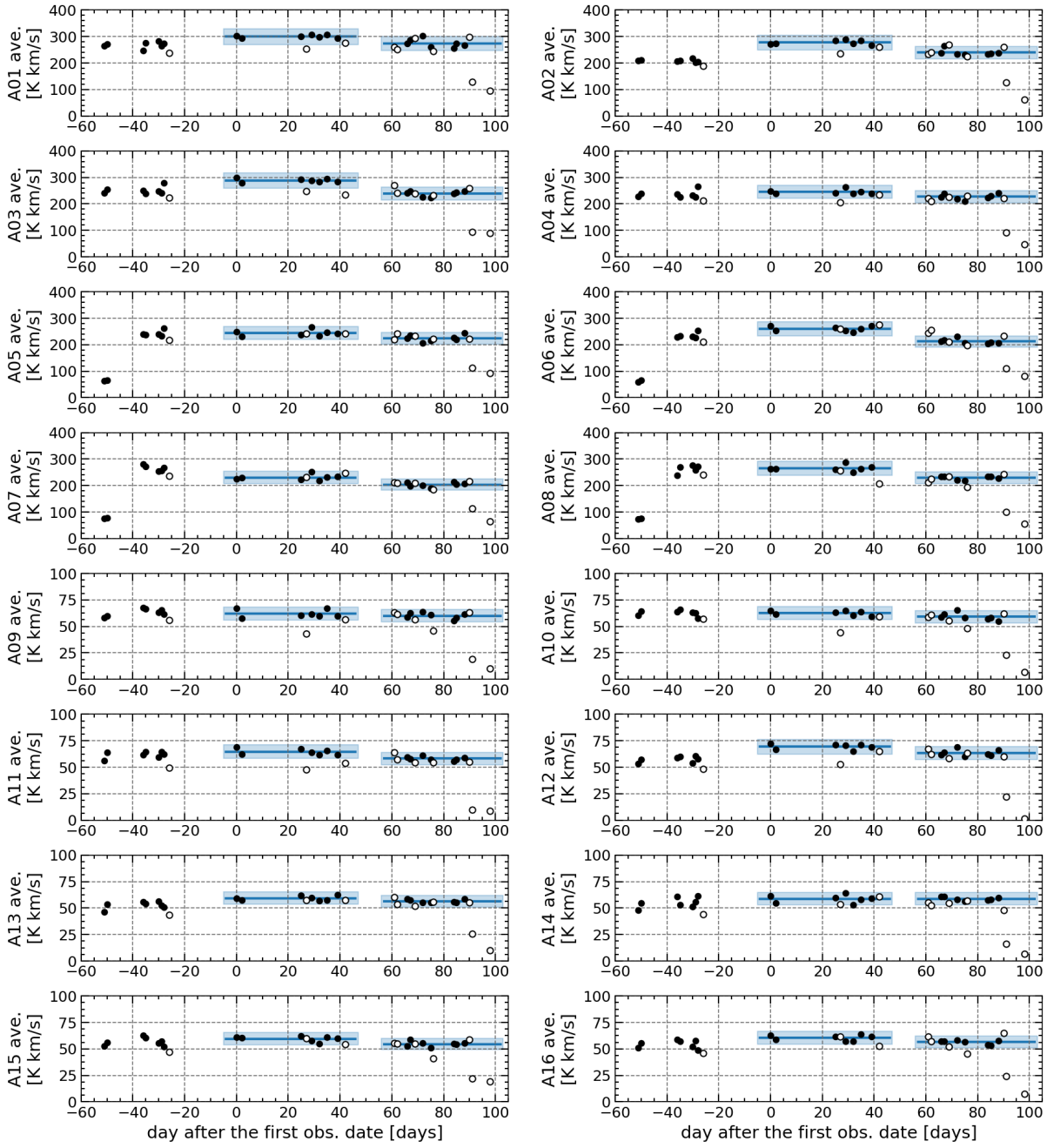

Figure 4.12: Daily variation of mean integrated-intensity in each array averaged over 7×7 pixels. Solid markers represent used data and open markers is unused data. Horizontal blue lines indicate mean integrated-intensity averaged over the term of main observations and compensated observations. Shaded areas indicate the $\pm 10\%$ range (typical uncertainty of intensity calibration by the chopper-wheel method) of mean integrated-intensity averaged over the terms. Error of mean integrated-intensity is negligible. Data for negative values of the horizontal axis is those obtained in the semester 2017 by Sorai et al. (2019).

correlation plots between the standard array and another array like figure 4.15. Scaling factors from the standard array into each array were derived by fitting the regression line between integrated intensities within the 7×7 area of the two arrays. The intercept of the vertical axis

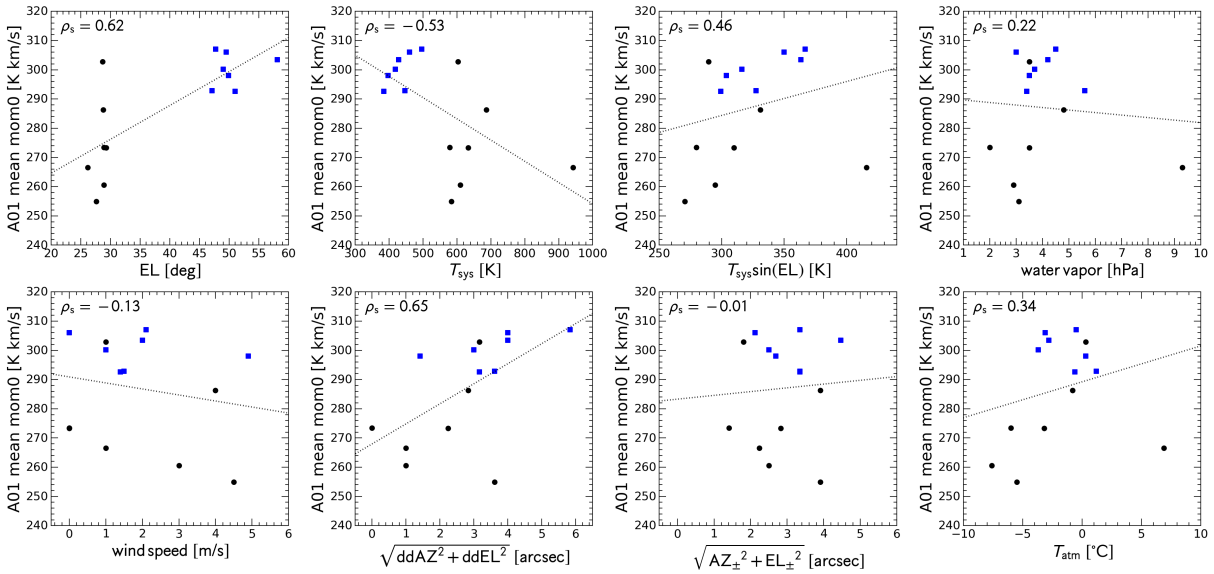

Figure 4.13: Correlation plots between mean integrated-intensity around the peak of the standard array for ^{12}CO($J = 1$–0). Compared quantities are elevation angle of the telescope, system noise temperature, system noise temperature corrected for the effect of elevation angle, water vapor, wind speed, pointing offset during the standard-source observation, scatter of pointing accuracy (how the pointing is shaken), atmospheric (outside) temperature, from left to right, top to bottom. Blue square markers indicate results for the main observation and black circles indicate results for the compensated observation. The Spearman's rank correlation coefficient is denoted in the top left in each panel.

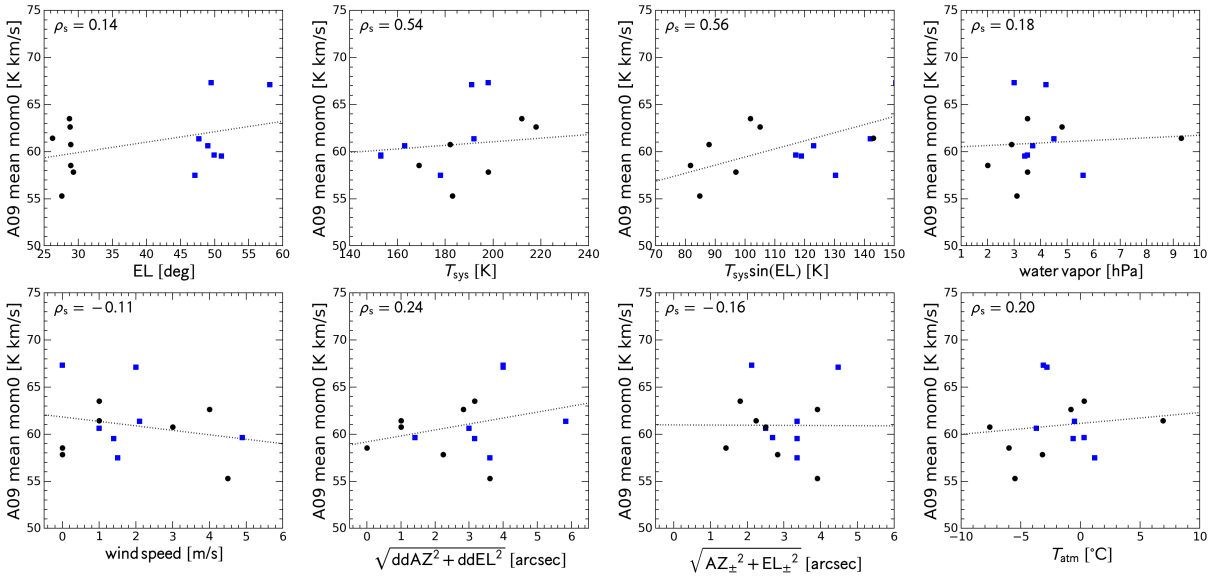

Figure 4.14: The same as figure 4.13 but for the ^{13}CO($J = 1$–0) standard array.

for the regression line is fixed to zero, because the relation among intensities of each array is considered as linear. From this method, intensity of each array except for the standard array was calibrated. We made use of the task Scaling of the Nobeyama OTF Software Tools for Analysis (NOSTAR) distributed by NRO for the calibration procedure.

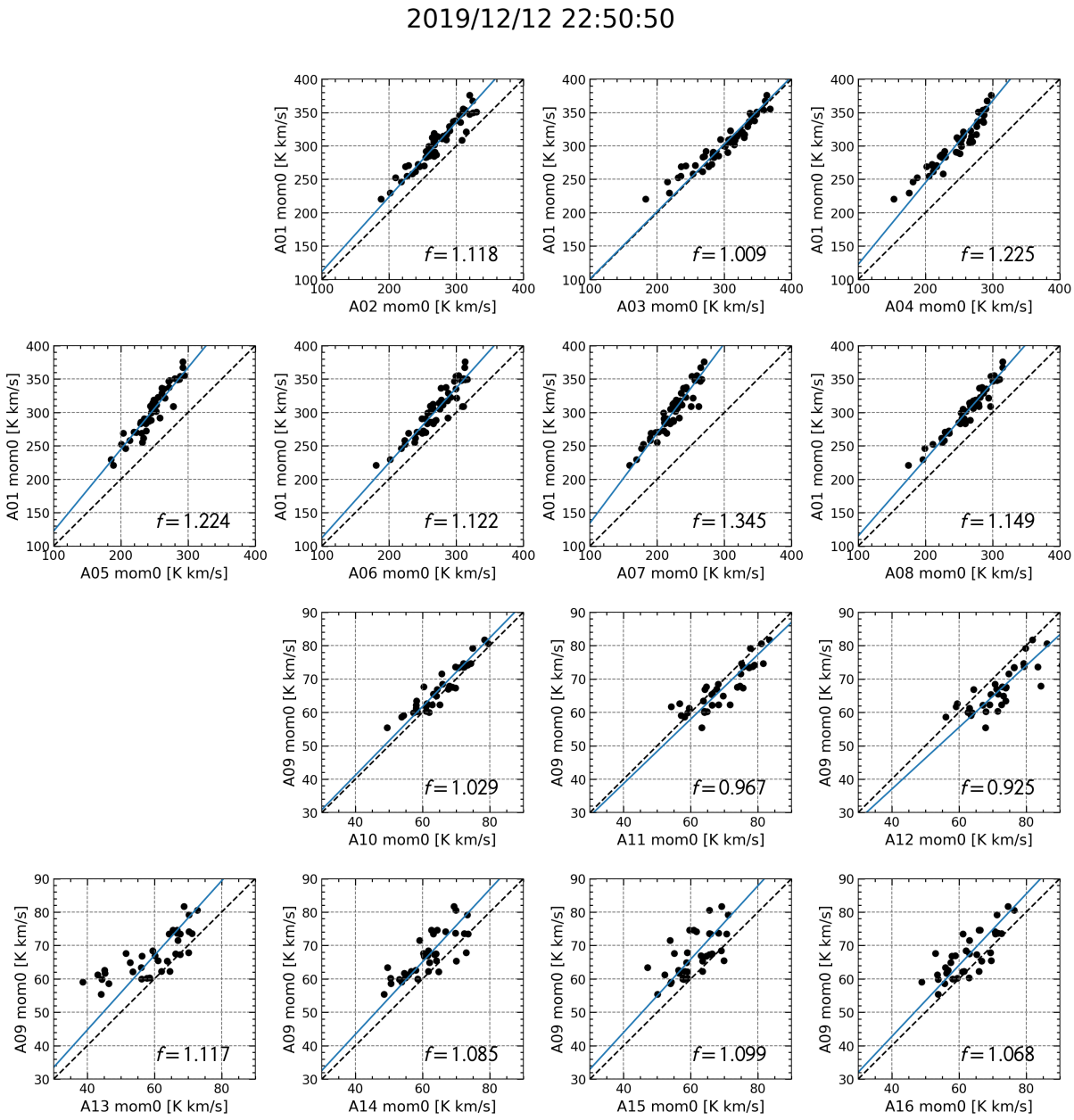

Figure 4.15: Correlation plots between integrated intensities of the standard array and another array for calibration of each array. Shown data is obtained on December 12, 2019. Blue solid lines are the regression line of each panel and black dashed orthogonal lines indicate $y = x$. For fitting, the intercept of the vertical axis was fixed to zero (i.e., $y = ax$ where a is a constant). Scaling factor from the standard array into each array is denoted in the bottom right.

4.3.3 Data reduction

Data reduction was performed using the Python-based automatic reduction system developed by the CO Multi-line Imaging of Nearby Galaxies (COMING; Sorai et al. 2019) team, COMING Auto-Reduction Tool (COMING ART) based on NOSTAR (see section 4.2 in Sorai et al. 2019 for more detail). COMING ART consists of flagging for bad data, binning up of velocity channels, basket weaving (Emerson and Gräve 1988), re-gridding, and subtracting the baseline. The final

velocity resolution and the grid spacing was set to be 10 km s^{-1} for ^{13}CO($J=1$–0) and 5 km s^{-1} for ^{12}CO($J=1$–0), and 6″, respectively. The resultant angular resolution is 17″. The root mean square (RMS) noise-level is 12.1 mK for ^{13}CO($J=1$–0), 34.1 mK for ^{12}CO($J=1$–0), respectively in the $T_{\rm MB}$ scale at the velocity resolution.

The ^{12}CO($J=1$–0) cube whose velocity resolution is 10 km s^{-1} was also made by binning velocity channels of the cube of velocity resolution 5 km s^{-1}. For channel binning, intensities at channels whose velocities can be divided by 10 km s^{-1} without a remainder is weighted by 2 and those at channels whose velocities can be divided by 5 km s^{-1} but not by 10 km s^{-1} is not weighted. This is because the value of coordinates of Flexible Image Transport System (FITS) files is determined as that at its center by the regulation of the FITS format (Greisen and Calabretta 2002). The baseline of this velocity binned ^{12}CO($J=1$–0) cube is also subtracted after binning up with the same algorithm of COMING ART. The RMS noise level of this cube is 23.0 mK. Corresponding sensitivity of H_2 column density at one velocity channel is 1.8×10^{20} cm^{-2} at $4\,\sigma$ when using the standard conversion factor $X_{\rm CO}=2.0\times10^{20}$ cm^{-2} (K km s^{-1})$^{-1}$ (Bolatto et al. 2013b).

The baseline of ^{13}CO($J=1$–0) cube is subtracted again based on the baseline range of ^{12}CO($J=1$–0) whose velocity resolution is 10 km s^{-1} after COMING ART. ^{13}CO($J=1$–0) voxels are determined as "signal" or "noise" when following conditions are satisfied:

$$T_{^{13}\rm CO}(\alpha_i,\delta_j,v_k)=\begin{cases}\text{signal}, & \text{if } T_{^{13}\rm CO}>2\sigma_{^{13}\rm CO} \text{ and } T_{^{12}\rm CO}(\alpha_i,\delta_j,v_k)>4\sigma_{^{12}\rm CO};\\ \text{noise}, & \text{otherwise;}\end{cases} \tag{4.3}$$

where $T_{^{13}\rm CO}$ is intensity at the position of (α_i,δ_j,v_k), $\sigma_{^{13}\rm CO}$ is RMS noise of ^{13}CO($J=1$–0) at the position, $T_{^{12}\rm CO}$ is intensity of ^{12}CO($J=1$–0) at the same position and velocity, and $\sigma_{^{12}\rm CO}$ is RMS noise level of ^{12}CO($J=1$–0) at the position.

Integrated-intensity maps of ^{12}CO($J=1$–0) and ^{13}CO($J=1$–0) were made by integrated intensities over channels determined as "signal". Error maps of them are derived in the same manner of Sorai et al. (2019). Namely, error of integrated intensity dI is derived with the following equation:

$$dI(\alpha_i,\delta_j)=\sqrt{[dI_n(\alpha_i,\delta_j)]^2+[dI_b(\alpha_i,\delta_j)]^2}, \tag{4.4}$$

where dI_n and dI_b are error caused by noise of intensity and baseline fitting, respectively. They are defined as the follows:

$$dI_n \equiv \sigma(\alpha_i,\delta_j)\times\Delta v_s(\alpha_i,\delta_j)\sqrt{\frac{\Delta v_{\rm ch}}{\Delta v_s(\alpha_i,\delta_j)}}, \tag{4.5}$$

$$dI_b \equiv \sigma(\alpha_i,\delta_j)\times\Delta v_s(\alpha_i,\delta_j)\sqrt{\frac{\Delta v_{\rm ch}}{\Delta v_b(\alpha_i,\delta_j)}}, \tag{4.6}$$

where Δv_s is velocity range of signal, $\Delta v_{\rm ch}$ is velocity resolution, and Δv_b is velocity range of the baseline. When the all velocity channels are "noise", median of Δv_s in the map is adopted as Δv_s at the position. Corresponding sensitivity of molecular gas surface density from ^{12}CO($J=1$–0) integrated intensity is 5.3 $M_\odot$ pc^{-2} at $4\,\sigma$ using the standard conversion factor of $\alpha_{\rm CO}=4.35$ $M_\odot$ (K km s^{-1} pc^2)$^{-1}$ (Bolatto et al. 2013b).

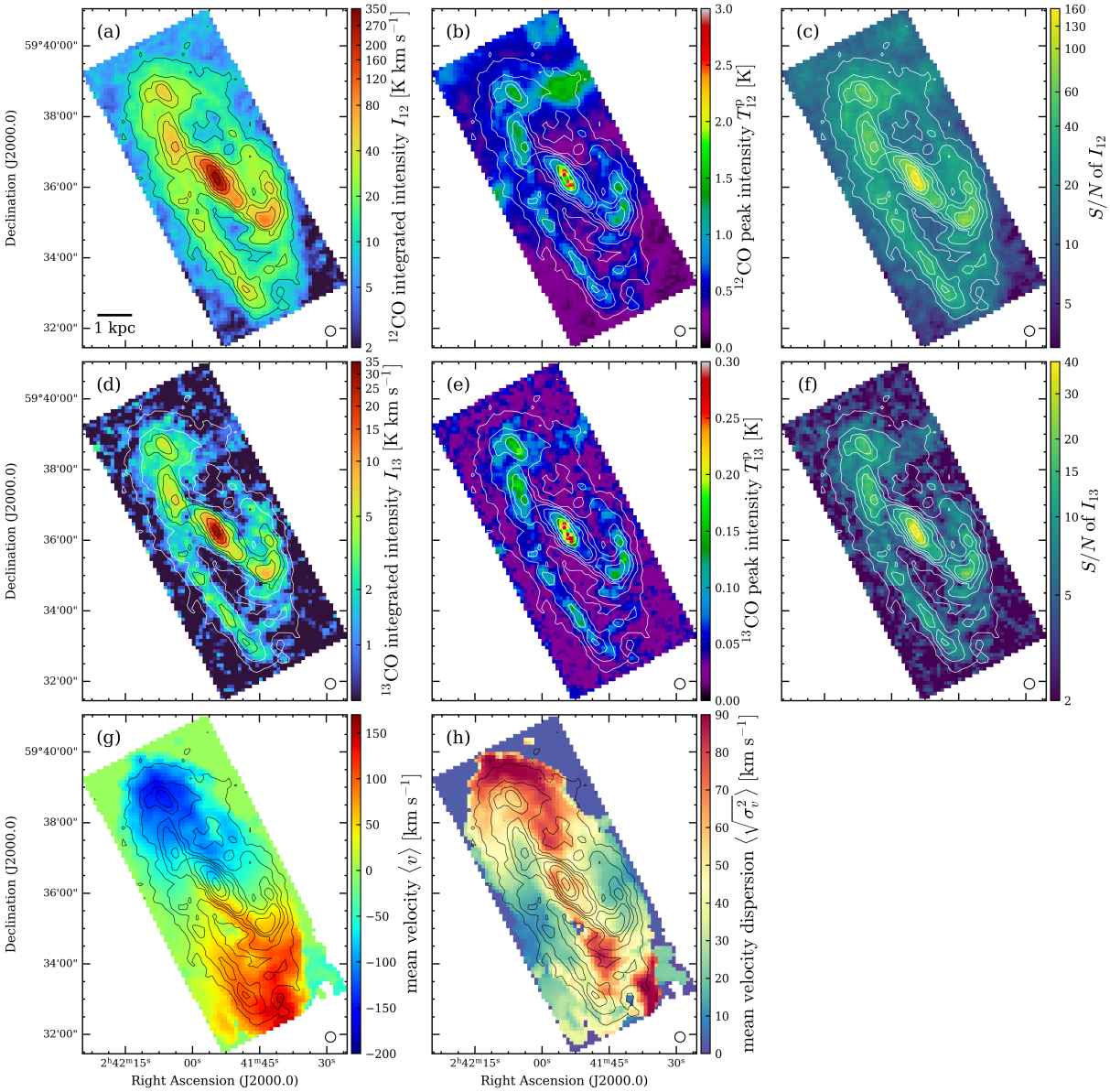

Figure 4.16: (a) Velocity-integrated intensity map of ^{12}CO($J=1$–0). (b) Peak intensity map of ^{12}CO($J=1$–0). (c) S/N map of ^{12}CO($J=1$–0) velocity-integrated intensity. (d) Velocity-integrated intensity map of ^{13}CO($J=1$–0). (e) Peak intensity map of ^{13}CO($J=1$–0). (f) S/N map of ^{13}CO($J=1$–0) velocity-integrated intensity. (g) Mean-velocity field (the first moment) map derived from ^{12}CO($J=1$–0). (h) Velocity dispersion (the second moment) map derived from ^{12}CO($J=1$–0). For (g) and (h), pixels below 5σ of ^{12}CO($J=1$–0) are masked. Open circles in the bottom right corner in each panel are the beam size of the Nobeyama 45 m Telescope. Contours indicate the integrated intensity of ^{12}CO($J=1$–0) at levels 10, 20, 30, 40, 60, 100, 160, and 250 K km s^{-1}.

4.4 Results

Figure 4.16 shows original results of the observations. Signal-to-noise ratio (S/N) of integrated intensity is achieved at $\gtrsim 15$ for ^{12}CO($J=1$–0) and $\gtrsim 5$ for ^{13}CO($J=1$–0) in the disk of Maffei 2. Both integrated-intensity maps of ^{12}CO($J=1$–0) and ^{13}CO($J=1$–0) trace galactic structures such as spiral arms and the bar of Maffei 2. This galaxy shows the strong concentration of

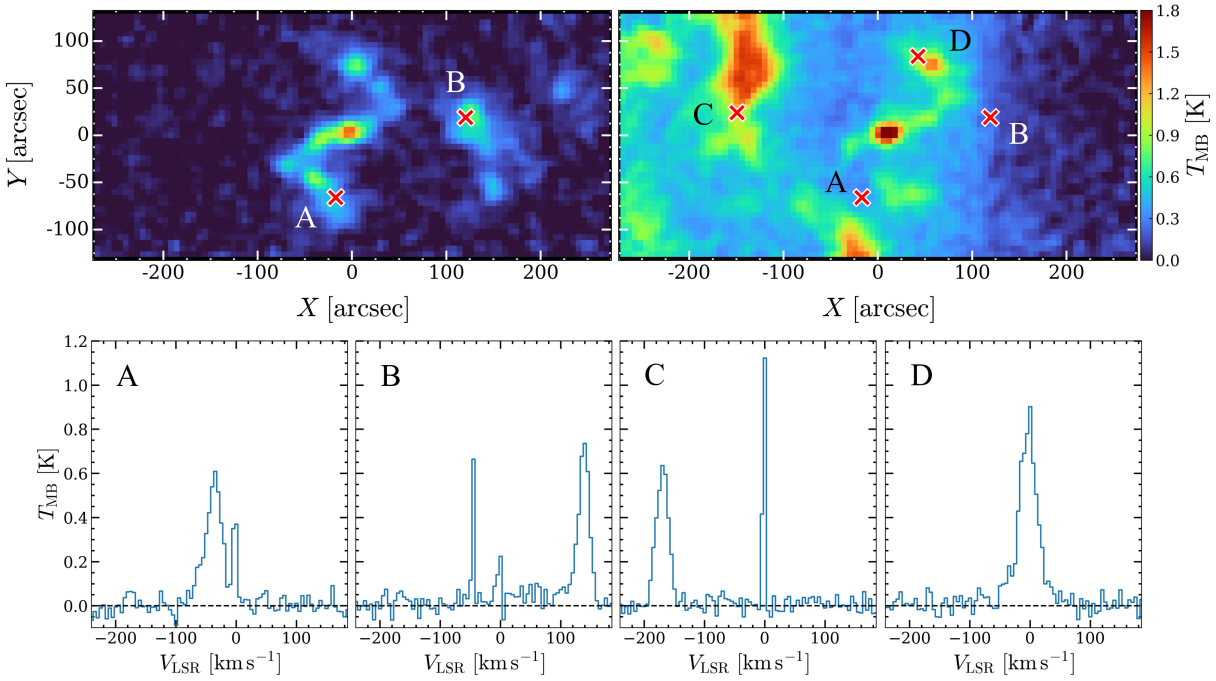

Figure 4.17: Representative Galactic ^{12}CO($J=1$–0) spectra at some positions. Maps shown in the top row are at the $v_{\rm LSR} = -45$ km s^{-1} channel (left) and the 0 km s^{-1} channel (right). The positive direction of the X- and Y-axis corresponds to the southwest and northwest, respectively (cf. figure 4.16). At position D, emission of Maffei 2 and the Galaxy are completely overlapped at the same position and the velocity.

molecular gas at the center. Molecular gas is also concentrated in bar ends and the lump structure in the north of the northern bar end. In the bar, it seems that molecular gas is rich in the leading side of offset ridges compared with the trailing side. In addition, there are gaps of molecular gas between bar ends and the inner part of the bar. These distributions are consistent with Kuno et al. (2007) and Sorai et al. (2012). The gaps are clear in the northern side in ^{13}CO($J=1$–0). Unlike integrated-intensity maps, peak-intensity maps show the double peak around the center in both ^{12}CO($J=1$–0) and ^{13}CO($J=1$–0). Their positions roughly coincide with intersections of offset ridges of the bar (arms in the bar) and the central ring, which harbor intense star-forming regions (Kuno et al. 2008; Meier et al. 2008; 2012). Stream features can be seen between the southern bar end and the eastern spiral arm, and in the southeast of the southern bar end. They would be caused by recent or undergoing interactions with another galaxy, because another interacting galaxy NGC 3627 shows the similar structure (e.g., Law et al. 2018; Sorai et al. 2019).

As well as galactic structures of Maffei 2, some large clumpy structures and diffuse emission can be seen. Both are clearly seen in the northern part of the galaxy in peak-intensity maps and S/N maps. These are foreground Galactic emission because the mapped area is very close to the midplane of the Galaxy (the map center is $l \sim 136°.5$, $b \sim -0°.325$) and the receding velocity of Maffei 2 is close to $v_{\rm LSR} = 0$ km s^{-1}. They can be seen at $v_{\rm LSR} = -55$, -50, -45, -40, -35, -10, -5, and 0 km s^{-1} for ^{12}CO($J=1$–0) and at 0 km s^{-1} for ^{13}CO($J=1$–0). Their spectra show very sharp, or spiky profiles. Galactic emission seen around -50 km s^{-1} is molecular gas in the Perseus Arm and seen around 0 km s^{-1} is in the Orion Spur (e.g., Dame et al. 2001).

Figure 4.17 shows representative Galactic spectra at some positions with maps at the −45 km s^{-1} channel and the 0 km s^{-1} channel. At position B and C, emission of Maffei 2 and the Galaxy at −45 and 0 km s^{-1} are separated along the velocity axis even though positions are overlapped. At position A, however, Galactic emission is overlapped in the wing of the spectrum of Maffei 2. As the worst case, the peaks of the spectrum of the Galaxy and Maffei 2 are completely overlapped at the same position and velocity like position D. Therefore, separating Galactic foreground emission by interpolating intensity along the velocity axis is not enough[2)]. Intensity of Galactic emission should be estimated along the spatial axis (i.e., X- and Y-axis) to deal with the worse case like the position D. We developed a new algorithm to remove Galactic foreground emission from the original data and describe it in the next subsection.

4.4.1 Extraction of Galactic emission

Figure 4.18 shows the flowchart of the algorithm for the removal of Galactic emission. Focusing its sharp and narrow spectra as shown in figure 4.17, we firstly identify and remove strong Galactic emission. We also consider the fact that Galactic emission is seen at only specific velocities, whereas positions where emission of Maffei 2 appears are continuously moving when the velocity is changing across wide velocity range. This process is referred to as "step 1" and described in the next sub-subsection in detail.

Step 1. Identification of Galactic emission

The process for identification of Galactic emission is performed at only the velocity where Galactic emission is seen; $v_{\rm LSR} = -55, -50, -45, -40, -35, -10, -5, 0$ km s^{-1} for ^{12}CO($J=1$–0) and 0 km s^{-1} for ^{13}CO($J=1$–0). To identify Galactic emission, the threshold of intensity at each channel is set as $3\,\sigma$ for both ^{12}CO($J=1$–0) and ^{13}CO($J=1$–0), i.e., at the position of (x_i, y_j) and the velocity v_k,

$$T_{\rm MB}(x_i, y_j, v_k) > 3\,\sigma(x_i, y_j), \tag{4.7}$$

where σ is the RMS noise level at the position. The profile of a spectrum is recognized as spiky, when at least either one of the following four conditions is satisfied;

$$\begin{cases} T_{\rm MB}(x_i, y_j, v_k) > 2\,T_{\rm MB}(x_i, y_j, v_{k+1}), \\ T_{\rm MB}(x_i, y_j, v_k) > 2\,T_{\rm MB}(x_i, y_j, v_{k-1}), \\ T_{\rm MB}(x_i, y_j, v_k) > 2\,T_{\rm MB}(x_i, y_j, v_{k+2}), \\ T_{\rm MB}(x_i, y_j, v_k) > 2\,T_{\rm MB}(x_i, y_j, v_{k-2}). \end{cases} \tag{4.8}$$

Note that $v_{k\pm1}$ is the velocity which is the adjacent velocity channel, so that when $v_k = -35$ km s^{-1}, $v_{k+1} = -30$ km s^{-1} for ^{12}CO($J=1$–0). The threshold of full-width at the half maximum (FWHM) of a spectrum ΔV we set is 15 km s^{-1} for both ^{12}CO($J=1$–0) and ^{13}CO($J=1$–0). This threshold is determined by measuring ΔV of some representative Galactic emission identified by eye. Thus, if ΔV is less than 15 km s^{-1}, the profile is distinguished as narrow;

$$\Delta V(x_i, y_j) < 15\,{\rm km\,s^{-1}}. \tag{4.9}$$

[2)] We attempted to extract Galactic emission by interpolating intensity of spectra of Maffei 2 along the velocity axis. However, vestiges of the distribution of Maffei 2 were seen in the image of the extracted Galactic emission. Hence, we have to develop another method to separate emission from the Galaxy and Maffei 2.

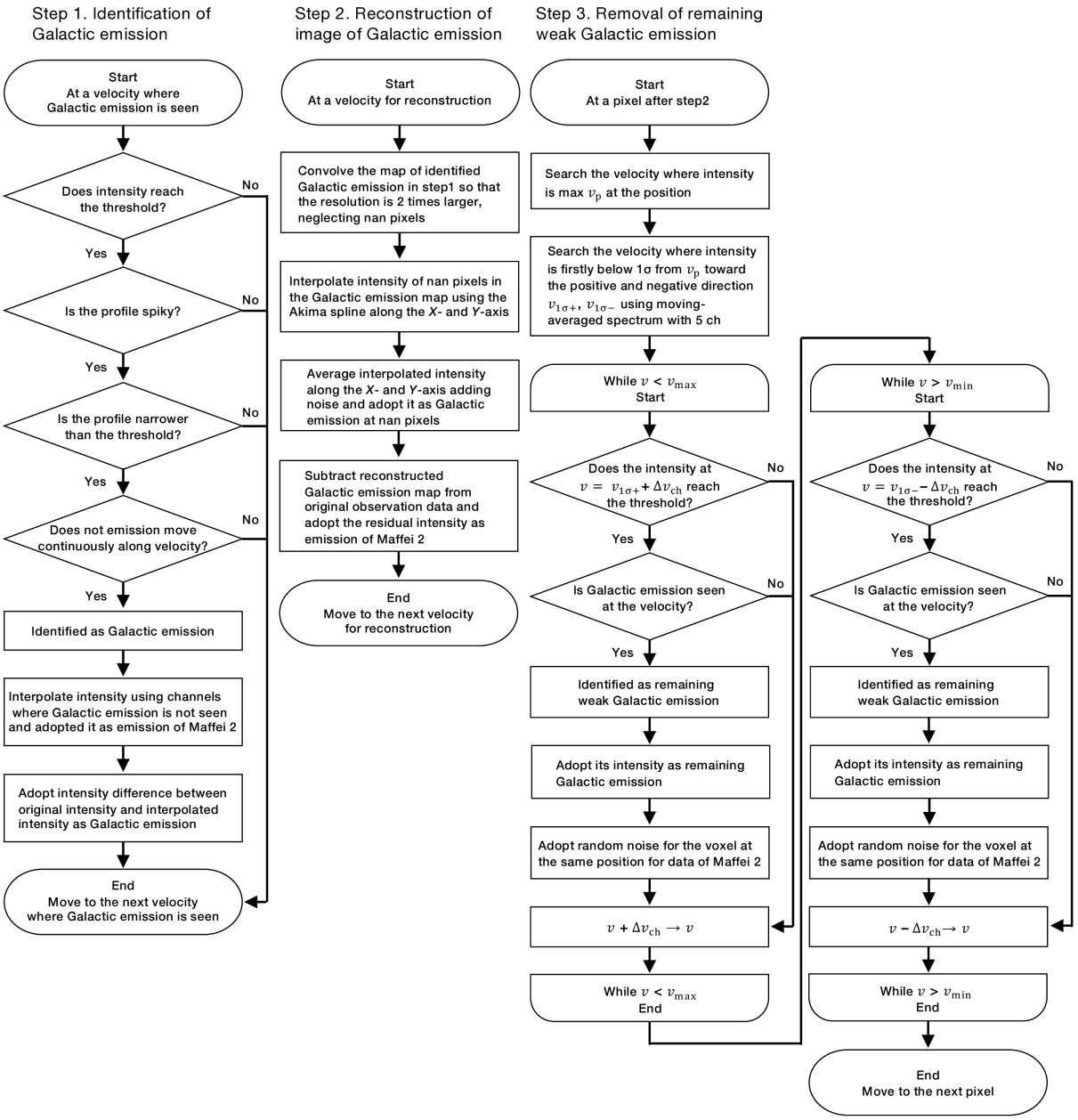

Figure 4.18: Flowchart of the algorithm to separate foreground Galactic emission and background emission of Maffei 2 from observational data. $\Delta v_{\rm ch}$ in the figure is velocity resolution.

Then, we set conditions to distinguish whether positions where emission appears are continuously moving when velocity changes or not. Since the disk of Maffei 2 is rotating, positions where its emission is seen change as velocity changes, while Galactic emission appears at only specific velocities. Conditions to recognize that the source of emission is rotating or not are as follows;

$$\begin{cases} T_{\rm MB}(x_{i\pm2}, y_j, v_k + 10\,{\rm km\,s^{-1}}) & < 2.5\,\sigma(x_{i\pm2}, y_j), \\ T_{\rm MB}(x_i, y_{j\pm2}, v_k + 10\,{\rm km\,s^{-1}}) & < 2.5\,\sigma(x_i, y_{j+2}), \\ T_{\rm MB}(x_{i\pm2}, y_{j\pm1}, v_k + 10\,{\rm km\,s^{-1}}) & < 2.5\,\sigma(x_{i\pm2}, y_{j\pm1}), \\ T_{\rm MB}(x_{i\pm1}, y_{j\pm2}, v_k + 10\,{\rm km\,s^{-1}}) & < 2.5\,\sigma(x_{i\pm1}, y_{j\pm2}), \end{cases} \tag{4.10}$$

or

$$\begin{cases} T_{\rm MB}(x_{i\pm2}, y_j, v_k - 10\,{\rm km\,s^{-1}}) & < 2.5\,\sigma(x_{i\pm2}, y_j), \\ T_{\rm MB}(x_i, y_{j\pm2}, v_k - 10\,{\rm km\,s^{-1}}) & < 2.5\,\sigma(x_i, y_{j+2}), \\ T_{\rm MB}(x_{i\pm2}, y_{j\pm1}, v_k - 10\,{\rm km\,s^{-1}}) & < 2.5\,\sigma(x_{i\pm2}, y_{j\pm1}), \\ T_{\rm MB}(x_{i\pm1}, y_{j\pm2}, v_k - 10\,{\rm km\,s^{-1}}) & < 2.5\,\sigma(x_{i\pm1}, y_{j\pm2}). \end{cases} \tag{4.11}$$

Equations (4.10) and (4.11) indicates that there is no emission at the velocity ±10 km s^{-1} in the edge of the surrounding 5×5 pixels. This ±10 km s^{-1} shift is common for both ^{12}CO($J=1$–0) and ^{13}CO($J=1$–0), because the rotating speed is independent of observed lines. If either all conditions of equation (4.10) or those of equation (4.11) are satisfied, the source of emission at (x_i, y_j, v_k) is not rotating and it is identified as Galactic emission. If not, it is identified as emission of Maffei 2.

With these conditions above, Galactic emission is identified. Intensity of Maffei 2 after the subtraction of Galactic emission is estimated by interpolating intensities at the nearest velocity channels where Galactic emission is not seen. The random noise which is equivalent to RMS at the position is added to the interpolated intensity. Intensity of Galactic emission is adopted as the residual intensity subtracted by interpolated intensity from the original. When these processes are completed for all pixels at the velocity, the same algorithm is done at the next velocity where Galactic emission is seen. Examples of results for step 1 are shown in panel (b) and (e) in figure 4.19.

As shown in panel (b) of figure 4.19, Galactic emission can be roughly removed in the case that Galactic spectra are not overlapped with emission of Maffei 2 at the same velocity like position B and C in figure 4.17 and the case that it is overlapped with the wing of spectra of Maffei 2 like position A in the figure. However, Galactic emission yet remains after step 1 like panel (e) in figure 4.19 and figure 4.20 when the peak of Galactic emission is completely overlapped with that of spectra of Maffei 2 at the same position and the velocity like position D in figure 4.17. This happens at $v_{\rm LSR} = -5$ and 0 km s^{-1} of ^{12}CO($J=1$–0) where extended Galactic emission is seen. We resolved this problem by reconstructing the identified foreground Galactic image as shown in figure 4.20 after step 1. This process is referred to as "step 2".

Step 2. Reconstruction for image of foreground emission

Step 2 is performed for only the maps at $v_{\rm LSR} = -5$ and 0 km s^{-1} of ^{12}CO($J=1$–0) that are velocities where the foreground image at the velocity is needed to be reconstructed. Namely, most of overlapped Galactic emission is the diffuse component traced by ^{12}CO($J=1$–0) alone. As the first process of step 2, Galactic emission images identified in step 1 are convolved to reduce effects of noise so that the angular resolution is 2 times larger than the original without considering nan pixels[3)] (pixels with missing value). After convolution, intensity at nan pixels is estimated by interpolation with the Akima spline (Akima 1970) along the X- and Y-axis using the convolved Galactic image. Figure 4.21 shows an example of interpolation for intensity with the Akima spline. The Akima spline produces more natural interpolation than the simple linear interpolation does. Moreover, this spline method does not tend to occur overshoot (significant vibration or deviation of an interpolated curve) compared with the usual spline interpolation. For these reasons, we adopt the Akima spline. Then, we get two reconstructed Galactic images

[3)] Usually, convolution with nan pixels is performed by replacing nan pixels with zero.

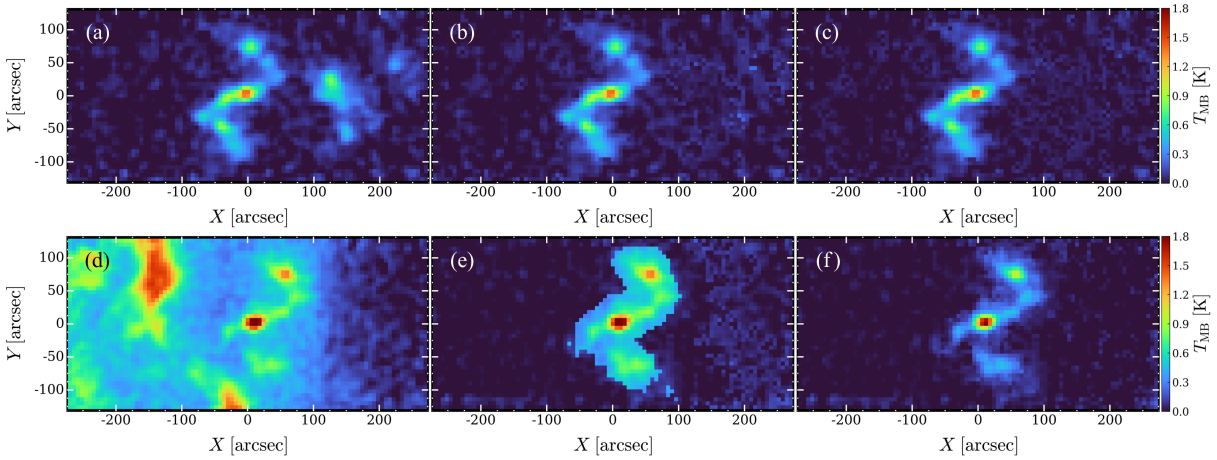

Figure 4.19: Channel maps at $v_{LSR} = -45$ km s^{-1} (top row) and 0 km $^{-1}$ (bottom row) after step 1 and step 3. Original maps are panel (a) and (d). Results after step 1 of the Galactic removal are shown in panel (b) and (e). Final results after step 3 are shown in panel (c) and (f).

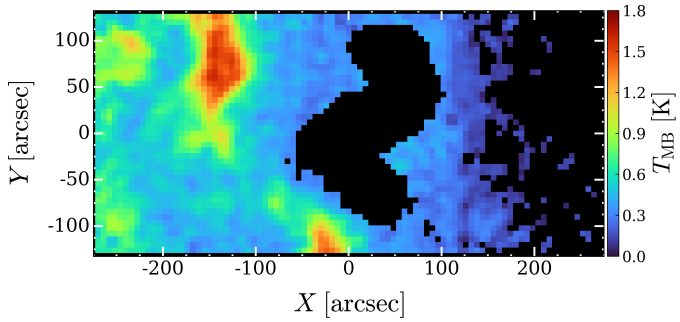

Figure 4.20: Extracted foreground Galactic emission at $v_{LSR} = 0$ km s^{-1} after step 1. Black pixels are nan (missing value) due to the inability to identify Galactic emission with the method in step 1, i.e., this is the subtracted image of panel (e) from (d) in figure 4.19.

interpolated along the X- and Y-axis. The final reconstructed Galactic image is created by averaging these two images and adding RMS noise at the positions. The reason the noise is added is that interpolated intensity is assumed from the convolved image (i.e., effects of noise are negligible). The residual intensity subtracted by reconstructed Galactic emission from the original data is adopted as emission of Maffei 2.

Since we set the threshold of intensity to identify Galactic emission in step 1, Galactic emission which is weaker than the threshold remains. It is significant in the envelope of small clouds seen around $v_{LSR} = -50$ km s^{-1}, e.g., around $(X, Y) \sim (200'', -50'')$ of panel (b) in figure 4.19. Hence, we developed the additional algorithm to remove such remaining weak Galactic emission. It is referred to as "step 3".

Step 3. Removal of remaining weak Galactic emission

Step 3 is also performed to only ^{12}CO($J = 1$–0) data, because ^{13}CO($J = 1$–0) does not show such remaining weak emission. In the first of step 3, the velocity where intensity is maximum v_p is searched at each pixel. We suppose that the component of emission including this peak intensity

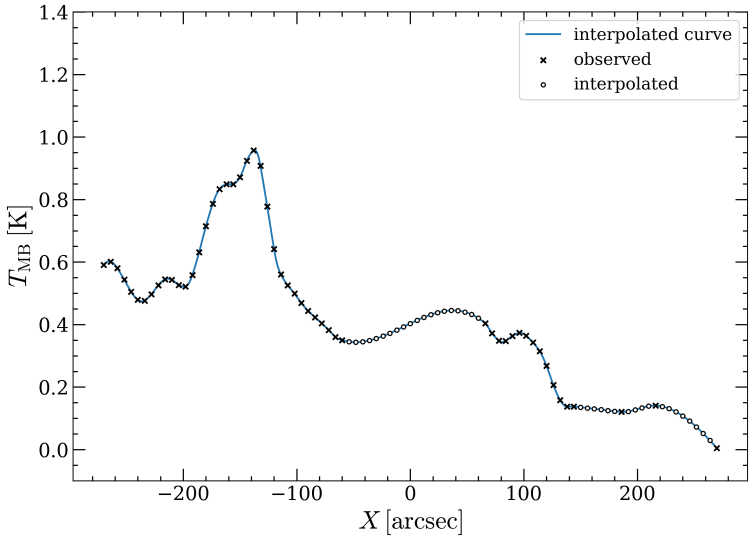

Figure 4.21: Example of interpolation for foreground intensity of the Galaxy along the X-axis in step 2 of the algorithm at 0 km s^{-1}, $Y = -6''$ (cf. figure 4.18, 4.20). Cross markers are observed value of intensity for identified Galactic emission in step 1 and open circles are interpolated intensity.

is from Maffei 2 because stronger Galactic emission than that of Maffei 2 is already removed in step 1. Next, the velocities where intensity is firstly below the $1\,\sigma$ level from the baseline are searched toward the positive (higher velocity) and negative (lower velocity) direction along the velocity axis using the 5 ch moving-averaged spectrum at the position. The velocity found on the positive side is denoted as $v_{1\sigma+}$ and that on the negative side is denoted as $v_{1\sigma-}$. Then, whether intensity reaches the $2\,\sigma$ level from the baseline or not is checked in the velocity range of $v > v_{1\sigma+}$ and $v < v_{1\sigma-}$ at each channel. If intensity is above $2\,\sigma$ and the velocity is those where Galactic emission is seen, it is identified as remaining weak Galactic emission and extracted from the data of Maffei 2 after step 2. Random noise which is equivalent to the $1\,\sigma$ RMS level at the position is adopted in data of Maffei 2 at the voxel. Results after step 3 of $v_{\rm LSR} = -45$ and 0 km s^{-1} are shown in panel (c) and (f) in figure 4.19.

4.4.2 Results of Galactic removal

Figure 4.22 shows final extracted Galactic emission. H_2 column density of Galactic molecular gas in this area is $\sim 10^{20}$–10^{21} cm^{-2} adopting the standard CO-to-H_2 conversion factor $X_{\rm CO} = 2.0 \times 10^{20}$ cm^{-2} (K km s^{-1})$^{-1}$ (Bolatto et al. 2013b). Small clouds are seen at $v_{\rm LSR} = -55 - -10$ km s^{-1}. The total molecular gas mass of clouds in the Perseus Arm ($v_{\rm LSR} = -55 - -35$ km s^{-1}) is 9.8 $M_\odot$ assuming the distance of them is the same as W3, which is also located in the Perseus Arm (1.95 kpc; Xu et al. 2006) and $\alpha_{\rm CO} = 4.3$ $M_\odot$ (K km s^{-1} pc^2)$^{-1}$. These small clouds are perhaps associated with other star-forming regions W4 (IC 1805) and W5 (IC 1848), which are adjacent to W3 and very close to Maffei 2 on the sky (e.g., Heyer et al. 1998; Megeath et al. 2008). Molecular gas mass in the Orion Spur ($v_{\rm LSR} = -10$–0 km s^{-1}) is not derived, because the distance to them cannot be assumed. Galactic emission can be seen at −55, −40, and −35 km s^{-1} in ^{12}CO($J = 1$–0), however, the number of detected pixels is a few and its distribution does not show cloud-like structures.

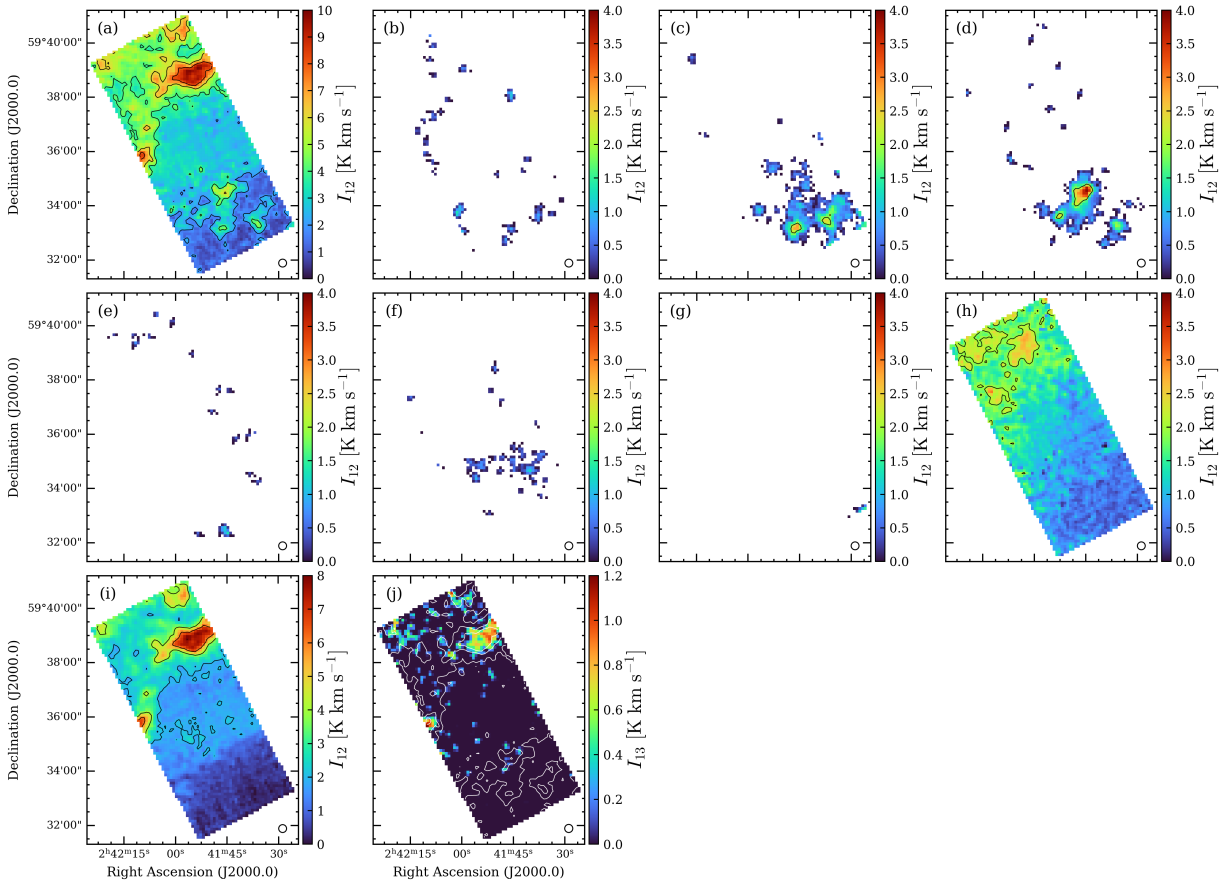

Figure 4.22: Extracted foreground emission of the Galaxy. (a) ^{12}CO($J=1$–0) integrated-intensity map of the Galaxy integrated over the all velocity range. (b)–(i) ^{12}CO($J=1$–0) integrated-intensity map at the velocity channel of $v_{\rm LSR} = -55$ km s^{-1} (b), at $v_{\rm LSR} = -50$ km s^{-1} (c), at $v_{\rm LSR} = -45$ km s^{-1} (d), at $v_{\rm LSR} = -40$ km s^{-1} (e), at $v_{\rm LSR} = -35$ km s^{-1} (f), at $v_{\rm LSR} = -10$ km s^{-1} (g), at $v_{\rm LSR} = -5$ km s^{-1} (h), at $v_{\rm LSR} = 0$ km s^{-1} (i). (j) The same as (a) but for ^{13}CO($J=1$–0) (Galactic ^{13}CO $J=1$–0 emission is detected at only 0 km s^{-1}). Contours indicate the integrated intensity of ^{12}CO($J=1$–0) at levels 2, 4, 6, and 8 K km s^{-1}. Note that color scales are different between (a), (b)–(h), (i), and (j).

For Maffei 2, figure 4.23 shows moment maps, peak-intensity maps, and sensitivity maps after the removal of Galactic emission. Baselines for ^{12}CO($J=1$–0) and ^{13}CO($J=1$–0) cubes were rebased again after the removal of Galactic emission. Hereafter, we call this process "rebase". The threshold of ^{12}CO($J=1$–0) intensity for rebase is set to be $2.5\,\sigma$. For ^{13}CO($J=1$–0) rebase, the signal and baseline range at each pixel is defined according to S/N of ^{12}CO($J=1$–0) and ^{13}CO($J=1$–0) intensities. Each ^{13}CO($J=1$–0) voxel is defined as "signal", when ^{13}CO($J=1$–0) is above $2\,\sigma$ and ^{12}CO($J=1$–0) is above $4\,\sigma$. Since ^{12}CO($J=1$–0) data can achieve high S/N, this ^{13}CO($J=1$–0) threshold using ^{12}CO($J=1$–0) does not eliminate ^{13}CO($J=1$–0) emission. According to figure 4.23, foreground Galactic emission is completely removed with our developed method. For instance, there are no clumpy and filamentary structures in peak-intensity maps and S/N maps, and significant deviations and extended components are not seen in the first and second moment map unlike seen in figure 4.16.

The removal of Galactic emission reveals more detailed structures of Maffei 2. For example, the diffuse disk which extends beyond spiral arms can be seen in ^{12}CO($J=1$–0) images. In

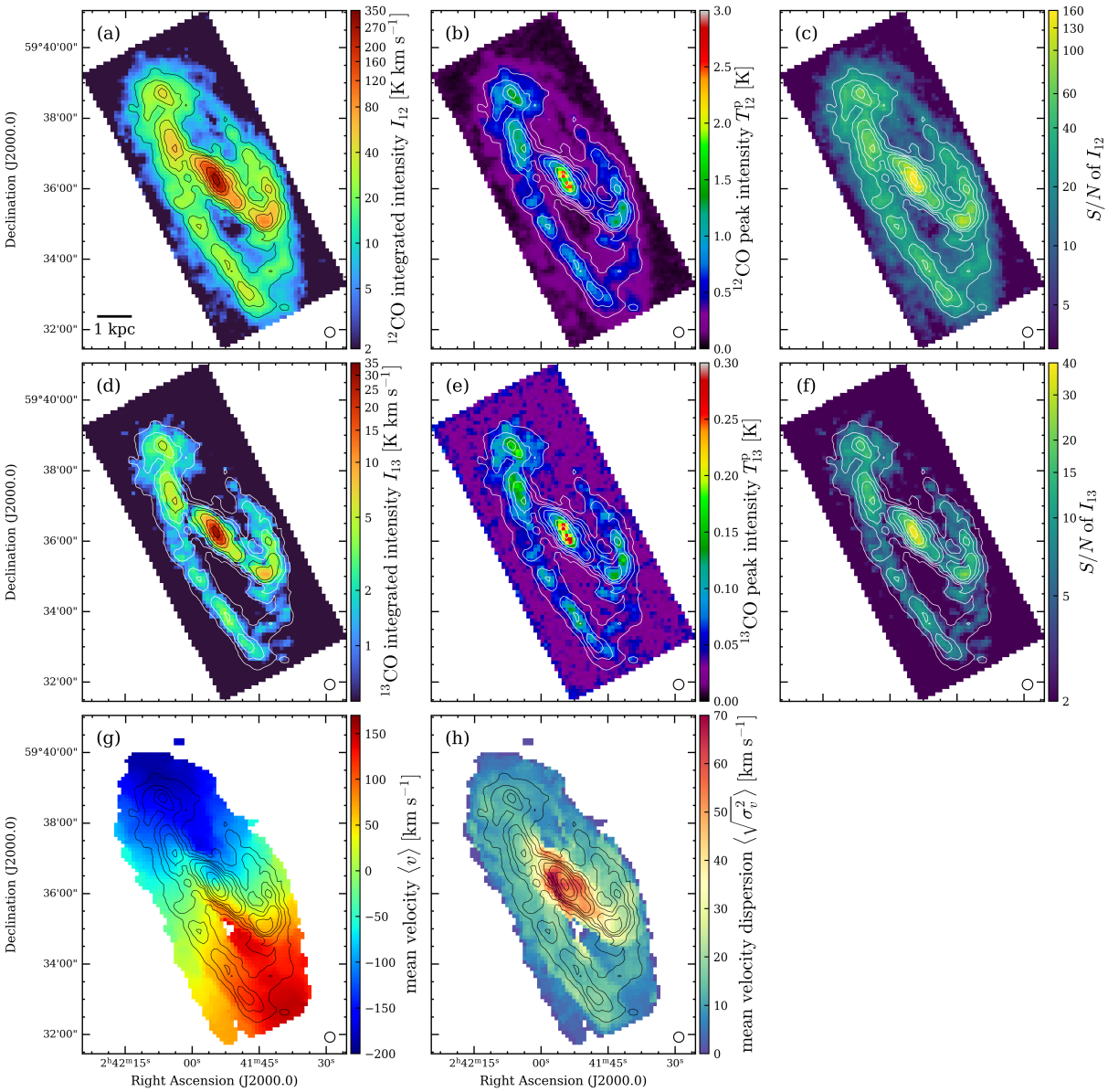

Figure 4.23: The same as figure 4.16 but for after the removal of Galactic emission. Contour levels are also the same as figure 4.16.

contrast to ^{12}CO($J=1$–0), ^{13}CO($J=1$–0) traces galactic structures and is not extended as seen in the Galaxy (e.g., Sawada et al. 2012b; Umemoto et al. 2017) at the sensitivity of our data ($S/N \gtrsim 4$ in galactic structures). We cannot see any offsets of ^{13}CO($J=1$–0) relative to ^{12}CO($J=1$–0) toward the downstream of arms like M 51 reported by Schinnerer et al. (2010), which is originally argued by Tosaki et al. (2002). The diffuse northwestern arm continues to the northern lump region.

In the northern lump region, the "?"-shaped structure that indicates that it is strongly influenced by an interaction (e.g., Hurt et al. 1993a) is seen more clearly compared to images prior to the Galactic removal, especially in peak-intensity maps. Molecular gas distribution in this region is similar to the 12 μm image (see figure 4.2). It is suggested that the possibility

for this structure is a companion of Maffei 2 (Hurt et al. 1993a). However, we cannot see any large deviations from the circular motion in this region as shown in the mean velocity map in figure 4.23. Moreover, we fitted molecular gas kinematics to the circular motion with tilted-rings model using the 3D-Based Analysis of Rotating Objects from Line Observations (^{3D}BAROLO; Di Teodoro and Fraternali 2015). We found that molecular gas in the structure follows the circular rotation of the disk of Maffei 2 as expected in the mean velocity field (figure 4.23). This structure may be just an elongated arm of Maffei 2 and not be a companion suggested by Hurt et al. (1993a).

A bridge feature connecting the tip of the southeastern arm and the southwestern bar end is also seen. The surface density of molecular gas in the region is less than the two arms. Toward the southeast of the southwestern bar end, there is the stream structure. ^{13}CO($J=1$–0) there is relatively strong considering its ^{12}CO($J=1$–0) intensity.

The mean velocity field (the first-moment map) shows strong non-circular motion along the offset ridges of the bar as seen in other barred spiral galaxies (e.g., Sorai et al. 2012; Salak et al. 2019b). The system velocity derived from ^{12}CO($J=1$–0) spectra within the central 500 pc is $v_{\rm LSR} = -31.6$ km s^{-1}, which is a very close value to previous studies (e.g., Hurt et al. 1993b; Mason and Wilson 2004). The second-moment map shows significant large velocity dispersion along the ridges of the bar as indicated by Sorai et al. (2012).

The total luminosity of ^{12}CO($J=1$–0) and ^{13}CO($J=1$–0) excluding Galactic emission is 4.84×10^8 K km s^{-1} pc^2 and 3.21×10^7 K km s^{-1} pc^2, respectively. Corresponding total molecular gas mass from ^{12}CO($J=1$–0) is 2.1×10^9 $M_\odot$ adopting the standard CO-to-H_2 conversion factor of $X_{\rm CO} = 2.0\times10^{20}$ cm^{-2} (K km s^{-1})$^{-1}$ (Bolatto et al. 2013b), which is equivalent to $\alpha_{\rm CO} = 4.3$ $M_\odot$ (K km s^{-1} pc^2)$^{-1}$. When the lower conversion factor of $X_{\rm CO} = 0.75\times10^{20}$ cm^{-2} (K km s^{-1})$^{-1}$ (Meier et al. 2008) is adopted in the inner 500 pc region which includes the nuclear molecular ring that harbors starburst (e.g., Ishiguro et al. 1989; Hurt and Turner 1991; Meier and Turner 2012), total molecular gas mass is 2.0×10^9 $M_\odot$.

In the IF band containing ^{13}CO($J=1$–0), C^{18}O($J=1$–0) line is also included. We conducted data reduction for this line. Figure 4.24 shows integrated intensity of C^{18}O($J=1$–0). Galactic C^{18}O($J=1$–0) emission is not detected. Since C^{18}O($J=1$–0) is very weak, velocity channels were binned up so that the velocity resolution is 20 km s^{-1}. The typical RMS noise level over the map of this line is 7.3 mK for the velocity resolution. The baseline range was determined by the threshold of $2\,\sigma$ and whether ^{13}CO($J=1$–0) is detected above $2\,\sigma$ at the same velocity. C^{18}O($J=1$–0) is significantly detected in bar ends, some positions in arms and the northern lump region, and especially the center. This line is scarcely detected in the bar, indicating very dense gas is poor in the bar. In the bar ends, C^{18}O($J=1$–0) emission has offset to local peaks of ^{12}CO($J=1$–0). However, the sensitivity for the line is yet poor, even though velocity channels are binned up.

4.4.3 Decomposition of ^{12}CO emission using that of ^{13}CO

To distinguish whether ^{12}CO($J=1$–0) emission is from the cloud component or the diffuse component, ^{12}CO($J=1$–0) emission is three-dimensionally decomposed into the two components based on ^{13}CO($J=1$–0) detection at the same position and velocity, taking advantage of optically thin ^{13}CO($J=1$–0). Prior to the decomposition of ^{12}CO($J=1$–0) emission, velocity

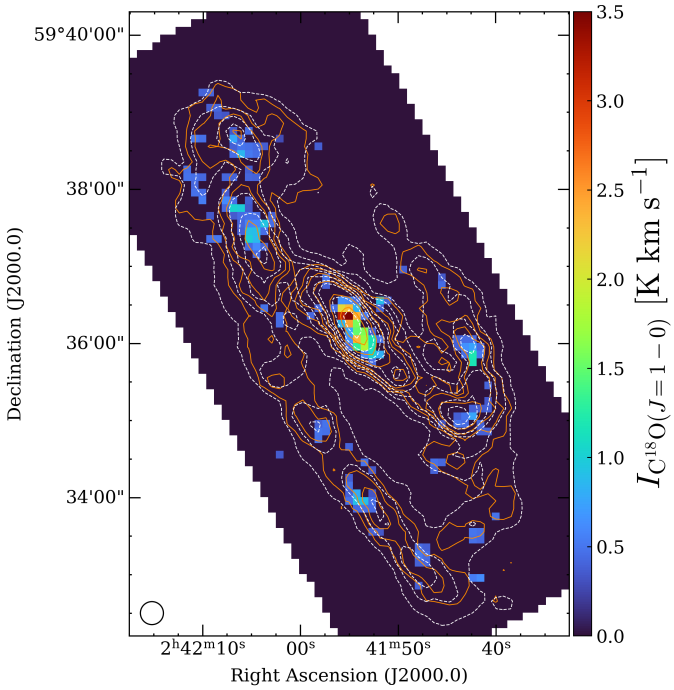

Figure 4.24: Integrated-intensity map of $C^{18}O(J=1–0)$. White dashed contours are $^{12}CO(J=1–0)$ integrated intensity which are the same as figure 4.23. Orange solid contours are $^{13}CO(J=1–0)$ integrated intensity at levels 1, 2, 3, 5, 10, 20 K km s^{-1}. Pixels below $2\,\sigma$ are masked.

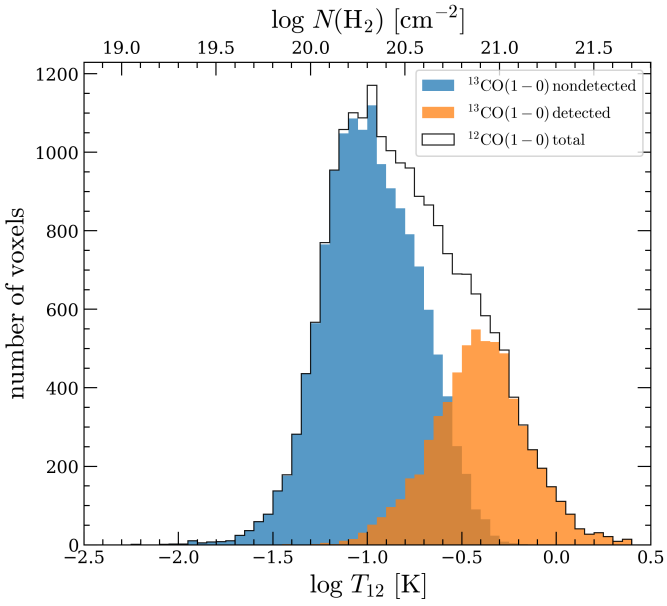

Figure 4.25: Histogram of $^{13}CO(J=1–0)$-nondetected and detected $^{12}CO(J=1–0)$ intensity. The upper x-axis indicates the corresponding column density of H_2 deriving from $^{12}CO(J=1–0)$ intensity on the assumption of the standard conversion factor of $X_{CO} = 2.0 \times 10^{20}$ cm^{-2} (K km s^{-1})$^{-1}$.

channels of $^{12}CO(J=1–0)$ were binned up from 5 km s^{-1} into 10 km s^{-1} so that the velocity resolution of $^{12}CO(J=1–0)$ is matched to that of $^{13}CO(J=1–0)$. After binning up of velocity

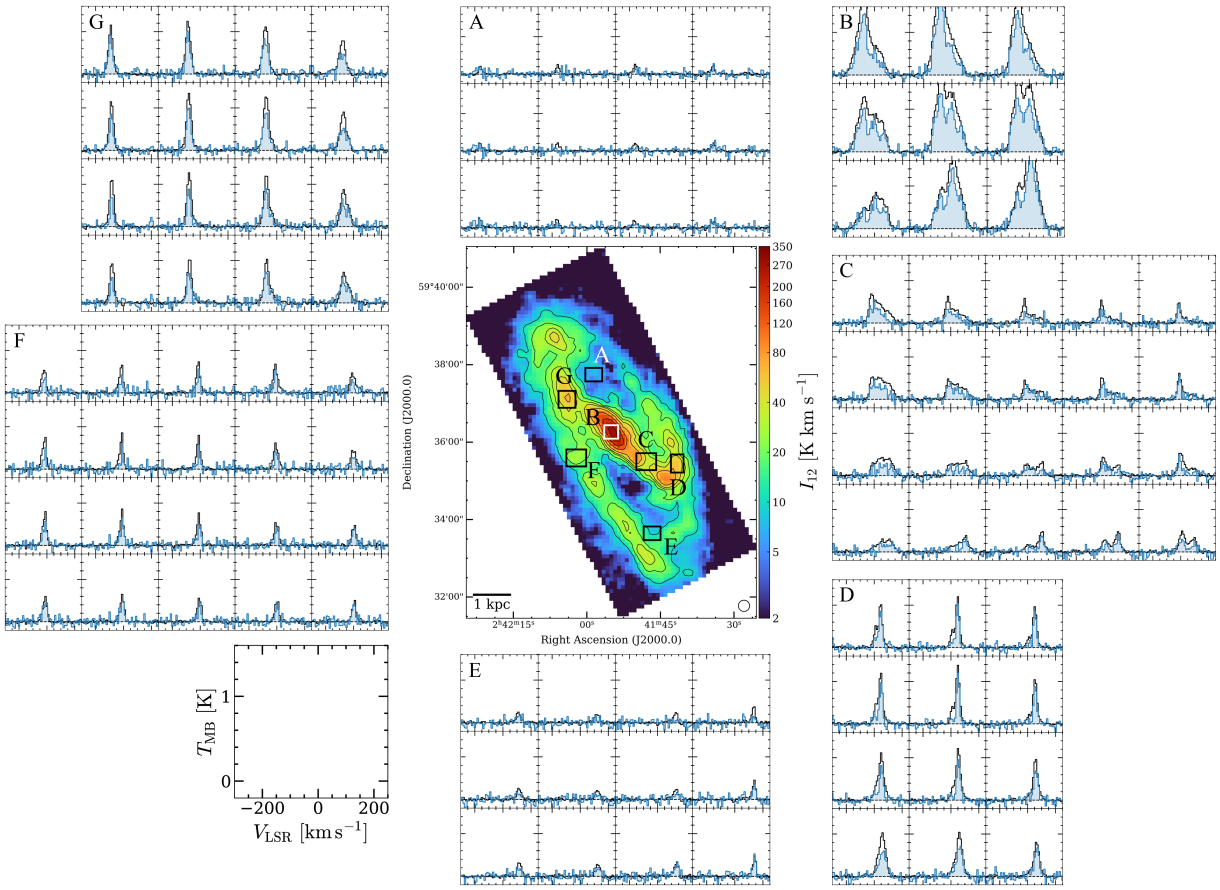

Figure 4.26: Spectra of ^{12}CO($J=1$–0) (black) and ^{13}CO($J=1$–0) (blue hatched) in rectangular areas in representative galactic structures on the ^{12}CO($J=1$–0) integrated intensity I_{12} map. Intensity of ^{13}CO($J=1$–0) is multiplied by seven. Contours in the I_{12} map are the same in figure 4.23.

channels of ^{12}CO($J=1$–0), each channel of ^{12}CO($J=1$–0) and ^{13}CO($J=1$–0) was defined as "signal" or "noise" and their baselines were subtracted by the same method of COMING ART (see section 2). Intensity threshold for ^{12}CO($J=1$–0) is $2.5\,\sigma$. Each ^{13}CO($J=1$–0) channel is defined as "signal" when ^{13}CO($J=1$–0) intensity is above $2\,\sigma$ and ^{12}CO($J=1$–0) intensity at the same position and velocity is above $4\,\sigma$. The resultant RMS noise level of ^{12}CO($J=1$–0) is decreased to 23.0 mK. That of ^{13}CO($J=1$–0) is nearly unchanged. Then, each velocity channel of ^{12}CO($J=1$–0) defined as "signal" is classified into "^{13}CO($J=1$–0)-detected" and "^{13}CO($J=1$–0)-nondetected" based on detection of ^{13}CO($J=1$–0) at the same voxel.

Figure 4.25 shows the histogram of ^{12}CO($J=1$–0) intensity in each voxel T_{12} with ^{13}CO($J=1$–0) detection and without detection, and corresponding H_2 column density $N(H_2)$ using the standard conversion factor $X_{\rm CO} = 2.0 \times 10^{20}$ cm^{-2} (K km s^{-1})$^{-1}$. ^{13}CO($J=1$–0)-detected ^{12}CO($J=1$–0) emission gradually appears from $\log T_{12}$ [K] $\gtrsim -1.1$ ($T_{12} \gtrsim 0.08$ K). This intensity is not so strong for Maffei 2, e.g., see panel (b) of figure 4.23. Hence, ^{13}CO($J=1$–0) is not always detected because of high column density. Whether ^{13}CO($J=1$–0) is detected or not does not represent only intensity of ^{12}CO($J=1$–0) emission.

On the other hand, T_{12} without ^{13}CO($J=1$–0) detection extends up to $\log T_{12}$ [K] ~ -0.3 (~ 0.5 K). Its corresponding $N(H_2)$ is $\sim 10^{21}$ cm^{-2}. This value is relatively higher column

density measured in one velocity channel, at least higher than the mode of $N(H_2)$ for the total emission channels $\sim 2\times10^{20}$ cm^{-2} [$\log N(H_2)$ [cm^{-2}] ~ 20.3] as shown in figure 4.25. Therefore, ^{13}CO($J=1$–0) is not detected even though $N(H_2)$ is relatively high when there is no cloud-phase molecular gas at a line of sight.

Figure 4.26 shows ^{12}CO($J=1$–0) and ^{13}CO($J=1$–0) spectra in representative galactic structures. ^{12}CO($J=1$–0) emission without ^{13}CO($J=1$–0) detection is often seen in wings of ^{12}CO($J=1$–0) spectra. In inter-arm regions such as position A and a part of E in figure 4.26, ^{13}CO($J=1$–0) is completely not detected in some pixels. In the bar (position C in figure 4.26), asymmetric profiles and multiple velocity-components can be seen in both ^{12}CO($J=1$–0) and ^{13}CO($J=1$–0) at some points, whereas ^{13}CO($J=1$–0)-nondetected secondary peaks are also seen. These multiple components correspond to inflowing gas along the offset ridges of the leading side and spraying gas to the offset ridges (e.g., Downes et al. 1996; Regan et al. 1999). At position D, there are secondary components or wing structures on the lower-velocity side. In the components, ^{13}CO($J=1$–0) is often not detected. It may be because wing structures without ^{13}CO($J=1$–0) detection reflect diffuse molecular gas having an outward radial velocity component.

We derived integrated intensity of ^{12}CO($J=1$–0) for ^{13}CO($J=1$–0)-detected channels, $I_{12(13\mathrm{det})}$, and for ^{13}CO($J=1$–0)-nondetected channels, $I_{12(13\mathrm{nondet})}$;

$$I_{12(13\mathrm{det})}(\alpha_i,\delta_j) \equiv \sum_{k\in{}^{13}\mathrm{CO\text{-}det\ ch}} T_{12}(\alpha_i,\delta_j,v_k)\Delta v_{\mathrm{ch}}, \tag{4.12}$$

and

$$I_{12(13\mathrm{nondet})}(\alpha_i,\delta_j) \equiv I_{12}(\alpha_i,\delta_j) - I_{12(13\mathrm{det})}(\alpha_i,\delta_j), \tag{4.13}$$

where I_{12} is integrated intensity of ^{12}CO($J=1$–0) integrated over all signal channels and Δv_{ch} is the velocity resolution (10 km s^{-1}). Panel (a) and (b) of figure 4.27 show maps of $I_{12(13\mathrm{det})}$ and $I_{12(13\mathrm{nondet})}$, respectively. The distribution of $I_{12(13\mathrm{det})}$ is similar to integrated intensity of ^{13}CO($J=1$–0), I_{13}, shown in panel (d) of figure 4.23. This indicates that there is good linearity between $I_{12(13\mathrm{det})}$ and I_{13}. The distribution of $I_{12(13\mathrm{nondet})}$ shows the cavity in the center like that of H I usually seen in massive spiral galaxies (e.g., Walter et al. 2008). In addition, $I_{12(13\mathrm{nondet})}$ decreases along the ridge (centerline, or spine) of arms, whereas it is high in the bar, peripheries of spiral arms, inter-arm, and the outer disk.

Total luminosity of ^{13}CO($J=1$–0)-detected ^{12}CO($J=1$–0) is 3.02×10^8 K km s^{-1} pc^2. It accounts for 62.4% of total $L'_{^{12}\mathrm{CO}(1-0)}$ within the whole galaxy. Therefore, 37.6% of ^{12}CO($J=1$–0) emission comes from the gas which is not associated with ^{13}CO($J=1$–0) emission. That is, approximately 40% of total molecular gas exists as the diffuse component if α_{CO} for the cloud and diffuse component is nearly the same (Liszt et al. 2010).

4.5 Discussion

4.5.1 Line ratios for decomposed ^{12}CO emission and comparison with the conventional line ratio

First of all, we discuss the fraction of the cloud component over the entire area of the galaxy. The fraction of ^{13}CO($J=1$–0)-detected ^{12}CO($J=1$–0) luminosity of 62.4% is roughly close to

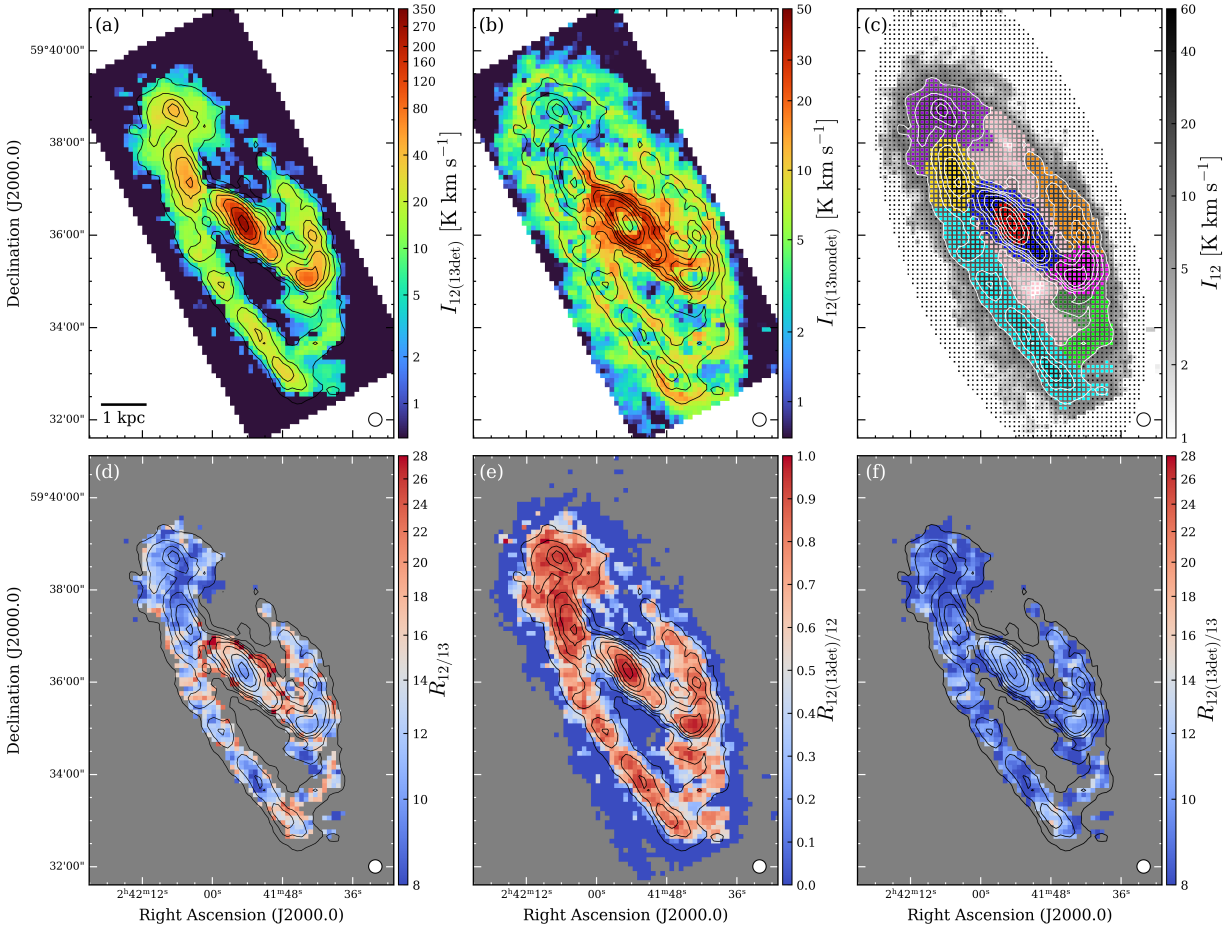

Figure 4.27: (a) Velocity-integrated intensity of ^{13}CO($J=1$–0)-detected ^{12}CO($J=1$–0). (b) The same as (a) but for ^{13}CO($J=1$–0)-nondetected ^{12}CO($J=1$–0). (c) Defined galactic regions; center (red), bar (blue), northeastern bar end (yellow), southwestern bar end (magenta), southeastern arm (cyan), northwestern arm (orange), northern lump (purple), southwestern stream (green), southern bridge (lime), interarm (pink), outer disk (black). (d) ^{12}CO($J=1$–0)/^{13}CO($J=1$–0) integrated-intensity ratio, $R_{12/13}$. (e) Integrated-intensity ratio of ^{13}CO($J=1$–0)-detected ^{12}CO($J=1$–0) to total ^{12}CO($J=1$–0), $R_{12(13\mathrm{det})/12}$. (f) Integrated-intensity ratio of ^{13}CO($J=1$–0)-detected ^{12}CO($J=1$–0) to ^{13}CO($J=1$–0), $R_{12(13\mathrm{det})/13}$. Contours in all panels are the same as those in figure 4.23. For panel (d)–(f), pixels below 3.5 σ are masked.

the fraction of recovered flux by only the PdBI in M 51 ($50 \pm 10\%$) reported by Pety et al. (2013). We note that nevertheless, it is not certain that whether the cloud component with ^{13}CO($J=1$–0) detection in Maffei 2 and GMCs traced by ^{12}CO($J=1$–0) alone with only the PdBI is the same.

Goldsmith et al. (2008) two-dimensionally decomposed pixels where ^{12}CO($J=1$–0) integrated-intensity is significantly detected into the two components according to that of ^{13}CO($J=1$–0) detection for the Taurus Molecular Cloud. They reported that fraction of ^{13}CO($J=1$–0)-nondetected ^{12}CO($J=1$–0) luminosity is 37% (see their table 5), which is a very close value to our result. It may be unnatural, because the spatial resolution differs by the four orders of magnitude (100 pc order and 0.01 pc order) between ours and theirs, and the method of analysis is different (3D based or 2D based to decompose ^{12}CO emission). We interpret the reason

for the similar result as follows. The two-dimensional analysis makes ^{13}CO($J=1$–0)-nondetected ^{12}CO($J=1$–0) fraction decrease, because wings of spectra where ^{13}CO($J=1$–0) is not detected do not contribute to ^{13}CO($J=1$–0)-nondetected ^{12}CO($J=1$–0) in the two-dimensional analysis. In contrast, it is supposed that much higher spatial resolution tends to increase ^{13}CO($J=1$–0)-nondetected ^{12}CO($J=1$–0) fraction, because sources of ^{13}CO($J=1$–0) are usually more compact than that of ^{12}CO low-J lines (e.g., Goldsmith et al. 2008; Rebolledo et al. 2012; Umemoto et al. 2017; Bešlić et al. 2021). These two effects may be offset each other.

In the disk of the Galaxy, Roman-Duval et al. (2016) presented ^{13}CO($J=1$–0)-detected ^{12}CO($J=1$–0) fraction accounts for 75% of the total ^{12}CO($J=1$–0) luminosity. One possibility of this slightly higher value than ours is multiple arms of the Galaxy, considering ^{13}CO($J=1$–0)-detected ^{12}CO($J=1$–0) increases in arms. Their observational area may also bias the fraction. The area covers mainly the inner Galaxy, whereas ours includes the outer CO disk where ^{13}CO($J=1$–0) is scarcely detected, which is possibly due to dissipation of the cloud component seen in CO because of the low metallicity environment. As in the previous paragraph, spatial resolution can also change the fraction of the cloud component. Observation toward the Galaxy can completely resolve small and weak ^{13}CO($J=1$–0) sources. These sources cannot detect in galactic observation and it may increase ^{13}CO($J=1$–0)-nondetected ^{12}CO($J=1$–0) fraction.

Next, we discuss spatially resolved line ratios and dependences on galactic structures as shown in panel (c) in figure 4.27. We define 11 galactic structures; center, bar, NE bar end, SW bar end, SE arm, NW arm, N lump, SW stream, S bridge, inter-arm, and the outer disk. The definition of them is based on distributions of ^{12}CO($J=1$–0) and ^{13}CO($J=1$–0), and the IR image in figure 4.2. We derived ratio of $I_{12(13\mathrm{det})}$ to total I_{12}, $R_{12(13\mathrm{det})/12} \equiv I_{12(13\mathrm{det})}/I_{12}$ and ratio of $I_{12(13\mathrm{det})}$ to I_{13}, $R_{12(13\mathrm{det})/13} \equiv I_{12(13\mathrm{det})}/I_{13}$, as well as the conventional line ratio of ^{12}CO($J=1$–0)/^{13}CO($J=1$–0), $R_{12/13} \equiv I_{12}/I_{13}$ at each pixel. It is supposed that $R_{12(13\mathrm{det})/12}$ reflects proportion of the cloud-phase molecular gas to the total molecular gas, whereas $R_{12(13\mathrm{det})/13}$ indicates properties of the cloud-phase molecular gas as mentioned in section 4.2. Panel (d)–(f) of figure 4.27 show distributions of $R_{12/13}$, $R_{12(13\mathrm{det})/12}$, and $R_{12(13\mathrm{det})/13}$, respectively. $R_{12/13}$ is high in the bar and peripheries of arms, and low in a part of arms (especially the ridge of them), the northern lump region, and the stream structure in the southeast of the southwestern bar end. More detailed discussion for the dependence of line ratios on galactic structures is described in section 4.5.3.

The distribution of $R_{12(13\mathrm{det})/12}$ shows high values in the center, bar ends, and along the spine of arms, in contrast to the distribution of $I_{12(13\mathrm{nondet})}$. In the bar, $R_{12(13\mathrm{det})/12}$ is not as high as (slightly lower than) that along the spine of arms on average, nevertheless, it tends to have higher values along the offset ridges of the leading side compared to the other side. In inter-arm and the outer disk, it is zero in a large area. Increasing in arms and decreasing in inter-arm and the bar of $R_{12(13\mathrm{det})/12}$ is the same trend that found in the Galaxy (Torii et al. 2019), while their result is fraction of ^{13}CO($J=1$–0)-detected to ^{12}CO($J=1$–0)-detected voxels. In contrast to $R_{12/13}$ and $R_{12(13\mathrm{det})/12}$, $R_{12(13\mathrm{det})/13}$ seems to show a smaller variation. Rather uniform $R_{12(13\mathrm{det})/13}$ may be just in appearance due to a lower mean value, because $R_{12(13\mathrm{det})/13}$ is always lower than $R_{12/13}$. Validation of this is examined in the next subsection.

We compare $R_{12(13\mathrm{det})/12}$ and $R_{12(13\mathrm{det})/13}$ with the conventional line ratio $R_{12/13}$. Figure 4.28 shows correlations of $R_{12/12(13\mathrm{det})}$ and $R_{12(13\mathrm{det})/13}$ with $R_{12/13}$ (note that the numerator

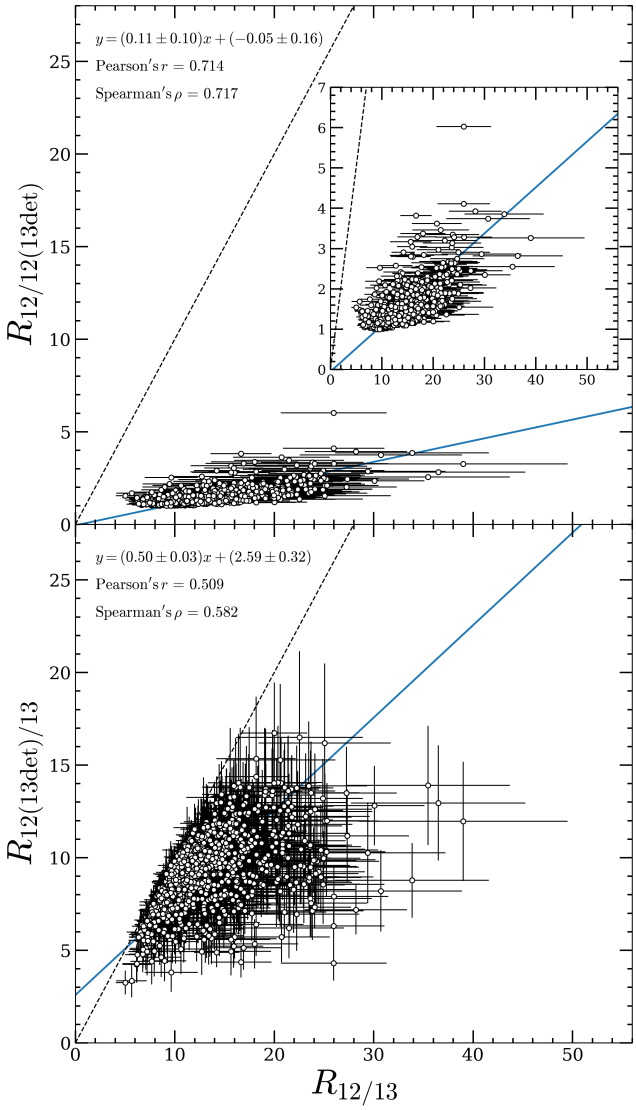

Figure 4.28: Correlation of $R_{12/12(13det)}$ (top) and $R_{12(13det)/13}$ (bottom) with conventional line ratio $R_{12/13}$. Dashed lines indicate $y = x$ and blue solid lines are the regression line with the ordinary least square bisector method for each panel. The expanded plot along the horizontal axis for the top panel is shown in the small panel.

and the denominator of $R_{12(13det)/12}$ is exchanged for the comparison to $R_{12/13}$). Since the dynamic range of $R_{12/12(13det)}$ is much smaller than that of $R_{12/13}$, the expanded plot is also shown in the top panel. Despite the small dynamic range of $R_{12/12(13det)}$, there is a strong positive correlation between $R_{12/12(13det)}$ with $R_{12/13}$ (the Pearson's product-moment correlation coefficient r is 0.71 and the Spearman's rank correlation coefficient ρ is 0.72). $R_{12(13det)/13}$ also has a positive correlation with $R_{12/13}$, although it is moderate and ambiguous (the Pearson's r is 0.51 and the Spearman's ρ is 0.58). Thus, there is a tendency that $R_{12/12(13det)}$ is high ($R_{12(13det)/12}$ is low) and $R_{12(13det)/13}$ is high where $R_{12/13}$ is high, and vice versa, though the relation of $R_{12/12(13det)}$ is clearer than that of $R_{12(13det)/13}$. Moreover, the correlation between $R_{12/12(13det)}$ and $R_{12/13}$ shows strong linearity, because the intercept is close to zero resulting from the ordinary least square bisector fitting (Isobe et al. 1990). It is also supported by almost

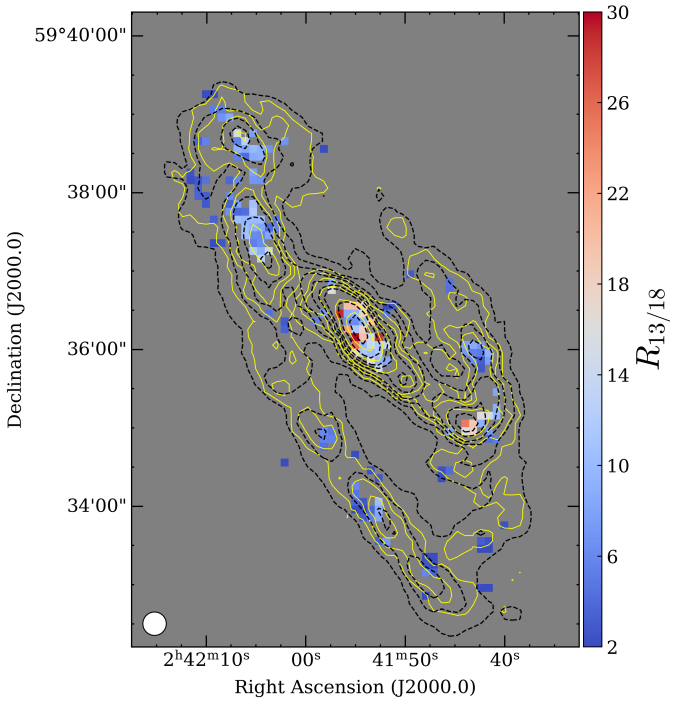

Figure 4.29: Integrated-intensity ratio of ^{13}CO($J=1$–0)/C^{18}O($J=1$–0). Contours are the same as figure 4.24. Pixels below $2\,\sigma$ are masked.

the same value of Pearson's r and the Spearman's ρ of the correlation[4)]. This indicates that $R_{12(13\mathrm{det})/13}$ has small variation (close to a constant) as seen in panel (f) in figure 4.27, because $R_{12(13\mathrm{det})/13} = R_{12/13}/R_{12/12(13\mathrm{det})}$.

As well as ^{12}CO/^{13}CO line ratios, we also derived the distribution of ^{13}CO($J=1$–0)/C^{18}O($J=1$–0) integrated-intensity ratio, $R_{13/18}$. Figure 4.29 shows the $R_{13/18}$ map. In arms, $R_{13/18}$ is similar values of 2–7. It shows asymmetry between the northwest bar end (~ 9) and southeast (~ 18). At the center, $R_{13/18}$ is intermediate (~ 14), while it is high around the center (~ 21). This may be due to difference in sensitivity; that is, C^{18}O($J=1$–0) is scarcely detected, whereas ^{13}CO($J=1$–0) is significantly detected in these pixels. Anyway, $R_{13/18}$ is barely derived and more detailed discussion and comparison with other studies about the line ratio needs new observations with much higher sensitivity.

4.5.2 Deviations of line ratios from each mean

$R_{12(13\mathrm{det})/13}$ has a small variation within the galaxy as shown in figure 4.27, however, it may be due to its lower mean than that of $R_{12/13}$. Thus, we derive deviations of line ratios from each mean to eliminate effects by different mean. Figure 4.30 shows distributions of deviations for $R_{12/13}$, $R_{12(13\mathrm{det})/12}$, and $R_{12(13\mathrm{det})/13}$ from their weighted mean in the whole galaxy. Each

[4)] When a relation is non-linear and monotonically increasing, Spearman's ρ is larger than Pearson's r. For instance, if data points are distributed along $y = x^3$, Spearman's $\rho = 1$, whereas $0 <$ Pearson's $r < 1$. Therefore, similar values of Pearson's r and Spearman's ρ indicate a high degree of linearity for the relation.

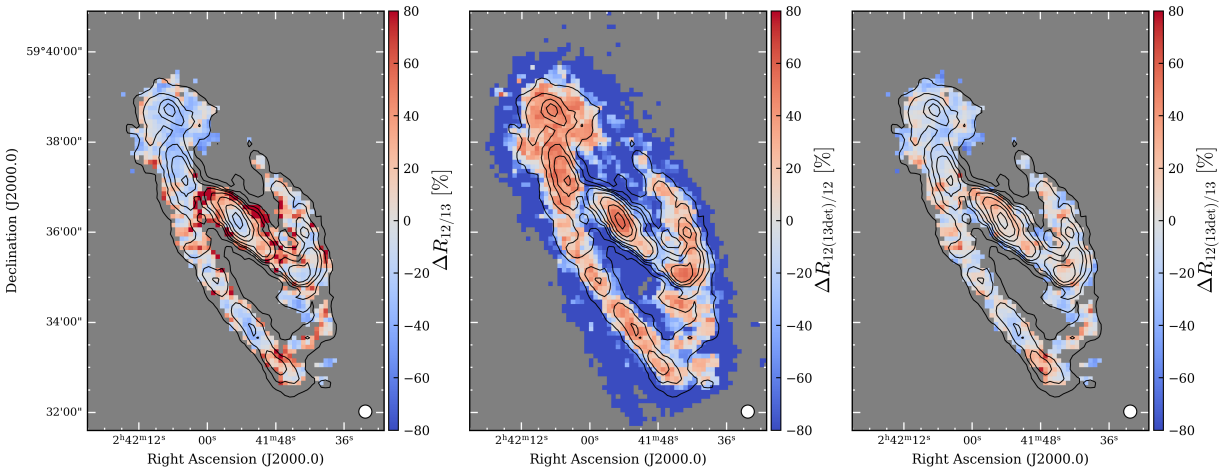

Figure 4.30: Deviations of $R_{12/13}$ (left), $R_{12(13\mathrm{det})/12}$ (center), $R_{12(13\mathrm{det})/13}$ (right) from each weighted mean in the entire galaxy. Contours are the same as figure 4.23.

weighted mean ratio is derived as following equations;

$$\begin{aligned}\langle R_{12/13}\rangle &= \frac{\sum_{i,j} R_{12/13}(\alpha_i,\delta_j) I_{13}(\alpha_i,\delta_j)}{\sum_{i,j} I_{13}(\alpha_i,\delta_j)} \\ &= \frac{\sum_{i,j} I_{12}(\alpha_i,\delta_j)}{\sum_{i,j} I_{13}(\alpha_i,\delta_j)},\end{aligned} \tag{4.14}$$

$$\begin{aligned}\langle R_{12(13\mathrm{det})/12}\rangle &= \frac{\sum_{i,j} R_{12(13\mathrm{det})/12}(\alpha_i,\delta_j) I_{12}(\alpha_i,\delta_j)}{\sum_{i,j} I_{12}(\alpha_i,\delta_j)} \\ &= \frac{\sum_{i,j} I_{12(13\mathrm{det})}(\alpha_i,\delta_j)}{\sum_{i,j} I_{12}(\alpha_i,\delta_j)},\end{aligned} \tag{4.15}$$

$$\begin{aligned}\langle R_{12(13\mathrm{det})/13}\rangle &= \frac{\sum_{i,j} R_{12(13\mathrm{det})/13}(\alpha_i,\delta_j) I_{13}(\alpha_i,\delta_j)}{\sum_{i,j} I_{13}(\alpha_i,\delta_j)} \\ &= \frac{\sum_{i,j} I_{12(13\mathrm{det})}(\alpha_i,\delta_j)}{\sum_{i,j} I_{13}(\alpha_i,\delta_j)}.\end{aligned} \tag{4.16}$$

Only ^{13}CO-detected pixels are used for these calculations.

According to the distribution of deviations for $R_{12/13}$, it differs by $\sim -30-60\%$ within the galaxy. At some positions, it is $\gtrsim 80\%$ ($\sim 200\%$ at most). Deviation of $R_{12(13\mathrm{det})/12}$ also shows significant variations; it is higher by $\sim 40\%$ and lower by $\sim 100\%$ (excluding ^{13}CO-nondetected pixels, deviation of $R_{12(13\mathrm{det})/12}$ is lower by $\sim 30\%$ at most) than $\langle R_{12(13\mathrm{det})/12}\rangle$ in the whole galaxy. On the other hand, there are small deviations of $R_{12(13\mathrm{det})/13}$. Their variations are within $\sim \pm 30\%$ at most positions. Scatter of $R_{12/13}$, $R_{12(13\mathrm{det})/12}$, and $R_{12(13\mathrm{det})/13}$ is 35.1%, 55.9%, and 19.9%, respectively, measured as the ratio of standard deviation to weighted mean. Weighted mean and standard deviation of each ratio are listed in table 4.2–4.4. $R_{12(13\mathrm{det})/12}$ indicates the largest scatter within the galaxy. Hence, variations of $R_{12/13}$ seen in galaxies so far is mainly produced by that of $R_{12(13\mathrm{det})/12}$ as suggested by previous studies (e.g., Polk et al. 1988; Wilson and Walker 1994; Hüttemeister et al. 2000; Hirota et al. 2010; Morokuma-Matsui et al. 2015).

Table 4.2: Statistics of $R_{12/13}$.

Region	$\langle R_{12/13} \rangle$ (1)	L'_{12}/L'_{13} (2)	$Q_2(R_{12/13})$ (3)	$Q_1(R_{12/13})$ (4)	$Q_3(R_{12/13})$ (5)	$\sigma(R_{12/13})$ (6)
All	12.4	15.1	12.3	10.3	15.3	4.34
Center	12.0	12.0	13.0	11.1	14.9	3.28
Bar	17.4	19.9	17.2	15.2	22.9	5.48
NE bar end	10.7	11.3	10.4	9.37	12.6	3.14
SW bar end	12.6	13.0	12.9	10.9	15.7	3.52
SE arm	12.8	14.9	12.9	11.1	15.9	3.70
NW arm	12.9	14.6	12.9	11.3	15.0	3.59
N lump	10.0	10.3	10.4	8.89	12.0	2.43
SW stream	10.4	10.9	10.0	8.42	12.8	2.78
S bridge	13.4	17.6	13.9	11.8	16.0	3.45
Inter-arm	12.7	36.3	13.3	9.56	15.3	4.00
Outer disk	9.54	54.7	9.27	8.26	10.7	2.34

(1) Weighted mean of $R_{12/13}$.
(2) Luminosity ratio of ^{12}CO($J=1$–0)/^{13}CO($J=1$–0).
(3) Median of $R_{12/13}$.
(4) First quartile of $R_{12/13}$.
(5) Third quartile of $R_{12/13}$.
(6) Standard deviation of $R_{12/13}$.

4.5.3 Statistical difference of the line ratios among galactic structures

Next, we investigate statistical differences in $R_{12/13}$, $R_{12(13\mathrm{det})/12}$, and $R_{12(13\mathrm{det})/13}$ among galactic structures. Figure 4.31 shows violin plots of $R_{12/13}$, $R_{12(13\mathrm{det})/12}$, and $R_{12(13\mathrm{det})/13}$ as well as median, Q_2, weighted mean, luminosity ratio, interquartile range (IQR) in each region and the whole galaxy. Median, luminosity ratio, first quartile Q_1, third quartile Q_3 of each ratio are also summarized in table 4.2–4.4.

As indicated by figure 4.27 and 4.30, $R_{12/13}$ in the bar is systematically higher than that in other regions and the entire galaxy; its weighted mean ratio is higher by $\sim 40\%$ than that in the entire galaxy. Higher $R_{12/13}$ in the bar is also found in other barred spiral galaxies (e.g., Watanabe et al. 2011; Yajima et al. 2019). NE bar end, N lump, SW stream, and the outer disk tend to show lower $R_{12/13}$. The former three may be due to effects of an interaction with another galaxy. Other regions (center, SW bar end, two arms, inter-arm) have a similar value, while SE arm is also heavily affected by an interaction as seen as the elongated one. One may expect that line ratio in the elongated arm is different from other structures. However, it is reported that line ratio in an elongated arm by interaction is not systematically different from that in the other arm in another interacting galaxy (e.g., in NGC 3627, Watanabe et al. 2011; Law et al. 2018).

Table 4.3: Statistics of $R_{12(13\mathrm{det})/12}$.

Region	$\langle R_{12(13\mathrm{det})/12}\rangle$	$L'_{12(13\mathrm{det})}/L'_{12}$	$Q_2(R_{12(13\mathrm{det})/12})$	$Q_1(R_{12(13\mathrm{det})/12})$	$Q_3(R_{12(13\mathrm{det})/12})$	$\sigma(R_{12(13\mathrm{det})/12})$
	(1)	(2)	(3)	(4)	(5)	(6)
All	0.626	0.624	0.327	0.000	0.714	0.350
Center	0.877	0.877	0.861	0.773	0.941	0.144
Bar	0.493	0.493	0.417	0.195	0.569	0.235
NE bar end	0.816	0.816	0.857	0.712	0.907	0.235
SW bar end	0.747	0.747	0.720	0.538	0.835	0.210
SE arm	0.642	0.642	0.687	0.446	0.791	0.261
NW arm	0.634	0.634	0.642	0.400	0.763	0.233
N lump	0.813	0.813	0.840	0.693	0.893	0.174
SW stream	0.739	0.739	0.763	0.689	0.831	0.126
S bridge	0.559	0.559	0.582	0.356	0.729	0.228
Inter-arm	0.192	0.192	0.000	0.000	0.336	0.216
Outer disk	0.116	0.113	0.000	0.000	0.000	0.169

(1)–(6) The same as table 4.2 but for $R_{12(13\mathrm{det})/12}$.

Table 4.4: Statistics of $R_{12(13\mathrm{det})/13}$.

Region	$\langle R_{12(13\mathrm{det})/13}\rangle$	$L'_{12(13\mathrm{det})}/L'_{13}$	$Q_2(R_{12(13\mathrm{det})/13})$	$Q_1(R_{12(13\mathrm{det})/13})$	$Q_3(R_{12(13\mathrm{det})/13})$	$\sigma(R_{12(13\mathrm{det})/13})$
	(1)	(2)	(3)	(4)	(5)	(6)
All	9.53	9.42	9.18	8.04	10.3	1.89
Center	10.5	10.5	10.6	9.93	11.7	1.18
Bar	9.94	9.79	9.37	8.17	10.8	2.19
NE bar end	9.19	9.20	9.10	8.35	10.1	1.53
SW bar end	9.73	9.72	9.66	8.60	10.3	1.59
SE arm	9.48	9.55	9.37	8.40	10.6	1.87
NW arm	9.30	9.27	9.48	8.28	10.2	1.64
N lump	8.37	8.41	8.50	7.51	9.33	1.54
SW stream	7.87	8.09	7.71	7.04	8.72	1.32
S bridge	9.44	9.87	9.31	8.40	10.4	1.98
Inter-arm	7.19	6.94	6.94	5.85	8.45	1.72
Outer disk	5.63	6.17	5.50	4.70	6.45	1.22

(1)–(6) The same as table 4.2 but for $R_{12(13\mathrm{det})/13}$.

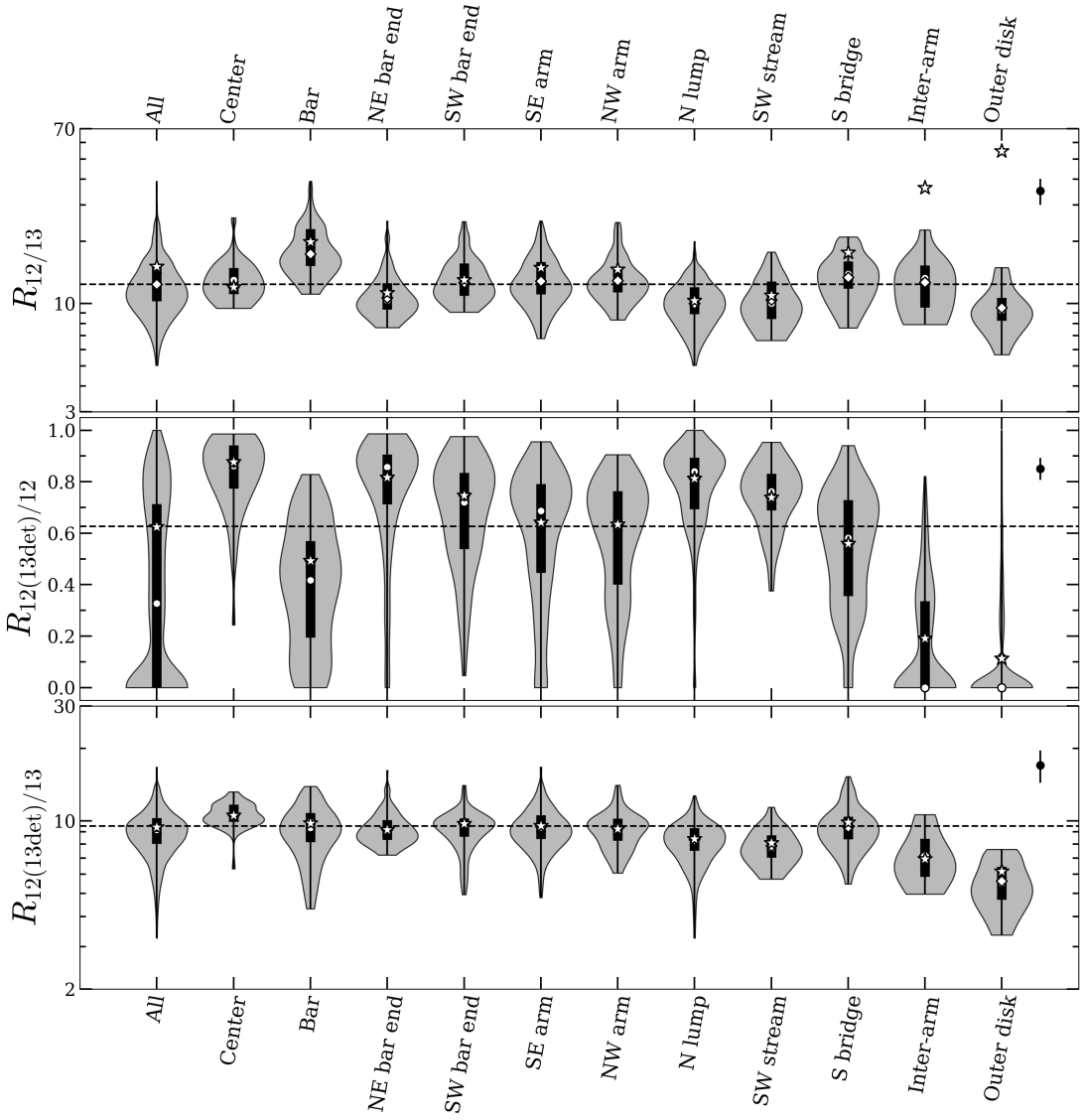

Figure 4.31: Violin plots of $R_{12/13}$ (top), $R_{12(13\mathrm{det})/12}$ (middle), $R_{12(13\mathrm{det})/13}$ (bottom) in each region. Circle, diamond, and star markers represent median, weighted mean ratio, and luminosity ratio, respectively. Thick bars in violin plots indicate the interquartile range. Horizontal dashed lines are each weighted mean ratio within the entire galaxy. Typical errors in logarithmic scale for each ratio are also represented in the top right corner with solid circle markers.

The similar value of $R_{12/13}$ at the galactic center to that in the disk (in especial, arms) is not ubiquitous. Galactic centers with active star formation tend to be higher $R_{12/13}$ associated with warm, diffuse molecular gas (e.g., Paglione et al. 2001; Hirota et al. 2010), however, centers harboring moderate or quiescent star-formation activity have close values of $R_{12/13}$ to the disk (Yajima et al. 2021). Although Maffei 2 has the moderate starburst nucleus, its effect may be limited according to our derived $R_{12/13}$. $\langle R_{12/13} \rangle$ and $Q_2(R_{12/13})$ in inter-arm and the outer disk is somewhat low, although luminosity ratio is high (it is due to considering ^{13}CO-nondetected pixels). Its possible cause is discussed in two paragraphs later.

The $R_{12(13\mathrm{det})/12}$ distribution shows that a large fraction of ^{12}CO($J = 1$–0) emission involves

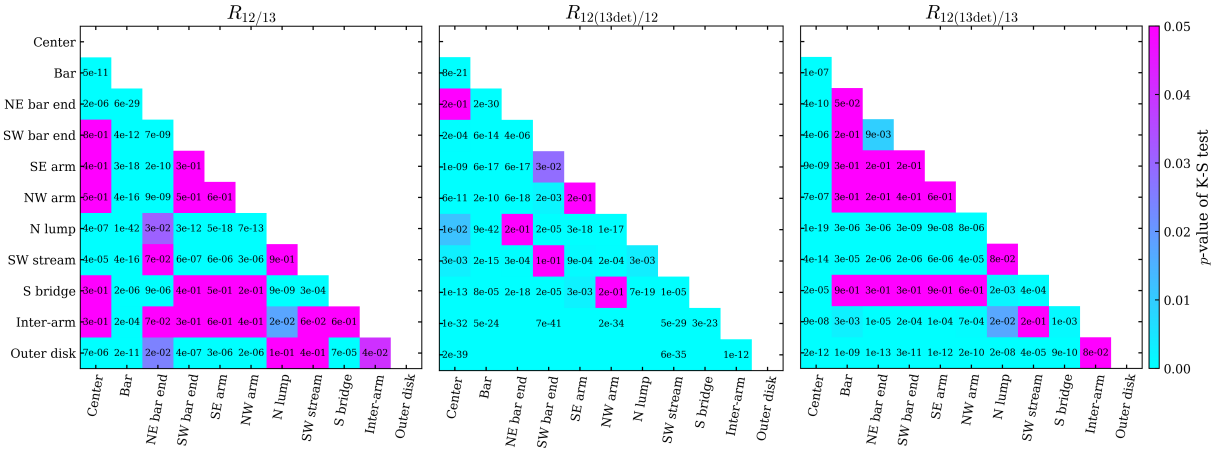

Figure 4.32: Matrices of p-values of the Kolmogorov–Smirnov test between each region for $R_{12/13}$ (left), $R_{12(13\mathrm{det})/12}$ (center), $R_{12(13\mathrm{det})/13}$ (right). Each p-value is denoted in each pixel, unless it is $< 10^{-100}$.

^{13}CO($J = 1$–0) emission in the center, NE bar end, N lump, and SW stream. Their $\langle R_{12(13\mathrm{det})/12} \rangle$ are higher by $\sim$ 30–40% than that of the entire galaxy. Like $R_{12/13}$, higher $R_{12(13\mathrm{det})/12}$ in the latter three structures would be caused by the interaction. Although $R_{12(13\mathrm{det})/12}$ in SW bar end is not as high as that in NE bar end, it is also slightly higher than the average. The two arms show almost averaged values. The bar prefers low $R_{12(13\mathrm{det})/12}$ like its $R_{12/13}$ tendency; $R_{12(13\mathrm{det})/12}$ is lower by $\sim$ 21% than the average. In inter-arm and the outer disk, ^{13}CO($J = 1$–0) is barely detected, as a result, $R_{12(13\mathrm{det})/12}$ there is much lower than other regions.

Unlike $R_{12/13}$ and $R_{12(13\mathrm{det})/12}$, $R_{12(13\mathrm{det})/13}$ in each region shows a very small variation as seen in figure 4.27 and 4.30. Except for the center, N lump, SW stream, inter-arm, and the outer disk, all regions have similar values. $R_{12(13\mathrm{det})/13}$ of the center is slightly high. $R_{12(13\mathrm{det})/13}$ is also relatively lower in N lump and SW stream, which is the same tendency as $R_{12/13}$ and $R_{12(13\mathrm{det})/12}$. Thus, the interaction may also exert influences on not only proportion of the cloud-component molecular gas but also properties of clouds through some processes such as compression of clouds by their distorted and crowded orbits. As a consequence, $R_{12(13\mathrm{det})/13}$ decreases.

Lower ^{12}CO/^{13}CO line ratio in inter-arm and the outer disk is not consistent with results of other galaxies (e.g., Morokuma-Matsui et al. 2015; Muraoka et al. 2016; Yajima et al. 2021). The lower line ratio indicates that molecular clouds in these regions are relatively denser than those in other regions. It is unlikely because star-formation activity in inter-arm and the outer disk is usually quiescent (e.g., Leroy et al. 2008; Momose et al. 2010; Muraoka et al. 2019). Moreover, virial parameter for GMCs and GMAs in inter-arm is higher than that in arms (e.g., Muraoka et al. 2009; Pan and Kuno 2017; Hirota et al. 2018) and H_2 number density of there is lower than that in arms (Topal et al. 2014). A theoretical simulation shows that survived molecular clouds from strong shear in inter-arm show lower virial parameter (Pettitt et al. 2018). It might be a possible mechanism to explain low ^{12}CO/^{13}CO line ratio in inter-arm and the outer disk. However, a more natural interpretation of low ^{12}CO/^{13}CO line ratio in these regions is relative lack of ^{13}CO($J = 1$–0) sensitivity to that of ^{12}CO($J = 1$–0). Namely, relatively bright ^{13}CO($J = 1$–0) to ^{12}CO($J = 1$–0) is biased at locations where ^{12}CO($J = 1$–0) is weak. It leads to unexpected low line ratio.

Mean $I_{12(13\mathrm{det})}$ in inter-arm and the outer disk for non-zero pixels is 3.8 and 3.0 K km s^{-1}, respectively. Thus, if $R_{12(13\mathrm{det})/13} = 9.5$, which is the typical value within the galaxy, the expected mean I_{13} in inter-arm and the outer disk is 0.40 and 0.32 K km s^{-1}, respectively. They correspond to $2.9\,\sigma$ and $2.3\,\sigma$, respectively. Such pixels where S/N is too low are masked in the current analysis. Lower $R_{12(13\mathrm{det})/13}$ in inter-arm and the outer disk than other regions is in fact due to poor S/N of ^{13}CO($J=1$–0) and weak ^{12}CO($J=1$–0) (since ^{12}CO emission is weak in these regions, higher sensitivity of ^{13}CO is needed to produce a similar value in other regions).

To check statistical differences in ratios among the regions, the Kolmogorov–Smirnov (K–S) test is applied. The p-values resulting in the K–S test are shown in figure 4.32 as matrices. Those of $R_{12(13\mathrm{det})/12}$ are significantly and systematically less than those of $R_{12/13}$. In particular, peculiarities of the bar, inter-arm, and the outer disk become more significant. In figure 4.32, the number of tiles where p-values is higher than 0.05 decreases from 21 (in $R_{12/13}$) to 5 (in $R_{12(13\mathrm{det})/12}$). Thus, the null hypothesis that the distributions are the same can be rejected with higher accuracy in $R_{12(13\mathrm{det})/12}$ (difference of the ratio between different regions is more significant in $R_{12(13\mathrm{det})/12}$ compared to $R_{12/13}$).

In contrast, p-values of $R_{12(13\mathrm{det})/13}$ are systematically higher than those of $R_{12/13}$ in disk regions (bar, bar ends, arms, and the bridge structure). Statistical difference in $R_{12(13\mathrm{det})/13}$ among these regions cannot be recognized at the 5% significance level. Note that the small p-value between NE bar end and SW bar end is not due to different mean but different profile of their distributions. Their weighted mean ratio, luminosity ratio, and IQR are so close. Therefore, it is considered that there is no systematic difference in $R_{12(13\mathrm{det})/13}$ between bar ends. In figure 4.32, the number of pairs where p-values are higher than 0.05 decreases from 21 to 17 in $R_{12(13\mathrm{det})/13}$ comparing to $R_{12/13}$. Although p-values for a majority of pairs do not increase in $R_{12(13\mathrm{det})/13}$, when inter-arm and the outer disk, which would not achieve enough S/N are excluded, the number of pairs where p-values are higher than 0.05 increases from 12 (in $R_{12/13}$) to 15 (in $R_{12(13\mathrm{det})/13}$). Therefore, statistical differences in $R_{12(13\mathrm{det})/13}$ for a majority of regions in the disk (in particular, the bar, bar ends, arms, and S bridge as in figure 4.32) tend to be unrecognizable.

According to these results, differences in ratios among regions are larger in the order of $R_{12(13\mathrm{det})/12} > R_{12/13} > R_{12(13\mathrm{det})/13}$. Hence, structures of the galaxy can exert strong influences on the proportion of the cloud/diffuse-phase molecular gas (i..e., formation and destruction of the cloud-phase molecular gas) inferred from $R_{12(13\mathrm{det})/12}$. On the other hand, their effects are not strong enough to change properties of the cloud-phase molecular gas as seen in Pan and Kuno (2017).

4.5.4 Effects of the cloud-component fraction on star formation

The results above suggest that an important factor to characterize physical properties of molecular gas is proportion of cloud-phase (diffuse-phase) molecular gas to total molecular gas. Therefore, we examine the Kennicutt–Schmidt (K–S) relation using I_{12}, $I_{12(13\mathrm{det})}$, and I_{13}, to investigate effects of cloud-phase fraction and properties of clouds on star formation. As a tracer of SFR, intensity of WISE 12 μm, $I_{12\,\mu\mathrm{m}}$, is used. It is often adopted as a SFR tracer (e.g., Cluver et al. 2017). Unlike our CO data, the 12 μm data does not show any clumpy structures associated with clouds in the Galaxy, although a few foreground stars are seen outside the disk of

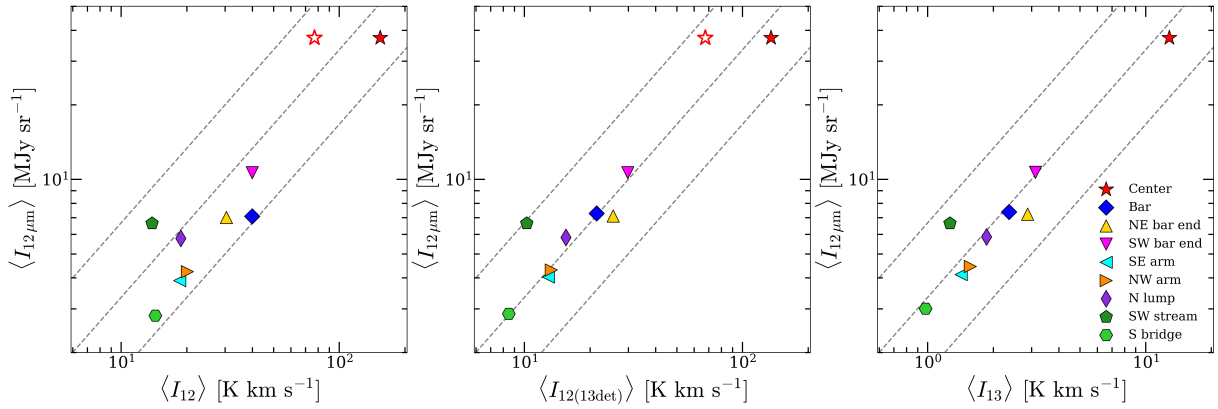

Figure 4.33: Kennicutt–Schmidt relations using I_{12} (left), $I_{12(13\mathrm{det})}$ (center), and I_{13} (left) as a tracer of molecular gas surface density and WISE 12 μm intensity as a SFR surface density averaging over each region. Inter-arm and outer disk regions are excluded, because there are a few ^{13}CO($J=1$–0)-detected pixels. Dashed lines from the bottom left to the top right indicate that $I_{12\,\mu\mathrm{m}}/I_{12}$, $I_{12\,\mu\mathrm{m}}/I_{12(13\mathrm{det})}$ are 2/3, 1/3, 1/6 (MJy sr^{-1})/(K km s^{-1}) for the left and center panel, and $I_{12\,\mu\mathrm{m}}/I_{13}$ is 20/3, 10/3, 5/3 (MJy sr^{-1})/(K km s^{-1}). Along these dashed lines, SFE is a constant. Open star markers in the left and center panels are the result for the central region considering lower X_{CO} of 0.75×10^{20} cm^{-2} (K km s^{-1})$^{-1}$ (Meier et al. 2008). Note that the range of the x-axis is different from the left and central panel, and the right, but its dynamic range is fixed (about 1.5 dex) for all panels.

Maffei 2 (see figure 4.2)[5]. Therefore, we derived intensity of foreground emission as the median of intensity outside the disk of Maffei 2 and made use of the foreground-subtracted data as a SFR traser.

Figure 4.33 shows K–S relations derived from I_{12}, $I_{12(13\mathrm{det})}$, and I_{13} as a tracer of molecular gas surface density. Mean $I_{12\,\mu\mathrm{m}}$, I_{12}, $I_{12(13\mathrm{det})}$, and I_{13} averaged over each structure are plotted. Results of inter-arm and the outer disk are not shown, because diffuse IR emission (e.g., Liu et al. 2011; Rahman et al. 2011) remains, which comes from stochastically heated small dust grains (e.g., Desert et al. 1990) and old stars (e.g., Draine et al. 2007; Verley et al. 2009), even if the foreground Galactic emission is subtracted by deriving it from mean $I_{12\mu\mathrm{m}}$ outside the disk of Maffei 2. The diffuse IR emission leads to unreliable high SFE in these regions with weak CO emission. For I_{12} and $I_{12(13\mathrm{det})}$ of the center, we plot two results considering the standard X_{CO} and the lower X_{CO} derived by Meier et al. (2008). However, the discussed area by Meier et al. (2008) is within the nuclear starburst ring. It is a smaller area than our defined region as the center, so that the expected mean molecular gas surface density in the center region is somewhere in the range between these two results.

Figure 4.33 clearly shows differences in ratios of $I_{12\,\mu\mathrm{m}}$ to each CO integrated-intensity (equivalent to SFE) among regions except for SW stream decrease, when $I_{12(13\mathrm{det})}$ and I_{13} are used instead of I_{12}. Variation of SFE among all regions derived from I_{12}, $I_{12(13\mathrm{det})}$, and I_{13} is 36%, 31%, and 24%, respectively as the ratio of standard deviation of SFE to mean SFE of all regions. It decreases by 12% from I_{12} to $I_{12(13\mathrm{det})}$, and by 22% from $I_{12(13\mathrm{det})}$ to I_{13}. When SW stream, which seems to be heavily affected by interaction excluded, the variation of SFE is 18%, 11%, and 8.9%, respectively. It decreases by 39% from I_{12} to $I_{12(13\mathrm{det})}$, and by 19% from $I_{12(13\mathrm{det})}$ to I_{13}. Namely, by removing the diffuse component which is difficult to contribute to star for-

[5] These point sources are recognized as stars in the Galaxy, because they are disappeared in the WISE 22 μm image

mation, SFE becomes close to uniform, excepting SW stream as the peculiar region. Hence, proportion of cloud (diffuse)-phase molecular gas to total molecular gas also affects star formation. Variations of SFE seen in other galaxies so far introduced in section 1 would be attributed to this proportion.

The slope (index) of the K–S relation becomes closer to unity from I_{12} to $I_{12(13\mathrm{det})}$ and I_{13}. This tendency would be relevant to the linear K–S relation by dense gas (e.g., Gao and Solomon 2004b; Narayanan et al. 2008; Lada et al. 2010). Molecular gas more related to star formation would produce such a linear relation. Moreover, it is found that SFE is correlated with number density of molecular gas and molecular gas density is affected by large-scale velocity dispersion of gas in the barred spiral galaxy NGC 4303 (Yajima et al. 2019). According to our result, molecular gas dynamics on a large scale changes the proportion of the cloud phase of molecular gas and as a result, SFE is changed. Moreover, molecular clouds would be robust against dynamical environment, considering rather constant $R_{12(13\mathrm{det})/13}$ in the galaxy.

4.5.5 Implications

Our results indicate that the proportion of the cloud/diffuse component to total molecular gas has large variations within Maffei 2. In contrast, the cloud-phase molecular gas is insensitive to its environments induced by galactic structures as other studies indicate (e.g., Donovan Meyer et al. 2013; Colombo et al. 2014; Maeda et al. 2020a). Decreasing the cloud-component molecular gas in the bar is attributed to large velocity dispersion and velocity gradient due to the non-axisymmetric potential. In inter-arm, shear is strong (e.g., Miyamoto et al. 2014; Pettitt et al. 2018). A large fraction of the diffuse component in inter-arm is produced by the reason. In addition to the outer disk, it is also possible that low transition between H I and H_2 because of low column density (shelf shielding of hydrogen is not enough). In these regions, even if H_2 is formed, molecular gas is easily dissociated and it is difficult to form cloud-like structures.

Rather constant properties of the cloud component can be interpreted as follows. One possibility is that GMCs are stable, so that they cannot become dense by shrinking due to self-gravity. Meidt et al. (2021) derived that fraction of self-gravitating molecular gas to total molecular gas is only $\sim$ 40–60%. About half of molecular gas is just collected by the galactic potential. Meidt et al. (2018, 2020) showed that when molecular clouds are not associated with the potential of the galaxy, they are stabilized and collapsing timescale becomes long. In addition, most molecular clouds traced by ^{12}CO lines are gravitationally unbound or sub-virialized (Schruba et al. 2019; Zetterlund et al. 2019; Evans et al. 2021). Several simulations also support these scenarios (e.g., Dobbs et al. 2011a; Ward et al. 2014; Treß et al. 2021). Even for molecular clouds traced by ^{13}CO($J=1$–0), they are sub-viriarized in the Galaxy ($\alpha_{\mathrm{vir}} > 1$ for most of clouds and its median is 1.9; Heyer et al. 2009). Dense clumps detected in HCO^+ line are still pressure confined objects (Barnes et al. 2016). Inoue et al. (2021) also showed that arms of local spiral galaxies are gravitationally stable and arms will not be fragmented. It is expected that clouds are difficult to contract due to such weak contribution of self-gravity.

Focusing on only arms, recent studies have revealed that effects of arms on molecular gas. For example, streaming motion across arms can stabilize molecular clouds by reducing surface pressure on them (Meidt et al. 2013). In the Galaxy, dense gas fraction, SFE within each GMC, and fraction of star-forming dense clumps to total clumps are not enhanced across arms (e.g.,

Ragan et al. 2018; Urquhart et al. 2021). Moreover, properties of molecular clouds are not so different between arms and inter-arm (e.g., Colombo et al. 2021). Differences in properties of dense clumps are much greater from one clump to another than those between arms and inter-arm (Rigby et al. 2019). Since the Galaxy is considered to be a multiple-armed spiral galaxy, spiral shock may not be strong enough to affect molecular gas properties.

However, even in the grand-design galaxy M 51 where strong spiral shock is expected, there is no gradient of age for star clusters across an arm (Schinnerer et al. 2017), whereas more massive clumps are observed and the onset of star formation seems to be occurred in the downstream of an arm (e.g., Egusa et al. 2011). In addition, virial parameter and depletion time of molecular gas are not systematically different between arms and inter-arm in M 51 (Colombo et al. 2014; Leroy et al. 2017a). Elmegreen and Elmegreen (1986) showed that there is no difference of SFR between grand-design galaxies and galaxies without grand-design spirals. Foyle et al. (2010) reported that enhancement of SFE in arms is limited in M 51 and another grand-design galaxy NGC 628, although SFE in arms may be underestimated, because they derived molecular gas mass from ^{12}CO($J=2$–1) with a fixed ^{12}CO($J=2$–1)/^{12}CO($J=1$–0) line ratio and the line ratio is usually higher in arms than that in inter-arm (e.g., Koda et al. 2012; Koda et al. 2020; Yajima et al. 2021). Elmegreen et al. (2018) also estimated SFR of star-forming clumps found by the composite image of Spitzer/IRAC four-band images of M 100 and concluded that effects of arms on star formation are small. Querejeta et al. (2021b) found that impacts of galactic structures such as bars and bulges as well as arms on SFE are elusive. It may also be possible that variations of SFE among structures are underestimated, because they used ^{12}CO($J=2$–1) as a tracer of molecular gas with a fixed ^{12}CO $J=2$–1/$J=1$–0 ratio and the K–S relation by ^{12}CO($J=2$–1) is linear (e.g., Bigiel et al. 2011; Momose et al. 2013; Yajima et al. 2021).

Our results do not show $R_{12(13\mathrm{det})/13}$ gradient across arms in Maffei 2. It suggests that the cloud-phase molecular gas is not compressed by spiral shock. Tosaki et al. (2007) found a GMA with lower ^{12}CO($J=1$–0)/^{13}CO($J=1$–0) line ratio (both in integrated-intensity and peak intensity maps) in the downstream of an arm than that in upstream in M 31. They argued that the GMA is compressed by spiral shock. Since their spatial resolution is $\sim$ 50 pc, compressed molecular clouds might be observed in other galaxies with as high resolution as theirs, nevertheless, this anticipation is in contradiction with observational results in the Galaxy. Hence, the GMA they found may be compressed by another process except for spiral shock.

Theoretical studies also indicate that effects of spiral arms on gas properties and star formation are limited (e.g., Dobbs et al. 2011b; Dobbs et al. 2015; Kim et al. 2020; Pettitt et al. 2020; Treß et al. 2021). The role of arms is collecting molecular gas, enhancing the conversion of H I gas into molecular gas, and forming molecular clouds (e.g., Tokuda et al. 2020). Arms do not compress molecular clouds, make further clouds dense, nor enhance dense gas fraction and SFE. In this sense, arms indirectly induce star formation.

Bar ends often show active star formation (e.g., Watanabe et al. 2011; Yajima et al. 2019; Bešlić et al. 2021). The Galaxy also has the massive-star forming region W43 at its bar end. Converging gas from a bar and an arm is suggested as its reason (e.g., Motte et al. 2014; Kohno et al. 2021b). Mean molecular gas density in bar ends is actually higher than that in arms and bar (Yajima et al. 2019). However, $R_{12(13\mathrm{det})/13}$ in bar ends of Maffei 2 is comparable to other regions. Its discrepancy would originate from the fact that dense clumps formed by gas

convergence are spatially small ($\sim$ 10 pc; Kohno et al. 2021b). At the current spatial resolution of our data, these clumps cannot be observed. Moreover, Kohno et al. (2021b) found that PDF of ^{12}CO($J=1$–0) and ^{13}CO($J=1$–0) are similar between W43 and other star-forming regions W51 and M 17, however, that of C^{18}O($J=1$–0) for W43 has the bright-end tail and others do not. Therefore, dense gas formed by gas converging in bar ends is traced by not ^{13}CO($J=1$–0) but C^{18}O($J=1$–0) and it is not reflected by $R_{12(13\mathrm{det})/13}$ in our measurements.

The high-resolution observation of dense gas traced by C^{18}O, HNC, and HCO$^+$ toward NGC 3627 shows enhanced higher dense gas fraction in its bar ends (Bešlić et al. 2021). They used ^{12}CO($J=2$–1) as a tracer of total molecular gas, however, ^{12}CO($J=2$–1)/^{12}CO($J=1$–0) line ratio systematically increases in high SFR regions and decreases when SFR is low (e.g., Yajima et al. 2021) and actually the line ratio is high in the center and bar ends in this galaxy (Law et al. 2018). Thus, Σ_{mol} would be overestimated in the center and bar ends, and underestimated in the bar and arms. As a result, higher dense gas fraction in bar ends than that in the bar and arms would appear.

It is not likely that the small variation of $R_{12(13\mathrm{det})/13}$ in the galaxy is due to the saturation of ^{12}CO($J=1$–0)/^{13}CO($J=1$–0) line ratio. The line ratio can attain saturation when molecular gas density exceeds $\sim 10^4$ cm^{-3} according to a non-LTE calculation (Leroy et al. 2017b). Such high density is reached in dense and small clumps (the typical size is a few pc) which are traced by dust (Zetterlund et al. 2019). Such small dense clumps would not contribute to our observational data. Hence, ^{13}CO($J=1$–0) observed here is not thermalized and somewhat uniform $R_{12(13\mathrm{det})/13}$ over the galaxy reflects uniformity of the cloud-phase molecular gas properties.

Our results provide a clue to unexpected low SFE per free-fall time $\varepsilon_{\mathrm{ff}}$ and conversion efficiency of gas into stars $\varepsilon_{\mathrm{SF}}$ (i.e., "star-formation efficiency" in the context of studies for ISM in the Galaxy) reported by many studies (e.g., Murray 2011; Utomo et al. 2018; Schruba et al. 2019). If self-gravity in GMCs is not superior as inferred from small variation of $R_{12(13\mathrm{det})/13}$ as well as results found in other studies (e.g., Dobbs et al. 2011a; Evans et al. 2021), it is difficult for GMCs to contract and become dense. This may be also a reason for low dense gas fraction which induces the gap of two orders of magnitude between depletion time of molecular gas and that of dense molecular gas (Torii et al. 2019). Moreover, not all molecular gas contributes to star formation or the time scale of star formation for the diffuse-component molecular gas is long as seen in section 4.4. These factors may be partially responsible for low $\varepsilon_{\mathrm{ff}}$ and $\varepsilon_{\mathrm{SF}}$.

4.6 Summary of this chapter

We investigate that how significant the fraction of the cloud/diffuse-component molecular gas is for characterizing properties of molecular gas and star formation, in comparison with effects of properties of clouds. To that end, the simultaneous mapping of ^{13}CO($J=1$–0) and ^{12}CO($J=1$–0) was conducted toward the nearby barred spiral galaxy Maffei 2 with the Nobeyama 45 m telescope. ^{12}CO($J=1$–0) is considered as a tracer of total molecular gas and ^{13}CO($J=1$–0) is considered as a tracer of more structured, the cloud component inside molecular gas because of its low opacity. The main results and implications of this paper are as follows.

1. Galactic emission is seen at some velocities. We developed a new algorithm to automatically separate observational data into foreground Galactic emission and background emission

of Maffei 2. Thanks to it, Galactic emission is successfully removed Extracted Galactic emission shows clumpy structures around -50 km s^{-1} (corresponding to the Perseus Arm) and an extended distribution around 0 km s^{-1} (corresponding to the Orion Spur). Mass of clumps in the Perseus Arm is $\sim 10\ M_\odot$ and column density of H_2, $N(H_2)$, for Galactic emission is 10^{20}–10^{21} cm^{-2} (section 4.4.1–4.4.2, figure 4.16–4.22).

2. The removal of Galactic emission reveals characteristic distributions of molecular gas such as the "?"-shaped structure in N lump, the bridge feature connecting SE arm and SW bar end, and the stream from SW bar end toward the southeast. ^{12}CO($J=1$–0) shows the extended and diffuse disk beyond spiral arms and in inter-arm (section 4.4.2, figure 4.23).

3. ^{12}CO($J=1$–0) emission is three-dimensionally decomposed into the cloud component and the diffuse component based on detection of ^{13}CO($J=1$–0) at each voxel. It is found that intensity of ^{13}CO($J=1$–0)-detected ^{12}CO($J=1$–0) appears from 0.08 K, which corresponds to $N(H_2) \sim 1.6 \times 10^{20}$ cm^{-2}. ^{13}CO($J=1$–0)-nondetected ^{12}CO($J=1$–0) can be seen up to 0.5 K [$N(H_2) \sim 10^{21}$ cm^{-2}]. Namely, ^{13}CO($J=1$–0) is not always detected because of high column density. ^{13}CO-nondetected ^{12}CO($J=1$–0) is often seen in wings of its spectra. In some positions, secondary peaks of ^{12}CO($J=1$–0) does not show ^{13}CO emission (section 4.4.3, figure 4.25 and 4.26).

4. The luminosity of ^{12}CO($J=1$–0) without ^{13}CO($J=1$–0) detection accounts for 37.6% of total ^{12}CO($J=1$–0) luminosity. Integrated intensity of ^{13}CO-detected ^{12}CO($J=1$–0), $I_{12(13\mathrm{det})}$, is distributed like that of ^{13}CO($J=1$–0). That of ^{13}CO-nondetected ^{12}CO($J=1$–0), $I_{12(13\mathrm{nondet})}$, shows the extended disk and the cavity at the center, and is remarkable in the bar (section 4.4.3, figure 4.27).

5. $R_{12/13} \equiv I_{12}/I_{13}$ is high in the bar and periphery of arms, and low in a part of arms and the N lump. $R_{12(13\mathrm{det})/12} \equiv I_{12(13\mathrm{det})}/I_{12}$, which reflects proportion of the cloud-phase molecular gas, is high at the center, bar ends, and along the spine of arms. In the bar, $R_{12(13\mathrm{det})/12}$ is quite low on average, however, it is relatively higher along the offset ridge of the leading side than that in other positions of the bar. In contrast, $R_{12(13\mathrm{det})/13} \equiv I_{12(13\mathrm{det})}/I_{13}$, which indicates properties of the cloud-phase molecular gas, is rather constant over the galaxy (section 4.5.1, figure 4.27).

6. Comparing $R_{12(13\mathrm{det})/12}$ and $R_{12(13\mathrm{det})/13}$ with the conventional line ratio $R_{12/13}$, the correlation of $R_{12/12(13\mathrm{det})}$ (note that the numerator and denominator are exchanged) and $R_{12/13}$ is tight and prefers strong linearity. It indicates $R_{12(13\mathrm{det})/13}$ has small variations in Maffei 2. The correlation of $R_{12(13\mathrm{det})/13}$ with $R_{12/13}$ also shows the positive one, however, it is more ambiguous (section 4.5.1, figure 4.28).

7. The scatter of $R_{12/13}$, $R_{12(13\mathrm{det})/12}$, and $R_{12(13\mathrm{det})/13}$ within the galaxy is 35.1%, 55.9%, and 19.9%, respectively, as derived by their standard deviation over weighted mean. Since $R_{12(13\mathrm{det})/12}$ has the largest scatter, variations of $R_{12/13}$ seen in other galaxies so far are caused by that of $R_{12(13\mathrm{det})/12}$. The small variation seen in $R_{12(13\mathrm{det})/13}$ is not due to a small mean of $R_{12(13\mathrm{det})/13}$ (section 4.5.2, figure 4.30, table 4.2–4.4).

8. The statistical comparison of each ratio between 11 galactic regions reveals that $R_{12/13}$ is systematically higher by $\sim 40\%$ in the bar and lower in NE bar end, N lump, SW stream,

and the outer disk (for the outer disk, its luminosity ratios is higher) than the weighted mean over the galaxy. $R_{12(13\mathrm{det})/12}$ is high in the center, NE bar end, N lump, and SW stream and low in the bar, inter-arm, and the outer disk. $R_{12(13\mathrm{det})/13}$ is not so different among the bar, bar ends, arms, and S bridge. In N lump, NE bar end, and SW stream, effects by an interaction would change these ratios (section 4.5.3, figure 4.31, table 4.2–4.4).

9. According to results of the Kolmogorov–Smirnov test for each ratio between regions, the number of combinations of regions whose p-values are less than 0.05 is larger in $R_{12(13\mathrm{det})/12}$ than that in $R_{12/13}$. Moreover, peculiarities of the bar, inter-arm, and the outer disk become more significant in $R_{12(13\mathrm{det})/12}$ seen as their decreased p-values. On the other hand, the number of combinations of the regions in the disk (the bar, bar ends, arms, S bridge) whose p-values are less than 0.05 is less in $R_{12(13\mathrm{det})/13}$ than that in $R_{12/13}$. From these results, the hypothesis that there are no differences among regions can be rejected with higher accuracy in $R_{12(13\mathrm{det})/12}$ compared to $R_{12/13}$. In contrast, statistical differences among regions tend to be unrecognizable in $R_{12(13\mathrm{det})/13}$. Importance to characterize properties of molecular gas is $R_{12(13\mathrm{det})/12} > R_{12/13} > R_{12(13\mathrm{det})/13}$ (section 4.5.3, figure 4.32).

10. When I_{12}, $I_{12(13\mathrm{det})}$, and I_{13} are used for the Kennicutt–Schmidt relation, differences of SFE between galactic regions become smaller if $I_{12(13\mathrm{det})}$ and I_{13} are used instead of I_{12} except for SW stream. Excluding SW stream, the difference of SFE derived from $I_{12(13\mathrm{det})}$ and I_{13} among galactic regions is lower by $\sim 40\%$ than that using I_{12}. Thus, SFE is close to uniform when diffuse-phase molecular gas which seems to be difficult to contribute to star formation is not considered. This result indicates that proportion of cloud (diffuse)-phase molecular gas also affects star formation; it is also an important factor for star formation (section 4.5.4, figure 4.33).

11. Our results indicate that structures in the galaxy promote formation and destruction of the cloud/diffuse-component molecular gas as seen in variations of $R_{12(13\mathrm{det})/12}$. However, properties of the cloud-phase molecular gas are not so changed by them as far as referring $R_{12(13\mathrm{det})/13}$. The cloud-phase molecular gas is insensitive to galactic structures. A possibility for the interpretation of rather unchanged properties of cloud-component molecular gas is low contribution of its self-gravity. Structures of the galaxy just collect molecular gas, however, they further do not compress molecular gas and enhance dense gas formation and star formation. This study would also provide a clue to the unexpected low efficiency of star formation per free-fall time and inefficient conversion from molecular gas into stars (section 4.5.5).

Chapter 5

Properties of giant molecular clouds and molecular gas in the starburst galaxy NGC 1808

5.1 Abstract of this chapter

Galaxies show differences in star formation among their structures, and one of the possible reasons for this is that the properties of the molecular clouds differ among the associated structures. We investigate dependence of the global molecular gas state and the properties of giant molecular clouds (GMCs) on environments in the nearby barred spiral galaxy NGC 1808, which harbor the starburst activity at its center using data obtained by Atacama Large Millimeter/submillimeter Array (ALMA). We found that the ratio of the missing flux for the ALMA 12 m array in the bar is approximately 30% to 60% as it approaches the center. It may indicate that molecular gas is gradually converted into a diffuse component due to the shear and velocity gradient as it falls along the offset ridge of the bar. 275 GMCs are identified in this galaxy. Comparing the properties of the GMCs between galaxy regions, we find that virial parameter $\alpha_{\rm vir}$ of GMCs in the bar is significantly higher than that in arms. It implies that the internal motion of the GMC is activated by the global intense gas motion in the bar. In the center, mass and mass density of GMCs significantly increase and $\alpha_{\rm vir}$ decreases as they approach the center. These tendencies remains even when missing flux exists. This result is consistent with implications by Salak et al. (2017) that the accretion of molecular gas on clouds is accelerated as GMCs fall into the center. Moreover, increasing density of GMCs and gravitational instability in the galactic center can be one of the reasons for the starburst in NGC 1808.

5.2 Background of this study

Giant molecular clouds (GMCs) are a main component of interstellar medium (ISM). In addition, stars form in molecular clouds including GMCs. Therefore, to investigate properties of GMCs such as density and gravitational boundness known as virial parameter $\alpha_{\rm vir}$ is important, because they can affect star formation. Since spatially resolved observations for GMCs in extragalaxies need high resolution, such observations are limited to has been revealed that For instance, $\alpha_{\rm vir}$ for GMCs associated with H II regions are systematically lower than those without H II regions

(e.g., Hirota et al. 2011).

It is expected that properties of GMCs are influenced by surrounding environments in galaxies and characters of galaxies. For example, massive, high surface density, and large velocity dispersion GMCs tend to be preferred at galactic centers (e.g., Leroy et al. 2015; Hirota et al. 2018). This tendency is more significant for barred spiral galaxies than non-barred galaxies (Sun et al. 2020). Starburst is also often associated with such extreme environments.

The mechanism of the trigger for starburst is important to understand evolution of galaxies, because it drives quenching of star formation due to removal of gas by galactic wind and outflow (e.g., Bolatto et al. 2013a). In addition, many galaxies in the early universe is in the starburst phase seen in the current universe (e.g., Elbaz et al. 2007; Daddi et al. 2010; Schreiber et al. 2015). Investigating physical properties of molecular gas in starburst regions may give us a clue of galaxy evolution and the activeness of galaxies in the early universe and "cosmic noon". To achieve it, comparing GMC properties between the normal environment for nearby, normal star-forming galaxies and the starburst environment is critical and crucial.

NGC 1808 is a nearby barred spiral galaxy seen mainly from the southern hemisphere ($\delta_{\rm J2000.0} \sim -37^\circ.5$). Optical studies show dust lanes from the center toward the perpendicular direction to the disk (Burbidge and Burbidge 1968; Phillips 1993) indicating outflow, or galactic wind. Many H II regions, young star cluster, and supernova remnants are found in the center (e.g., Forbes et al. 1992; Krabbe et al. 1994; Kotilainen et al. 1996; Tacconi-Garman et al. 1996; Galliano et al. 2005; Galliano and Alloin 2008). They are reported as "hot spots" in more past studies (Morgan 1958; Sérsic and Pastoriza 1965). The nucleus harbors starburst and low-luminosity active galactic nucleus (AGN; Véron-Cetty and Véron 1985; Awaki et al. 1996; Jiménez-Bailón et al. 2005; Heike and Awaki 2007).

This galaxy also has spiral arms and the bar and molecular gas is distributed along them. GMC environments in these structures are expected to be more moderate than the starburst region in the center. Therefore, the comparison of GMC properties among these regions is available in this galaxy. Moreover, we can trace the evolutionary sequence of GMCs from the quiescent environment of spiral arm to the extreme environment of starburst in the galactic center. It will be powerful to attain the goal mentioned above.

Previous studies of molecular gas in NGC 1808 are based on single-dish observations (Salak et al. 2014) or focus on the central region within the circumnuclear ring ($r \lesssim 500$ pc) with high resolution (Salak et al. 2016; 2017; 2018; 2019a). However, GMC properties across the galactic disk are not yet discussed, although Salak et al. (2016) showed the molecular gas distribution in the entire disk and derived non-circular motion in the disk using the ALMA 12-m array data alone. Hence, we investigate GMC properties, their differences, and evolutionary sequences across galactic structures in this study using ALMA feathered (the 12 m array + 7 m array + total power array, the latter two arrays configure the Atacama Compact Array: ACA) data, i.e., no missing-flux data.

5.3 Data and its reduction

Observations toward NGC 1808 with ALMA was carried out on March 8, 2014 in the cycle 1 based on the proposal #2012.1.01004 (PI: Dragan Salak). Both the 12 m array and the ACA

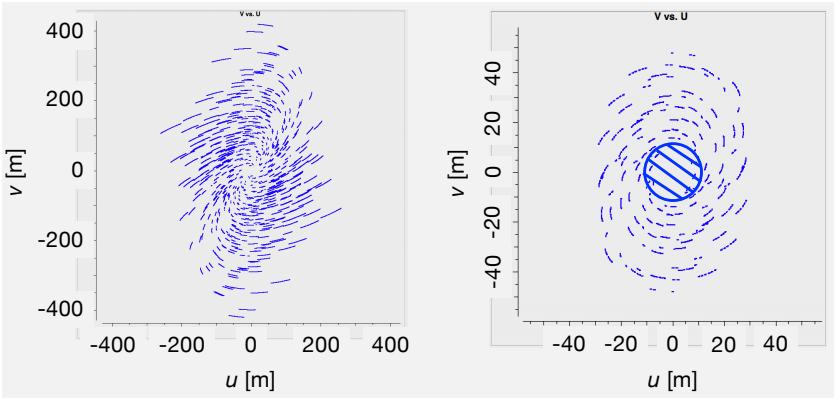

Figure 5.1: *uv* coverage of the 12 m array observation (left) and the Atacama Compact Array (ACA) observation (right). The *uv* coverage corresponding the TP observation is indicated the hatched circle in the right panel.

observations cover the entire disk of this galaxy using the Nyquist sampling of the primary beam. The size of the primary beam and the number of fields for the 12 m array are 50″.8 and 39, respectively. Those for the 7 m array is 86″.4 and 14 respectively. The configuration for the 12 m array is C27-4, thus the number of the 12 m antenna is only 27 because of the early stage of ALMA and this configuration is the fourth most compact out of 10 levels. The shortest and longest baseline for the 12 m array is 15 and 423 m, respectively, The maximum recoverable scale (MRS) $\theta_{\rm MRS}$ ($\approx 0.6\lambda_{\rm obs}/D_{\rm min}$, where $D_{\rm min}$ is the minimum length of baselines) estimated from the former is $21'' \sim 0.92$ kpc. Figure 5.1 shows *uv* coverages for observations with the 12 m array and the 7 m array. The calibrators for flux density, bandpass, and phase are Callisto, the quasar J0609-1542, and the quasar J0522-3627, respectively. More detailed information for the 12 m array observations is described in Salak et al. (2016).

We made use of already intensity-calibrated data by Dr. D. Salak. The subtraction of continua was performed using the task `uvcontsub` of the Common Astronomy Software Applications (CASA; McMullin et al. 2007) ver 5.0.0. Figure 5.2 shows the original dirty (before deconvolu-

Table 5.1: Parameters of NGC 1808.

Parameter	Value
Right Ascension (J2000.0)*	$05^{\rm h}07^{\rm m}42^{\rm s}.343$
Declination (J2000.0)*	$-37°30'45''.95$
Morphological type†	(R)SAB(s)a
Distance‡	9.08 Mpc
Inclination angle§	57°
Position angle*	−36°
Linear scale	44.0 parsec arcsec^{-1}
System velocity (LSR)*	963.9 ± 2.5 km s^{-1}
Nucleus activity‖	H II, Seyfert 2

* Salak et al. (2016).
† de Vaucouleurs et al. (1991).
‡ Tully et al. (2013).
§ Reif et al. (1982).
‖ Véron-Cetty and Véron (2006), NED.

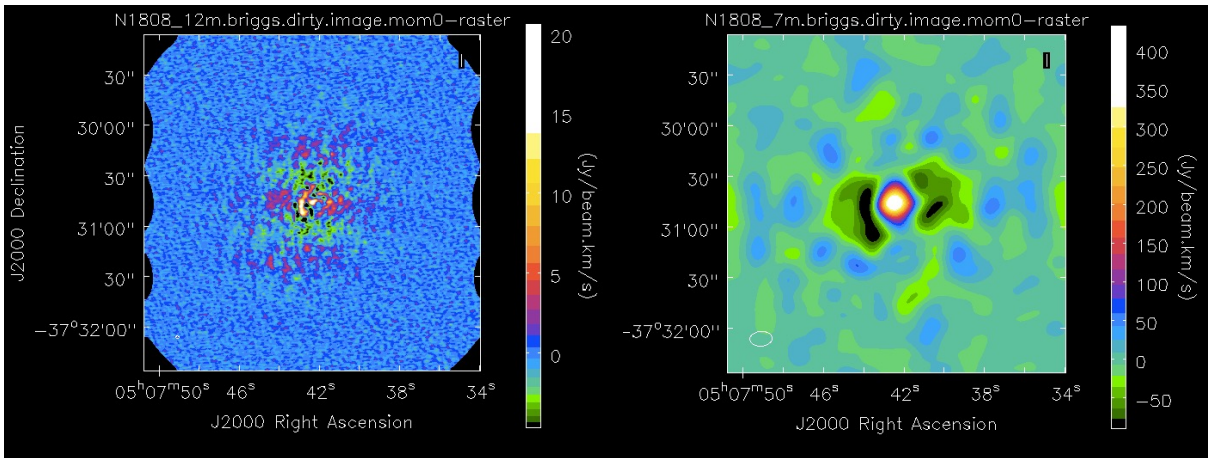

Figure 5.2: Flux distribution of dirty images (before CLEAN) by the ALMA 12 m array (left) and the 7 m array (right). Open ellipticals in the bottom left corner indicate angular resolutions in each panel.

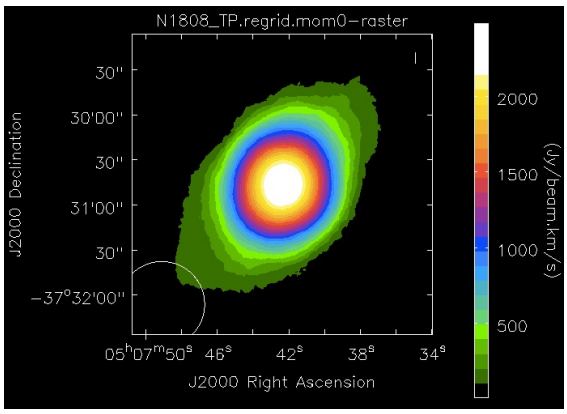

Figure 5.3: Flux distribution by the ALMA total power (TP) array. The large open circle in the bottom left corner indicate angular resolution.

tion, or CLEAN) images of flux[1)] distrubution for the 12 m array and 7 m array. The Briggs weighting at robust = 0.5 (Briggs 1995) was adopted to make maps. Observational data without any process from the raw data is severely affected by the side lobes. This is because sampled visibilities are limited in interferometric observations. We cannot recognize image of the galaxy and analyze the data as it is. Therefore, the CLEAN algorithm (equivalent to deconvolution) was performed using the task `tclean` of CASA. For our scientific analysis, we performed the CLEAN algorithm for the data combining the 12 m and 7 m array with the task `concat`. In addition, we corrected weighing of visibilities for these arrays using the task `statwt` of CASA with reference to https://casaguides.nrao.edu/index.php/DataWeightsAndCombination before the combine of 12 m and 7 m array data, because the definition of weighting for visibilities is different before the ALMA cycle 3. Also, we performed the CLEAN algorithm for the 12 m

[1)] In radio astronomy, "flux density" is referred as radiant power through unit area per unit frequency. The term "flux" is referred to as frequency- or velocity-integrated flux density. Therefore, the unit of flux density and flux are usually "Jy beam^{-1}" and "Jy beam^{-1} km s^{-1}", respectively. Here, "Jy beam^{-1}" is flux coming from the solid angle of the synthesized beam. Thus, it is not normalized by the solid angle.

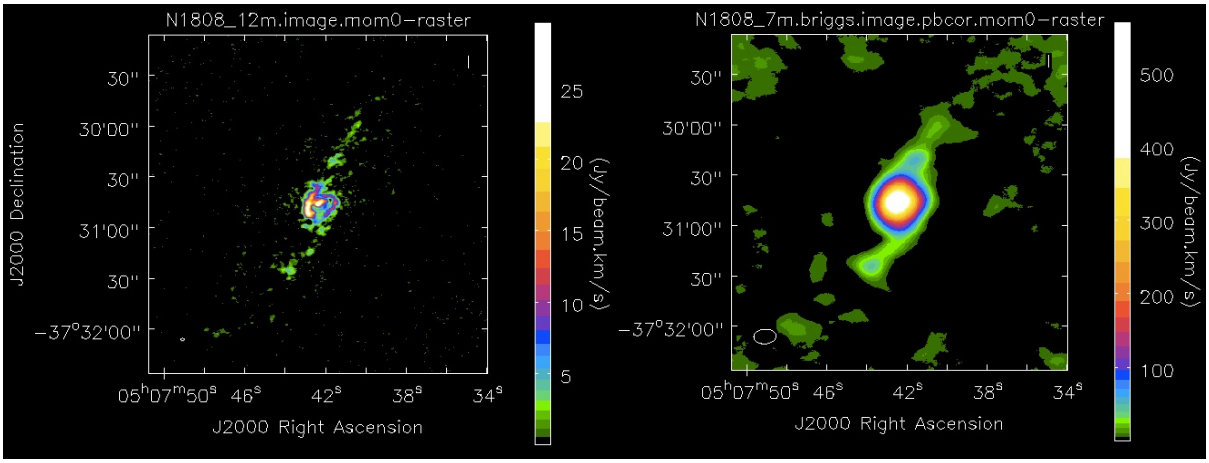

Figure 5.4: The same as figure 5.2 but for maps after the CLEAN process.

array and 7 m array alone, respectively.

Note that the CLEAN algorithm is for interferometric data, thus it is no need to perform CLEAN for the ALMA TP array. In the TP array, four 12 m telescopes are used as single dish. We also show the original data obtained by the TP array in figure 5.3. TP data was combined to the 12 m + 7 m array data using the task `feather`. We referred to the CASA guidelines https://casaguides.nrao.edu/index.php/M100_Band3_Combine_5.1 for these procedures above.

Figure 5.4 shows flux distribution after the CLEAN process. Owing to it, the effects of side lobes seen in figure 5.2 almost disappears and galactic structures can bee seen. The pixel size and the velocity resolution is set to be $0''.5$ and 5 km s^{-1}. The former is smaller than the Nyquist sampling and close to 1/3 of the size for the minor axis of the synthesized beam. The latter is considered to be enough to discuss properties of GMCs based on previous studies (e.g., Colombo et al. 2014; Hirota et al. 2018; Sun et al. 2018). Thus, we set these values.

The resultant synthesized beam size is $2''.37 \times 1''.37$ with the position angle (PA) of $-87°.4$ at the Briggs weighting at robust = 0.5 (Briggs 1995). It corresponds to 104 pc × 60.3 pc. The beam size is slightly lower than that for data by the 12 m array alone ($2''.26 \times 1''.23$) because of the contribution of visibilities by the 7 m array and TP. The final RMS error at the weighting, pixel size, and velocity resolution is 7.19 mJy beam^{-1}, which is equivalent to 204 mK.

Figure 5.5 shows the feathered (the 12 m array + 7 m array + TP array) integrated intensity map. Flux density $S_{\rm CO}$ is converted into brightness temperature (intensity) by the following equation;

$$\left(\frac{T_{\rm CO}}{\rm K}\right) = 1.222 \times 10^6 \left(\frac{\theta_{\rm maj}}{\rm arcsec}\right)^{-1} \left(\frac{\theta_{\rm min}}{\rm arcsec}\right)^{-1} \left(\frac{\nu}{\rm GHz}\right)^{-2} \left(\frac{S_{\rm CO}}{\rm Jy\ beam^{-1}}\right), \tag{5.1}$$

where $\theta_{\rm maj}$ is the beam size along its major axis, $\theta_{\rm min}$ is that along the minor axis. In making the map of figure 5.5, we applied the COMING ART algorithm (Sorai et al. 2019) to define the baseline range of spectra and make error map of integrated intensity. The typical RMS integrated-intensity error over the map is 69.2 mJy beam^{-1} km s^{-1}, which is equivalent to 1.96 K km s^{-1}. It corresponds to 4.64 $M_\odot$ pc^{-2} adopting the standard conversion factor $\alpha_{\rm CO} = 4.35$ $M_\odot$ pc^{-2} (K km s^{-1})$^{-1}$ (Bolatto et al. 2013b).

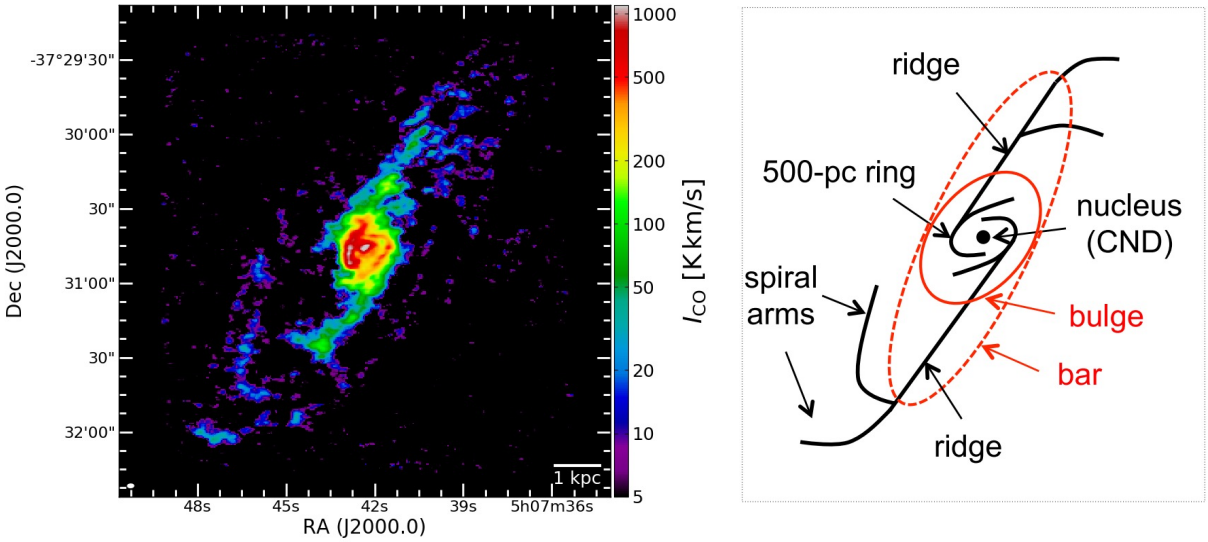

Figure 5.5: Integrated intensity map of the feathered (the 12 m array + 7 m array + TP array) data (left) and the schematic view of structures in NGC 1808 by Salak et al. (2016) (right).

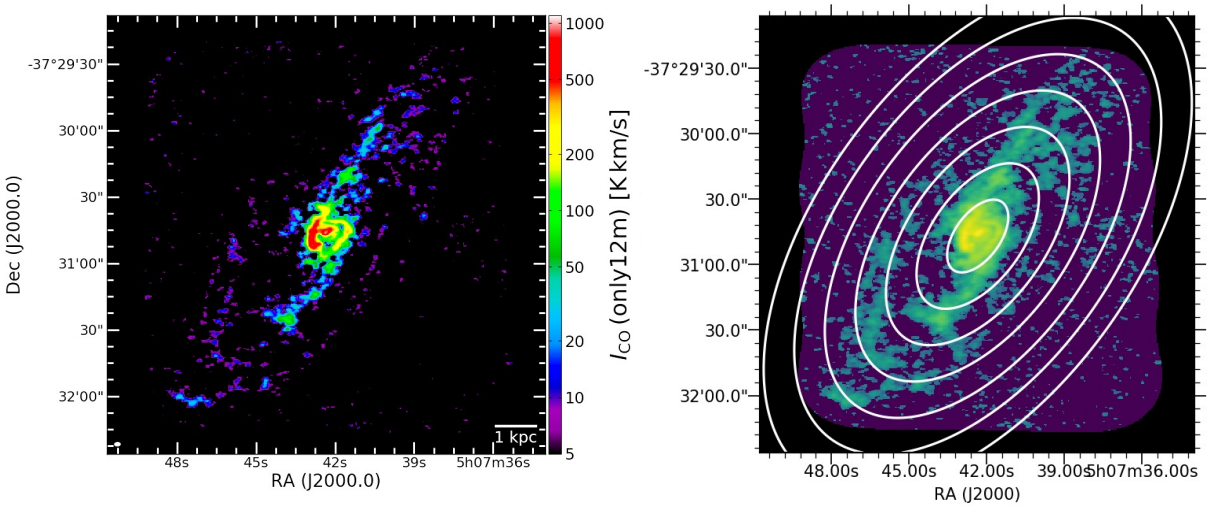

Figure 5.6: (Left) Integrated intensity map of data by the 12 m array alone. The color scale is the same as figure 5.5. (Right) Radii on the integrated intensity map of the feathered data. Indicated radii are 1, 2, . . ., 7 kpc.

5.4 Results

The right panel of figure 5.5 shows the schematic view of structures for NGC 1808. The feathered image clearly traces the structures. The comparison to the integrated intensity image by the 12 m array, which is already reported by Salak et al. (2016), indicates that the feathered data shows more extending molecular gas surrounding small clumpy structures seen in the 12 array data. It is especially significant along the bar and around the 500-pc ring indicated in the right panel of figure 5.5. The fraction of missing flux is different between galactic environments. Therefore, we investigate radial distribution of missing flux fraction as shown in the next subsection. In the all area of the map, the total flux of CO for the feathered data is 1.12×10^6 K km s^{-1}. That

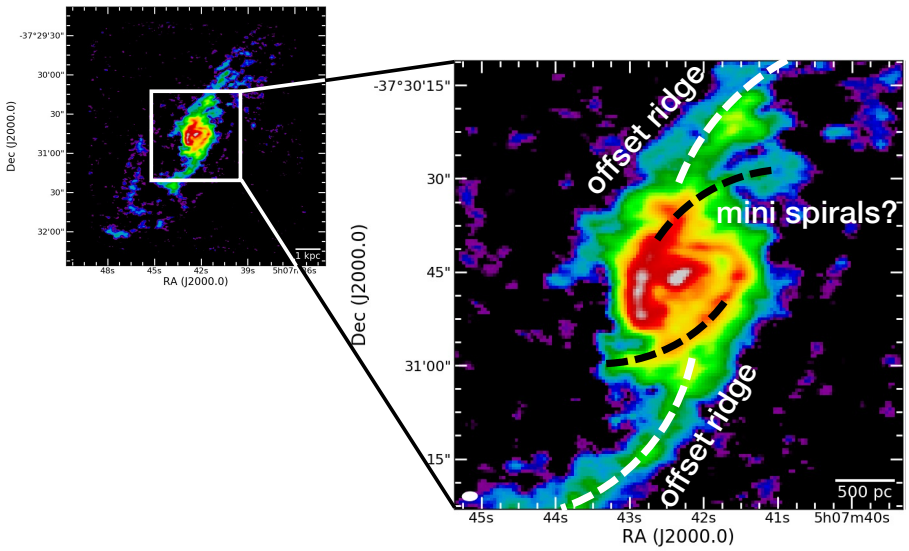

Figure 5.7: Mini spiral features in the 500-pc ring.

for the data by the 12 m array is 0.539×10^6 K km s^{-1}. The fraction of missing flux is 51.9% in the all area of this galaxy. This is comparable to results found in other galaxies (e.g., Pety et al. 2013; Caldú-Primo et al. 2015; 2016). Note that the missing flux fraction depends on the array configuration.

We also would like to mention that we can see mini spiral features in the trailing size of the offset ridges of the bar in the 500-pc ring. It may be relatively rare structures. Barred spiral galaxies usually shows molecular gas and star forming ring around their own centers connecting the offset ridges of the bar (e.g., Regan et al. 1999; Schinnerer et al. 2002; Koda and Sofue 2006; Sun et al. 2018; Harada et al. 2019). It is known as x_2 orbits (e.g., Athanassoula 1992b; Downes et al. 1996). In most barred spiral galaxies, molecular gas is distributed along the offset ridges and x_2 orbits as the central ring. According the recent high resolution CO data for barred spiral galaxies, NGC 1672 has the similar mini spiral structures (see figures in Sun et al. 2018). Although we now cannot distinguish whether the strictures are material or density-wave-like ones, specific and detailed analysis for gas motion and orbits may reveal rare properties of x_2 orbits.

5.5 Discussion and summary

5.5.1 Missing flux of the 12 m array

As we see figure 5.5 and 5.6, fraction of missing flux varies depending on galactic regions. Therefore, we investigate dependency of missing flux fraction on galactic environments. Figure 5.8 shows radial distribution of the missing flux fraction. See also the right panel of figure 5.6 for the reference of radius. The fraction of missing flux is derived as $1 - I_{12\mathrm{m}}/I_{12\mathrm{m+7m+TP}}$, where $I_{12\mathrm{m}}$ is integrated intensity by the 12 m array and $I_{12\mathrm{m+7m+TP}}$ is that by the data combining the all arrays. We derived total $I_{12\mathrm{m}}$ and $I_{12\mathrm{m+7m+TP}}$ in each concentric annuli with the width of 0.5 kpc and calculated $1 - I_{12\mathrm{m}}/I_{12\mathrm{m+7m+TP}}$.

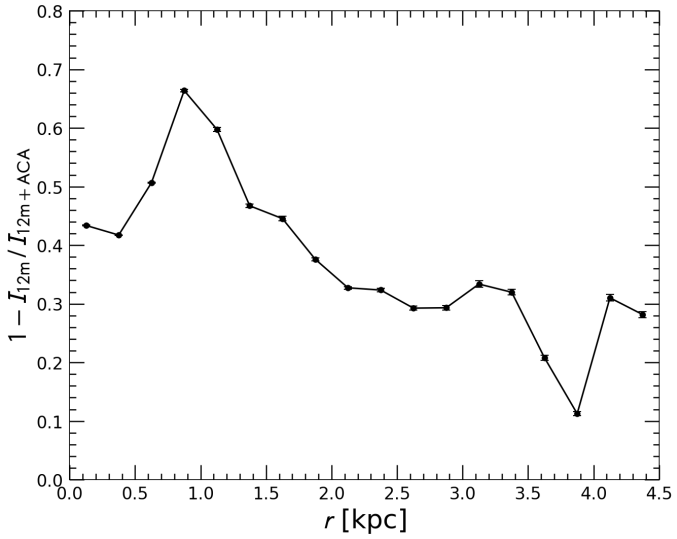

Figure 5.8: Fraction of missing flux for the 12 m array as a function of radius. Each radius bin is 0.5 kpc. Approximately $r < 0.91$ kpc, 0.91 kpc $< r <$ 2.4 kpc, and 2.4 kpc $< r$ correspond to the CNR, bar, and arms, respectively.

Figure 5.8 indicates that the degree of clumpiness is high in arms. Approximately 30% of integrated intensity is missing flux there. Missing flux fraction increases from $\sim$ 30% to 60% toward the center in the bar. Within the 500-pc ring, clumpiness increases toward the nucleus. Increasing missing flux fraction in the bar would be attributed to the strong shear or velocity gradient in the bar. As a result, GMCs are shredded and converted into small clouds or the diffuse, extended component. In fact, strong non-circular motion is observed in the bar of NGC 1808 (Salak et al. 2016).

5.5.2 Dependence of GMC properties on environments

To investigate dependence of GMC properties on galactic environments, GMCs are identified. Prior to the identification, we make the mask of signal channels. Signal channels at each spatial position are determined as the at least two continuous channels which include peak above $4\,\sigma$ from the baseline. The threshold of intensity at the edge of the signal range exceeds $0.5\,\sigma$ from the baseline. For the identification, `FINDCLUMPS`[2)], one of tasks of A 3D Clump Identification And Analysis Package (CUPID; Berry et al. 2007). It is is built in the Starlink package (Currie et al. 2014)[3)] distributed by the East Asian Observatory (EAO). `FINDCLUMPS` can specify the identification algorithm. We set it to the ClumpFind algorithm (Williams et al. 1994). The shape of clumps is set to be ellipse. The threshold to search local peaks is set to be $4\,\sigma$. The definition of adjacent voxel to the local peak voxel is defined as the corner of voxels. The beam FWHM for identification is input to be $\theta_{\rm min}$. With the settings above, 275 GMCs are identified. Their positions are shown in figure 5.9 with the feathered data. We also identify GMCs using the data by the 12-m array alone to check effects of missing flux on GMC properties. In this case, 141 GMCs are identified and their positions are shown in figure 5.10.

[2)] http://starlink.eao.hawaii.edu/docs/sun255.htx/sun255ss5.html
[3)] https://starlink.eao.hawaii.edu/starlink/WelcomePage

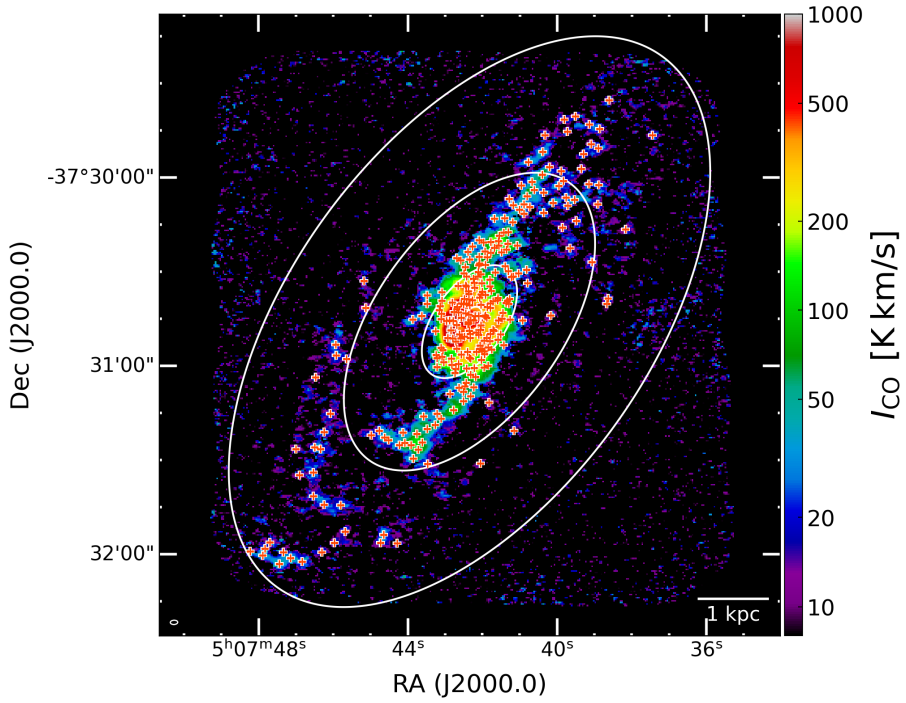

Figure 5.9: Positions of identified GMCs are denoted as plus markers overlaiding on the feathered integrated intensity map. Ellipses are boundaries of galactic regions we defined. "Nucleus" is within the innermost ellipse. "500-pc ring" is between the innermost and the second ellipse from the center. "Bar" is between the second and third ellipses. "Arm" is between the third and fourth ellipses. Their radii are 0.24, 0.91, 2.4, and 4.6 kpc.

We derived representative properties of GMCs, mass $M_{\rm GMC}$, effective radius $R_{\rm eff}$, surface density $\Sigma_{\rm GMC}$, peak intensity $T_{\rm peak}$, 1D velocity dispersion σ_v, mass density $\rho_{\rm GMC}$, virial parameter $\alpha_{\rm vir}$, and free-fall time $\tau_{\rm ff}$. $T_{\rm peak}$ and σ_v are direct observed quantities within each GMC. The latter is derived as the second moment along the velocity axis within each GMC. Others are derived from the following equations based on Leroy et al. (2015) and Hirota et al. (2018);

$$M_{\rm GMC} = L_{\rm CO}\alpha_{\rm CO}, \tag{5.2}$$

$$R_{\rm eff} = \frac{3.4}{\sqrt{\pi}}\sqrt{\sigma_{\rm maj}\sigma_{\rm min}}, \tag{5.3}$$

$$\Sigma_{\rm GMC} = \frac{M_{\rm GMC}}{\pi R_{\rm eff}^2}, \tag{5.4}$$

$$\rho_{\rm GMC} = 1.26\frac{M_{\rm GMC}}{4\pi R_{\rm eff}^3/3}, \tag{5.5}$$

$$\alpha_{\rm vir} = \frac{M_{\rm vir}}{M_{\rm GMC}}, \tag{5.6}$$

$$\tau_{\rm ff} = \sqrt{\frac{3\pi}{32G\rho_{\rm GMC}}}, \tag{5.7}$$

where $L_{\rm CO}$ is luminosity of the CO line, $\alpha_{\rm CO}$ is the CO-to-H_2 conversion factor, $\sigma_{\rm maj}$ is the cloud size determined by the second moment along the major axis of GMCs, $\sigma_{\rm min}$ is the same

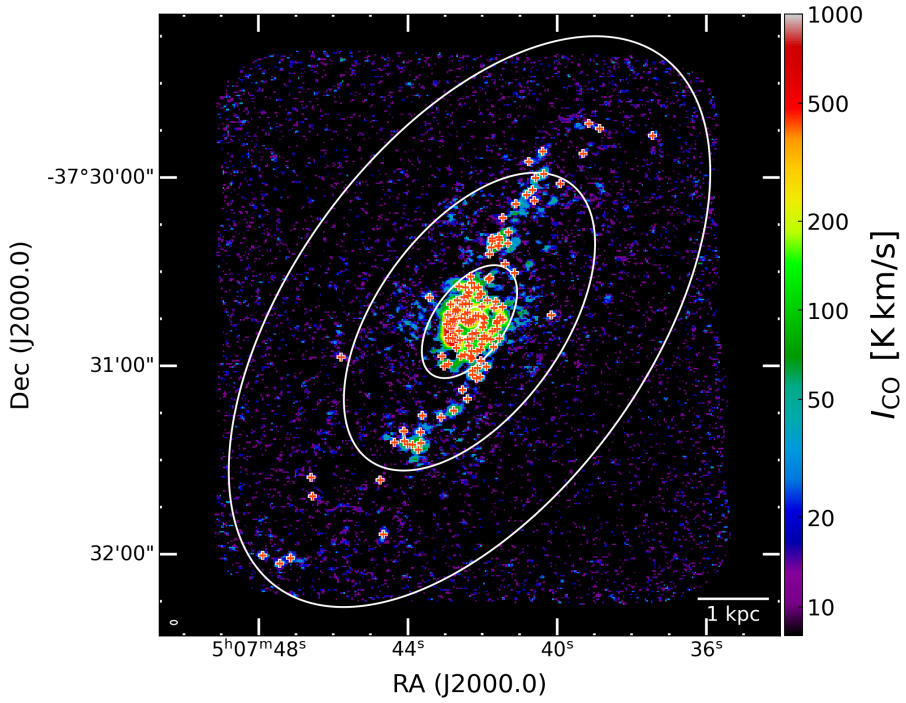

Figure 5.10: The same as figure 5.9 but GMCs in the data of the 12-m array alone.

as $\sigma_{\rm maj}$ but along the minor axis of GMCs, $M_{\rm vir}$ is the virial mass, and G is the gravitational constant. For $\alpha_{\rm CO}$, the standard value of 4.35 $M_\odot$ pc^{-2} (K km s^{-1})$^{-1}$, which is equivalent to $X_{\rm CO} = 2.0 \times 10^{20}$ cm^{-2} (K km s^{-1})$^{-1}$ is adopted for the disk region ($r > 0.95$ kpc). In the bulge ($r < 0.95$ kpc), the lower $\alpha_{\rm CO}$ of 1.09 $M_\odot$ pc^{-2} (K km s^{-1})$^{-1}$ corresponding to $X_{\rm CO} = 0.5 \times 10^{20}$ cm^{-2} (K km s^{-1})$^{-1}$ that is applicable for starburst galaxies and (ultra-)luminous infrared galaxies (ULIRGs; Bolatto et al. 2013b). $M_{\rm vir}$ is derived from

$$M_{\rm vir} = \frac{1}{a_1} \frac{5 R_{\rm eff} \sigma_v^2}{G}, \tag{5.8}$$

and a_1 is

$$a_1 = \frac{1 - k/3}{1 - 2n/5}, \tag{5.9}$$

where k is power-law index of density profile $\rho(r) \propto r^{-k}$ (Bertoldi and McKee 1992). We adopt $k = 1$ (Solomon et al. 1987).

To investigate environmental dependence of GMC properties, we define galactic regions: nucleus, 500-pc ring, bar, and arm based on radius. Figure 5.9 also shows their boundaries. The nucleus region is referred to as the region within $r < 0.4$ kpc. The 500-pc ring is qualitatively defined as the range of 0.4 kpc $< r <$ 0.95 kpc. The bar is 0.95 kpc $< r <$ 2 kpc. Outside of 2 kpc, we refer to as the arm region. These boundaries are defined by eye according to the distribution of molecular gas and positions of identified GMCs.

Figure 5.11 shows properties of GMCs in each galactic environment with box-whisker plots. Median of each properties is also plotted in each panel. Mass of most identified GMCs are of the order of 10^6 $M_\odot$, which is the typical value of GMCs (e.g., Koda et al. 2009; Donovan Meyer et al. 2013; Hirota et al. 2018). GMCs in arms are relatively less massive; about a half of them

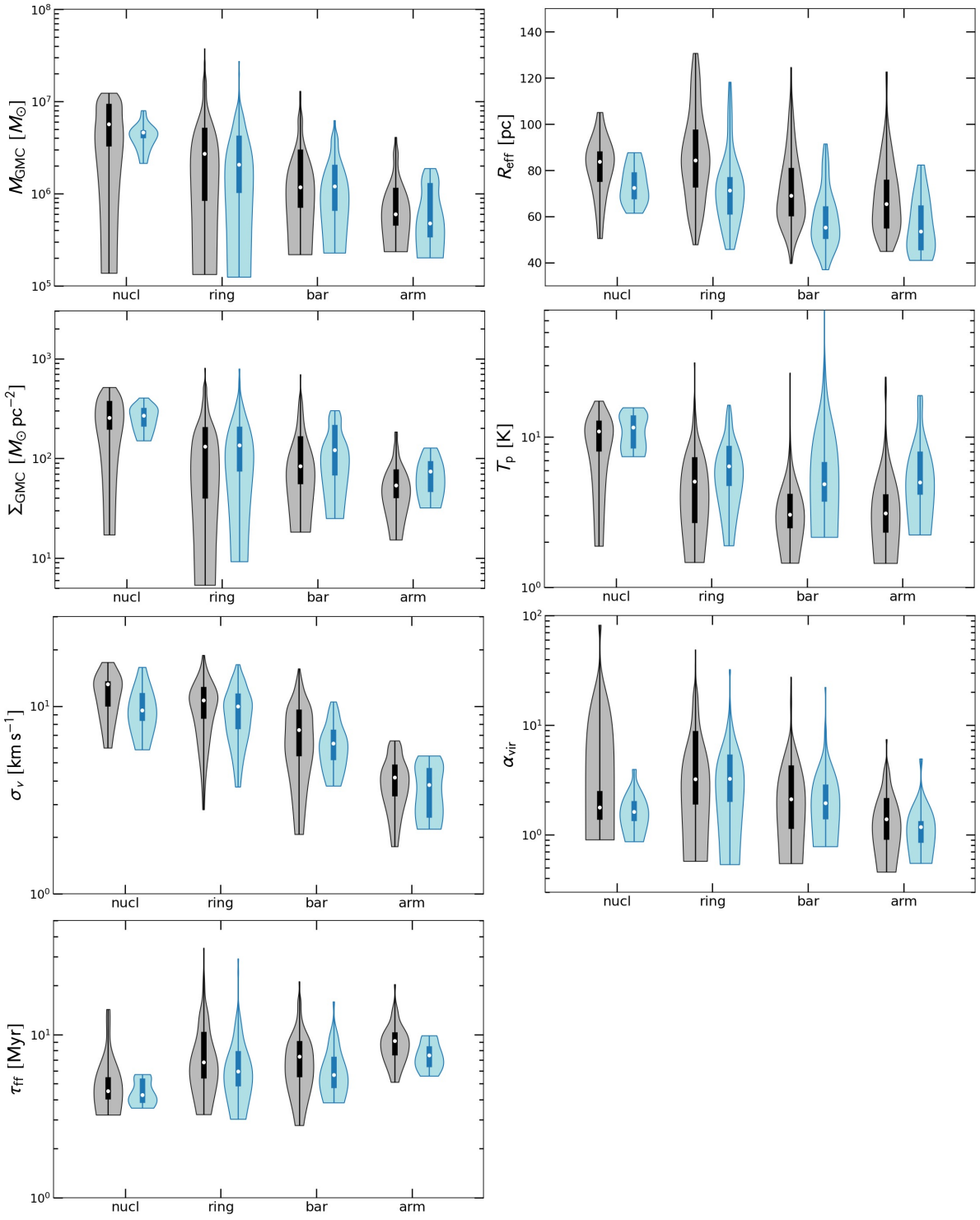

Figure 5.11: Dependence of representative GMC properties, mass, effective radius, surface density, peak intensity, 1D velocity dispersion, mass density, virial parameter, and free-fall time from left to right, top to bottom, on the four galactic environments. Back violin plots are results of the feathered data and blue ones are the data of the 12-m array alone. Thick bars and open markers indicate IQR and median, respectively.

is less than 10^6 $M_\odot$. Mass has large variation in the bar. In the central region of NGC 1808 (nucleus + 500-pc ring regions), massive ($M > 10^7 M_\odot$) ones are preferred even though lower $\alpha_{\rm CO}$ is dopted. This is the similar tendency seen in other galaxies with high concentration at the center (e.g., Pan and Kuno 2017; Hirota et al. 2018).

Effective radius increases toward the center in the disk region (bar + arm), however, it is almost constant in the bulge. According to increasing mass in the bulge, perhaps size of GMCs cannot blow due to high external pressure (external pressure is high in the bulge considering missing flux fraction there and total integrated intensity; see figure 5.5 and 5.8). Surface density of GMCs also roughly increase as radius decrease, whereas there is not systematic difference between the bar and the 500-pc ring. This is a natural result from the tendency of $M_{\rm GMC}$ and small dynamic range of $R_{\rm eff}$. The peak intensity in GMCs systematically increase toward the center as well as $M_{\rm GMC}$. There is no difference between the bar and arms. Velocity dispersion is roughly higher in the bulge than that in the disk. It is natural because of the tendency of $R_{\rm eff}$ and the Larson's scaling relation (Larson 1981).

Virial parameter clearly increases toward the center in arms, the bar, and 500-pc ring, and decreases from the 500-pc ring to the nucleus. $\alpha_{\rm vir}$ is significantly higher than that in arms with the significance level of 5%. Therefore, GMCs in the bar may be influenced by the surrounding strong gas dynamics. The 500-pc scale ring shows the highest $\alpha_{\rm vir}$ in all regions. In fact, the region does not seem to be associated with active star formation inferred from Hα line and radio continua considering richness of molecular gas, except for the end of flow from the offset ridge of the bar (Salak et al. 2016; 2017). Perhaps GMCs in the 500-pc ring, especially in its upstream are stable. Moreover, the median of $\alpha_{\rm vir}$ in the entire galaxy is ~ 2. Hence, about a half of GMCs are gravitationally unbound or pressure confined objects as indicated by Evans et al. (2021).

Free-fall time of most GMCs are of the order of 1–10 Myr, which is the typical value for other galaxies (e.g., Utomo et al. 2018). Also, Shorter $\tau_{\rm ff}$ in the galactic center is seen in another galaxy (Hirota et al. 2018). $\tau_{\rm ff}$ seems to decrease systematically, there is no difference between the bar and 500-pc ring. Taking account of deceased $\alpha_{\rm vir}$ and increasing $M_{\rm GMC}$ and $\Sigma_{\rm GMC}$ in the nucleus, the starburst at the center of NGC 1808 is caused by these unstable GMCs which are easy to form stars. These tendencies remain even when missing flux exists (GMC properties by the 12-m array alone).

These properties of GMCs are consistent with the picture of starburst in NGC 1808 proposed by Salak et al. (2017) with the higher resolution observational data of CO($J = 3$–2) than this data. GMCs traced CO($J = 3$–2) become massive as falling to the nucleus along the 500-pc ring from the offset ridges of the bar. This result indicate GMCs grows as molecular gas accretes onto them. GMCs by CO($J = 1$–0) become massive and dense (for density, it is the case at least except for the bar). Gravitational boundness gat stronger in the nucleus. In addition, $\alpha_{\rm vir}$ is high and missing flux fraction is large. Thus, molecular gas in the bar would be difficult to participate in star formation as it is. Molecular gas in the 500-pc ring, especially in its upstream also seems to be difficult to contribute to star formation because of high $\alpha_{\rm vir}$. Such GMCs rapidly glows by accretion of molecular gas and are compressed by external pressure, and possibly deep gravitational potential well of the galaxy (stellar surface density of the bulge of NGC 1808 is actually higher by about 1–2 orders of magnitude than normal spiral galaxies; Salak et al. 2016).

Finally, molecular gas can be the fuel of starburst in the nucleus and the downstream of the 500-pc ring. We traced the evolutionally sequence of GMCs to reach the nuclear starburst.

Chapter 6

Conclusions of this dissertation

In the end, I summarize and conclude the dissertation. In chapter 2, we show ^{12}CO($J=2$–1)/^{12}CO($J=1$–0) variations in nearby galaxies and reveal influences of the assumption that the line ratio is constant on derived molecular gas mass and the K–S relation. Although observation efficiency is higher for ^{12}CO($J=2$–1) than ^{12}CO($J=1$–0), the usage of ^{12}CO($J=2$–1) as a tracer of molecular gas needs consideration and attention. In particular, classifying analysis and systematic analysis for molecular gas related to star formation activity are carefully done, because ^{12}CO($J=2$–1)/^{12}CO($J=1$–0) line ratio has a trend with star formation and molecular gas temperature which seems to be affected by star formation. ^{12}CO($J=1$–0) would be a good tracer of total molecular gas. Note that the consequence is applicable to metal rich galaxies; CO emission lines are weak or not detected in low-metallicity galaxies.

In chapter 3, we showed that the qualitative relation between regionally averaged SFE and $n(H_2)$ in three barred spiral galaxies NGC 2903, NGC 3627, and NGC 4303. Positive correlations between them are seen in both compiled all galaxies and plotted for each galaxy. However, the former case has a large scatter and the correlation is rough. The scatter is originated from different slopes and intercepts between the galaxies. To investigate what determine them is a new theme of molecular gas and star formation studies for nearby galaxies.

We also discover that the increasing and decreasing tendency of $n(H_2)$ with large-scale molecular gas velocity dispersion. When velocity dispersion is moderate, $n(H_2)$ increases as velocity dispersion increases, however, the tendency of $n(H_2)$ changes a decrease. Thus, $n(H_2)$ traces asymmetric "Λ" and the letter of "へ" ("*he*") in hiragana as a function of velocity dispersion. Increasing $n(H_2)$ with velocity dispersion would be interpreted by the increased probability of cloud-cloud collisions and efficient compression by them. Decreasing $n(H_2)$ would be attributed to destruction and dissipation of molecular clouds due to high collision speed. Strong shear and velocity gradient can also explain it without considering cloud-cloud collisions. In contrast to the SFE–$n(H_2)$ relation, most galactic regions tightly follow the $n(H_2)$–velocity dispersion relation. Thus, this relation may be universal for galaxies.

In chapter 4, we investigate effects of the fraction of the cloud/diffuse component molecular gas and properties of the cloud component in Maffei 2 using ^{12}CO($J=1$–0) and ^{13}CO($J=1$–0) data obtained by the new observation with the Nobeyama 45 m Telescope. According to the three-dimensional decomposition of ^{12}CO($J=1$–0) based on ^{13}CO($J=1$–0), about 40% of total molecular gas is in the diffuse phase in the entire galaxy. Moreover, we found that the cloud/diffuse component fraction reflected by $R_{12(13\mathrm{det})/12}$ significantly depends on galactic en-

vironments. $R_{12(13\mathrm{det})/12}$ is high in the center, bar ends, and arms and low in the bar, inter-arm, and outer disk. However, properties of the cloud component inferred from $R_{12(13\mathrm{det})/13}$ is somewhat uniform within the galaxy. In particular, galactic regions in the disk (i.e., bar, bar ends, arms, and the bridge feature) show statistically similar values according to the K–S test. These results suggest that structures of galaxies promote formation and destruction of the cloud component molecular gas, however, their effects are not strong enough to change properties of the cloud component molecular gas. That is, they perhaps do not compress clouds further. In fact, previous studies suggest that self-gravity of molecular clouds are weak and clouds are just collected by the potential of galaxies. We also found that differences in SFE between galactic regions become small when SFE is derived from ^{13}CO($J=1$–0)-detected ^{12}CO($J=1$–0) and ^{13}CO($J=1$–0). It indicates that SFE is close to a constant by removing molecular gas which is difficult to participate in star formation, i.e., the diffuse component. The fraction of the cloud/diffuse component of molecular gas is important factor to characterize properties of molecular gas and star formation.

In chapter 5, we can trace the evolutionary sequence of GMCs in the starburst barred spiral galaxy NGC 1808 with the high resolution ^{12}CO($J=1$–0) data by ALMA. Virial parameter of GMCs in the bar is statistically higher than those in arms. The fraction of missing flux of the ALMA 12 m array also increases toward the center in the bar. GMCs in the bar would be influenced by the surrounding strong gas dynamics environment and some of them are shredded and converted into small clouds or diffuse molecular clouds. Virial parameter in the central ring, which is referred to as the 500-pc ring further increases from those in the bar. Since distributions of Hα line and radio continua show low star forming activity in its upstream considering its strong ^{12}CO emission, GMCs may be stable and it may be hard to form stars. However, GMCs rapidly grow by accreting molecular gas or agglomeration and become massive as they are moving to the downstream and fall into the nucleus. As well as them, α_{vir} and τ_{ff} decreases. These gravitationally unstable GMCs may be a cause of starburst in the center of NGC 1808.

Regarding ^{12}CO($J=1$–0) as a good tracer of molecular gas, this line traces diffuse molecular gas, which is difficult to contribute to star formation. In this sense, ^{12}CO($J=1$–0) is not good tracer of molecular gas which is related to star formation. It is also expected from the linear K–S relations using higher energy transitions of ^{12}CO, high critical density tracers, and ^{13}CO as seen in chapter 4. In addition, ^{12}CO($J=1$–0) reflect spatially extended molecular gas. Therefore, observers should choose observed emission lines according to what they would like to investigate. For instance, studies for molecular gas at the Galactic center often make use of ^{12}CO($J=3$–2) instead of ^{12}CO($J=1$–0), because structures of molecular gas by ^{12}CO($J=1$–0) are ambiguous.

Considering decreased differences in SFE by ^{13}CO($J=1$–0)-detected ^{12}CO($J=1$–0) and ^{13}CO($J=1$–0) seen in chapter 4, the positive correlation between SFE and $n(\mathrm{H_2})$ may reflect the cloud component variations. That is, high $n(\mathrm{H_2})$ indicates high fraction of the cloud component and vise versa. If so, large-scale velocity dispersion control the fraction of the cloud component molecular gas. It may be a natural consequence for the decreasing $n(\mathrm{H_2})$ in the range of large velocity dispersion. Although we attribute the increasing $n(\mathrm{H_2})$ to compressed GMCs by frequent cloud-cloud collisions, it may be also possible that increased fraction of the cloud component increases mean $n(\mathrm{H_2})$.

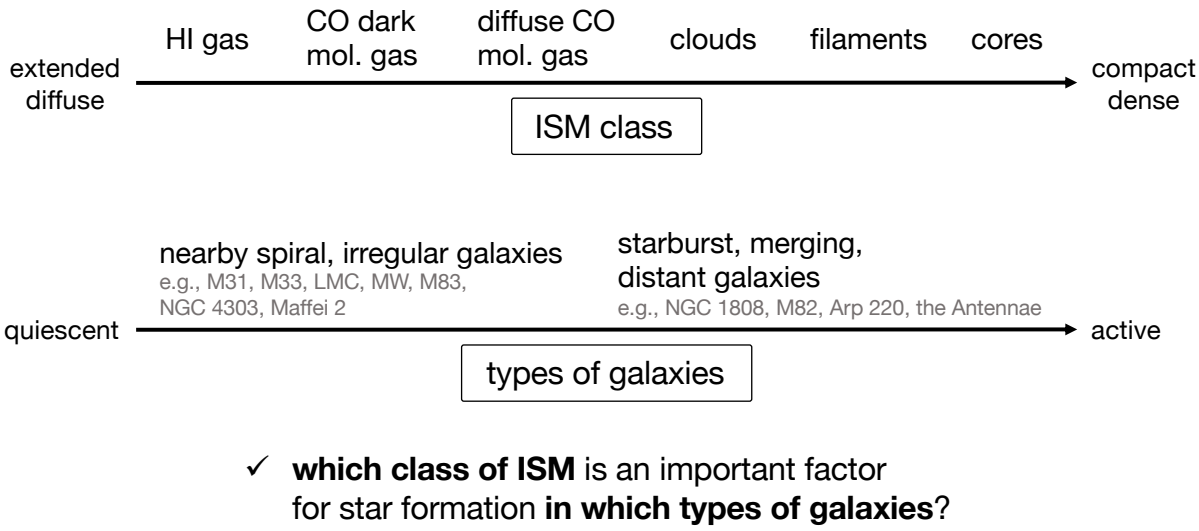

Figure 6.1: Classes of the hierarchical structure of ISM and types of galaxies.

The conclusion of chapter 4 and 5 seem to contradict each other. We see almost unchanged properties of the cloud component of molecular gas inferred from $R_{12(13\mathrm{det})/13}$ in Maffei 2. On the other hand, properties of GMCs in NGC 1808 do very between galactic environments. This would be because used tracers of molecular gas is different. The cloud component molecular gas in Maffei 2 is derived from the combination of ^{12}CO($J=1$–0) and ^{13}CO($J=1$–0), whereas identified GMCs in NGC 1808 is from ^{12}CO($J=1$–0) alone. Since sources of ^{13}CO($J=1$–0) is spatially compact than GMCs found in ^{12}CO($J=1$–0) data, ^{13}CO($J=1$–0) traces denser part of GMCs, which would be insensitive to surrounding environments. The usage of the feathered data for NGC 1808 may also affect variations of GMC properties. It will be helpful to derive them from the 12 m array alone. Note that derived properties of GMCs in NGC 1808 and $R_{12(13\mathrm{det})/13}$ in Maffei 2 are different in the first place.

$R_{12(13\mathrm{det})/12}$ as an effective factor found in Maffei 2 and missing flux variations in NGC 1808 suggest importance of hierarchical structures of molecular gas, i.e., the compact cloud component and the extended diffuse component. When we broaden our view to other phases in ISM, hierarchical structures is universal (figure 6.1). For example, H I gas is extended outside the molecular phase. There is CO-dark gas which can trace [C I] and [C II] lines outside the diffuse molecular gas seen in only ^{12}CO. In the cloud component of molecular gas and GMCs, filament-like structures traced by ^{12}CO, ^{13}CO, and C^{18}O are found. Denser and more compact structures known as molecular cloud cores which is cradles of stars exist in filaments and observed in C^{18}O, dust, HCN, HCO$^+$ (H^{13}CO$^+$), and N_2H^+.

In the end of the dissertation, I would like to suggest that it is important to investigate which class is effective and crucial to characterize ISM properties and for star formation activity in various environments (e.g., arms, inter-arm, bars, bar ends, galactic centers) and in various types of galaxies (normal star forming galaxies, dwarfs/irregulars, very late-type galaxies, starbursts, LIRGs, and major mergers) as shown in figure 6.1. In fact, properties of GMCs differ among galactic regions in NGC 1808, which has extreme environments for GMCs (high pressure, high surface density). More violent environments can be expected in wet major mergers such as the

Antennae galaxy. In a more normal star-forming galaxy than NGC 1808, the cloud component in Maffei 2 is rather uniform, while gas tracers are different from the study of NGC 1808. Moreover, Koch et al. (2019) reported that line width of CO is narrower than that of H I in M 33 unlike the results of Caldú-Primo et al. (2013) and Caldú-Primo et al. (2015). It indicates that this galaxy has the marginal thick CO disk, i.e., diffuse CO molecular gas is poor and may not a key factor. M 33 is a less massive, more quiescent over the whole disk (although it has the giant H II region NGC 604), and H I dominated galaxy and CO is mainly distributed as clumpy structures (e.g., Tosaki et al. 2011; Druard et al. 2014). Key factors to characterize ISM properties, and subsequent star-formation activity would vary depending on types of galaxies and GMC environments. Toward the unified view of the relation between star formation and ISM, it is important to observe various classes of ISM in various types of galaxies.

Acknowledgment

In the first, I would like to heartily express my gratitude to my supervisor Professor Kazuo Sorai for his dedicated and helpful discussions, suggestions, and comments in my research life since I joined in the laboratory. I am also grateful to Professor Naoki Watanabe, Dr. Takashi Okamoto, Professor Masaaki Kimura, and Professor Mitsuteru Sato as well as Professor Kazuo Sorai (the chief) for undertaking the referees of the dissertation and giving me many useful advices with active discussions in defenses. I would like to thank COMING members, especially Professor Nario Kuno, Dr. Kazuyuki Muraoka, Dr. Yusuke Miyamoto, Dr. Hiroyuki Kaneko, Dr. Kana Morokuma-Matsui, Dr. Salak Dragan, Dr. Takahiro Tanaka, and Atsushi Yasuda for discussions, cooperation of extensive data reduction of COMING and teaching how to produce observations, since I was an undergraduate student. I appreciate giving helpful and constructive comments and suggestion for our works by Dr. Fumi Egusa, Dr. Jin Koda, Dr. Toshiki Saito, Dr. Fumiya Maeda, Dr. Yusuke Fujimoto, Dr. Kazuki Tokuda, Dr. Alex R. Pettitt, Dr. Masato I. N. Kobayashi, Professor Toshihiro Handa, Professor Keiichi Wada, and Professor Emeritus Tetsuo Hasegawa in seminars, meetings, and workshops. I thank students in our laboratory including graduates and students in other universities for discussions of studies on ordinary days and my private life. I also give thanks to members and graduates of our laboratory for helping my observations of Maffei 2. At last, I would like to emphasize that this dissertation can be accomplished by continuous helps and dedications by my parents and my girlfriend Aoi. I deeply express my gratitude about it.

Bibliography

S. Aalto, J. H. Black, L. E. B. Johansson, and R. S. Booth. Large 12CO/13CO intensity ratios in luminous mergers. *A&A*, 249:323, Sept. 1991.

S. Aalto, R. S. Booth, J. H. Black, and L. E. B. Johansson. Molecular gas in starburst galaxies: line intensities and physical conditions. *A&A*, 300:369, Aug. 1995.

S. Aalto, R. Beswick, and E. Jütte. ^{13}CO 1-0 imaging of the Medusa merger, NGC 4194. Large scale variations in molecular cloud properties. *A&A*, 522:A59, Nov. 2010. doi: 10.1051/0004-6361/200913511.

H. Akima. A new method of interpolation and smooth curve fitting based on local procedures. *Journal of Association for Computing Machinery*, 17(4):589–602, Oct. 1970. ISSN 0004-5411. doi: 10.1145/321607.321609. URL https://doi.org/10.1145/321607.321609.

P. André, A. Men'shchikov, S. Bontemps, V. Könyves, F. Motte, N. Schneider, P. Didelon, V. Minier, P. Saraceno, D. Ward-Thompson, J. di Francesco, G. White, S. Molinari, L. Testi, A. Abergel, M. Griffin, T. Henning, P. Royer, B. Merín, R. Vavrek, M. Attard, D. Arzoumanian, C. D. Wilson, P. Ade, H. Aussel, J. P. Baluteau, M. Benedettini, J. P. Bernard, J. A. D. L. Blommaert, L. Cambrésy, P. Cox, A. di Giorgio, P. Hargrave, M. Hennemann, M. Huang, J. Kirk, O. Krause, R. Launhardt, S. Leeks, J. Le Pennec, J. Z. Li, P. G. Martin, A. Maury, G. Olofsson, A. Omont, N. Peretto, S. Pezzuto, T. Prusti, H. Roussel, D. Russeil, M. Sauvage, B. Sibthorpe, A. Sicilia-Aguilar, L. Spinoglio, C. Waelkens, A. Woodcraft, and A. Zavagno. From filamentary clouds to prestellar cores to the stellar IMF: Initial highlights from the Herschel Gould Belt Survey. *A&A*, 518: L102, July 2010. doi: 10.1051/0004-6361/201014666.

R. W. Argyle and P. Eldridge. Optical positions of Seyfert galaxies - III. *MNRAS*, 243:504, Apr. 1990.

E. Athanassoula. The existence and shapes of dust lanes in galactic bars. *MNRAS*, 259:345–364, Nov. 1992a. doi: 10.1093/mnras/259.2.345.

E. Athanassoula. Morphology of bar orbits. *MNRAS*, 259:328–344, Nov. 1992b. doi: 10.1093/mnras/259.2.328.

H. Awaki, S. Ueno, K. Koyama, T. Tsuru, and K. Iwasawa. ASCA Observation of NGC 1808. *PASJ*, 48:409–416, June 1996. doi: 10.1093/pasj/48.3.409.

J. Baba, K. Morokuma-Matsui, and T. R. Saitoh. Eventful evolution of giant molecular clouds in dynamically evolving spiral arms. *MNRAS*, 464(1):246–263, Jan. 2017. doi: 10.1093/mnras/stw2378.

C. Bacchini, F. Fraternali, G. Iorio, and G. Pezzulli. Volumetric star formation laws of disc galaxies. *A&A*, 622: A64, Feb. 2019. doi: 10.1051/0004-6361/201834382.

I. K. Baldry, K. Glazebrook, J. Brinkmann, Ž. Ivezić, R. H. Lupton, R. C. Nichol, and A. S. Szalay. Quantifying the Bimodal Color-Magnitude Distribution of Galaxies. *ApJ*, 600(2):681–694, Jan. 2004. doi: 10.1086/380092.

P. J. Barnes, A. K. Hernandez, S. N. O'Dougherty, I. Schap, William J., and E. Muller. The Galactic Census of High- and Medium-mass Protostars. III. ^{12}CO Maps and Physical Properties of Dense Clump Envelopes and Their Embedding GMCs. *ApJ*, 831(1):67, Nov. 2016. doi: 10.3847/0004-637X/831/1/67.

E. Bayet, M. Gerin, T. G. Phillips, and A. Contursi. Are ^{12}CO lines good indicators of the star formation rate in galaxies? *MNRAS*, 399(1):264–272, Oct. 2009. doi: 10.1111/j.1365-2966.2009.15258.x.

G. J. Bendo, F. Galliano, and S. C. Madden. MIPS 24-160 μm photometry for the Herschel-SPIRE Local Galaxies Guaranteed Time Programs. *MNRAS*, 423(1):197–212, June 2012. doi: 10.1111/j.1365-2966.2012.20784.x.

M. Benedettini, A. Traficante, L. Olmi, S. Pezzuto, A. Baldeschi, S. Molinari, D. Elia, E. Schisano, M. Merello, F. Fontani, K. L. J. Rygl, J. Brand, M. T. Beltrán, R. Cesaroni, S. J. Liu, and L. Testi. Molecular cloud catalogue from ^{13}CO (1-0) data of the Forgotten Quadrant Survey. *A&A*, 654:A144, Oct. 2021. doi: 10.1051/0004-6361/202141433.

D. S. Berry, K. Reinhold, T. Jenness, and F. Economou. CUPID: A Clump Identification and Analysis Package. In R. A. Shaw, F. Hill, and D. J. Bell, editors, *Astronomical Data Analysis Software and Systems XVI*, volume 376 of *Astronomical Society of the Pacific Conference Series*, page 425, Oct. 2007.

F. Bertoldi and C. F. McKee. Pressure-confined Clumps in Magnetized Molecular Clouds. *ApJ*, 395:140, Aug. 1992. doi: 10.1086/171638.

I. Bešlić, A. T. Barnes, F. Bigiel, J. Puschnig, J. Pety, C. Herrera Contreras, A. K. Leroy, A. Usero, E. Schinnerer, S. E. Meidt, E. Emsellem, A. Hughes, C. Faesi, K. Kreckel, F. M. C. Belfiore, M. Chevance, J. S. den Brok, C. Eibensteiner, S. C. O. Glover, K. Grasha, M. J. Jimenez-Donaire, R. S. Klessen, J. M. D. Kruijssen, D. Liu, I. Pessa, M. Querejeta, E. Rosolowsky, T. Saito, F. Santoro, A. Schruba, M. C. Sormani, and T. G. Williams. Dense molecular gas properties on 100 pc scales across the disc of NGC 3627. *MNRAS*, 506(1):963–988, Sept. 2021. doi: 10.1093/mnras/stab1776.

F. Bigiel, A. Leroy, F. Walter, E. Brinks, W. J. G. de Blok, B. Madore, and M. D. Thornley. The Star Formation Law in Nearby Galaxies on Sub-Kpc Scales. *AJ*, 136(6):2846–2871, Dec. 2008. doi: 10.1088/0004-6256/136/6/2846.

F. Bigiel, A. K. Leroy, F. Walter, E. Brinks, W. J. G. de Blok, C. Kramer, H. W. Rix, A. Schruba, K. F. Schuster, A. Usero, and H. W. Wiesemeyer. A Constant Molecular Gas Depletion Time in Nearby Disk Galaxies. *ApJL*, 730(2):L13, Apr. 2011. doi: 10.1088/2041-8205/730/2/L13.

F. Bigiel, A. K. Leroy, M. J. Jiménez-Donaire, J. Pety, A. Usero, D. Cormier, A. Bolatto, S. Garcia-Burillo, D. Colombo, M. González-García, A. Hughes, A. A. Kepley, C. Kramer, K. Sandstrom, E. Schinnerer, A. Schruba, K. Schuster, N. Tomicic, and L. Zschaechner. The EMPIRE Survey: Systematic Variations in the Dense Gas Fraction and Star Formation Efficiency from Full-disk Mapping of M51. *ApJL*, 822(2):L26, May 2016. doi: 10.3847/2041-8205/822/2/L26.

L. Blitz, J. Binney, K. Y. Lo, J. Bally, and P. T. P. Ho. The centre of the Milky Way. *Nature*, 361:417–424, Feb. 1993. doi: 10.1038/361417a0.

A. D. Bolatto, A. K. Leroy, E. Rosolowsky, F. Walter, and L. Blitz. The Resolved Properties of Extragalactic Giant Molecular Clouds. *ApJ*, 686(2):948–965, Oct. 2008. doi: 10.1086/591513.

A. D. Bolatto, S. R. Warren, A. K. Leroy, F. Walter, S. Veilleux, E. C. Ostriker, J. Ott, M. Zwaan, D. B. Fisher, A. Weiss, E. Rosolowsky, and J. Hodge. Suppression of star formation in the galaxy NGC 253 by a starburst-driven molecular wind. *Nature*, 499(7459):450–453, July 2013a. doi: 10.1038/nature12351.

A. D. Bolatto, M. Wolfire, and A. K. Leroy. The CO-to-H_2 Conversion Factor. *ARA&A*, 51(1):207–268, Aug. 2013b. doi: 10.1146/annurev-astro-082812-140944.

A. Boselli, L. Cortese, M. Boquien, S. Boissier, B. Catinella, C. Lagos, and A. Saintonge. Cold gas properties of the Herschel Reference Survey. II. Molecular and total gas scaling relations. *A&A*, 564:A66, Apr. 2014. doi: 10.1051/0004-6361/201322312.

J. Braine and F. Combes. A CO(1-0) and CO(2-1) survey of nearby spiral galaxies. II. Physical conditions in the nuclear gas. *A&A*, 264:433–443, Oct. 1992.

D. S. Briggs. *High fidelity deconvolution of moderately resolved sources*. PhD thesis, New Mexico Institute of Mining and Technology, United States, Jan. 1995.

T. Brown, C. D. Wilson, N. Zabel, T. A. Davis, A. Boselli, A. Chung, S. L. Ellison, C. D. P. Lagos, A. R. H. Stevens, L. Cortese, Y. M. Bahé, D. Bisaria, A. D. Bolatto, C. R. Cashmore, B. Catinella, R. Chown, B. Diemer, P. J. Elahi, M. H. Hani, M. J. Jiménez-Donaire, B. Lee, K. Leidig, A. Mok, K. P. Olsen, L. C. Parker, I. D. Roberts, R. Smith, K. Spekkens, M. Thorp, S. Tonnesen, E. Vienneau, V. Villanueva, S. N. Vogel, J. Wadsley, C. Welker, and H. Yoon. VERTICO: The Virgo Environment Traced in CO Survey. *ApJS*, 257(2):21, Dec. 2021. doi: 10.3847/1538-4365/ac28f5.

P. M. Bryant and N. Z. Scoville. High-Resolution CO Observations of Luminous Infrared Galaxies. *AJ*, 117(6):2632–2655, June 1999. doi: 10.1086/300879.

J. V. Buckle, R. E. Hills, H. Smith, W. R. F. Dent, G. Bell, E. I. Curtis, R. Dace, H. Gibson, S. F. Graves, J. Leech, J. S. Richer, R. Williamson, S. Withington, G. Yassin, R. Bennett, P. Hastings, I. Laidlaw, J. F. Lightfoot, T. Burgess, P. E. Dewdney, G. Hovey, A. G. Willis, R. Redman, B. Wooff, D. S. Berry, B. Cavanagh, G. R. Davis, J. Dempsey, P. Friberg, T. Jenness, R. Kackley, N. P. Rees, R. Tilanus, C. Walther, W. Zwart, T. M. Klapwijk, M. Kroug, and T. Zijlstra. HARP/ACSIS: a submillimetre spectral imaging system on the James Clerk Maxwell Telescope. *MNRAS*, 399(2):1026–1043, Oct. 2009. doi: 10.1111/j.1365-2966.2009.15347.x.

E. M. Burbidge and G. R. Burbidge. The Rotation and Mass of NGC 1808. *ApJ*, 151:99, Jan. 1968. doi: 10.1086/149421.

M. P. Busch, P. D. Engelke, R. J. Allen, and D. E. Hogg. Observational Evidence for a Thick Disk of Dark Molecular Gas in the Outer Galaxy. *ApJ*, 914(1):72, June 2021. doi: 10.3847/1538-4357/abf832.

A. Caldú-Primo and A. Schruba. Molecular Gas Velocity Dispersions in the Andromeda Galaxy. *AJ*, 151(2):34, Feb. 2016. doi: 10.3847/0004-6256/151/2/34.

A. Caldú-Primo, A. Schruba, F. Walter, A. Leroy, K. Sandstrom, W. J. G. de Blok, R. Ianjamasimanana, and K. M. Mogotsi. A High-dispersion Molecular Gas Component in Nearby Galaxies. *AJ*, 146(6):150, Dec. 2013. doi: 10.1088/0004-6256/146/6/150.

A. Caldú-Primo, A. Schruba, F. Walter, A. Leroy, A. D. Bolatto, and S. Vogel. Spatially Extended and High-Velocity Dispersion Molecular Component in Spiral Galaxies: Single-Dish Versus Interferometric Observations. *AJ*, 149(2):76, Feb. 2015. doi: 10.1088/0004-6256/149/2/76.

D. Calzetti, J. Kennicutt, R. C., L. Bianchi, D. A. Thilker, D. A. Dale, C. W. Engelbracht, C. Leitherer, M. J. Meyer, M. L. Sosey, M. Mutchler, M. W. Regan, M. D. Thornley, L. Armus, G. J. Bendo, S. Boissier, A. Boselli, B. T. Draine, K. D. Gordon, G. Helou, D. J. Hollenbach, L. Kewley, B. F. Madore, D. C. Martin, E. J. Murphy, G. H. Rieke, M. J. Rieke, H. Roussel, K. Sheth, J. D. Smith, F. Walter, B. A. White, S. Yi, N. Z. Scoville, M. Polletta, and D. Lindler. Star Formation in NGC 5194 (M51a): The Panchromatic View from GALEX to Spitzer. *ApJ*, 633(2):871–893, Nov. 2005. doi: 10.1086/466518.

D. Calzetti, R. C. Kennicutt, C. W. Engelbracht, C. Leitherer, B. T. Draine, L. Kewley, J. Moustakas, M. Sosey, D. A. Dale, K. D. Gordon, G. X. Helou, D. J. Hollenbach, L. Armus, G. Bendo, C. Bot, B. Buckalew, T. Jarrett, A. Li, M. Meyer, E. J. Murphy, M. Prescott, M. W. Regan, G. H. Rieke, H. Roussel, K. Sheth, J. D. T. Smith, M. D. Thornley, and F. Walter. The Calibration of Mid-Infrared Star Formation Rate Indicators. *ApJ*, 666(2): 870–895, Sept. 2007. doi: 10.1086/520082.

Y. Cao, T. Wong, R. Xue, A. D. Bolatto, L. Blitz, S. N. Vogel, A. K. Leroy, and E. Rosolowsky. CARMA Survey toward Infrared-bright Nearby Galaxies (STING). IV. Spatially Resolved ^{13}CO in Spiral Galaxies. *ApJ*, 847 (1):33, Sept. 2017. doi: 10.3847/1538-4357/aa88c5.

V. Casasola, L. P. Cassarà, S. Bianchi, S. Verstocken, E. Xilouris, L. Magrini, M. W. L. Smith, I. De Looze, M. Galametz, S. C. Madden, M. Baes, C. Clark, J. Davies, P. De Vis, R. Evans, J. Fritz, F. Galliano, A. P. Jones, A. V. Mosenkov, S. Viaene, and N. Ysard. Radial distribution of dust, stars, gas, and star-formation rate in DustPedia face-on galaxies. *A&A*, 605:A18, Sept. 2017. doi: 10.1051/0004-6361/201731020.

J. I. Castor. Spectral line formation in Wolf-Rayet envelopes. *MNRAS*, 149:111, Jan. 1970. doi: 10.1093/mnras/149.2.111.

V. Cayatte, J. H. van Gorkom, C. Balkowski, and C. Kotanyi. VLA Observations of Neutral Hydrogen in Virgo Cluster Galaxies. I. The Atlas. *AJ*, 100:604, Sept. 1990. doi: 10.1086/115545.

G. Chabrier. Galactic Stellar and Substellar Initial Mass Function. *PASP*, 115(809):763–795, July 2003. doi: 10.1086/376392.

A. Chung, J. H. van Gorkom, J. D. P. Kenney, H. Crowl, and B. Vollmer. VLA Imaging of Virgo Spirals in Atomic Gas (VIVA). I. The Atlas and the H I Properties. *AJ*, 138(6):1741–1816, Dec. 2009. doi: 10.1088/0004-6256/138/6/1741.

A. Cimatti, E. Daddi, M. Mignoli, L. Pozzetti, A. Renzini, G. Zamorani, T. Broadhurst, A. Fontana, P. Saracco, F. Poli, S. Cristiani, S. D'Odorico, E. Giallongo, R. Gilmozzi, and N. Menci. The K20 survey. I. Disentangling old and dusty star-forming galaxies in the ERO population. *A&A*, 381:L68–L72, Jan. 2002. doi: 10.1051/0004-6361:20011696.

P. C. Clark, I. A. Bonnell, H. Zinnecker, and M. R. Bate. Star formation in unbound giant molecular clouds: the origin of OB associations? *MNRAS*, 359(3):809–818, May 2005. doi: 10.1111/j.1365-2966.2005.08942.x.

D. D. Clayton and L. R. Nittler. Astrophysics with Presolar Stardust. *ARA&A*, 42(1):39–78, Sept. 2004. doi: 10.1146/annurev.astro.42.053102.134022.

M. E. Cluver, T. H. Jarrett, D. A. Dale, J. D. T. Smith, T. August, and M. J. I. Brown. Calibrating Star Formation in WISE Using Total Infrared Luminosity. *ApJ*, 850(1):68, Nov. 2017. doi: 10.3847/1538-4357/aa92c7.

D. Colombo, A. Hughes, E. Schinnerer, S. E. Meidt, A. K. Leroy, J. Pety, C. L. Dobbs, S. García-Burillo, G. Dumas, T. A. Thompson, K. F. Schuster, and C. Kramer. The PdBI Arcsecond Whirlpool Survey (PAWS): Environmental Dependence of Giant Molecular Cloud Properties in M51. *ApJ*, 784(1):3, Mar. 2014. doi: 10.1088/0004-637X/784/1/3.

D. Colombo, V. Kalinova, D. Utomo, E. Rosolowsky, A. D. Bolatto, R. C. Levy, T. Wong, S. F. Sanchez, A. K. Leroy, E. Ostriker, L. Blitz, S. Vogel, D. Mast, R. García-Benito, B. Husemann, H. Dannerbauer, L. Ellmeier, and Y. Cao. The EDGE-CALIFA survey: the influence of galactic rotation on the molecular depletion time across the Hubble sequence. *MNRAS*, 475(2):1791–1808, Apr. 2018. doi: 10.1093/mnras/stx3233.

D. Colombo, A. Duarte-Cabral, A. R. Pettitt, J. S. Urquhart, F. Wyrowski, T. Csengeri, K. R. Neralwar, F. Schuller, K. M. Menten, L. Anderson, P. Barnes, H. Beuther, L. Bronfman, D. Eden, A. Ginsburg, T. Henning, C. Koenig, M. Y. Lee, M. Mattern, S. Medina, S. E. Ragan, A. J. Rigby, A. Sanchez-Monge, A. Traficante, A. Y. Yang, and M. Wienen. The SEDIGISM survey: The influence of spiral arms on the molecular gas distribution of the inner Milky Way. *arXiv e-prints*, art. arXiv:2110.06071, Oct. 2021.

D. Cormier, F. Bigiel, M. J. Jiménez-Donaire, A. K. Leroy, M. Gallagher, A. Usero, K. Sandstrom, A. Bolatto, A. Hughes, C. Kramer, M. R. Krumholz, D. S. Meier, E. J. Murphy, J. Pety, E. Rosolowsky, E. Schinnerer, A. Schruba, K. Sliwa, and F. Walter. Full-disc ^{13}CO(1-0) mapping across nearby galaxies of the EMPIRE survey and the CO-to-H_2 conversion factor. *MNRAS*, 475(3):3909–3933, Apr. 2018. doi: 10.1093/mnras/sty059.

M. J. Currie, D. S. Berry, T. Jenness, A. G. Gibb, G. S. Bell, and P. W. Draper. Starlink Software in 2013. In N. Manset and P. Forshay, editors, *Astronomical Data Analysis Software and Systems XXIII*, volume 485 of *Astronomical Society of the Pacific Conference Series*, page 391, May 2014.

E. Daddi, A. Cimatti, A. Renzini, A. Fontana, M. Mignoli, L. Pozzetti, P. Tozzi, and G. Zamorani. A New Photometric Technique for the Joint Selection of Star-forming and Passive Galaxies at $1.4 \lesssim z \lesssim 2.5$. *ApJ*, 617 (2):746–764, Dec. 2004. doi: 10.1086/425569.

E. Daddi, D. Elbaz, F. Walter, F. Bournaud, F. Salmi, C. Carilli, H. Dannerbauer, M. Dickinson, P. Monaco, and D. Riechers. Different Star Formation Laws for Disks Versus Starbursts at Low and High Redshifts. *ApJL*, 714 (1):L118–L122, May 2010. doi: 10.1088/2041-8205/714/1/L118.

T. M. Dame, D. Hartmann, and P. Thaddeus. The Milky Way in Molecular Clouds: A New Complete CO Survey. *ApJ*, 547(2):792–813, Feb. 2001. doi: 10.1086/318388.

T. A. Davis. Systematic variation of the ^{12}CO/^{13}CO ratio as a function of star formation rate surface density. *MNRAS*, 445(3):2378–2384, Dec. 2014. doi: 10.1093/mnras/stu1850.

T. de Jong, S. Chu, and A. Dalgarno. Carbon monoxide in collapsing interstellar clouds. *ApJ*, 199:69–78, July 1975. doi: 10.1086/153665.

G. de Vaucouleurs. Classification and Morphology of External Galaxies. *Handbuch der Physik*, 53:275, Jan. 1959. doi: 10.1007/978-3-642-45932-0_7.

G. de Vaucouleurs, A. de Vaucouleurs, J. Corwin, Herold G., R. J. Buta, G. Paturel, and P. Fouque. *Third Reference Catalogue of Bright Galaxies*. Springer-Verlag, New York, NY, USA, 1991.

J. S. den Brok, D. Chatzigiannakis, F. Bigiel, J. Puschnig, A. T. Barnes, A. K. Leroy, M. J. Jiménez-Donaire, A. Usero, E. Schinnerer, E. Rosolowsky, C. M. Faesi, K. Grasha, A. Hughes, J. M. D. Kruijssen, D. Liu, L. Neumann, J. Pety, M. Querejeta, T. Saito, A. Schruba, and S. Stuber. New constraints on the ^{12}CO(2-1)/(1-0) line ratio across nearby disc galaxies. *MNRAS*, 504(3):3221–3245, July 2021. doi: 10.1093/mnras/stab859.

F. X. Desert, F. Boulanger, and J. L. Puget. Interstellar dust models for extinction and emission. *A&A*, 500: 313–334, Oct. 1990.

E. M. Di Teodoro and F. Fraternali. ^{3D} BAROLO: a new 3D algorithm to derive rotation curves of galaxies. *MNRAS*, 451(3):3021–3033, Aug. 2015. doi: 10.1093/mnras/stv1213.

S. Díaz-García, U. Lisenfeld, I. Pérez, A. Zurita, S. Verley, F. Combes, D. Espada, S. Leon, V. Martínez-Badenes, J. Sabater, and L. Verdes-Montenegro. Molecular gas and star formation within 12 strong galactic bars observed with IRAM-30m. *accepted to A&A, arXiv e-prints*, art. arXiv:2106.13099, June 2021.

R. L. Dickman, R. L. Snell, and F. P. Schloerb. Carbon Monoxide as an Extragalactic Mass Tracer. *ApJ*, 309: 326, Oct. 1986. doi: 10.1086/164604.

C. L. Dobbs, A. Burkert, and J. E. Pringle. Why are most molecular clouds not gravitationally bound? *MNRAS*, 413(4):2935–2942, June 2011a. doi: 10.1111/j.1365-2966.2011.18371.x.

C. L. Dobbs, A. Burkert, and J. E. Pringle. The properties of the interstellar medium in disc galaxies with stellar feedback. *MNRAS*, 417(2):1318–1334, Oct. 2011b. doi: 10.1111/j.1365-2966.2011.19346.x.

C. L. Dobbs, J. E. Pringle, and A. Duarte-Cabral. The frequency and nature of 'cloud-cloud collisions' in galaxies. *MNRAS*, 446(4):3608–3620, Feb. 2015. doi: 10.1093/mnras/stu2319.

J. Donovan Meyer, J. Koda, R. Momose, T. Mooney, F. Egusa, M. Carty, R. Kennicutt, N. Kuno, D. Rebolledo, T. Sawada, N. Scoville, and T. Wong. Resolved Giant Molecular Clouds in Nearby Spiral Galaxies: Insights from the CANON CO (1-0) Survey. *ApJ*, 772(2):107, Aug. 2013. doi: 10.1088/0004-637X/772/2/107.

D. Downes and P. M. Solomon. Rotating Nuclear Rings and Extreme Starbursts in Ultraluminous Galaxies. *ApJ*, 507(2):615–654, Nov. 1998. doi: 10.1086/306339.

D. Downes, D. Reynaud, P. M. Solomon, and S. J. E. Radford. CO in the Barred Galaxy NGC 1530. *ApJ*, 461: 186, Apr. 1996. doi: 10.1086/177046.

B. T. Draine. *Physics of the Interstellar and Intergalactic Medium*. Princeton series in astrophysics. PRINCETON UNIVERSITY PRESS, Princeton, New Jersey, 2011.

B. T. Draine, D. A. Dale, G. Bendo, K. D. Gordon, J. D. T. Smith, L. Armus, C. W. Engelbracht, G. Helou, J. Kennicutt, R. C., A. Li, H. Roussel, F. Walter, D. Calzetti, J. Moustakas, E. J. Murphy, G. H. Rieke, C. Bot, D. J. Hollenbach, K. Sheth, and H. I. Teplitz. Dust Masses, PAH Abundances, and Starlight Intensities in the SINGS Galaxy Sample. *ApJ*, 663(2):866–894, July 2007. doi: 10.1086/518306.

C. Druard, J. Braine, K. F. Schuster, N. Schneider, P. Gratier, S. Bontemps, M. Boquien, F. Combes, E. Corbelli, C. Henkel, F. Herpin, C. Kramer, F. van der Tak, and P. van der Werf. The IRAM M 33 CO(2-1) survey. A complete census of molecular gas out to 7 kpc. *A&A*, 567:A118, July 2014. doi: 10.1051/0004-6361/201423682.

F. Egusa, J. Koda, and N. Scoville. Molecular Gas Evolution Across a Spiral Arm in M51. *ApJ*, 726(2):85, Jan. 2011. doi: 10.1088/0004-637X/726/2/85.

D. Elbaz, E. Daddi, D. Le Borgne, M. Dickinson, D. M. Alexander, R. R. Chary, J. L. Starck, W. N. Brandt, M. Kitzbichler, E. MacDonald, M. Nonino, P. Popesso, D. Stern, and E. Vanzella. The reversal of the star formation-density relation in the distant universe. *A&A*, 468(1):33–48, June 2007. doi: 10.1051/0004-6361:20077525.

S. L. Ellison, M. D. Thorp, L. Lin, H.-A. Pan, A. F. L. Bluck, J. M. Scudder, H. Teimoorinia, S. F. Sánchez, and M. Sargent. The ALMaQUEST survey - III. Scatter in the resolved star-forming main sequence is primarily due to variations in star formation efficiency. *MNRAS*, 493(1):L39–L43, Mar. 2020. doi: 10.1093/mnrasl/slz179.

S. L. Ellison, L. Lin, M. D. Thorp, H.-A. Pan, J. M. Scudder, S. F. Sánchez, A. F. L. Bluck, and R. Maiolino. The ALMaQUEST Survey - V. The non-universality of kpc-scale star formation relations and the factors that drive them. *MNRAS*, 501(4):4777–4797, Mar. 2021. doi: 10.1093/mnras/staa3822.

B. G. Elmegreen. The H to H 2 Transition in Galaxies: Totally Molecular Galaxies. *ApJ*, 411:170, July 1993. doi: 10.1086/172816.

B. G. Elmegreen. Star Formation from Galaxies to Globules. *ApJ*, 577(1):206–220, Sept. 2002. doi: 10.1086/342177.

B. G. Elmegreen. On the Star Formation Law for Spiral and Irregular Galaxies. *ApJL*, 814(2):L30, Dec. 2015. doi: 10.1088/2041-8205/814/2/L30.

B. G. Elmegreen and D. M. Elmegreen. Do Density Waves Trigger Star Formation? *ApJ*, 311:554, Dec. 1986. doi: 10.1086/164795.

B. G. Elmegreen, D. M. Elmegreen, and Y. N. Efremov. Regularly Spaced Infrared Peaks in the Dusty Spirals of Messier 100. *ApJ*, 863(1):59, Aug. 2018. doi: 10.3847/1538-4357/aacf9a.

D. T. Emerson and R. Gräve. The reduction of scanning noise in raster scanned data. *A&A*, 190:353–358, Jan. 1988.

E. Emsellem, E. Schinnerer, F. Santoro, F. Belfiore, I. Pessa, R. McElroy, G. A. Blanc, E. Congiu, B. Groves, I.-T. Ho, K. Kreckel, A. Razza, P. Sanchez-Blazquez, O. Egorov, C. Faesi, R. S. Klessen, A. K. Leroy, S. Meidt, M. Querejeta, E. Rosolowsky, F. Scheuermann, G. S. Anand, A. T. Barnes, I. Bešlić, F. Bigiel, M. Boquien, Y. Cao, M. Chevance, D. A. Dale, C. Eibensteiner, S. C. O. Glover, K. Grasha, J. D. Henshaw, A. Hughes, E. W. Koch, J. M. D. Kruijssen, J. Lee, D. Liu, H.-A. Pan, J. Pety, T. Saito, K. M. Sandstrom, A. Schruba, J. Sun, D. A. Thilker, A. Usero, E. J. Watkins, and T. G. Williams. The PHANGS-MUSE survey – Probing the chemo-dynamical evolution of disc galaxies. *submitted to A&A, arXiv e-prints*, art. arXiv:2110.03708, Oct. 2021.

G. Engargiola, R. L. Plambeck, E. Rosolowsky, and L. Blitz. Giant Molecular Clouds in M33. I. BIMA All-Disk Survey. *ApJS*, 149(2):343–363, Dec. 2003. doi: 10.1086/379165.

C. W. Engelbracht, M. Blaylock, K. Y. L. Su, J. Rho, G. H. Rieke, J. Muzerolle, D. L. Padgett, D. C. Hines, K. D. Gordon, D. Fadda, A. Noriega-Crespo, D. M. Kelly, W. B. Latter, J. L. Hinz, K. A. Misselt, J. E. Morrison, J. A. Stansberry, D. L. Shupe, S. Stolovy, W. A. Wheaton, E. T. Young, G. Neugebauer, S. Wachter, P. G. Pérez-González, D. T. Frayer, and F. R. Marleau. Absolute Calibration and Characterization of the Multiband Imaging Photometer for Spitzer. I. The Stellar Calibrator Sample and the 24 μm Calibration. *PASP*, 119(859): 994–1018, Sept. 2007. doi: 10.1086/521881.

R. Enokiya, K. Torii, and Y. Fukui. Cloud-cloud collisions in the common foot point of molecular loops 1 and 2 in the Galactic Center. *PASJ*, 73:S75–S90, Jan. 2021. doi: 10.1093/pasj/psz119.

I. Evans, Neal J., A. Heiderman, and N. Vutisalchavakul. Star Formation Relations in Nearby Molecular Clouds. *ApJ*, 782(2):114, Feb. 2014. doi: 10.1088/0004-637X/782/2/114.

I. Evans, Neal J., M. Heyer, M.-A. Miville-Deschênes, Q. Nguyen-Luong, and M. Merello. Which Molecular Cloud Structures Are Bound? *ApJ*, 920(2):126, Oct. 2021. doi: 10.3847/1538-4357/ac1425.

I. N. Evans, F. A. Primini, K. J. Glotfelty, C. S. Anderson, N. R. Bonaventura, J. C. Chen, J. E. Davis, S. M. Doe, J. D. Evans, G. Fabbiano, E. C. Galle, I. Gibbs, Danny G., J. D. Grier, R. M. Hain, D. M. Hall, P. N. Harbo, X. H. He, J. C. Houck, M. Karovska, V. L. Kashyap, J. Lauer, M. L. McCollough, J. C. McDowell, J. B. Miller, A. W. Mitschang, D. L. Morgan, A. E. Mossman, J. S. Nichols, M. A. Nowak, D. A. Plummer, B. L. Refsdal, A. H. Rots, A. Siemiginowska, B. A. Sundheim, M. S. Tibbetts, D. W. Van Stone, S. L. Winkelman, and P. Zografou. The Chandra Source Catalog. *ApJS*, 189(1):37–82, July 2010. doi: 10.1088/0067-0049/189/1/37.

C. M. Faesi, C. J. Lada, and J. Forbrich. The ALMA View of GMCs in NGC 300: Physical Properties and Scaling Relations at 10 pc Resolution. *ApJ*, 857(1):19, Apr. 2018. doi: 10.3847/1538-4357/aaad60.

C. Federrath and R. S. Klessen. The Star Formation Rate of Turbulent Magnetized Clouds: Comparing Theory, Simulations, and Observations. *ApJ*, 761(2):156, Dec. 2012. doi: 10.1088/0004-637X/761/2/156.

R. Feldmann, N. Y. Gnedin, and A. V. Kravtsov. The X-factor in Galaxies. I. Dependence on Environment and Scale. *ApJ*, 747(2):124, Mar. 2012. doi: 10.1088/0004-637X/747/2/124.

A. V. Filippenko and W. L. W. Sargent. A search for "dwarf" Seyfert 1 nuclei. I. The initial data and results. *ApJS*, 57:503–522, Mar. 1985. doi: 10.1086/191012.

D. J. Fixsen, C. L. Bennett, and J. C. Mather. COBE Far Infrared Absolute Spectrophotometer Observations of Galactic Lines. *ApJ*, 526(1):207–214, Nov. 1999. doi: 10.1086/307962.

D. A. Forbes, C. Boisson, and M. J. Ward. NGC 1808 : active galactic nucleus or starburst ? *MNRAS*, 259: 293–301, Nov. 1992. doi: 10.1093/mnras/259.2.293.

K. Foyle, H. W. Rix, F. Walter, and A. K. Leroy. Arm and Interarm Star Formation in Spiral Galaxies. *ApJ*, 725(1):534–541, Dec. 2010. doi: 10.1088/0004-637X/725/1/534.

P. Freeman, E. Rosolowsky, J. M. D. Kruijssen, N. Bastian, and A. Adamo. The varying mass distribution of molecular clouds across M83. *MNRAS*, 468(2):1769–1781, June 2017. doi: 10.1093/mnras/stx499.

M. A. Frerking, W. D. Langer, and R. W. Wilson. The relationship between carbon monoxide abundance and visual extinction in interstellar clouds. *ApJ*, 262:590–605, Nov. 1982. doi: 10.1086/160451.

Y. Fujimoto, E. J. Tasker, M. Wakayama, and A. Habe. Do giant molecular clouds care about the galactic structure? *MNRAS*, 439(1):936–953, Mar. 2014. doi: 10.1093/mnras/stu014.

Y. Fujimoto, F. Maeda, A. Habe, and K. Ohta. Fast cloud-cloud collisions in a strongly barred galaxy: suppression of massive star formation. *MNRAS*, 494(2):2131–2146, May 2020. doi: 10.1093/mnras/staa840.

Y. Fukui and A. Kawamura. Molecular Clouds in Nearby Galaxies. *ARA&A*, 48:547–580, Sept. 2010. doi: 10.1146/annurev-astro-081309-130854.

Y. Fukui, A. Kawamura, T. Minamidani, Y. Mizuno, Y. Kanai, N. Mizuno, T. Onishi, Y. Yonekura, A. Mizuno, H. Ogawa, and M. Rubio. The Second Survey of the Molecular Clouds in the Large Magellanic Cloud by NANTEN. I. Catalog of Molecular Clouds. *ApJS*, 178(1):56–70, Sept. 2008. doi: 10.1086/589833.

M. J. Gallagher, A. K. Leroy, F. Bigiel, D. Cormier, M. J. Jiménez-Donaire, A. Hughes, J. Pety, E. Schinnerer, J. Sun, A. Usero, D. Utomo, A. Bolatto, M. Chevance, C. Faesi, S. C. O. Glover, A. A. Kepley, J. M. D. Kruijssen, M. R. Krumholz, S. E. Meidt, D. S. Meier, E. Murphy, M. Querejeta, E. Rosolowsky, T. Saito, and A. Schruba. Do Spectroscopic Dense Gas Fractions Track Molecular Cloud Surface Densities? *ApJL*, 868(2): L38, Dec. 2018a. doi: 10.3847/2041-8213/aaf16a.

M. J. Gallagher, A. K. Leroy, F. Bigiel, D. Cormier, M. J. Jiménez-Donaire, E. Ostriker, A. Usero, A. D. Bolatto, S. García-Burillo, A. Hughes, A. A. Kepley, M. Krumholz, S. E. Meidt, D. S. Meier, E. J. Murphy, J. Pety, E. Rosolowsky, E. Schinnerer, A. Schruba, and F. Walter. Dense Gas, Dynamical Equilibrium Pressure, and Star Formation in Nearby Star-forming Galaxies. *ApJ*, 858(2):90, May 2018b. doi: 10.3847/1538-4357/aabad8.

E. Galliano and D. Alloin. Embedded clusters in NGC 1808 central starburst. Near-infrared imaging and spectroscopy. *A&A*, 487(2):519–525, Aug. 2008. doi: 10.1051/0004-6361:200809732.

E. Galliano, D. Alloin, E. Pantin, P. O. Lagage, and O. Marco. Mid-infrared imaging of active galaxies. Active nuclei and embedded star clusters. *A&A*, 438(3):803–820, Aug. 2005. doi: 10.1051/0004-6361:20053049.

Y. Gao and P. M. Solomon. HCN Survey of Normal Spiral, Infrared-luminous, and Ultraluminous Galaxies. *ApJS*, 152(1):63–80, May 2004a. doi: 10.1086/383003.

Y. Gao and P. M. Solomon. The Star Formation Rate and Dense Molecular Gas in Galaxies. *ApJ*, 606(1):271–290, May 2004b. doi: 10.1086/382999.

Y. Gao, C. L. Carilli, P. M. Solomon, and P. A. Vanden Bout. HCN Observations of Dense Star-forming Gas in High-Redshift Galaxies. *ApJL*, 660(2):L93–L96, May 2007. doi: 10.1086/518244.

S. Garcia-Burillo, M. Guelin, J. Cernicharo, and M. Dahlem. Molecular gas distribution and dynamics of the edge-on spiral galaxy NGC 891. Discovery of a molecular halo. *A&A*, 266:21–36, Dec. 1992.

A. Gil de Paz, S. Boissier, B. F. Madore, M. Seibert, Y. H. Joe, A. Boselli, T. K. Wyder, D. Thilker, L. Bianchi, S.-C. Rey, R. M. Rich, T. A. Barlow, T. Conrow, K. Forster, P. G. Friedman, D. C. Martin, P. Morrissey, S. G. Neff, D. Schiminovich, T. Small, J. Donas, T. M. Heckman, Y.-W. Lee, B. Milliard, A. S. Szalay, and S. Yi. The GALEX Ultraviolet Atlas of Nearby Galaxies. *ApJS*, 173(2):185–255, Dec. 2007. doi: 10.1086/516636.

S. C. O. Glover and M. M. Mac Low. On the relationship between molecular hydrogen and carbon monoxide abundances in molecular clouds. *MNRAS*, 412(1):337–350, Mar. 2011. doi: 10.1111/j.1365-2966.2010.17907.x.

P. Goldreich and J. Kwan. Molecular Clouds. *ApJ*, 189:441–454, May 1974. doi: 10.1086/152821.

P. F. Goldsmith. Molecular Clouds: An Overview. In D. J. Hollenbach and J. Thronson, Harley A., editors, *Interstellar Processes*, volume 134, page 51, Jan. 1987. doi: 10.1007/978-94-009-3861-8_3.

P. F. Goldsmith, M. Heyer, G. Narayanan, R. Snell, D. Li, and C. Brunt. Large-Scale Structure of the Molecular Gas in Taurus Revealed by High Linear Dynamic Range Spectral Line Mapping. *ApJ*, 680(1):428–445, June 2008. doi: 10.1086/587166.

M. Gong, E. C. Ostriker, C.-G. Kim, and J.-G. Kim. The Environmental Dependence of the X_{CO} Conversion Factor. *ApJ*, 903(2):142, Nov. 2020. doi: 10.3847/1538-4357/abbdab.

E. W. Greisen and M. R. Calabretta. Representations of world coordinates in FITS. *A&A*, 395:1061–1075, Dec. 2002. doi: 10.1051/0004-6361:20021326.

J. E. Gunn and I. Gott, J. Richard. On the Infall of Matter Into Clusters of Galaxies and Some Effects on Their Evolution. *ApJ*, 176:1, Aug. 1972. doi: 10.1086/151605.

D. Guszejnov, M. Y. Grudić, S. S. R. Offner, M. Boylan-Kolchin, C.-A. Faucher-Giguère, A. Wetzel, S. M. Benincasa, and S. Loebman. Evolution of giant molecular clouds across cosmic time. *MNRAS*, 492(1):488–502, Feb. 2020. doi: 10.1093/mnras/stz3527.

S. Haan, E. Schinnerer, E. Emsellem, S. García-Burillo, F. Combes, C. G. Mundell, and H.-W. Rix. Dynamical Evolution of AGN Host Galaxies-Gas In/Out-Flow Rates in Seven NUGA Galaxies. *ApJ*, 692(2):1623–1661, Feb. 2009. doi: 10.1088/0004-637X/692/2/1623.

A. Habe and K. Ohta. Gravitational Instability Induced by a Cloud-Cloud Collision: The Case of Head-on Collisions between Clouds with Different Sizes and Densities. *PASJ*, 44:203–226, June 1992.

A. Hacar, J. Alves, A. Burkert, and P. Goldsmith. Opacity broadening and interpretation of suprathermal CO linewidths: Macroscopic turbulence and tangled molecular clouds. *A&A*, 591:A104, June 2016. doi: 10.1051/0004-6361/201527319.

T. Handa, Y. Sofue, and N. Nakai. The Molecular Bar and Arm of the Barred-Spiral Galaxy M83. In F. Combes and F. Casoli, editors, *Dynamics of Galaxies and Their Molecular Cloud Distributions*, volume 146, page 156, Jan. 1991.

C.-N. Hao, R. C. Kennicutt, B. D. Johnson, D. Calzetti, D. A. Dale, and J. Moustakas. Dust-corrected Star Formation Rates of Galaxies. II. Combinations of Ultraviolet and Infrared Tracers. *ApJ*, 741(2):124, Nov. 2011. doi: 10.1088/0004-637X/741/2/124.

N. Harada, K. Sakamoto, S. Martín, Y. Watanabe, R. Aladro, D. Riquelme, and A. Hirota. Chemical Evolution along the Circumnuclear Ring of M83. *ApJ*, 884(2):100, Oct. 2019. doi: 10.3847/1538-4357/ab41ff.

T. Hatakeyama, N. Kuno, K. Sorai, H. Kaneko, Y. Miyamoto, K. Muraoka, M. Takeda, K. Yanagitani, N. Kishida, M. Umei, T. Tanaka, Y. Tomiyasu, H. Nakanishi, C. Saita, S. Ueno, D. Salak, N. Matsumoto, K. Morokuma-Matsui, H.-A. Pan, and N. Nakai. CO Multi-line Imaging of Nearby Galaxies (COMING). II. Transitions between atomic and molecular gas, diffuse and dense gas, gas and stars in the dwarf galaxy NGC 2976. *PASJ*, 69(4):67, Aug. 2017. doi: 10.1093/pasj/psx044.

C. C. Hayward and P. F. Hopkins. How stellar feedback simultaneously regulates star formation and drives outflows. *MNRAS*, 465(2):1682–1698, Feb. 2017. doi: 10.1093/mnras/stw2888.

K. Heike and H. Awaki. X-Ray Study of Discrete Sources in NGC 1808 with Chandra. *PASJ*, 59:531–540, June 2007. doi: 10.1093/pasj/59.3.531.

C. Henkel, R. Mauersberger, T. Wiklind, S. Huettemeister, C. Lemme, and T. J. Millar. Dense gas in nearby galaxies. VI. A large 12C/13C ratio in a nuclear starburst environnement. *A&A*, 268:L17–L20, Feb. 1993.

C. Henkel, Y. N. Chin, R. Mauersberger, and J. B. Whiteoak. Dense gas in nearby galaxies. XI. Interstellar $^{12}C/^{13}C$ ratios in the central regions of M82 and IC342. *A&A*, 329:443–450, Jan. 1998.

P. Hennebelle and G. Chabrier. Analytical Star Formation Rate from Gravoturbulent Fragmentation. *ApJL*, 743 (2):L29, Dec. 2011. doi: 10.1088/2041-8205/743/2/L29.

P. Hennebelle and E. Falgarone. Turbulent molecular clouds. *The Astronomy and Astrophysics Review*, 20:55, Nov. 2012. doi: 10.1007/s00159-012-0055-y.

M. Heyer, C. Krawczyk, J. Duval, and J. M. Jackson. Re-Examining Larson's Scaling Relationships in Galactic Molecular Clouds. *ApJ*, 699(2):1092–1103, July 2009. doi: 10.1088/0004-637X/699/2/1092.

M. H. Heyer, C. Brunt, R. L. Snell, J. E. Howe, F. P. Schloerb, and J. M. Carpenter. The Five College Radio Astronomy Observatory CO Survey of the Outer Galaxy. *ApJS*, 115(2):241–258, Apr. 1998. doi: 10.1086/313086.

M. H. Heyer, J. M. Carpenter, and R. L. Snell. The Equilibrium State of Molecular Regions in the Outer Galaxy. *ApJ*, 551(2):852–866, Apr. 2001. doi: 10.1086/320218.

M. H. Heyer, E. Corbelli, S. E. Schneider, and J. S. Young. The Molecular Gas Distribution and Schmidt Law in M33. *ApJ*, 602(2):723–729, Feb. 2004. doi: 10.1086/381196.

A. Hirota, N. Kuno, N. Sato, H. Nakanishi, T. Tosaki, and K. Sorai. Variation of Molecular Gas Properties Across the Spiral Arms in IC 342: Large-Scale ^{13}CO (1-0) Emission. *PASJ*, 62:1261–1275, Oct. 2010. doi: 10.1093/pasj/62.5.1261.

A. Hirota, N. Kuno, N. Sato, H. Nakanishi, T. Tosaki, and K. Sorai. Giant Molecular Clouds in the Spiral Arm of IC 342. *ApJ*, 737(1):40, Aug. 2011. doi: 10.1088/0004-637X/737/1/40.

A. Hirota, N. Kuno, J. Baba, F. Egusa, A. Habe, K. Muraoka, A. Tanaka, H. Nakanishi, and R. Kawabe. Wide-field ^{12}CO (J = 1-0) imaging of the nearby barred galaxy M 83 with NMA and Nobeyema 45 m telescope: Mole cular gas kinematics and star formation along the bar. *PASJ*, 66(2):46, Apr. 2014. doi: 10.1093/pasj/psu006.

A. Hirota, F. Egusa, J. Baba, N. Kuno, K. Muraoka, T. Tosaki, R. Miura, H. Nakanishi, and R. Kawabe. ALMA ^{12}CO (J = 1-0) imaging of the nearby galaxy M 83: Variations in the efficiency of star formation in giant molecular clouds. *PASJ*, 70(4):73, Aug. 2018. doi: 10.1093/pasj/psy071.

L. C. Ho, A. V. Filippenko, and W. L. W. Sargent. A Search for "Dwarf" Seyfert Nuclei. III. Spectroscopic Parameters and Properties of the Host Galaxies. *ApJS*, 112(2):315–390, Oct. 1997. doi: 10.1086/313041.

E. P. Hubble. *Realm of the Nebulae*. Yale University Press, 1936.

R. L. Hurt and J. L. Turner. The Molecular Structure of a Starburst: 13CO in the Nucleus of Maffei 2. *ApJ*, 377:434, Aug. 1991. doi: 10.1086/170373.

R. L. Hurt, K. M. Merrill, I. Gatley, and J. L. Turner. Maffei 2 Revealed: The Infared Morphology of a Hidden Galaxy. *AJ*, 105:121, Jan. 1993a. doi: 10.1086/116412.

R. L. Hurt, J. L. Turner, P. T. P. Ho, and R. N. Martin. Warm Molecular Gas in a Starburst: CO (3–2) Observations of Maffei 2. *ApJ*, 404:602, Feb. 1993b. doi: 10.1086/172313.

R. L. Hurt, J. L. Turner, and P. T. P. Ho. H i and the Maffei 2 Starburst: A Merger Scenario. *ApJ*, 466:135, July 1996. doi: 10.1086/177498.

S. Hüttemeister, S. Aalto, M. Das, and W. F. Wall. Changing molecular gas properties in the bar and center of NGC 7479. *A&A*, 363:93–107, Nov. 2000.

A. P. S. Hygate, J. M. D. Kruijssen, M. Chevance, A. Schruba, D. T. Haydon, and S. N. Longmore. An uncertainty principle for star formation - IV. On the nature and filtering of diffuse emission. *MNRAS*, 488(2):2800–2824, Sept. 2019. doi: 10.1093/mnras/stz1779.

E. J. Iles, A. R. Pettitt, and T. Okamoto. Differences in star formation activity between tidally triggered and isolated bars: a case study of NGC 4303 and NGC 3627. *MNRAS*, 510(3):3899–3916, Mar. 2022. doi: 10.1093/mnras/stab3330.

S. Inoue, T. Takagi, A. Miyazaki, E. M. Cooper, F. Egusa, and H. Yajima. Instability analysis for spiral arms of local galaxies: M51, NGC 3627, and NGC 628. *MNRAS*, 506(1):84–97, Sept. 2021. doi: 10.1093/mnras/stab1729.

D. Iono, C. D. Wilson, S. Takakuwa, M. S. Yun, G. R. Petitpas, A. B. Peck, P. T. P. Ho, S. Matsushita, Y. M. Pihlstrom, and Z. Wang. High-Resolution Imaging of Warm and Dense Molecular Gas in the Nuclear Region of the Luminous Infrared Galaxy NGC 6240. *ApJ*, 659(1):283–295, Apr. 2007. doi: 10.1086/512362.

D. Iono, C. D. Wilson, M. S. Yun, A. J. Baker, G. R. Petitpas, A. B. Peck, M. Krips, T. J. Cox, S. Matsushita, J. C. Mihos, and Y. Pihlstrom. Luminous Infrared Galaxies with the Submillimeter Array. II. Comparing the CO (3-2) Sizes and Luminosities of Local and High-Redshift Luminous Infrared Galaxies. *ApJ*, 695(2): 1537–1549, Apr. 2009. doi: 10.1088/0004-637X/695/2/1537.

M. Ishiguro, R. Kawabe, K. I. Morita, S. Okumura, Y. Chikada, T. Kasuga, T. Kanzawa, H. Iwashita, K. Handa, T. Takahashi, H. Kobayashi, Y. Murata, S. Ishizuki, and N. Nakai. Molecular Gas Bar and Expanding Molecular Ring in the Nucleus of the Spiral Galaxy Maffei 2. *ApJ*, 344:763, Sept. 1989. doi: 10.1086/167840.

T. Isobe, E. D. Feigelson, M. G. Akritas, and G. J. Babu. Linear Regression in Astronomy. I. *ApJ*, 364:104, Nov. 1990. doi: 10.1086/169390.

F. P. Israel. H_2 and its relation to CO in the LMC and other magellanic irregular galaxies. *A&A*, 328:471–482, Dec. 1997.

F. P. Israel. Central molecular zones in galaxies: ^{12}CO-to-^{13}CO ratios, carbon budget, and X factors. *A&A*, 635: A131, Mar. 2020. doi: 10.1051/0004-6361/201834198.

F. P. Israel and F. Baas. CI and CO in the nearby spiral galaxies IC 342 and Maffei 2. *A&A*, 404:495–504, June 2003. doi: 10.1051/0004-6361:20030479.

P. Jáchym, J. D. P. Kenney, M. Sun, F. Combes, L. Cortese, T. C. Scott, S. Sivanandam, E. Brinks, E. Roediger, J. Palouš, and M. Fumagalli. ALMA Unveils Widespread Molecular Gas Clumps in the Ram Pressure Stripped Tail of the Norma Jellyfish Galaxy. *ApJ*, 883(2):145, Oct. 2019. doi: 10.3847/1538-4357/ab3e6c.

T. H. Jarrett, T. Chester, R. Cutri, S. E. Schneider, and J. P. Huchra. The 2MASS Large Galaxy Atlas. *AJ*, 125 (2):525–554, Feb. 2003. doi: 10.1086/345794.

S. M. R. Jeffreson, J. M. D. Kruijssen, B. W. Keller, M. Chevance, and S. C. O. Glover. The role of galactic dynamics in shaping the physical properties of giant molecular clouds in Milky Way-like galaxies. *MNRAS*, 498(1):385–429, Oct. 2020. doi: 10.1093/mnras/staa2127.

E. Jiménez-Bailón, M. Santos-Lleó, M. Dahlem, M. Ehle, J. M. Mas-Hesse, M. Guainazzi, T. M. Heckman, and K. A. Weaver. X-ray emission from NGC 1808: more than a complex starburst. *A&A*, 442(3):861–877, Nov. 2005. doi: 10.1051/0004-6361:20053022.

M. J. Jiménez-Donaire, D. Cormier, F. Bigiel, A. K. Leroy, M. Gallagher, M. R. Krumholz, A. Usero, A. Hughes, C. Kramer, D. Meier, E. Murphy, J. Pety, E. Schinnerer, A. Schruba, K. Schuster, K. Sliwa, and N. Tomicic. ^{13}CO/C^{18}O Gradients across the Disks of Nearby Spiral Galaxies. *ApJL*, 836(2):L29, Feb. 2017. doi: 10.3847/2041-8213/836/2/L29.

M. J. Jiménez-Donaire, F. Bigiel, A. K. Leroy, A. Usero, D. Cormier, J. Puschnig, M. Gallagher, A. Kepley, A. Bolatto, S. García-Burillo, A. Hughes, C. Kramer, J. Pety, E. Schinnerer, A. Schruba, K. Schuster, and F. Walter. EMPIRE: The IRAM 30 m Dense Gas Survey of Nearby Galaxies. *ApJ*, 880(2):127, Aug. 2019. doi: 10.3847/1538-4357/ab2b95.

S. Jogee, N. Scoville, and J. D. P. Kenney. The Central Region of Barred Galaxies: Molecular Environment, Starbursts, and Secular Evolution. *ApJ*, 630(2):837–863, Sept. 2005. doi: 10.1086/432106.

T. Kamazaki, S. K. Okumura, Y. Chikada, T. Okuda, Y. Kurono, S. Iguchi, S. Mitsuishi, Y. Murakami, N. Nishimura, H. Mita, and R. Sano. Digital Spectro-Correlator System for the Atacama Compact Array of the Atacama Large Millimeter/submillimeter Array. *PASJ*, 64:29, Apr. 2012. doi: 10.1093/pasj/64.2.29.

J. D. P. Kenney, J. H. van Gorkom, and B. Vollmer. VLA H I Observations of Gas Stripping in the Virgo Cluster Spiral NGC 4522. *AJ*, 127(6):3361–3374, June 2004. doi: 10.1086/420805.

J. Kennicutt, R. C. Stellar Structure of the Galaxy: Overview. In C. E. Woodward, M. D. Bicay, and J. M. Shull, editors, *Tetons 4: Galactic Structure, Stars and the Interstellar Medium*, volume 231 of *Astronomical Society of the Pacific Conference Series*, page 2, Jan. 2001.

J. Kennicutt, Robert C. The Star Formation Law in Galactic Disks. *ApJ*, 344:685, Sept. 1989. doi: 10.1086/167834.

J. Kennicutt, Robert C. Star Formation in Galaxies Along the Hubble Sequence. *ARA&A*, 36:189–232, Jan. 1998a. doi: 10.1146/annurev.astro.36.1.189.

J. Kennicutt, Robert C. The Global Schmidt Law in Star-forming Galaxies. *ApJ*, 498(2):541–552, May 1998b. doi: 10.1086/305588.

J. Kennicutt, Robert C., D. Calzetti, F. Walter, G. Helou, D. J. Hollenbach, L. Armus, G. Bendo, D. A. Dale, B. T. Draine, C. W. Engelbracht, K. D. Gordon, M. K. M. Prescott, M. W. Regan, M. D. Thornley, C. Bot, E. Brinks, E. de Blok, D. de Mello, M. Meyer, J. Moustakas, E. J. Murphy, K. Sheth, and J. D. T. Smith. Star Formation in NGC 5194 (M51a). II. The Spatially Resolved Star Formation Law. *ApJ*, 671(1):333–348, Dec. 2007. doi: 10.1086/522300.

J. Kennicutt, Robert C., C.-N. Hao, D. Calzetti, J. Moustakas, D. A. Dale, G. Bendo, C. W. Engelbracht, B. D. Johnson, and J. C. Lee. Dust-corrected Star Formation Rates of Galaxies. I. Combinations of Hα and Infrared Tracers. *ApJ*, 703(2):1672–1695, Oct. 2009. doi: 10.1088/0004-637X/703/2/1672.

R. C. Kennicutt and N. J. Evans. Star Formation in the Milky Way and Nearby Galaxies. *ARA&A*, 50:531–608, Sept. 2012. doi: 10.1146/annurev-astro-081811-125610.

W.-T. Kim, C.-G. Kim, and E. C. Ostriker. Local Simulations of Spiral Galaxies with the TIGRESS Framework. I. Star Formation and Arm Spurs/Feathers. *ApJ*, 898(1):35, July 2020. doi: 10.3847/1538-4357/ab9b87.

E. W. Koch, E. W. Rosolowsky, A. Schruba, A. Leroy, A. Kepley, J. Braine, J. Dalcanton, and M. C. Johnson. Relationship between the line width of the atomic and molecular ISM in M33. *MNRAS*, 485(2):2324–2342, May 2019. doi: 10.1093/mnras/stz484.

J. Koda and Y. Sofue. The Virgo High-Resolution CO Survey: VI. Gas Dynamics and Star Formation along the Bar in NGC 4303. *PASJ*, 58:299–312, Apr. 2006. doi: 10.1093/pasj/58.2.299.

J. Koda, N. Scoville, T. Sawada, M. A. La Vigne, S. N. Vogel, A. E. Potts, J. M. Carpenter, S. A. Corder, M. C. H. Wright, S. M. White, B. A. Zauderer, J. Patience, A. I. Sargent, D. C. J. Bock, D. Hawkins, M. Hodges, A. Kemball, J. W. Lamb, R. L. Plambeck, M. W. Pound, S. L. Scott, P. Teuben, and D. P. Woody. Dynamically Driven Evolution of the Interstellar Medium in M51. *ApJL*, 700(2):L132–L136, Aug. 2009. doi: 10.1088/0004-637X/700/2/L132.

J. Koda, T. Sawada, M. C. H. Wright, P. Teuben, S. A. Corder, J. Patience, N. Scoville, J. Donovan Meyer, and F. Egusa. CO(J = 1-0) Imaging of M51 with CARMA and the Nobeyama 45 m Telescope. *ApJS*, 193(1):19, Mar. 2011. doi: 10.1088/0067-0049/193/1/19.

J. Koda, N. Scoville, T. Hasegawa, D. Calzetti, J. Donovan Meyer, F. Egusa, R. Kennicutt, N. Kuno, M. Louie, R. Momose, T. Sawada, K. Sorai, and M. Umei. Physical Conditions in Molecular Clouds in the Arm and Interarm Regions of M51. *ApJ*, 761(1):41, Dec. 2012. doi: 10.1088/0004-637X/761/1/41.

J. Koda, N. Scoville, and M. Heyer. Evolution of Molecular and Atomic Gas Phases in the Milky Way. *ApJ*, 823 (2):76, June 2016. doi: 10.3847/0004-637X/823/2/76.

J. Koda, T. Sawada, K. Sakamoto, A. Hirota, F. Egusa, S. Boissier, D. Calzetti, J. D. Meyer, B. G. Elmegreen, A. G. de Paz, N. Harada, L. C. Ho, M. I. N. Kobayashi, N. Kuno, S. Martín, K. Muraoka, K. Nakanishi, N. Scoville, M. Seibert, C. Vlahakis, and Y. Watanabe. Systematic Variations of CO J = 2-1/1-0 Ratio and Their Implications in The Nearby Barred Spiral Galaxy M83. *ApJL*, 890(1):L10, Feb. 2020. doi: 10.3847/2041-8213/ab70b7.

M. Kohno, A. Nishimura, S. Fujita, K. Tachihara, T. Onishi, K. Tokuda, Y. Fukui, Y. Miyamoto, S. Ueda, R. Kiridoshi, D. Tsutsumi, K. Torii, T. Minamidani, K. Saigo, T. Handa, and H. Sano. Nobeyama 45 m Local Spur CO survey. I. Giant molecular filaments and cluster formation in the Vulpecula OB association. *arXiv e-prints*, art. arXiv:2110.08841, Oct. 2021a.

M. Kohno, K. Tachihara, K. Torii, S. Fujita, A. Nishimura, N. Kuno, T. Umemoto, T. Minamidani, M. Matsuo, R. Kiridoshi, K. Tokuda, M. Hanaoka, Y. Tsuda, M. Kuriki, A. Ohama, H. Sano, T. Hasegawa, Y. Sofue, A. Habe, T. Onishi, and Y. Fukui. FOREST unbiased Galactic plane imaging survey with the Nobeyama 45 m telescope (FUGIN). VI. Dense gas and mini-starbursts in the W 43 giant molecular cloud complex. *PASJ*, 73:S129–S171, Jan. 2021b. doi: 10.1093/pasj/psaa015.

S. Komugi, Y. Sofue, and F. Egusa. Threshold between Spontaneous and Cloud-Collisional Star Formation. *PASJ*, 58:793–796, Oct. 2006. doi: 10.1093/pasj/58.5.793.

J. K. Kotilainen, D. A. Forbes, A. F. M. Moorwood, P. P. van der Werf, and M. J. Ward. Near-infrared line and continuum imaging of the nuclear starburst region of NGC 1808. *A&A*, 313:771–782, Sept. 1996.

H. Koyama and E. C. Ostriker. Pressure Relations and Vertical Equilibrium in the Turbulent, Multiphase Interstellar Medium. *ApJ*, 693(2):1346–1359, Mar. 2009. doi: 10.1088/0004-637X/693/2/1346.

A. Krabbe, A. Sternberg, and R. Genzel. Near-Infrared Spectral Imaging of NGC 1808: Probing the Starburst. *ApJ*, 425:72, Apr. 1994. doi: 10.1086/173964.

K. Kreckel, C. Faesi, J. M. D. Kruijssen, A. Schruba, B. Groves, A. K. Leroy, F. Bigiel, G. A. Blanc, M. Chevance, C. Herrera, A. Hughes, R. McElroy, J. Pety, M. Querejeta, E. Rosolowsky, E. Schinnerer, J. Sun, A. Usero, and D. Utomo. A 50 pc Scale View of Star Formation Efficiency across NGC 628. *ApJL*, 863(2):L21, Aug. 2018. doi: 10.3847/2041-8213/aad77d.

P. Kroupa. On the variation of the initial mass function. *MNRAS*, 322(2):231–246, Apr. 2001. doi: 10.1046/j.1365-8711.2001.04022.x.

J. M. D. Kruijssen, A. Schruba, M. Chevance, S. N. Longmore, A. P. S. Hygate, D. T. Haydon, A. F. McLeod, J. J. Dalcanton, L. J. Tacconi, and E. F. van Dishoeck. Fast and inefficient star formation due to short-lived molecular clouds and rapid feedback. *Nature*, 569(7757):519–522, May 2019. doi: 10.1038/s41586-019-1194-3.

M. R. Krumholz and C. F. McKee. A General Theory of Turbulence-regulated Star Formation, from Spirals to Ultraluminous Infrared Galaxies. *ApJ*, 630(1):250–268, Sept. 2005. doi: 10.1086/431734.

M. R. Krumholz, C. F. McKee, and J. Tumlinson. The Atomic-to-Molecular Transition in Galaxies. II: H I and H_2 Column Densities. *ApJ*, 693(1):216–235, Mar. 2009a. doi: 10.1088/0004-637X/693/1/216.

M. R. Krumholz, C. F. McKee, and J. Tumlinson. The Star Formation Law in Atomic and Molecular Gas. *ApJ*, 699(1):850–856, July 2009b. doi: 10.1088/0004-637X/699/1/850.

M. R. Krumholz, J. M. D. Kruijssen, and R. M. Crocker. A dynamical model for gas flows, star formation and nuclear winds in galactic centres. *MNRAS*, 466(1):1213–1233, Apr. 2017. doi: 10.1093/mnras/stw3195.

N. Kuno, N. Sato, H. Nakanishi, A. Hirota, T. Tosaki, Y. Shioya, K. Sorai, N. Nakai, K. Nishiyama, and B. Vila-Vilaró. Nobeyama CO Atlas of Nearby Spiral Galaxies: Distribution of Molecular Gas in Barred and Nonbarred Spiral Galaxies. *PASJ*, 59:117–166, Feb. 2007. doi: 10.1093/pasj/59.1.117.

N. Kuno, K. Nakanishi, K. Sorai, and T. Shibatsuka. Central Spiral Structure of Molecular Gas in Maffei 2. *PASJ*, 60:475, June 2008. doi: 10.1093/pasj/60.3.475.

N. Kuno, S. Takano, D. Iono, T. Nakajima, H. Iwashita, K. Handa, B. Hatsukade, A. Higuchi, A. Hirota, S. Ishikawa, H. Kaneko, N. Kawaguchi, R. Kawabe, K. Kimura, K. Kohno, J. Maekawa, H. Mikoshiba, C. Miyazawa, K. Miyazawa, K. Muraoka, H. Ogawa, S. Onodera, Y. Saito, S. Takahashi, and T. Yonezu. New observing system of the 45-m telescope at nobeyama radio observatory. In *2011 XXXth URSI General Assembly and Scientific Symposium*, pages 1–4, 2011. doi: 10.1109/URSIGASS.2011.6051296.

C. J. Lada, M. Lombardi, and J. F. Alves. On the Star Formation Rates in Molecular Clouds. *ApJ*, 724(1):687–693, Nov. 2010. doi: 10.1088/0004-637X/724/1/687.

W. D. Langer and A. A. Penzias. 12C/ 13C Isotope Ratio across the Galaxy from Observations of 13C 18O in Molecular Clouds. *ApJ*, 357:477, July 1990. doi: 10.1086/168935.

W. D. Langer, T. E. Graedel, M. A. Frerking, and P. B. Armentrout. Carbon and oxygen isotope fractionation in dense interstellar clouds. *ApJ*, 277:581–604, Feb. 1984. doi: 10.1086/161730.

W. D. Langer, R. W. Wilson, P. F. Goldsmith, and C. A. Beichman. Dust and Gas Emission in Barnard 5. *ApJ*, 337:355, Feb. 1989. doi: 10.1086/167108.

R. B. Larson. Turbulence and star formation in molecular clouds. *MNRAS*, 194:809–826, Mar. 1981. doi: 10.1093/mnras/194.4.809.

C. J. Law, Q. Zhang, L. Ricci, G. Petitpas, M. J. Jiménez-Donaire, J. Ueda, X. Lu, and M. M. Dunham. Submillimeter Array Observations of Extended CO (J = 2 - 1) Emission in the Interacting Galaxy NGC 3627. *ApJ*, 865(1):17, Sept. 2018. doi: 10.3847/1538-4357/aadca9.

E. J. Lee, M.-A. Miville-Deschênes, and N. W. Murray. Observational Evidence of Dynamic Star Formation Rate in Milky Way Giant Molecular Clouds. *ApJ*, 833(2):229, Dec. 2016. doi: 10.3847/1538-4357/833/2/229.

C. Leitherer, D. Schaerer, J. D. Goldader, R. M. G. Delgado, C. Robert, D. F. Kune, D. F. de Mello, D. Devost, and T. M. Heckman. Starburst99: Synthesis Models for Galaxies with Active Star Formation. *ApJS*, 123(1):3–40, July 1999. doi: 10.1086/313233.

A. K. Leroy, F. Walter, E. Brinks, F. Bigiel, W. J. G. de Blok, B. Madore, and M. D. Thornley. The Star Formation Efficiency in Nearby Galaxies: Measuring Where Gas Forms Stars Effectively. *AJ*, 136(6):2782–2845, Dec. 2008. doi: 10.1088/0004-6256/136/6/2782.

A. K. Leroy, F. Walter, F. Bigiel, A. Usero, A. Weiss, E. Brinks, W. J. G. de Blok, R. C. Kennicutt, K.-F. Schuster, C. Kramer, H. W. Wiesemeyer, and H. Roussel. Heracles: The HERA CO Line Extragalactic Survey. *AJ*, 137(6):4670–4696, June 2009. doi: 10.1088/0004-6256/137/6/4670.

A. K. Leroy, A. Bolatto, K. Gordon, K. Sandstrom, P. Gratier, E. Rosolowsky, C. W. Engelbracht, N. Mizuno, E. Corbelli, Y. Fukui, and A. Kawamura. The CO-to-H_2 Conversion Factor from Infrared Dust Emission across the Local Group. *ApJ*, 737(1):12, Aug. 2011. doi: 10.1088/0004-637X/737/1/12.

A. K. Leroy, F. Walter, K. Sandstrom, A. Schruba, J.-C. Munoz-Mateos, F. Bigiel, A. Bolatto, E. Brinks, W. J. G. de Blok, S. Meidt, H.-W. Rix, E. Rosolowsky, E. Schinnerer, K.-F. Schuster, and A. Usero. Molecular Gas and Star Formation in nearby Disk Galaxies. *AJ*, 146(2):19, Aug. 2013. doi: 10.1088/0004-6256/146/2/19.

A. K. Leroy, A. D. Bolatto, E. C. Ostriker, E. Rosolowsky, F. Walter, S. R. Warren, J. Donovan Meyer, J. Hodge, D. S. Meier, J. Ott, K. Sandstrom, A. Schruba, S. Veilleux, and M. Zwaan. ALMA Reveals the Molecular Medium Fueling the Nearest Nuclear Starburst. *ApJ*, 801(1):25, Mar. 2015. doi: 10.1088/0004-637X/801/1/25.

A. K. Leroy, E. Schinnerer, A. Hughes, J. M. D. Kruijssen, S. Meidt, A. Schruba, J. Sun, F. Bigiel, G. Aniano, G. A. Blanc, A. Bolatto, M. Chevance, D. Colombo, M. Gallagher, S. Garcia-Burillo, C. Kramer, M. Querejeta, J. Pety, T. A. Thompson, and A. Usero. Cloud-scale ISM Structure and Star Formation in M51. *ApJ*, 846(1): 71, Sept. 2017a. doi: 10.3847/1538-4357/aa7fef.

A. K. Leroy, A. Usero, A. Schruba, F. Bigiel, J. M. D. Kruijssen, A. Kepley, G. A. Blanc, A. D. Bolatto, D. Cormier, M. Gallagher, A. Hughes, M. J. Jiménez-Donaire, E. Rosolowsky, and E. Schinnerer. Millimeter-wave Line Ratios and Sub-beam Volume Density Distributions. *ApJ*, 835(2):217, Feb. 2017b. doi: 10.3847/1538-4357/835/2/217.

A. K. Leroy, A. Hughes, D. Liu, J. Pety, E. Rosolowsky, T. Saito, E. Schinnerer, A. Schruba, A. Usero, C. M. Faesi, C. N. Herrera, M. Chevance, A. P. S. Hygate, A. A. Kepley, E. W. Koch, M. Querejeta, K. Sliwa, D. Will, C. D. Wilson, G. S. Anand, A. Barnes, F. Belfiore, I. Bešlić, F. Bigiel, G. A. Blanc, A. D. Bolatto, M. Boquien, Y. Cao, R. Chandar, J. Chastenet, I. D. Chiang, E. Congiu, D. A. Dale, S. Deger, J. S. den Brok, C. Eibensteiner, E. Emsellem, A. García-Rodríguez, S. C. O. Glover, K. Grasha, B. Groves, J. D. Henshaw, M. J. Jiménez Donaire, J. Kim, R. S. Klessen, K. Kreckel, J. M. D. Kruijssen, K. L. Larson, J. C. Lee, N. Mayker, R. McElroy, S. E. Meidt, A. Mok, H.-A. Pan, J. Puschnig, A. Razza, P. Sánchez-Bl'azquez, K. M. Sandstrom, F. Santoro, A. Sardone, F. Scheuermann, J. Sun, D. A. Thilker, J. A. Turner, L. Ubeda, D. Utomo, E. J. Watkins, and T. G. Williams. PHANGS-ALMA Data Processing and Pipeline. *ApJS*, 255(1):19, July 2021a. doi: 10.3847/1538-4365/abec80.

A. K. Leroy, E. Rosolowsky, A. Usero, K. Sandstrom, E. Schinnerer, A. Schruba, A. D. Bolatto, J. Sun, A. T. Barnes, F. Belfiore, F. Bigiel, J. S. den Brok, Y. Cao, I.-D. Chiang, M. Chevance, D. A. Dale, C. Eibensteiner, C. M. Faesi, S. C. O. Glover, A. Hughes, M. J. Jiménez Donaire, R. S. Klessen, E. W. Koch, J. M. D. Kruijssen, D. Liu, S. E. Meidt, H.-A. Pan, J. Pety, J. Puschnig, M. Querejeta, T. Saito, A. Sardone, E. J. Watkins, A. Weiss, and T. G. Williams. Low-J CO Line Ratios From Single Dish CO Mapping Surveys and PHANGS-ALMA. *arXiv e-prints*, art. arXiv:2109.11583, Sept. 2021b.

A. K. Leroy, E. Schinnerer, A. Hughes, E. Rosolowsky, J. Pety, A. Schruba, A. Usero, G. A. Blanc, M. Chevance, E. Emsellem, C. M. Faesi, C. N. Herrera, D. Liu, S. E. Meidt, M. Querejeta, T. Saito, K. M. Sandstrom, J. Sun, T. G. Williams, G. S. Anand, A. T. Barnes, E. A. Behrens, F. Belfiore, S. M. Benincasa, I. Bešlić, F. Bigiel, A. D. Bolatto, J. S. den Brok, Y. Cao, R. Chandar, J. Chastenet, I.-D. Chiang, E. Congiu, D. A. Dale, S. Deger, C. Eibensteiner, O. V. Egorov, A. García-Rodríguez, S. C. O. Glover, K. Grasha, J. D. Henshaw, I.-T. Ho, A. A. Kepley, J. Kim, R. S. Klessen, K. Kreckel, E. W. Koch, J. M. D. Kruijssen, K. L. Larson, J. C. Lee, L. A. Lopez, J. Machado, N. Mayker, R. McElroy, E. J. Murphy, E. C. Ostriker, H.-A. Pan, I. Pessa, J. Puschnig, A. Razza, P. Sánchez-Blázquez, F. Santoro, A. Sardone, F. Scheuermann, K. Sliwa, M. C. Sormani, S. K. Stuber, D. A. Thilker, J. A. Turner, D. Utomo, E. J. Watkins, and B. Whitmore. PHANGS-ALMA: Arcsecond CO(2-1) Imaging of Nearby Star-Forming Galaxies. *acceepted to ApJS, arXiv e-prints*, art. arXiv:2104.07739, Apr. 2021c.

C. M. Leung and H. S. Liszt. Radiation transport and non-LTE analysis of interstellar molecular lines. I. Carbon monoxide. *ApJ*, 208:732–746, Sept. 1976. doi: 10.1086/154657.

Z. Li, Z. Li, M. W. L. Smith, C. D. Wilson, Y. Gao, S. A. Eales, Y. Ao, M. Bureau, A. Chung, T. A. Davis, R. de Grijs, D. J. Eden, J. He, T. M. Hughes, X. Jiang, F. Kemper, I. Lamperti, B. Lee, C.-H. Lee, M. J. Michałowski, H. Parsons, S. Ragan, P. Scicluna, Y. Shi, X. Tang, N. Tomičić, S. Viaene, T. G. Williams, and M. Zhu. The HASHTAG project I. A survey of CO(3-2) emission from the star forming disc of M31. *MNRAS*, 492(1):195–209, Feb. 2020. doi: 10.1093/mnras/stz3409.

L. Lin, H.-A. Pan, S. L. Ellison, F. Belfiore, Y. Shi, S. F. Sánchez, B.-C. Hsieh, K. Rowlands, S. Ramya, M. D. Thorp, C. Li, and R. Maiolino. The ALMaQUEST Survey: The Molecular Gas Main Sequence and the Origin of the Star-forming Main Sequence. *ApJL*, 884(2):L33, Oct. 2019. doi: 10.3847/2041-8213/ab4815.

L. Lin, S. L. Ellison, H.-A. Pan, M. D. Thorp, Y.-C. Su, S. F. Sánchez, F. Belfiore, M. S. Bothwell, K. Bundy, Y.-M. Chen, A. Concas, B.-C. Hsieh, P.-Y. Hsieh, C. Li, R. Maiolino, K. Masters, J. A. Newman, K. Rowlands, Y. Shi, R. Smethurst, D. V. Stark, T. Xiao, and P.-C. Yu. ALMaQUEST. IV. The ALMA-MaNGA QUEnching and STar Formation (ALMaQUEST) Survey. *ApJ*, 903(2):145, Nov. 2020. doi: 10.3847/1538-4357/abba3a.

H. S. Liszt. Formation, fractionation, and excitation of carbon monoxide in diffuse clouds. *A&A*, 476(1):291–300, Dec. 2007. doi: 10.1051/0004-6361:20078502.

H. S. Liszt, J. Pety, and R. Lucas. The CO luminosity and CO-H_2 conversion factor of diffuse ISM: does CO emission trace dense molecular gas? *A&A*, 518:A45, July 2010. doi: 10.1051/0004-6361/201014510.

G. Liu, J. Koda, D. Calzetti, M. Fukuhara, and R. Momose. The Super-linear Slope of the Spatially Resolved Star Formation Law in NGC 3521 and NGC 5194 (M51a). *ApJ*, 735(1):63, July 2011. doi: 10.1088/0004-637X/735/1/63.

I. MacLaren, K. M. Richardson, and A. W. Wolfendale. Corrections to Virial Estimates of Molecular Cloud Masses. *ApJ*, 333:821, Oct. 1988. doi: 10.1086/166791.

P. Madau and M. Dickinson. Cosmic Star-Formation History. *ARA&A*, 52:415–486, Aug. 2014. doi: 10.1146/annurev-astro-081811-125615.

F. Maeda, K. Ohta, Y. Fujimoto, A. Habe, and J. Baba. Large velocity dispersion of molecular gas in bars of strongly barred galaxies NGC 1300 and NGC 5383. *PASJ*, 70(3):37, June 2018. doi: 10.1093/pasj/psy028.

F. Maeda, K. Ohta, Y. Fujimoto, and A. Habe. Properties of giant molecular clouds in the strongly barred galaxy NGC 1300. *MNRAS*, 493(4):5045–5061, Apr. 2020a. doi: 10.1093/mnras/staa556.

F. Maeda, K. Ohta, Y. Fujimoto, A. Habe, and K. Ushio. A large amount of diffuse molecular gases in the bar of the strongly barred galaxy NGC 1300: cause of the low star formation efficiency. *MNRAS*, 495(4):3840–3858, July 2020b. doi: 10.1093/mnras/staa1296.

F. Maeda, K. Ohta, Y. Fujimoto, and A. Habe. Connection among environment, cloud-cloud collision speed, and star formation activity in the strongly barred galaxy NGC 1300. *MNRAS*, 502(2):2238–2250, Apr. 2021. doi: 10.1093/mnras/stab130.

P. Maffei. Infrared Object in the Region of IC 1805. *PASP*, 80(476):618–621, Oct. 1968. doi: 10.1086/128698.

R. Q. Mao, C. Henkel, A. Schulz, M. Zielinsky, R. Mauersberger, H. Störzer, T. L. Wilson, and P. Gensheimer. Dense gas in nearby galaxies. XIII. CO submillimeter line emission from the starburst galaxy M 82. *A&A*, 358:433–450, June 2000.

R.-Q. Mao, A. Schulz, C. Henkel, R. Mauersberger, D. Muders, and Dinh-V-Trung. An Extragalactic ^{12}CO J = 3-2 Survey with the Heinrich Hertz Telescope. *ApJ*, 724(2):1336–1356, Dec. 2010. doi: 10.1088/0004-637X/724/2/1336.

S. Martín, R. Aladro, J. Martín-Pintado, and R. Mauersberger. A large ^{12}C/^{13}C isotopic ratio in M 82 and NGC 253. *A&A*, 522:A62, Nov. 2010. doi: 10.1051/0004-6361/201014972.

A. M. Mason and C. D. Wilson. Extended Molecular Gas in the Nearby Starburst Galaxy Maffei 2. *ApJ*, 612(2):860–866, Sept. 2004. doi: 10.1086/422676.

J. P. McMullin, B. Waters, D. Schiebel, W. Young, and K. Golap. CASA Architecture and Applications. In R. A. Shaw, F. Hill, and D. J. Bell, editors, *Astronomical Data Analysis Software and Systems XVI*, volume 376 of *Astronomical Society of the Pacific Conference Series*, page 127, Oct. 2007.

S. T. Megeath, L. K. Townsley, M. S. Oey, and A. R. Tieftrunk. *Low and High Mass Star Formation in the W3, W4, and W5 Regions*, volume 4, page 264. 2008.

S. Mei, J. P. Blakeslee, P. Côté, J. L. Tonry, M. J. West, L. Ferrarese, A. Jordán, E. W. Peng, A. Anthony, and D. Merritt. The ACS Virgo Cluster Survey. XIII. SBF Distance Catalog and the Three-dimensional Structure of the Virgo Cluster. *ApJ*, 655(1):144–162, Jan. 2007. doi: 10.1086/509598.

S. E. Meidt, E. Schinnerer, S. García-Burillo, A. Hughes, D. Colombo, J. Pety, C. L. Dobbs, K. F. Schuster, C. Kramer, A. K. Leroy, G. Dumas, and T. A. Thompson. Gas Kinematics on Giant Molecular Cloud Scales in M51 with PAWS: Cloud Stabilization through Dynamical Pressure. *ApJ*, 779(1):45, Dec. 2013. doi: 10.1088/0004-637X/779/1/45.

S. E. Meidt, A. K. Leroy, E. Rosolowsky, J. M. D. Kruijssen, E. Schinnerer, A. Schruba, J. Pety, G. Blanc, F. Bigiel, M. Chevance, A. Hughes, M. Querejeta, and A. Usero. A Model for the Onset of Self-gravitation and Star Formation in Molecular Gas Governed by Galactic Forces. I. Cloud-scale Gas Motions. *ApJ*, 854(2):100, Feb. 2018. doi: 10.3847/1538-4357/aaa290.

S. E. Meidt, S. C. O. Glover, J. M. D. Kruijssen, A. K. Leroy, E. Rosolowsky, A. Hughes, E. Schinnerer, A. Schruba, A. Usero, F. Bigiel, G. Blanc, M. Chevance, J. Pety, M. Querejeta, and D. Utomo. A Model for the Onset of Self-gravitation and Star Formation in Molecular Gas Governed by Galactic Forces. II. The Bottleneck to Collapse Set by Cloud-Environment Decoupling. *ApJ*, 892(2):73, Apr. 2020. doi: 10.3847/1538-4357/ab7000.

S. E. Meidt, A. K. Leroy, M. Querejeta, E. Schinnerer, J. Sun, A. van der Wel, E. Emsellem, J. Henshaw, A. Hughes, J. M. D. Kruijssen, E. Rosolowsky, A. Schruba, A. Barnes, F. Bigiel, G. A. Blanc, M. Chevance, Y. Cao, D. A. Dale, C. Faesi, S. C. O. Glover, K. Grasha, B. Groves, C. Herrera, R. S. Klessen, K. Kreckel, D. Liu, H.-A. Pan, J. Pety, T. Saito, A. Usero, E. Watkins, and T. G. Williams. The Organization of Cloud-scale Gas Density Structure: High-resolution CO versus 3.6 μm Brightness Contrasts in Nearby Galaxies. *ApJ*, 913(2):113, June 2021. doi: 10.3847/1538-4357/abf35b.

D. S. Meier and J. L. Turner. Molecular Gas and Star Formation in the Nucleus of IC 342: $C^{18}O$ and Millimeter Continuum Imaging. *ApJ*, 551(2):687–701, Apr. 2001. doi: 10.1086/320243.

D. S. Meier and J. L. Turner. Dynamically Influenced Molecular Clouds in the Nucleus of NGC 6946: Variations in the CO Isotopic Line Ratios. *AJ*, 127(4):2069–2084, Apr. 2004. doi: 10.1086/382904.

D. S. Meier and J. L. Turner. Spatially Resolved Chemistry in nearby Galaxies. II. The Nuclear Bar in Maffei 2. *ApJ*, 755(2):104, Aug. 2012. doi: 10.1088/0004-637X/755/2/104.

D. S. Meier, J. L. Turner, and R. L. Hurt. Molecular Gas Properties of the Starburst Nucleus of IC 342: High-Resolution ^{13}CO (2-1) Imaging. *ApJ*, 531(1):200–209, Mar. 2000. doi: 10.1086/308429.

D. S. Meier, J. L. Turner, and R. L. Hurt. Nuclear Bar Catalyzed Star Formation: ^{13}CO, $C^{18}O$, and Molecular Gas Properties in the Nucleus of Maffei 2. *ApJ*, 675(1):281–302, Mar. 2008. doi: 10.1086/524932.

S. N. Milam, C. Savage, M. A. Brewster, L. M. Ziurys, and S. Wyckoff. The $^{12}C/^{13}C$ Isotope Gradient Derived from Millimeter Transitions of CN: The Case for Galactic Chemical Evolution. *ApJ*, 634(2):1126–1132, Dec. 2005. doi: 10.1086/497123.

T. Minamidani, T. Tanaka, Y. Mizuno, N. Mizuno, A. Kawamura, T. Onishi, T. Hasegawa, K. Tatematsu, T. Takekoshi, K. Sorai, N. Moribe, K. Torii, T. Sakai, K. Muraoka, K. Tanaka, H. Ezawa, K. Kohno, S. Kim, M. Rubio, and Y. Fukui. Dense Clumps in Giant Molecular Clouds in the Large Magellanic Cloud: Density and Temperature Derived from ^{13}CO(J = 3-2) Observations. *AJ*, 141(3):73, Mar. 2011. doi: 10.1088/0004-6256/141/3/73.

T. Minamidani, A. Nishimura, Y. Miyamoto, H. Kaneko, H. Iwashita, C. Miyazawa, H. Nishitani, T. Wada, Y. Fujii, T. Takahashi, Y. Iizuka, H. Ogawa, K. Kimura, Y. Kozuki, Y. Hasegawa, M. Matsuo, S. Fujita, S. Ohashi, K. Morokuma-Matsui, J. Maekawa, K. Muraoka, T. Nakajima, T. Umemoto, K. Sorai, F. Nakamura, N. Kuno, and M. Saito. Development of the new multi-beam 100 GHz band SIS receiver FOREST for the Nobeyama 45-m Telescope. In W. S. Holland and J. Zmuidzinas, editors, *Millimeter, Submillimeter, and Far-Infrared Detectors and Instrumentation for Astronomy VIII*, volume 9914 of *Society of Photo-Optical Instrumentation Engineers (SPIE) Conference Series*, page 99141Z, July 2016. doi: 10.1117/12.2232137.

Y. Miyamoto, N. Nakai, and N. Kuno. Influence of shear motion on evolution of molecular clouds in the spiral galaxy M 51. *PASJ*, 66(2):36, Apr. 2014. doi: 10.1093/pasj/psu017.

N. Mizuno, M. Rubio, A. Mizuno, R. Yamaguchi, T. Onishi, and Y. Fukui. First Results of a CO Survey of the Small Magellanic Cloud with NANTEN. *PASJ*, 53(6):L45–L49, Dec. 2001. doi: 10.1093/pasj/53.6.L45.

R. Momose, S. K. Okumura, J. Koda, and T. Sawada. Star Formation Efficiency in the Barred Spiral Galaxy NGC 4303. *ApJ*, 721(1):383–394, Sept. 2010. doi: 10.1088/0004-637X/721/1/383.

R. Momose, J. Koda, J. Kennicutt, Robert C., F. Egusa, D. Calzetti, G. Liu, J. Donovan Meyer, S. K. Okumura, N. Z. Scoville, T. Sawada, and N. Kuno. Star Formation on Subkiloparsec Scale Triggered by Non-linear Processes in Nearby Spiral Galaxies. *ApJL*, 772(1):L13, July 2013. doi: 10.1088/2041-8205/772/1/L13.

W. W. Morgan. A Preliminary Classification of the Forms of Galaxies According to Their Stellar Population. *PASP*, 70(415):364, Aug. 1958. doi: 10.1086/127243.

K. Morokuma-Matsui and K. Muraoka. Kennicutt-Schmidt Relation Variety and Star-forming Cloud Fraction. *ApJ*, 837(2):137, Mar. 2017. doi: 10.3847/1538-4357/aa6115.

K. Morokuma-Matsui, K. Sorai, Y. Watanabe, and N. Kuno. Stacking analysis of ^{12}CO and ^{13}CO spectra of NGC 3627: Existence of non-optically thick ^{12}CO emission? *PASJ*, 67(1):2, Feb. 2015. doi: 10.1093/pasj/psu126.

K. Morokuma-Matsui, K. Sorai, Y. Sato, N. Kuno, T. T. Takeuchi, D. Salak, Y. Miyamoto, Y. Yajima, K. Muraoka, and H. Kaneko. CO Multi-line Imaging of Nearby Galaxies (COMING). X. Physical conditions of molecular gas and the local SFR-mass relation. *PASJ*, 72(5):90, Oct. 2020. doi: 10.1093/pasj/psaa084.

K. Morokuma-Matsui, T. Kodama, T. Morokuma, K. Nakanishi, Y. Koyama, T. Yamashita, S. Koyama, and T. Okamoto. A Phase-space View of Cold-gas Properties of Virgo Cluster Galaxies: Multiple Quenching Processes at Work? *ApJ*, 914(2):145, June 2021. doi: 10.3847/1538-4357/abedb6.

P. Morrissey, T. Conrow, T. A. Barlow, T. Small, M. Seibert, T. K. Wyder, T. Budavári, S. Arnouts, P. G. Friedman, K. Forster, D. C. Martin, S. G. Neff, D. Schiminovich, L. Bianchi, J. Donas, T. M. Heckman, Y.-W. Lee, B. F. Madore, B. Milliard, R. M. Rich, A. S. Szalay, B. Y. Welsh, and S. K. Yi. The Calibration and Data Products of GALEX. *ApJS*, 173(2):682–697, Dec. 2007. doi: 10.1086/520512.

F. Motte, P. Andre, and R. Neri. The initial conditions of star formation in the rho Ophiuchi main cloud: wide-field millimeter continuum mapping. *A&A*, 336:150–172, Aug. 1998.

F. Motte, Q. Nguyên Luong, N. Schneider, F. Heitsch, S. Glover, P. Carlhoff, T. Hill, S. Bontemps, P. Schilke, F. Louvet, M. Hennemann, P. Didelon, and H. Beuther. The formation of the W43 complex: constraining its atomic-to-molecular transition and searching for colliding clouds. *A&A*, 571:A32, Nov. 2014. doi: 10.1051/0004-6361/201323001.

H. Murakami, H. Baba, P. Barthel, D. L. Clements, M. Cohen, Y. Doi, K. Enya, E. Figueredo, N. Fujishiro, H. Fujiwara, M. Fujiwara, P. Garcia-Lario, T. Goto, S. Hasegawa, Y. Hibi, T. Hirao, N. Hiromoto, S. S. Hong, K. Imai, M. Ishigaki, M. Ishiguro, D. Ishihara, Y. Ita, W.-S. Jeong, K. S. Jeong, H. Kaneda, H. Kataza, M. Kawada, T. Kawai, A. Kawamura, M. F. Kessler, D. Kester, T. Kii, D. C. Kim, W. Kim, H. Kobayashi, B. C. Koo, S. M. Kwon, H. M. Lee, R. Lorente, S. Makiuti, H. Matsuhara, T. Matsumoto, H. Matsuo, S. Matsuura, T. G. MÜller, N. Murakami, H. Nagata, T. Nakagawa, T. Naoi, M. Narita, M. Noda, S. H. Oh, A. Ohnishi, Y. Ohyama, Y. Okada, H. Okuda, S. Oliver, T. Onaka, T. Ootsubo, S. Oyabu, S. Pak, Y.-S. Park, C. P. Pearson, M. Rowan-Robinson, T. Saito, I. Sakon, A. Salama, S. Sato, R. S. Savage, S. Serjeant, H. Shibai, M. Shirahata, J. Sohn, T. Suzuki, T. Takagi, H. Takahashi, T. TanabÉ, T. T. Takeuchi, S. Takita, M. Thomson, K. Uemizu, M. Ueno, F. Usui, E. Verdugo, T. Wada, L. Wang, T. Watabe, H. Watarai, G. J. White, I. Yamamura, C. Yamauchi, and A. Yasuda. The Infrared Astronomical Mission AKARI. *PASJ*, 59: S369–S376, Oct. 2007. doi: 10.1093/pasj/59.sp2.S369.

K. Muraoka, K. Kohno, T. Tosaki, N. Kuno, K. Nakanishi, K. Sorai, T. Okuda, S. Sakamoto, A. Endo, B. Hatsukade, K. Kamegai, K. Tanaka, J. Cortes, H. Ezawa, N. Yamaguchi, T. Sakai, and R. Kawabe. ASTE CO (3-2) Observations of the Barred Spiral Galaxy M 83: I. Correlation between CO (3-2)/ CO (1-0) Ratios and Star Formation Efficiencies. *PASJ*, 59:43–54, Feb. 2007. doi: 10.1093/pasj/59.1.43.

K. Muraoka, K. Kohno, T. Tosaki, N. Kuno, K. Nakanishi, T. Handa, K. Sorai, S. Ishizuki, and T. Okuda. Nobeyama Millimeter Array Observations of the Nuclear Starburst of M 83: A GMA Scale Correlation between Dense Gas Fraction and Star Formation Efficiency. *PASJ*, 61:163, Feb. 2009. doi: 10.1093/pasj/61.2.163.

K. Muraoka, T. Tosaki, R. Miura, S. Onodera, N. Kuno, K. Nakanishi, H. Kaneko, and S. Komugi. ^{13}CO(J = 1-0) On-the-Fly Mapping of the Giant H II Region NGC 604: Variation in Molecular Gas Density and Temperature due to Sequential Star Formation. *PASJ*, 64:3, Feb. 2012. doi: 10.1093/pasj/64.1.3.

K. Muraoka, K. Sorai, N. Kuno, N. Nakai, H. Nakanishi, M. Takeda, K. Yanagitani, H. Kaneko, Y. Miyamoto, N. Kishida, T. Hatakeyama, M. Umei, T. Tanaka, Y. Tomiyasu, C. Saita, S. Ueno, N. Matsumoto, D. Salak, and K. Morokuma-Matsui. CO Multi-line Imaging of Nearby Galaxies (COMING). I. Physical properties of molecular gas in the barred spiral galaxy NGC 2903. *PASJ*, 68(5):89, Oct. 2016. doi: 10.1093/pasj/psw080.

K. Muraoka, K. Sorai, Y. Miyamoto, M. Yoda, K. Morokuma-Matsui, M. I. N. Kobayashi, M. Kuroda, H. Kaneko, N. Kuno, T. T. Takeuchi, H. Nakanishi, Y. Watanabe, T. Tanaka, A. Yasuda, Y. Yajima, S. Shibata, D. Salak, D. Espada, N. Matsumoto, Y. Noma, S. Kita, R. Komatsuzaki, A. Kajikawa, Y. Yashima, H.-A. Pan, N. Oi, M. Seta, and N. Nakai. CO Multi-line Imaging of Nearby Galaxies (COMING). VI. Radial variations in star formation efficiency. *PASJ*, 71:S15, Dec. 2019. doi: 10.1093/pasj/psz015.

K. Muraoka, H. Kondo, K. Tokuda, A. Nishimura, R. E. Miura, S. Onodera, N. Kuno, S. Zahorecz, K. Tsuge, H. Sano, S. Fujita, T. Onishi, K. Saigo, K. Tachihara, Y. Fukui, and A. Kawamura. ALMA Observations of Giant Molecular Clouds in M33. II. Triggered High-mass Star Formation by Multiple Gas Colliding Events at the NGC 604 Complex. *ApJ*, 903(2):94, Nov. 2020. doi: 10.3847/1538-4357/abb822.

E. J. Murphy, J. J. Condon, E. Schinnerer, R. C. Kennicutt, D. Calzetti, L. Armus, G. Helou, J. L. Turner, G. Aniano, P. Beirão, A. D. Bolatto, B. R. Brandl, K. V. Croxall, D. A. Dale, J. L. Donovan Meyer, B. T. Draine, C. Engelbracht, L. K. Hunt, C. N. Hao, J. Koda, H. Roussel, R. Skibba, and J. D. T. Smith. Calibrating Extinction-free Star Formation Rate Diagnostics with 33 GHz Free-free Emission in NGC 6946. *ApJ*, 737(2): 67, Aug. 2011. doi: 10.1088/0004-637X/737/2/67.

N. Murray. Star Formation Efficiencies and Lifetimes of Giant Molecular Clouds in the Milky Way. *ApJ*, 729(2): 133, Mar. 2011. doi: 10.1088/0004-637X/729/2/133.

P. C. Myers. A compilation of interstellar gas properties. *ApJ*, 225:380–389, Oct. 1978. doi: 10.1086/156500.

N. Nakai, N. Kuno, T. Handa, and Y. Sofue. Distribution and Dynamics of Molecular Gas in the Galaxy M51. I. Data and Spiral Structure. *PASJ*, 46:527–538, Dec. 1994.

H. Nakanishi and Y. Sofue. Three-dimensional distribution of the ISM in the Milky Way galaxy. III. The total neutral gas disk. *PASJ*, 68(1):5, Feb. 2016. doi: 10.1093/pasj/psv108.

H. Nakanishi, N. Kuno, Y. Sofue, N. Sato, N. Nakai, Y. Shioya, T. Tosaki, S. Onodera, K. Sorai, F. Egusa, and A. Hirota. Environmental Effects on Gaseous Disks of the Virgo Spiral Galaxies. *ApJ*, 651(2):804–810, Nov. 2006. doi: 10.1086/507974.

D. Narayanan, T. J. Cox, Y. Shirley, R. Davé, L. Hernquist, and C. K. Walker. Molecular Star Formation Rate Indicators in Galaxies. *ApJ*, 684(2):996–1008, Sept. 2008. doi: 10.1086/588720.

D. Narayanan, M. Krumholz, E. C. Ostriker, and L. Hernquist. The CO-H_2 conversion factor in disc galaxies and mergers. *MNRAS*, 418(1):664–679, Nov. 2011. doi: 10.1111/j.1365-2966.2011.19516.x.

D. Narayanan, M. R. Krumholz, E. C. Ostriker, and L. Hernquist. A general model for the CO-H_2 conversion factor in galaxies with applications to the star formation law. *MNRAS*, 421(4):3127–3146, Apr. 2012. doi: 10.1111/j.1365-2966.2012.20536.x.

N. K. Nguyen, A. R. Pettitt, E. J. Tasker, and T. Okamoto. The impact of galactic disc environment on star-forming clouds. *MNRAS*, 475(1):27–42, Mar. 2018. doi: 10.1093/mnras/stx3143.

Q. Nguyen Luong, F. Motte, F. Schuller, N. Schneider, S. Bontemps, P. Schilke, K. M. Menten, F. Heitsch, F. Wyrowski, P. Carlhoff, L. Bronfman, and T. Henning. W43: the closest molecular complex of the Galactic bar? *A&A*, 529:A41, May 2011. doi: 10.1051/0004-6361/201016271.

M. Nimori, A. Habe, K. Sorai, Y. Watanabe, A. Hirota, and D. Namekata. Dense cloud formation and star formation in a barred galaxy. *MNRAS*, 429(3):2175–2182, Mar. 2013. doi: 10.1093/mnras/sts487.

A. Nishimura, K. Tokuda, K. Kimura, K. Muraoka, H. Maezawa, H. Ogawa, K. Dobashi, T. Shimoikura, A. Mizuno, Y. Fukui, and T. Onishi. Revealing the Physical Properties of Molecular Gas in Orion with a Large-scale Survey in J = 2-1 Lines of ^{12}CO, ^{13}CO, and C^{18}O. *ApJS*, 216(1):18, Jan. 2015. doi: 10.1088/0067-0049/216/1/18.

K. Nishiyama and N. Nakai. CO Survey of Nearby Spiral Galaxies with the Nobeyama 45-m Telescope: I. The Data. *PASJ*, 53(5):713–756, Oct. 2001. doi: 10.1093/pasj/53.5.713.

T. Oka, T. Hasegawa, M. Hayashi, T. Handa, and S. Sakamoto. CO (J = 2–1) Line Observations of the Galactic Center Molecular Cloud Complex. II. Dynamical Structure and Physical Conditions. *ApJ*, 493(2):730–761, Jan. 1998. doi: 10.1086/305133.

T. Oka, T. Hasegawa, F. Sato, M. Tsuboi, A. Miyazaki, and M. Sugimoto. Statistical Properties of Molecular Clouds in the Galactic Center. *ApJ*, 562(1):348–362, Nov. 2001. doi: 10.1086/322976.

S. Onodera, N. Kuno, T. Tosaki, K. Kohno, K. Nakanishi, T. Sawada, K. Muraoka, S. Komugi, R. Miura, H. Kaneko, A. Hirota, and R. Kawabe. Breakdown of Kennicutt-Schmidt Law at Giant Molecular Cloud Scales in M33. *ApJL*, 722(2):L127–L131, Oct. 2010. doi: 10.1088/2041-8205/722/2/L127.

D. E. Osterbrock and G. J. Ferland. *Astrophysics of gaseous nebulae and active galactic nuclei*. 2006.

P. Padoan and Å. Nordlund. The Star Formation Rate of Supersonic Magnetohydrodynamic Turbulence. *ApJ*, 730(1):40, Mar. 2011. doi: 10.1088/0004-637X/730/1/40.

B. E. J. Pagel. *Nucleosynthesis and Chemical Evolution of Galaxies*. Cambridge University Press, Cambridge, 1997.

T. A. D. Paglione, W. F. Wall, J. S. Young, M. H. Heyer, M. Richard, M. Goldstein, Z. Kaufman, J. Nantais, and G. Perry. A Mapping Survey of the ^{13}CO and ^{12}CO Emission in Galaxies. *ApJS*, 135(2):183–200, Aug. 2001. doi: 10.1086/321785.

H.-A. Pan and N. Kuno. Variation in GMC Association Properties across the Bars, Spiral Arms, Inter-arms, and Circumnuclear Region of M100 (NGC 4321) Extracted from ALMA Observations. *ApJ*, 839(2):133, Apr. 2017. doi: 10.3847/1538-4357/aa60c2.

H.-A. Pan, N. Kuno, J. Koda, A. Hirota, K. Sorai, and H. Kaneko. Molecular Gas and Star-formation Properties in the Central and Bar Regions of NGC 6946. *ApJ*, 815(1):59, Dec. 2015a. doi: 10.1088/0004-637X/815/1/59.

H.-A. Pan, N. Kuno, K. Sorai, and M. Umei. Constraints on the minor merging and star formation history of the Wolf-Rayet galaxy NGC 5430 through observations. *PASJ*, 67(6):116, Dec. 2015b. doi: 10.1093/pasj/psv086.

H.-A. Pan, E. Schinnerer, A. Hughes, A. Leroy, B. Groves, A. T. Barnes, F. Belfiore, F. Bigiel, G. A. Blanc, Y. Cao, M. Chevance, E. Congiu, D. A. Dale, C. Eibensteiner, E. Emsellem, C. M. Faesi, S. C. O. Glover, K. Grasha, C. N. Herrera, I.-T. Ho, R. S. Klessen, J. M. D. Kruijssen, P. Lang, D. Liu, R. McElroy, S. E. Meidt, E. J. Murphy, J. Pety, M. Querejeta, A. Razza, E. Rosolowsky, T. Saito, F. Santoro, A. Schruba, J. Sun, N. Tomicic, A. Usero, D. Utomo, and T. G. Williams. The Gas-Star Formation Cycle in Nearby Star-forming Galaxies II. Resolved Distributions of CO and Hα Emission for 49 PHANGS Galaxies. *ApJ, in press*, art. arXiv:2201.01403, Jan. 2022.

P. P. Papadopoulos, P. van der Werf, E. Xilouris, K. G. Isaak, and Y. Gao. The Molecular Gas in Luminous Infrared Galaxies. II. Extreme Physical Conditions and Their Effects on the X $_{co}$ Factor. *ApJ*, 751(1):10, May 2012a. doi: 10.1088/0004-637X/751/1/10.

P. P. Papadopoulos, P. P. van der Werf, E. M. Xilouris, K. G. Isaak, Y. Gao, and S. Mühle. The molecular gas in luminous infrared galaxies - I. CO lines, extreme physical conditions and their drivers. *MNRAS*, 426(4): 2601–2629, Nov. 2012b. doi: 10.1111/j.1365-2966.2012.21001.x.

D. Paradis, K. Dobashi, T. Shimoikura, A. Kawamura, T. Onishi, Y. Fukui, and J. P. Bernard. Dark gas in the solar neighborhood from extinction data. *A&A*, 543:A103, July 2012. doi: 10.1051/0004-6361/201118740.

N. N. Patra. Theoretical modelling of two-component molecular discs in spiral galaxies. *A&A*, 638:A66, June 2020. doi: 10.1051/0004-6361/201936483.

N. N. Patra. Thick disc molecular gas fraction in NGC 6946. *MNRAS*, 501(3):3527–3539, Mar. 2021. doi: 10.1093/mnras/staa3929.

C. H. Peñaloza, P. C. Clark, S. C. O. Glover, R. Shetty, and R. S. Klessen. Using CO line ratios to trace the physical properties of molecular clouds. *MNRAS*, 465(2):2277–2285, Feb. 2017. doi: 10.1093/mnras/stw2892.

C. H. Peñaloza, P. C. Clark, S. C. O. Glover, and R. S. Klessen. CO line ratios in molecular clouds: the impact of environment. *MNRAS*, 475(2):1508–1520, Apr. 2018. doi: 10.1093/mnras/stx3263.

Y. Peng, R. Maiolino, and R. Cochrane. Strangulation as the primary mechanism for shutting down star formation in galaxies. *Nature*, 521(7551):192–195, May 2015. doi: 10.1038/nature14439.

A. R. Pettitt, F. Egusa, C. L. Dobbs, E. J. Tasker, Y. Fujimoto, and A. Habe. The changing GMC population in galaxy interactions. *MNRAS*, 480(3):3356–3375, Nov. 2018. doi: 10.1093/mnras/sty2040.

A. R. Pettitt, C. L. Dobbs, J. Baba, D. Colombo, A. Duarte-Cabral, F. Egusa, and A. Habe. How do different spiral arm models impact the ISM and GMC population? *MNRAS*, 498(1):1159–1174, Oct. 2020. doi: 10.1093/mnras/staa2242.

J. Pety, E. Schinnerer, A. K. Leroy, A. Hughes, S. E. Meidt, D. Colombo, G. Dumas, S. García-Burillo, K. F. Schuster, C. Kramer, C. L. Dobbs, and T. A. Thompson. The Plateau de Bure + 30 m Arcsecond Whirlpool Survey Reveals a Thick Disk of Diffuse Molecular Gas in the M51 Galaxy. *ApJ*, 779(1):43, Dec. 2013. doi: 10.1088/0004-637X/779/1/43.

A. C. Phillips. Nuclear and large-Scale Outflows in NGC 1808. *AJ*, 105:486, Feb. 1993. doi: 10.1086/116447.

A. C. Phillips. Star Formation in Barred Galaxies. In R. Buta, D. A. Crocker, and B. G. Elmegreen, editors, *IAU Colloq. 157: Barred Galaxies*, volume 91 of *Astronomical Society of the Pacific Conference Series*, page 44, Jan. 1996.

G. L. Pilbratt, J. R. Riedinger, T. Passvogel, G. Crone, D. Doyle, U. Gageur, A. M. Heras, C. Jewell, L. Metcalfe, S. Ott, and M. Schmidt. Herschel Space Observatory. An ESA facility for far-infrared and submillimetre astronomy. *A&A*, 518:L1, July 2010. doi: 10.1051/0004-6361/201014759.

J. E. Pineda, P. Caselli, and A. A. Goodman. CO Isotopologues in the Perseus Molecular Cloud Complex: the X-factor and Regional Variations. *ApJ*, 679(1):481–496, May 2008. doi: 10.1086/586883.

J. L. Pineda, P. F. Goldsmith, N. Chapman, R. L. Snell, D. Li, L. Cambrésy, and C. Brunt. The Relation Between Gas and Dust in the Taurus Molecular Cloud. *ApJ*, 721(1):686–708, Sept. 2010. doi: 10.1088/0004-637X/721/1/686.

Planck Collaboration, P. A. R. Ade, N. Aghanim, M. Arnaud, M. Ashdown, J. Aumont, C. Baccigalupi, A. Balbi, A. J. Banday, R. B. Barreiro, J. G. Bartlett, E. Battaner, K. Benabed, A. Benoît, J. P. Bernard, M. Bersanelli, R. Bhatia, J. J. Bock, A. Bonaldi, J. R. Bond, J. Borrill, F. R. Bouchet, F. Boulanger, M. Bucher, C. Burigana, P. Cabella, J. F. Cardoso, A. Catalano, L. Cayón, A. Challinor, A. Chamballu, L. Y. Chiang, C. Chiang, P. R. Christensen, D. L. Clements, S. Colombi, F. Couchot, A. Coulais, B. P. Crill, F. Cuttaia, T. M. Dame, L. Danese, R. D. Davies, R. J. Davis, P. de Bernardis, G. de Gasperis, A. de Rosa, G. de Zotti, J. Delabrouille, J. M. Delouis, F. X. Désert, C. Dickinson, K. Dobashi, S. Donzelli, O. Doré, U. Dörl, M. Douspis, X. Dupac, G. Efstathiou, T. A. Enßlin, H. K. Eriksen, E. Falgarone, F. Finelli, O. Forni, P. Fosalba, M. Frailis, E. Franceschi, Y. Fukui,

S. Galeotta, K. Ganga, M. Giard, G. Giardino, Y. Giraud-Héraud, J. González-Nuevo, K. M. Górski, S. Gratton, A. Gregorio, I. A. Grenier, A. Gruppuso, F. K. Hansen, D. Harrison, G. Helou, S. Henrot-Versillé, D. Herranz, S. R. Hildebrandt, E. Hivon, M. Hobson, W. A. Holmes, W. Hovest, R. J. Hoyland, K. M. Huffenberger, A. H. Jaffe, W. C. Jones, M. Juvela, A. Kawamura, E. Keihänen, R. Keskitalo, T. S. Kisner, R. Kneissl, L. Knox, H. Kurki-Suonio, G. Lagache, J. M. Lamarre, A. Lasenby, R. J. Laureijs, C. R. Lawrence, S. Leach, R. Leonardi, C. Leroy, P. B. Lilje, M. Linden-Vørnle, M. López-Caniego, P. M. Lubin, J. F. Macías-Pérez, C. J. MacTavish, B. Maffei, D. Maino, N. Mandolesi, R. Mann, M. Maris, P. Martin, E. Martínez-González, S. Masi, S. Matarrese, F. Matthai, P. Mazzotta, P. McGehee, P. R. Meinhold, A. Melchiorri, L. Mendes, A. Mennella, M. A. Miville-Deschênes, A. Moneti, L. Montier, G. Morgante, D. Mortlock, D. Munshi, A. Murphy, P. Naselsky, P. Natoli, C. B. Netterfield, H. U. Nørgaard-Nielsen, F. Noviello, D. Novikov, I. Novikov, I. J. O'Dwyer, T. Onishi, S. Osborne, F. Pajot, R. Paladini, D. Paradis, F. Pasian, G. Patanchon, O. Perdereau, L. Perotto, F. Perrotta, F. Piacentini, M. Piat, S. Plaszczynski, E. Pointecouteau, G. Polenta, N. Ponthieu, T. Poutanen, G. Prézeau, S. Prunet, J. L. Puget, W. T. Reach, M. Reinecke, C. Renault, S. Ricciardi, T. Riller, I. Ristorcelli, G. Rocha, C. Rosset, M. Rowan-Robinson, J. A. Rubiño-Martín, B. Rusholme, M. Sandri, D. Santos, G. Savini, D. Scott, M. D. Seiffert, P. Shellard, G. F. Smoot, J. L. Starck, F. Stivoli, V. Stolyarov, R. Stompor, R. Sudiwala, J. F. Sygnet, J. A. Tauber, L. Terenzi, L. Toffolatti, M. Tomasi, J. P. Torre, M. Tristram, J. Tuovinen, G. Umana, L. Valenziano, P. Vielva, F. Villa, N. Vittorio, L. A. Wade, B. D. Wandelt, A. Wilkinson, D. Yvon, A. Zacchei, and A. Zonca. Planck early results. XIX. All-sky temperature and dust optical depth from Planck and IRAS. Constraints on the "dark gas" in our Galaxy. *A&A*, 536:A19, Dec. 2011. doi: 10.1051/0004-6361/201116479.

B. M. Poggianti, A. Moretti, M. Gullieuszik, J. Fritz, Y. Jaffé, D. Bettoni, G. Fasano, C. Bellhouse, G. Hau, B. Vulcani, A. Biviano, A. Omizzolo, A. Paccagnella, M. D'Onofrio, A. Cava, Y. K. Sheen, W. Couch, and M. Owers. GASP. I. Gas Stripping Phenomena in Galaxies with MUSE. *ApJ*, 844(1):48, July 2017. doi: 10.3847/1538-4357/aa78ed.

A. Poglitsch, C. Waelkens, N. Geis, H. Feuchtgruber, B. Vandenbussche, L. Rodriguez, O. Krause, E. Renotte, C. van Hoof, P. Saraceno, J. Cepa, F. Kerschbaum, P. Agnèse, B. Ali, B. Altieri, P. Andreani, J. L. Augueres, Z. Balog, L. Barl, O. H. Bauer, N. Belbachir, M. Benedettini, N. Billot, O. Boulade, H. Bischof, J. Blommaert, E. Callut, C. Cara, R. Cerulli, D. Cesarsky, A. Contursi, Y. Creten, W. De Meester, V. Doublier, E. Doumayrou, L. Duband, K. Exter, R. Genzel, J. M. Gillis, U. Grözinger, T. Henning, J. Herreros, R. Huygen, M. Inguscio, G. Jakob, C. Jamar, C. Jean, J. de Jong, R. Katterloher, C. Kiss, U. Klaas, D. Lemke, D. Lutz, S. Madden, B. Marquet, J. Martignac, A. Mazy, P. Merken, F. Montfort, L. Morbidelli, T. Müller, M. Nielbock, K. Okumura, R. Orfei, R. Ottensamer, S. Pezzuto, P. Popesso, J. Putzeys, S. Regibo, V. Reveret, P. Royer, M. Sauvage, J. Schreiber, J. Stegmaier, D. Schmitt, J. Schubert, E. Sturm, M. Thiel, G. Tofani, R. Vavrek, M. Wetzstein, E. Wieprecht, and E. Wiezorrek. The Photodetector Array Camera and Spectrometer (PACS) on the Herschel Space Observatory. *A&A*, 518:L2, July 2010. doi: 10.1051/0004-6361/201014535.

K. S. Polk, G. R. Knapp, A. A. Stark, and R. W. Wilson. Molecules in Galaxies. VI. Diffuse and Dense Cloud Contributions to the Large-Scale CO Emission of the Galaxy. *ApJ*, 332:432, Sept. 1988. doi: 10.1086/166667.

M. Querejeta, E. Schinnerer, A. Schruba, E. Murphy, S. Meidt, A. Usero, A. K. Leroy, J. Pety, F. Bigiel, M. Chevance, C. M. Faesi, M. Gallagher, S. García-Burillo, S. C. O. Glover, A. P. S. Hygate, M. J. Jiménez-Donaire, J. M. D. Kruijssen, E. Momjian, E. Rosolowsky, and D. Utomo. Dense gas is not enough: environmental variations in the star formation efficiency of dense molecular gas at 100 pc scales in M 51. *A&A*, 625: A19, May 2019. doi: 10.1051/0004-6361/201834915.

M. Querejeta, F. Lelli, E. Schinnerer, D. Colombo, U. Lisenfeld, C. G. Mundell, F. Bigiel, S. García-Burillo, C. N. Herrera, A. Hughes, J. M. D. Kruijssen, S. E. Meidt, T. J. T. Moore, J. Pety, and A. J. Rigby. ALMA resolves giant molecular clouds in a tidal dwarf galaxy. *A&A*, 645:A97, Jan. 2021a. doi: 10.1051/0004-6361/202038955.

M. Querejeta, E. Schinnerer, S. Meidt, J. Sun, A. K. Leroy, E. Emsellem, R. S. Klessen, J. C. Munoz-Mateos, H. Salo, E. Laurikainen, I. Beslic, G. A. Blanc, M. Chevance, D. A. Dale, C. Eibensteiner, C. Faesi, A. Garcia-Rodriguez, S. C. O. Glover, K. Grasha, J. Henshaw, C. Herrera, A. Hughes, K. Kreckel, J. M. D. Kruijssen, D. Liu, E. J. Murphy, H. A. Pan, J. Pety, A. Razza, E. Rosolowsky, T. Saito, A. Schruba, A. Usero, E. J. Watkins, and T. G. Williams. Stellar structures, molecular gas, and star formation across the PHANGS sample of nearby galaxies. *accepted to A&A, arXiv e-prints*, art. arXiv:2109.04491, Sept. 2021b.

S. E. Ragan, T. J. T. Moore, D. J. Eden, M. G. Hoare, J. S. Urquhart, D. Elia, and S. Molinari. The role of spiral arms in Milky Way star formation. *MNRAS*, 479(2):2361–2373, Sept. 2018. doi: 10.1093/mnras/sty1672.

N. Rahman, A. D. Bolatto, T. Wong, A. K. Leroy, F. Walter, E. Rosolowsky, A. A. West, F. Bigiel, J. Ott, R. Xue, R. Herrera-Camus, K. Jameson, L. Blitz, and S. N. Vogel. CARMA Survey Toward Infrared-bright Nearby Galaxies (STING): Molecular Gas Star Formation Law in NGC 4254. *ApJ*, 730(2):72, Apr. 2011. doi: 10.1088/0004-637X/730/2/72.

N. Rahman, A. D. Bolatto, R. Xue, T. Wong, A. K. Leroy, F. Walter, F. Bigiel, E. Rosolowsky, D. B. Fisher, S. N. Vogel, L. Blitz, A. A. West, and J. Ott. CARMA Survey Toward Infrared-bright Nearby Galaxies (STING). II. Molecular Gas Star Formation Law and Depletion Time across the Blue Sequence. *ApJ*, 745(2):183, Feb. 2012. doi: 10.1088/0004-637X/745/2/183.

D. Rebolledo, T. Wong, A. Leroy, J. Koda, and J. Donovan Meyer. Giant Molecular Clouds and Star Formation in the Non-grand Design Spiral Galaxy NGC 6946. *ApJ*, 757(2):155, Oct. 2012. doi: 10.1088/0004-637X/757/2/155.

M. W. Regan, K. Sheth, and S. N. Vogel. Molecular Gas Kinematics in Barred Spiral Galaxies. *ApJ*, 526(1): 97–113, Nov. 1999. doi: 10.1086/307960.

K. Reif, U. Mebold, W. M. Goss, H. van Woerden, and B. Siegman. An H II survey of southern galaxies. *A&A*, 50:451–479, Dec. 1982.

F. Renaud, F. Bournaud, E. Emsellem, O. Agertz, E. Athanassoula, F. Combes, B. Elmegreen, K. Kraljic, F. Motte, and R. Teyssier. Environmental regulation of cloud and star formation in galactic bars. *MNRAS*, 454(3):3299–3310, Dec. 2015. doi: 10.1093/mnras/stv2223.

D. Reynaud and D. Downes. Kinematics of the gas in a barred galaxy: do strong shocks inhibit star formation? *A&A*, 337:671–680, Sept. 1998.

L. J. Rickard, B. E. Turner, and P. Palmer. Carbon monoxide in Maffei 2. *ApJL*, 218:L51–L55, Dec. 1977. doi: 10.1086/182574.

G. H. Rieke, A. Alonso-Herrero, B. J. Weiner, P. G. Pérez-González, M. Blaylock, J. L. Donley, and D. Marcillac. Determining Star Formation Rates for Infrared Galaxies. *ApJ*, 692(1):556–573, Feb. 2009. doi: 10.1088/0004-637X/692/1/556.

A. J. Rigby, T. J. T. Moore, D. J. Eden, J. S. Urquhart, S. E. Ragan, N. Peretto, R. Plume, M. A. Thompson, M. J. Currie, and G. Park. CHIMPS: physical properties of molecular clumps across the inner Galaxy. *A&A*, 632:A58, Dec. 2019. doi: 10.1051/0004-6361/201935236.

J. Roman-Duval, J. M. Jackson, M. Heyer, J. Rathborne, and R. Simon. Physical Properties and Galactic Distribution of Molecular Clouds Identified in the Galactic Ring Survey. *ApJ*, 723(1):492–507, Nov. 2010. doi: 10.1088/0004-637X/723/1/492.

J. Roman-Duval, M. Heyer, C. M. Brunt, P. Clark, R. Klessen, and R. Shetty. Distribution and Mass of Diffuse and Dense CO Gas in the Milky Way. *ApJ*, 818(2):144, Feb. 2016. doi: 10.3847/0004-637X/818/2/144.

E. Rosolowsky and L. Blitz. Giant Molecular Clouds in M64. *ApJ*, 623(2):826–845, Apr. 2005. doi: 10.1086/428897.

E. Rosolowsky, E. Keto, S. Matsushita, and S. P. Willner. High-Resolution Molecular Gas Maps of M33. *ApJ*, 661(2):830–844, June 2007. doi: 10.1086/516621.

E. Rosolowsky, A. Hughes, A. K. Leroy, J. Sun, M. Querejeta, A. Schruba, A. Usero, C. N. Herrera, D. Liu, J. Pety, T. Saito, I. Bešlić, F. Bigiel, G. Blanc, M. Chevance, D. A. Dale, S. Deger, C. M. Faesi, S. C. O. Glover, J. D. Henshaw, R. S. Klessen, J. M. D. Kruijssen, K. Larson, J. Lee, S. Meidt, A. Mok, E. Schinnerer, D. A. Thilker, and T. G. Williams. Giant molecular cloud catalogues for PHANGS-ALMA: methods and initial results. *MNRAS*, 502(1):1218–1245, Mar. 2021. doi: 10.1093/mnras/stab085.

T. Saito, D. Iono, M. S. Yun, J. Ueda, K. Nakanishi, H. Sugai, D. Espada, M. Imanishi, K. Motohara, Y. Hagiwara, K. Tateuchi, M. Lee, and R. Kawabe. ALMA Multi-line Observations of the IR-bright Merger VV 114. *ApJ*, 803(2):60, Apr. 2015. doi: 10.1088/0004-637X/803/2/60.

K. Sakamoto, S. K. Okumura, S. Ishizuki, and N. Z. Scoville. Bar-driven Transport of Molecular Gas to Galactic Centers and Its Consequences. *ApJ*, 525(2):691–701, Nov. 1999. doi: 10.1086/307910.

S. Sakamoto, M. Hayashi, T. Hasegawa, T. Handa, and T. Oka. A Large Area CO(J = 2–1) Mapping of the Giant Molecular Clouds in Orion. *ApJ*, 425:641, Apr. 1994. doi: 10.1086/174011.

S. Sakamoto, T. Hasegawa, M. Hayashi, T. Handa, and T. Oka. An Out-of-Plane CO (J = 2–1) Survey of the Milky Way. I. The Data. *ApJS*, 100:125, Sept. 1995. doi: 10.1086/192210.

S. Sakamoto, T. Handa, Y. Sofue, M. Honma, and K. Sorai. An Isotope Study of Carbon Monoxide in the Edge-on Galaxy NGC 891. *ApJ*, 475(1):134–143, Jan. 1997a. doi: 10.1086/303515.

S. Sakamoto, T. Hasegawa, T. Handa, M. Hayashi, and T. Oka. An Out-of-Plane CO (J = 2-1) Survey of the Milky Way. II. Physical Conditions of Molecular Gas. *ApJ*, 486(1):276–290, Sept. 1997b. doi: 10.1086/304479.

D. Salak, N. Nakai, and S. Kitamoto. CO (J = 3 $\rightarrow$ 2) observations of the starburst galaxy NGC 1808 with ASTE. *PASJ*, 66(5):96, Oct. 2014. doi: 10.1093/pasj/psu074.

D. Salak, N. Nakai, T. Hatakeyama, and Y. Miyamoto. Gas Dynamics and Outflow in the Barred Starburst Galaxy NGC 1808 Revealed with ALMA. *ApJ*, 823(1):68, May 2016. doi: 10.3847/0004-637X/823/1/68.

D. Salak, Y. Tomiyasu, N. Nakai, N. Kuno, Y. Miyamoto, and H. Kaneko. Evolution of Molecular Clouds in the Superwind Galaxy NGC 1808 Probed by ALMA Observations. *ApJ*, 849(2):90, Nov. 2017. doi: 10.3847/1538-4357/aa91cb.

D. Salak, Y. Tomiyasu, N. Nakai, N. Kuno, Y. Miyamoto, and H. Kaneko. Dense Molecular Gas in the Starburst Nucleus of NGC 1808. *ApJ*, 856(2):97, Apr. 2018. doi: 10.3847/1538-4357/aab2ac.

D. Salak, N. Nakai, M. Seta, and Y. Miyamoto. ALMA Observations of Atomic Carbon [C I] (^{3} P $_1$ $\rightarrow$ ^{3} P $_0$) and Low-J CO Lines in the Starburst Galaxy NGC 1808. *ApJ*, 887(2):143, Dec. 2019a. doi: 10.3847/1538-4357/ab55dc.

D. Salak, Y. Noma, K. Sorai, Y. Miyamoto, N. Kuno, A. R. Pettitt, H. Kaneko, T. Tanaka, A. Yasuda, S. Kita, Y. Yajima, S. Shibata, N. Nakai, M. Seta, K. Muraoka, M. Kuroda, H. Nakanishi, T. T. Takeuchi, M. Yoda, K. Morokuma-Matsui, Y. Watanabe, N. Matsumoto, N. Oi, H.-A. Pan, A. Kajikawa, Y. Yashima, and R. Komatsuzaki. CO Multi-line Imaging of Nearby Galaxies (COMING). VII. Fourier decomposition of molecular gas velocity fields and bar pattern speed. *PASJ*, 71:S16, Dec. 2019b. doi: 10.1093/pasj/psz004.

H. Salo, E. Laurikainen, J. Laine, S. Comerón, D. A. Gadotti, R. Buta, K. Sheth, D. Zaritsky, L. Ho, J. Knapen, E. Athanassoula, A. Bosma, S. Laine, M. Cisternas, T. Kim, J. C. Muñoz-Mateos, M. Regan, J. L. Hinz, A. Gil de Paz, K. Menendez-Delmestre, T. Mizusawa, S. Erroz-Ferrer, S. E. Meidt, and M. Querejeta. The Spitzer Survey of Stellar Structure in Galaxies (S^4G): Multi-component Decomposition Strategies and Data Release. *ApJS*, 219(1):4, July 2015. doi: 10.1088/0067-0049/219/1/4.

E. E. Salpeter. The Luminosity Function and Stellar Evolution. *ApJ*, 121:161, Jan. 1955. doi: 10.1086/145971.

K. M. Sandstrom, A. K. Leroy, F. Walter, A. D. Bolatto, K. V. Croxall, B. T. Draine, C. D. Wilson, M. Wolfire, D. Calzetti, R. C. Kennicutt, G. Aniano, J. Donovan Meyer, A. Usero, F. Bigiel, E. Brinks, W. J. G. de Blok, A. Crocker, D. Dale, C. W. Engelbracht, M. Galametz, B. Groves, L. K. Hunt, J. Koda, K. Kreckel, H. Linz, S. Meidt, E. Pellegrini, H. W. Rix, H. Roussel, E. Schinnerer, A. Schruba, K. F. Schuster, R. Skibba, T. van der Laan, P. Appleton, L. Armus, B. Brandl, K. Gordon, J. Hinz, O. Krause, E. Montiel, M. Sauvage, A. Schmiedeke, J. D. T. Smith, and L. Vigroux. The CO-to-H_2 Conversion Factor and Dust-to-gas Ratio on Kiloparsec Scales in Nearby Galaxies. *ApJ*, 777(1):5, Nov. 2013. doi: 10.1088/0004-637X/777/1/5.

T. Sawada, T. Hasegawa, T. Handa, J.-I. Morino, T. Oka, R. Booth, L. Bronfman, M. Hayashi, A. Luna Castellanos, L.-Å. Nyman, S. Sakamoto, M. Seta, P. Shaver, K. Sorai, and K. S. Usuda. The Tokyo-Onsala-ESO-Calán Galactic CO J=2-1 Survey. I. The Galactic Center Region. *ApJS*, 136(1):189–219, Sept. 2001. doi: 10.1086/321793.

T. Sawada, N. Ikeda, K. Sunada, N. Kuno, T. Kamazaki, K.-I. Morita, Y. Kurono, N. Koura, K. Abe, S. Kawase, J. Maekawa, O. Horigome, and K. Yanagisawa. On-The-Fly Observing System of the Nobeyama 45-m and ASTE 10-m Telescopes. *PASJ*, 60:445, June 2008. doi: 10.1093/pasj/60.3.445.

T. Sawada, T. Hasegawa, and J. Koda. Structured Molecular Gas Reveals Galactic Spiral Arms. *ApJL*, 759(1):L26, Nov. 2012a. doi: 10.1088/2041-8205/759/1/L26.

T. Sawada, T. Hasegawa, M. Sugimoto, J. Koda, and T. Handa. Structural Variation of Molecular Gas in the Sagittarius Arm and Interarm Regions. *ApJ*, 752(2):118, June 2012b. doi: 10.1088/0004-637X/752/2/118.

E. Schinnerer, W. Maciejewski, N. Scoville, and L. A. Moustakas. Toward the Secondary Bar: Gas Morphology and Dynamics in NGC 4303. *ApJ*, 575(2):826–844, Aug. 2002. doi: 10.1086/341348.

E. Schinnerer, T. Böker, E. Emsellem, and U. Lisenfeld. Molecular Gas Dynamics in NGC 6946: A Bar-driven Nuclear Starburst "Caught in the Act". *ApJ*, 649(1):181–200, Sept. 2006. doi: 10.1086/506265.

E. Schinnerer, A. Weiß, S. Aalto, and N. Z. Scoville. Multi-transition Study of M51'S Molecular Gas Spiral Arms. *ApJ*, 719(2):1588–1601, Aug. 2010. doi: 10.1088/0004-637X/719/2/1588.

E. Schinnerer, S. E. Meidt, J. Pety, A. Hughes, D. Colombo, S. García-Burillo, K. F. Schuster, G. Dumas, C. L. Dobbs, A. K. Leroy, C. Kramer, T. A. Thompson, and M. W. Regan. The PdBI Arcsecond Whirlpool Survey (PAWS). I. A Cloud-scale/Multi-wavelength View of the Interstellar Medium in a Grand-design Spiral Galaxy. *ApJ*, 779(1):42, Dec. 2013. doi: 10.1088/0004-637X/779/1/42.

E. Schinnerer, S. E. Meidt, D. Colombo, R. Chandar, C. L. Dobbs, S. García-Burillo, A. Hughes, A. K. Leroy, J. Pety, M. Querejeta, C. Kramer, and K. F. Schuster. The PdBI Arcsecond Whirlpool Survey (PAWS): The Role of Spiral Arms in Cloud and Star Formation. *ApJ*, 836(1):62, Feb. 2017. doi: 10.3847/1538-4357/836/1/62.

E. Schinnerer, A. Hughes, A. Leroy, B. Groves, G. A. Blanc, K. Kreckel, F. Bigiel, M. Chevance, D. Dale, E. Emsellem, C. Faesi, S. Glover, K. Grasha, J. Henshaw, A. Hygate, J. M. D. Kruijssen, S. Meidt, J. Pety, M. Querejeta, E. Rosolowsky, T. Saito, A. Schruba, J. Sun, and D. Utomo. The Gas-Star Formation Cycle in Nearby Star-forming Galaxies. I. Assessment of Multi-scale Variations. *ApJ*, 887(1):49, Dec. 2019. doi: 10.3847/1538-4357/ab50c2.

M. Schmidt. The Rate of Star Formation. *ApJ*, 129:243, Mar. 1959. doi: 10.1086/146614.

C. Schreiber, M. Pannella, D. Elbaz, M. Béthermin, H. Inami, M. Dickinson, B. Magnelli, T. Wang, H. Aussel, E. Daddi, S. Juneau, X. Shu, M. T. Sargent, V. Buat, S. M. Faber, H. C. Ferguson, M. Giavalisco, A. M. Koekemoer, G. Magdis, G. E. Morrison, C. Papovich, P. Santini, and D. Scott. The Herschel view of the dominant mode of galaxy growth from z = 4 to the present day. *A&A*, 575:A74, Mar. 2015. doi: 10.1051/0004-6361/201425017.

A. Schruba, A. K. Leroy, F. Walter, F. Bigiel, E. Brinks, W. J. G. de Blok, G. Dumas, C. Kramer, E. Rosolowsky, K. Sandstrom, K. Schuster, A. Usero, A. Weiss, and H. Wiesemeyer. A Molecular Star Formation Law in the Atomic-gas-dominated Regime in Nearby Galaxies. *AJ*, 142(2):37, Aug. 2011. doi: 10.1088/0004-6256/142/2/37.

A. Schruba, J. M. D. Kruijssen, and A. K. Leroy. How Galactic Environment Affects the Dynamical State of Molecular Clouds and Their Star Formation Efficiency. *ApJ*, 883(1):2, Sept. 2019. doi: 10.3847/1538-4357/ab3a43.

N. Z. Scoville and P. M. Solomon. Radiative Transfer, Excitation, and Cooling of Molecular Emission Lines (CO and CS). *ApJL*, 187:L67, Jan. 1974. doi: 10.1086/181398.

N. Z. Scoville, M. S. Yun, D. P. Clemens, D. B. Sanders, and W. H. Waller. Molecular Clouds and Cloud Cores in the Inner Galaxy. *ApJS*, 63:821, Apr. 1987. doi: 10.1086/191185.

E. R. Seaquist, J. Pfund, and R. C. Bignell. High resolution studies of spiral and irregular galaxies at 2695 and 8085 MHz I: Maffei 2. *A&A*, 48(3):413–419, May 1976.

J. L. Sérsic and M. Pastoriza. Peculiar Nuclei of Galaxies. *PASP*, 77(457):287, Aug. 1965. doi: 10.1086/128217.

K. Sheth, M. W. Regan, S. N. Vogel, and P. J. Teuben. Molecular Gas, Dust, and Star Formation in the Barred Spiral NGC 5383. *ApJ*, 532(1):221–237, Mar. 2000. doi: 10.1086/308530.

K. Sheth, S. N. Vogel, M. W. Regan, P. J. Teuben, A. I. Harris, and M. D. Thornley. Molecular Gas and Star Formation in Bars of Nearby Spiral Galaxies. *AJ*, 124(5):2581–2599, Nov. 2002. doi: 10.1086/343835.

K. Sheth, M. Regan, J. L. Hinz, A. Gil de Paz, K. Menéndez-Delmestre, J.-C. Muñoz-Mateos, M. Seibert, T. Kim, E. Laurikainen, H. Salo, D. A. Gadotti, J. Laine, T. Mizusawa, L. Armus, E. Athanassoula, A. Bosma, R. J. Buta, P. Capak, T. H. Jarrett, D. M. Elmegreen, B. G. Elmegreen, J. H. Knapen, J. Koda, G. Helou, L. C. Ho, B. F. Madore, K. L. Masters, B. Mobasher, P. Ogle, C. Y. Peng, E. Schinnerer, J. A. Surace, D. Zaritsky, S. Comerón, B. de Swardt, S. E. Meidt, M. Kasliwal, and M. Aravena. The Spitzer Survey of Stellar Structure in Galaxies (S4G). *PASP*, 122(898):1397, Dec. 2010. doi: 10.1086/657638.

R. Shetty, P. C. Clark, and R. S. Klessen. Interpreting the sub-linear Kennicutt-Schmidt relationship: the case for diffuse molecular gas. *MNRAS*, 442(3):2208–2215, Aug. 2014a. doi: 10.1093/mnras/stu919.

R. Shetty, B. C. Kelly, N. Rahman, F. Bigiel, A. D. Bolatto, P. C. Clark, R. S. Klessen, and L. K. Konstandin. Indications of a sub-linear and non-universal Kennicutt-Schmidt relationship. *MNRAS*, 437(1):L61–L65, Jan. 2014b. doi: 10.1093/mnrasl/slt156.

V. V. Sobolev. *Moving envelopes of stars*. Harvard University Press, Cambridge, MA, 1960.

P. M. Solomon, N. Z. Scoville, and D. B. Sanders. Giant molecular clouds in the Galaxy: the distribution of ^{13}CO emission in the galactic plane. *ApJL*, 232:L89–L93, Sept. 1979. doi: 10.1086/183042.

P. M. Solomon, A. R. Rivolo, J. Barrett, and A. Yahil. Mass, Luminosity, and Line Width Relations of Galactic Molecular Clouds. *ApJ*, 319:730, Aug. 1987. doi: 10.1086/165493.

P. M. Solomon, D. Downes, and S. J. E. Radford. Dense Molecular Gas and Starbursts in Ultraluminous Galaxies. *ApJL*, 387:L55, Mar. 1992. doi: 10.1086/186304.

K. Sorai, N. Nakai, N. Kuno, K. Nishiyama, and T. Hasegawa. Distribution and Kinematics of Molecular Gas in Barred Spiral Galaxies. II. NGC 253. *PASJ*, 52:785–802, Oct. 2000. doi: 10.1093/pasj/52.5.785.

K. Sorai, T. Hasegawa, R. S. Booth, M. Rubio, J. I. Morino, L. Bronfman, T. Handa, M. Hayashi, L. Å. Nyman, T. Oka, S. Sakamoto, M. Seta, and K. S. Usuda. The CO J=2-1/J=1-0 Ratio in the Large Magellanic Cloud. *ApJ*, 551(2):794–802, Apr. 2001. doi: 10.1086/320212.

K. Sorai, N. Nakai, N. Kuno, and K. Nishiyama. Radial Distributions of the HCN/CO Ratio in Nearby CO Bright Galaxies. *PASJ*, 54:179–194, Apr. 2002. doi: 10.1093/pasj/54.2.179.

K. Sorai, N. Kuno, K. Nishiyama, Y. Watanabe, H. Matsui, A. Habe, A. Hirota, Y. Ishihara, and N. Nakai. Properties of Molecular Gas in the Bar of Maffei 2. *PASJ*, 64:51, June 2012. doi: 10.1093/pasj/64.3.51.

K. Sorai, N. Kuno, K. Muraoka, Y. Miyamoto, H. Kaneko, H. Nakanishi, N. Nakai, K. Yanagitani, T. Tanaka, Y. Sato, D. Salak, M. Umei, K. Morokuma-Matsui, N. Matsumoto, S. Ueno, H.-A. Pan, Y. Noma, T. T. Takeuchi, M. Yoda, M. Kuroda, A. Yasuda, Y. Yajima, N. Oi, S. Shibata, M. Seta, Y. Watanabe, S. Kita, R. Komatsuzaki, A. Kajikawa, Y. Yashima, S. Cooray, H. Baji, Y. Segawa, T. Tashiro, M. Takeda, N. Kishida, T. Hatakeyama, Y. Tomiyasu, and C. Saita. CO Multi-line Imaging of Nearby Galaxies (COMING). Ⅳ. Overview of the project. *PASJ*, 71:S14, Dec. 2019. doi: 10.1093/pasj/psz115.

L. S. Sparke and I. Gallagher, John S. *Galaxies in the Universe*. Cambridge University Press, Cambridge, 2nd edition edition, 2007.

L. Spitzer. *Physical processes in the interstellar medium*. 1978. doi: 10.1002/9783527617722.

A. W. Strong and J. R. Mattox. Gradient model analysis of EGRET diffuse Galactic γ-ray emission. *A&A*, 308: L21–L24, Apr. 1996.

Y. Su, J. Yang, Q.-Z. Yan, S. Zhang, H. Wang, Y. Sun, Z. Chen, C. Wang, X. Zhou, X. Chen, Z. Jiang, and M. Wang. Molecular Gas Distribution Perpendicular to the Galactic Plane. *ApJ*, 910(2):131, Apr. 2021. doi: 10.3847/1538-4357/abe5ab.

J. Sun, A. K. Leroy, A. Schruba, E. Rosolowsky, A. Hughes, J. M. D. Kruijssen, S. Meidt, E. Schinnerer, G. A. Blanc, F. Bigiel, A. D. Bolatto, M. Chevance, B. Groves, C. N. Herrera, A. P. S. Hygate, J. Pety, M. Querejeta, A. Usero, and D. Utomo. Cloud-scale Molecular Gas Properties in 15 Nearby Galaxies. *ApJ*, 860(2):172, June 2018. doi: 10.3847/1538-4357/aac326.

J. Sun, A. K. Leroy, E. Schinnerer, A. Hughes, E. Rosolowsky, M. Querejeta, A. Schruba, D. Liu, T. Saito, C. N. Herrera, C. Faesi, A. Usero, J. Pety, J. M. D. Kruijssen, E. C. Ostriker, F. Bigiel, G. A. Blanc, A. D. Bolatto, M. Boquien, M. Chevance, D. A. Dale, S. Deger, E. Emsellem, S. C. O. Glover, K. Grasha, B. Groves, J. Henshaw, M. J. Jimenez-Donaire, J. J. Kim, R. S. Klessen, K. Kreckel, J. C. Lee, S. Meidt, K. Sandstrom, A. E. Sardone, D. Utomo, and T. G. Williams. Molecular Gas Properties on Cloud Scales across the Local Star-forming Galaxy Population. *ApJL*, 901(1):L8, Sept. 2020. doi: 10.3847/2041-8213/abb3be.

L. Szűcs, S. C. O. Glover, and R. S. Klessen. The ^{12}CO/^{13}CO ratio in turbulent molecular clouds. *MNRAS*, 445 (4):4055–4072, Dec. 2014. doi: 10.1093/mnras/stu2013.

F. S. Tabatabaei, R. Beck, E. Krügel, M. Krause, E. M. Berkhuijsen, K. D. Gordon, and K. M. Menten. High-resolution radio continuum survey of M 33. II. Thermal and nonthermal emission. *A&A*, 475(1):133–143, Nov. 2007. doi: 10.1051/0004-6361:20078174.

L. E. Tacconi-Garman, A. Sternberg, and A. Eckart. Sub-Arcsecond 2.2 micron Imaging of the Starburst Galaxy NGC 1808: Infrared Observations of Super Star Clusters. *AJ*, 112:918, Sept. 1996. doi: 10.1086/118065.

K. Takahira, E. J. Tasker, and A. Habe. Do Cloud-Cloud Collisions Trigger High-mass Star Formation? I. Small Cloud Collisions. *ApJ*, 792(1):63, Sept. 2014. doi: 10.1088/0004-637X/792/1/63.

J. C. Tan. A Test of Star Formation Laws in Disk Galaxies. *ApJL*, 710(1):L88–L91, Feb. 2010. doi: 10.1088/2041-8205/710/1/L88.

F. X. Timmes, S. E. Woosley, and T. A. Weaver. Galactic Chemical Evolution: Hydrogen through Zinc. *ApJS*, 98:617, June 1995. doi: 10.1086/192172.

K. Tokuda, K. Muraoka, H. Kondo, A. Nishimura, T. Tosaki, S. Zahorecz, S. Onodera, R. E. Miura, K. Torii, N. Kuno, S. Fujita, H. Sano, T. Onishi, K. Saigo, Y. Fukui, A. Kawamura, and K. Tachihara. ALMA Observations of Giant Molecular Clouds in M33. I. Resolving Star Formation Activities in the Giant Molecular Filaments Possibly Formed by a Spiral Shock. *ApJ*, 896(1):36, June 2020. doi: 10.3847/1538-4357/ab8ad3.

S. Topal, E. Bayet, M. Bureau, T. A. Davis, and W. Walsh. Molecular gas properties of the giant molecular cloud complexes in the arms and inter-arms of the spiral galaxy NGC 6946. *MNRAS*, 437(2):1434–1455, Jan. 2014. doi: 10.1093/mnras/stt1976.

K. Torii, S. Fujita, A. Nishimura, K. Tokuda, M. Kohno, K. Tachihara, S.-i. Inutsuka, M. Matsuo, M. Kuriki, Y. Tsuda, T. Minamidani, T. Umemoto, N. Kuno, and Y. Miyamoto. FOREST Unbiased Galactic Plane Imaging Survey with the Nobeyama 45 m telescope (FUGIN). V. Dense gas mass fraction of molecular gas in the Galactic plane. *PASJ*, 71:S2, Dec. 2019. doi: 10.1093/pasj/psz033.

K. Torii, Y. Hattori, M. Matsuo, S. Fujita, A. Nishimura, M. Kohno, M. Kuriki, Y. Tsuda, T. Minamidani, T. Umemoto, N. Kuno, S. Yoshiike, A. Ohama, K. Tachihara, Y. Fukui, K. Shima, A. Habe, and T. J. Haworth. CO observations of the molecular gas in the Galactic H II region Sh2-48: Evidence for cloud-cloud collision as a trigger of high-mass star formation. *PASJ*, 73:S368–S384, Jan. 2021. doi: 10.1093/pasj/psy098.

T. Tosaki, T. Hasegawa, Y. Shioya, N. Kuno, and S. Matsushita. Variation of Molecular Cloud Properties across the Spiral Arm in M 51. *PASJ*, 54:209–221, Apr. 2002. doi: 10.1093/pasj/54.2.209.

T. Tosaki, Y. Shioya, N. Kuno, T. Hasegawa, K. Nakanishi, S. Matsushita, and K. Kohno. Giant Molecular Association in Spiral Arms of M 31: I. Evidence for Dense Gas Formation via Spiral Shock Associated with Density Waves? *PASJ*, 59:33–42, Feb. 2007. doi: 10.1093/pasj/59.1.33.

T. Tosaki, N. Kuno, R. Onodera, Sachiko Miura, T. Sawada, K. Muraoka, K. Nakanishi, S. Komugi, H. Nakanishi, H. Kaneko, A. Hirota, K. Kohno, and R. Kawabe. NRO M33 All-Disk Survey of Giant Molecular Clouds (NRO MAGiC). I. H I to H_2 Transition. *PASJ*, 63:1171–1179, Dec. 2011. doi: 10.1093/pasj/63.6.1171.

R. G. Treß, M. C. Sormani, R. J. Smith, S. C. O. Glover, R. S. Klessen, M.-M. Mac Low, P. Clark, and A. Duarte-Cabral. Simulations of the star-forming molecular gas in an interacting M51-like galaxy: cloud population statistics. *MNRAS*, 505(4):5438–5459, Aug. 2021. doi: 10.1093/mnras/stab1683.

A. D. Tubbs. The inhibition of star formation in barred spiral galaxies. *ApJ*, 255:458–466, Apr. 1982. doi: 10.1086/159846.

R. B. Tully, H. M. Courtois, A. E. Dolphin, J. R. Fisher, P. Héraudeau, B. A. Jacobs, I. D. Karachentsev, D. Makarov, L. Makarova, S. Mitronova, L. Rizzi, E. J. Shaya, J. G. Sorce, and P.-F. Wu. Cosmicflows-2: The Data. *AJ*, 146(4):86, Oct. 2013. doi: 10.1088/0004-6256/146/4/86.

J. L. Turner and P. T. P. Ho. Bright Radio Continuum Emission from Star Formation in the Cores of Nearby Spiral Galaxies. *ApJ*, 421:122, Jan. 1994. doi: 10.1086/173631.

B. L. Ulich and R. W. Haas. Absolute calibration of millimeter-wavelength spectral lines. *ApJS*, 30:247–258, Mar. 1976. doi: 10.1086/190361.

T. Umemoto, T. Minamidani, N. Kuno, S. Fujita, M. Matsuo, A. Nishimura, K. Torii, T. Tosaki, M. Kohno, M. Kuriki, Y. Tsuda, A. Hirota, S. Ohashi, M. Yamagishi, T. Handa, H. Nakanishi, T. Omodaka, N. Koide, N. Matsumoto, T. Onishi, K. Tokuda, M. Seta, Y. Kobayashi, K. Tachihara, H. Sano, Y. Hattori, S. Onodera, Y. Oasa, K. Kamegai, M. Tsuboi, Y. Sofue, A. E. Higuchi, J. O. Chibueze, N. Mizuno, M. Honma, E. Muller, T. Inoue, K. Morokuma-Matsui, H. Shinnaga, T. Ozawa, R. Takahashi, S. Yoshiike, J. Costes, and S. Kuwahara. FOREST unbiased Galactic plane imaging survey with the Nobeyama 45 m telescope (FUGIN). I. Project overview and initial results. *PASJ*, 69(5):78, Oct. 2017. doi: 10.1093/pasj/psx061.

J. S. Urquhart, C. Figura, J. R. Cross, M. R. A. Wells, T. J. T. Moore, D. J. Eden, S. E. Ragan, A. R. Pettitt, A. Duarte-Cabral, D. Colombo, F. Schuller, T. Csengeri, M. Mattern, H. Beuther, K. M. Menten, F. Wyrowski, L. D. Anderson, P. J. Barnes, M. T. Beltrán, S. J. Billington, L. Bronfman, A. Giannetti, J. Kainulainen, J. Kauffmann, M. Y. Lee, S. Leurini, S. N. X. Medina, F. M. Montenegro-Montes, M. Riener, A. J. Rigby, A. Sánchez-Monge, P. Schilke, E. Schisano, A. Traficante, and M. Wienen. SEDIGISM-ATLASGAL: dense gas fraction and star formation efficiency across the Galactic disc. *MNRAS*, 500(3):3050–3063, Jan. 2021. doi: 10.1093/mnras/staa2512.

A. Usero, A. K. Leroy, F. Walter, A. Schruba, S. García-Burillo, K. Sandstrom, F. Bigiel, E. Brinks, C. Kramer, E. Rosolowsky, K.-F. Schuster, and W. J. G. de Blok. Variations in the Star Formation Efficiency of the Dense Molecular Gas across the Disks of Star-forming Galaxies. *AJ*, 150(4):115, Oct. 2015. doi: 10.1088/0004-6256/150/4/115.

D. Utomo, A. D. Bolatto, T. Wong, E. C. Ostriker, L. Blitz, S. F. Sanchez, D. Colombo, A. K. Leroy, Y. Cao, H. Dannerbauer, R. Garcia-Benito, B. Husemann, V. Kalinova, R. C. Levy, D. Mast, E. Rosolowsky, and S. N. Vogel. The EDGE-CALIFA Survey: Variations in the Molecular Gas Depletion Time in Local Galaxies. *ApJ*, 849(1):26, Nov. 2017. doi: 10.3847/1538-4357/aa88c0.

D. Utomo, J. Sun, A. K. Leroy, J. M. D. Kruijssen, E. Schinnerer, A. Schruba, F. Bigiel, G. A. Blanc, M. Chevance, E. Emsellem, C. Herrera, A. P. S. Hygate, K. Kreckel, E. C. Ostriker, J. Pety, M. Querejeta, E. Rosolowsky, K. M. Sandstrom, and A. Usero. Star Formation Efficiency per Free-fall Time in nearby Galaxies. *ApJL*, 861(2):L18, July 2018. doi: 10.3847/2041-8213/aacf8f.

F. F. S. van der Tak, J. H. Black, F. L. Schöier, D. J. Jansen, and E. F. van Dishoeck. A computer program for fast non-LTE analysis of interstellar line spectra. With diagnostic plots to interpret observed line intensity ratios. *A&A*, 468(2):627–635, June 2007. doi: 10.1051/0004-6361:20066820.

S. Verley, E. Corbelli, C. Giovanardi, and L. K. Hunt. Star formation in M 33: multiwavelength signatures across the disk. *A&A*, 493(2):453–466, Jan. 2009. doi: 10.1051/0004-6361:200810566.

M. P. Véron-Cetty and P. Véron. NGC 1808 : a nearby galaxy with a faint Seyfert nucleus. *A&A*, 145:425–429, Apr. 1985.

M. P. Véron-Cetty and P. Véron. A catalogue of quasars and active nuclei: 12th edition. *A&A*, 455(2):773–777, Aug. 2006. doi: 10.1051/0004-6361:20065177.

V. Villanueva, A. Bolatto, S. Vogel, R. C. Levy, S. F. Sanchez, J. Barrera-Ballesteros, T. Wong, E. Rosolowsky, D. Colombo, M. Rubio, Y. Cao, V. Kalinova, A. Leroy, D. Utomo, R. Herrera-Camus, L. Blitz, and Y. Luo. The EDGE-CALIFA survey: The resolved star formation efficiency and local physical conditions. *arXiv e-prints*, art. arXiv:2109.14167, Sept. 2021.

K. Wada and C. A. Norman. Density Structure of the Interstellar Medium and the Star Formation Rate in Galactic Disks. *ApJ*, 660(1):276–287, May 2007. doi: 10.1086/513002.

F. Walter, E. Brinks, W. J. G. de Blok, F. Bigiel, J. Kennicutt, Robert C., M. D. Thornley, and A. Leroy. THINGS: The H I Nearby Galaxy Survey. *AJ*, 136(6):2563–2647, Dec. 2008. doi: 10.1088/0004-6256/136/6/2563.

R. L. Ward, J. Wadsley, and A. Sills. Unbound star-forming molecular clouds. *MNRAS*, 439(1):651–658, Mar. 2014. doi: 10.1093/mnras/stu004.

Y. Watanabe, K. Sorai, N. Kuno, and A. Habe. Refined molecular gas mass and star-formation efficiency in NGC 3627. *MNRAS*, 411(3):1409–1417, Mar. 2011. doi: 10.1111/j.1365-2966.2010.17746.x.

J. C. Weingartner and B. T. Draine. Dust Grain-Size Distributions and Extinction in the Milky Way, Large Magellanic Cloud, and Small Magellanic Cloud. *ApJ*, 548(1):296–309, Feb. 2001. doi: 10.1086/318651.

G. Westerhout. A survey of the continuous radiation from the Galactic System at a frequency of 1390 Mc/s. *Bull. Astron. Inst. Netherlands*, 14:215, Dec. 1958.

J. P. Williams, E. J. de Geus, and L. Blitz. Determining Structure in Molecular Clouds. *ApJ*, 428:693, June 1994. doi: 10.1086/174279.

C. D. Wilson and C. E. Walker. Diffuse Molecular Clouds and the Molecular Interstellar Medium from 13CO Observations of M33. *ApJ*, 432:148, Sept. 1994. doi: 10.1086/174556.

M. G. Wolfire, D. Hollenbach, and C. F. McKee. The Dark Molecular Gas. *ApJ*, 716(2):1191–1207, June 2010. doi: 10.1088/0004-637X/716/2/1191.

T. Wong, A. Hughes, J. Ott, E. Muller, J. L. Pineda, J.-P. Bernard, Y.-H. Chu, Y. Fukui, R. A. Gruendl, C. Henkel, A. Kawamura, U. Klein, L. W. Looney, S. Maddison, Y. Mizuno, D. Paradis, J. Seale, and D. E. Welty. The Magellanic Mopra Assessment (MAGMA). I. The Molecular Cloud Population of the Large Magellanic Cloud. *ApJS*, 197(2):16, Dec. 2011. doi: 10.1088/0067-0049/197/2/16.

J. G. A. Wouterloot, C. Henkel, J. Brand, and G. R. Davis. Galactic interstellar $^{18}O/^{17}O$ ratios - a radial gradient? *A&A*, 487(1):237–246, Aug. 2008. doi: 10.1051/0004-6361:20078156.

E. L. Wright, P. R. M. Eisenhardt, A. K. Mainzer, M. E. Ressler, R. M. Cutri, T. Jarrett, J. D. Kirkpatrick, D. Padgett, R. S. McMillan, M. Skrutskie, S. A. Stanford, M. Cohen, R. G. Walker, J. C. Mather, D. Leisawitz, I. Gautier, Thomas N., I. McLean, D. Benford, C. J. Lonsdale, A. Blain, B. Mendez, W. R. Irace, V. Duval, F. Liu, D. Royer, I. Heinrichsen, J. Howard, M. Shannon, M. Kendall, A. L. Walsh, M. Larsen, J. G. Cardon, S. Schick, M. Schwalm, M. Abid, B. Fabinsky, L. Naes, and C.-W. Tsai. The Wide-field Infrared Survey Explorer (WISE): Mission Description and Initial On-orbit Performance. *AJ*, 140(6):1868–1881, Dec. 2010. doi: 10.1088/0004-6256/140/6/1868.

E. M. Xilouris, F. S. Tabatabaei, M. Boquien, C. Kramer, C. Buchbender, F. Bertoldi, S. Anderl, J. Braine, S. Verley, M. Relaño, G. Quintana-Lacaci, S. Akras, R. Beck, D. Calzetti, F. Combes, M. Gonzalez, P. Gratier, C. Henkel, F. Israel, B. Koribalski, S. Lord, B. Mookerjea, E. Rosolowsky, G. Stacey, R. P. J. Tilanus, F. van der Tak, and P. van der Werf. Cool and warm dust emission from M 33 (HerM33es). *A&A*, 543:A74, July 2012. doi: 10.1051/0004-6361/201219291.

Y. Xu, M. J. Reid, X. W. Zheng, and K. M. Menten. The Distance to the Perseus Spiral Arm in the Milky Way. *Science*, 311(5757):54–57, Jan. 2006. doi: 10.1126/science.1120914.

Y. Yajima and K. Sorai. Key factor in molecular gas properties and star formation by decomposition of CO emission in Maffei 2. *submitted to PASJ*, 2022.

Y. Yajima, K. Sorai, N. Kuno, K. Muraoka, Y. Miyamoto, H. Kaneko, H. Nakanishi, N. Nakai, T. Tanaka, Y. Sato, D. Salak, K. Morokuma-Matsui, N. Matsumoto, H.-A. Pan, Y. Noma, T. T. Takeuchi, M. Yoda, M. Kuroda, A. Yasuda, N. Oi, S. Shibata, M. Seta, Y. Watanabe, S. Kita, R. Komatsuzaki, A. Kajikawa, and Y. Yashima. CO Multi-line Imaging of Nearby Galaxies (COMING). Ⅲ. Dynamical effect on molecular gas density and star formation in the barred spiral galaxy NGC 4303. *PASJ*, 71:S13, Dec. 2019. doi: 10.1093/pasj/psz022.

Y. Yajima, K. Sorai, Y. Miyamoto, K. Muraoka, N. Kuno, H. Kaneko, T. T. Takeuchi, A. Yasuda, T. Tanaka, K. Morokuma-Matsui, and M. I. N. Kobayashi. CO Multi-line Imaging of Nearby Galaxies (COMING). Ⅸ. $^{12}CO(J = 2–1)/^{12}CO(J = 1–0)$ line ratio on kiloparsec scales. *PASJ*, 73(2):257–285, Apr. 2021. doi: 10.1093/pasj/psaa119.

A. Yasuda, N. Kuno, K. Sorai, K. Muraoka, Y. Miyamoto, H. Kaneko, Y. Yajima, T. Tanaka, K. Morokuma-Matsui, T. T. Takeuchi, and M. I. N. Kobayashi. CO Multi-line Imaging of Nearby Galaxies (COMING). XII. CO-H_2 conversion factor and Dust-to-Gas Ratio. *submitted to PASJ*, 2021.

J. S. Young and N. Z. Scoville. Molecular gas in galaxies. *ARA&A*, 29:581–625, Jan. 1991. doi: 10.1146/annurev.aa.29.090191.003053.

E. Zetterlund, J. Glenn, and E. Rosolowsky. Northern Galactic Molecular Cloud Clumps in Hi-GAL: Clump and Star Formation within Clouds. *ApJ*, 881(2):90, Aug. 2019. doi: 10.3847/1538-4357/ab2e03.

B. Zuckerman and I. Evans, N. J. Models of Massive Molecular Clouds. *ApJL*, 192:L149, Sept. 1974. doi: 10.1086/181613.